**MARMARA UNIVERSITY**
**INSTITUTE FOR GRADUATE STUDIES IN PURE AND APPLIED SCIENCES**

# DEVELOPMENT OF FLAT BOTTOM DRILL CUTTING TOOL FOR MACHINING OF BRASS ALLOYS

NIMA ZOGHIPOUR

**Ph.D. THESIS**

Department of Mechanical Engineering

**Thesis Supervisor**

Prof. Dr. Yusuf KAYNAK

ISTANBUL, 2023

# PREFACE

First and foremost, I would like to express my gratitude to my supervisor, Prof. Yusuf Kaynak, for his invaluable supervision and motivation during my PhD. Besides my advisor, I would like to thank my thesis committee members, Prof. Alper Uysal and Assist. Prof. Selim Hartomacıoğlu, for all the valuable insights and the precious points that they have raised in our discussions.

I would like to thank Torun Copper Alloys Company, for all the opportunities and equipment devoted to me to discover my passions. In addition, I want to acknowledge the technical help provided by my colleagues in the engineering, tool shop, and R&D departments.

I also thank TÜBİTAK (The Scientific and Technological Research Council of Turkey) for partial supports granted under project number 118C069.

Last but not least, my parents' love, prayers, care, patience, education, and preparation for my future are all things for which I would want to convey my sincere gratitude. Additionally, I want to convey my sincere appreciation to my brother, Pouya Zoghipour, for his continuous encouragement, energy, vision, honesty, and genuine interest in seeing my thesis through to completion. I am really indebting to my family for their steadfastness in giving me the enthusiasm and inspiration for my whole achievements.

# CONTENTS

ABSTRACT ..... III

ÖZET ..... V

INNOVATION STATEMENT ..... VII

SYMBOLS ..... VIII

A B B R E V I A T I O N S ..... X

LIST OF FIGURES ..... XI

LIST OF TABLES ..... XXXVI

1. INTRODUCTION ..... 1
2. EXPERIMENTAL METHODOLOGY ..... 10
   - 2.1 Mechanical and metallographic analysis ..... 10
   - 2.2 Microstructure Analyses ..... 14
   - 2.3 Tensile tests ..... 22
   - 2.4 Micro Hardness ..... 27
   - 2.5 Impact charpy ..... 29

3. MECHANICS OF FLAT BOTTOM DRILLING ..... 34
   - 3.1. Scenario 1 ..... 39
   - 3.2. Scenario 2 ..... 46

4. TESTS WITH REFERENCE CUTTING TOOLS ..... 54

5. MODAL ANALYSIS OF THE DESIGNED FLAT BOTTOM DRILLS ..... 84

6. TESTS WITH DESIGNED FLAT BOTTOM DRILL CUTTING TOOLS ..... 111
   - 6.1. Evaluation of the cutting forces ..... 130
   - 6.1.1. Determination of the cutting force coefficients ..... 135
   - 6.2. Evaluation of the formed burr heights ..... 146
   - 6.3. Evaluation of the surface quality ..... 149
   - 6.4. Evaluation of the dimensional accuracy ..... 153

6.5. Analysis of variance (ANOVA) for the obtained results .....154

6.6. Evaluation of the surface and sub-surface microhardness .....278

7. EVALUATION OF DIFFERENT COATINGS ON THE MACHINABILITY OF THE MANUFACTURED TOOLS .....283

8. APPLICATION OF ARTIFICIAL INTELLIGENCE AND POLYNOMIAL REGRESSION MODELS IN PREDICTION OF THE PRODUCT QUALITY .....290

8.1. Fuzzy Logic Modeling .....290

8.2. Regression Modeling .....291

8.3. Artificial Neural Networks (ANN) Modeling .....297

9. CONCLUSION .....303

# ABSTRACT


## DEVELOPMENT OF FLAT BOTTOM DRILL CUTTING TOOL FOR MACHINING OF BRASS ALLOYS

Owing to their superior properties, brass alloys constitute a significant percentage of the industrial components used in water systems and pumping equipment. These materials are manufactured using extrusion or hot forging processes, depending on their specified application. Regarding the permissible lead concentration levels in items, particularly for drinking water applications, recent regulation has focused on the hazardous character of lead as an alloying element in brass products. These limitations have promoted the invention and use of novel solutions, such as the development of brass alloys free of lead. In this context, the material characterization, metallographic, and mechanical properties of the eco-friendly brass alloys CuZn40Pb2 (CW617N), CuZn38As (CW511L), and CuZn21Si3P (CW724R) has been explored in chapter 2. The experimental data on microstructure, phasic composition, tensile strength, impact fracture energy, fracture toughness, and microhardness has undergone careful inspection. Prior to being a final product, the majority of brass components go through several machining operations including drilling. In order to fulfill design and application requirements, such as the assembly of screws, pins, or passing channels for fluids, a significant portion of these components have holes. These holes are being drilled even in vertical or inclined orientations with respect to the jig and fixturing systems, depending on the production method being used and the positioning of these components during machining processes. The design and utilization of new types of cutting tools with complex geometries is driven by the development of technologies in components with difficult features and the competition among manufacturers in rapid and precise manufacturing. These tools must have setup stiffness, static and dynamic strength, sufficient cutting performance, and dimensional accuracy in addition to these other properties to prevent damage themselves, holders, and machine components. Conventional or indexable inserted drills are frequently employed in vertical drilling of flat surfaces. However, due to vibrations and run-out that occur when using these types of tools in sloped features, they do not perform as effectively on surfaces where holes are drilled. Therefore, in order to be used for curved

or sloped surfaces, flat bottom drills have been designed. By concentrating on the flat bottom drilling operation, the effects of the process and alloying type have been assessed in order to carry out an extensive study on the machinability. In chapter 3, a mechanistic method is used to develop a predictive analytical cutting force model for flat bottom drills for both vertical and inclined plunging. According to the concepts of orthogonal and oblique cuts, the model is built on distributed elemental cutting throughout the tool radius while taking into account rake and relief faces. Five effective industrial bottom drills made by various firms were the subject of chapter 4's attempt to narrow the topic. These tools' geometries have been measured, and machining experiments have been used to assess each tool's performance. According to the findings of existing research, the geometrical characteristics that have the greatest influence have been identified. In Chapter 5, flat bottom drills with varied axial and radial rake angles have been designed and put through modal analysis using finite element methods in order to explore the dynamic behavior of the tools. For the designed tools, the first six natural frequencies, maximum total displacements, stiffnesses, as well as the period of oscillation corresponding to the modes form, have all been computed. The effects of the cutting tool geometries, including axial rake, radial rake angles, edge radius, and plunging angle to the work material, with a focus on the cutting forces, formed entrance, exit burr sizes, hole quality (surface roughness and dimensional correctness), as well as surface, sub-surface integrity, have been studied in chapter 6. The outcomes of the developed predictive analytic model from chapter 3 have also been compared with the experimental data in the meantime. Regression modeling and analysis of variance (ANOVA) techniques have also been employed to explain the outcomes of the experiments. The optimum cutting tool has been selected based on the results attained. In chapter 7, the performance of three different industrial coatings for non-ferrous materials, including brass alloys, was compared to that of uncoated carbide flat bottom drills. In chapter 8, artificial neural networks, fuzzy logic, and regression models have been developed in order to predict the manufactured production quality and their obtainability has been compared with the measured results.

**Keywords:** Lead-Free Brass, Machinability, Flat Bottom Drill, Mechanistic Model, Modal Analysis, Finite Element Methods, Artificial Neural Networks, Fuzzy Logic

# ÖZET

## PİRİNÇ ALAŞIMLARININ TALAŞLI İMALAT SÜREÇLERİ İÇİN DÜZ AĞIZLI MATKAP KESİCİ TAKIM GELİŞTİRİLMESİ

Pirinç alaşımları üstün özellikleri nedeniyle su sistemlerinde ve pompa ekipmanlarında kullanılan endüstriyel bileşenlerin önemli bir yüzdesini oluşturmaktadır. Bu malzemeler, belirtilen uygulamalarına bağlı olarak ekstrüzyon veya sıcak dövme işlemleri kullanılarak üretilir. Özellikle içme suyu uygulamaları için kalemlerdeki izin verilen kurşun konsantrasyonu seviyeleri ile ilgili olarak, son düzenlemeler pirinç ürünlerde bir alaşım elementi olarak kurşunun tehlikeli karakterine odaklanmıştır. Bu sınırlamalar, kurşunsuz pirinç alaşımlarının geliştirilmesi gibi yeni çözümlerin icadını ve kullanımını teşvik etmiştir. Bu bağlamda, çevre dostu pirinç alaşımları CuZn40Pb2 (CW617N), CuZn38As (CW511L) ve CuZn21Si3P (CW724R)'nin malzeme karakterizasyonu, metalografik ve mekanik özellikleri 2. bölümde incelenmiştir. Mikroyapı, faz yapısı, çekme mukavemeti, darbe kırılma enerjisi, kırılma tokluğu ve mikrosertlik dikkatli bir incelemeden geçmiştir. Nihai ürün olmadan önce, pirinç bileşenlerin çoğu delme dahil olmak üzere çeşitli işleme işlemlerinden geçer. Akışkanlar için vidaların, pimlerin veya geçiş kanallarının montajı gibi tasarım ve uygulama gereksinimlerini karşılamak için bu bileşenlerin önemli bir kısmında delikler bulunur. Bu delikler, kullanılan üretim yöntemine ve bu bileşenlerin talaşlı imalat işlemleri sırasındaki konumlarına bağlı olarak, mastar ve fikstür sistemlerine göre dikey veya eğimli yönlerde dahi delinmektedir. Karmaşık geometrilere sahip yeni tip kesici takımların tasarımı ve kullanımı, zor özelliklere sahip bileşenlerdeki teknolojilerin gelişmesi ve hızlı ve hassas üretimde üreticiler arasındaki rekabetten kaynaklanmaktadır. Bu takımlar, kendilerine, tutuculara ve makine bileşenlerine zarar vermemek için bu diğer özelliklere ek olarak kurulum sertliği, statik ve dinamik mukavemet, yeterli kesme performansı ve boyutsal doğruluğa sahip olmalıdır. Düz yüzeylerin dikey olarak delinmesi için geleneksel veya değiştirilebilir insörtlü matkaplar sıklıkla kullanılır. Ancak bu tip takımların eğimli özelliklerde kullanılması sırasında oluşan titreşimler ve salgılar nedeniyle delik açılmış yüzeylerde etkili bir şekilde çalışmazlar. Bu nedenle kavisli veya eğimli yüzeylerde kullanılmak üzere düz ağızlı matkaplar tasarlanmıştır. Düz dipli delme işlemine odaklanılarak, işlenebilirlik

konusunda kapsamlı bir çalışma yapmak için işlemin ve alaşım tipinin etkileri değerlendirilmiştir. Bölüm 3'te, hem dikey hem de eğimli dalma için düz tabanlı matkaplar için tahmine dayalı bir analitik mekanistik yöntem ile kesme kuvveti modeli geliştirmiştir. Ortogonal ve oblique kesim presnsiplerine göre, model, talaş ve kabartma yüzleri dikkate alınarak takım yarıçapı boyunca dağıtılmış temel kesme üzerine kurulmuştur. Bölüm 4'te konuyu daraltmak çeşitli firmalar tarafından yapılan beş yüksek performanslı endüstriyel düz ağızlı matkap incelenmiştir. Bu takımların geometrileri ölçülmüş ve her takımın performansını değerlendirmek için işleme deneyleri kullanılmıştır. Mevcut araştırma bulgularına göre, en büyük etkiye sahip olan geometrik özellikler tespit edilmiştir. Bölüm 5'te, çeşitli eksenel ve radyal eğim açılarına sahip düz tabanlı matkaplar tasarlanmış ve takımların dinamik davranışını keşfetmek için sonlu elemanlar yöntemleri kullanılarak modal analize tabi tutulmuştur. Tasarlanan takımlar için, ilk altı doğal frekans, maksimum toplam deplasmanlar, rijitlikler ve mod formuna karşılık gelen salınım periyodu hesaplanmıştır. Eksenel talaş, radyal talaş açıları, yuvarlanma uç yarıçapı ve dalma açısı dahil olmak üzere kesici takım geometrilerinin, kesme kuvvetleri, oluşturulan giriş, çıkış çapak boyutları, delik kalitesi (yüzey pürüzlülüğü ve boyutsal doğruluk) odaklı olarak iş malzemesine etkileri) yanı sıra yüzey, yüzey altı bütünlüğü, 6. bölümde incelenmiştir. Deneylerin sonuçlarını açıklamak için regresyon modelleme ve varyans analizi (ANOVA) teknikleri de kullanılmıştır. Elde edilen sonuçlara göre en iyilenmiş kesici takım geometrileri seçilmiştir. 7. Bölümde ise, pirinç alaşımları da dahil olmak üzere demir dışı malzemeler için üç farklı endüstriyel kaplamanın performansı, kaplanmamış karbür düz ağızlı matkapların performansıyla karşılaştırılmıştır. 8. bölümde ise, üretilen üretim kalitesini tahmin etmek için yapay sinir ağları, bulanık mantık ve regresyon modelleri geliştirilmiş ve modellerin elde edilebilirliklerinin hassasiyeti deneysel olarak ölçülen sonuçlarla karşılaştırılmıştır.

**Anahtar Kelimeler:** Kurşunsuz Pirinç, İşlenebilirlik, Düz Ağızlı Matkap, Analitik Model, Modal Analiz, Sonlu Elemanlar Yöntemi, Yapay Sinir Ağları, Bulanık Mantık

# INNOVATION STATEMENT

It is undeniable that low-lead and lead-free brasses are prevailing over traditional ones, notwithstanding the importance of human health and the environment, as well as the upgrading needs of modern industry. As a result, in order for manufacturers to stay competitive in the industrial market, a thorough understanding of these materials and the ability to machine them using newly designed cutting tools is a must. The majority of studies have been conducted on generic, conventional, and straightforward machining operations such as turning, it can be deduced from a review of the literature. Therefore, three types of available brasses in EUA7038 (Brass for European Potable Water Applications List), leaded (CW617N), low-leaded (CW511L), and lead-free (CW724R), have been taken into consideration when drilling with flat bottom drill tools in order to close the knowledge gap in the literature as well as develop a know-how meeting the industrial needs. For calculating the cutting forces and torques during plunging to an inclined workpiece as well as plunging to a flat surface, analytical and experimental methods have been developed and utilized. Utilizing the ANCA tool room, cutting tools with various geometries and coatings have been manufactured. Additionally, the machinability has been assessed using measurements of the cutting forces, torques, entry and exit burr heights, surface roughness, diameters, and microstructures. Furthermore, using Finite Element Methods, a modal analysis of the designed cutting tools was accomplished.

# SYMBOLS

$\sigma_y$ : Yield strength

$\sigma_{UTS}$ : Ultimate tensile strength

$K_{IC}$ : First mode fracture toughness

$P_n$ : Normal plane

$F_n$ : Normal force

$F_s$ : Shear force

$P_s$ : Shear plane

$F_R$ : Resultant force

$\Gamma$ : Inclination angle

$\eta$ : Chip flow angle

$\Phi_n$ : Normal shear angle

$\Phi_\Gamma$ : Inclined shear angle

$\alpha_n$ : Normal rake angle

$\beta_a$ : Friction angle

$\beta_n$ : Normal friction angle

$V_c$ : Chip velocity

$V_s$ : Shear velocity

$V$ : Cutting velocity

$K_{tc}$ : Tangential cutting force coefficient

$K_{fc}$ : Feed cutting force coefficient

$K_{rc}$ : Radial cutting force coefficient

$d$ : Cutting tool diameter

$R$ : Cutting tool radius

$\psi$ : Plunge angle

$\Phi_{st}$ : Start angle of the cutting

$\Phi_{ex}$ : Exit angle of the cutting

$\Phi$ : Instantaneous angle

$\omega$ : Width of the cut area

$\omega_L$ : Axial elemental integration

$(St.)_a$ : Differential axial step

$\Phi_p$ : Pitch angle

$K$ : Number of the angular steps

$L$ : Number of the axial steps

$m$ : Number of the radial steps

$n_t$ : Number of teeth

$dr$ : Differential element

$dF_t$ : Differential element tangential force

$dF_f$ : Differential element feed force

$dF_r$ : Differential element radial force

$l_{cu}$ : Uncut chip length

$A_{cu}$ : Cross section of the uncut chip

$f_t$ : Feed per tooth

$h$ : Angular feed rate

$F_x$ : Cutting force in X direction

$F_y$ : Cutting force in Y direction

$F_z$ : Cutting force in Z direction

$CL$ : Chisel edge length

$\alpha_e$ : Effective rake angle

$r_t$ : Tool edge radius

$V_f$ : Feed rate

$N$ : Spindle speed

$V_c$ : Cutting speed

$f$ : Natural frequency

$\omega$ : Angular frequency

$T$ : Period of the oscillation

$\alpha$ : Alpha phase

$\beta$ : Beta phase

$\beta`$ : Beta prime (ordinated) phase

$\kappa$ : Kappa phase

$\gamma$ : Gamma phase

# ABBREVIATIONS

**FCC** : Face-Centered Cubic

**BCC** : Body-Centered Cubic

**HCP** : Hexagonal Close-Packed

**P/M** : Powder metallurgical

**PCD** : Polycrystalline diamond

**DLC** : Diamond like carbon

**Ra** : Arithmetic mean roughness of the surface

**Rt** : Total height of the surface roughness

**Rz** : The mean value of the absolute the heights peaks and deepest depths

**DF** : Desirability function

**GA** : Genetic algorithms-based analysis

**EUA7038** : Brass for European Potable Water Applications List

**Rohs** : Restriction of Hazardous Substances Directive

**HV** : Hardness of Vickers

**CC** : Cutting condition

**VHM** : Vollhartmetall, Solid carbide

**BHEN** : Burr height at entrance

**BHEX** : Burr height at exit

**BWEN** : Burr width at entrance

**BWEX** : Burr width at exit

**RRA** : Radial rake angle

**ARA** : Axial rake angle

**CER** : Cutting-edge radius

**PA** : Plunge angle

**ANN** : Artificial neural network

**AI** : Artificial Intelligence

# LIST OF FIGURES

**Figure 1.1.** Cu-Zn phase diagram .....2

**Figure 2.1.** The used spectrum analysis device .....11

**Figure 2.2.** Designed forged specimen .....12

**Figure 2.3.** Hot forging procedure of the designed test specimens .....13

**Figure 2.4.** Annealing images of the hot forged specimens .....14

**Figure 2.5.** The design of the specimen and die sets used in this thesis .....14

**Figure 0.6.** The utilized equipment in the microstructural analysis .....15

**Figure 2.7.** Optical images of the microstructure .....17

**Figure 2.8.** SEM images of the microstructure .....18

**Figure 2.9.** EDS analysis images of the microstructure .....22

**Figure 2.10.** Tensile test experimental setup .....23

**Figure 2.11.** Tensile test plots .....24

**Figure 2.12.** The yeild stress for the test materials .....26

**Figure 2.13.** Ruptured images of the specimens after tensile test .....27

**Figure 2.14.** The utilized micro hardness measurement device .....28

**Figure 2.15.** The measured micro hardness value for the brass alloys .....29

**Figure 2.16.** The Charpy impact energy test setup .....30

**Figure 2.17.** The Charpy impact energy of the extruded, forged and annealed brass alloys .....31

**Figure 2.18.** Fractographic images of the impact fractures .....31

**Figure 2.19.** Schematic view of the first mode intensity factor and stresses .....32

**Figure 2.20.** The calculated first mode fracture toughness values for the brass alloys .....33

**Figure 3.1.** Cross sectional of drilling .....34

**Figure 3.2.** A schematic view of the forces orientation in the flat bottom drill with respect

to a reference coordinate system ……..35

**Figure 3.3.** Mechanism of oblique cutting ……..36

**Figure 3.4.** Cross sectional of the flat bottom drill during inclined drilling …….....39

**Figure 3.5**. The top view of the tool movement in the vertical direction into a workpiece …….……40

**Figure 3.6.** Schematic view for difference of the cut width for two different axial steps ……..……41

**Figure 3.7**. Schematic view of the subjected cutting forces for an element on the cutting edge ……43

**Figure 3.8.** A top view of the geometrical specifications of a pattern flat bottom drill ..48

**Figure 3.9.** A side view of the cutting tool and an element on the edge ……...…49

**Figure 3.10.** A top view of the flat bottom drill tool geometry including indentation and cutting sections ……..…..49

**Figure 3.11.** A schematic depiction for the tool edge radius effect during cut $f_t < r_t$ …51

**Figure 3.12.** Cutting forces for an oblique cut for $f_t > r_t$ ……...…52

**Figure 3.13.** Flow chart of the developed model ……53

**Figure 4.1.** The measurement operation of the cutting tools in Zoller and Keyence optical microscope ……..57

**Figure 4.2.** Test setup for extruded specimens .....58

**Figure 4.3.** Measured resultant cutting forces during blind drilling at 90° of extruded specimens using reference tools .....59

**Figure 4.4.** Measured entry burr height during blind drilling at 90° of extruded specimens using reference tools .....59

**Figure 4.5.** Measured hole bottom surface roughness during blind drilling at 90° of extruded specimens using reference tools .....60

**Figure 4.6.** Measured hole wall surface roughness during blind drilling at 90° of extruded specimens using reference tools .....60

**Figure 4.7.** Measured hole diameter during blind drilling at 90° of extruded specimens using reference tools .....61

**Figure 4.8.** Measured resultant cutting forces during blind drilling at 45° of extruded specimens using reference tools .....61

**Figure 4.9.** Measured entry burr height during blind drilling at 45° of extruded specimens using reference tools .....62

**Figure 4.10.** Measured hole bottom surface roughness during blind drilling at 45° of extruded specimens using reference tools .....62

**Figure 4.11.** Measured hole diameter during blind drilling at 45° of extruded specimens using reference tools .....63

**Figure 4.12.** Measured resultant cutting forces during through all drilling at 90° of extruded specimens using reference tools .....63

**Figure 4.13.** Measured entry burr height during through all drilling at 90° of extruded specimens using reference tools .....63

**Figure 4.14.** Measured exit burr height during through all drilling at 90° of extruded specimens using reference tools .....64

**Figure 4.15.** Measured resultant cutting forces during through all drilling at 60° of extruded specimens using reference tools .....64

**Figure 4.16.** Measured entry burr height during through all drilling at 60° of extruded specimens using reference tools .....65

**Figure 4.17.** Measured exit burr height during through all drilling at 60° of extruded specimens using reference tools .....65

**Figure 4.18.** Measured hole diameter during through all drilling at 60° of extruded specimens using reference tools .....65

**Figure 4.19.** Test setup for forged and annealed specimens .....66

**Figure 4.20.** Measured cutting forces during blind drilling at 90° of forged and annealed specimens using reference tools .....67

**Figure 4.21.** Measured entry burr height during blind drilling at 90° of forged and

annealed specimens using reference tools .....68

**Figure 4.22.** Measured hole bottom surface roughness during blind drilling at 90° of forged and annealed specimens using reference tools .....68

**Figure 4.23.** Measured hole wall surface roughness during blind drilling at 90° of forged and annealed specimens using reference tools .....69

**Figure 4.24.** Measured cutting forces during blind drilling at 45° of forged and annealed specimens using reference tools .....70

**Figure 4.25.** Measured entry burr height during blind drilling at 45° of forged and annealed specimens using reference tools .....71

**Figure 4.26.** Measured hole bottom surface roughness during blind drilling at 45° of forged and annealed specimens using reference tools .....71

**Figure 4.27.** Measured cutting forces during blind drilling at 60° of forged and annealed specimens using reference tools .....73

**Figure 4.28.** Measured entry burr height during blind drilling at 60° of forged and annealed specimens using reference tools .....73

**Figure 4.29.** Measured hole bottom surface roughness during blind drilling at 60° of forged and annealed specimens using reference tools .....74

**Figure 4.30.** Measured cutting forces during through all drilling at 90° of forged and annealed specimens using reference tools .....75

**Figure 4.31.** Measured entry burr height during through all drilling at 90° of forged and annealed specimens using reference tools .....76

**Figure 4.32.** Measured exit burr height during through all drilling at 90° of forged and annealed specimens using reference tools .....76

**Figure 4.33.** Measured hole diameter during through all drilling at 90° of forged and annealed specimens using reference tools .....76

**Figure 4.34.** Measured cutting forces during through all drilling at 45° of forged and annealed specimens using reference tools .....78

**Figure 4.35.** Measured entry burr height during through all drilling at 45° of forged and

annealed specimens using reference tools .....78

**Figure 4.36.** Measured exit burr height during through all drilling at 45° of forged and annealed specimens using reference tools .....79

**Figure 4.37.** Measured hole diameter during through all drilling at 45° of forged and annealed specimens using reference tools .....79

**Figure 4.38.** Measured cutting forces during through all drilling at 60° of forged and annealed specimens using reference tools .....80

**Figure 4.39.** Measured entry burr height during through all drilling at 60° of forged and annealed specimens using reference tools .....80

**Figure 4.40.** Measured exit burr height during through all drilling at 60° of forged and annealed specimens using reference tools .....81

**Figure 4.41.** Measured hole diameter during through all drilling at 60° of forged and annealed specimens using reference tools .....81

**Figure 5.1.** Single degree of freedom, undamped lumped parameter model .....85

**Figure 5.2.** Single degree of freedom, damped lumped parameter model .....87

**Figure 5.3.** The applied boundary conditions for the designed flat bottom drills .....91

**Figure 5.4.** Modal analysis results for the flat bottom drill No.1 .....94

**Figure 5.5.** Modal analysis results for the flat bottom drill No.2 .....95

**Figure 5.6.** Modal analysis results for the flat bottom drill No.3 .....96

**Figure 5.7.** Modal analysis results for the flat bottom drill No.4 .....97

**Figure 5.8.** Modal analysis results for the flat bottom drill No.5 .....98

**Figure 5.9.** Modal analysis results for the flat bottom drill No.6 .....98

**Figure 5.10.** Modal analysis results for the flat bottom drill No.7 .....99

**Figure 5.11.** Modal analysis results for the flat bottom drill No.8 .....100

**Figure 5.12.** Modal analysis results for the flat bottom drill No.9 .....100

**Figure 5.13.** The variation of the natural frequencies with radial and axial rake angle of flat bottom drill .....102

**Figure 5.14.** The variation of the natural frequencies with radial and axial rake angle of flat bottom drill .....104

**Figure 5.15.** The variation of the natural frequencies with radial and axial rake angle of flat bottom drill .....105

**Figure 6.1.** The designed flat bottom drill cutting tool .....112

**Figure 6.2.** The process of the flat bottom drill design and its manufacturing .....112

**Figure 6.3.** Drag finishing operation on the manufactured flat bottom drills .....113

**Figure 6.4.** The utilized micrometer for measurement of the drilled holes diameter .....114

**Figure 6.5.** The used experimental and operational form setup in this study .....116

**Figure 6.6.** The measured forces in X direction (Fx) with 90° of plunging angle .....132

**Figure 6.7.** The measured forces in X direction (Fx) with 60° of plunging angle .....133

**Figure 6.8.** The measured forces in X direction (Fx) with 45° of plunging angle .....133

**Figure 6.9.** The measured forces in Y direction (Fy) with 90° of plunging angle .....133

**Figure 6.10.** The measured forces in Y direction (Fy) with 60° of plunging angle .....133

**Figure 6.11.** The measured forces in Y direction (Fy) with 45° of plunging angle .....133

**Figure 6.12.** The measured forces in Z direction (Fz) with 90° of plunging angle .....134

**Figure 6.13.** The measured forces in Z direction (Fz) with 60° of plunging angle .....134

**Figure 6.14.** The measured forces in Z direction (Fz) with 45° of plunging angle .....134

**Figure 6.15.** The measured resultant cutting forces (FR) with 90° of plunging angle .....134

**Figure 6.16.** The measured resultant cutting forces (FR) with 60° of plunging angle .....134

**Figure 6.17.** The measured resultant cutting forces (FR) with 45° of plunging angle .....135

**Figure 6.18.** Oblique cutting tests setup .....135

**Figure 6.19.** The generated chips .....136

**Figure 6.20.** Comparison between experimental measurements and analytical model prediction for cutting forces of extruded CW617N with 90° of plunging angle .....137

**Figure 6.21.** Comparison between experimental measurements and analytical model

prediction for cutting forces of extruded CW617N with 60° of plunging angle .....137

**Figure 6.22.** Comparison between experimental measurements and analytical model prediction for cutting forces of extruded CW617N with 45° of plunging angle .....138

**Figure 6.23.** Comparison between experimental measurements and analytical model prediction for cutting forces of extruded CW511L with 90° of plunging angle .....138

**Figure 6.24.** Comparison between experimental measurements and analytical model prediction for cutting forces of extruded CW511L with 60° of plunging angle .....139

**Figure 6.25.** Comparison between experimental measurements and analytical model prediction for cutting forces of extruded CW511L with 45° of plunging angle .....139

**Figure 6.26.** Comparison between experimental measurements and analytical model prediction for cutting forces of extruded CW724R with 90° of plunging angle .....140

**Figure 6.27.** Comparison between experimental measurements and analytical model prediction for cutting forces of extruded CW724R with 60° of plunging angle .....140

**Figure 6.28.** Comparison between experimental measurements and analytical model prediction for cutting forces of extruded CW724R with 45° of plunging angle .....141

**Figure 6.29.** Comparison between experimental measurements and analytical model prediction for cutting forces of forged+annealed CW617N with 90° of plunging angle ..141

**Figure 6.30.** Comparison between experimental measurements and analytical model prediction for cutting forces of forged+annealed CW617N with 60° of plunging angle ..142

**Figure 6.31.** Comparison between experimental measurements and analytical model prediction for cutting forces of forged+annealed CW617N with 45° of plunging angle ..142

**Figure 6.32.** Comparison between experimental measurements and analytical model prediction for cutting forces of forged+annealed CW511L with 90° of plunging angle ..143

**Figure 6.33.** Comparison between experimental measurements and analytical model prediction for cutting forces of forged+annealed CW511L with 60° of plunging angle ..143

**Figure 6.34.** Comparison between experimental measurements and analytical model prediction for cutting forces of forged+annealed CW511L with 45° of plunging angle ..144

**Figure 6.35.** Comparison between experimental measurements and analytical model

prediction for cutting forces of forged+annealed CW724R with 90° of plunging angle ..144

**Figure 6.36.** Comparison between experimental measurements and analytical model prediction for cutting forces of forged+annealed CW724R with 60° of plunging angle .145

**Figure 6.37.** Comparison between experimental measurements and analytical model prediction for cutting forces of forged+annealed CW724R with 45° of plunging angle ..145

**Figure 6.38.** The measured cutting forces of blind flat bottom drilling.....146

**Figure 6.39.** The measured burr heights at hole entry (BHEN) with 90° of plunging angle .....147

**Figure 6.40.** The measured burr heights at hole entry (BHEN) with 60° of plunging angle .....147

**Figure 6.41.** The measured burr heights at hole entry (BHEN) with 45° of plunging angle .....148

**Figure 6.42.** The measured burr heights at hole exit (BHEX) with 90° of plunging angle .....148

**Figure 6.43.** The measured burr heights at hole exit (BHEX) with 60° of plunging angle .....148

**Figure 6.44.** The measured burr heights at hole exit (BHEX) with 45° of plunging angle .....148

**Figure 6.45.** The images of the formed entry burrs on hot forged+annealed .....149

**Figure 6.46.** The measured surface roughness at hole wall with 90° of plunging angle ..151

**Figure 6.47.** The measured surface roughness at hole wall with 60° of plunging angle ..151

**Figure 6.48.** The measured surface roughness at hole wall with 45° of plunging angle ..152

**Figure 6.49.** The measured surface roughness at hole bottom with 90° of plunging angle .....152

**Figure 6.50.** The measured surface roughness at hole bottom with 60° of plunging angle .....152

**Figure 6.51.** The measured surface roughness at hole bottom with 45° of plunging angle .....152

**Figure 6.52.** Surface topography images of the drilled holes on extruded .....153

**Figure 6.53.** The measured hole diameter with 90° of plunging angle .....154

**Figure 6.54.** The measured hole diameter with 60° of plunging angle .....154

**Figure 6.55.** The measured hole diameter with 45° of plunging angle .....154

**Figure 6.56.** 3D surface plot of the measured forces in X direction (Fx) variation during drilling of extruded CW617N with 90° of plunging angle with respect to the studied cutting tool geometry .....155

**Figure 6.57.** 3D surface plot of the measured forces in Y direction (Fy) variation during drilling of extruded CW617N with 90° of plunging angle with respect to the studied cutting tool geometry .....156

**Figure 6.58.** 3D surface plot of the measured forces in Z direction (Fz) variation during drilling of extruded CW617N with 90° of plunging angle with respect to the studied cutting tool geometry .....157

**Figure 6.59.** 3D surface plot of the measured resultant forces variation during drilling of extruded CW617N with 90° of plunging angle with respect to the studied cutting tool geometry .....158

**Figure 6.60.** 3D surface plot of the measured burr heights at hole entry (BHEN) variation during drilling of extruded CW617N with 90° of plunging angle with respect to the studied cutting tool geometry .....158

**Figure 6.61.** 3D surface plot of the measured burr heights at hole exit (BHEX) variation during drilling of extruded CW617N with 90° of plunging angle with respect to the studied cutting tool geometry .....159

**Figure 6.62.** 3D surface plot of the measured surface roughness at hole bottom (Ra) variation during drilling of extruded CW617N with 90° of plunging angle with respect to the studied cutting tool geometry .....159

**Figure 6.63.** 3D surface plot of the measured surface roughness at hole wall (Ra) variation during drilling of extruded CW617N with 90° of plunging angle with respect to the studied cutting tool geometry .....160

**Figure 6.64.** 3D surface plot of the measured hole diameter variation during drilling of

extruded CW617N with 90° of plunging angle with respect to the studied cutting tool geometry .....161

**Figure 6.65.** 3D surface plot of the measured forces in X direction (Fx) variation during drilling of extruded CW617N with 60° of plunging angle with respect to the studied cutting tool geometry .....162

**Figure 6.66.** 3D surface plot of the measured forces in Y direction (Fy) variation during drilling of extruded CW617N with 60° of plunging angle with respect to the studied cutting tool geometry .....163

**Figure 6.67.** 3D surface plot of the measured forces in Z direction (Fz) variation during drilling of extruded CW617N with 60° of plunging angle with respect to the studied cutting tool geometry .....163

**Figure 6.68.** 3D surface plot of the measured resultant forces variation during drilling of extruded CW617N with 60° of plunging angle with respect to the studied cutting tool geometry .....164

**Figure 6.69.** 3D surface plot of the measured burr heights at hole entry (BHEN) variation during drilling of extruded CW617N with 60° of plunging angle with respect to the studied cutting tool geometry .....165

**Figure 6.70.** 3D surface plot of the measured burr heights at hole exit (BHEX) variation during drilling of extruded CW617N with 60° of plunging angle with respect to the studied cutting tool geometry .....165

**Figure 6.71.** 3D surface plot of the measured surface roughness at hole bottom (Ra) variation during drilling of extruded CW617N with 60° of plunging angle with respect to the studied cutting tool geometry .....166

**Figure 6.72.** 3D surface plot of the measured surface roughness at hole wall (Ra) variation during drilling of extruded CW617N with 60° of plunging angle with respect to the studied cutting tool geometry .....166

**Figure 6.73.** 3D surface plot of the measured hole diameter variation during drilling of extruded CW617N with 60° of plunging angle with respect to the studied cutting tool geometry .....167

**Figure 6.74.** 3D surface plot of the measured forces in X direction (Fx) variation during drilling of extruded CW617N with 45° of plunging angle with respect to the studied cutting tool geometry .....168

**Figure 6.75.** 3D surface plot of the measured forces in Y direction (Fy) variation during drilling of extruded CW617N with 45° of plunging angle with respect to the studied cutting tool geometry .....169

**Figure 6.76.** 3D surface plot of the measured forces in Z direction (Fz) variation during drilling of extruded CW617N with 45° of plunging angle with respect to the studied cutting tool geometry .....170

**Figure 6.77.** 3D surface plot of the measured resultant forces variation during drilling of extruded CW617N with 45° of plunging angle with respect to the studied cutting tool geometry .....170

**Figure 6.78.** 3D surface plot of the measured burr heights at hole entry (BHEN) variation during drilling of extruded CW617N with 45° of plunging angle with respect to the studied cutting tool geometry .....171

**Figure 6.79.** 3D surface plot of the measured burr heights at hole exit (BHEX) variation during drilling of extruded CW617N with 45° of plunging angle with respect to the studied cutting tool geometry .....171

**Figure 6.80.** 3D surface plot of the measured surface roughness at hole bottom (Ra) variation during drilling of extruded CW617N with 45° of plunging angle with respect to the studied cutting tool geometry .....172

**Figure 6.81.** 3D surface plot of the measured surface roughness at hole wall (Ra) variation during drilling of extruded CW617N with 45° of plunging angle with respect to the studied cutting tool geometry .....173

**Figure 6.82.** 3D surface plot of the measured hole diameter variation during drilling of extruded CW617N with 45° of plunging angle with respect to the studied cutting tool geometry .....173

**Figure 6.83.** 3D surface plot of the measured forces in X direction (Fx) variation during drilling of extruded CW511L with 90° of plunging angle with respect to the studied cutting tool geometry .....175

**Figure 6.84.** 3D surface plot of the measured forces in Y direction (Fy) variation during drilling of extruded CW511L with 90° of plunging angle with respect to the studied cutting tool geometry .....176

**Figure 6.85.** 3D surface plot of the measured forces in Z direction (Fz) variation during drilling of extruded CW511L with 90° of plunging angle with respect to the studied cutting tool geometry .....176

**Figure 6.86.** 3D surface plot of the measured resultant forces variation during drilling of extruded CW511L with 90° of plunging angle with respect to the studied cutting tool geometry .....177

**Figure 6.87.** 3D surface plot of the measured burr heights at hole entry (BHEN) variation during drilling of extruded CW511L with 90° of plunging angle with respect to the studied cutting tool geometry .....178

**Figure 6.88.** 3D surface plot of the measured burr heights at hole exit (BHEX) variation during drilling of extruded CW511L with 90° of plunging angle with respect to the studied cutting tool geometry .....179

**Figure 6.89.** 3D surface plot of the measured surface roughness at hole bottom (Ra) variation during drilling of extruded CW511L with 90° of plunging angle with respect to the studied cutting tool geometry .....179

**Figure 6.90.** 3D surface plot of the measured surface roughness at hole wall (Ra) variation during drilling of extruded CW511L with 90° of plunging angle with respect to the studied cutting tool geometry .....180

**Figure 6.91.** 3D surface plot of the measured hole diameter variation during drilling of extruded CW511L with 90° of plunging angle with respect to the studied cutting tool geometry .....181

**Figure 6.92.** 3D surface plot of the measured forces in X direction (Fx) variation during drilling of extruded CW511L with 60° of plunging angle with respect to the studied cutting tool geometry .....182

**Figure 6.93.** 3D surface plot of the measured forces in Y direction (Fy) variation during drilling of extruded CW511L with 60° of plunging angle with respect to the studied cutting tool geometry .....183

**Figure 6.94.** 3D surface plot of the measured forces in Z direction (Fz) variation during drilling of extruded CW511L with 60° of plunging angle with respect to the studied cutting tool geometry .....183

**Figure 6.95.** 3D surface plot of the measured resultant forces variation during drilling of extruded CW511L with 60° of plunging angle with respect to the studied cutting tool geometry .....184

**Figure 6.96.** 3D surface plot of the measured burr heights at hole entry (BHEN) variation during drilling of extruded CW511L with 60° of plunging angle with respect to the studied cutting tool geometry .....185

**Figure 6.97.** 3D surface plot of the measured burr heights at hole exit (BHEX) variation during drilling of extruded CW511L with 60° of plunging angle with respect to the studied cutting tool geometry .....186

**Figure 6.98.** 3D surface plot of the measured surface roughness at hole bottom (Ra) variation during drilling of extruded CW511L with 60° of plunging angle with respect to the studied cutting tool geometry .....186

**Figure 6.99.** 3D surface plot of the measured surface roughness at hole wall (Ra) variation during drilling of extruded CW511L with 60° of plunging angle with respect to the studied cutting tool geometry .....187

**Figure 6.100.** 3D surface plot of the measured hole diameter variation during drilling of extruded CW511L with 60° of plunging angle with respect to the studied cutting tool geometry .....188

**Figure 6.101.** 3D surface plot of the measured forces in X direction (Fx) variation during drilling of extruded CW511L with 45° of plunging angle with respect to the studied cutting tool geometry .....189

**Figure 6.102.** 3D surface plot of the measured forces in Y direction (Fy) variation during drilling of extruded CW511L with 45° of plunging angle with respect to the studied cutting tool geometry .....190

**Figure 6.103.** 3D surface plot of the measured forces in Z direction (Fz) variation during drilling of extruded CW511L with 45° of plunging angle with respect to the studied cutting tool geometry .....190

**Figure 6.104.** 3D surface plot of the measured resultant forces variation during drilling of extruded CW511L with 45° of plunging angle with respect to the studied cutting tool geometry .....191

**Figure 6.105.** 3D surface plot of the measured burr heights at hole entry (BHEN) variation during drilling of extruded CW511L with 45° of plunging angle with respect to the studied cutting tool geometry .....192

**Figure 6.106.** 3D surface plot of the measured burr heights at hole exit (BHEX) variation during drilling of extruded CW511L with 45° of plunging angle with respect to the studied cutting tool geometry .....192

**Figure 6.107.** 3D surface plot of the measured surface roughness at hole bottom (Ra) variation during drilling of extruded CW511L with 45° of plunging angle with respect to the studied cutting tool geometry .....193

**Figure 6.108.** 3D surface plot of the measured surface roughness at hole wall (Ra) variation during drilling of extruded CW511L with 45° of plunging angle with respect to the studied cutting tool geometry .....194

**Figure 6.109.** 3D surface plot of the measured hole diameter variation during drilling of extruded CW511L with 45° of plunging angle with respect to the studied cutting tool geometry .....194

**Figure 6.110.** 3D surface plot of the measured forces in X direction (Fx) variation during drilling of extruded CW724R with 90° of plunging angle with respect to the studied cutting tool geometry .....196

**Figure 6.111.** 3D surface plot of the measured forces in Y direction (Fy) variation during drilling of extruded CW724R with 90° of plunging angle with respect to the studied cutting tool geometry .....197

**Figure 6.112.** 3D surface plot of the measured forces in Z direction (Fz) variation during drilling of extruded CW724R with 90° of plunging angle with respect to the studied cutting tool geometry .....198

**Figure 6.113.** 3D surface plot of the measured resultant forces variation during drilling of extruded CW724R with 90° of plunging angle with respect to the studied cutting tool geometry .....198

**Figure 6.114.** 3D surface plot of the measured burr heights at hole entry (BHEN) variation during drilling of extruded CW724R with 90° of plunging angle with respect to the studied cutting tool geometry .....199

**Figure 6.115.** 3D surface plot of the measured burr heights at hole exit (BHEX) variation during drilling of extruded CW724R with 90° of plunging angle with respect to the studied cutting tool geometry .....200

**Figure 6.116.** 3D surface plot of the measured surface roughness at hole bottom (Ra) variation during drilling of extruded CW724R with 90° of plunging angle with respect to the studied cutting tool geometry .....200

**Figure 6.117.** 3D surface plot of the measured surface roughness at hole wall (Ra) variation during drilling of extruded CW724R with 90° of plunging angle with respect to the studied cutting tool geometry .....201

**Figure 6.118.** 3D surface plot of the measured hole diameter variation during drilling of extruded CW724R with 90° of plunging angle with respect to the studied cutting tool geometry .....202

**Figure 6.119.** 3D surface plot of the measured forces in X direction (Fx) variation during drilling of extruded CW724R with 60° of plunging angle with respect to the studied cutting tool geometry .....203

**Figure 6.120.** 3D surface plot of the measured forces in Y direction (Fy) variation during drilling of extruded CW724R with 60° of plunging angle with respect to the studied cutting tool geometry .....204

**Figure 6.121.** 3D surface plot of the measured forces in Z direction (Fz) variation during drilling of extruded CW724R with 60° of plunging angle with respect to the studied cutting tool geometry .....204

**Figure 6.122.** 3D surface plot of the measured resultant forces variation during drilling of extruded CW724R with 60° of plunging angle with respect to the studied cutting tool geometry .....205

**Figure 6.123.** 3D surface plot of the measured burr heights at hole entry (BHEN) variation during drilling of extruded CW724R with 60° of plunging angle with respect to the studied cutting tool geometry .....206

**Figure 6.124.** 3D surface plot of the measured burr heights at hole exit (BHEX) variation during drilling of extruded CW724R with 60° of plunging angle with respect to the studied cutting tool geometry .....206

**Figure 6.125.** 3D surface plot of the measured surface roughness at hole bottom (Ra) variation during drilling of extruded CW724R with 60° of plunging angle with respect to the studied cutting tool geometry .....207

**Figure 6.126.** 3D surface plot of the measured surface roughness at hole wall (Ra) variation during drilling of extruded CW724R with 60° of plunging angle with respect to the studied cutting tool geometry .....208

**Figure 6.127.** 3D surface plot of the measured hole diameter variation during drilling of extruded CW724R with 60° of plunging angle with respect to the studied cutting tool geometry .....208

**Figure 6.128.** 3D surface plot of the measured forces in X direction (Fx) variation during drilling of extruded CW724R with 45° of plunging angle with respect to the studied cutting tool geometry .....210

**Figure 6.129.** 3D surface plot of the measured forces in Y direction (Fy) variation during drilling of extruded CW724R with 45° of plunging angle with respect to the studied cutting tool geometry .....210

**Figure 6.130.** 3D surface plot of the measured forces in Z direction (Fz) variation during drilling of extruded CW724R with 45° of plunging angle with respect to the studied cutting tool geometry .....211

**Figure 6.131.** 3D surface plot of the measured resultant forces variation during drilling of extruded CW724R with 45° of plunging angle with respect to the studied cutting tool geometry .....212

**Figure 6.132.** 3D surface plot of the measured burr heights at hole entry (BHEN) variation during drilling of extruded CW724R with 45° of plunging angle with respect to the studied cutting tool geometry .....212

**Figure 6.133.** 3D surface plot of the measured burr heights at hole exit (BHEX) variation during drilling of extruded CW724R with 45° of plunging angle with respect to the studied cutting tool geometry .....213

**Figure 6.134.** 3D surface plot of the measured surface roughness at hole bottom (Ra) variation during drilling of extruded CW724R with 45° of plunging angle with respect to the studied cutting tool geometry .....214

**Figure 6.135.** 3D surface plot of the measured surface roughness at hole wall (Ra) variation during drilling of extruded CW724R with 45° of plunging angle with respect to the studied cutting tool geometry .....214

**Figure 6.136.** 3D surface plot of the measured hole diameter variation during drilling of extruded CW724R with 45° of plunging angle with respect to the studied cutting tool geometry .....215

**Figure 6.137.** 3D surface plot of the measured forces in X direction (Fx) variation during drilling of forged CW617N with 90° of plunging angle with respect to the studied cutting tool geometry .....217

**Figure 6.138.** 3D surface plot of the measured forces in Y direction (Fy) variation during drilling of forged CW617N with 90° of plunging angle with respect to the studied cutting tool geometry .....218

**Figure 6.139.** 3D surface plot of the measured forces in Z direction (Fz) variation during drilling of forged CW617N with 90° of plunging angle with respect to the studied cutting tool geometry .....218

**Figure 6.140.** 3D surface plot of the measured resultant forces variation during drilling of forged CW617N with 90° of plunging angle with respect to the studied cutting tool geometry .....219

**Figure 6.141.** 3D surface plot of the measured burr heights at hole entry (BHEN) variation during drilling of forged CW617N with 90° of plunging angle with respect to the studied cutting tool geometry .....220

**Figure 6.142.** 3D surface plot of the measured burr heights at hole exit (BHEX) variation during drilling of forged CW617N with 90° of plunging angle with respect to the studied cutting tool geometry .....220

**Figure 6.143.** 3D surface plot of the measured surface roughness at hole bottom (Ra) variation during drilling of forged CW617N with 90° of plunging angle with respect to the studied cutting tool geometry .....221

**Figure 6.144.** 3D surface plot of the measured surface roughness at hole wall (Ra) variation during drilling of forged CW617N with 90° of plunging angle with respect to the studied cutting tool geometry .....221

**Figure 6.145.** 3D surface plot of the measured hole diameter variation during drilling of forged CW617N with 90° of plunging angle with respect to the studied cutting tool geometry .....222

**Figure 6.146.** 3D surface plot of the measured forces in X direction (Fx) variation during drilling of forged CW617N with 60° of plunging angle with respect to the studied cutting tool geometry .....224

**Figure 6.147.** 3D surface plot of the measured forces in Y direction (Fy) variation during drilling of forged CW617N with 60° of plunging angle with respect to the studied cutting tool geometry .....224

**Figure 6.148.** 3D surface plot of the measured forces in Z direction (Fz) variation during drilling of forged CW617N with 60° of plunging angle with respect to the studied cutting tool geometry .....225

**Figure 6.149.** 3D surface plot of the measured resultant forces variation during drilling of forged CW617N with 60° of plunging angle with respect to the studied cutting tool geometry .....226

**Figure 6.150.** 3D surface plot of the measured burr heights at hole entry (BHEN) variation during drilling of forged CW617N with 60° of plunging angle with respect to the studied cutting tool geometry .....226

**Figure 6.151.** 3D surface plot of the measured burr heights at hole exit (BHEX) variation during drilling of forged CW617N with 60° of plunging angle with respect to the studied cutting tool geometry .....227

**Figure 6.152.** 3D surface plot of the measured surface roughness at hole bottom (Ra) variation during drilling of forged CW617N with 60° of plunging angle with respect to the studied cutting tool geometry .....227

**Figure 6.153.** 3D surface plot of the measured surface roughness at hole wall (Ra) variation during drilling of forged CW617N with 60° of plunging angle with respect to the studied cutting tool geometry .....228

**Figure 6.154.** 3D surface plot of the measured hole diameter variation during drilling of forged CW617N with 60° of plunging angle with respect to the studied cutting tool geometry .....229

**Figure 6.155.** 3D surface plot of the measured forces in X direction (Fx) variation during drilling of forged CW617N with 45° of plunging angle with respect to the studied cutting tool geometry .....230

**Figure 6.156.** 3D surface plot of the measured forces in Y direction (Fy) variation during drilling of forged CW617N with 45° of plunging angle with respect to the studied cutting tool geometry .....231

**Figure 6.157.** 3D surface plot of the measured forces in Z direction (Fz) variation during drilling of forged CW617N with 45° of plunging angle with respect to the studied cutting tool geometry .....231

**Figure 6.158.** 3D surface plot of the measured resultant forces variation during drilling of forged CW617N with 45° of plunging angle with respect to the studied cutting tool geometry .....232

**Figure 6.159.** 3D surface plot of the measured burr heights at hole entry (BHEN) variation during drilling of forged CW617N with 45° of plunging angle with respect to the studied cutting tool geometry .....233

**Figure 6.160.** 3D surface plot of the measured burr heights at hole exit (BHEX) variation during drilling of forged CW617N with 45° of plunging angle with respect to the studied cutting tool geometry .....233

**Figure 6.161.** 3D surface plot of the measured surface roughness at hole bottom (Ra) variation during drilling of forged CW617N with 45° of plunging angle with respect to the studied cutting tool geometry .....234

**Figure 6.162.** 3D surface plot of the measured surface roughness at hole wall (Ra) variation during drilling of forged CW617N with 45° of plunging angle with respect to the studied cutting tool geometry .....234

**Figure 6.163.** 3D surface plot of the measured hole diameter variation during drilling of forged CW617N with 45° of plunging angle with respect to the studied cutting tool geometry .....235

**Figure 6.164.** 3D surface plot of the measured forces in X direction (Fx) variation during drilling of forged CW511L with 90° of plunging angle with respect to the studied cutting tool geometry .....237

**Figure 6.165.** 3D surface plot of the measured forces in Y direction (Fy) variation during drilling of forged CW511L with 90° of plunging angle with respect to the studied cutting tool geometry .....238

**Figure 6.166.** 3D surface plot of the measured forces in Z direction (Fz) variation during drilling of forged CW511L with 90° of plunging angle with respect to the studied cutting tool geometry .....238

**Figure 6.167.** 3D surface plot of the measured resultant forces variation during drilling of forged CW511L with 90° of plunging angle with respect to the studied cutting tool geometry .....239

**Figure 6.168.** 3D surface plot of the measured burr heights at hole entry (BHEN) variation during drilling of forged CW511L with 90° of plunging angle with respect to the studied cutting tool geometry .....240

**Figure 6.169.** 3D surface plot of the measured burr heights at hole exit (BHEX) variation during drilling of forged CW511L with 90° of plunging angle with respect to the studied cutting tool geometry .....241

**Figure 6.170.** 3D surface plot of the measured surface roughness at hole bottom (Ra) variation during drilling of forged CW511L with 90° of plunging angle with respect to the studied cutting tool geometry .....241

**Figure 6.171.** 3D surface plot of the measured surface roughness at hole wall (Ra) variation during drilling of forged CW511L with 90° of plunging angle with respect to the studied cutting tool geometry .....242

**Figure 6.172.** 3D surface plot of the measured hole diameter variation during drilling of forged CW511L with 90° of plunging angle with respect to the studied cutting tool geometry .....242

**Figure 6.173.** 3D surface plot of the measured forces in X direction (Fx) variation during drilling of forged CW511L with 60° of plunging angle with respect to the studied cutting tool geometry .....244

**Figure 6.174.** 3D surface plot of the measured forces in Y direction (Fy) variation during drilling of forged CW511L with 60° of plunging angle with respect to the studied cutting tool geometry .....245

**Figure 6.175.** 3D surface plot of the measured forces in Z direction (Fz) variation during drilling of forged CW511L with 60° of plunging angle with respect to the studied cutting tool geometry .....246

**Figure 6.176.** 3D surface plot of the measured resultant forces variation during drilling of forged CW511L with 60° of plunging angle with respect to the studied cutting tool geometry .....246

**Figure 6.177.** 3D surface plot of the measured burr heights at hole entry (BHEN) variation during drilling of forged CW511L with 60° of plunging angle with respect to the studied cutting tool geometry .....247

**Figure 6.178.** 3D surface plot of the measured burr heights at hole exit (BHEX) variation during drilling of forged CW511L with 60° of plunging angle with respect to the studied cutting tool geometry .....248

**Figure 6.179.** 3D surface plot of the measured surface roughness at hole bottom (Ra) variation during drilling of forged CW511L with 60° of plunging angle with respect to the studied cutting tool geometry .....248

**Figure 6.180.** 3D surface plot of the measured surface roughness at hole wall (Ra) variation during drilling of forged CW511L with 60° of plunging angle with respect to the studied cutting tool geometry .....249

**Figure 6.181.** 3D surface plot of the measured hole diameter variation during drilling of forged CW511L with 60° of plunging angle with respect to the studied cutting tool geometry .....250

**Figure 6.182.** 3D surface plot of the measured forces in X direction (Fx) variation during drilling of forged CW511L with 45° of plunging angle with respect to the studied cutting tool geometry .....251

**Figure 6.183.** 3D surface plot of the measured forces in Y direction (Fy) variation during drilling of forged CW511L with 45° of plunging angle with respect to the studied cutting tool geometry .....252

**Figure 6.184.** 3D surface plot of the measured forces in Z direction (Fz) variation during drilling of forged CW511L with 45° of plunging angle with respect to the studied cutting tool geometry .....253

**Figure 6.185.** 3D surface plot of the measured resultant forces variation during drilling of forged CW511L with 45° of plunging angle with respect to the studied cutting tool geometry .....253

**Figure 6.186.** 3D surface plot of the measured burr heights at hole entry (BHEN) variation during drilling of forged CW511L with 45° of plunging angle with respect to the studied cutting tool geometry .....254

**Figure 6.187.** 3D surface plot of the measured burr heights at hole exit (BHEX) variation during drilling of forged CW511L with 45° of plunging angle with respect to the studied cutting tool geometry .....255

**Figure 6.188.** 3D surface plot of the measured surface roughness at hole bottom (Ra) variation during drilling of forged CW511L with 45° of plunging angle with respect to the studied cutting tool geometry .....255

**Figure 6.189.** 3D surface plot of the measured surface roughness at hole wall (Ra) variation during drilling of forged CW511L with 45° of plunging angle with respect to the studied cutting tool geometry .....256

**Figure 6.190.** 3D surface plot of the measured hole diameter variation during drilling of forged CW511L with 45° of plunging angle with respect to the studied cutting tool geometry .....257

**Figure 6.191.** 3D surface plot of the measured forces in X direction (Fx) variation during drilling of forged CW724R with 90° of plunging angle with respect to the studied cutting tool geometry .....258

**Figure 6.192.** 3D surface plot of the measured forces in Y direction (Fy) variation during drilling of forged CW724R with 90° of plunging angle with respect to the studied cutting tool geometry .....259

**Figure 6.193.** 3D surface plot of the measured forces in Z direction (Fz) variation during drilling of forged CW724R with 90° of plunging angle with respect to the studied cutting tool geometry .....260

**Figure 6.194.** 3D surface plot of the measured resultant forces variation during drilling of forged CW724R with 90° of plunging angle with respect to the studied cutting tool geometry .....261

**Figure 6.195.** 3D surface plot of the measured burr heights at hole entry (BHEN) variation during drilling of forged CW724R with 90° of plunging angle with respect to the studied cutting tool geometry .....261

**Figure 6.196.** 3D surface plot of the measured burr heights at hole exit (BHEX) variation during drilling of forged CW724R with 90° of plunging angle with respect to the studied cutting tool geometry .....262

**Figure 6.197.** 3D surface plot of the measured surface roughness at hole bottom (Ra) variation during drilling of forged CW724R with 90° of plunging angle with respect to the studied cutting tool geometry .....263

**Figure 6.198.** 3D surface plot of the measured surface roughness at hole wall (Ra) variation during drilling of forged CW724R with 90° of plunging angle with respect to the studied cutting tool geometry .....263

**Figure 6.199.** 3D surface plot of the measured hole diameter variation during drilling of forged CW724R with 90° of plunging angle with respect to the studied cutting tool geometry .....264

**Figure 6.200.** 3D surface plot of the measured forces in X direction (Fx) variation during drilling of forged CW724R with 60° of plunging angle with respect to the studied cutting tool geometry .....266

**Figure 6.201.** 3D surface plot of the measured forces in Y direction (Fy) variation during drilling of forged CW724R with 60° of plunging angle with respect to the studied cutting tool geometry .....266

**Figure 6.202.** 3D surface plot of the measured forces in Z direction (Fz) variation during drilling of forged CW724R with 60° of plunging angle with respect to the studied cutting tool geometry .....267

**Figure 6.203.** 3D surface plot of the measured resultant forces variation during drilling of forged CW724R with 60° of plunging angle with respect to the studied cutting tool geometry .....268

**Figure 6.204.** 3D surface plot of the measured burr heights at hole entry (BHEN) variation during drilling of forged CW724R with 60° of plunging angle with respect to the studied cutting tool geometry .....268

**Figure 6.205.** 3D surface plot of the measured burr heights at hole exit (BHEX) variation during drilling of forged CW724R with 60° of plunging angle with respect to the studied cutting tool geometry .....269

**Figure 6.206.** 3D surface plot of the measured surface roughness at hole bottom (Ra) variation during drilling of forged CW724R with 60° of plunging angle with respect to the studied cutting tool geometry .....269

**Figure 6.207.** 3D surface plot of the measured surface roughness at hole wall (Ra) variation during drilling of forged CW724R with 60° of plunging angle with respect to the studied cutting tool geometry .....270

**Figure 6.208.** 3D surface plot of the measured hole diameter variation during drilling of forged CW724R with 60° of plunging angle with respect to the studied cutting tool geometry .....271

**Figure 6.209.** 3D surface plot of the measured forces in X direction (Fx) variation during drilling of forged CW724R with 45° of plunging angle with respect to the studied cutting tool geometry .....272

**Figure 6.210.** 3D surface plot of the measured forces in Y direction (Fy) variation during drilling of forged CW724R with 45° of plunging angle with respect to the studied cutting tool geometry .....273

**Figure 6.211.** 3D surface plot of the measured forces in Z direction (Fz) variation during drilling of forged CW724R with 45° of plunging angle with respect to the studied cutting tool geometry .....273

**Figure 6.212.** 3D surface plot of the measured resultant forces variation during drilling of forged CW724R with 45° of plunging angle with respect to the studied cutting tool geometry .....274

**Figure 6.213.** 3D surface plot of the measured burr heights at hole entry (BHEN) variation during drilling of forged CW724R with 45° of plunging angle with respect to the studied cutting tool geometry .....275

**Figure 6.214.** 3D surface plot of the measured burr heights at hole exit (BHEX) variation during drilling of forged CW724R with 45° of plunging angle with respect to the studied cutting tool geometry .....275

**Figure 6.215.** 3D surface plot of the measured surface roughness at hole bottom (Ra) variation during drilling of forged CW724R with 45° of plunging angle with respect to the studied cutting tool geometry .....276

**Figure 6.216.** 3D surface plot of the measured surface roughness at hole wall (Ra) variation during drilling of forged CW724R with 45° of plunging angle with respect to the studied cutting tool geometry .....277

**Figure 6.217.** 3D surface plot of the measured hole diameter variation during drilling of forged CW724R with 45° of plunging angle with respect to the studied cutting tool geometry .....277

**Figure 6.218.** Measured surface and sub-surface microhardness of the extruded specimens .....280

**Figure 6.219.** The SEM images of the deformation on the sub-surfaces of the machined holes .....282

**Figure 7.1.** 3D topography images of the drilled holes on extruded CW511L .....289

**Figure 8.1.** The schematic of a fuzzy logic system .....291

**Figure 8.2.** The generated inputs FIS model .....293

**Figure 8.3.** The schematic of the developed fuzzy logic model .....293

**Figure 8.4.** The variation of the average entry burr height and surface roughness in a combined mode of the influencing cutting tool geometries .....294

**Figure 8.5.** The developed fuzzy logic model in this study .....295

**Figure 8.6.** Comparison of the model predictions with the experimental results .....297

**Figure 8.7.** The schematic of neural network model and back propagation algorithm ..298

**Figure 8.8.** The schematic of the formed burrs .....299

**Figure 8.9.** The MSE of training of the selected ANN .....301

**Figure 8.10.** Comparison between the measured and predicted results by ANN .....302

# LIST OF TABLES

**Table 2.1.** Chemical composition of the studied brass alloys .....10

**Table 2.2.** Technical specifications of the as received (extruded) brass alloys .....10

**Table 2.3.** The results obtained for the chemical composition of the studied brass alloys .....11

**Table 2.4.** The phasic percentages of the studied brass alloys .....22

**Table 2.5.** The experimental mechanical properties of the studied brass alloys .....25

**Table 2.6.** The microhardness results of the studied brass alloys .....28

**Table 2.7.** The toughness results of the studied brass alloys .....30

**Table 2.8.** The first mode fracture toughness results of the studied brass alloys .....33

**Table 4.1.** the performance evaluated refence tools specifications .....55

**Table 4.2.** The geometric measurements of the cutting tools.....57

**Table 4.3.** The utilized test parameters for the experiments.....58

**Table 4.4.** The best performance evaluation results for the extruded specimens using reference cutting tools .....81

**Table 4.5.** The best performance evaluation results for the forged and annealed specimens using reference cutting tools .....82

**Table 4.6.** The most influencing geometric parameters on the machining responses .....83

**Table 5.1.** Geometrical parameters of the designed cutting tools .....90

**Table 5.2.** The calculated masses of the designed flat bottom drills .....90

**Table 5.3.** Technical specifications of the used carbide in the manufacture cutting tools……..…90

**Table 5.4.** The calculated natural frequencies in different shape modes of the designed flat bottom drills .....91

**Table 5.5.** The calculated total displacements in different shape modes of the designed flat bottom drills .....92

**Table 5.6.** The calculated stiffness values for different shape modes of the designed flat bottom drills .....92

**Table 5.7.** The calculated oscillation period time for different shape modes of the designed flat bottom drills .....93

**Table 5.8.** ANOVA results of first mode natural frequencies .....105

**Table 5.9.** ANOVA results of second mode natural frequencies .....106

**Table 5.10.** ANOVA results of third mode natural frequencies .....107

**Table 5.11.** ANOVA results of fourth mode natural frequencies .....107

**Table 5.12.** ANOVA results of fifth mode natural frequencies .....108

**Table 5.13.** ANOVA results of sixth mode natural frequencies .....109

**Table 5.14.** The quadratic order developed regression model for different shape modes of the designed flat bottom drills .....110

**Table 6.1.** The geometric specification of the utilized cutting tools .....111

**Table 6.2.** Technical specifications of the utilized carbide material .....112

**Table 6.3.** The utilized test parameters for the experiments.....113

**Table 6.4.** The measurement results for the extruded CW617N with 90° of plunging angle .....116

**Table 6.5.** The measurement results for the extruded CW617N with 60° of plunging angle .....117

**Table 6.6.** The measurement results for the extruded CW617N with 45° of plunging angle .....118

**Table 6.7.** The measurement results for the extruded CW511L with 90° of plunging angle .....118

**Table 6.8.** The measurement results for the extruded CW511L with 60° of plunging angle .....119

**Table 6.9.** The measurement results for the extruded CW511L with 45° of plunging angle .....120

**Table 6.10.** The measurement results for the extruded CW724R with 90° of plunging angle .....121

**Table 6.11.** The measurement results for the extruded CW724R with 60° of plunging angle .....121

**Table 6.12.** The measurement results for the extruded CW724R with 45° of plunging angle .....122

**Table 6.13.** The measurement results for the forged CW617N with 90° of plunging angle .....123

**Table 6.14.** The measurement results for the forged CW617N with 60° of plunging angle .....124

**Table 6.15.** The measurement results for the forged CW617N with 45° of plunging angle .....124

**Table 6.16.** The measurement results for the forged CW511L with 90° of plunging angle .....125

**Table 6.17.** The measurement results for the forged CW511L with 60° of plunging angle .....126

**Table 6.18.** The measurement results for the forged CW511L with 45° of plunging angle .....127

**Table 6.19.** The measurement results for the forged CW724R with 90° of plunging angle .....127

**Table 6.20.** The measurement results for the forged CW724R with 60° of plunging angle .....128

**Table 6.21.** The measurement results for the forged CW724R with 45° of plunging angle .....129

**Table 6.22.** The specific cutting forces in flat bottom drilling .....136

**Table 6.23.** The ANOVA results for measured forces in X direction (Fx) during drilling of extruded CW617N with 90° of plunging angle .....155

**Table 6.24.** The ANOVA results for measured forces in Y direction (Fy) during drilling

of extruded CW617N with 90° of plunging angle .....156

**Table 6.25.** The ANOVA results for measured forces in Z direction (Fz) during drilling of extruded CW617N with 90° of plunging angle .....157

**Table 6.26.** The ANOVA results for measured resultant forces (FR) during drilling of extruded CW617N with 90° of plunging angle .....157

**Table 6.27.** The ANOVA results for measured burr heights at hole entry (BHEN) during drilling of extruded CW617N with 90° of plunging angle .....158

**Table 6.28.** The ANOVA results for measured burr heights at hole exit (BHEX) during drilling of extruded CW617N with 90° of plunging angle .....158

**Table 6.29.** The ANOVA results for measured surface roughness at hole bottom (Ra) during drilling of extruded CW617N with 90° of plunging angle .....159

**Table 6.30.** The ANOVA results for measured surface roughness at hole wall (Ra) during drilling of extruded CW617N with 90° of plunging angle .....160

**Table 6.31.** The developed regression model for drilling of extruded CW617N with 90° of plunging angle .....160

**Table 6.32.** The developed regression model for drilling of extruded CW724R with 90° of plunging angle .....161

**Table 6.33.** The ANOVA results for measured forces in X direction (Fx) during drilling of extruded CW617N with 60° of plunging angle .....162

**Table 6.34.** The ANOVA results for measured forces in Y direction (Fy) during drilling of extruded CW617N with 60° of plunging angle .....162

**Table 6.35.** The ANOVA results for measured forces in Z direction (Fz) during drilling of extruded CW617N with 60° of plunging angle .....163

**Table 6.36.** The ANOVA results for measured resultant forces (FR) during drilling of extruded CW617N with 60° of plunging angle .....163

**Table 6.37.** The ANOVA results for measured burr heights at hole entry (BHEN) during drilling of extruded CW617N with 60° of plunging angle .....164

**Table 6.38.** The ANOVA results for measured burr heights at hole exit (BHEX) during

drilling of extruded CW617N with 60° of plunging angle .....165

**Table 6.39.** The ANOVA results for measured surface roughness at hole bottom (Ra) during drilling of extruded CW617N with 60° of plunging angle .....165

**Table 6.40.** The ANOVA results for measured surface roughness at hole wall (Ra) during drilling of extruded CW617N with 60° of plunging angle .....166

**Table 6.41.** The ANOVA results for measured hole diameter during drilling of extruded CW617N with 60° of plunging angle .....167

**Table 6.42.** The developed regression model for drilling of extruded CW617N with 60° of plunging angle .....167

**Table 6.43.** The ANOVA results for measured forces in X direction (Fx) during drilling of extruded CW617N with 45° of plunging angle .....168

**Table 6.44.** The ANOVA results for measured forces in Y direction (Fy) during drilling of extruded CW617N with 45° of plunging angle .....168

**Table 6.45.** The ANOVA results for measured forces in Z direction (Fz) during drilling of extruded CW617N with 45° of plunging angle .....169

**Table 6.46.** The ANOVA results for measured resultant forces (FR) during drilling of extruded CW617N with 45° of plunging angle .....170

**Table 6.47.** The ANOVA results for measured burr heights at hole entry (BHEN) during drilling of extruded CW617N with 45° of plunging angle .....170

**Table 6.48.** The ANOVA results for measured burr heights at hole exit (BHEX) during drilling of extruded CW617N with 45° of plunging angle .....171

**Table 6.49.** The ANOVA results for measured surface roughness at hole bottom (Ra) during drilling of extruded CW617N with 45° of plunging angle .....172

**Table 6.50.** The ANOVA results for measured surface roughness at hole wall (Ra) during drilling of extruded CW617N with 45° of plunging angle .....172

**Table 6.51.** The ANOVA results for measured hole diameter during drilling of extruded CW617N with 45° of plunging angle .....173

**Table 6.52.** The developed regression model for drilling of extruded CW617N with 45°

of plunging angle .....173

**Table 6.53.** The ANOVA results for measured forces in X direction (Fx) during drilling of extruded CW511L with 90° of plunging angle .....174

**Table 6.54.** The ANOVA results for measured forces in Y direction (Fy) during drilling of extruded CW511L with 90° of plunging angle .....175

**Table 6.55.** The ANOVA results for measured forces in Z direction (Fz) during drilling of extruded CW511L with 90° of plunging angle .....176

**Table 6.56.** The ANOVA results for measured resultant forces (FR) during drilling of extruded CW511L with 90° of plunging angle .....177

**Table 6.57.** The ANOVA results for measured burr heights at hole entry (BHEN) during drilling of extruded CW511L with 90° of plunging angle .....177

**Table 6.58.** The ANOVA results for measured burr heights at hole exit (BHEX) during drilling of extruded CW511L with 90° of plunging angle .....178

**Table 6.59.** The ANOVA results for measured surface roughness at hole bottom (Ra) during drilling of extruded CW511L with 90° of plunging angle .....178

**Table 6.60.** The ANOVA results for measured surface roughness at hole wall (Ra) during drilling of extruded CW511L with 90° of plunging angle .....180

**Table 6.61.** The ANOVA results for measured hole diameter during drilling of extruded CW511L with 90° of plunging angle .....180

**Table 6.62.** The developed regression model for drilling of extruded CW511L with 90° of plunging angle .....181

**Table 6.63.** The ANOVA results for measured forces in X direction (Fx) during drilling of extruded CW511L with 60° of plunging angle .....181

**Table 6.64.** The ANOVA results for measured forces in Y direction (Fy) during drilling of extruded CW511L with 60° of plunging angle .....182

**Table 6.65.** The ANOVA results for measured forces in Z direction (Fz) during drilling of extruded CW511L with 60° of plunging angle .....183

**Table 6.66.** The ANOVA results for measured resultant forces (FR) during drilling of

extruded CW511L with 60° of plunging angle .....183

**Table 6.67.** The ANOVA results for measured burr heights at hole entry (BHEN) during drilling of extruded CW511L with 60° of plunging angle .....184

**Table 6.68.** The ANOVA results for measured burr heights at hole exit (BHEX) during drilling of extruded CW511L with 60° of plunging angle .....185

**Table 6.69.** The ANOVA results for measured surface roughness at hole bottom (Ra) during drilling of extruded CW511L with 60° of plunging angle .....186

**Table 6.70.** The ANOVA results for measured surface roughness at hole wall (Ra) during drilling of extruded CW511L with 60° of plunging angle .....186

**Table 6.71.** The ANOVA results for measured hole diameter during drilling of extruded CW511L with 60° of plunging angle .....187

**Table 6.72.** The developed regression model for drilling of extruded CW511L with 60° of plunging angle .....188

**Table 6.73.** The ANOVA results for measured forces in X direction (Fx) during drilling of extruded CW511L with 45° of plunging angle .....189

**Table 6.74.** The ANOVA results for measured forces in Y direction (Fy) during drilling of extruded CW511L with 45° of plunging angle .....189

**Table 6.75.** The ANOVA results for measured forces in Z direction (Fz) during drilling of extruded CW511L with 45° of plunging angle .....190

**Table 6.76.** The ANOVA results for measured resultant forces (FR) during drilling of extruded CW511L with 45° of plunging angle .....190

**Table 6.77.** The ANOVA results for measured burr heights at hole entry (BHEN) during drilling of extruded CW511L with 45° of plunging angle .....191

**Table 6.78.** The ANOVA results for measured burr heights at hole exit (BHEX) during drilling of extruded CW511L with 45° of plunging angle .....192

**Table 6.79.** The ANOVA results for measured surface roughness at hole bottom (Ra) during drilling of extruded CW511L with 45° of plunging angle .....193

**Table 6.80.** The ANOVA results for measured surface roughness at hole wall (Ra) during

drilling of extruded CW511L with 45° of plunging angle .....193

**Table 6.81.** The ANOVA results for measured hole diameter during drilling of extruded CW511L with 45° of plunging angle .....194

**Table 6.82.** The developed regression model for drilling of extruded CW511L with 45° of plunging angle .....195

**Table 6.83.** The ANOVA results for measured forces in X direction (Fx) during drilling of extruded CW724R with 90° of plunging angle .....195

**Table 6.84.** The ANOVA results for measured forces in Y direction (Fy) during drilling of extruded CW724R with 90° of plunging angle .....196

**Table 6.85.** The ANOVA results for measured forces in Z direction (Fz) during drilling of extruded CW724R with 90° of plunging angle .....197

**Table 6.86.** The ANOVA results for measured resultant forces (FR) during drilling of extruded CW724R with 90° of plunging angle .....198

**Table 6.87.** The ANOVA results for measured burr heights at hole entry (BHEN) during drilling of extruded CW724R with 90° of plunging angle .....198

**Table 6.88.** The ANOVA results for measured burr heights at hole exit (BHEX) during drilling of extruded CW724R with 90° of plunging angle .....199

**Table 6.89.** The ANOVA results for measured surface roughness at hole bottom (Ra) during drilling of extruded CW724R with 90° of plunging angle .....200

**Table 6.90.** The ANOVA results for measured surface roughness at hole wall (Ra) during drilling of extruded CW724R with 90° of plunging angle .....200

**Table 6.91.** The ANOVA results for measured hole diameter during drilling of extruded CW724R with 90° of plunging angle .....201

**Table 6.92.** The developed regression model for drilling of extruded CW724R with 90° of plunging angle .....202

**Table 6.93.** The ANOVA results for measured forces in X direction (Fx) during drilling of extruded CW724R with 60° of plunging angle .....202

**Table 6.94.** The ANOVA results for measured forces in Y direction (Fy) during drilling

of extruded CW724R with 60° of plunging angle .....203

**Table 6.95.** The ANOVA results for measured forces in Z direction (Fz) during drilling of extruded CW724R with 60° of plunging angle .....204

**Table 6.96.** The ANOVA results for measured resultant forces (FR) during drilling of extruded CW724R with 60° of plunging angle .....204

**Table 6.97.** The ANOVA results for measured burr heights at hole entry (BHEN) during drilling of extruded CW724R with 60° of plunging angle .....205

**Table 6.98.** The ANOVA results for measured burr heights at hole exit (BHEX) during drilling of extruded CW724R with 60° of plunging angle .....206

**Table 6.99.** The ANOVA results for measured surface roughness at hole bottom (Ra) during drilling of extruded CW724R with 60° of plunging angle .....206

**Table 6.100.** The ANOVA results for measured surface roughness at hole wall (Ra) during drilling of extruded CW724R with 60° of plunging angle .....207

**Table 6.101.** The ANOVA results for measured hole diameter during drilling of extruded CW724R with 60° of plunging angle .....208

**Table 6.102.** The developed regression model for drilling of extruded CW724R with 60° of plunging angle .....209

**Table 6.103.** The ANOVA results for measured forces in X direction (Fx) during drilling of extruded CW724R with 45° of plunging angle .....209

**Table 6.104.** The ANOVA results for measured forces in Y direction (Fy) during drilling of extruded CW724R with 45° of plunging angle .....210

**Table 6.105.** The ANOVA results for measured forces in Z direction (Fz) during drilling of extruded CW724R with 45° of plunging angle .....210

**Table 6.106.** The ANOVA results for measured resultant forces (FR) during drilling of extruded CW724R with 45° of plunging angle .....211

**Table 6.107.** The ANOVA results for measured burr heights at hole entry (BHEN) during drilling of extruded CW724R with 45° of plunging angle .....212

**Table 6.108.** The ANOVA results for measured burr heights at hole exit (BHEX) during

drilling of extruded CW724R with 45° of plunging angle .....212

**Table 6.109.** The ANOVA results for measured surface roughness at hole bottom (Ra) during drilling of extruded CW724R with 45° of plunging angle .....213

**Table 6.110.** The ANOVA results for measured surface roughness at hole wall (Ra) during drilling of extruded CW724R with 45° of plunging angle .....214

**Table 6.111.** The ANOVA results for measured hole diameter during drilling of extruded CW724R with 45° of plunging angle .....214

**Table 6.112.** The developed regression model for drilling of extruded CW724R with 45° of plunging angle .....215

**Table 6.113.** The ANOVA results for measured forces in X direction (Fx) during drilling of forged CW617N with 90° of plunging angle .....216

**Table 6.114.** The ANOVA results for measured forces in Y direction (Fy) during drilling of forged CW617N with 90° of plunging angle .....217

**Table 6.115.** The ANOVA results for measured forces in Z direction (Fz) during drilling of forged CW617N with 90° of plunging angle .....218

**Table 6.116.** The ANOVA results for measured resultant forces (FR) during drilling of forged CW617N with 90° of plunging angle .....218

**Table 6.117.** The ANOVA results for measured burr heights at hole entry (BHEN) during drilling of forged CW617N with 90° of plunging angle .....219

**Table 6.118.** The ANOVA results for measured burr heights at hole exit (BHEX) during drilling of forged CW617N with 90° of plunging angle .....220

**Table 6.119.** The ANOVA results for measured surface roughness at hole bottom (Ra) during drilling of forged CW617N with 90° of plunging angle .....220

**Table 6.120.** The ANOVA results for measured surface roughness at hole wall (Ra) during drilling of forged CW617N with 90° of plunging angle .....221

**Table 6.121.** The ANOVA results for measured hole diameter during drilling of forged CW617N with 90° of plunging angle .....222

**Table 6.122.** The developed regression model for drilling of forged CW617N with 90°

of plunging angle .....222

**Table 6.123.** The ANOVA results for measured forces in X direction (Fx) during drilling of forged CW617N with 60° of plunging angle .....223

**Table 6.124.** The ANOVA results for measured forces in Y direction (Fy) during drilling of forged CW617N with 60° of plunging angle .....224

**Table 6.125.** The ANOVA results for measured forces in Z direction (Fz) during drilling of forged CW617N with 60° of plunging angle .....224

**Table 6.126.** The ANOVA results for measured resultant forces (FR) during drilling of forged CW617N with 60° of plunging angle .....225

**Table 6.127.** The ANOVA results for measured burr heights at hole entry (BHEN) during drilling of forged CW617N with 60° of plunging angle .....226

**Table 6.128.** The ANOVA results for measured burr heights at hole exit (BHEX) during drilling of forged CW617N with 60° of plunging angle .....226

**Table 6.129.** The ANOVA results for measured surface roughness at hole bottom (Ra) during drilling of forged CW617N with 60° of plunging angle .....227

**Table 6.130.** The ANOVA results for measured surface roughness at hole wall (Ra) during drilling of forged CW617N with 60° of plunging angle .....228

**Table 6.131.** The ANOVA results for measured hole diameter during drilling of forged CW617N with 60° of plunging angle .....228

**Table 6.132.** The developed regression model for drilling of forged CW617N with 60° of plunging angle .....229

**Table 6.133.** The ANOVA results for measured forces in X direction (Fx) during drilling of forged CW617N with 45° of plunging angle .....230

**Table 6.134.** The ANOVA results for measured forces in Y direction (Fy) during drilling of forged CW617N with 45° of plunging angle .....230

**Table 6.135.** The ANOVA results for measured forces in Z direction (Fz) during drilling of forged CW617N with 45° of plunging angle .....231

**Table 6.136.** The ANOVA results for measured resultant forces (FR) during drilling of

forged CW617N with 45° of plunging angle .....231

**Table 6.137.** The ANOVA results for measured burr heights at hole entry (BHEN) during drilling of forged CW617N with 45° of plunging angle .....232

**Table 6.138.** The ANOVA results for measured burr heights at hole exit (BHEX) during drilling of forged CW617N with 45° of plunging angle .....233

**Table 6.139.** The ANOVA results for measured surface roughness at hole bottom (Ra) during drilling of forged CW617N with 45° of plunging angle .....233

**Table 6.140.** The ANOVA results for measured surface roughness at hole wall (Ra) during drilling of forged CW617N with 45° of plunging angle .....234

**Table 6.141.** The ANOVA results for measured hole diameter during drilling of forged CW617N with 45° of plunging angle .....234

**Table 6.142.** The developed regression model for drilling of forged CW617N with 45° of plunging angle .....235

**Table 6.143.** The ANOVA results for measured forces in X direction (Fx) during drilling of forged CW511L with 90° of plunging angle .....236

**Table 6.144.** The ANOVA results for measured forces in Y direction (Fy) during drilling of forged CW511L with 90° of plunging angle .....237

**Table 6.145.** The ANOVA results for measured forces in Z direction (Fz) during drilling of forged CW511L with 90° of plunging angle .....238

**Table 6.146.** The ANOVA results for measured resultant forces (FR) during drilling of forged CW511L with 90° of plunging angle .....239

**Table 6.147.** The ANOVA results for measured burr heights at hole entry (BHEN) during drilling of forged CW511L with 90° of plunging angle .....239

**Table 6.148.** The ANOVA results for measured burr heights at hole exit (BHEX) during drilling of forged CW511L with 90° of plunging angle .....240

**Table 6.149.** The ANOVA results for measured surface roughness at hole bottom (Ra) during drilling of forged CW511L with 90° of plunging angle .....241

**Table 6.150.** The ANOVA results for measured surface roughness at hole wall (Ra)

during drilling of forged CW511L with 90° of plunging angle .....241

**Table 6.151.** The ANOVA results for measured hole diameter during drilling of forged CW511L with 90° of plunging angle .....242

**Table 6.152.** The developed regression model for drilling of forged CW511L with 90° of plunging angle .....243

**Table 6.153.** The ANOVA results for measured forces in X direction (Fx) during drilling of forged CW511L with 60° of plunging angle .....244

**Table 6.154.** The ANOVA results for measured forces in Y direction (Fy) during drilling of forged CW511L with 60° of plunging angle .....245

**Table 6.155.** The ANOVA results for measured forces in Z direction (Fz) during drilling of forged CW511L with 60° of plunging angle .....245

**Table 6.156.** The ANOVA results for measured resultant forces (FR) during drilling of forged CW511L with 60° of plunging angle .....246

**Table 6.157.** The ANOVA results for measured burr heights at hole entry (BHEN) during drilling of forged CW511L with 60° of plunging angle .....247

**Table 6.158.** The ANOVA results for measured burr heights at hole exit (BHEX) during drilling of forged CW511L with 60° of plunging angle .....247

**Table 6.159.** The ANOVA results for measured surface roughness at hole bottom (Ra) during drilling of forged CW511L with 60° of plunging angle .....248

**Table 6.160.** The ANOVA results for measured surface roughness at hole wall (Ra) during drilling of forged CW511L with 60° of plunging angle .....249

**Table 6.161.** The ANOVA results for measured hole diameter during drilling of forged CW511L with 60° of plunging angle .....249

**Table 6.162.** The developed regression model for drilling of forged CW511L with 60° of plunging angle .....250

**Table 6.163.** The ANOVA results for measured forces in X direction (Fx) during drilling of forged CW511L with 45° of plunging angle .....251

**Table 6.164.** The ANOVA results for measured forces in Y direction (Fy) during drilling

of forged CW511L with 45° of plunging angle .....251

**Table 6.165.** The ANOVA results for measured forces in Z direction (Fz) during drilling of forged CW511L with 45° of plunging angle .....252

**Table 6.166.** The ANOVA results for measured resultant forces (FR) during drilling of forged CW511L with 45° of plunging angle .....253

**Table 6.167.** The ANOVA results for measured burr heights at hole entry (BHEN) during drilling of forged CW511L with 45° of plunging angle .....253

**Table 6.168.** The ANOVA results for measured burr heights at hole exit (BHEX) during drilling of forged CW511L with 45° of plunging angle .....254

**Table 6.169.** The ANOVA results for measured surface roughness at hole bottom (Ra) during drilling of forged CW511L with 45° of plunging angle .....255

**Table 6.170.** The ANOVA results for measured surface roughness at hole wall (Ra) during drilling of forged CW511L with 45° of plunging angle .....256

**Table 6.171.** The ANOVA results for measured hole diameter during drilling of forged CW511L with 45° of plunging angle .....256

**Table 6.172.** The developed regression model for drilling of forged CW511L with 45° of plunging angle .....257

**Table 6.173.** The ANOVA results for measured forces in X direction (Fx) during drilling of forged CW724R with 90° of plunging angle .....258

**Table 6.174.** The ANOVA results for measured forces in Y direction (Fy) during drilling of forged CW724R with 90° of plunging angle .....259

**Table 6.175.** The ANOVA results for measured forces in Z direction (Fz) during drilling of forged CW724R with 90° of plunging angle .....260

**Table 6.176.** The ANOVA results for measured resultant forces (FR) during drilling of forged CW724R with 90° of plunging angle .....260

**Table 6.177.** The ANOVA results for measured burr heights at hole entry (BHEN) during drilling of forged CW724R with 90° of plunging angle .....261

**Table 6.178.** The ANOVA results for measured burr heights at hole exit (BHEX) during

drilling of forged CW724R with 90° of plunging angle .....261

**Table 6.179.** The ANOVA results for measured surface roughness at hole bottom (Ra) during drilling of forged CW724R with 90° of plunging angle .....262

**Table 6.180.** The ANOVA results for measured surface roughness at hole wall (Ra) during drilling of forged CW724R with 90° of plunging angle .....263

**Table 6.181.** The ANOVA results for measured hole diameter during drilling of forged CW724R with 90° of plunging angle .....263

**Table 6.182.** The developed regression model for drilling of forged CW724R with 90° of plunging angle .....264

**Table 6.183.** The ANOVA results for measured forces in X direction (Fx) during drilling of forged CW724R with 60° of plunging angle .....265

**Table 6.184.** The ANOVA results for measured forces in Y direction (Fy) during drilling of forged CW724R with 60° of plunging angle .....266

**Table 6.185.** The ANOVA results for measured forces in Z direction (Fz) during drilling of forged CW724R with 60° of plunging angle .....266

**Table 6.186.** The ANOVA results for measured resultant forces (FR) during drilling of forged CW724R with 60° of plunging angle .....267

**Table 6.187.** The ANOVA results for measured burr heights at hole entry (BHEN) during drilling of forged CW724R with 60° of plunging angle .....268

**Table 6.188.** The ANOVA results for measured burr heights at hole exit (BHEX) during drilling of forged CW724R with 60° of plunging angle .....268

**Table 6.189.** The ANOVA results for measured surface roughness at hole bottom (Ra) during drilling of forged CW724R with 60° of plunging angle .....269

**Table 6.190.** The ANOVA results for measured surface roughness at hole wall (Ra) during drilling of forged CW724R with 60° of plunging angle .....270

**Table 6.191.** The ANOVA results for measured hole diameter during drilling of forged CW724R with 60° of plunging angle .....270

**Table 6.192.** The developed regression model for drilling of forged CW724R with 60° of

plunging angle .....271

**Table 6.193.** The ANOVA results for measured forces in X direction (Fx) during drilling of forged CW724R with 45° of plunging angle .....272

**Table 6.194.** The ANOVA results for measured forces in Y direction (Fy) during drilling of forged CW724R with 45° of plunging angle .....272

**Table 6.195.** The ANOVA results for measured forces in Z direction (Fz) during drilling of forged CW724R with 45° of plunging angle .....273

**Table 6.196.** The ANOVA results for measured resultant forces (FR) during drilling of forged CW724R with 45° of plunging angle .....273

**Table 6.197.** The ANOVA results for measured burr heights at hole entry (BHEN) during drilling of forged CW724R with 45° of plunging angle .....274

**Table 6.198.** The ANOVA results for measured burr heights at hole exit (BHEX) during drilling of forged CW724R with 45° of plunging angle .....275

**Table 6.199.** The ANOVA results for measured surface roughness at hole bottom (Ra) during drilling of forged CW724R with 45° of plunging angle .....275

**Table 6.200.** The ANOVA results for measured surface roughness at hole wall (Ra) during drilling of forged CW724R with 45° of plunging angle .....276

**Table 6.201.** The ANOVA results for measured hole diameter during drilling of forged CW724R with 45° of plunging angle .....277

**Table 6.202.** The developed regression model for drilling of forged CW724R with 45° of plunging angle .....278

**Table 7.1.** Technical specifications of Raptor coating .....283

**Table 7.2.** Technical specifications of AlTiCN coating .....283

**Table 7.3.** Technical specifications of CrN coating .....284

**Table 7.4.** Obtained results extruded CW617N at 90° of plunging angle .....284

**Table 7.5.** Obtained results extruded CW617N at 60° of plunging angle .....284

**Table 7.6.** Obtained results extruded CW617N at 45° of plunging angle .....284

**Table 7.7.** Obtained results extruded CW511L at 90° of plunging angle .....285

**Table 7.8.** Obtained results extruded CW511L at 60° of plunging angle .....285

**Table 7.9.** Obtained results extruded CW511L at 45° of plunging angle .....285

**Table 7.10.** Obtained results extruded CW724R at 90° of plunging angle .....285

**Table 7.11.** Obtained results extruded CW617N at 60° of plunging angle .....285

**Table 7.12.** Obtained results extruded CW617N at 45° of plunging angle .....286

**Table 7.13.** Obtained results foged+annealed CW617N at 90° of plunging angle ….....286

**Table 7.14.** Obtained results foged+annealed CW617N at 60° of plunging angle .....286

**Table 7.15.** Obtained results foged+annealed CW617N at 45° of plunging angle .....286

**Table 7.16.** Obtained results foged+annealed CW511L at 90° of plunging angle .....287

**Table 7.17.** Obtained results foged+annealed CW511L at 60° of plunging angle .....287

**Table 7.18.** Obtained results foged+annealed CW511L at 45° of plunging angle .....287

**Table 7.19.** Obtained results foged+annealed CW724R at 90° of plunging angle .....287

**Table 7.20.** Obtained results foged+annealed CW724R at 60° of plunging angle .....287

**Table 7.21.** Obtained results foged+annealed CW724R at 45° of plunging angle ….....288

**Table 8.1.** The utilized linguistic coding for the developed model .....291

**Table 8.2.** The developed regression model .....295

**Table 8.3.** The obtained experimental and model results .....295

**Table 8.4.** Measured experimental results .....299

# 1. INTRODUCTION

Brass materials are within the group of copper-based alloys. These materials are widely recognized for having outstanding qualities including high strength, ductility, wear and corrosion resistance, hardness, high thermal and electric conductivity, recyclability, anti-bacterial, sanitary, and also acceptable machinability and formability. Brass alloys are widely utilized in a variety of industries, including the electrical and electronic, automotive, irrigation, pumping/plumbing, and sterile industries [1].

The mechanical and metallurgical (corrosion) characteristics, crystal structure, chemical composition content, and alloying element percentages are used to classify brass materials. Zinc is used as the primary alloying element in the copper-based alloys' chemical composition. Therefore, it can be concluded that brass is the generic abstraction form of copper-zinc alloy. Brass alloys are composed in a single phase when they contain up to 35% zinc and display high strength, ductility, and forming is even possible with cold work. However, when zinc concentration is between 32% and 39%, the material exhibits superior hot working and machinability features. In this case, the cold workability of the brass is limited, and the material is constituted from a dual phase structure (α-β, α-γ) [2, 3]. Withal, the material exhibits higher strength but lower ductility at room temperature when the Zinc is higher than 39% [2, 3]. The brasses have a microstructure with almost 39% zinc comprising α dendrites along with β surrounding the dendrites. A Widmanstatten structure is formed when the material is cooled slowly resulting in the α precipitating out of the solution at the crystal boundaries [3]. Brasses that contain in excess of 45% zinc, known as white/β brasses, are neither hot nor cold formable. However, a granulated structure is utilized in brazing (soldering); they likewise structure the reason for certain alloys utilized in die-casting [4]. These brasses are less ductile but stronger and thus are suitable for the manufacture of faucet handles, sprinkler heads, window and door fittings, and other fixtures [4]. Furthermore, depending on the Zinc element percentage the color of the brass alloys varies and new branches of categorization such as yellow/golden, red and cartridge brass is formed. Single phase brasses are used for producing fasteners, wood screws and spring contacts. Figure 1.1 demonstrates the Cu-Zn phase diagram for different temperatures.

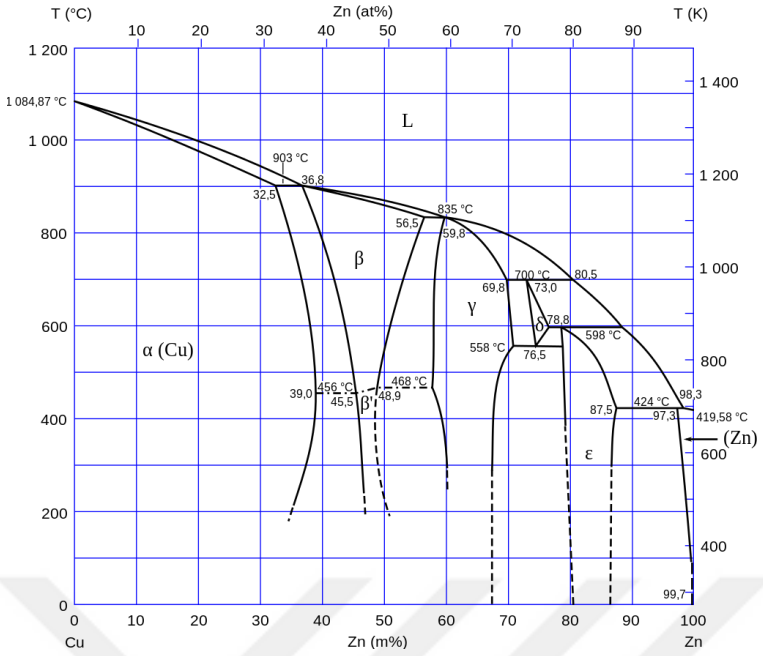


**Figure 1.1.** Cu-Zn phase diagram [5]

It is worth mentioning that the lattice structure of α, β, β` and γ phases are Face-Centered Cubic (FCC), Body-Centered Cubic (BCC), BCC and intermetallic brittle complex, respectively. Hence, it is concluded that the β phase is much harder and less formable as compared to α [6]. Moreover, the machinability of the brass alloys improves with the increase of the β phase in the microstructure whereas the dezincification and corrosion resistance deteriorate [6, 7]. In excess of the mentioned phases, dependent to the alloying elements different phases such as brittle and highly abrasive κ can be found in the microstructure due to the existence of Silicon [6].

Besides Zinc content, addition of elements such as Lead, Sulfur, Aluminum, Silisium, Silicon, Arsenic, Bismuth, Tin, Iron, Tellurium, Manganese, Nickel, etc. is carried out in order to change the microstructure of the material for different purposes including machinability or corrosion resistance enhancement depending on the applications [8-11]. In order to increase the dezincification resistance, Arsenic is being added to brass alloys [12-14]. However, this benefit is lost even by poor heat treatments [15]. Thanks to the low solubility of Lead, it can isolate in the whole microstructure and grain boundaries. In addition, having low, 327.5 °C, of melting temperature concludes in executing of Lead as a lubricant during machining [1, 16]. Accordingly, the rise of Lead amount is considered as bringing about sufficient machinability through further developing the chip breaking,

reducing the cutting forces, diminishing the tool wear, just as giving better surface roughness and tolerances. [1, 16]. While all of these elements result in improvement in any of the desired properties, some of them including Lead and Arsenic are toxic and contain human health and ecological hazards. For this reason, the first regulations in the usage of Lead element in drinking water systems for both municipalities and rural water districts was established in 1996 namely, The Safe Drinking Water Act (SDWA) in U.S. Under the Act, EPA also establishes minimum standards for state programs to protect underground sources of drinking water from endangerment by minimizing chemical and bacterial contaminants in drinking water [17]. Soon after, the Restriction of Hazardous Substances directive (RoHS) constituted legislations on the use and production of lead-free materials were in Europe [18, 19]. According to these restrictions, plumbing fittings, fixtures, faucets, drinking fountains, water coolers and other drinking water conveyance devices must pass standard control measures regulations [17-19]. Furthermore, new compulsions are being published by minimizing the amount of these elements in the chemical composition of the brass alloys. Taking into consideration all of these restrictions, the need for developing new types of brass alloys in which the mentioned toxic elements have been minimized is being intensified. Therefore, low-lead and lead-free brass alloys are being at the point of attraction as alternatives for conventional ones. Meanwhile, being aware of that a huge scale of all the brass products need to be machined to their designed final shape. These tasks frequently include cutting operations of many kinds, such as milling, turning, drilling, grinding, etc. [1, 16, 19]. Accordingly, in order to subject low-lead and lead-free brass alloys to machining operation, comprehensive studies including mechanical, metallurgical properties and machinability should be carried out.

In this context, several researchers have evaluated the machinability of lead-free brasses by altering the other elements content such as Si and Al [20]. Imai et al. [21] investigated the influences of the dispersed graphite and bismuth particles in the brass alloying compositions by focusing on the machinability and mechanical properties of the extruded lead-free brass alloys. By adding the mixed powder containing 0.5 wt.% graphite particles and 2.2 wt.% Bi, a lead-free machinable brass (CuZn40) was obtained which exhibits good balance between the elongation and the machinability. They claimed that the combination of bismuth and graphite particles improved the elongation and machinability of brass alloys in comparison to brass that included solely those two materials. In another work

[22], with the purpose of producing a lead-free machinable brass dispersed with graphite particles by powder metallurgy process, the characteristics and machinability of lead-free P/M Cu60–Zn40 brass alloys dispersed with graphite was investigated. According to the results of this study, a reduction in the weight of the brass powder was obtained with increasing the heat treatment temperature over 873 °K by vaporized zinc. Moreover, according to Kirkendall effect risen from the difference of diffusion velocity between Cu and Zn in the brass powder surface voids were observed. Schultheiss et al. [23] conducted a comparative study on the machinability of the CuZn39Pb3 brass with the commercially available CuZn21Si3P lead-free alternative. They carried out longitudinal turning using cemented carbides tools. To evaluate the potential for tool life improvements, they also run experiments on CuZn21Si3P using different tool coatings. Klocke et al. [24] investigated the influence of the coating type including TiN, TiAlN, TiB2 and DLC on carbide tools besides using polycrystalline diamond (PCD) tools on cutting forces, chip formation and workpiece quality during machining of CuZn38As, CuZn42, and CuZn21Si3P. According to their obtained results, when using a diamond-like carbon coating on the tool, the friction in the secondary shear zone was reduced and the machining problems were abated. Nobel et al. [25] studied the machinability of CW724R, CW508L, CW511L, CW510L, CW510L (W), and CW614N brasses in terms of the influences of the material microstructure and silicon content during external turning operations. In their study, different tool coatings, PCD tools and high-pressure coolants were taken into consideration. Upon their results, PCD tools demonstrated high abrasion resistance and low adhesion tendency as well as the possibility to achieve sharp cutting edges. In order to abstain formation of long chips especially in continuous cutting operations like turning, they recommended using inserts possessing chip breaking geometries. The friction conditions between low-leaded brass alloys (CuZn38As, CuZn42 and CuZn21Si3P) were analyzed and compared to the high-leaded free-cutting brass CuZn39Pb3 using uncoated, TiB2 and DLC, TaC coated carbide tools by Nobel et al. [25]. They also focused on the effect of low lead contents ranging from Pb=0.003–0.19% on friction and compared the achieved results with high lead content of Pb=1.9%. They observed a significant role of Pb amount in the frictional behavior of the materials. A comparative study was carried out on the machinability of leaded (CuZn39Pb3) and lead-free brass (CuZn21Si3P) alloys focus on the tool wear during machining by Schultheiss et al. [23]. Higher cutting forces,

longer chips and, ultimately, higher tool-wear rates using cemented carbides was experienced when machining of CuZn21Si3P lead-free brass alloy. Ti, V, Zr, Hf, Nb, TaN coatings were recommended to avoid higher tool wear rates. Several studies [26-28] considered the influence of existent lead element in brass alloys on friction conditions performing pin-on-disc tribometer tests. Notwithstanding, these tests were described by a few deficiencies. Most importantly, steel alloys were applied as friction accomplices. However, steel does not address the present cutting tools material. Additionally, the contact forces, process temperatures and relative speeds were altogether beneath the qualities that are generated and applied in a cutting. Additionally, pin-on-disk tribometer have the overall detriment that the contact surface is not completely mathematically characterized because of point, line, or circular contact in combination with plastic deformation of the softer material. Consequently, the direction of the generated forces cannot be resolved unequivocally. Toulfatzis et al. [29] conducted heat treatments in CuZn42, CuZn38As and CuZn36 lead-free brass alloys to modify the microstructure and increase the β-phase percentage for an exceeding chip breakability and enhanced machinability while keeping the mechanical properties of the brass within the EN standard, since β-phase augmentation can result in embrittlement. They prepared 27 heat treatment protocols for modifying the microstructure and material properties of the mentioned lead-free brasses. The best heat treatment was picked for each concentrated-on alloy as indicated by the above measurements. The chose conventions prompted a combination of β-phase expansion with mechanical properties adjusting to principles giving a promising ground to further developed machinability execution. According to Sundberg et al. [30], with careful heat treatment, skipping the precipitation of both β-phase and arsenide particles is possible. Brasses containing arsenic are appropriately associated as dezincification resistant brass alloys. In order to improve the machinability of extruded and drawn lead-free brasses, namely, CW510L, CW511L, and C27450, Toulfatzis et al. [31] carried out heat treatments based on the concept of microstructural modification. They selected heat treatment condition sets for CW510L (775 °C for 60 min), CW511L (850 °C for 120 min), and C27450 (850 °C for 120 min). They investigated the machinability considering chip morphology, power consumption, cutting force, and surface roughness in turning of as received and heat-treated specimens. According to their results, heat treatment led to a marginal reduction in cutting forces of CW510L and CW511L. The

surface roughness (Ra) was not affected by heat treatment. Atay [32] studied the machinability of the forged and cryogenically treated CW511L with different contents of Cu. According to him, for the samples cryogenic treated and annealed after the forging process, the desired dimensional accuracy and quality properties can be achieved facilitating the machinability depending on the cutting forces in machining, and desired outputs can be obtained. The corrosion–microstructure interrelations in low-lead CW625N, CW626N, and lead-free CW511L brass alloys was investigated by Stålnacke et al. [15]. According to their research, the loss of corrosion resistance was only the most severe for alloys with higher aluminum and iron content. These alloys showed significant precipitation of intermetallic aluminum arsenide particles on grain boundaries, twins and lead particles, as well as the formation of β phase along grain boundaries. Zoghipour et al. [1] studied the effect of drilling process on surface integrity characteristics of CW511L brass alloy by focusing on dimensional accuracy and the surface quality of the holes, subsurface characteristics including microhardness and microstructure. Their results revealed that cutting tools have strong influence on both microstructural aspects of lead-free alloy and resulting to hardening of the surface and subsurface along with deformation twinning. Aytekin [33] carried out a comprehensive study has been conducted to characterize the machinability of lead-free brass alloys by evaluating the cutting forces and chip formation during turning and drilling. The purpose of his turning experiments was to characterize the machinability by comparing two lead-free alloys (CW511L and AquaNordic®) with a leaded alloy (CW625N), whereas he aimed to characterize machinability of the lead-free AquaNordic® alloy, with the focus on the impact of tool geometry on machinability in drilling tests. According to his results, when turning of lead-free alloys higher cutting forces are generated than to the leaded. Yet, no significant difference between the two lead-free alloys regarding the cutting forces was obtained while the chip formation enhanced for AquaNordic. Furthermore, from the conducted drilling experiments, he concluded that by increasing the tool rake angle and decreasing tool diameter, the machinability of the lead-free AquaNordic alloy can be augmented. The machinability of the leaded CuZn39Pb3 brass as compared to the lead-free alternative CuZn21Si3P was studied by Schultheiss et al. [23]. They reported significantly higher tool wear and cutting forces in machining of CuZn21Si3P as compared to CuZn39Pb3 under similar conditions. Atsumi et al. [34] obtained compromising results when machining lead-

free Cu40ZnCrFeSnBi alloy as compared to the leaded alternative. According to them, using alloying elements such as Bi and Ti which have higher prices as compared to Pb, is a magnificent obstacle in discouraging the lead-free brass alloy to become widespread. However, due to the availability and abundant supply of Si in the world, it can be considered as reasonable alternative for Pb in brass industry [35]. Amaral1 et al. [36] studied the machinability characterization of leaded, medium leaded and minimally leaded brass alloys running external turning with polycrystalline diamond inserts. They focused on the evaluation of the cutting forces, chip morphology and surface roughness besides microstructural and mechanical characterization. Results have demonstrated that with the reduction in Pb, higher cutting forces and longer chips are achieved. Tam et al. [37] compared the machinability of lead-free and free machining brasses by face turning tests and investigated the cutting forces besides the machining residual stresses. Lead-free brass alloy demonstrated higher strength and lower residual stresses. The mechanical behavior under static and dynamic loading of CW510L-CW511L-C27450 lead-free brass alloys in comparison to CW614N was investigated by Toulfatzis et al. [29]. In order to determine the involved fracture mechanisms and their relation to the alloy microstructure, they carried out fractographic evaluation of the texture of conjugate fracture surfaces. According to their achieved results, due to the prevalence of β phase in the microstructure of CW510L, it seems to be a potential candidate in replacing conventional CW614N, combining high tensile strength and fracture toughness. Cicek et al. [38] designed two teeth form brazed carbide boring tools with different geometries in terms of radial rake angle and cutting-edge radius and evaluated them for the purpose of high-performance boring process of CuZN40Pb2 brass alloy in mass production. In this study, they applied drag finishing to enhance the edge radius of brazed carbide cutting tools for better surface quality of machined parts. Tascioglu et al. [39] studied the machining performance, and subsurface properties in terms of cutting forces, cutting temperatures, surface quality, subsurface microhardness and microstructures of leaded (CW617N), low-leaded (CW511L) and lead-free (CW724R) brasses. According to their results, higher subsurface deformation was observed in low-leaded and lead-free brass materials compared to leaded brass materials. Zoghipour et al. [40] investigated the machining performance of lead-free, low-lead and leaded brass alloys in terms of cutting forces, surface roughness, and burr height during milling operations. Moreover, they took the edge radius of cutting tools and

its role on machining the performance into account. Empirical equations were derived to predict the machining behavior for each material. Their results revealed that increasing the edge radius results in larger cutting forces and tool vibration during the process, but better surface quality. Furthermore, reduction/elimination of the Lead element in alloy content concludes into higher burr size on the machined surface edges. To define the machinability parameters including depth of cut, and the feed rate and to obtain their optimum values for high-performance machining, Taguchi technique was used by Toulfatzis et al. [41] in turning of CW510L, CW511L and C27450 lead-free brass alloys, compared with a leaded brass CW614N. cutting force and surface roughness was taken into consideration to be optimized. Various cutting responses such as machining time, cutting forces, metal removal rate, and dimensional accuracy during the rough pocket milling of the lead-free brass alloys with various toolpath strategies has been studied by Zoghipour et. al [42]. The optimization was carried out using the desirability function (DF) and Genetic algorithms-based analysis (GA). The optimization resulted in minimum production time, cutting forces, dimensional accuracy error and maximum material removal rate considering technological and industrial constraints. Fountas et al. [43] studied the influences of cutting conditions on the cutting force and surface roughness parameters Ra and Rt in turning of CuZn39Pb3. Moreover, they implemented artificial grey wolf optimization algorithm for optimization of the responses. Zoghipour et al. [7] addressed data on cutting forces, dimensional accuracy, and surface quality of the holes drilling process using form cutting tools with different geometries, feed rates and rotational speeds on hot forged lead-free brass alloys with various copper content. In order to predict and optimize the machining process and related responses, artificial neural networks modelling, and genetic algorithm-based optimization methods were used. The computational results demonstrated that the developed model and optimization procedure can notably improve the efficiency of the process by reducing the production cost with the obtained optimum machining conditions.

Following the previous conducted researches as well as the upgrading needs in modern industry, besides the significance of human health and ecological environment, it is completely indisputable that low-lead and lead-free brasses are being prevail as compared to the conventional ones. Therefore, the need for a deep knowledge of these materials as well as their machining with newly developed cutting tools is being a deal for the manufacturers to keep the pace in the industrial competition. Furthermore, considering the

literature, it is seen that most of the research has been carried out on general, standard and simple machining processes such as turning. Thus, in order to fill the gap in the literature as well as developing a know-how meeting the industrial needs, three type of available brasses in EUA7038 (Brass for European Potable Water Applications List) leaded (CW617N), low-leaded (CW511L) and lead-free (CW724R) brasses has been taken into consideration when drilling with flat bottom drill tools. Analytical and experimental methods have been utilized for calculating the cutting forces and torques during plunging to an inclined workpiece as well as plunging to a flat surface. Cutting tools with different geometries and coatings have been designed and manufactured using ANCA tool room. And the machinability has been evaluated through measurements on the cutting forces, torques, entry and exit burr heights, surface roughness, diameters and microstructures. Moreover, modal analysis has been performed on the designed cutting tools using Finite Element Analysis methods.

# 2. EXPERIMENTAL METHODOLOGY

## 2.1 Mechanical and metallographic analysis

In this research, three different types of brass alloys consisted of leaded CuZn40Pb2 (CW617N), low-lead CuZn38As (CW511L), and lead-free CuZn21Si3P (CW724R) with a diameter 35 mm extruded bars were selected as the case study. The chemical composition and technical specifications of the mentioned materials are given in Table 2.1 and 2.2. The test materials have been subjected to spectrum analysis at metallography laboratory in Torun Copper Metal Alloys Inc. Ltd. Ind. in order to confirm the chemical composition and standard requirements as shown in Figure 2.1. The result of the spectrum analysis is given in Table 2.3.

**Table 2.1.** Chemical composition of the studied brass alloys [44]

| Composition | | Cu | Zn | Pb | Sn | Fe | Ni | Al | As | Mn | P | Si |
|---|---|---|---|---|---|---|---|---|---|---|---|---|
| CuZn40Pb2 (CW617N) | %Min. | 57.0 | Rem. | 1.6 | - | - | - | - | - | - | | - |
| | %Max. | 59.0 | Rem. | 2.5 | 0.3 | 0.3 | 0.3 | 0.05 | - | - | - | - |
| CuZn38As (CW511L) | %Min. | 61.5 | Rem. | - | - | - | - | - | 0.02 | - | - | - |
| | %Max. | 63.5 | Rem. | 0.2 | 0.1 | 0.1 | 0.3 | 0.05 | 0.15 | - | - | - |
| CuZn21Si3P (CW724R) | %Min. | 75.0 | Rem. | - | - | - | - | - | - | - | 0.02 | 2.7 |
| | %Max. | 77.0 | Rem. | 0.09 | 0.3 | 0.3 | 0.2 | 0.05 | - | 0.05 | 0.10 | 3.5 |

**Table 2.2.** Technical specifications of the as received (extruded) brass alloys

| Brass Alloy | Elasticity Module, (GPa) | Density ($g/cm^3$) | Electrical Conductivity, (MS/m) | Thermal Conductivity, (W/(m.K)) | Coe. of Thermal Expansion, ($10^{-6}$/K) | Melting Point, (°C) | Hot Forming, (°C) | Soft Annealing, (°C) | Soft Annealing Duration, (h) | Stress Relieving, (°C) | Stress Relieving Duration, (h) |
|---|---|---|---|---|---|---|---|---|---|---|---|
| CW617N | 96 | 8.43 | 14.9 | 113 | 21.1 | 880-895 | 650-800 | 450-600 | 1-3 | 200-300 | 1-3 |
| CW511L | 100 | 8.41 | 14.7 | 114 | 21.7 | 850-900 | 600-800 | 450-550 | 1-3 | 200-250 | 1-3 |
| CW724R | 100 | 8.25 | 4.5 | 35 | - | 680-750 | 530-650 | 450-550 | 1-3 | 200-300 | 1-3 |

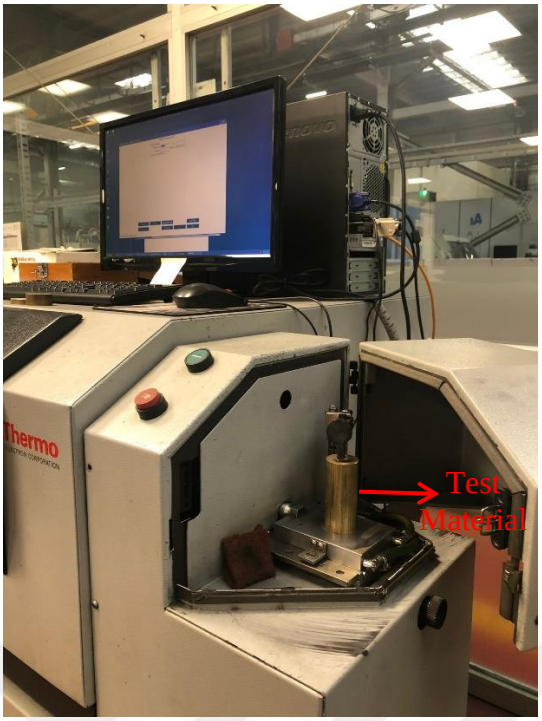


**Figure 2.1.** The used spectrum analysis device

**Table 2.3.** The results obtained for the chemical composition of the studied brass alloys

| Composition | CW617N | CW511L | CW724R |
|---|---|---|---|
| Cu | 57.4330 | 62.1040 | 76.0490 |
| Pb | 1.7030 | 0.1560 | 0.0620 |
| Al | 0.0110 | 0.0050 | 0.0030 |
| Fe | 0.0990 | 0.0050 | 0.0230 |
| As | 0.0070 | 0.0100 | 0.0001 |
| Mn | 0.0060 | 0.1000 | 0.0000 |
| Ni | 0.0270 | 0.0080 | 0.0050 |
| Sn | 0.0680 | 0.0040 | 0.0070 |
| S | 0.0020 | 0.0700 | 0.0020 |
| Cd | 0.0010 | 0.0020 | 0.0006 |
| P | 0.0040 | 0.0006 | 0.0540 |

| | | | |
|---|---|---|---|
| Si | 0.0040 | 0.0016 | 2.9000 |
| Sb | 0.0140 | 0.0043 | 0.0030 |
| Mg | 0.0010 | 0.0040 | 0.0004 |
| Bi | 0.0030 | 0.0030 | 0.0003 |
| Zn | 40.6100 | 37.5220 | 20.8840 |

Brass alloys are being utilized in pumping and watering systems as industrial applications. Therefore, high pressure endurance and strength is a requirement for these products. Thus, in order to meet this purpose, industrial brass components are generally manufactured by forging. In this thesis, besides the extruded bars, experiments have also been carried out on forged and annealed specimens. For this reason, a specimen which fulfills performing different sorts of machining tests such as drilling, boring, milling, turning, and a combination of the required dies and punches have been designed. Figure 2.2 demonstrates the designed geometry of the specimen and its forging die. The rods were cut into the billets of Ø35 mm and 86 mm in length, and then forged at 730±10 °C with a rate of 11 stroke/min under a 165 tons of press load in a Hydromec 550 eccentric press machine at forging department of Torun Copper Metal Alloys Inc. Ltd. Ind. Thereafter, the forged specimens were annealed at 550 °C for 150 minutes. Meanwhile, a design for forging a tensile test sample according to ASTM E8/E8M – 09 standards has been added to the dies. The billets for the tensile test were prepared as 20 and 120 mm in diameter and length, respectively. Subsequently, they were subjected to hot forging at 730±10 °C with 70 tons of press with a rate of 9 stroke/min. These specimens were annealed at the same conditions as mentioned before.

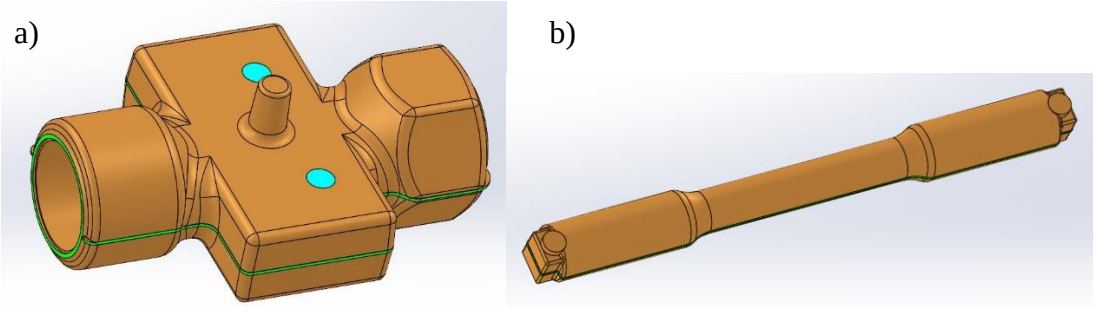


**Figure 2.2.** Designed forged specimen for; a) machining tests, b) tensile test.

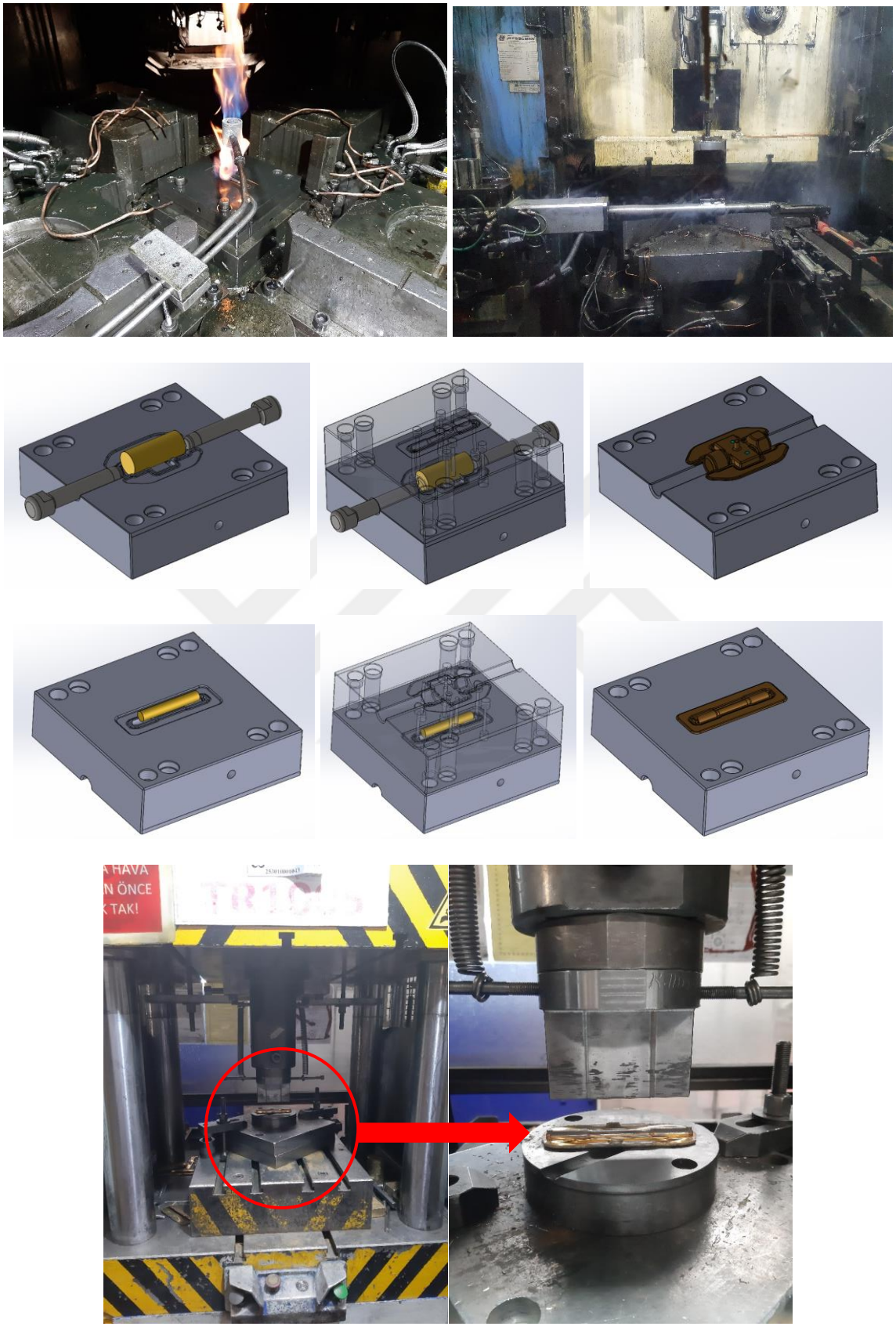

**Figure 2.3.** Hot forging procedure of the designed test specimens



**Figure 2.4.** Annealing images of the hot forged specimens

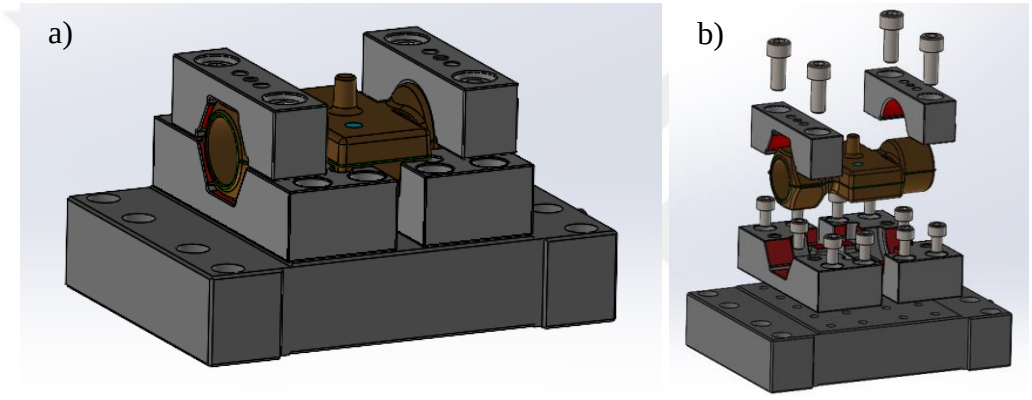


**Figure 2.5.** The design of the specimen and die sets used in this thesis; a) test specimen geometry, b) die and punch sets

## 2.2 Microstructure Analyses

In order to carry out microstructural studies on the brasses, the specimens were cut into small pieces. Then, they were subjected to bakelite and polishing operations with 500, 1000, 2000 sandpapers and 3 and 1 μm solution as shown in Figure 2.6 a, b, c. the microstructural analyses of the specimens performed by Keyence digital optical microscope and SEM (Scanning electron microscope) as demonstrated in Figure 2.6 d, e. Before analysis, the specimens were etched with 30 mL aqueous solution of H2O, 3.5 mL of H2O2 and 4.25 g (NH4)2S2O8 at room temperature for about 20 seconds, then were washed with alcohol and deionized water and dried again. The microstructural and phases of the extruded, extruded-annealed, forged and forged-annealed of CW617N, CW511L and CW724R brasses is demonstrated in Figure 2.7 and 2.8. According to the

microstructure analysis, it is seen that the leaded (CW617N) and low-lead brasses are formed of α and β phases. The Pb particles are also obvious in CW617N. However, the lead-free brass (CW724R) is formed of α, κ and γ phases. It is essential to note however the lattice structure of α is FCC (Face centered cubic), the β, γ and Si-rich κ phases are BCC (Body centered cubic), and hexagonal, respectively.

The phasic percentages of the mentioned brasses for extruded, extruded-annealed, forged and forged-annealed specimens are given in Table 2.4. An increase has been obtained in %β by forging in all types of CW617N and CW511L. However, an inverse relation is achieved by annealing on the mentioned alloys. The positive contribution of β to enhancement of machinability has been discussed by several authors [29, 31]. Furthermore, annealing leads to a less hard surface and tool wear. The amount of the γ is very low as compared to α and κ. Therefore, by measuring the %κ in the microstructure, we can conclude to that the %α has increased with annealing whereas it has been decreased by forging. The EDS analysis images are illustrated in Figure 2.9.

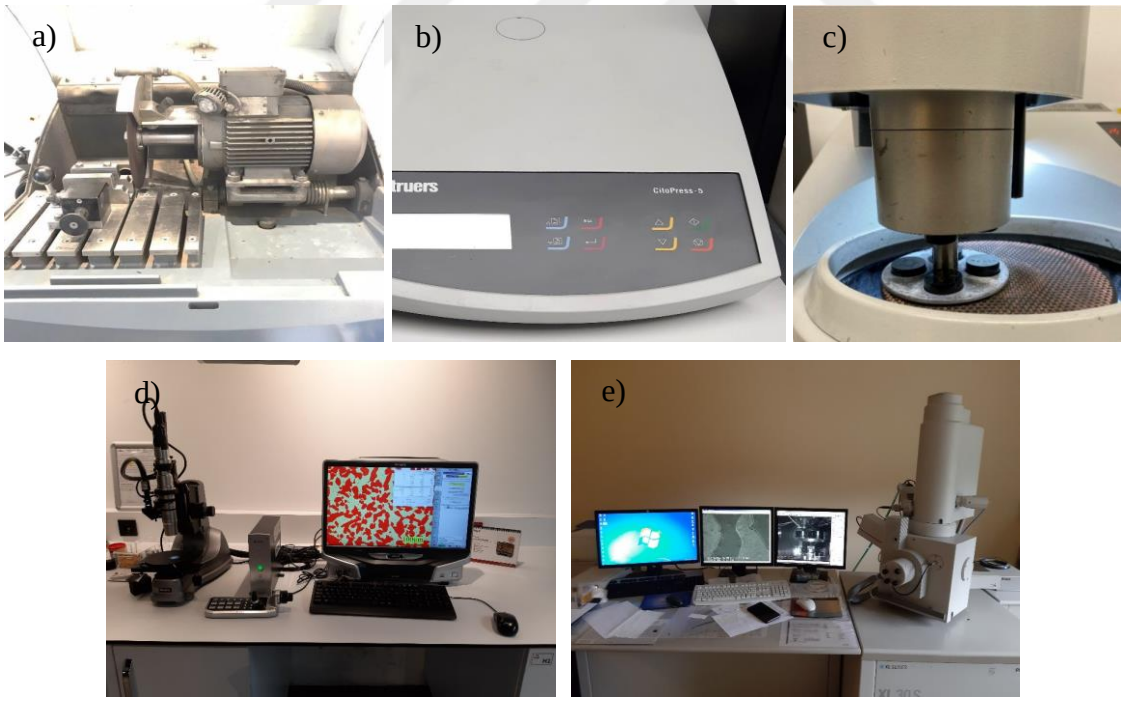


**Figure 0.6.** The utilized equipment in the microstructural analysis; a) accurate cutting, b) bakelite, c) polishing, d) optical microscope, e) SEM analyzes steps

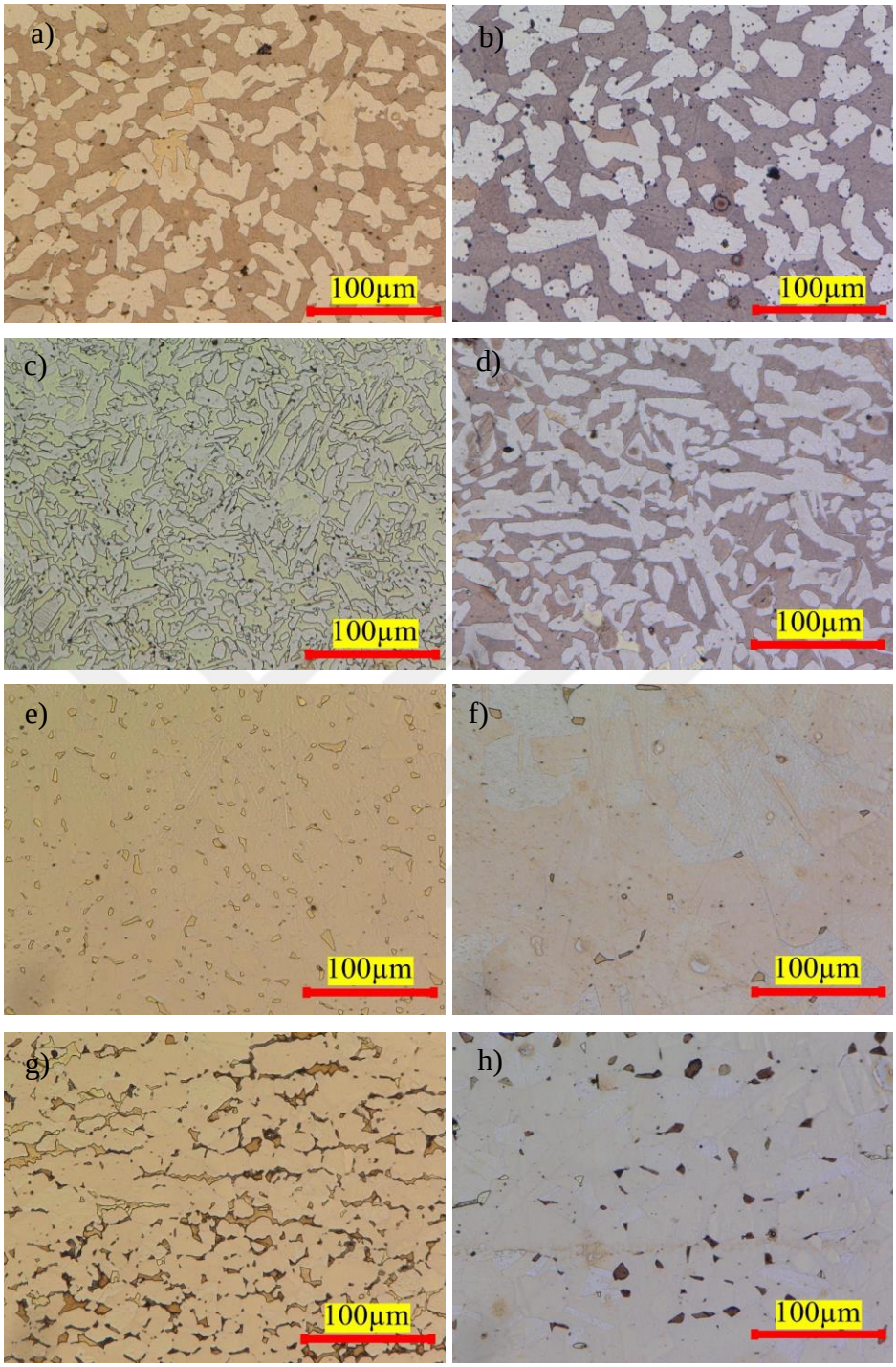
a)
100µm
b)
100µm
c)
100µm
d)
100µm
e)
100µm
f)
100µm
g)
100µm
h)
100µm

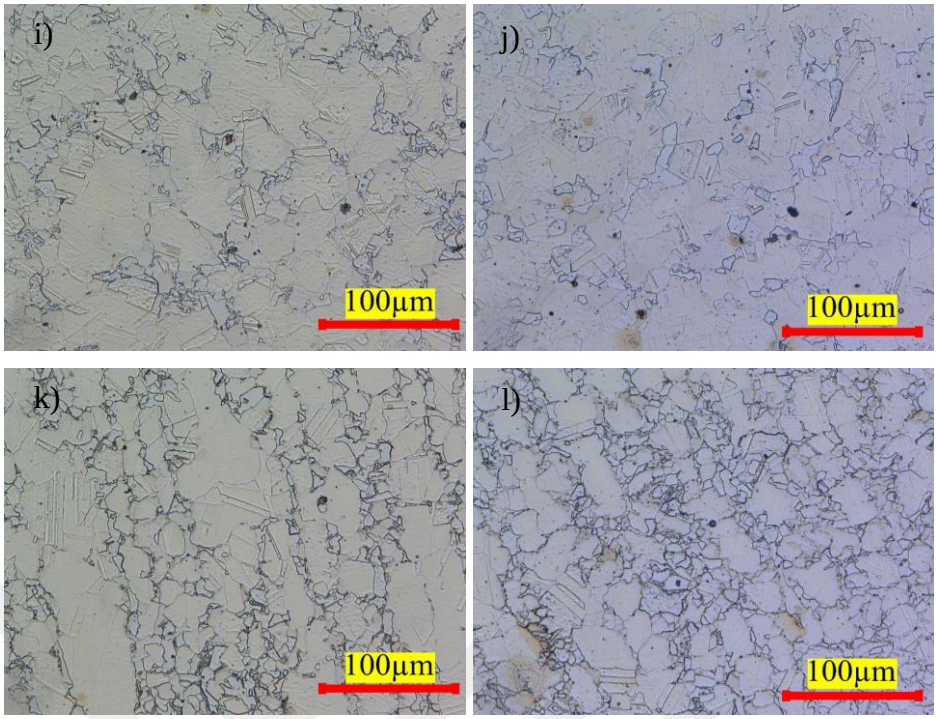


**Figure 2.7.** Optical images of the microstructure of, CW617N; a) extruded, b) extruded-annealed, c) forged, d) forgred-annealed, CW511L; e) extruded, f) extruded-annealed, g) forged, h) forgred-annealed, CW724R; i) extruded, j) extruded-annealed, k) forged, l) forgred-annealed.

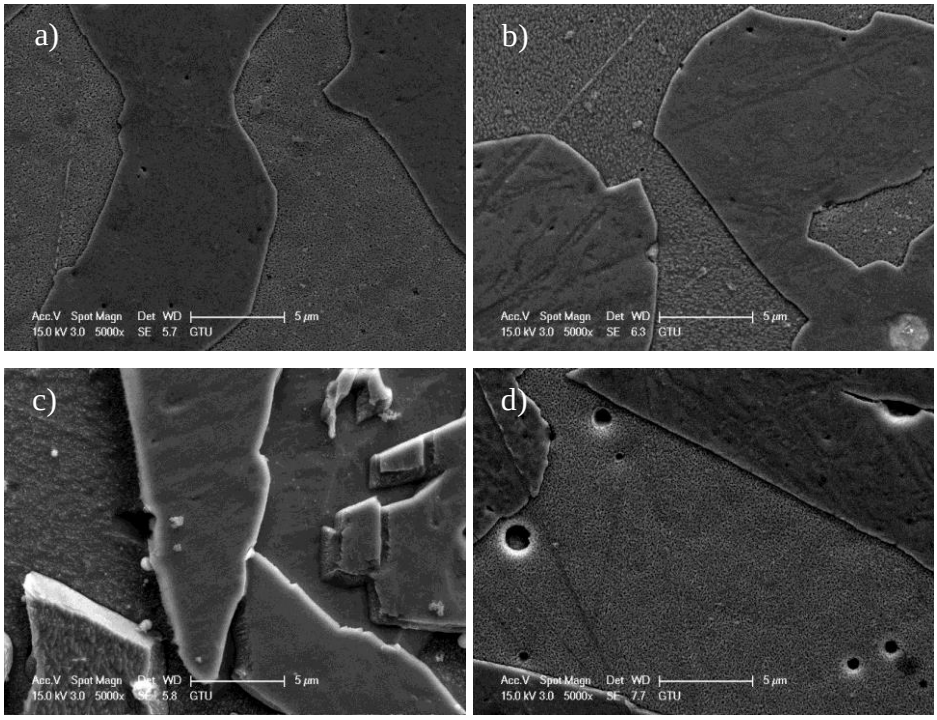

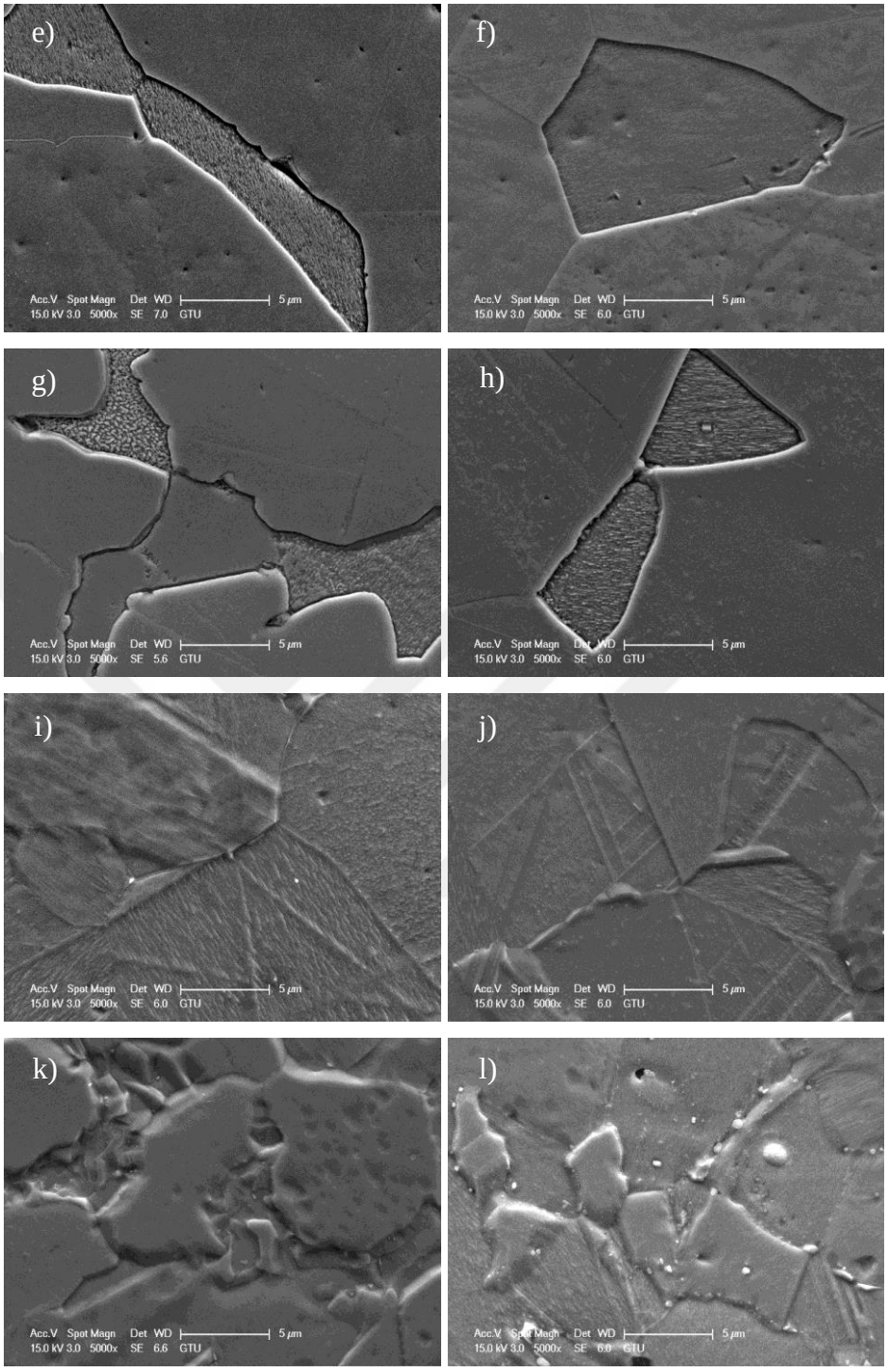


**Figure 2.8.** SEM images of the microstructure of, CW617N; a) extruded, b) extruded-annealed, c) forged, d) forgred-annealed, CW511L; e) extruded, f) extruded-annealed, g) forged, h) forgred-annealed, CW724R; i) extruded, j) extruded-annealed, k) forged, l) forgred-annealed.

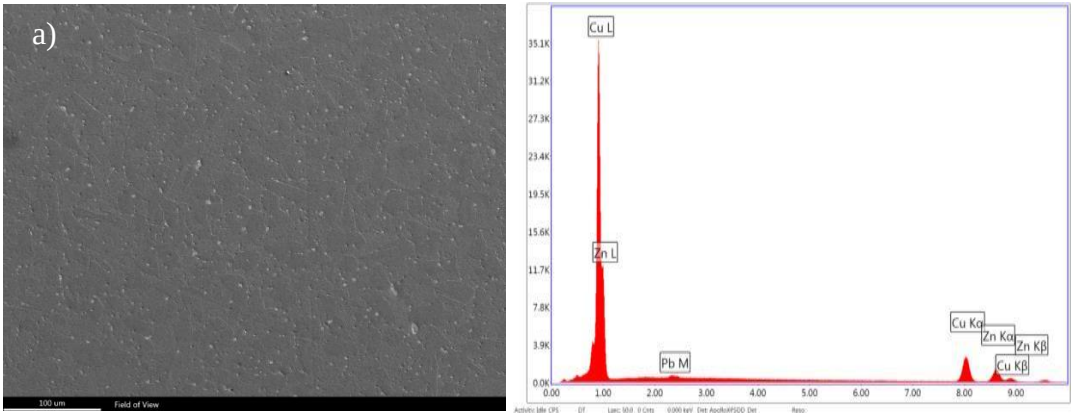
a)
100 um
Field of View
Cu L
Zn L
Pb M
Cu Kα
Zn Kα
Zn Kβ
Cu Kβ

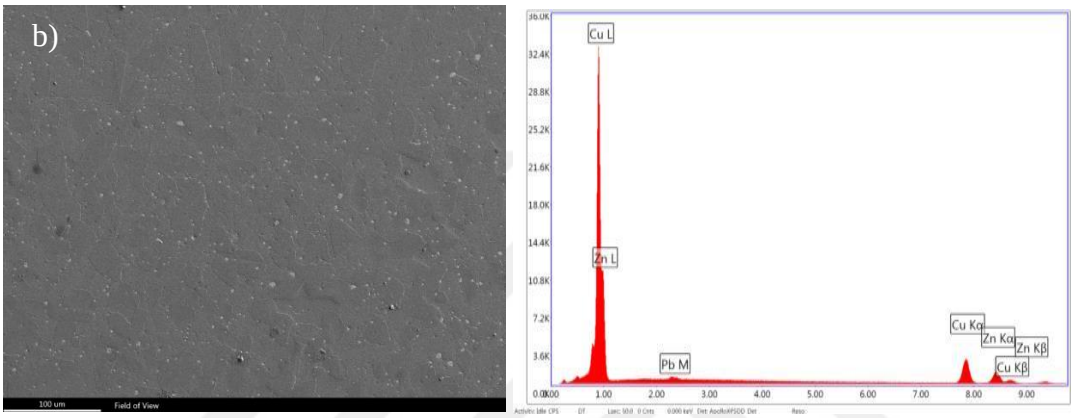
b)
100 um
Field of View
Cu L
Zn L
Pb M
Cu Kα
Zn Kα
Zn Kβ
Cu Kβ

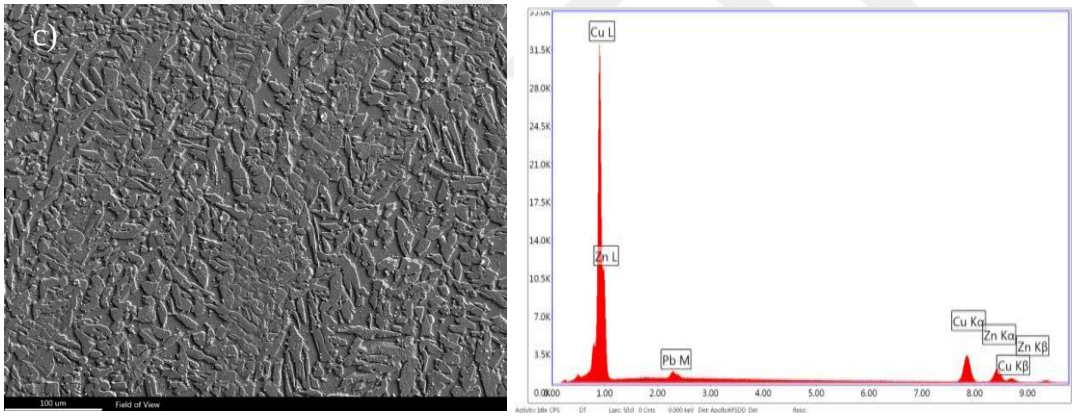
c)
100 um
Field of View
Cu L
Zn L
Pb M
Cu Kα
Zn Kα
Zn Kβ
Cu Kβ

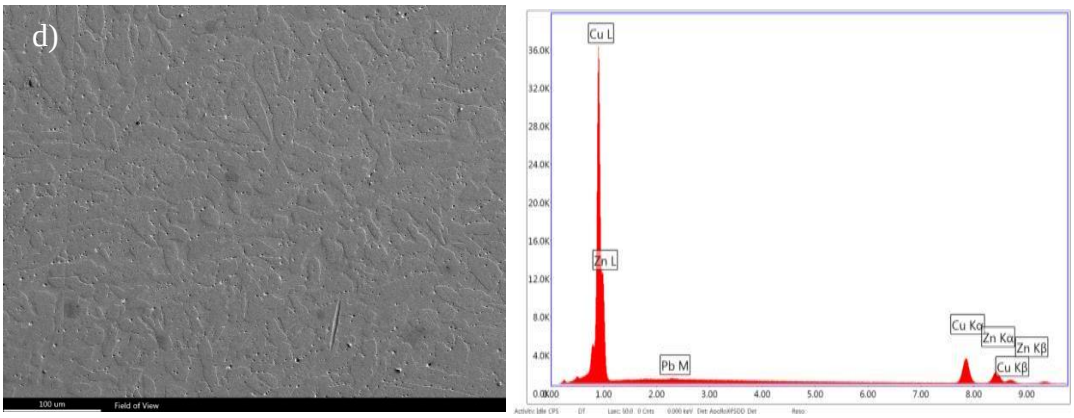
d)
100 um
Field of View
Cu L
Zn L
Pb M
Cu Kα
Zn Kα
Zn Kβ
Cu Kβ

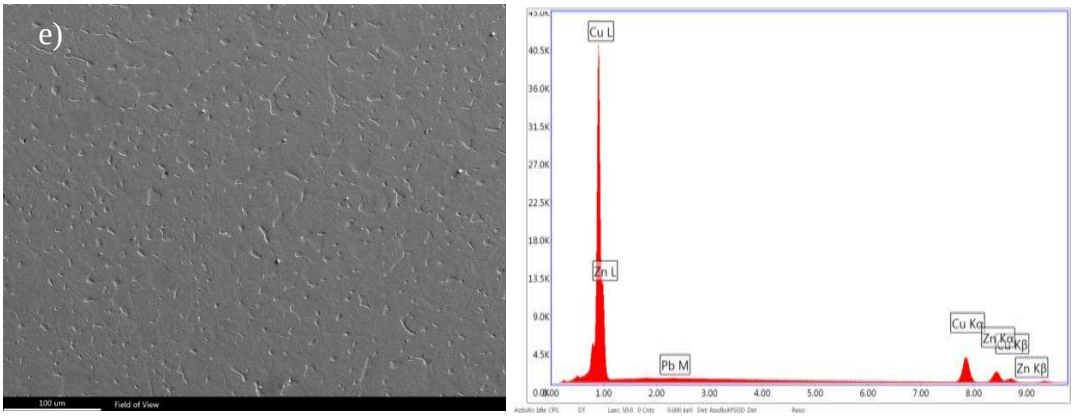
e)
100 um
Field of View
Cu L
Zn L
Pb M
Cu Kα
Zn Kα
Cu Kβ
Zn Kβ

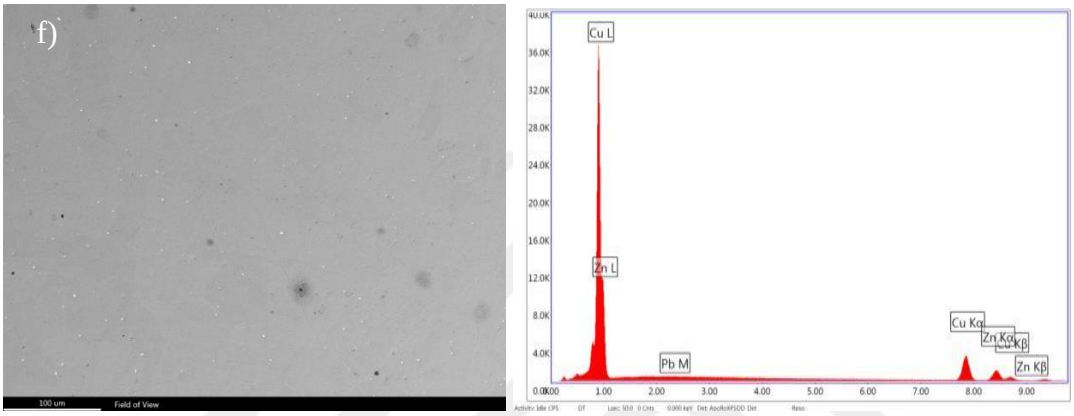
f)
100 um
Field of View
Cu L
Zn L
Pb M
Cu Kα
Zn Kα
Cu Kβ
Zn Kβ

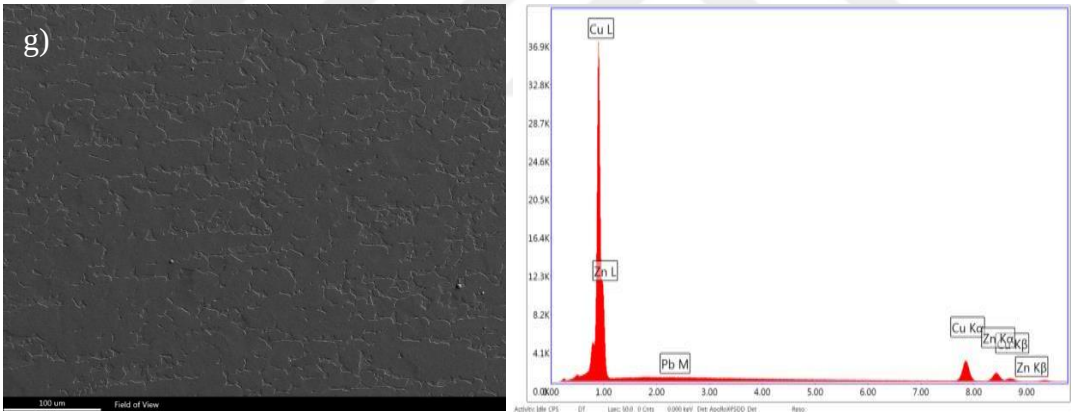
g)
100 um
Field of View
Cu L
Zn L
Pb M
Cu Kα
Zn Kα
Cu Kβ
Zn Kβ

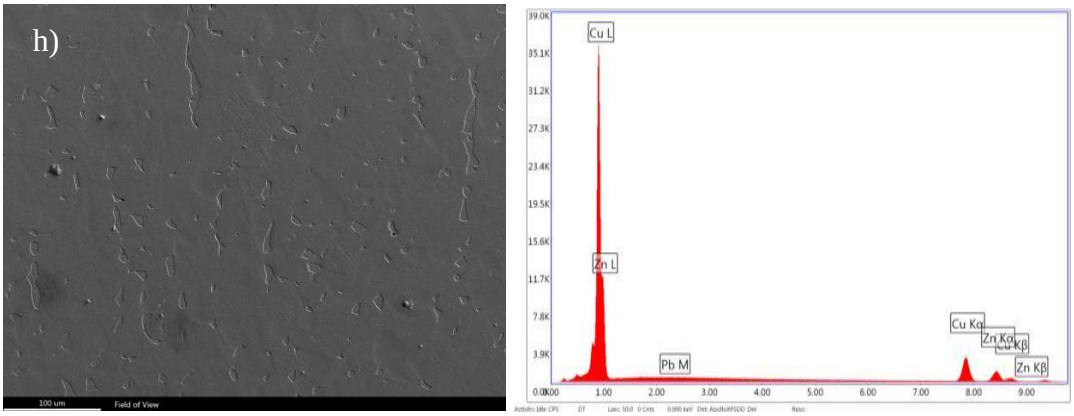
h)
100 um
Field of View
Cu L
Zn L
Pb M
Cu Kα
Zn Kα
Cu Kβ
Zn Kβ

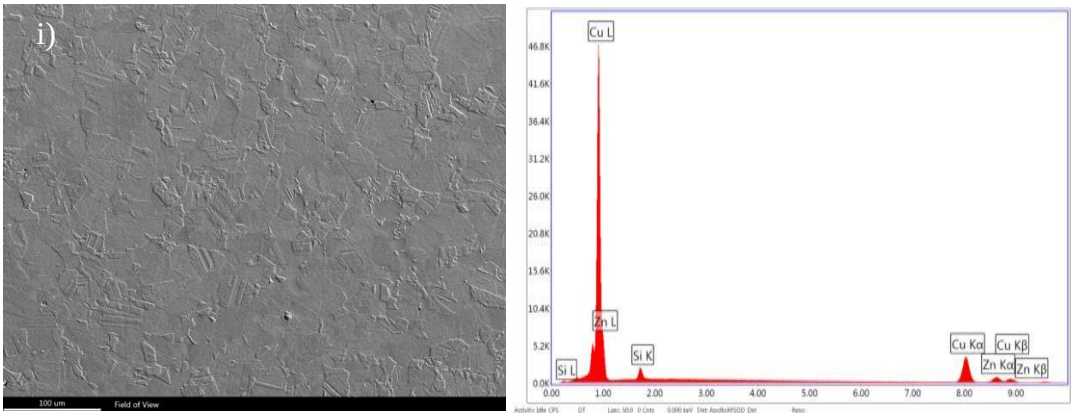
i)
100 um
Field of View
Cu L
Zn L
Si K
Si L
Cu Kα
Cu Kβ
Zn Kα
Zn Kβ

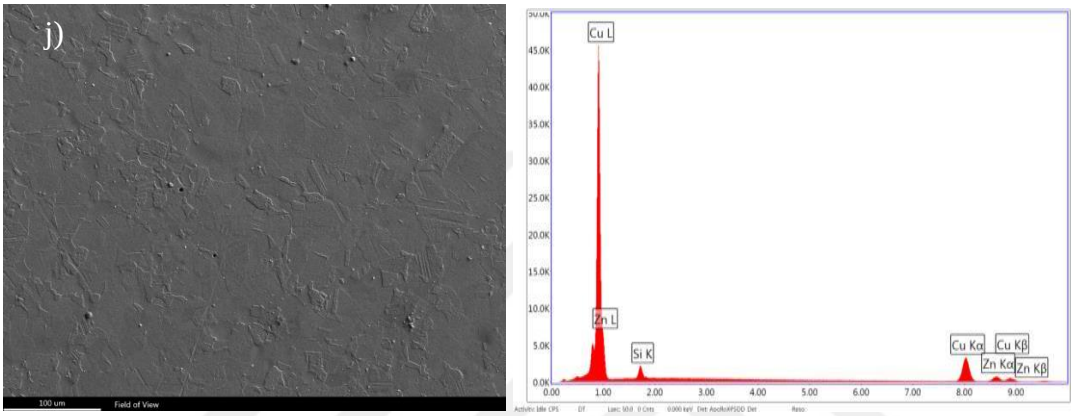
j)
100 um
Field of View
Cu L
Zn L
Si K
Cu Kα
Cu Kβ
Zn Kα
Zn Kβ

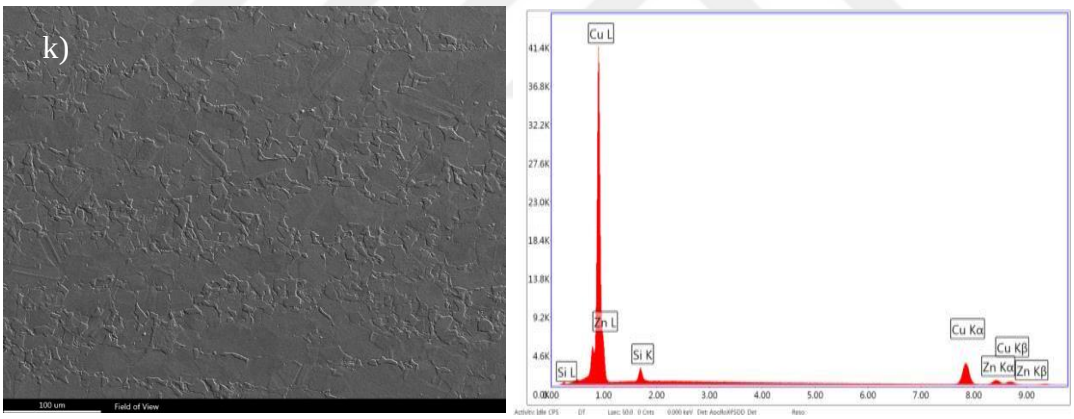
k)
100 um
Field of View
Cu L
Zn L
Si K
Si L
Cu Kα
Cu Kβ
Zn Kα
Zn Kβ

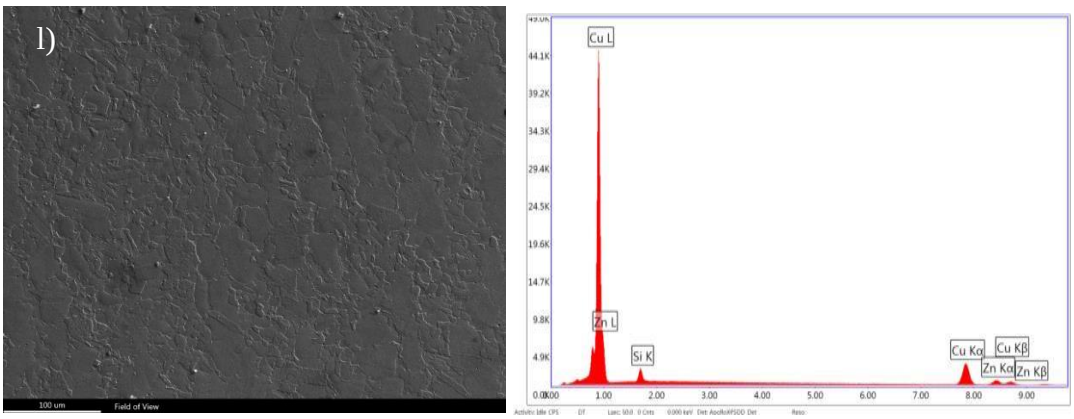
l)
100 um
Field of View
Cu L
Zn L
Si K
Cu Kα
Cu Kβ
Zn Kα
Zn Kβ

**Figure 2.9.** EDS analysis images of the microstructure of, CW617N; a) extruded, b) extruded-annealed, c) forged, d) forgred-annealed, CW511L; e) extruded, f) extruded-annealed, g) forged, h) forgred-annealed, CW724R; i) extruded, j) extruded-annealed, k) forged, l) forgred-annealed.

**Table 2.4.** The phasic percentages of the studied brass alloys

| Brass Type | | α% | β% | κ% + γ% |
|---|---|---|---|---|
| CW617N | Extruded | 54 | 46 | - |
| | Extruded & annealed | 56 | 44 | - |
| | Forged | 49 | 61 | - |
| | Forged & annealed | 39 | 51 | - |
| CW511L | Extruded | 94 | 6 | - |
| | Extruded & annealed | 99 | 1 | - |
| | Forged | 83 | 17 | - |
| | Forged & annealed | 96 | 4 | - |
| CW724R | Extruded | 84 | - | 16 |
| | Extruded & annealed | 89 | - | 11 |
| | Forged | 81 | - | 19 |
| | Forged & annealed | 84 | - | 16 |

### 2.3 Tensile tests

The specimens have been subjected to tensile tests at 2 mm/min rate of strain by Instron 5569 machine at mechanical tests laboratory of Gebze technical university as shown in Figure 2.10. The results of the tensile tests are shown in Figure 2.11. As it is seen the forged specimens have demonstrated a brittle like behavior during the tests by sudden rupture. The lowest yield point was observed for annealed CW511L bar as equal to 110 MPa. However, the highest value was measured for forged CW724R as 387 MPa. Furthermore, by annealing of the extruded bar the yield stress of has decreased %15, %19 and %2 for CW617N, CW511L and CW724R, respectively, while these percentages were %16, %41 and %22 for the same forged materials. It is evident to note that annealing has led to reduction in durability and earlier initiation of permanent plastic deformation region

for both extruded and forged brass alloys due to declination in the dislocations inside the crystal structures. However, the yield stress increased by forging %58, %52 and %77 by forging for CW617N, CW511L and CW724R, respectively. This result is an illustrative of the double working under tension compacts on the metal and formation of a dense and refined grain structure gained by twice applied high pressures during; rod extrusion and forging [1]. Moreover, the calculation of the elastic modulus for the test specimens which are also given in Table 2.5 confirms the obtained results for the yield stress values and their change according to the annealing and forging operations. The ruptured images of the specimens after tensile test are shown in Figure 2.13. As it is seen all the materials have been experienced 45° of fracture/rupture which is a clue for a ductile fracture. Accordingly, it is expected to notice an expansion in the brittlely yet greater durability with the ascent in the β progressively work in CW617N and CW511L in regard to the larger number of slip frameworks and dislocation lattice friction stresses when contrasted with α phase which is FCC. Moreover, because of the easier movement of dislocations in HCP (Hexagonal Close-Packed) due to 3 slip frameworks when contrasted with FCC and BCC, it is anticipated for CW724R to show brittlely.

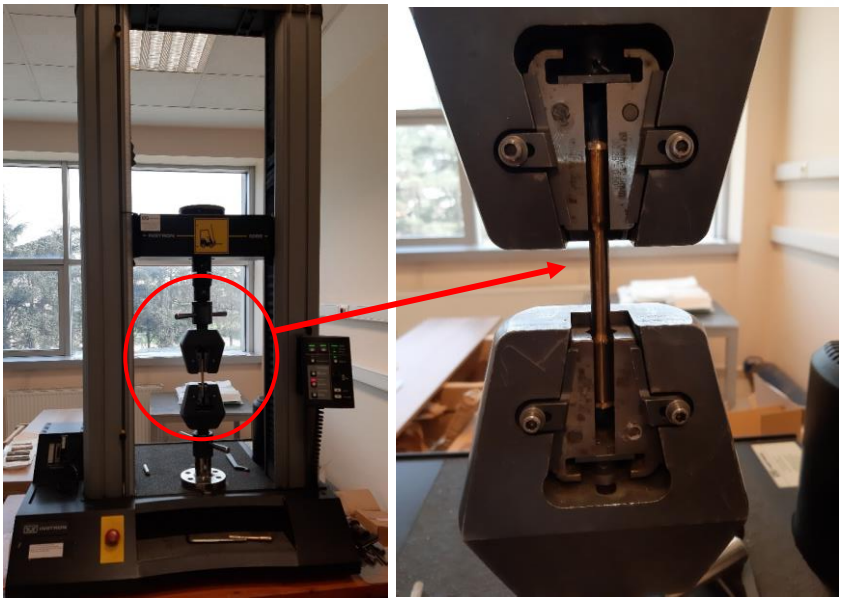

**Figure 2.10.** Tensile test experimental setup

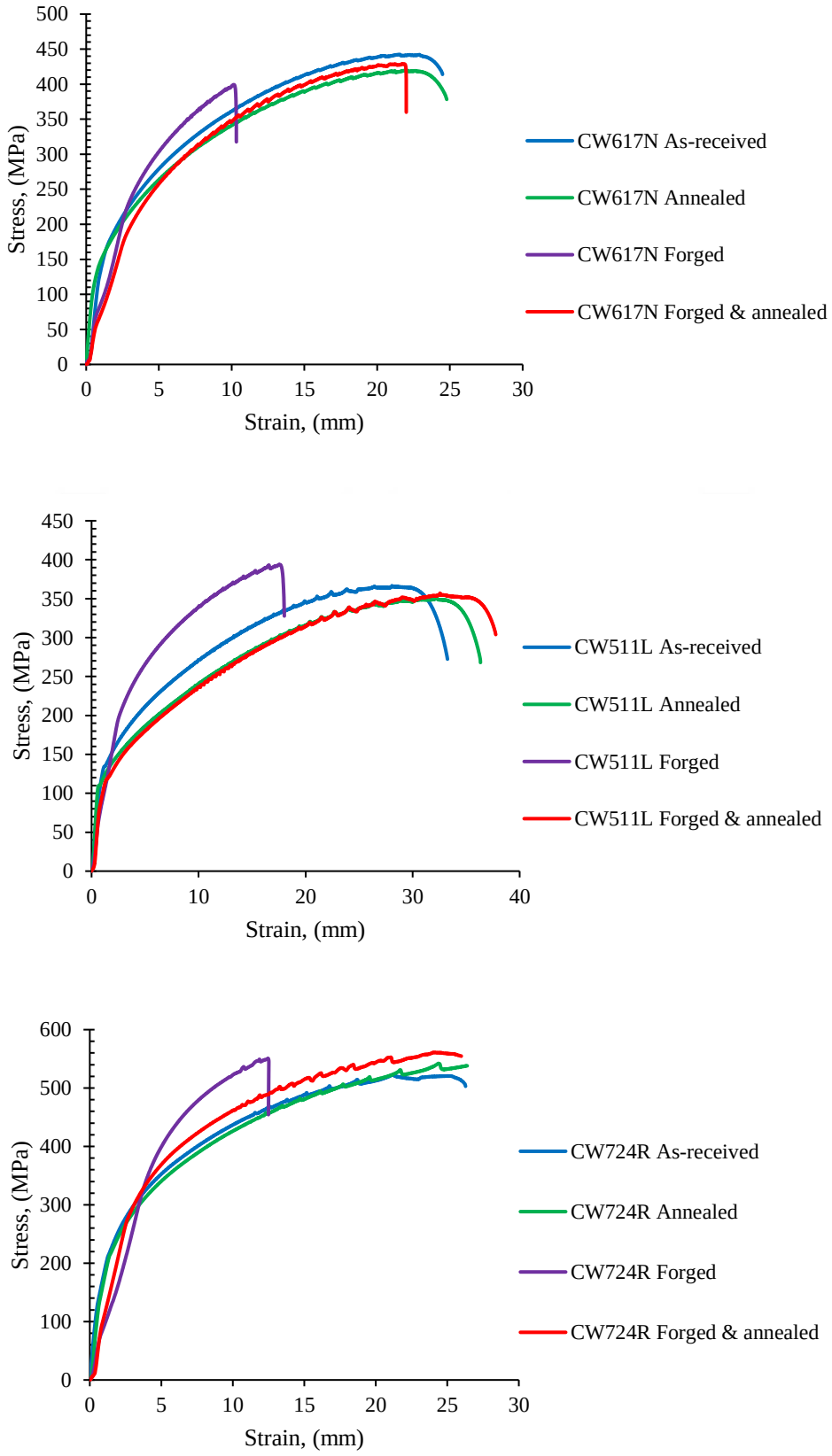


**Figure 2.11.** Tensile test plots; a) CW617N, b) CW511L, c) CW724R.

**Table 2.5.** The experimental mechanical properties of the studied brass alloys

| | Brass alloy type | Yield stress, (MPa) | Ultimate tensile stress, (MPa) | Elastic modulus, (GPa) |
|---|---|---|---|---|
| CW617N | Extruded | 153 | 442.4 | 84.8 |
| | Extruded+annealed | 130 | 420 | 85.48 |
| | Forged | 243 | 399.2 | 77.35 |
| | Forged+annealed | 203 | 428.9 | 74.48 |
| CW511L | Extruded | 136 | 366.6 | 82.81 |
| | Extruded+annealed | 110 | 351.2 | 87.07 |
| | Forged | 208 | 393.9 | 80.46 |
| | Forged+annealed | 141 | 356.9 | 79.33 |
| CW724R | Extruded | 218 | 522.7 | 78.76 |
| | Extruded+annealed | 213 | 547.3 | 78.40 |
| | Forged | 387 | 550.9 | 75.71 |
| | Forged+annealed | 299 | 563.9 | 77.01 |

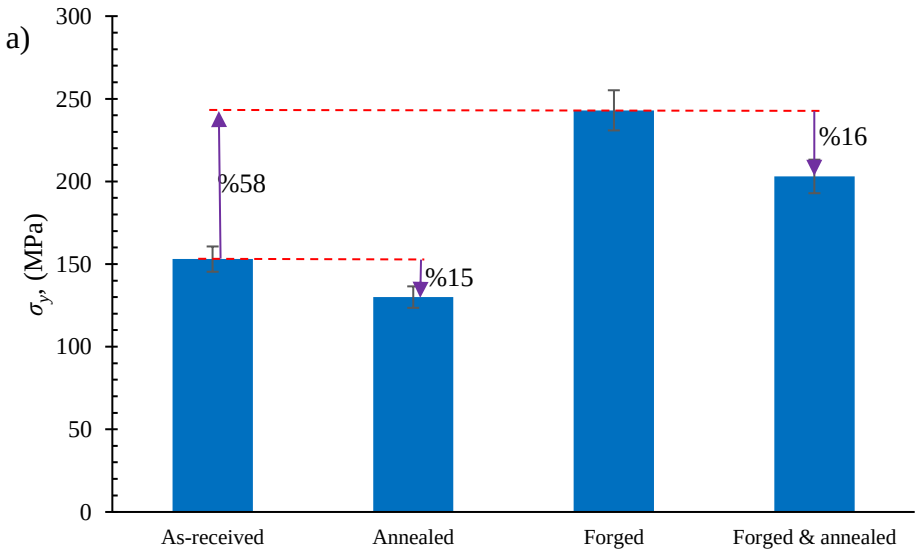

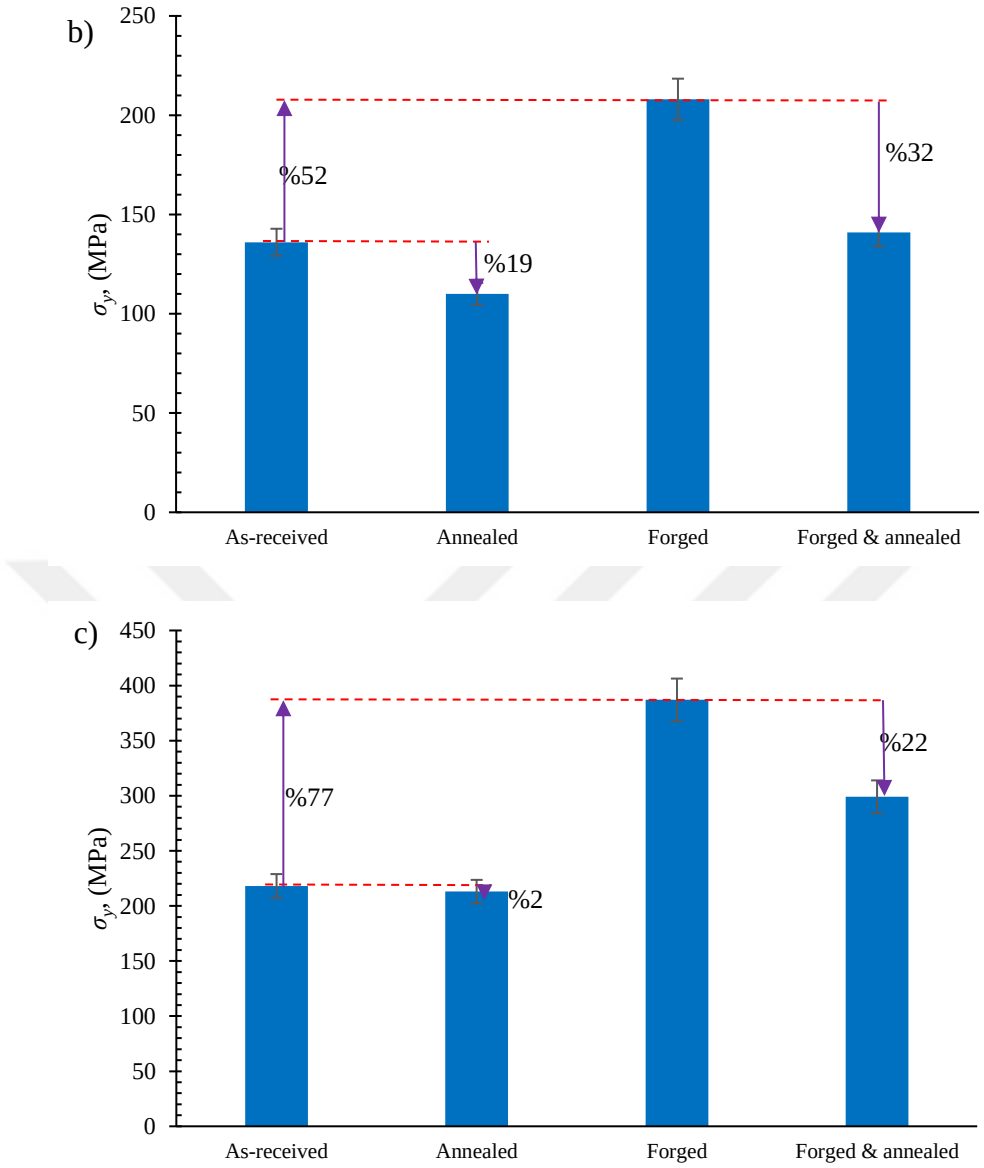


**Figure 2.12.** The yeild stress for the test materials; a) CW617N, b) CW511L, c) CW724R

| | Extruded Bar | Annealed Extruded Bar | Forged | Forged and Annealed |
|---|---|---|---|---|
| CW617N | | | | |
| CW511L | | | | |




**Figure 2.13.** Ruptured images of the specimens after tensile test

## 2.4 Micro Hardness

Micro-hardness tests of the studied specimens were carried out under 100 g applied load for 10 seconds using MHVD 1000 IS microhardness tester machine according to ASTM E 384 standards and the average value of five measurements is reported in Table 2.6. The lowest hardness has been measured for extruded and annealed CW511L as 88.8 HV. However, the highest value was obtained for forged CW724R as equal to 138.9 HV. Considering the obtained results in a broad perspective, it is obvious that annealing plays a major role in reduction of the hardness property for the test materials. Meanwhile, owing to the movement of the dislocations and grain refinements in the alloy structures extracted by forging process, an increase in the hardness value is achieved. This hardness can be explained by Hal-Petch equation as given in below:

$$\sigma_y = \sigma_0 + K\sqrt{d} \tag{2.1}$$

where $\sigma_y$ , $\sigma_0$ , $K$ and $d$ stand for the yield stress, materials constant for the starting stress for dislocation movement, the strengthening coefficient, and the average grain diameter, respectively [45]. And according to the Hal-Petch equation, it can be concluded that smaller grain sizes result in an increase on micro hardness value due to the hindering of the movement of the dislocations in the crystalline microstructure.

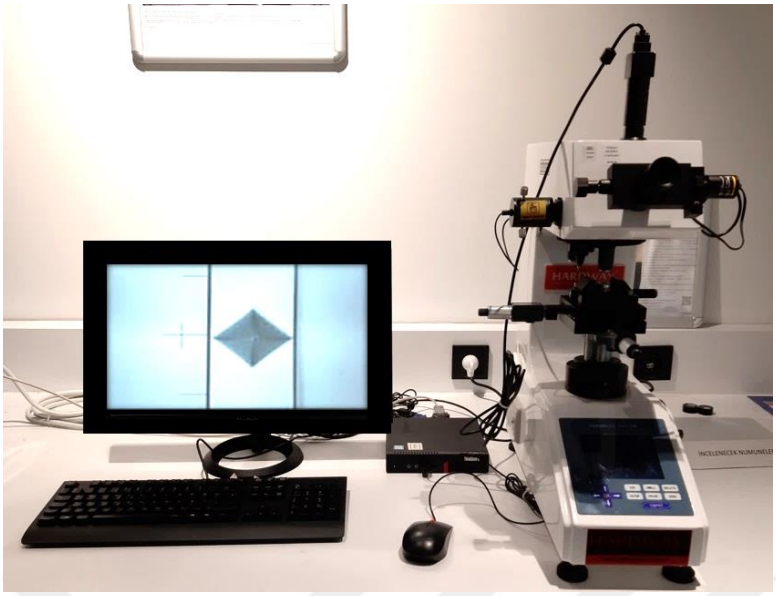

**Figure 2.14.** The utilized micro hardness measurement device

**Table 2.6.** The microhardness results of the studied brass alloys

| Brass Type | | Microhardness, (HV) |
|---|---|---|
| CW617N | Extruded | 95.6 |
| | Extruded & annealed | 92.3 |
| | Forged | 107.9 |
| | Forged & annealed | 98.5 |
| CW511L | Extruded | 92.1 |
| | Extruded & annealed | 88.8 |
| | Forged | 102.3 |
| | Forged & annealed | 96.7 |
| CW724R | Extruded | 118.2 |
| | Extruded & annealed | 107.4 |
| | Forged | 138.9 |
| | Forged & annealed | 125.6 |

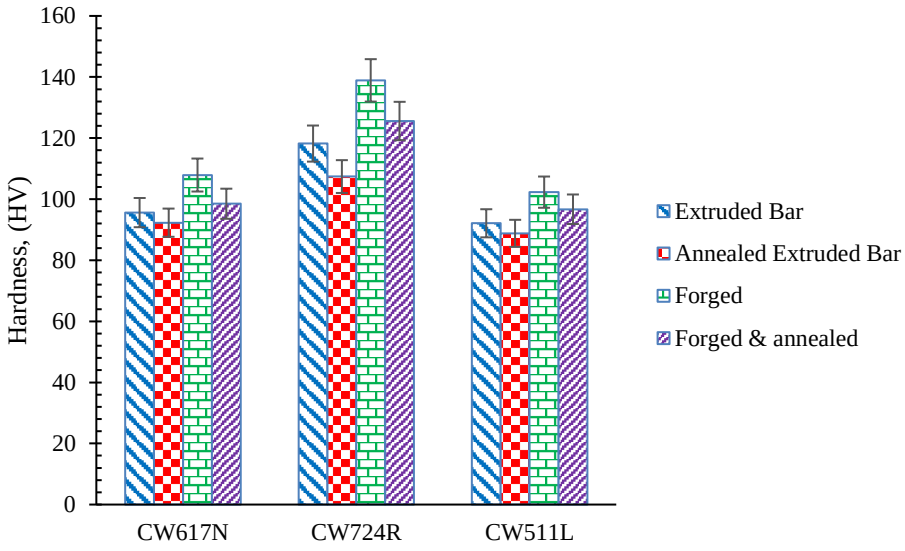


**Figure 2.15.** The measured micro hardness value for the brass alloys

## 2.5 Impact charpy

Impact charpy test is method which is executed in order to determine the amount of required energy to fracture under dynamic loads for different types of materials. In other words, the result of this test reveals the fracture energy as a mechanical property [46, 47]. Notch type, yield stress of the material, alloying elements, crystal structures, temperature, cooling, annealing, and forming conditions/ procedures play an important role in the microstructural phase, grain size type and on the fracture behavior of the material. Therefore, it is evident that the fracture property is directly associated with the machinability and chip breakability of the materials [10, 48]. In this thesis, the impact Charpy tests have been carried out with V-notched specimens according to ASTM E23 at R & D center of Torun Copper Metal Alloys Inc. Ltd. Ind. as shown in Figure 2.16, and the average of two measurement of the Notch impact energy is reported in Table 2.7. The obtained results illustrate that the toughness value has increased %11.34, %88.02 and %14.24 by annealing for CW617N, CW724R and CW511L, respectively. This trend is in discrepancy for CW511L in [48]. However, they had different annealing parameters as compared to the deployed ones in this thesis. For the case of forged specimens, annealing has led to %4.03, %20.70 and %2.64 increase in the fracture energy value for CW617N, CW724R and CW511L, respectively. Throughout the Charpy impact experiment results, the absorbed energy of the material increases with annealing. In α+β brasses, annealing

results in the increase of the β phase percentage as demonstrated in microstructural studies section of this chapter. Subsequently, the hardness value decreases. The harder the material, the less tough and more plastic deformation is achieved. There is no available performed previous studies on CW74R including annealing and impact fracture up until the preparation of this thesis. But in total the microstructural studies exhibited that annealing leads to formation of smaller grain sizes and boundaries.



**Figure 2.16.** The Charpy impact energy test setup

**Table 2.7.** The toughness results of the studied brass alloys

| | Extruded Bar | Annealed Extruded Bar | Forged | Forged & annealed |
|---|---|---|---|---|
| CW617N | 35.71 | 39.76 | 27.41 | 28.51 |
| CW724R | 29.97 | 56.35 | 26.51 | 32 |
| CW511L | 86.26 | 98.55 | 57.6 | 59.12 |

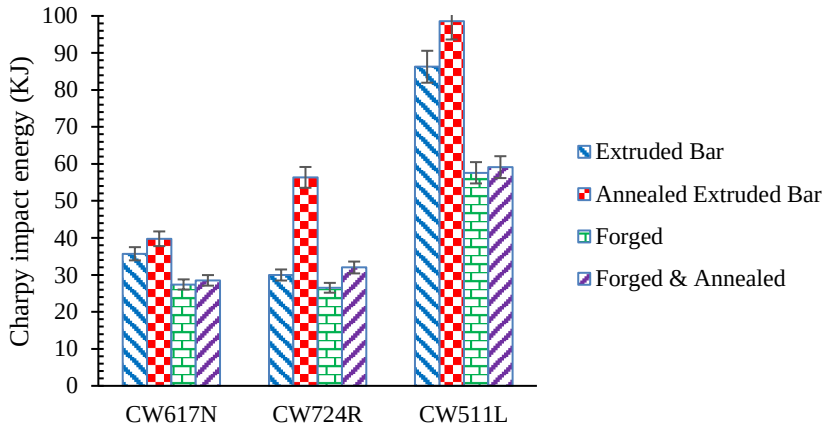


**Figure 2.17.** The Charpy impact energy of the extruded, forged and annealed brass alloys

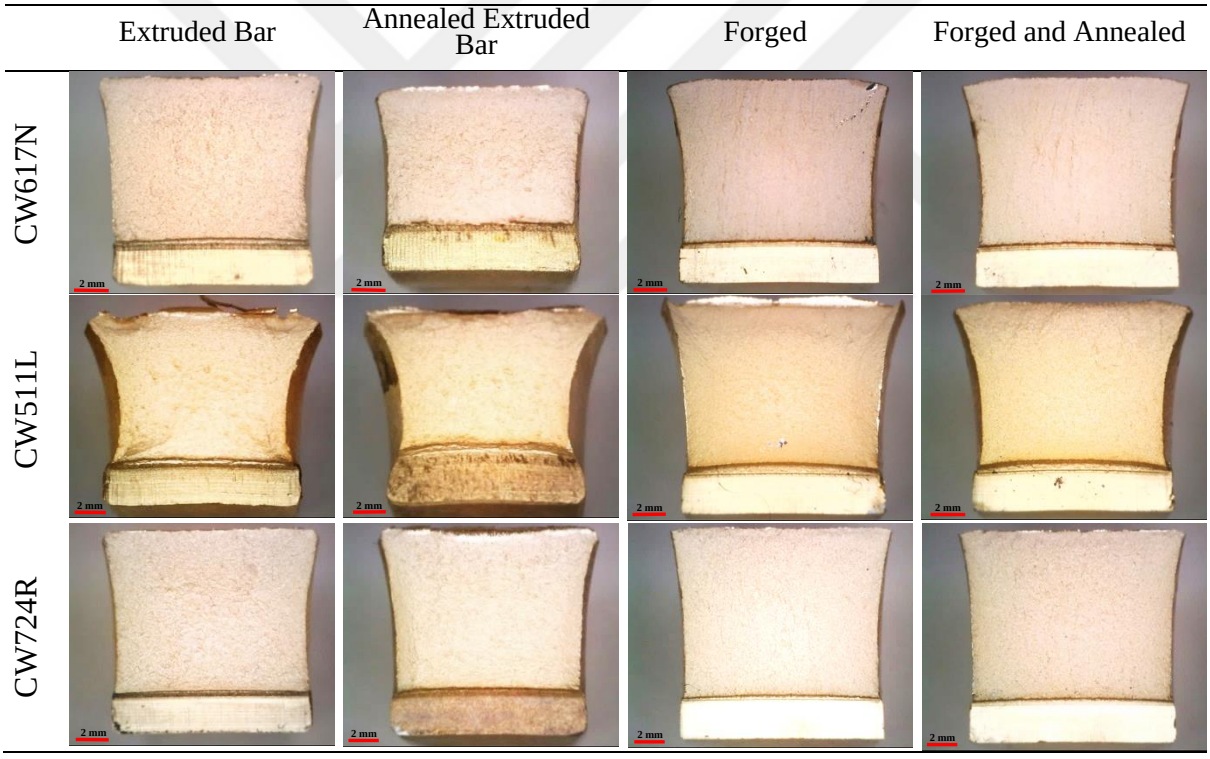


**Figure 2.18.** Fractographic images of the impact fractures

Figure 2.18 demonstrates the fractographic images of the impact fractures. The lowest fracture energy was measured for forged CW724R as 26.51 KJ. However, the highest value was obtained in 98.55 KJ for annealed extruded bar. As it is seen from Figure 2.18, an expressive deformation in visual shape of CW511L illustrating of higher strain before fracture is obtained as an Charpy impact toughness effect. This shape and absorbed energy

value is in agreement with [48]. However, the shape deformation in CW724R and CW617N is lower than CW511L due to movement restraint of the molecules and lower required energy for breaking the atomic bonds, subsequently lower absorbed energy. Furthermore, it is seen that annealing has resulted in boosting of the absorbed energy due to the reasons which have been explained in the tensile test section of this chapter. However, this rate has decreased by forging for all the test specimens.

Depending on the loading type, mode I, II, III or mixed one can occur on the crack tip of linear elastic material. These stresses can be declared as a function of the polar or cartesian coordinate system and stress intensity factor for the fracture modes. Considering the impact Charpy test, it can be assumed that the process can be reduced into plane strain of mode I fracture as shown in Figure 2.19. Therefore, the first mode intensity factor and stresses can be expressed from Equation 2.2 and 2.3.

$$K_{IC} = Y\sigma\sqrt{\pi a} \tag{2.2}$$

$$\sigma_{xx} = \frac{K_{IC}}{\sqrt{2\pi r}}\cos\left(\frac{\theta}{2}\right)\left[1 - sin\left(\frac{\theta}{2}\right)sin\left(\frac{3\theta}{2}\right)\right] \tag{2.3}$$

$$\sigma_{yy} = \frac{K_{IC}}{\sqrt{2\pi r}}\cos\left(\frac{\theta}{2}\right)\left[1 + sin\left(\frac{\theta}{2}\right)sin\left(\frac{3\theta}{2}\right)\right] \tag{2.4}$$

$$\sigma_{yy} = \begin{cases} 0 & plane\ stress \\ \nu(\sigma_{xx} + \sigma_{yy}) & plane\ strain \end{cases} \tag{2.5}$$

$$\tau_{xy} = \frac{K_{IC}}{\sqrt{2\pi r}}\cos\left(\frac{\theta}{2}\right)sin\left(\frac{\theta}{2}\right)cos\left(\frac{3\theta}{2}\right) \tag{2.6}$$

$$\tau_{yz} = \tau_{xz} = 0 \tag{2.7}$$

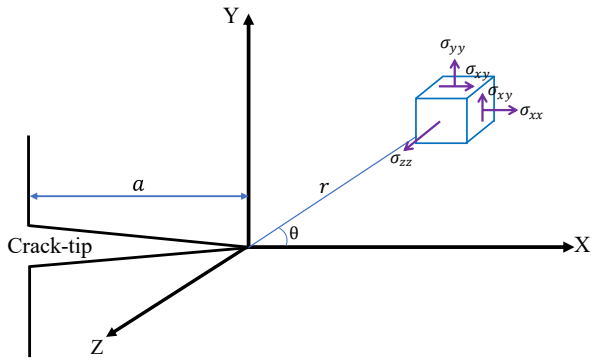


**Figure 2.19.** Schematic view of the first mode intensity factor and stresses

Where $K_{IC}$, $Y$, $\sigma$ and $a$ are the first mode fracture toughness, geometric constant, yield stress and crack/notch length, respectively [49, 50].

Table 2.8 and Figure 2.20 illustrates the first mode fracture toughness values for the mentioned brass alloys with different operational conditions. The lowest first mode fracture toughness was calculated for annealed extruded bar CW511L as 308.82 MPa.m1/2. However, the highest one was observed in forged CW724R specimen as 1086.47 MPa.m1/2. Based on the obtained results, it can be concluded that a significant improvement in the mechanical properties of the test materials is attained by forging process due to the refinement in the structure. Moreover, by annealing an enhancement is also accomplished due to the acquirement of ductility in the specimens.

**Table 2.8.** The first mode fracture toughness results of the studied brass alloys

| | Extruded Bar | Annealed Extruded Bar | Forged | Forged & annealed |
|---|---|---|---|---|
| CW617N | 429.54 | 364.97 | 682.20 | 569.91 |
| CW724R | 612.02 | 597.98 | 1086.47 | 839.42 |
| CW511L | 381.81 | 308.82 | 583.94 | 339.70 |

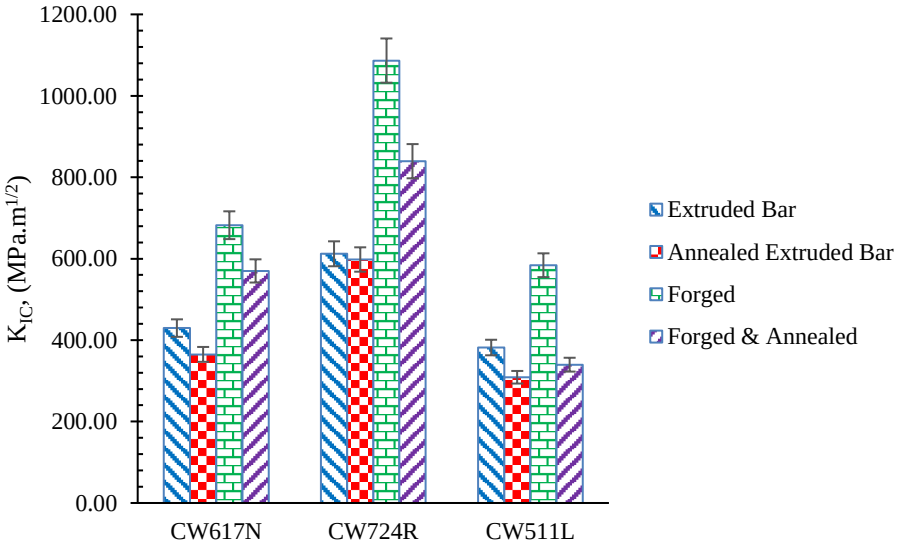


**Figure 2.20.** The calculated first mode fracture toughness values for the brass alloys

# 3. MECHANICS OF FLAT BOTTOM DRILLING

In this chapter, the geometry and mechanics of flat bottom drilling is introduced. Moreover, a mechanistic cutting force and torque prediction approach as a function of cutting tool geometry, cutting conditions and work material properties is developed and presented using analytical models for two different scenarios of inclined and vertical flat drilling.

In flat drilling processes deploying bottom drills, the cutting is carried out by transaction of the tool or work material along chisel edge and lips. Therefore, complicated mechanisms of orthogonal and oblique mechanisms participate in the cutting process by involvement of the flutes. In general, most of the flat bottom drills have a small (1°-3°) dish angle ensuring that the flat surface is produced by the cutter during machining. The existence of this angle concludes in performing of the tool center as a rotating indenter for extruding the work material on both sides of the chisel edges. By moving away from the tool center along chisel edge, the tool removes the material by orthogonal cutting mechanism and irregular chips form due to the negative rake angle and low cutting speed [51] as presented in Figure 3.1.

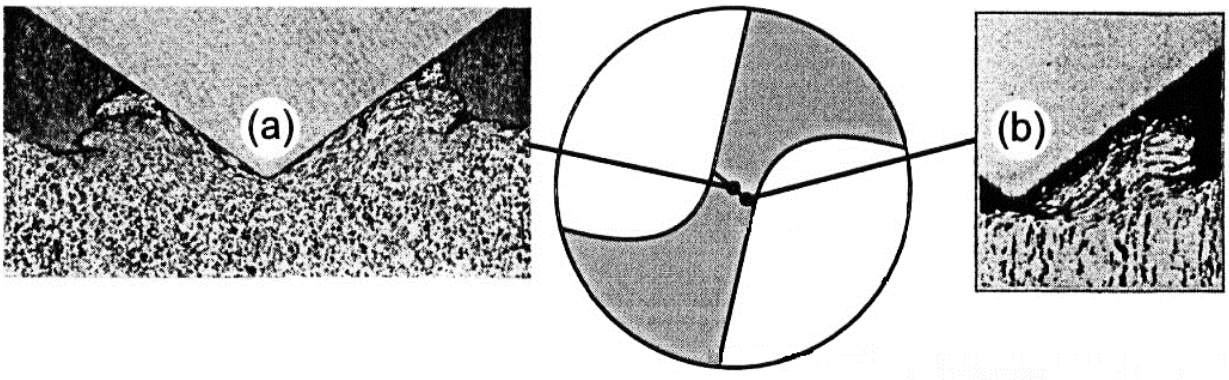


**Figure 3.1.** Cross sectional of drilling; a) indentation at the drill center of the chisel edge, b) orthogonal cutting with chisel edge [51]

Moving along the cutting edges, the mechanisms of the cut changes to oblique one due to the gash, rake and inclination angles. In this region, the chip formation is dramatically dependent on the positive or negative radial rake angle of the edges.

Figure 3.2 demonstrates the penetration and cutting, as well as forces orientation in the flat bottom drill reference coordinate system. In order to model the cutting forces and torques acting on the tool during the machining process, the elemental local forces should be projected mainly according to reference planes.

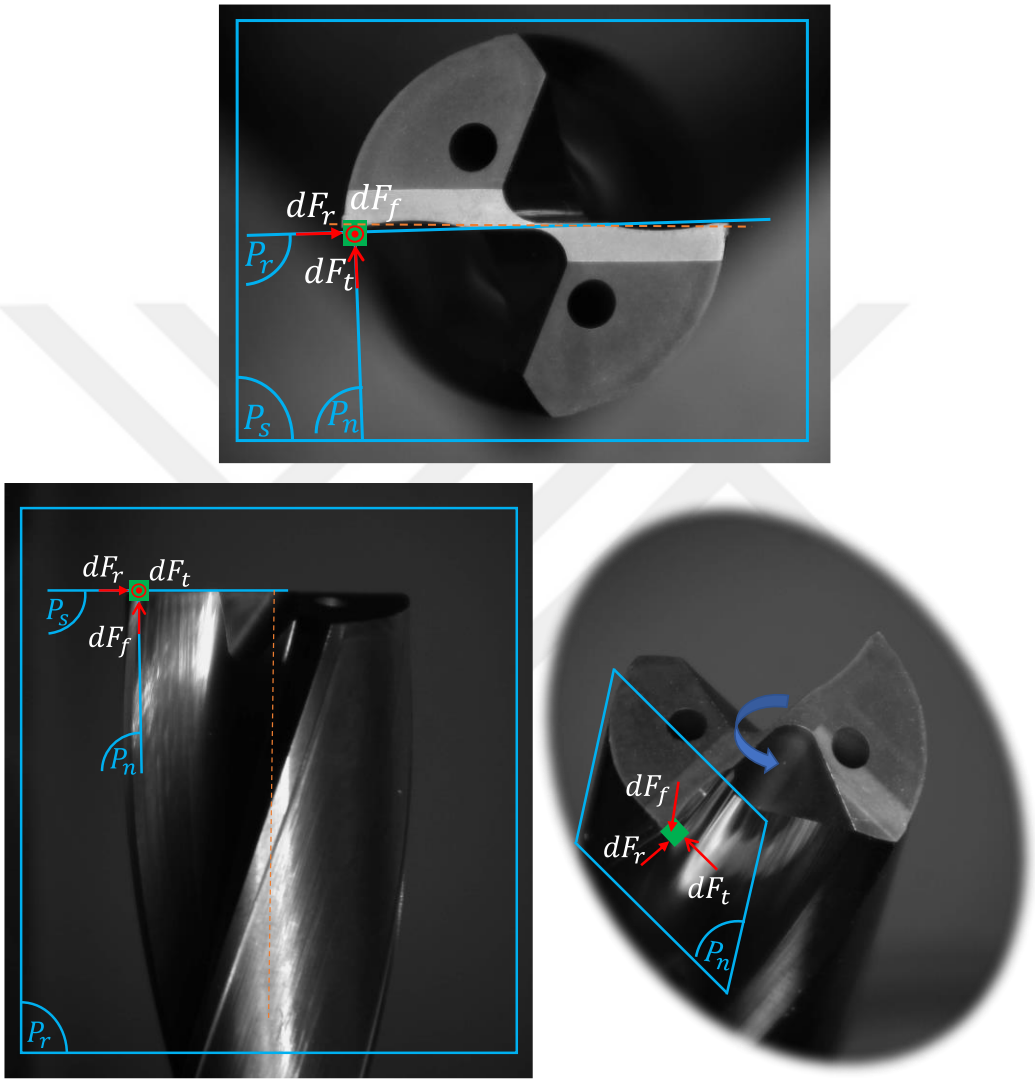


**Figure 3.2.** A schematic view of the forces orientation in the flat bottom drill with respect to a reference coordinate system

In orthogonal cutting mechanism, on the normal plane of $P_n$, the normal force $(F_n)$, shear force $(F_s)$ and as well as the resultant cutting force $(F_R)$, all are generated on the shear and chip–rake face contact zone [52]. Thereupon, the cutting tool or the work material is not subjected to any force in the third direction. However, in oblique cutting mechanism, due

to the inclination angle of Γ the orientation of the shear, friction, chip flow, and resultant cutting force vectors varies with respect to the Cartesian coordinate system [52]. For this reason, on the perpendicular planes $(P_r, P_s)$ to the $P_n$ and shear plane, the rake face of the tool, a third component of force appears. Accordingly, the motion of removed chip occurs on the rake face of the tool with a chip flow angle of $\eta$ as illustrated in Figure 3.3.

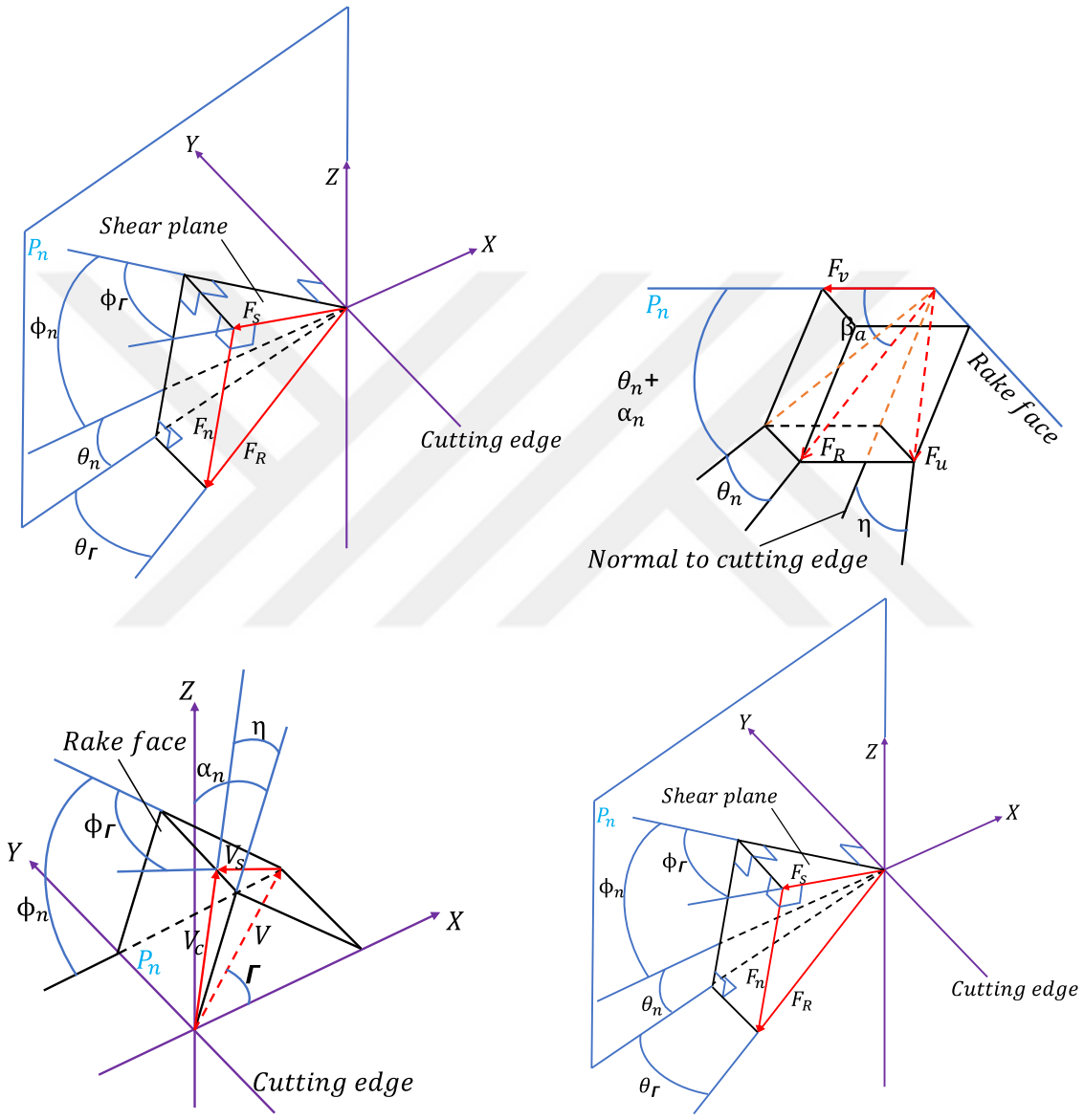


**Figure 3.3.** Mechanism of oblique cutting

where;

$\Phi_n$: normal shear angle; the angle between the shear and $P_s$ planes

$\Phi_\Gamma$: inclined shear angle; the angle between the shear velocity ($V_s$) and normal vector to the cutting edge on $P_n$

$\alpha_n$: normal rake angle

$\beta_a$: friction angle

$\theta_\Gamma$: the angle between $P_n$ and $F_R$

$\theta_n$: the angle between $P_n$ and $F_R$ on X axis

$V_c$: chip velocity

$V_s$: shear velocity

$V$: cutting velocity

In the light of the above given information, the following equations can be concluded:

$$F_u = F_R.\sin(\beta_a) = F_R.\frac{\sin(\theta_\Gamma)}{\sin(\eta)} \Rightarrow \theta_\Gamma = \sin^{-1}(\sin(\beta_a).\sin(\eta)) \quad (3.1)$$

$$F_u = F_v.\tan(\beta_a) = F_v.\frac{\tan(\theta_n+\alpha_n)}{\cos(\eta)} \Rightarrow \theta_n + \alpha_n = \tan^{-1}(\tan(\beta_a).\cos(\eta)) \quad (3.2)$$

$$\vec{V} = (V\cos(\Gamma), V\sin(\Gamma), 0) \quad (3.3)$$

$$\overrightarrow{V_c} = (V_c\cos(\eta)\sin(\alpha_n)\ , V_c\sin(\eta), V_c\cos(\eta)\cos(\alpha_n)) \quad (3.4)$$

$$\overrightarrow{V_s} = (-V_s\cos(\Phi_\Gamma)\sin(\Phi_n)\ , -V_s\sin(\Phi_\Gamma), V_s\cos(\Phi_\Gamma)\cos(\Phi_n)) \quad (3.5)$$

$$\overrightarrow{V_s} = \overrightarrow{V_c} - \vec{V} \quad (3.6)$$

Thus, the chip flow angle can be expressed by Equation 3.7:

$$\eta = \tan^{-1}\left(\frac{\tan(\Gamma).\cos(\Phi_n-\alpha_n)-\cos(\alpha_n).\tan(\Phi_\Gamma)}{\sin(\Phi_n)}\right) \quad (3.7)$$

Withal the (Equation 3.1, 3.2 and 3.7) equations, various arrangements in view of the empirical chip flow direction in [54-59] and other empirical assumptions given in [52] have been proposed. In addition, equations established by maximum shear stress theory in

[53, 54] and minimum energy principle in [55-56] have been expressed different equations for oblique cutting mechanism. Deploying the models developed by [57] and [58], the following expressions can be obtained [52]:

$$\Phi_n + \beta_n = \tan^{-1}\left(\frac{\tan(\Gamma).\cos(\alpha_n)}{\tan(\eta)-\sin(\alpha_n).\tan(\Gamma)}\right) \tag{3.8}$$

$$\beta_n = \tan^{-1}(\tan(\beta_a).\cos(\eta)) \tag{3.9}$$

$$\beta_n = \theta_n + \alpha_n \tag{3.10}$$

$$\Phi_n = \tan^{-1}\left(\frac{r_c.\left(\frac{\cos(\eta)}{\cos(\Gamma)}\right).\cos(\alpha_n)}{1-r_c.\left(\frac{\cos(\eta)}{\cos(\Gamma)}\right).\sin(\alpha_n)}\right) \tag{3.11}$$

where; $r_c$ is obtained by the measurement of the uncut chip thickness over cut chip thickness, known as chip ratio.

Assuming that the cutting of metals occurs by shearing phenomena, and the material failure during cut is contributed by shear stress, the cutting force coefficients for an oblique cutting can be calculated from Equation 3.12-14, [52, 57]:

$$K_{tc} = \frac{\tau_s(\cos(\beta_n-\alpha_n)+\tan(\Gamma)\tan(\eta)\sin(\beta_n))}{\sin(\Phi_n)\sqrt{\cos^2(\Phi_n+\beta_n-\alpha_n)+\tan^2(\eta)\sin^2(\beta_n)}} \tag{3.12}$$

$$K_{fc} = \frac{\tau_s(\sin(\beta_n-\alpha_n))}{\sin(\Phi_n)\cos(\Gamma)\sqrt{\cos^2(\Phi_n+\beta_n-\alpha_n)+\tan^2(\eta)\sin^2(\beta_n)}} \tag{3.13}$$

$$K_{rc} = \frac{\tau_s(\cos(\beta_n-\alpha_n)\tan(\Gamma)-\tan(\eta)\sin(\beta_n))}{\sin(\Phi_n)\sqrt{\cos^2(\Phi_n+\beta_n-\alpha_n)+\tan^2(\eta)\sin^2(\beta_n)}} \tag{3.14}$$

In order to analytically model the cutting forces and torques, an experimental pre-work has been conducted to identify the shear, friction, normal rake angles and cutting and edge force coefficients. Furthermore, the cutting coefficients have been calculated from an experimental and also the above given equations in this thesis. Afterwards, the cutting and chisel edges are discretized into small elements with constant assumption of the angles through the tool geometry. Lastly, using oblique transformation equations of Armarego [53-57] and Stabler's [58] the cutting forces has been calculated for each discretized

element and the integration operation has been carried out to calculate the total forces and torques.

### 3.1. Scenario 1:

In this section, in order to predict the cutting forces and torques, an analytical model is developed for an inclined plunge using flat bottom drilling tool in Matlab R2019a software.

The radial integration limits of the cutting edges are needed for each flute to implement the cutting force model. Furthermore, since during inclined drilling all the teeth are not involved in the cut, at each step in the axial direction $\phi_{st}$ and $\phi_{ex}$ angles defines an immersion section interacting with a tooth $j$ in which is involved in the cut as depicted in Figure 3.4a, b. $d$ and ψ stand for the cutting tool diameter and inclination angle of the plunge, respectively.

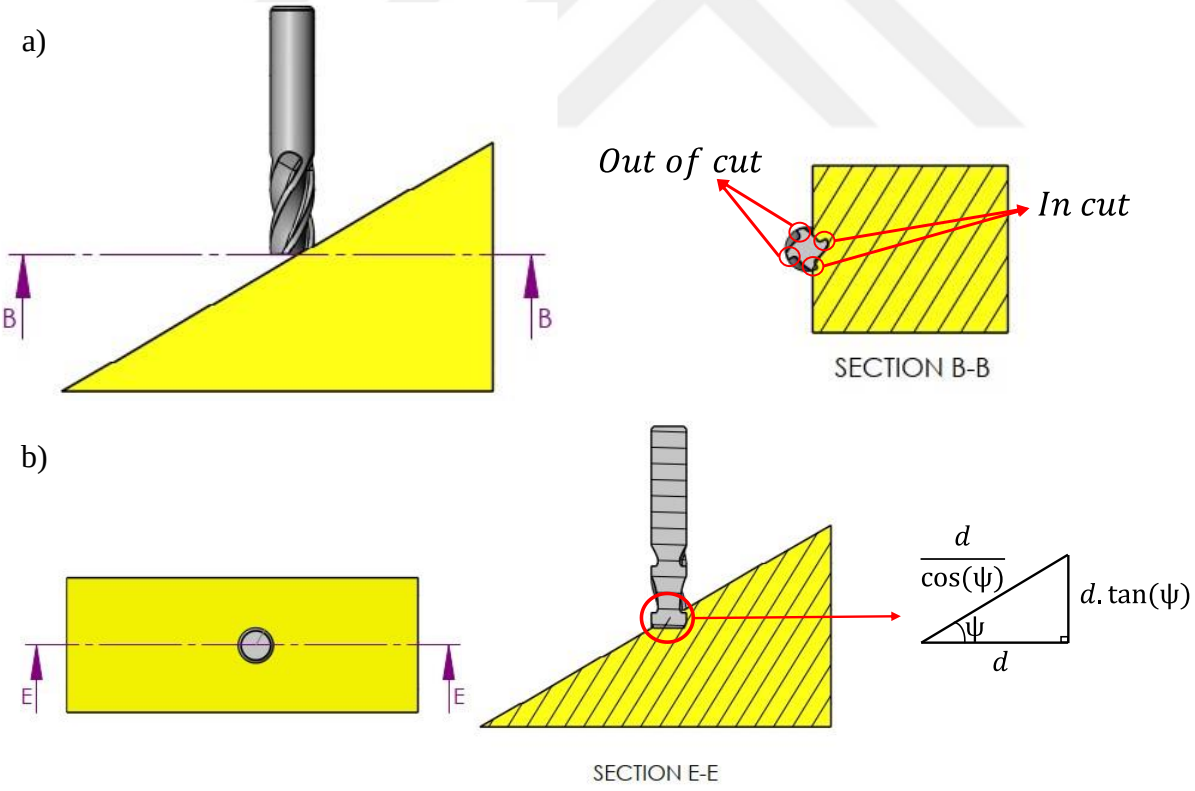


**Figure 3.4.** Cross sectional of the flat bottom drill during inclined drilling; a) involved teeth during cut, b) full immersion start of the cutting tool

The top segmental region which is formed with the tool movement in the vertical direction into the workpiece with an inclination angle of $\psi$ is demonstrated in Figure 3.5. As it is seen, the angle of the cutting start ($\phi_{st}$) and exit ($\phi_{ex}$) angles vary at each step of the axial elemental integration. Moreover, the width of the cut area ($\omega$) presents a variation as a function of the instantaneous angle of $\phi$ for the involved tooth in the cut. By using trigonometry and internal angles theorem of a triangle, the width of the cut area for a particular axial elemental integration ($\omega_L$) can be calculated for any instantaneous angle.

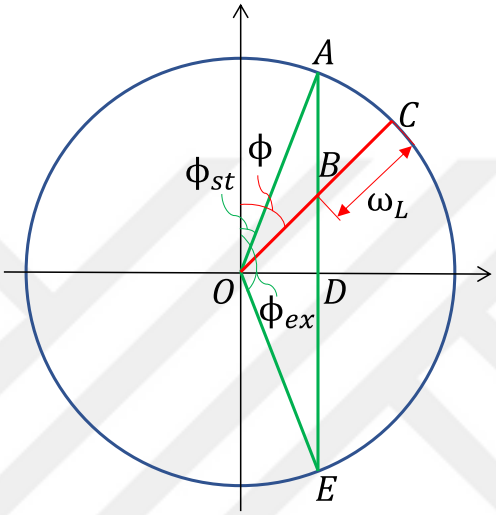


**Figure 3.5**. The top view of the tool movement in the vertical direction into a workpiece

$$|OA| = R \tag{3.15}$$

$$|OD| = R.\cos\left(\frac{\pi}{2} - \phi_{st}\right) = |R - \omega_L|.sin\ \phi \tag{3.16}$$

$$|\omega_L| = |R| - |OB| \tag{3.17}$$

$$\overrightarrow{AD} = \vec{R} - \overrightarrow{OD} \tag{3.18}$$

$$\left|\overrightarrow{BD}\right| = \left|\overrightarrow{OD}\right|.\tan\left(\frac{\pi}{2} - \phi\right) \tag{3.19}$$

$$\left|\overrightarrow{AB}\right| = \left|\overrightarrow{AD}\right| - \left|\overrightarrow{BD}\right| \tag{3.20}$$

$$\Delta OAB = \begin{cases} |OA| = \checkmark \\ |AB| = \checkmark \\ |OB| = \checkmark \end{cases} \tag{3.21}$$

$$\omega_L(\phi) = R - |OB| \tag{3.22}$$

As mentioned before, as the cutting tool moves downward, the value of $\omega$ varies at each step due to the change in the $\phi_{st}$ and $\phi_{ex}$. Therefore, in each step of the axial discretization, an increase in the width of the cut area is obtained as equal to $X$ which can be calculated by the following expressions:

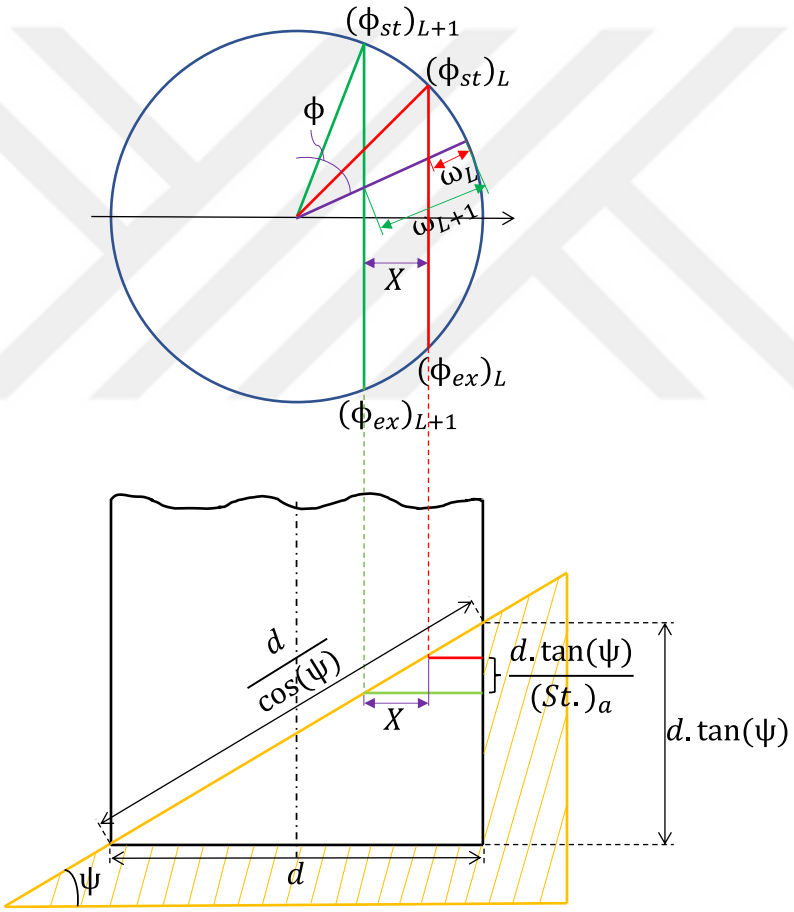


**Figure 3.6.** Schematic view for difference of the cut width for two different axial steps

$$tan(\psi) = \frac{\frac{d.tan(\psi)}{(St.)_a}}{X} \tag{3.23}$$

$$X = \frac{d}{(St.)_a} \tag{3.24}$$

For $L = 1: (St.)_a : d.\tan(\psi)$ (3.25)

$$\omega_{L+1} = \omega_L + X \quad (3.26)$$

End

where $(St.)_a$ is the elemental deviation being coincidence with the plunge axis.

After $\frac{d.tan(\psi)}{2}$, directions of the cutting forces in X and Y changes. The total plunging duration can be calculated from Equation 3.27.

$$t = \frac{a_{p_1} + a_{p_2}}{v_f} \times 60 = \frac{d.tan(\psi) + a_{p_2}}{v_f} \times 60 \quad (3.27)$$

Additionally, the pitch angle $(\phi_p)$, number of angular, axial and radial steps can be calculated with the below given equations; in which $n_t$ is the teeth number of the cutting tool.

Pitch Angle $\phi_p = \frac{2\pi}{n_t}$ (3.28)

Number of the angular steps $K = \frac{2\pi}{\Delta\phi}$ (3.29)

Number of the axial steps $L = \frac{2\pi}{(St.)_a}$ (3.30)

Number of the radial steps $m = \frac{R}{\Delta R}$ (3.31)

In order to analytically model the plunging operation, it is necessary to elementally discretize the cutting tool. A schematic view of a representative element with a width of $(dr)$ on the cutting tool is depicted in Figure 3.7. As it is seen, the element is subjected to cutting forces in three different directions with a distance of $r(i,j)$ form the tool center. Therefore, it is required to develop the model into the radial integration for the multi-teeth tool where each tooth location varies with respect to the $\phi_p$ and $n_t$ within the cutting tool integration boundaries. $\phi(i)$ and $\phi(i,j)$ represent the immersion of the flute at the bottom

and immersion of the ith flute. This implementation can be expressed in below given algorithm:

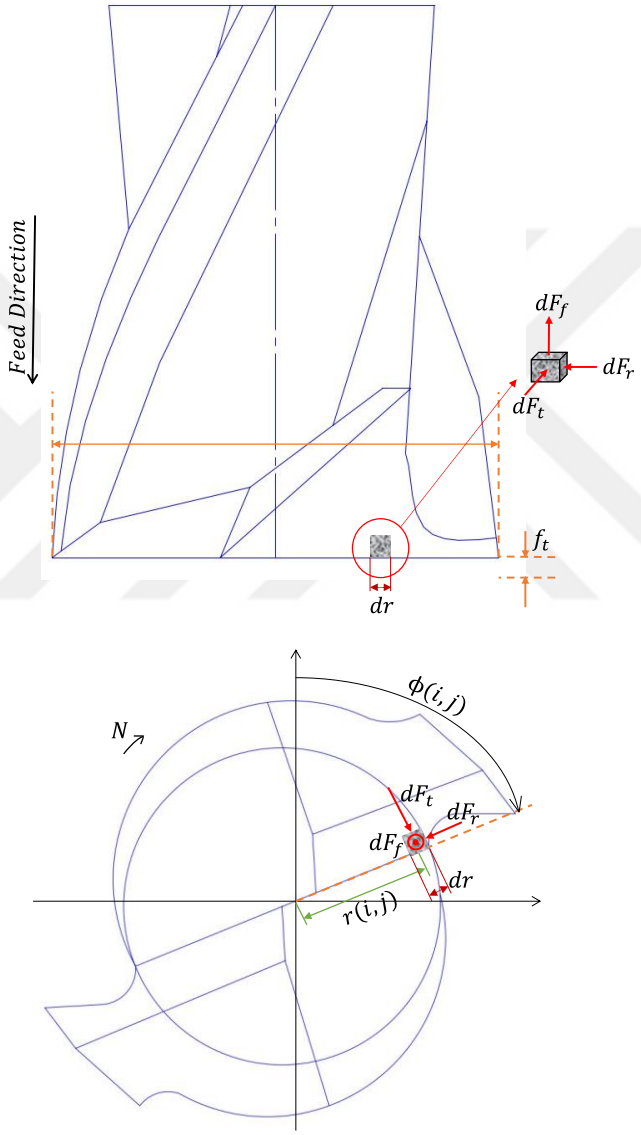


**Figure 3.7**. Schematic view of the subjected cutting forces for an element on the cutting edge

For $i = 1: n_t$ (3.32)

$$\phi(i) = \phi_{st} + i\Delta\phi \quad (3.33)$$

For $j = 1: m$ (3.34)

$$\phi(i,j) = \phi(j) + (i-1)\phi_p \quad (3.35)$$

$$R(j) = j\Delta R \quad (3.36)$$

End

End

The $\phi_{st}$ and $\phi_{ex}$ can be described for plunging into an inclined work material considering the tool geometry and width of the cut area for each axial step as given in Equation 3.35.

$$\phi_2 = \begin{cases} \phi_{st} = \arcsin\left(\frac{R-\omega_L}{R}\right) & 0 < a_{p_1} < \frac{d.\tan(\psi)}{2} \\ \phi_{st} = 0 & a_{p_1} = \frac{d.\tan(\psi)}{2} \\ \phi_{st} = \arcsin\left(\frac{-R+\omega_L}{R}\right) & a_{p_1} > \frac{d.\tan(\psi)}{2} \\ \phi_{ex} = \pi - \phi_{st} \end{cases} \quad (3.37)$$

The uncut chip thickness, length and its cross section can be calculated from the Equation 3.36-38.

The uncut chip width=$\begin{cases} 0 & \phi_2 < \phi_{st}\ ,\ \phi_2 > \phi_{ex} \\ \omega & \phi_{st} \le \phi_2 \le \phi_{ex} \end{cases}$ (3.38)

The uncut chip length=$l_{cu} = \frac{\pi.d}{360}.\phi_2$ (3.39)

Cross section of the uncut chip=$A_{cu}(\phi_2) = \omega(\phi_2).f_t$ (3.40)

The flat drilling process is consisted of two stages of cutting; first plunging to the inclined part and second, full diameter plunge. At the first stage, the depth of the cut is abbreviated by $a_{p_1}$. When this value becomes larger than $d.\tan(\psi)$, it indicates that the cutting tool has entered to the second stage and $a_{p_2}$ is the input. Thus, the expressions and calculations are not valid, and the algorithm should skip to Scenario 2 of this chapter as expressed below.

$$a_p = a_{p_1} + a_{p_2} \tag{3.41}$$

If $a_{p_1} > d.\tan(\psi)\ 0$ (3.42)

$$a_{p_1} = a_{p_2} \tag{3.43}$$

$$\phi_2 = \phi_1 + \phi_p \tag{3.44}$$

$$\phi_{st} \leq \phi_2 \leq \phi_{ex} \tag{3.45}$$

In contrary to turning and full diameter plunging operations, in flat bottom drilling of inclined workpieces, as a function of time and immersion angle of the involved tooth in the cut, the instantaneous chip thickness ($h$) varies regularly. The value of this variation can be calculated as in Equation 3.45.

$$h = f_t.\sin(\phi_2) \tag{3.46}$$

where $f_t$ and $\phi_2$ stand for the feed rate (mm/rev-tooth) and instantaneous angle of immersion, respectively.

The elemental tangential forces ($F_t$), radial forces ($F_r$) and feed forces ($F_f$) can be expressed as a function of inspected element width of cut ($dr$) and instantaneous chip thickness. Considering the multi-teeth cutting tool, the cutting condition ($CC$) can be applied to the force expressions in order to scrutinize the share of the teeth involved in the cut. $K_{tc}$, $K_{rc}$, and $K_{fc}$ are presentative for the cutting force coefficients in tangential, radial, and axial directions, respectively. Meanwhile, $K_{te}$ and $K_{re}$, and $K_{fe}$ are the edge forces coefficients. The torques of the cutting can be calculated from the cross product of the tangential force of the element and its distance to the tool center as demonstrated in Equation 3.49-52.

If $\phi_{st} \leq \phi_2 \leq \phi_{ex}$ (3.47)

$$CC = 1 \tag{3.48}$$

Else

$$CC = 0 \tag{3.49}$$

End

$$\Delta F_t = CC.[(K_{tc}.h.dr + K_{tc}.dr)] \tag{3.50}$$

$$\Delta F_r = CC.[(K_{rc}.h.dr + K_{rc}.dr)] \tag{3.51}$$

$$\Delta F_f = CC.[(K_{fc}.h.dr + K_{fc}.dr)] \tag{3.52}$$

$$\Delta T = -\Delta F_t.R(j) \tag{3.53}$$

The components of the forces and forces in cartesian coordinate system can be calculated from the multiply of a transformation matrix to the elemental cutting forces and torques in local coordinate system as given in Equation 3.53-54.

$$\begin{bmatrix} F_x \\ F_y \\ F_z \\ T \end{bmatrix} = \begin{bmatrix} -\cos(\phi) & -\sin(\phi) & 0 & 0 \\ sin(\phi) & -\cos(\phi) & 0 & 0 \\ 0 & 0 & 1 & 0 \\ 0 & 0 & 0 & 1 \end{bmatrix} \begin{bmatrix} F_t \\ F_r \\ F_f \\ T \end{bmatrix} \tag{3.54}$$

$$\begin{Bmatrix} F_x \\ F_y \\ F_z \\ T \end{Bmatrix} = \sum_{i=1}^{n_t} \sum_{p=1}^{K} \sum_{s=1}^{L} \sum_{j=1}^{m} \begin{Bmatrix} F_t \\ F_r \\ F_f \\ T \end{Bmatrix} \tag{3.55}$$

**3.2. Scenario 2:**

In this section, in order to predict the cutting forces and torques, an analytical model is developed for a vertical plunge using flat bottom drilling tool in Matlab R2019a software.

Developing technologies in cutting tool design, manufacturing techniques and precise machines has opened a new era in machining industry and led to complex shapes and geometries on the cutting tools. Entering all these complicated geometries into the

analytical model seems to be impossible and insufficient. For this reason, the curvature on the rake face is neglected on the developed model and the cutting edge has been assumed as straight. Furthermore, this simplification has not adversely influenced the obtained results of the researchers for milling and drilling tools and mostly has reported good and satisfactory notes on their results [59-65].

Chisel Edge

The intersection of the flank surfaces of the drill results in formation of the chisel edge. In addition, even flat bottom drills are formed of a small (1°-3°) dish angle as explained in this chapter. Therefore, the fundamental mechanism of the material removal in this area is indentation and smearing the workpiece on both sides of the chisel edge. Consequently, the contribution of the workpiece hardness and area of the contact are required to be considered when calculating the thrust force for cutting this region as demonstrated in Equation 3.55.

$$Thrust\ Force = A_c \times HB \tag{3.56}$$

where $A_c$ and $HB$ are the area of contact indentation and hardness of the work material, respectively.

The area of contact indentation can be calculated from

$$A_c = \frac{2w}{\cos(\Gamma)} \times f_t \tag{3.57}$$

A top view of the geometrical specifications of a pattern flat bottom drill is given in Figure 3.8. The chisel edge length ($CL$) and the local web angle ($\Gamma$) can be calculated from Equation 3.57-58.

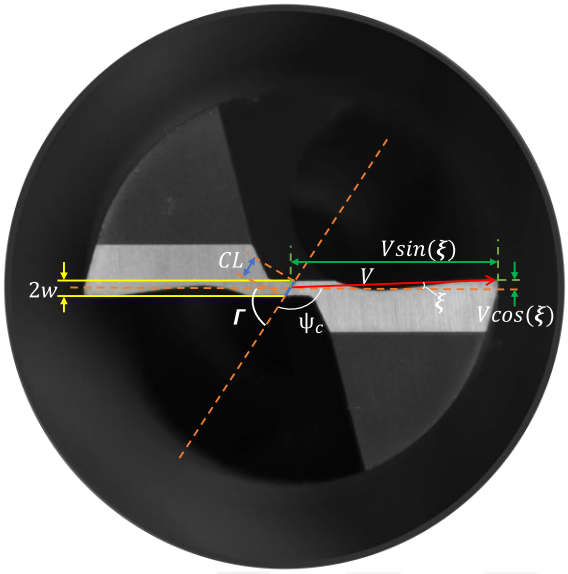


**Figure 3.8.** A top view of the geometrical specifications of a pattern flat bottom drill

$$CL = \frac{2w}{\sin(\pi - \psi_c)} = \frac{2w}{\cos(\Gamma)} \tag{3.58}$$

$$\Gamma = sin^{-1}(\frac{w}{\mathrm{R}}) \tag{3.59}$$

$$\begin{cases} V_x = V.\cos(\xi) \\ V_y = V.\sin(\xi) \end{cases} \tag{3.60}$$

where; $\boldsymbol{\xi}$ and V are the radial rake angle and the cutting velocity which is perpendicular to $R$, respectively.

It may be deduced that the accumulated indentation and cutting forces as shown in Equation 3.61 result in the overall cutting forces in vertical plunge to a flat surface. Given that the chisel width $(2w)$ and indentation region of the tool center are less than the tool diameter and cutting lips, it may be expected that the chisel forces are between 10% and 15% of the lip cutting forces [52]. Therefore, this region has been considered cutting-edge during material removal due to the simplicity of the established model. In a thin shear plane, the cut progress is then carried out on the involved cutting edges.

$$\sum F = \sum F_{indentation} + \sum F_{cutting} \tag{3.61}$$

In this case, if we divide the cutting tool into small elements, the width and height of the cut ($a_w$ and $a_c$) will be equal to the tool radius and feed as illustrated in Figure 3.9, respectively. The feed rate $(h)$ is calculated form the multiplication of the flute number to the feed per tooth as shown in Equation 3.64.

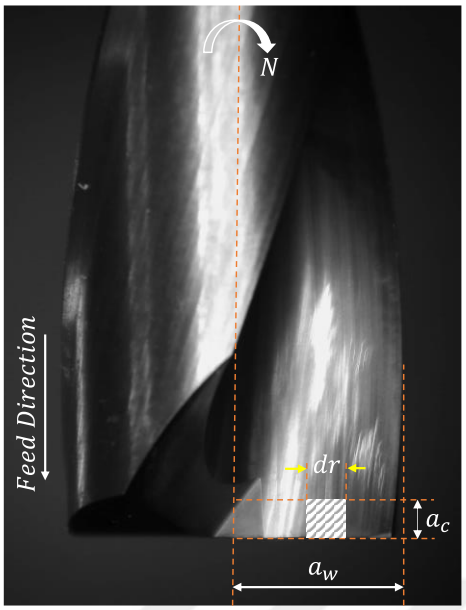


**Figure 3.9.** A side view of the cutting tool and an element on the edge

$$a_w = \frac{d}{2} \tag{3.62}$$

$$a_c = f_t \tag{3.63}$$

$$dx = dr \tag{3.64}$$

$$h = n_t . f_t \tag{3.65}$$

However, in reality the cutting edge ($r_c$) initiates at ($r_i$) as demonstrated in Figure 3.10 and the elemental discretization should be performed by the below given range.

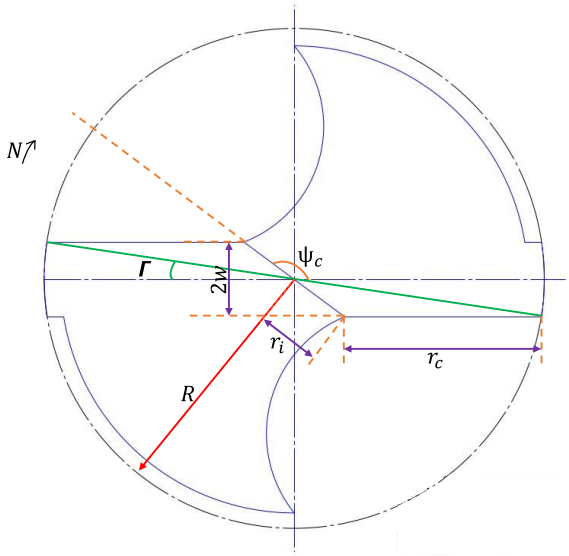


**Figure 3.10.** A top view of the flat bottom drill tool geometry including indentation and cutting sections

Start of cut:

$$r_c = \frac{w}{\cos(\Gamma)} : \Delta R : R \tag{3.66}$$

$$\begin{cases} V_x = V.\cos(\Gamma) \\ V_y = V.\sin(\Gamma) = V_t \end{cases} \tag{3.67}$$

$V$ is the cutting velocity, and it is perpendicular to $r_i$.

The angle between two velocity vectors can be expressed as:

$$\tan(\Gamma) = \frac{V.\sin(\Gamma)}{V.\cos(\Gamma)} \tag{3.68}$$

$$\Gamma = tan^{-1}(\frac{V_t}{V_x}) \tag{3.69}$$

The material flow and its friction between tool rake face as well as machinability performance evaluation criteria such as cutting forces, surface roughness and tool wear is significantly influenced by the tool cutting edge radius.

When drilling with tool cutting edge radius and lower values of the feed rate, the contact area of the uncut chip thickness is on the edge radius. Hence, consideration of the normal rake angle would cause miscalculation. In order to avoid this issue, the effective rake angle should be used as base in determination of elemental cutting forces. A schematic depiction for the mentioned occurrence is given in Figure 3.11. By drawing the cutting forces diagram, it is seen that the effective rake angle is influenced by the cutting tool edge radius, and it can be calculated from Equation 3.70.

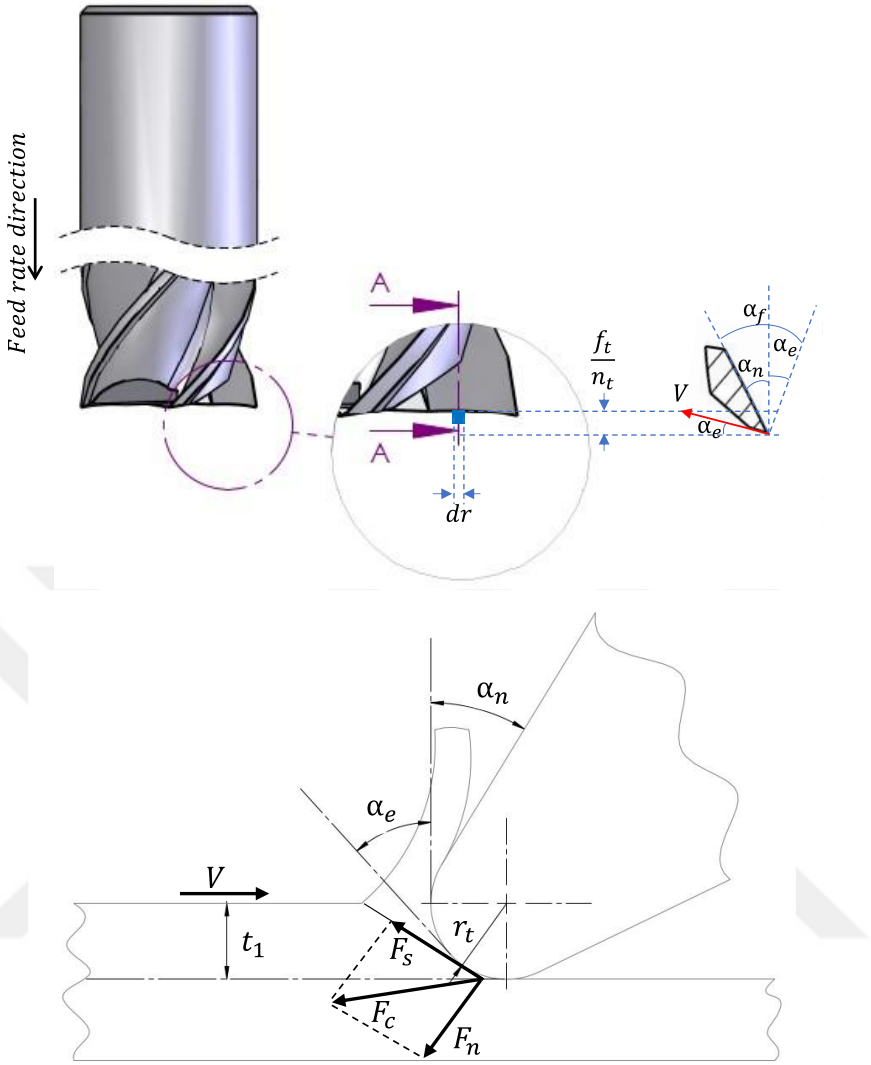


**Figure 3.11.** A schematic depiction for the tool edge radius effect during cut $f_t < r_t$

$$\alpha_e = sin^{-1}\left(\frac{h-r_t}{r_t}\right) \tag{3.70}$$

where $h$, $r_t$ , $F_s$ and $F_n$ stand for the uncut chip thickness, tool edge radius, shear, and normal forces, respectively.

The normal rake will be as equal to the effective rake angle ($\alpha_e = \alpha_n$) when $h = r_t(1 + \sin(\alpha_n)) = h_{max}$ . Moreover, if $h > h_{max}$ ; then $\alpha_n$ should be considered. The elemental cutting forces in this situation for an oblique cut with a single cutting edge may be computed using the following equations taking friction and normal forces into account.

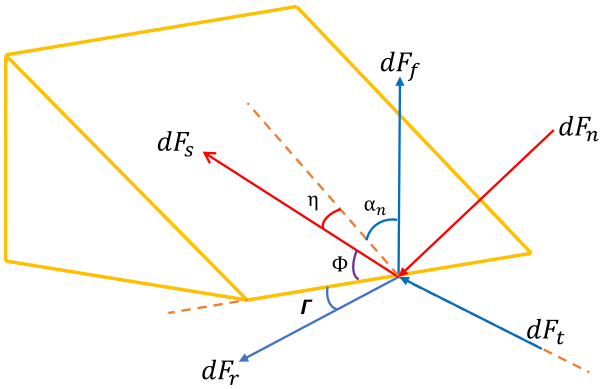


**Figure 3.12.** Cutting forces for an oblique cut for $f_t > r_t$

$$dF_t = dF_s.[\cos(\eta).\cos(\Gamma).\sin(\alpha_e) + \sin(\eta).\sin(\Gamma)] + dF_n.\cos(\alpha_e).\cos(\Gamma) \quad (3.71)$$

$$dF_r = dF_s.[\cos(\eta).\sin(\Gamma).\sin(\alpha_e) + \sin(\eta).\sin(\Gamma)] + dF_n.\cos(\alpha_e).\sin(\Gamma) \quad (3.72)$$

$$dF_f = dF_s.\cos(\eta).\cos(\alpha_e) - dF_n.\sin(\alpha_e) \quad (3.73)$$

In other words, the elemental tangential forces ($F_t$), radial forces ($F_r$) and feed forces ($F_f$) can be expressed as a function of inspected element width of cut ($dr$) and uncut chip thickness.

$$dF_t = [(K_{tc}.h.dr + K_{te}.dr)] \quad (3.74)$$

$$dF_r = [(K_{rc}.h.dr + K_{re}.dr)] \quad (3.75)$$

$$dF_f = \left[\left(K_{fc}.h.dr + K_{fe}.dr\right)\right] \quad (3.76)$$

$$dF_f = dF_z \quad (3.77)$$

$$dT = dM_z = r_c \times \Delta F_t \quad (3.78)$$

Figure 3.13 illustrates the developed algorithm for the analytical model.

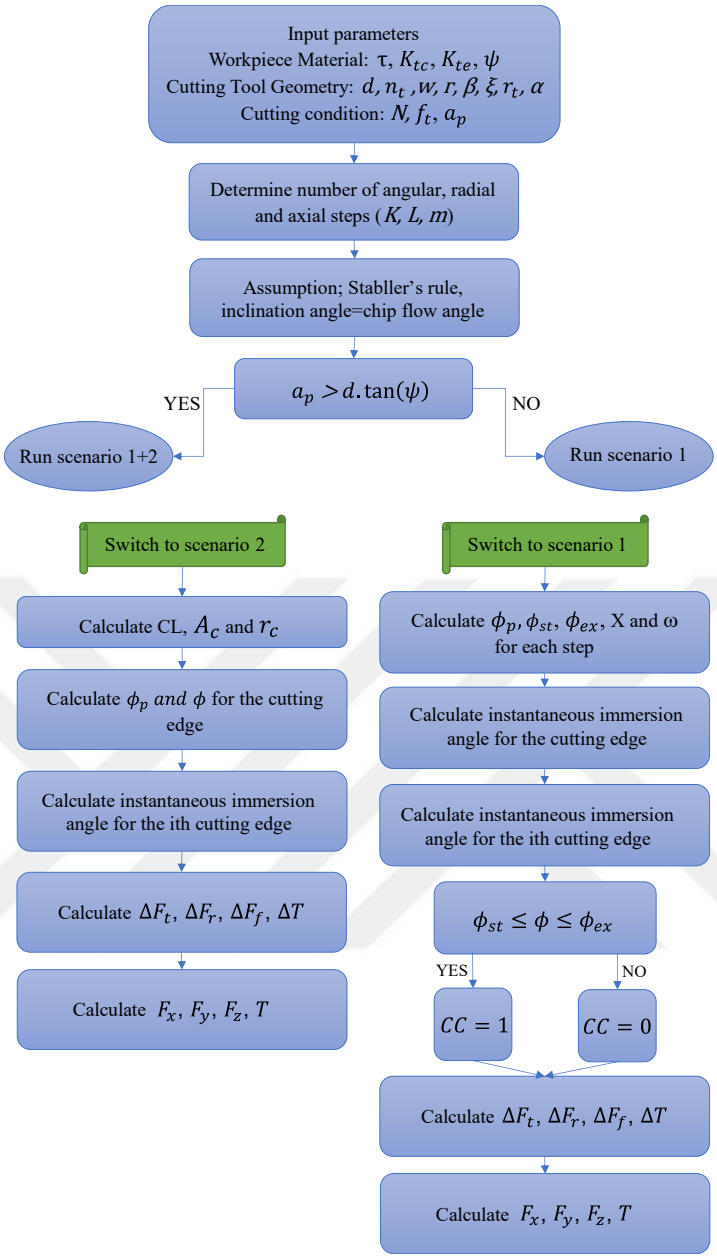


**Figure 3.13.** Flow chart of the developed model

# 4. TESTS WITH REFERENCE CUTTING TOOLS

In this chapter, cutting tests have been carried out using reference flat bottom drills provided by several famous companies on extruded and forged-annealed CW617N, CW511L, CW724R brass alloys. The technical specifications of the utilized Vollhartmetall (VHM) or solid carbide cutting tools are given in Table 4.1. The geometry of the cutting tools has been measured using ZOLLER measuring device type Genius 3s and Keyence digital optical microscope as demonstrated in Figure 4.1. The geometry measurement results of the cutting tools are illustrated in Table 4.2. It has made an endeavor to prevent from disclosing the names of the companies, along with the cutting tools geometries and legibility norms, due to commercial rules. The cutting tests were performed on the materials with 90°, 60° and 45° of plunging angles in order to make both blind and through all holes. Table 4.3 provides an illustration of the test parameters that were used in the experiments. For each test, cutting forces, entrance and exit burr heights, hole bottom and wall surface quality, as well as the drilled hole's dimensional accuracy, were assessed. The test configuration for extruded specimens is shown in Figure 4.2. From Figure 4.3 through Figure 4.18, the findings for the extruded specimens are exhibited. Fixturing equipment has been constructed and made in order to carry out the performance assessment of the cutting tools on the forged and annealed specimens, as shown in Figure 4.19. Figures 4.20 to 4.41 show the results that were attained for the extruded specimens. Following that, the cutting tool performances were assessed based on the findings for the extruded and forged-annealed specimens, taking into account the minimum average cutting forces, burr heights, and dimensional inaccuracy as shown in Table 4.4-5. Thus, the first two devices were chosen for the development of new flat bottom drills. The most influential geometrical features of the cutting tools have been identified and indicated by their relevance level on the machining responses in Table 4.6 based on the knowledge in the literature and cutting tool designers' experience.

**Table 4.1.** the performance evaluated refence tools specifications

| Company | Tool Diameter, (mm) | Material | Coating | Type | Cooling |
|---|---|---|---|---|---|
| A | Ø8 | VHM Carbide | Uncoated-Polished | N | Internal |
| B | Ø8 | VHM Carbide | PVD EgiAs | M, K, H, P, N | Internal |
| C | Ø8 | VHM Carbide | X | M, K, H, P, N | Internal |
| D | Ø8 | VHM Carbide | AQUA EX | N | Internal |
| E | Ø8 | VHM Carbide | TiAlN | P, M, K, N, S, H | External |

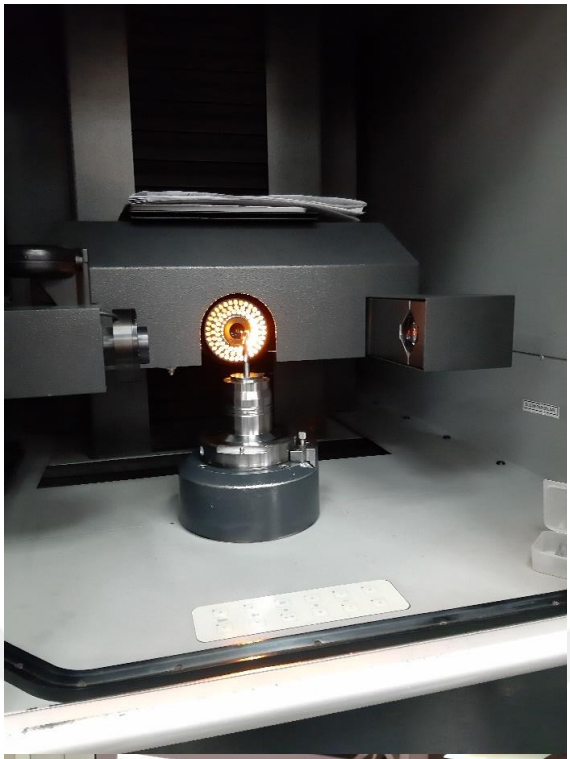

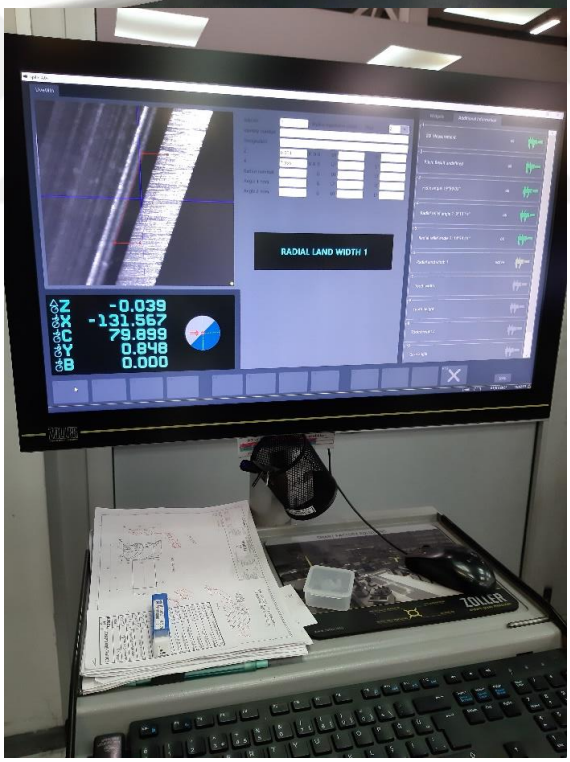
RADIAL LAND WIDTH 1
Z -0.039
X -131.567
C 79.899
Y 0.848
B 0.000

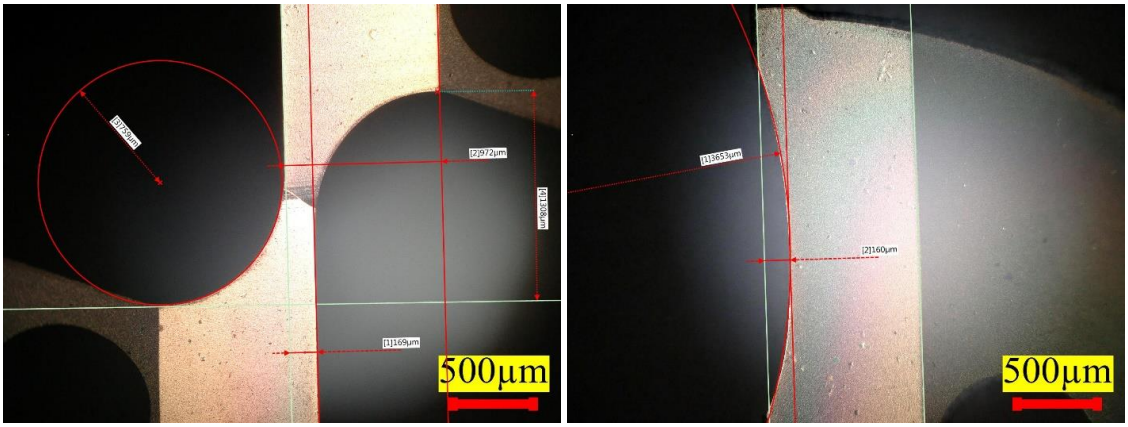


**Figure 4.1.** The measurement operation of the cutting tools in Zoller and Keyence optical microscope

**Table 4.2.** The geometric measurements of the cutting tools

| | A | B | C | D | E |
|---|---|---|---|---|---|
| Core diameter | 1.986 | 2.096 | 2.02 | 1.958 | 1.273 |
| Flute depth | 3.003 | 2.928 | 2.986 | 3.003 | 3.34 |
| Radial rake angle | -4°02'24" | 14°11'24" | 7°04'12" | 10°05'24" | 0°40'48" |
| Helix angle | 30°29'24" | 19°58'48" | 30°05'24" | 30°25'48" | 19°49'48" |
| Helical pitch | 42.747 | 68.698 | 43.326 | 42.597 | 69.281 |
| Radial relief angle 1 | 4°32'24" | 3°10'12" | 2°22'12" | 3°19'48" | 0°11'24" |
| Radial relief angle 2 | 26°55'12" | 14°39'00" | 17°08'24" | 19°21'36" | 17°45'36" |
| Radial land width 1 | 0.651 | 0.282 | 0.249 | 0.382 | 0.216 |
| Eff. radial land width 1 | 0.559 | 0.264 | 0.214 | 0.328 | 0.203 |
| Tooth width | 5.887 | 5.145 | 6.377 | 6.389 | 5.603 |
| Eff. tooth width | 5.051 | 4.809 | 5.476 | 5.487 | 5.25 |
| Tooth height | 0.138 | 0.061 | 0.039 | 0.229 | 0.036 |
| Tooth height 2 | 0.142 | 0.058 | 0.044 | 0.229 | 0.048 |
| Relief angle | 10°27'36" | 7°15'36" | 8°54'36" | 21°16'48" | 9°25'12" |
| Gash angle | 27°48'36" | 33°54'36" | 51°53'24" | 40°52'12" | 38°34'12" |
| Center offset | -0.184 | 0.018 | 0.063 | 0.092 | 0.055 |
| Axial relief angle 1 | 5°19'48" | 6°07'12" | 4°50'24" | 4°55'12" | 4°50'24" |
| Axial relief angle 2 | 11°25'48" | 16°06'36" | 20°05'24" | 19°47'24" | 0°06'00" |
| Axial land width | 0.419 | 0.97 | 0.611 | 0.924 | 0.982 |
| Axial land width SE | 0.352 | 0.977 | 0.595 | 0.926 | 0.988 |
| Axial rake angle | 0°11'24" | -0°48'00" | -0°31'12" | -0°38'24" | 0°52'48" |
| Chisel angle | 17°16'12" | 48°34'12" | 84°16'12" | | 26°45'00" |
| Lengthways dimension | 5.148 | 4.35 | 3.633 | 3.214 | 5.167 |
| Crossways dimension | 6.836 | 7.218 | 6.75 | 6.652 | 7.012 |

| | | | | | |
|---|---|---|---|---|---|
| Radius (μm) | 2.000 | 6.333 | 2.333 | 3.333 | 13.667 |
| Axial angle | 179°54'36" | 179°28'12" | 178°52'48" | 179°16'12" | 180°39'36" |
| Dish angle | -0°03'00" | -0°16'12" | -0°33'36" | -0°21'36" | 0°19'48" |

**Table 4.3.** The utilized test parameters for the experiments

| Material | Tool | Hole Type | Angle | Parameter | Value |
|---|---|---|---|---|---|
| CW617N<br>CW724R<br>CW511L | A<br>B<br>C<br>D<br>E | Blind<br>Through all | 90°<br>60°<br>45° | $V_f$, (mm/min) | 500.0 |
| | | | | $N$,(rpm) | 4000.0 |
| | | | | $V_c$, (m/min) | 100.5 |
| | | | | $V_f$, (mm/min) | 200.0 |
| | | | | $N$,(rpm) | 3000.0 |
| | | | | $V_c$, (m/min) | 70.4 |

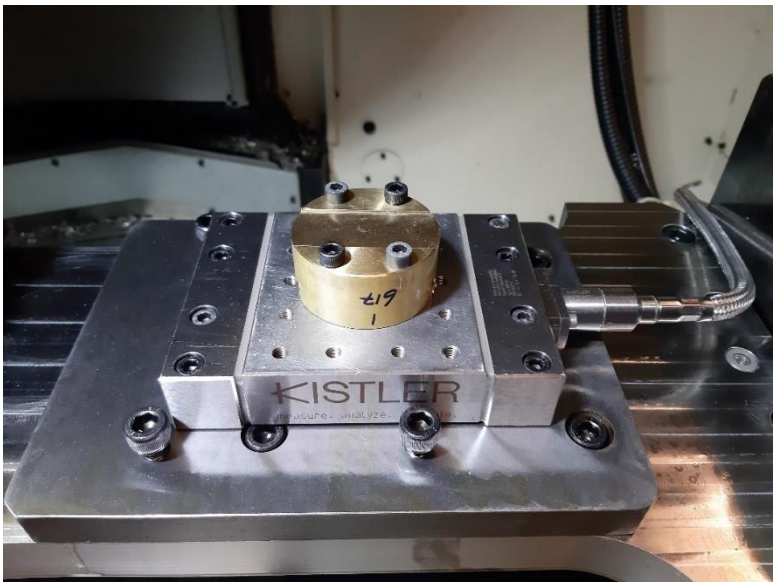


**Figure 4.2.** Test setup for extruded specimens

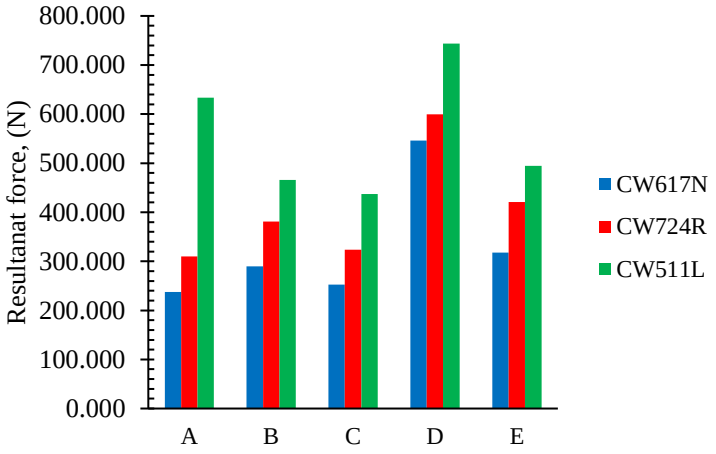


**Figure 4.3.** Measured resultant cutting forces during blind drilling at 90° of extruded specimens using reference tools

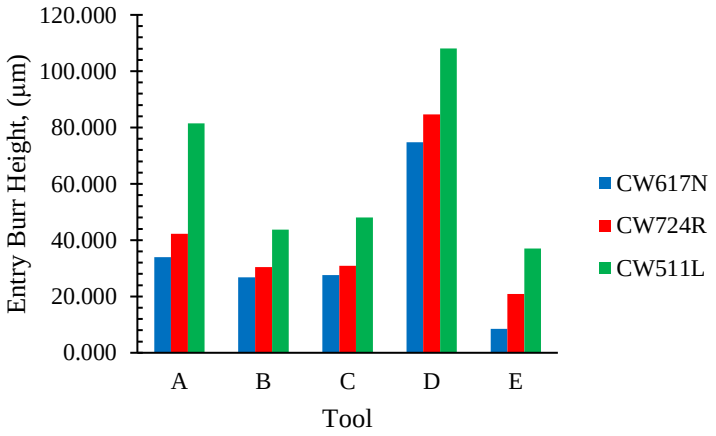


**Figure 4.4.** Measured entry burr height during blind drilling at 90° of extruded specimens using reference tools

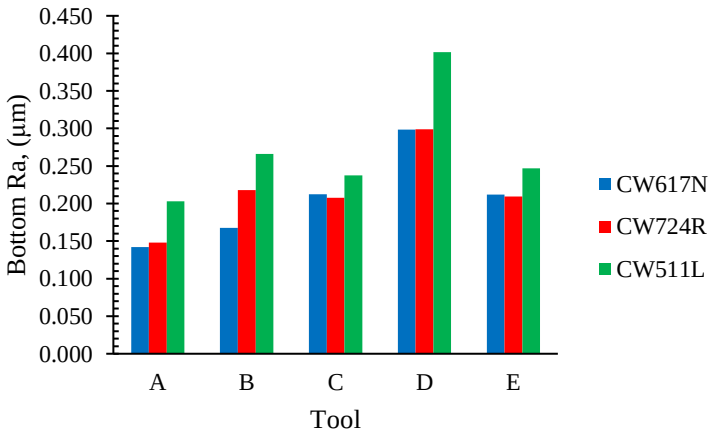

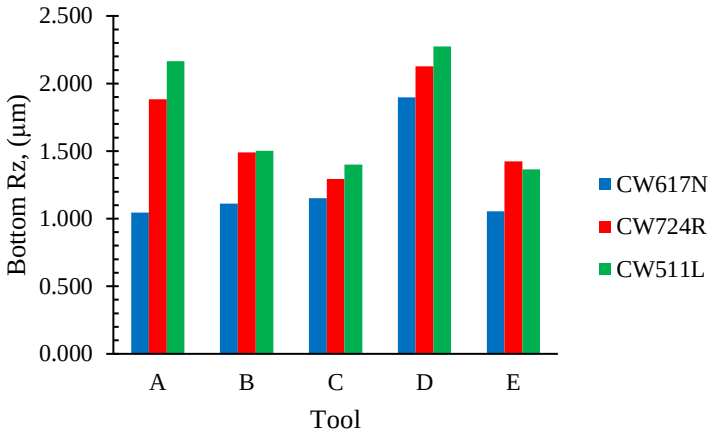


**Figure 4.5.** Measured hole bottom surface roughness during blind drilling at 90° of extruded specimens using reference tools

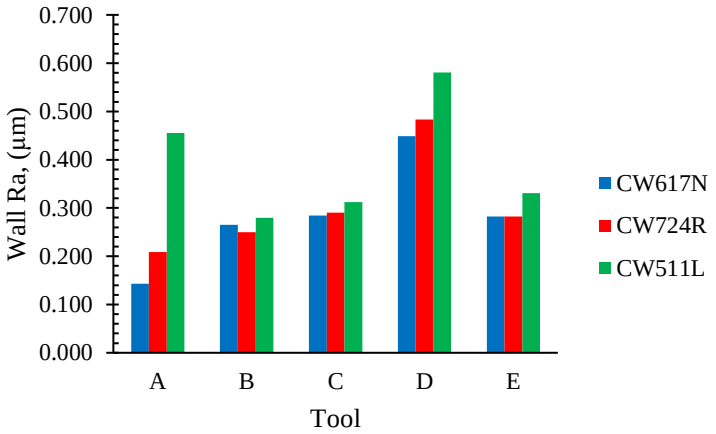


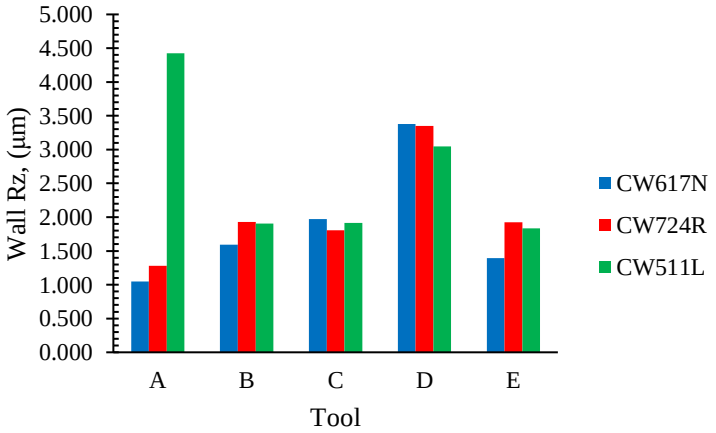


**Figure 4.6.** Measured hole wall surface roughness during blind drilling at 90° of extruded specimens using reference tools

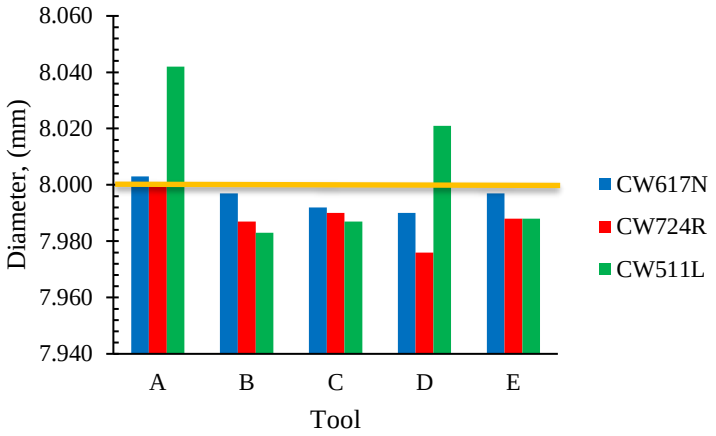


**Figure 4.7.** Measured hole diameter during blind drilling at 90° of extruded specimens using reference tools

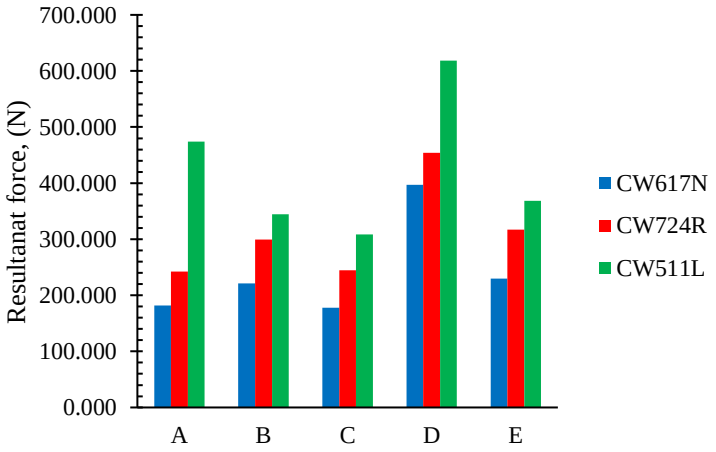


**Figure 4.8.** Measured resultant cutting forces during blind drilling at 45° of extruded specimens using reference tools

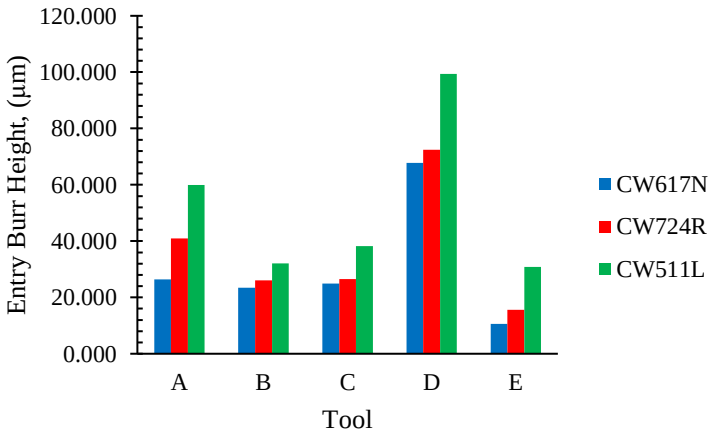

**Figure 4.9.** Measured entry burr height during blind drilling at 45° of extruded specimens using reference tools

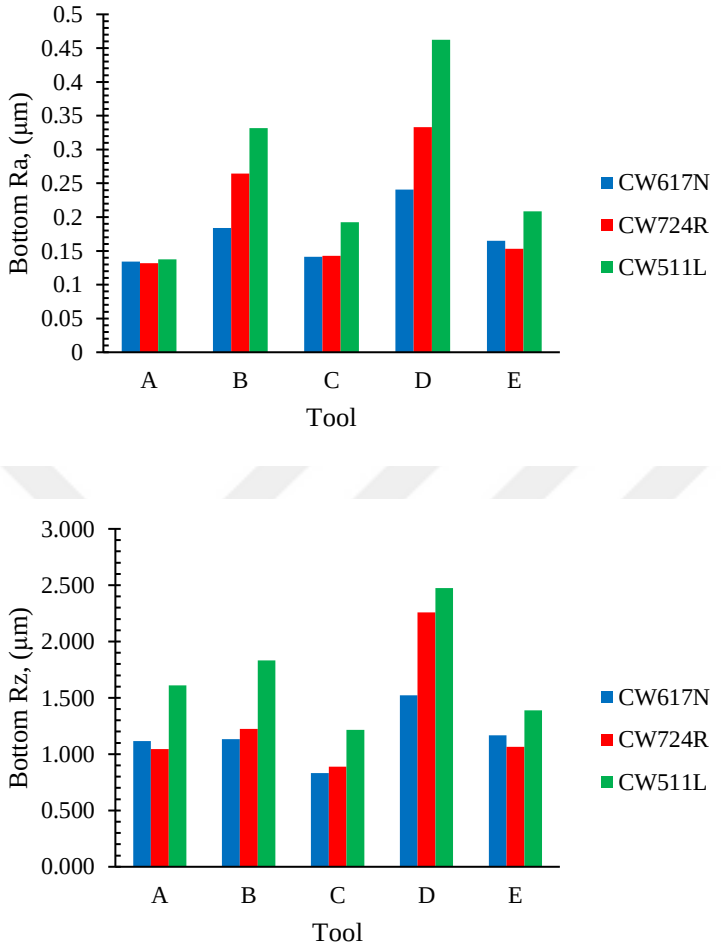


**Figure 4.10.** Measured hole bottom surface roughness during blind drilling at 45° of extruded specimens using reference tools

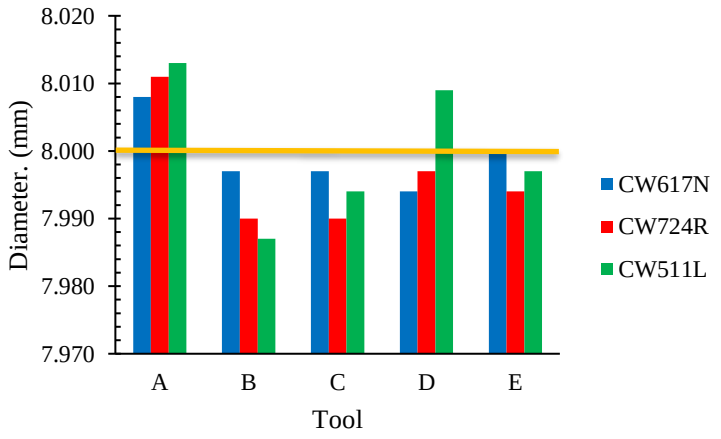

**Figure 4.11.** Measured hole diameter during blind drilling at 45° of extruded specimens using reference tools

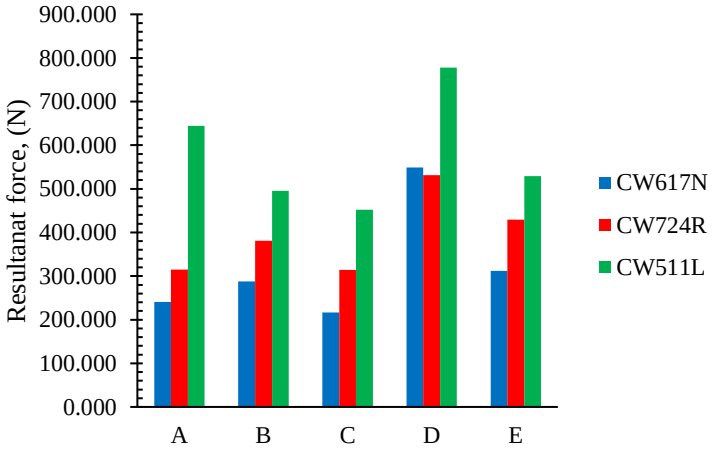


**Figure 4.12.** Measured resultant cutting forces during through all drilling at 90° of extruded specimens using reference tools

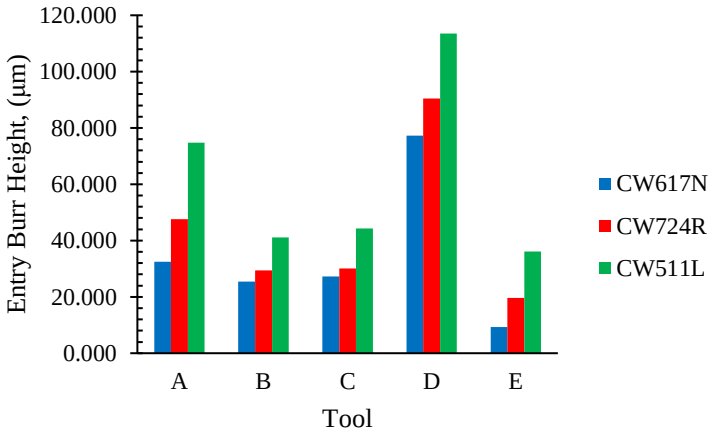


**Figure 4.13.** Measured entry burr height during through all drilling at 90° of extruded specimens using reference tools

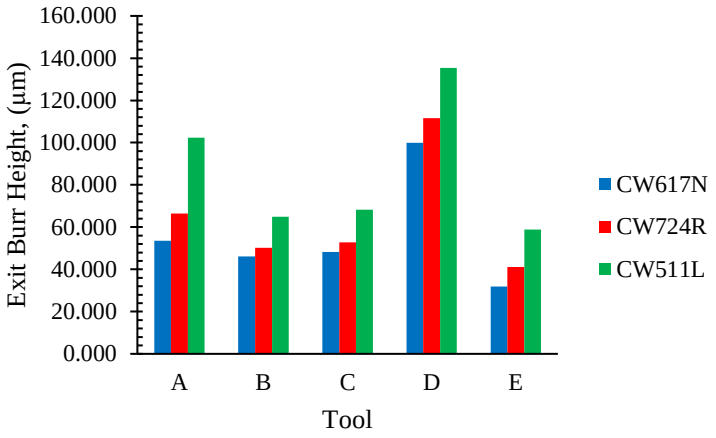


**Figure 4.14.** Measured exit burr height during through all drilling at 90° of extruded specimens using reference tools

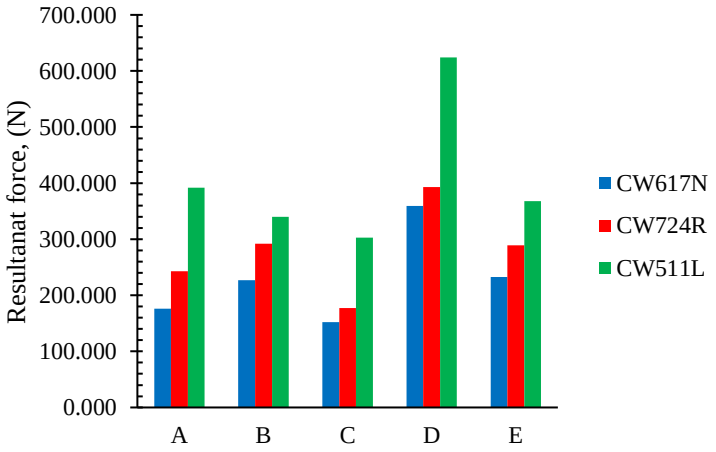


**Figure 4.15.** Measured resultant cutting forces during through all drilling at 60° of extruded specimens using reference tools

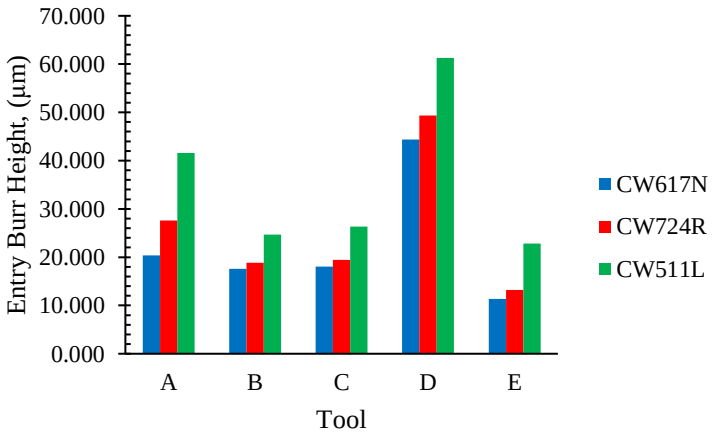

**Figure 4.16.** Measured entry burr height during through all drilling at 60° of extruded specimens using reference tools

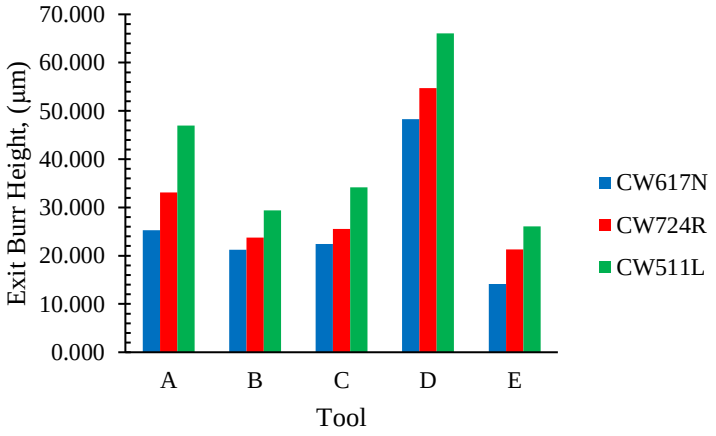


**Figure 4.17.** Measured exit burr height during through all drilling at 60° of extruded specimens using reference tools

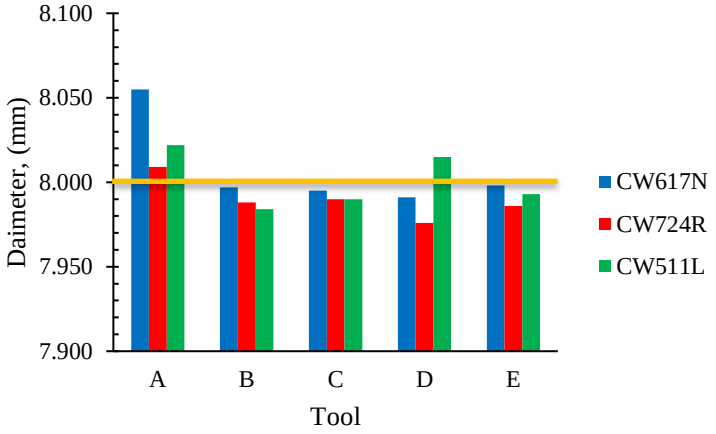


**Figure 4.18.** Measured hole diameter during through all drilling at 60° of extruded specimens using reference tools

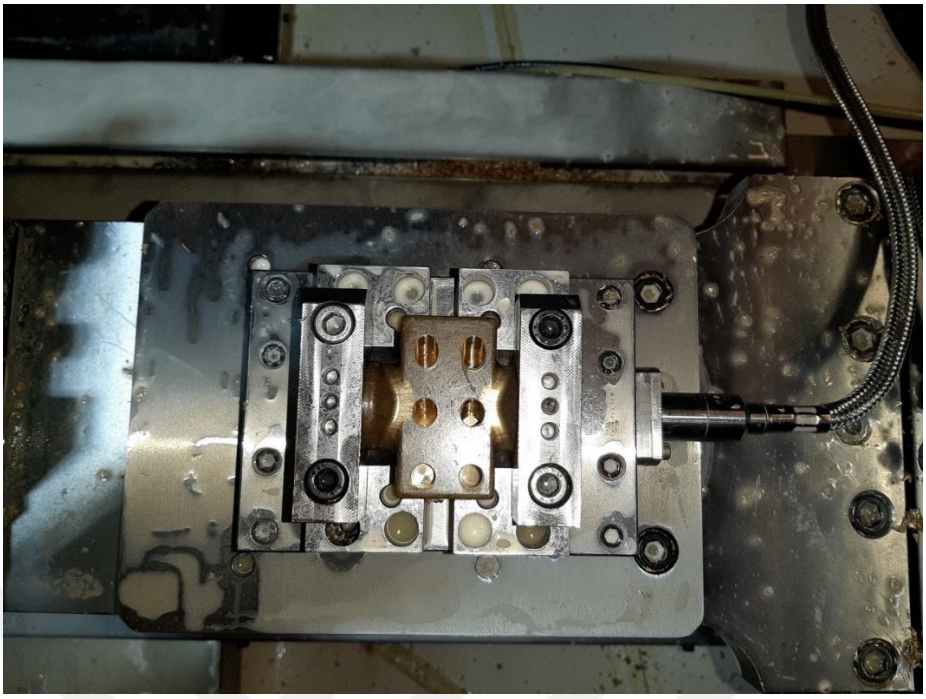

**Figure 4.19.** Test setup for forged and annealed specimens

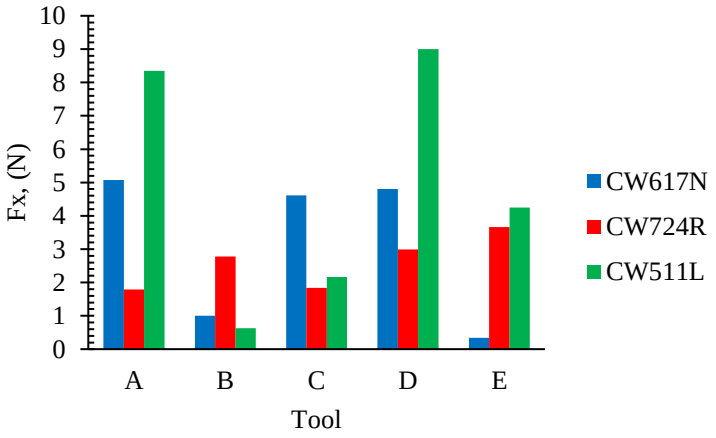

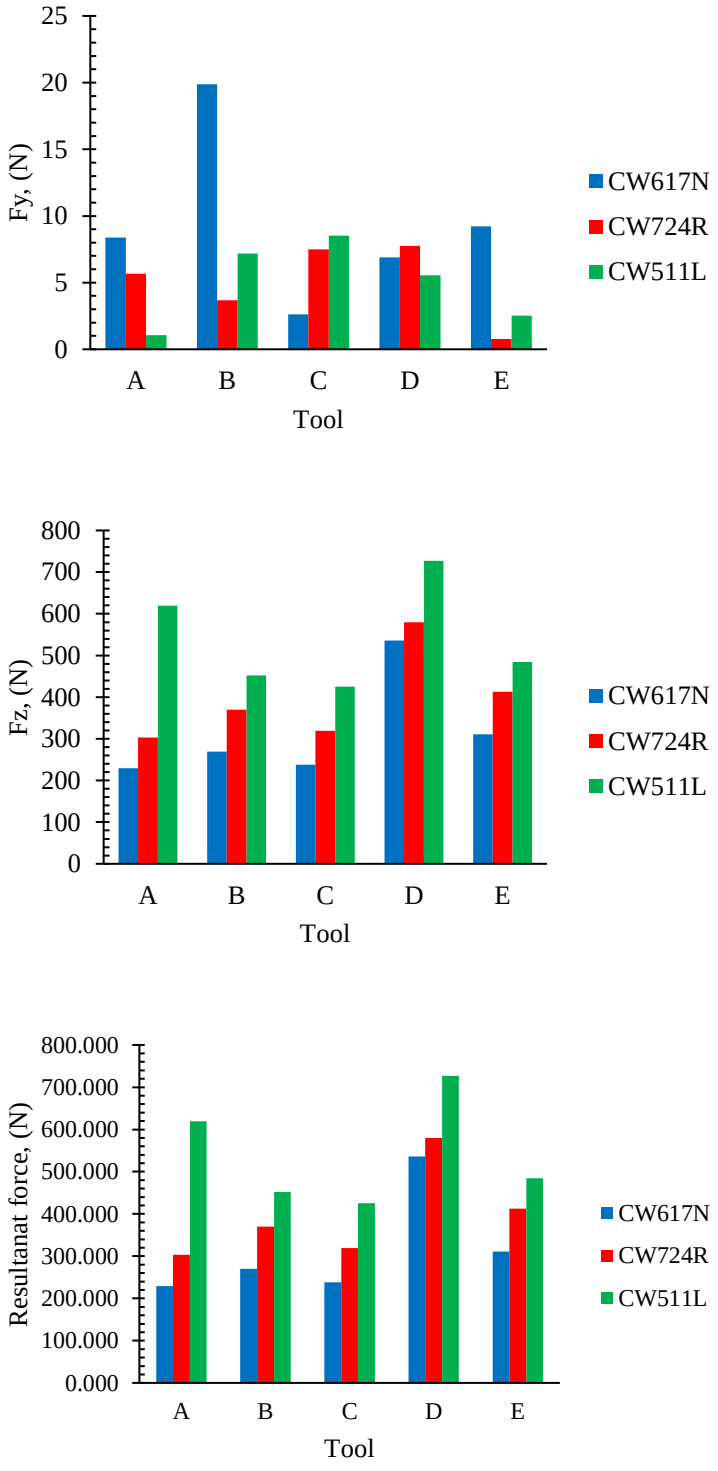


**Figure 4.20.** Measured cutting forces during blind drilling at 90° of forged and annealed specimens using reference tools

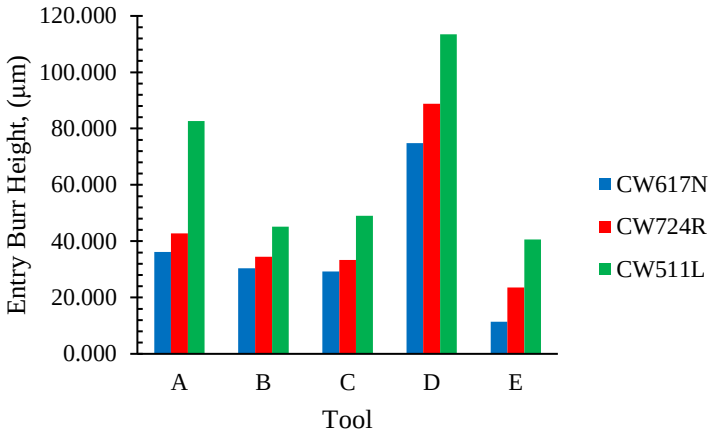


**Figure 4.21.** Measured entry burr height during blind drilling at 90° of forged and annealed specimens using reference tools

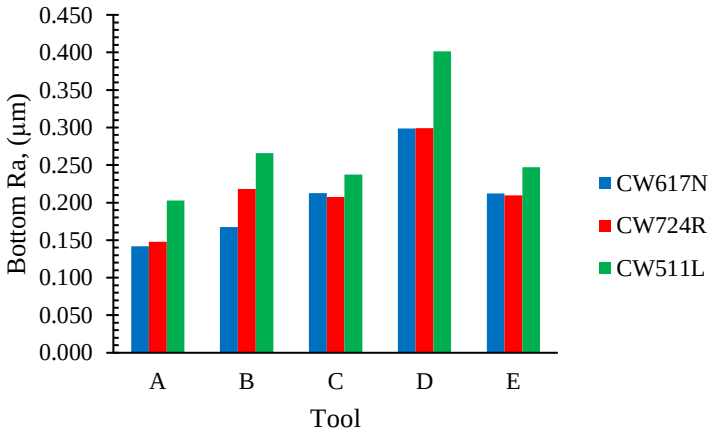


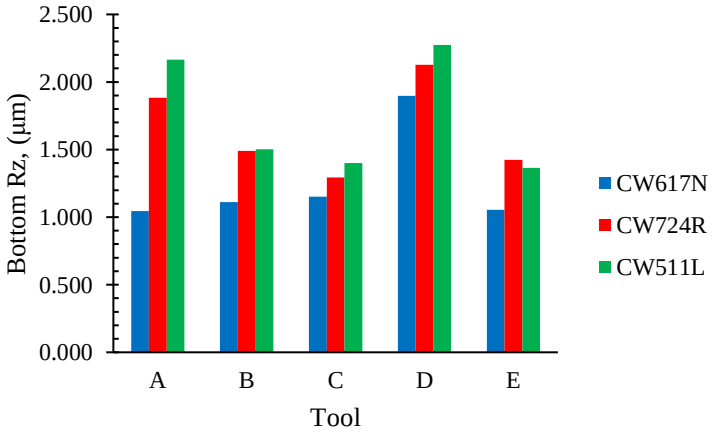


**Figure 4.22.** Measured hole bottom surface roughness during blind drilling at 90° of forged and annealed specimens using reference tools

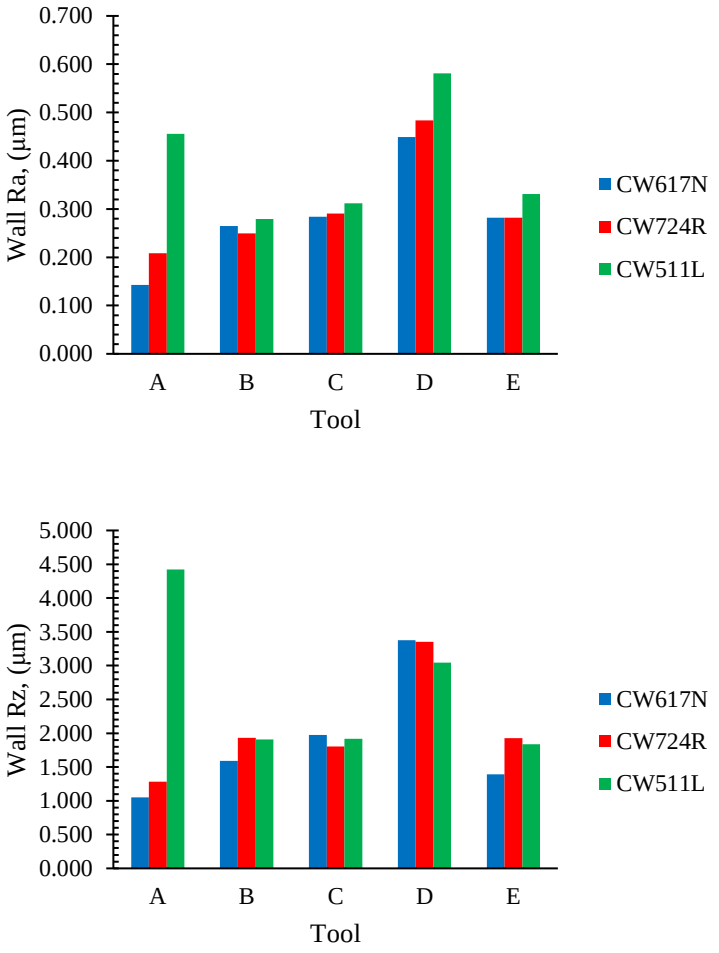


**Figure 4.23.** Measured hole wall surface roughness during blind drilling at 90° of forged and annealed specimens using reference tools

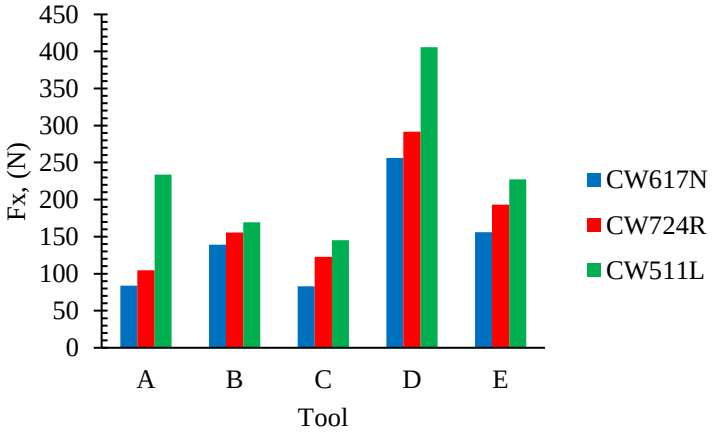

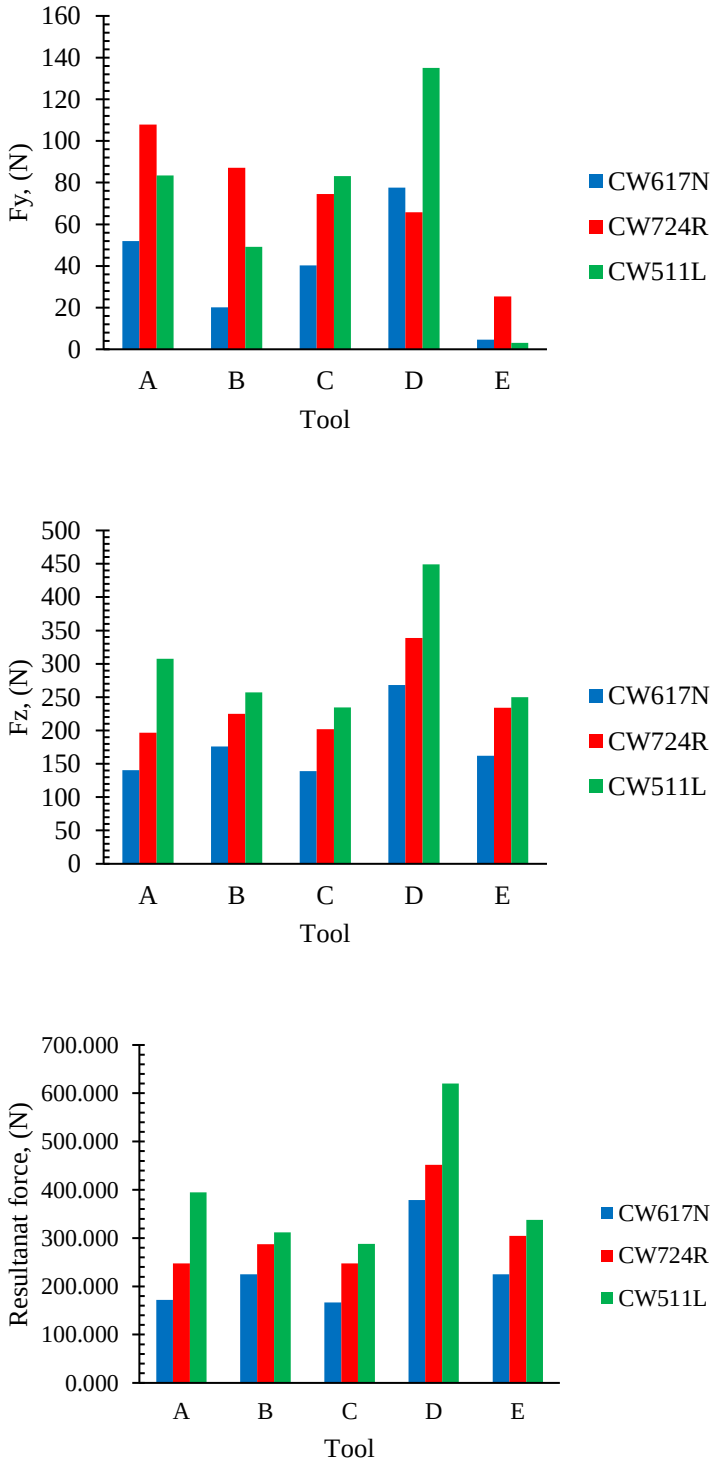


**Figure 4.24.** Measured cutting forces during blind drilling at 45° of forged and annealed specimens using reference tools

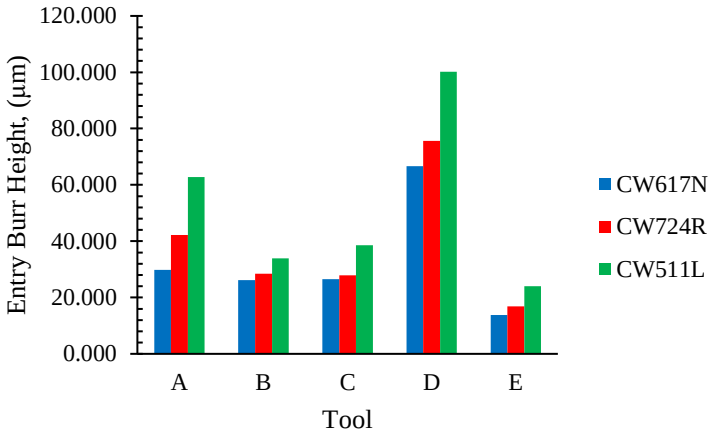


**Figure 4.25.** Measured entry burr height during blind drilling at 45° of forged and annealed specimens using reference tools

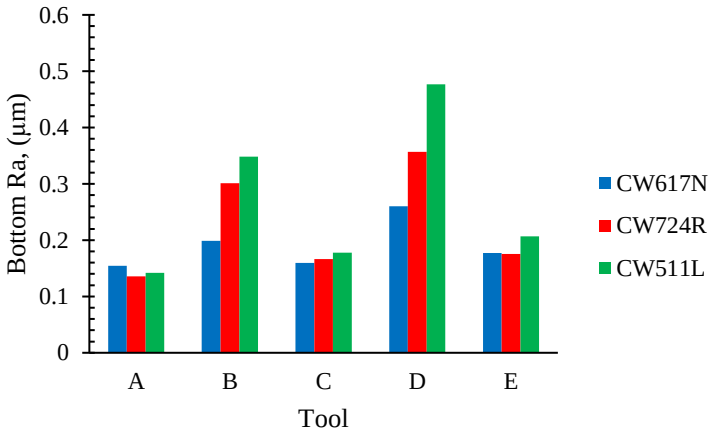


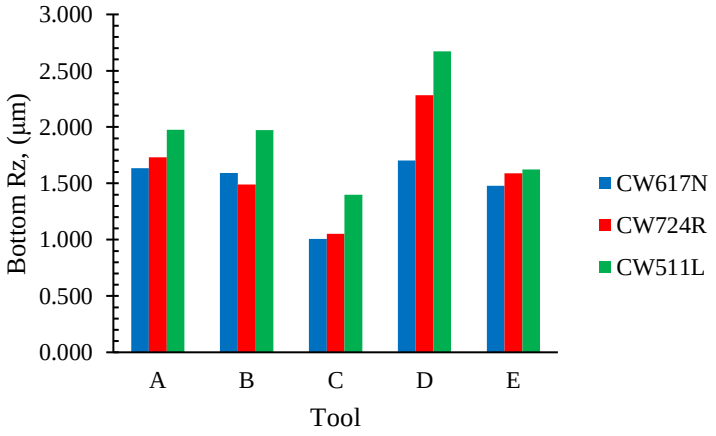


**Figure 4.26.** Measured hole bottom surface roughness during blind drilling at 45° of forged and annealed specimens using reference tools

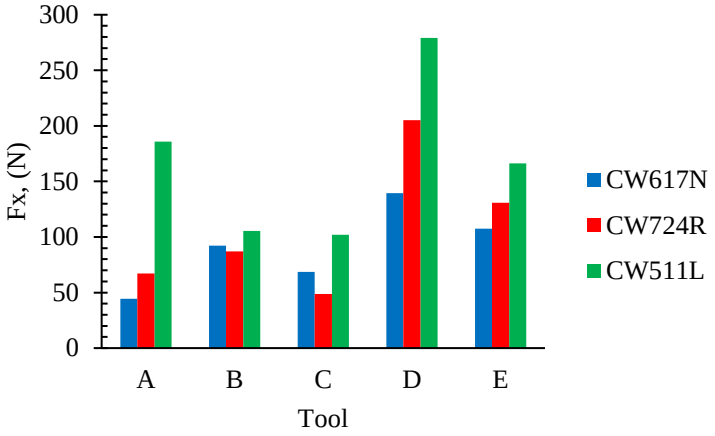
300
250
200
150
100
50
0
Fx, (N)
A
B
C
D
E
Tool
CW617N
CW724R
CW511L

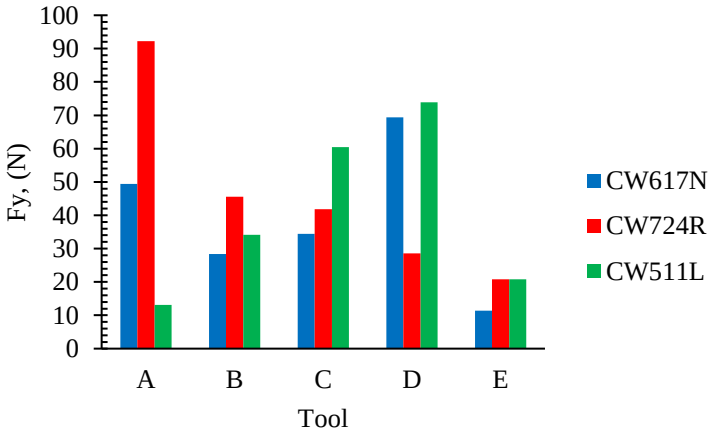
100
90
80
70
60
50
40
30
20
10
0
Fy, (N)
A
B
C
D
E
Tool
CW617N
CW724R
CW511L

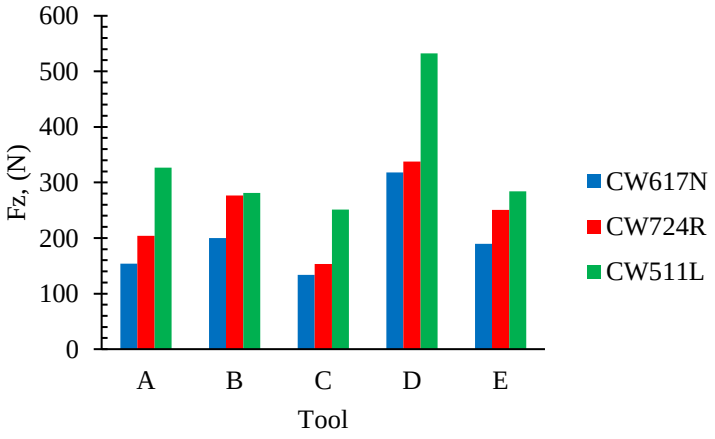
600
500
400
300
200
100
0
Fz, (N)
A
B
C
D
E
Tool
CW617N
CW724R
CW511L

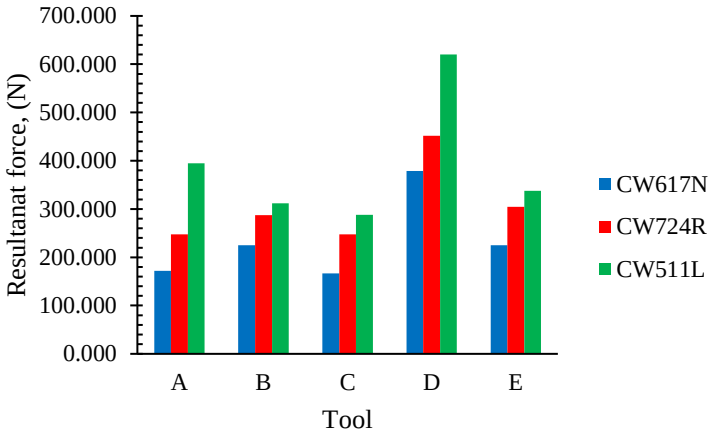


**Figure 4.27.** Measured cutting forces during blind drilling at 60° of forged and annealed specimens using reference tools

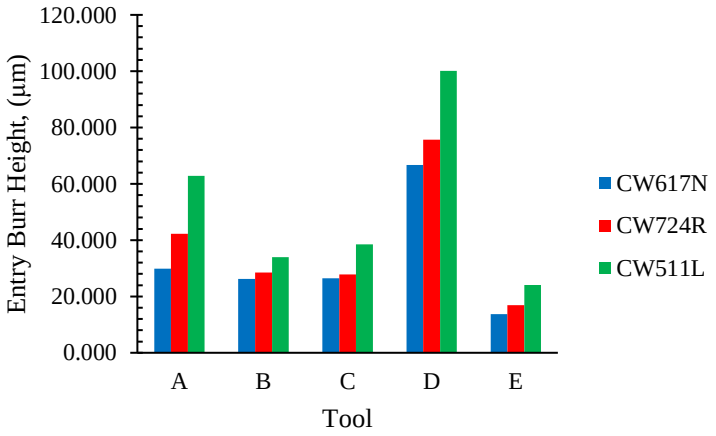


**Figure 4.28.** Measured entry burr height during blind drilling at 60° of forged and annealed specimens using reference tools

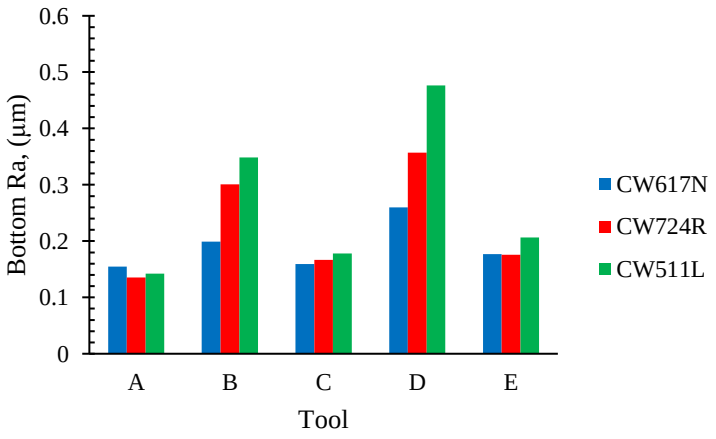

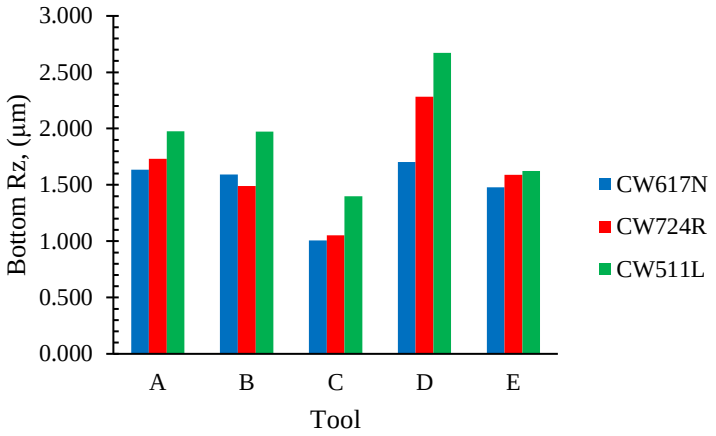


**Figure 4.29.** Measured hole bottom surface roughness during blind drilling at 60° of forged and annealed specimens using reference tools

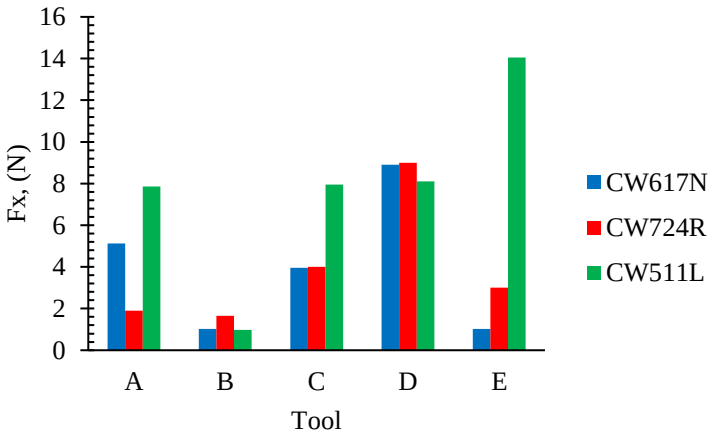


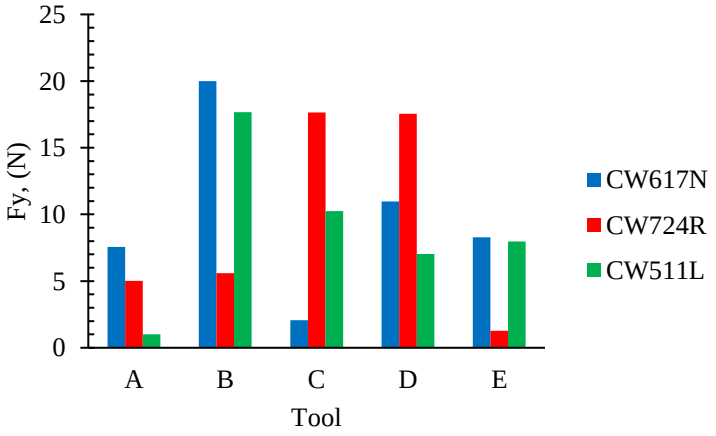

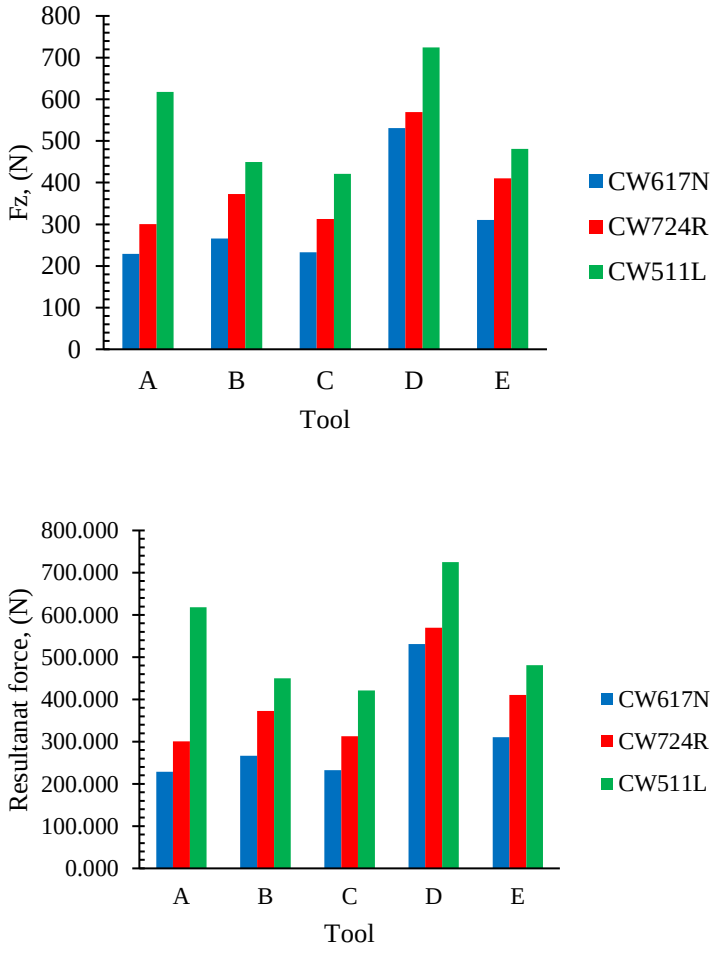


**Figure 4.30.** Measured cutting forces during through all drilling at 90° of forged and annealed specimens using reference tools

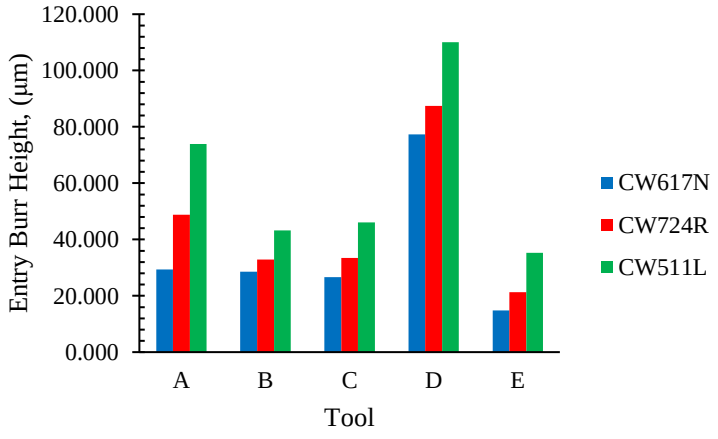

**Figure 4.31.** Measured entry burr height during through all drilling at 90° of forged and annealed specimens using reference tools

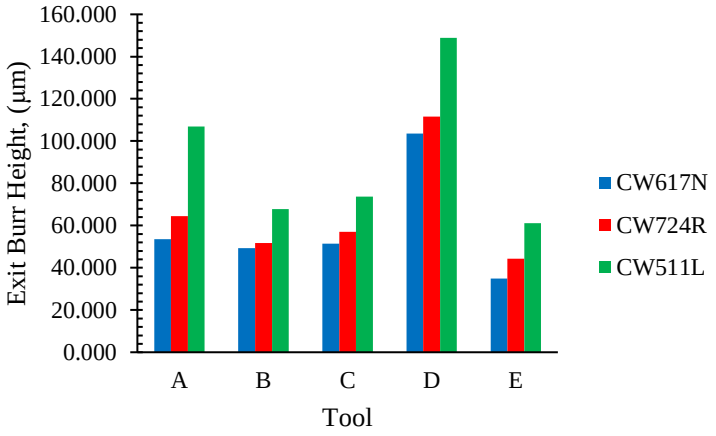


**Figure 4.32.** Measured exit burr height during through all drilling at 90° of forged and annealed specimens using reference tools

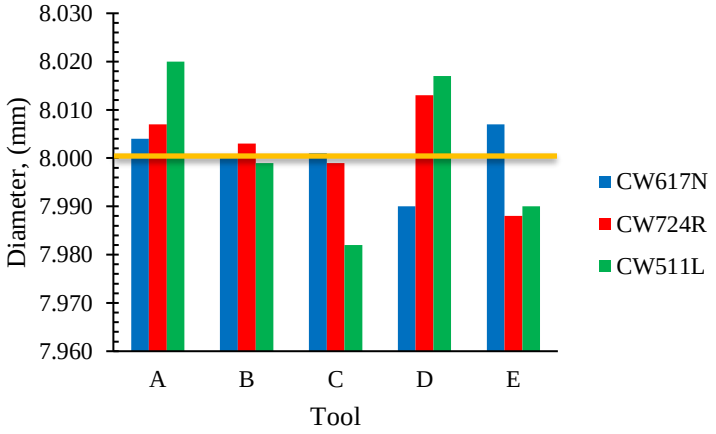


**Figure 4.33.** Measured hole diameter during through all drilling at 90° of forged and annealed specimens using reference tools

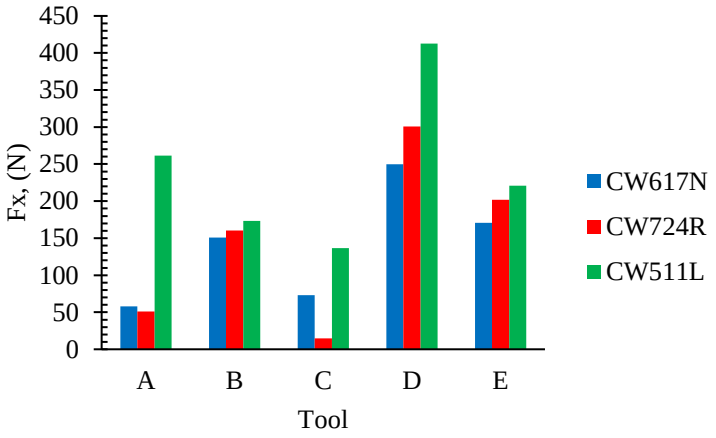
Fx, (N)
450
400
350
300
250
200
150
100
50
0
A
B
C
D
E
Tool
CW617N
CW724R
CW511L

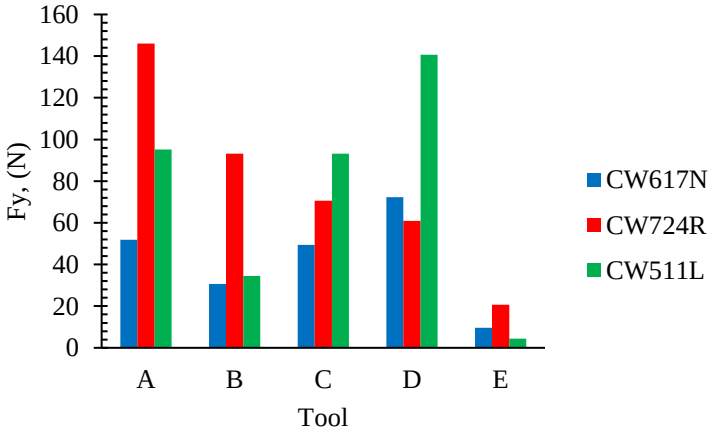
Fy, (N)
160
140
120
100
80
60
40
20
0
A
B
C
D
E
Tool
CW617N
CW724R
CW511L

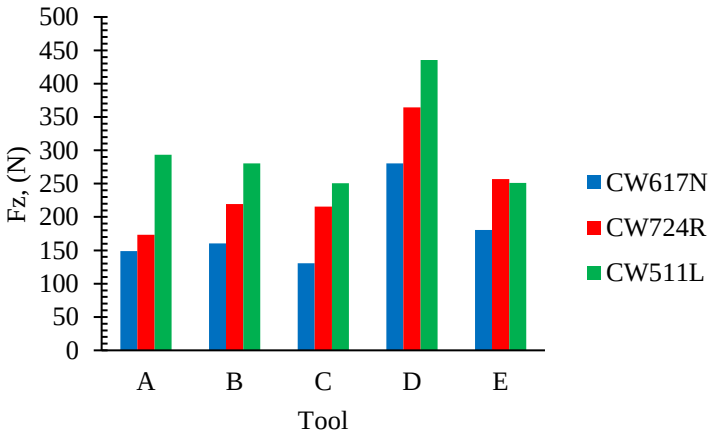
Fz, (N)
500
450
400
350
300
250
200
150
100
50
0
A
B
C
D
E
Tool
CW617N
CW724R
CW511L

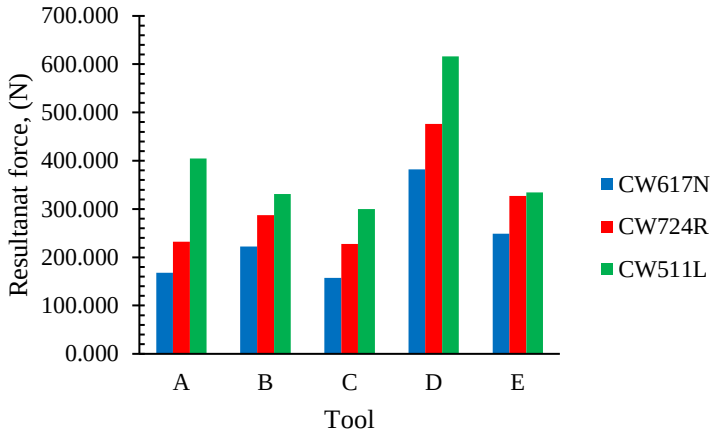


**Figure 4.34.** Measured cutting forces during through all drilling at 45° of forged and annealed specimens using reference tools

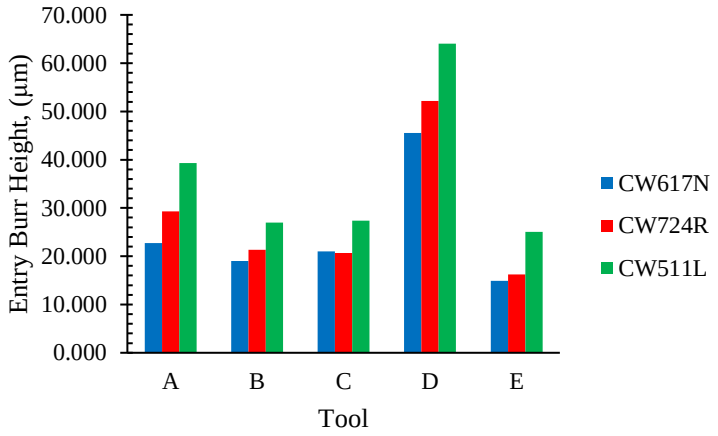


**Figure 4.35.** Measured entry burr height during through all drilling at 45° of forged and annealed specimens using reference tools

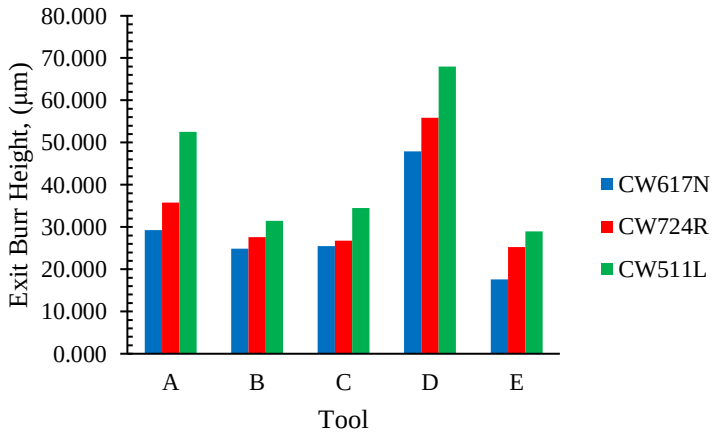

**Figure 4.36.** Measured exit burr height during through all drilling at 45° of forged and annealed specimens using reference tools

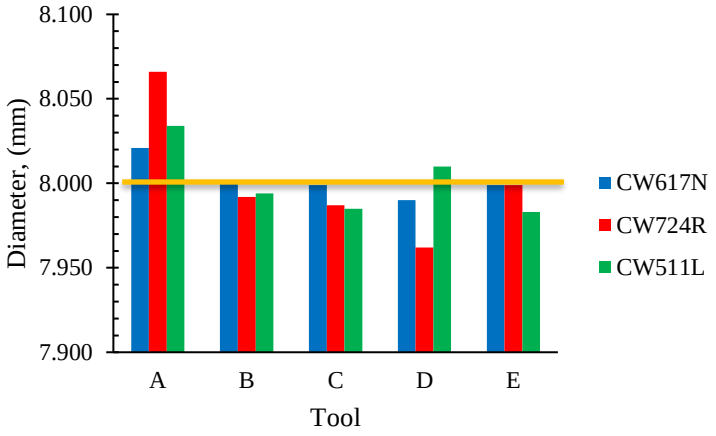


**Figure 4.37.** Measured hole diameter during through all drilling at 45° of forged and annealed specimens using reference tools

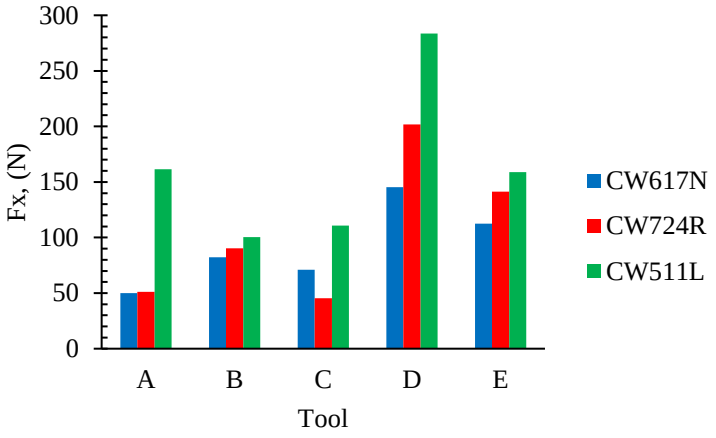


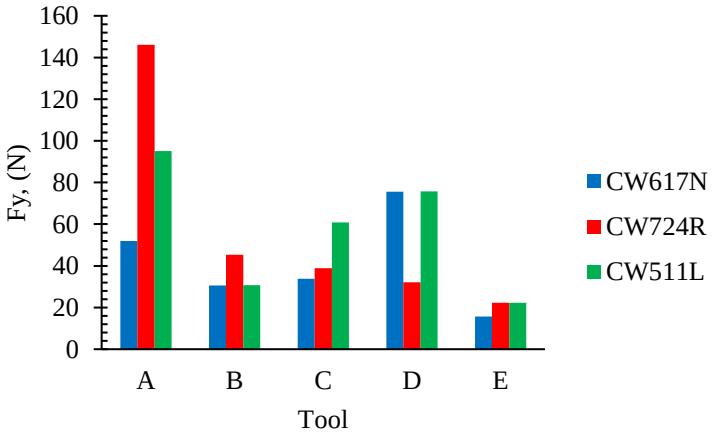

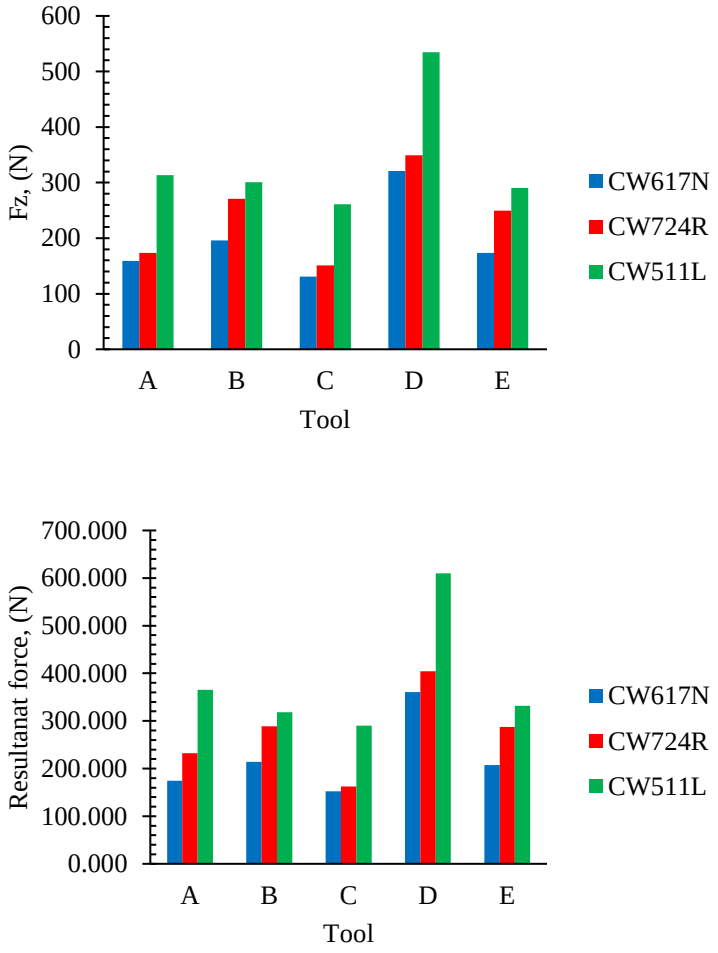


**Figure 4.38.** Measured cutting forces during through all drilling at 60° of forged and annealed specimens using reference tools

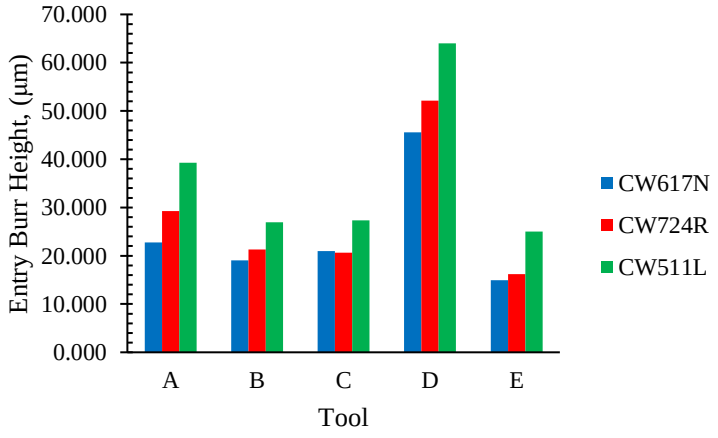


**Figure 4.39.** Measured entry burr height during through all drilling at 60° of forged and annealed specimens using reference tools

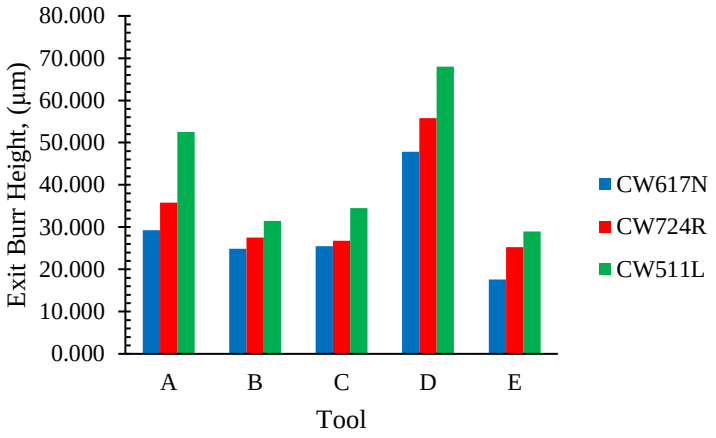


**Figure 4.40.** Measured exit burr height during through all drilling at 60° of forged and annealed specimens using reference tools

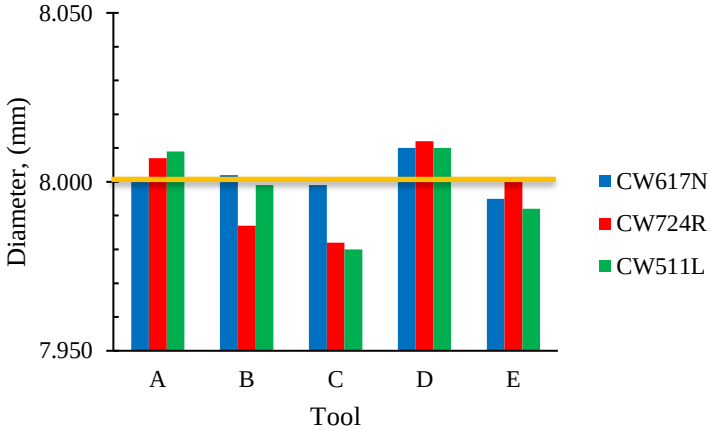


**Figure 4.41.** Measured hole diameter during through all drilling at 60° of forged and annealed specimens using reference tools

**Table 4.4.** The best performance evaluation results for the extruded specimens using reference cutting tools

| Extruded | | | CW617N | CW724R | CW511L |
|---|---|---|---|---|---|
| Entry Burr Size | Blind | 90° | E-B | E-B | E-B |
| | | 60° | - | - | - |
| | Through All | 45° | E-B | E-B | E-B |
| | | 90° | E-B | E-B | E-B |
| | | 60° | E-B | E-B | E-B |
| | | 45° | - | - | - |
| Exit Burr Size | Through All | 90° | E-B | E-B | E-B |
| | | 60° | E-B | E-B | E-B |

| | | | | | |
|---|---|---|---|---|---|
| | | 45° | - | - | - |
| | | 90° | A-B | C-E | A-C |
| Ra Bottom | Blind | 60° | - | - | - |
| | | 45° | A-C | A-C | A-C |
| | | 90° | A-B | A-B | B-C |
| | Blind | 60° | A-B | A-B | B-C |
| Ra Wall | | 45° | A-B | A-B | B-C |
| | Through All | 90° | - | - | - |
| | | 60° | - | - | - |
| | | 45° | - | - | - |
| | | 90° | - | - | - |
| | Blind | 60° | - | - | - |
| Diameter | | 90° | - | - | - |
| | Through All | 90° | B-C | C-B | E-B |
| | | 60° | B-C | E-B | B-C |
| | | 45° | B-A | E-A | B-E |
| | | 90° | A-C | A-C | C-B |
| | Blind | 60° | C-A | C-A | C-B |
| Cutting Forces | | 45° | C-A | C-A | C-B |
| | Through All | 90° | A-C | A-C | C-B |
| | | 60° | C-A | C-A | C-B |
| | | 45° | C-A | C-A | C-B |

**Table 4.5.** The best performance evaluation results for the forged and annealed specimens using reference cutting tools

| Forged & annealed | | | CW617N | CW724R | CW511L |
|---|---|---|---|---|---|
| | | 90° | C-B | C-B | E-B |
| | Blind | 60° | B-A | B-C | E-B |
| | | 45° | B-C | C-B | E-B |
| Entry Burr Size | | 90° | E-C | E-B | B-C |
| | Through All | 60° | E-B | E-C | E-B |
| | | 45° | E-B | E-C | E-B |
| | | 90° | E-B | E-B | E-B |
| Exit Burr Size | Through All | 60° | E-B | E-B | C-B |
| | | 45° | E-B | E-B | E-B |
| | | 90° | A-B | A-C | A-C |
| Ra Bottom | Blind | 60° | A-C | A-C | A-C |
| | | 45° | A-C | A-C | A-E |
| | | 90° | A-B | A-B | B-C |
| | Blind | 60° | A-B | A-B | B-C |
| Ra Wall | | 45° | A-B | A-B | B-C |
| | | 90° | - | - | - |
| | Through All | 60° | - | - | - |
| | | 45° | B-A | E-A | B-E |

| | | | | | |
|---|---|---|---|---|---|
| Diameter | Blind | 90° | - | - | - |
| | | 60° | - | - | - |
| | | 45° | - | - | - |
| | Through All | 90° | B-C | C-B | E-B |
| | | 60° | B-A | E-A | B-E |
| | | 45° | B-C | E-B | B-C |
| Cutting Forces | Blind | 90° | A-C | A-C | C-B |
| | | 60° | C-A | C-A | C-B |
| | | 45° | C-A | C-A | C-B |
| | Through All | 90° | A-C | A-C | C-B |
| | | 60° | C-A | C-A | C-B |
| | | 45° | C-A | C-A | C-B |

**Table 4.6.** The most influencing geometric parameters on the machining responses

| Response<br>Parameter | Surface Roughness-Bottom | Surface Roughness-Wall | Burr height | Diameter | Forces |
|---|---|---|---|---|---|
| Radial rake angle | ***** | **** | ***** | ***** | ***** |
| Helical pitch | *** | **** | - | ***** | ** |
| Helix angle | ** | **** | * | * | **** |
| Radial relief angle | ** | ***** | ***** | ** | * |
| Radial land width | * | ** | ** | ** | * |
| Axial relief angle | ***** | * | * | *** | *** |
| Axial rake angle | ***** | * | * | *** | *** |
| Edge Radius | ***** | * | **** | **** | ***** |
| Corner Chamfer | - | *** | ***** | * | *** |
| # Margin | - | ** | ** | ** | - |

# 5. MODAL ANALYSIS OF THE DESIGNED FLAT BOTTOM DRILLS

Machining outputs such as dimensional accuracy, eccentricity, roundness, and surface quality of the holes are extremely affected by the vibration of the cutting tool [66-67]. These vibrations are seen in different modes of lateral, torsional-axial chatters, and whirling for drilling processes. Chatter phenomenon develops at frequencies close to the natural modes of the cutting tool. However, whirling grows at the multiples of spindle frequency [67]. In other words, generated instabilities in the machining processes are raised from the self-excited or regenerative chatter [52]. Therefore, attaining a comprehend knowledge on the dynamic characteristics of the drilling systems using flat bottom drill tools for a further development of the process execution and capacities is one of the remarkable issues in the modern industries competition especially in mass production.

Modal analysis is a method for identification of the constitutional dynamic characteristics for a system. Eigenfrequencies, mode shapes and damping ratios are significant achievements of this analysis. The frequency at which a system vibration/oscillation initiates naturally when damping force is inadequate is called eigenfrequency or natural frequency. Being independent of gravity, natural frequencies are functions of the mass and stiffness of the component. Meanwhile, the structure motion or deflection raised by this vibration is called mode shape. In free vibration mode, if the system has a damping characteristic, the vibration/oscillation will diminish in a relatively short time span [68, 69]. Overall, it can be concluded that when the frequency of a system becomes equal to the natural frequency, resonance phenomenon occurs.

Prediction of the natural frequency, time and frequency domain analysis have been carried out on twist drilling tools by several researchers. Huang [66] considered a stepped pre-twisted beam to simulate the dynamics of micro-drills with the beam theory. They studied the boundary condition based on the Winkler-Type elastic foundation and developed a time-dependent vibration model. Moving is used to approximate the drilling process. Tekinalp et al. [70] used finite element modeling to study the dynamics of drill bits by derivation of the motion into an inertial frame and then transformed to a rotating fluted frame. They developed a finite element code for solving the eigenvalue problem for

various boundary conditions and drill cross sectional geometries. FEM was utilized to study the influences of the geometry and process parameters on the drill bit's transverse vibrations and frequency, and boundary conditions at the drill tip in [70,71]. Rincon et al. [72] they investigated the rotary inertia and gyroscopic moments effects on the drill vibration.

These modes are distributed sufficiently in most of the structures. For this reason, single degree of freedom system gives reasonable results for different applications [73]. In a single degree of freedom free vibration model, having a simple and lumped parameter, all the mass is accepted to be concentrated at the definite area and the spring has no mass. In other words, the system is consisted of a mass (m) which is attached to a spring having coefficient of k. therefore, the motion of the system can be expressed in one coordinate axis. The schematic view of the system and its dominant equation is illustrated in below:

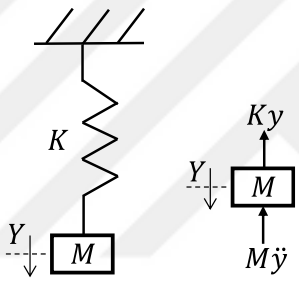


**Figure 5.1.** Single degree of freedom, undamped lumped parameter model

$$M\ddot{y} + Ky = F(t) \tag{4.1}$$

Assuming $y = Ye^{st}$ as a harmonic solution for the equation, where $Y$ is a coefficient, $s = i\omega$ and ω is the frequency with the unit of rad/s, the velocity and acceleration equations can be derived from displacement as given in Equation 4.2 and 4.3:

$$\frac{dy}{dt} = \dot{y} = sYe^{st} = i\omega Ye^{st} \tag{4.2}$$

$$\frac{d^2y}{dt^2} = \ddot{y} = s^2Ye^{st} = -\omega^2Ye^{st} \tag{4.3}$$

Where; $i = \sqrt{-1}$, substituting in Equation 4.2, the below given equation will be obtained.

$$Ye^{st}(Ms^2 + K) = 0 \tag{4.4}$$

In order to fulfill the equation conditions, taking $Ye^{st} = 0$ will result in the system to have no motion. Thereafter, $Ms^2 + K = 0$ will be considered as the solving approach.

Thus,

$$s_{1,2} = \pm\sqrt{-\frac{K}{M}} = \pm i\sqrt{-\frac{K}{M}} \tag{4.5}$$

Where the expression $\omega_n = \sqrt{\frac{K}{M}}$ stands for the natural frequency for the system. $M, K$ and $\omega_n$ are being represented in Kg, N/m and rad/s units for SI system. Hence, solving Equation 4.1 will conclude in:

$$y = Y_1 e^{\,i\omega_n t} + Y_2 e^{-i\omega_n t} \tag{4.6}$$

at the moment of $t = 0$, $y$ will be equal to $y_0$. Then,

$$y_0 = Y_1 + Y_2 \tag{4.7}$$

$$\dot{y} = \; i\omega_n Y_1 e^{\,i\omega_n t} - \; i\omega_n Y_2 e^{-i\omega_n t} \tag{4.8}$$

$$\text{At } t = 0 \qquad \dot{y}_0 = \; i\omega_n Y_1 - \; i\omega_n Y_2 \tag{4.9}$$

The complex coefficients, $Y_1$ and $Y_2$, can be described as in below:

$$Y_1 = \frac{-i\dot{y}_0 + \omega_n y_0}{2\omega_n} \tag{4.10}$$

$$Y_2 = \frac{i\dot{y}_0 + \omega_n y_0}{2\omega_n} \tag{4.11}$$

Substituting $Y_1$ and $Y_2$ in Equation 4.6 to will result in the time dependent displacement of the system.

In order to express this motion in exponential form, real ($Re$) and imaginary ($Im$) parts of the complex coefficients should be calculated:

$$Re(Y_1) = \frac{y_0}{2}, \; Im(Y_1) = \frac{-\dot{y}_0}{2\omega_n} \tag{4.12}$$

$$Re(Y_2) = \frac{y_0}{2}, \; Im(Y_2) = \frac{\dot{y}_0}{2\omega_n} \tag{4.13}$$

$$Y_1 = ¥e^{i Ж} = \sqrt{Re(Y_1)^2 + Im(Y_1)^2}\exp\,(i.tan^{-1}(\frac{Im(Y_1)}{Re(Y_1)})) \tag{4.14}$$

$$Y_1 = \sqrt{(\frac{y_0}{2})^2 + (\frac{-\dot{y}_0}{2\omega_n})^2}\exp\,(\,i.tan^{-1}(\frac{\frac{-\dot{y}_0}{2\omega_n}}{\frac{y_0}{2}})) \tag{4.15}$$

$$Y_1 = \sqrt{\frac{{y_0}^2{\omega_n}^2 + {\dot{y}_0}^2}{2{\omega_n}^2}}\,exp\,(i.tan^{-1}(-\frac{\dot{y}_0}{y_0\omega_n})) \tag{4.16}$$

Then, it can be expressed that

$$¥ = \sqrt{\frac{{y_0}^2{\omega_n}^2+{\dot{y}_0}^2}{2{\omega_n}^2}} \tag{4.17}$$

$$Ж = tan^{-1}(-\frac{\dot{y}_0}{y_0\omega_n}) \tag{4.18}$$

Being aware of that $Y_2 = ¥e^{-iЖ}$ and $e^{i(Ж+\omega_n t)} + e^{-i(Ж+\omega_n t)} = 2cos(Ж + \omega_n t)$. The total displacement can be expressed in Equation 4.19:

$$y = ¥e^{iЖ}e^{i\omega_n t} + ¥e^{-iЖ}e^{-i\omega_n t} = ¥\left(e^{i(Ж+\omega_n t)} + e^{-i(Ж+\omega_n t)}\right) = 2¥\cos(Ж + \omega_n t) \tag{4.19}$$

However, if we take damping and its influences on the system into account, a damping force as equal to $C\dot{y}$ will be applied as demonstrated in Figure 5.2 in which $C$ is the damping coefficient with the SI unit of N.s/m.

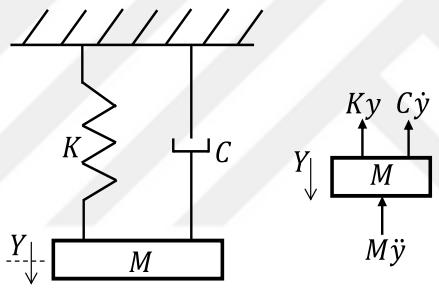


**Figure 5.2.** Single degree of freedom, damped lumped parameter model

Then, the motion equation can be expressed as:

$$M\ddot{y} + C\dot{y} + Ky = F(t) \tag{4.20}$$

Assuming $y = Ye^{st}$, the equation will yield into $Ms^2 + Cs + K = 0$. Therefore, the solutions for the equation and system condition can be determined by Equation 4.21 and 4.22.

$$s_{1,2} = -\frac{C}{2M} \pm \sqrt{(\frac{C}{2M})^2 - \frac{K}{M}} \tag{4.21}$$

$$\text{System condition} = \begin{cases} (\frac{C}{2M})^2 - \frac{K}{M} < 0 \ \rightarrow \ Underdamped \\ (\frac{C}{2M})^2 - \frac{K}{M} = 0 \rightarrow Critical\ damped \\ (\frac{C}{2M})^2 - \frac{K}{M} > 0 \ \rightarrow \ \ Overdamped \end{cases} \tag{4.22}$$

Excluding underdamped conditions, almost no vibration occurs in the other systems. Therefore, Equation 4.21 can be illustrated as in below:

$$s_{1,2} = -\zeta\omega_n \pm \mathrm{i}\omega_d \tag{4.23}$$

$$\zeta = \frac{C}{2\sqrt{KM}} \tag{4.24}$$

$$\omega_d = \omega_n\sqrt{1-\zeta^2} \tag{4.25}$$

Where $\zeta$ and $\omega_d$ are the damping ratio and damped natural frequency, respectively. Thus,

$$y = Y_1 e^{(-\zeta\omega_n + i\omega_d)t} + Y_2 e^{(-\zeta\omega_n + i\omega_d)t} = e^{-\zeta\omega_n t}(Y_1 e^{i\omega_d t} + Y_2 e^{-i\omega_d t}) \tag{4.26}$$

$$Y_1 = \frac{y_0}{2} - i\frac{\dot{y}_0 + \zeta\omega_n y_0}{2\omega_d} \tag{4.27}$$

$$Y_2 = \frac{y_0}{2} + i\frac{\dot{y}_0 + \zeta\omega_n y_0}{2\omega_d} \tag{4.28}$$

$$Re(Y_1) = \frac{y_0}{2},\ Im(Y_1) = -\frac{\dot{y}_0 + \zeta\omega_n y_0}{2\omega_d} \tag{4.29}$$

$$Re(Y_2) = \frac{y_0}{2},\ Im(Y_2) = \frac{\dot{y}_0 + \zeta\omega_n y_0}{2\omega_d} \tag{4.30}$$

$$Y_1 = ¥e^{i Ж} = \sqrt{Re(Y_1)^2 + Im(Y_1)^2}\,exp\,(i.tan^{-1}(\frac{Im(Y_1)}{Re(Y_1)})) \tag{4.31}$$

$$Y_1 = \sqrt{(\frac{y_0}{2})^2 + (-\frac{\dot{y}_0 + \zeta\omega_n y_0}{2\omega_d})^2}\,exp\,(i.tan^{-1}(\frac{-\frac{\dot{y}_0 + \zeta\omega_n y_0}{2\omega_d}}{\frac{y_0}{2}})) \tag{4.32}$$

$$¥ = \sqrt{(\frac{y_0}{2})^2 + (-\frac{\dot{y}_0 + \zeta\omega_n y_0}{2\omega_d})^2} \tag{4.33}$$

$$Ж = tan^{-1}(\frac{-\frac{\dot{y}_0 + \zeta\omega_n y_0}{2\omega_d}}{\frac{y_0}{2}}) \tag{4.34}$$

$$Y_2 = ¥e^{-i Ж} \tag{4.35}$$

The above given relations are representative of the dynamic model characteristics analysis equation of a cutting tool. Therefore, the general solution, when an external exciting force is zero $(F(t) = 0)$, of the dynamic model will be enough to identify the mode shapes and

the corresponding frequencies. In order to perform modal analysis, several methods such as experimental, numerical and analytical are being used. In the experimental method, by using an impact hammer different types of masses are used to excite the system. Thus, due to the applied force a vibration which has an amplitude and frequency is generated and the measurement is performed using a displacement sensor or an accelerometer. The frequency response function (FRF) of the system is $\Phi_a(i\omega) = \frac{\ddot{y}}{F}$ if an accelerometer is used. Thereafter, the FRF is processed to time domain by Fast Fourier Transfer Function through commercial programs such as Cut Pro, KiStudio, etc. Natural frequencies, modal damping and mode shapes can be obtained through the program results. The natural frequencies are exactly the oscillating frequencies in the unit of Hz which can be calculated by:

$$f = \frac{\omega}{2\pi} = \frac{\sqrt{\frac{k}{m}}}{2\pi} \tag{4.36}$$

$$T = \frac{1}{f} \tag{4.37}$$

where; f stands for the natural frequency, $\omega$ is the angular frequency, $k$ represents the stiffness of the system, $m$ is the mass and $T$ is symbolized for the period of the oscillation.

Only a few cutting parameters and geometries such as maximum value of depth for cut, cutting speed, point angle, etc. have been included into the models in [66, 70-73]. Since even a small variation in the cutting tool geometry can have a robust influence on the dynamic behaviors, in order to understand the effects of complex geometry of the designed flat bottom drills have been modeled with some simplifications in Solidworks with the given geometrical parameters in Table 5.1. To investigate the feasibility on resonance for an enhanced drilling operation and modal analysis numerical method in terms of Finite Element Methods have been taken advantage. For this purpose, the modal analyses of the designed and manufactured flat bottom drills have been executed in Explicit solver of Abaqus 2017 program to improve cutting tool performance and capabilities, especially for vertical and inclined drilling operations. Therefore, a deep knowledge on the dynamic characteristics rising from interaction of complex geometries and their effect on the natural frequencies as well as mode shapes can be obtained. The masses of the designed flat bottom drill cutting tools are given in Table 5.2. Table 5.3

illustrates the technical data of the used carbide material during the modal analyzes of the cutting tools.

**Table 5.1.** Geometrical parameters of the designed cutting tools

| Tool No. | Cuter diameter, (mm) | Tool length, (mm) | Helix angle, (deg) | Relief angle, (deg) | Flute radius, (mm) | Core diameter, (mm) | Axial relief angle, (deg) | Radial rake angle, (deg) | Axial rake angle, (deg) |
|---|---|---|---|---|---|---|---|---|---|
| 1 | | | | | | | | 6 | -2 |
| 2 | | | | | | | | 6 | 0 |
| 3 | | | | | | | | 6 | 2 |
| 4 | | | | | | | | 8 | -2 |
| 5 | 8 | 50 | 30 | 6 | 2 | 2.1 | 6 | 8 | 0 |
| 6 | | | | | | | | 8 | 2 |
| 7 | | | | | | | | 10 | -2 |
| 8 | | | | | | | | 10 | 0 |
| 9 | | | | | | | | 10 | 2 |

**Table 5.2.** The calculated masses of the designed flat bottom drills

| Tool No. | 1 | 2 | 3 | 4 | 5 | 6 | 7 | 8 | 9 |
|---|---|---|---|---|---|---|---|---|---|
| m (Kg) | 0.26660297 | 0.2680459 | 0.2697881 | 0.26649197 | 0.26797003 | 0.269229 | 0.265968 | 0.267929 | 0.268689 |

**Table 5.3.** Technical specifications of the used carbide in the manufacture cutting tools

| Grade | Classification | Co % | WC incl. doping | Density ($g/cm^3$) | Hardness HV30, ($Kg/mm^2$) | Tensile strength, (MPa) | Fracture Toughness $K_{IC}$, ($MPa.m^{1/2}$) | Transverse rupture strenght, ($N/mm^2$) | Average grain size, (μm) |
|---|---|---|---|---|---|---|---|---|---|
| DK500 UF | K20-K30 | 12.0 | 88.0 | 14.05 | 1690 | 550 | 10.4 | 4200 | 0.5 |

The modal analysis was performed by investigating the modes for the first ten natural frequencies up to 2000 Hz. In the simulation process, the element type was selected as tetrahedral elements and the element numbers for the designed tool were between 91610 and 92650. The boundary condition for tools were applied on the shank with U1=U2=U3=RU1=RU3=0 in order to simulate the tool-holder assembled situation as shown in Figure 5.3. The solved natural frequencies and total displacements are demonstrated in Table 4 and 5, respectively. Hopefully, the calculated natural frequencies

are higher than the real industrial application conditions and also tool manufacturer recommendations which means the design of the cutting tools are acceptable considering the modal dynamic analysis and can be utilized with no failure or damages to the system. Furthermore, it is seen that although small values, the natural frequencies of the cutting tool have decreased with increase in the radial rake angle for all of the shape modes. This can be attributed to the change in the cutting tool mass and stiffness which are illustrated in Table 5.2 and 5.6. However, no governing trends were seen for both natural frequencies and total displacement with the change in the axial rake angle of the cutting tool. As the resonant vibration results, total displacement and mode shapes of the cutting tools are illustrated in Figure 5.4 to Figure 5.12 for the studied flat bottom drills.

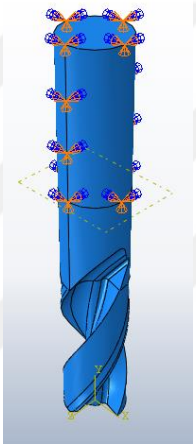

**Figure 5.3.** The applied boundary conditions for the designed flat bottom drills

**Table 5.4.** The calculated natural frequencies in different shape modes of the designed flat bottom drills

| Mode No. | 1 | 2 | 3 | 4 | 5 | 6 |
|---|---|---|---|---|---|---|
| 1 | 362.89 | 453.11 | 687.7 | 810.48 | 1019.8 | 1590.2 |
| 2 | 364.78 | 452.43 | 714.18 | 792.4 | 974.51 | 1586.2 |
| 3 | 363.65 | 448.87 | 722.97 | 784.12 | 953.09 | 1569.5 |
| 4 | 361.71 | 452.06 | 686.06 | 809.12 | 1019.4 | 1587.3 |

| | | | | | | |
|---|---|---|---|---|---|---|
| 5 | 363.53 | 451.36 | 712.61 | 791.13 | 974.08 | 1582.2 |
| 6 | 362.38 | 447.77 | 721.52 | 782.93 | 952.67 | 1562.5 |
| 7 | 361.68 | 451.83 | 682.72 | 803.34 | 1007.7 | 1579.7 |
| 8 | 362.37 | 450.36 | 711.3 | 789.93 | 973.68 | 1581.3 |
| 9 | 361.2 | 446.74 | 720.28 | 781.63 | 952.26 | 1559.6 |

**Table 5.5.** The calculated total displacements in different shape modes of the designed flat bottom drills

| Mode No. | 1 | 2 | 3 | 4 | 5 | 6 |
|---|---|---|---|---|---|---|
| 1 | 1.182 | 1.248 | 1.016 | 1.28 | 1.207 | 1.003 |
| 2 | 1.404 | 1.362 | 1.02 | 1.138 | 1.199 | 1.002 |
| 3 | 1.29 | 1.227 | 1.022 | 1.1 | 1.209 | 1.002 |
| 4 | 1.179 | 1.244 | 1.017 | 1.288 | 1.208 | 1.003 |
| 5 | 1.398 | 1.368 | 1.02 | 1.142 | 1.199 | 1.002 |
| 6 | 1.294 | 1.231 | 1.022 | 1.103 | 1.208 | 1.002 |
| 7 | 1.211 | 1.282 | 1.018 | 1.247 | 1.202 | 1.003 |
| 8 | 1.392 | 1.373 | 1.021 | 1.146 | 1.199 | 1.002 |
| 9 | 1.299 | 1.234 | 1.023 | 1.105 | 1.208 | 1.002 |

**Table 5.6.** The calculated stiffness values for different shape modes of the designed flat bottom drills

| Mode No. | 1 | 2 | 3 | 4 | 5 | 6 |
|---|---|---|---|---|---|---|
| 1 | 1386037 | 2160887 | 4977632 | 6913681 | 10945982 | 26615107 |
| 2 | 1408092 | 2166066 | 5397396 | 6644432 | 10049432 | 26624705 |
| 3 | 1408477 | 2145970 | 5567024 | 6548587 | 9674986 | 26236456 |
| 4 | 1376464 | 2149988 | 4951857 | 6887629 | 10932843 | 26507080 |
| 5 | 1398062 | 2155222 | 5372170 | 6621276 | 10037723 | 26483094 |
| 6 | 1395757 | 2131039 | 5533223 | 6515193 | 9646425 | 25949051 |
| 7 | 1373529 | 2143577 | 4894116 | 6776224 | 10662314 | 26202227 |
| 8 | 1388943 | 2145357 | 5351623 | 6600201 | 10027956 | 26448952 |
| 9 | 1383903 | 2116995 | 5503170 | 6480562 | 9618810 | 25801010 |

**Table 5.7.** The calculated oscillation period time for different shape modes of the designed flat bottom drills

| Mode No. | 1 | 2 | 3 | 4 | 5 | 6 |
|---|---|---|---|---|---|---|
| 1 | 0.0028 | 0.0022 | 0.0015 | 0.0012 | 0.0010 | 0.0006 |
| 2 | 0.0027 | 0.0022 | 0.0014 | 0.0013 | 0.0010 | 0.0006 |
| 3 | 0.0027 | 0.0022 | 0.0014 | 0.0013 | 0.0010 | 0.0006 |
| 4 | 0.0028 | 0.0022 | 0.0015 | 0.0012 | 0.0010 | 0.0006 |
| 5 | 0.0028 | 0.0022 | 0.0014 | 0.0013 | 0.0010 | 0.0006 |

| | | | | | | |
|---|---|---|---|---|---|---|
| 6 | 0.0028 | 0.0022 | 0.0014 | 0.0013 | 0.0010 | 0.0006 |
| 7 | 0.0028 | 0.0022 | 0.0015 | 0.0012 | 0.0010 | 0.0006 |
| 8 | 0.0028 | 0.0022 | 0.0014 | 0.0013 | 0.0010 | 0.0006 |
| 9 | 0.0028 | 0.0022 | 0.0014 | 0.0013 | 0.0011 | 0.0006 |

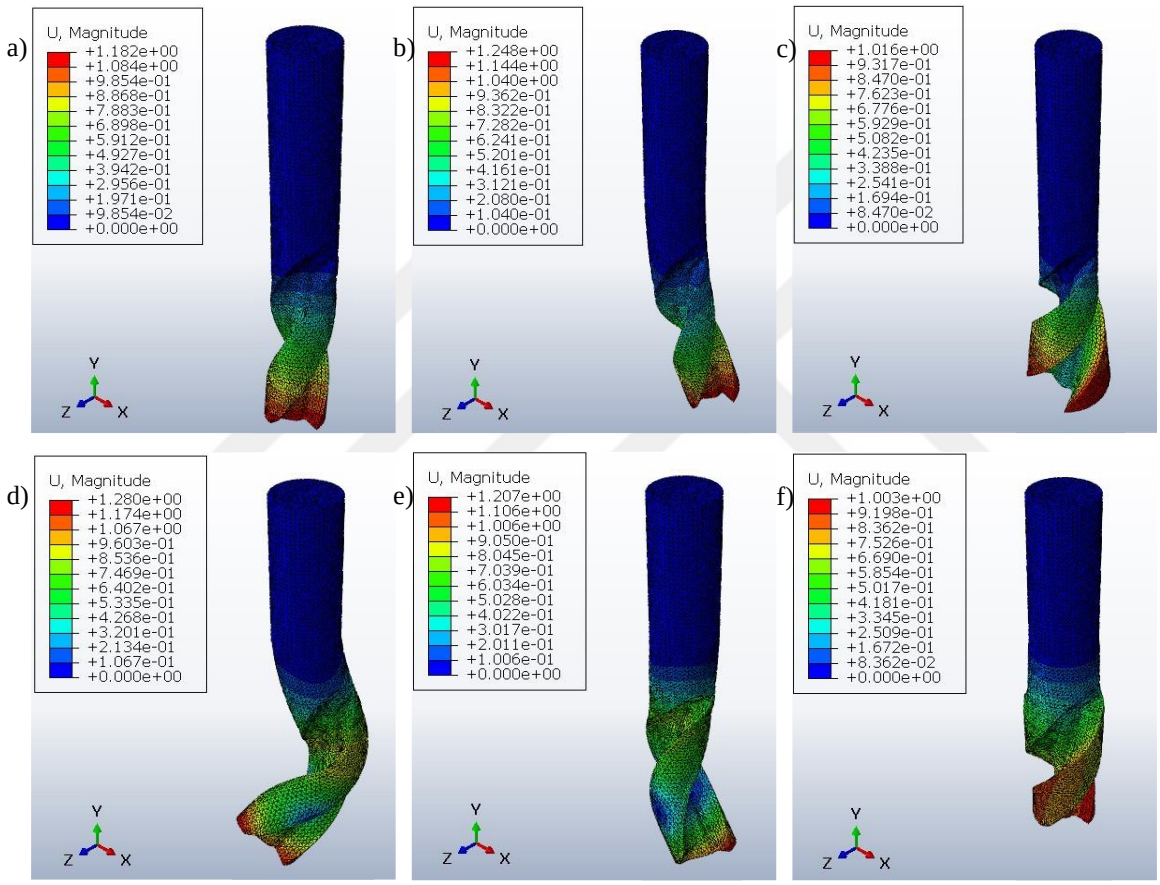


**Figure 5.4.** Modal analysis results for the flat bottom drill No.1; a) first, b) second, c) third, d) fourth, e) fifth, f) sixth, mode.

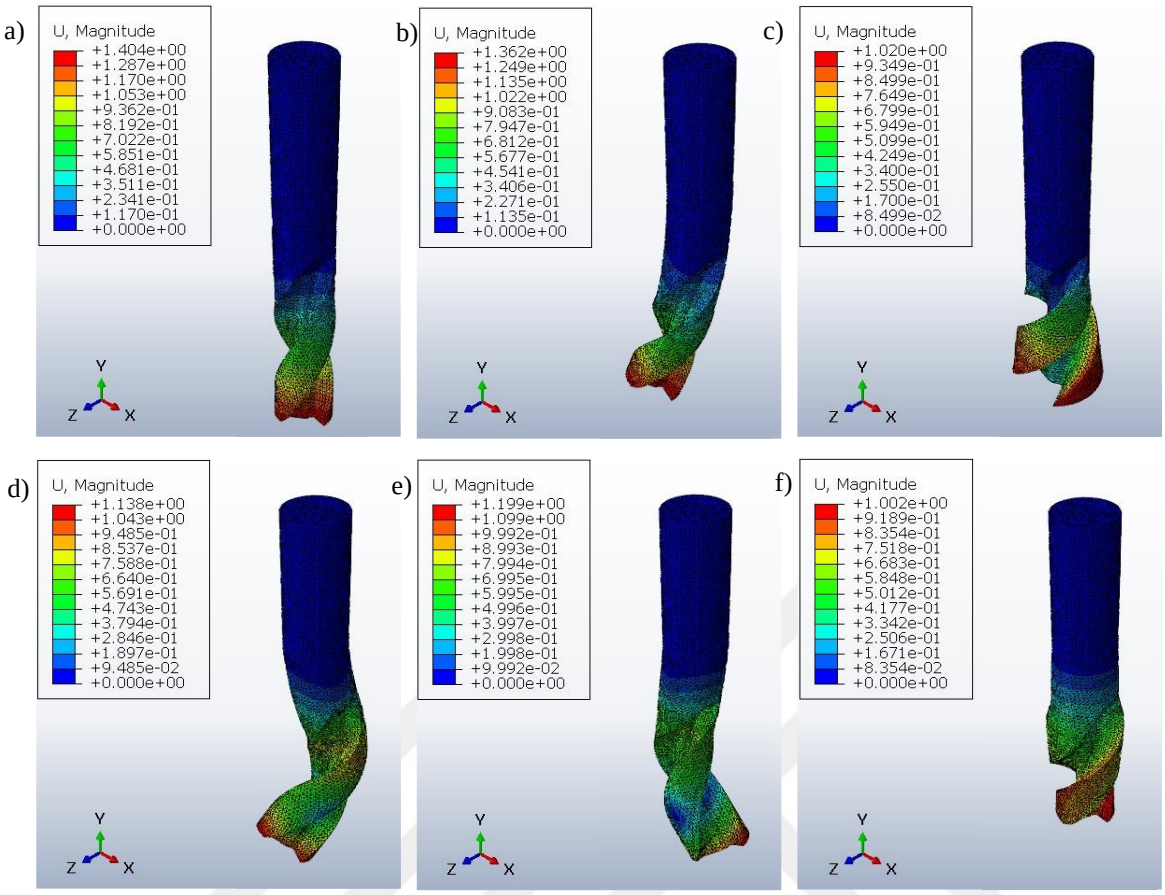


**Figure 5.5.** Modal analysis results for the flat bottom drill No.2; a) first, b) second, c) third, d) fourth, e) fifth, f) sixth, mode.

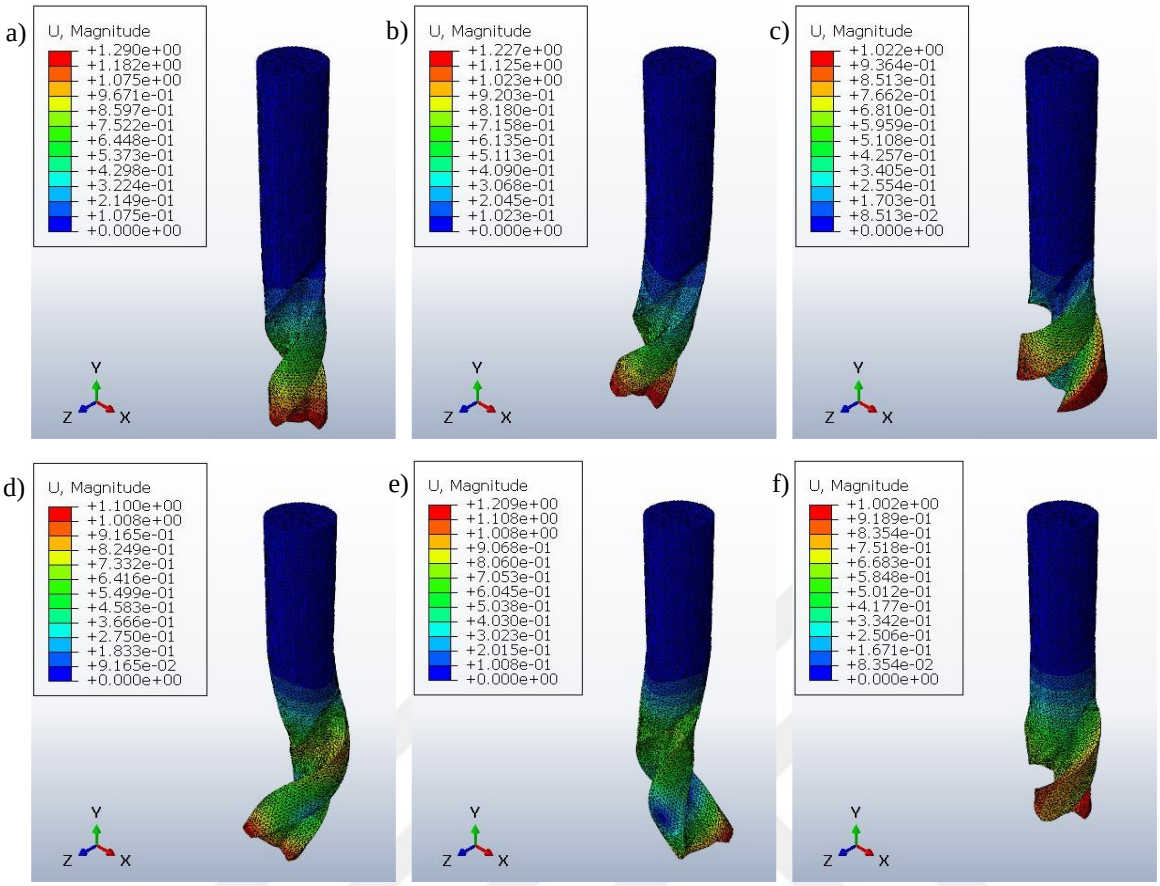


**Figure 5.6.** Modal analysis results for the flat bottom drill No.3; a) first, b) second, c) third, d) fourth, e) fifth, f) sixth, mode.

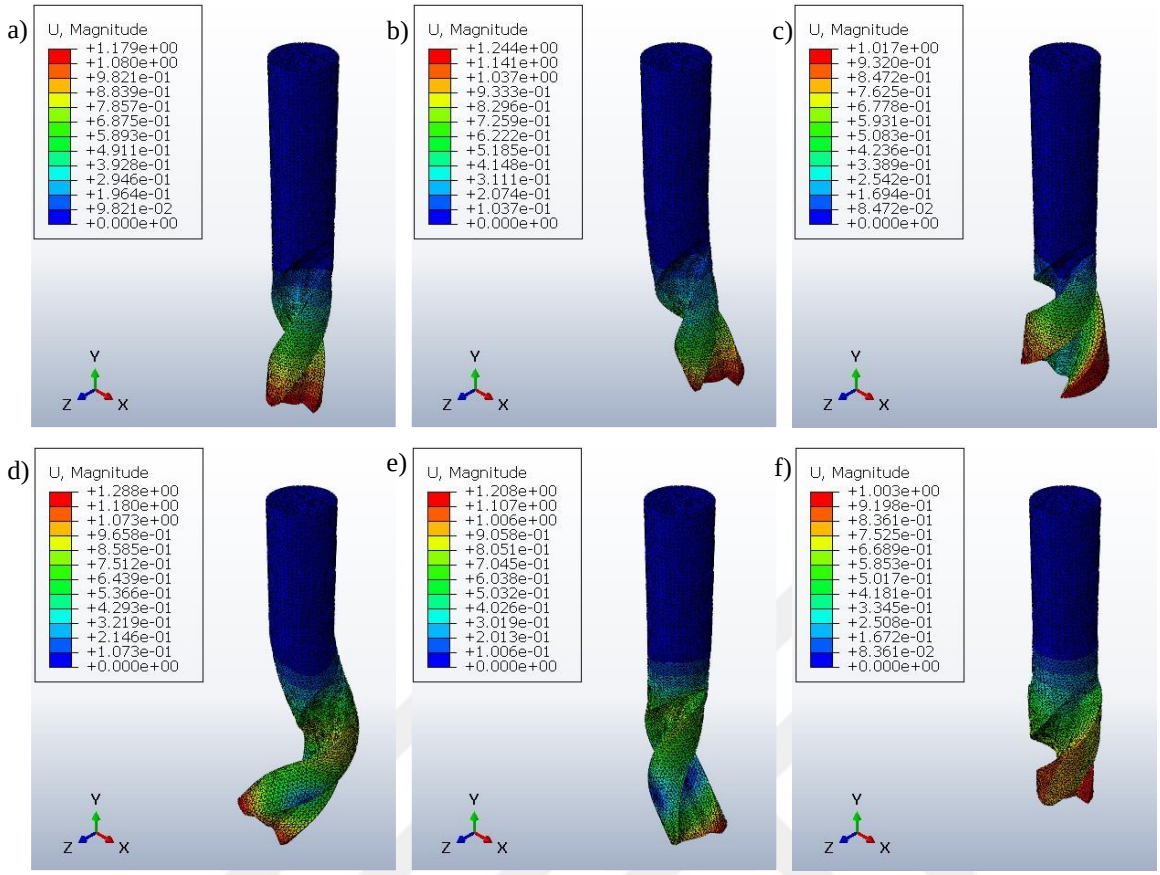


**Figure 5.7.** Modal analysis results for the flat bottom drill No.4; a) first, b) second, c) third, d) fourth, e) fifth, f) sixth, mode.

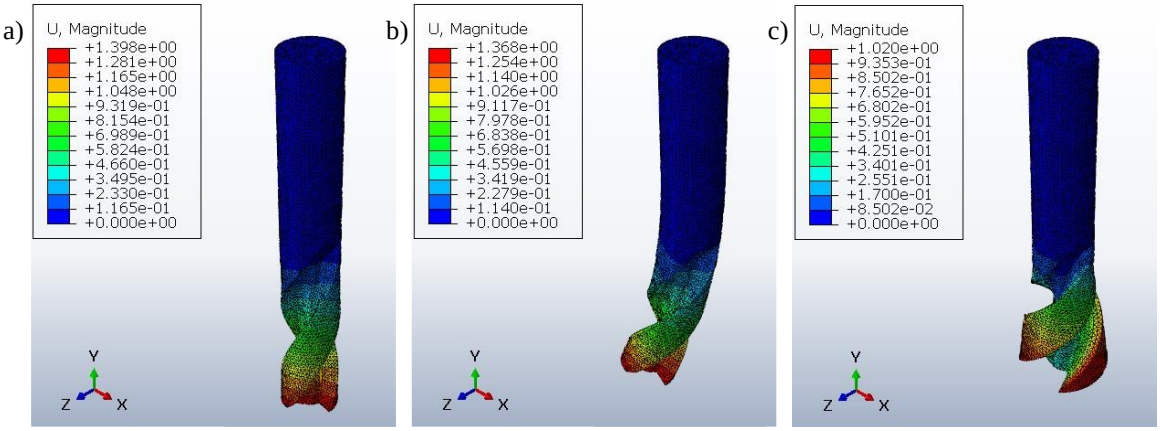

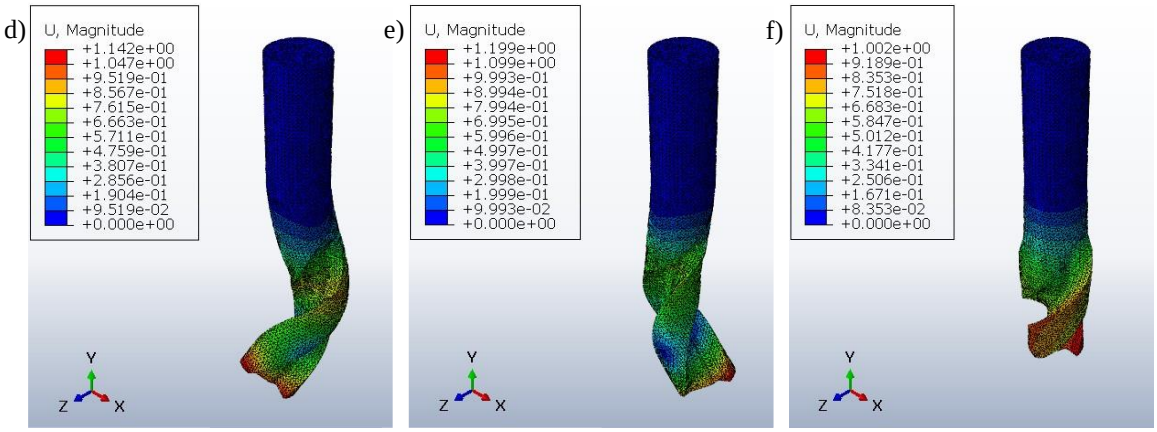


**Figure 5.8.** Modal analysis results for the flat bottom drill No.5; a) first, b) second, c) third, d) fourth, e) fifth, f) sixth, mode.

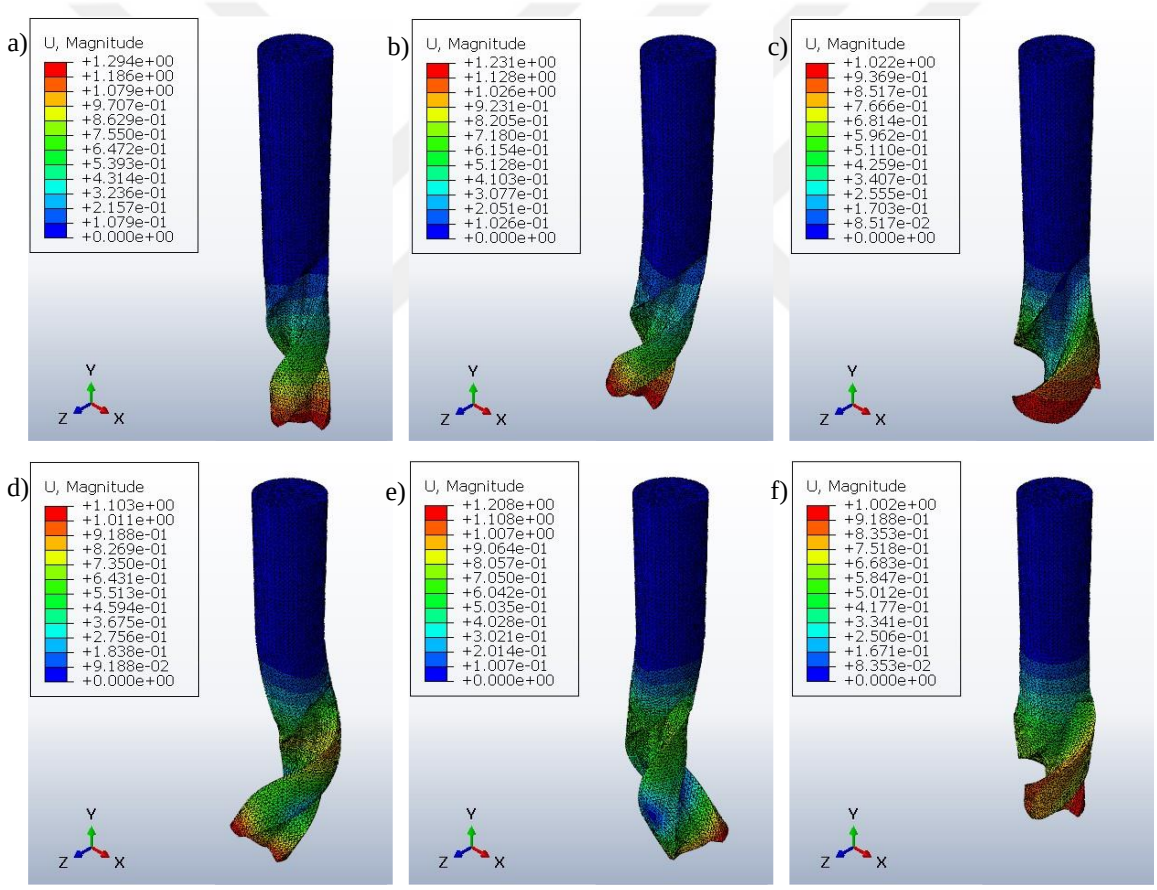


**Figure 5.9.** Modal analysis results for the flat bottom drill No.6; a) first, b) second, c) third, d) fourth, e) fifth, f) sixth, mode.

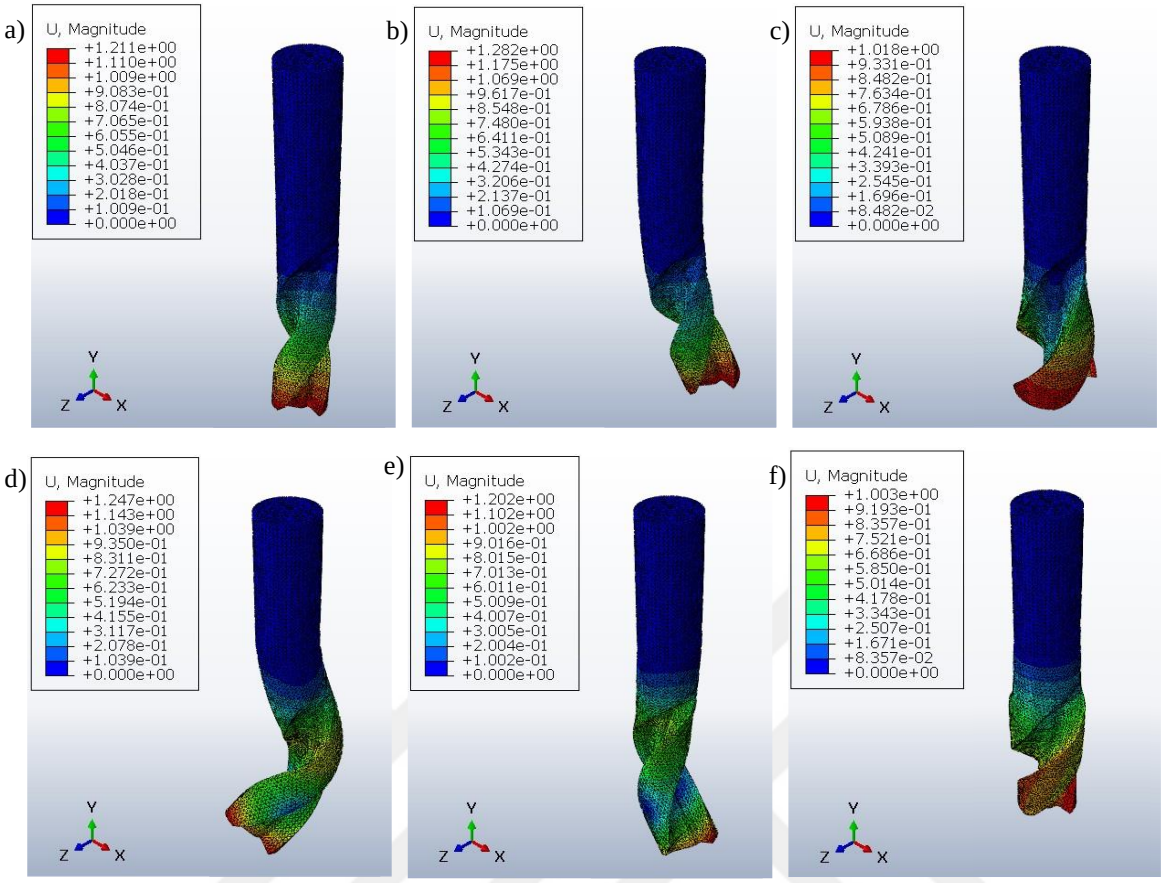


**Figure 5.10.** Modal analysis results for the flat bottom drill No.7; a) first, b) second, c) third, d) fourth, e) fifth, f) sixth, mode.

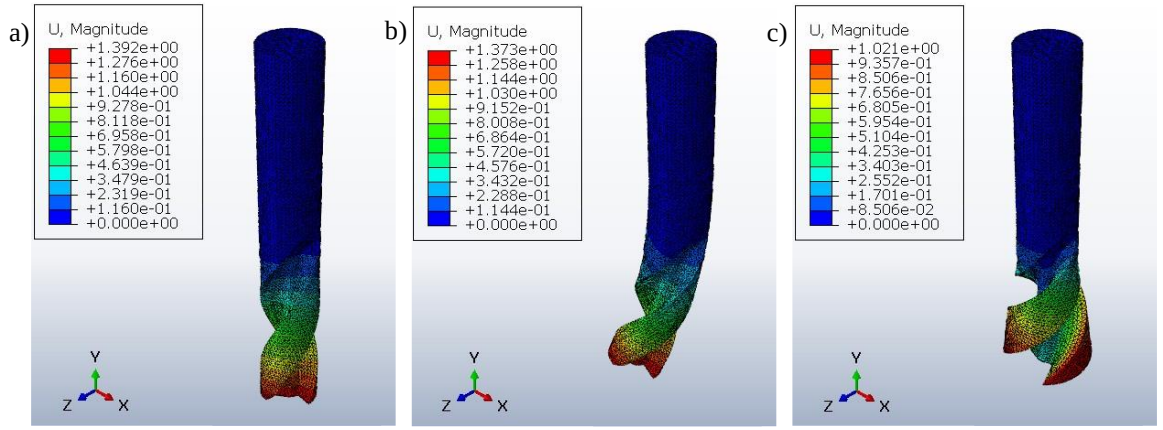

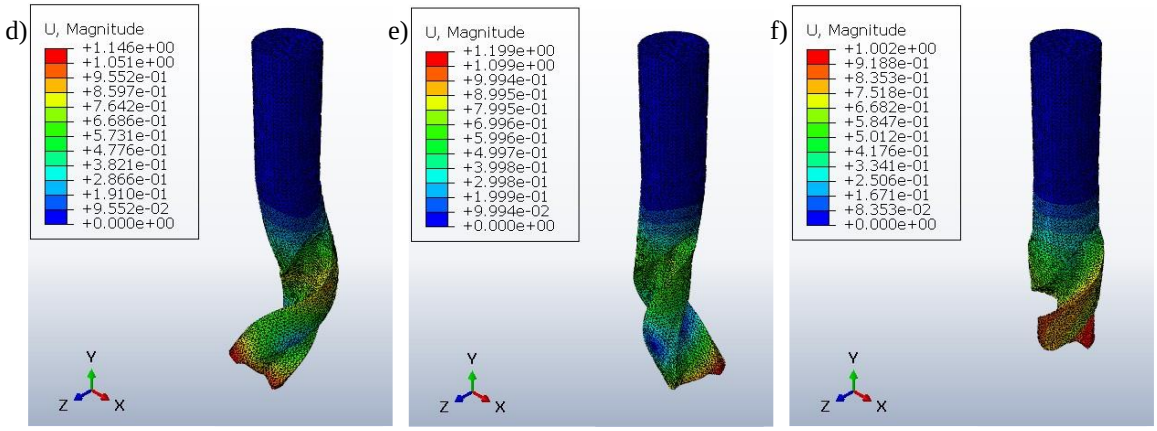


**Figure 5.11.** Modal analysis results for the flat bottom drill No.8; a) first, b) second, c) third, d) fourth, e) fifth, f) sixth, mode.

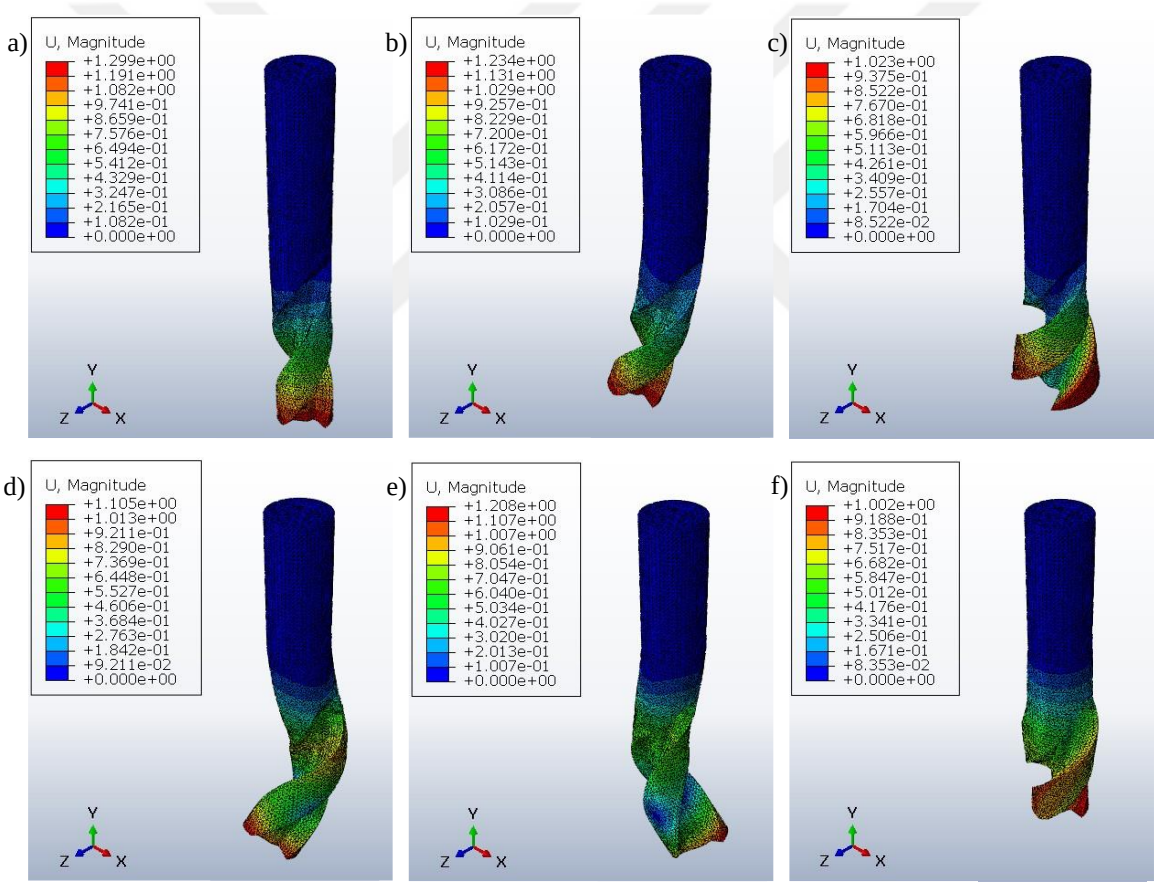


**Figure 5.12.** Modal analysis results for the flat bottom drill No.9; a) first, b) second, c) third, d) fourth, e) fifth, f) sixth, mode.

The lowest natural frequency has been determined as 361.20 Hz for tool number 9 at first mode. Be that as it may, the most noteworthy one was for tool number 1 with 1590.20 Hz at 6th mode. It should be noticed that the metallic materials are being machined utilizing

carbide tools at the most extreme 20000 rpm in industrial applications. Preferably, the determined natural frequencies for the tools are higher than the industrial application conditions and furthermore tool manufacturers' recommendations which is an implicant of an adequate cutting tools design thinking about the modal dynamic analyses and can be utilized with no failure or damages to the structure, for example, machine tools. Considering the stiffness results of the system for each mode shapes, it is seen that higher natural frequencies are consequents of higher stiffness values in any direction. Moreover, during the resonance, the system irritates, and associated displacement may intensify until the occurrence of buckling, yielding, fatigue, etc. on the cutting tool.

Figure 5.13 shows the variety of the natural frequencies for six modes of the designed flat bottom drills with radial and axial rake angles. The impacts of these parameters on natural frequency are displayed in Figure 5.14. It is seen that albeit little qualities, the natural frequencies of the cutting tool have diminished with expansion in the radial rake angle for all of the shape modes. This can be ascribed to the variation of the cutting tool mass and stiffness. In any case, no prevailing patterns were noticed for both natural frequencies and complete most extreme displacements with the variation of the axial rake angle of the cutting tool. The impacts of radial and axial rake angles on complete total displacement are displayed in Figure 5.15. To notice the impact of the cutting tool geometrical design parameters on the natural frequencies for every mode shape, analysis of variance (ANOVA) as a statistical method has been utilized. Statistical meaning of the fitted model and terms was surveyed by the P-upsides of ANOVA results. The analysis results are given in Tables 8 to 13 for six modes of natural frequencies, separately. The A and B parameters represent the radial and axial rake angles in the tables, separately. For all the mode shapes, the high model F-values infer that the examinees are significant. The possibilities of the mistake because of clamor are under 1%. P-esteems under 0.0500 demonstrate model terms are significant. Values more prominent than 0.1000 demonstrate the model terms are not significant.

To predict the natural frequencies for various shape modes of the designed flat bottom drills quadratic request relapse models have been developed and delineated in Table 5.14. The A, B, and $R^2$ parameters represent the radial, axial rake angles and model exactness, respectively.

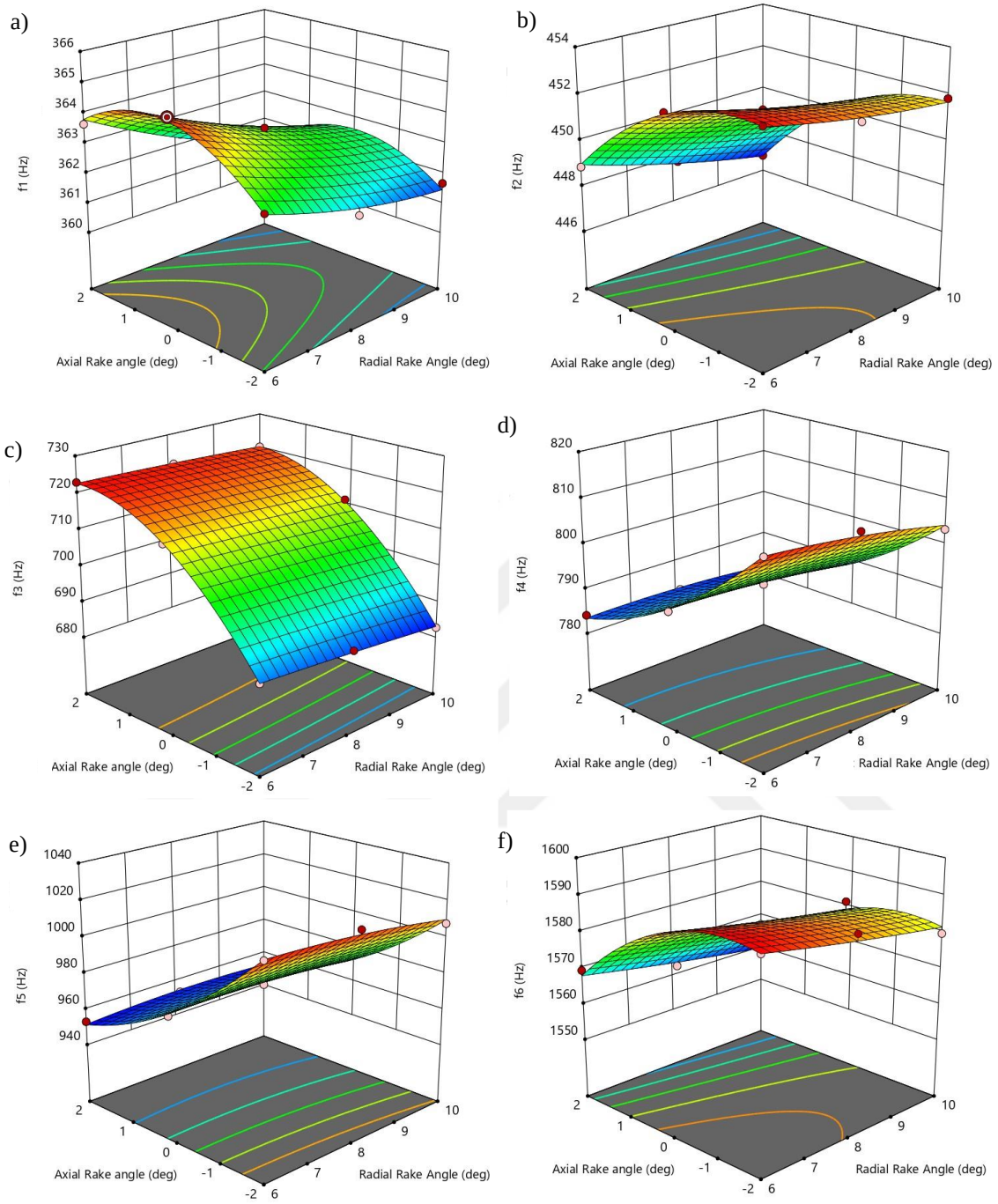


**Figure 5.13.** The variation of the natural frequencies with radial and axial rake angle of flat bottom drill; a) first, b) second, c) third, d) fourth, e) fifth, f) sixth modes.

a)

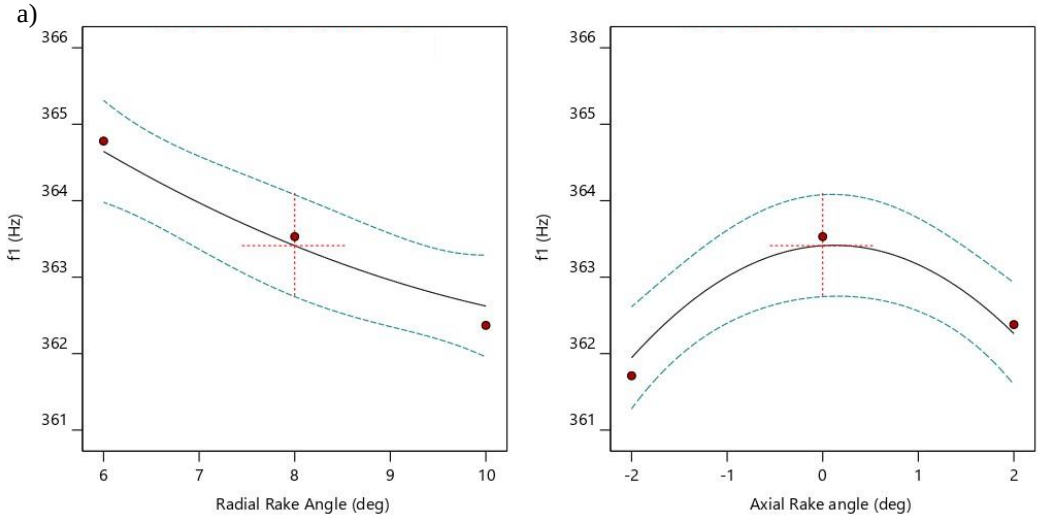
366
365
364
363
362
361
f1 (Hz)
6
7
8
9
10
Radial Rake Angle (deg)
-2
-1
0
1
2
Axial Rake angle (deg)

b)

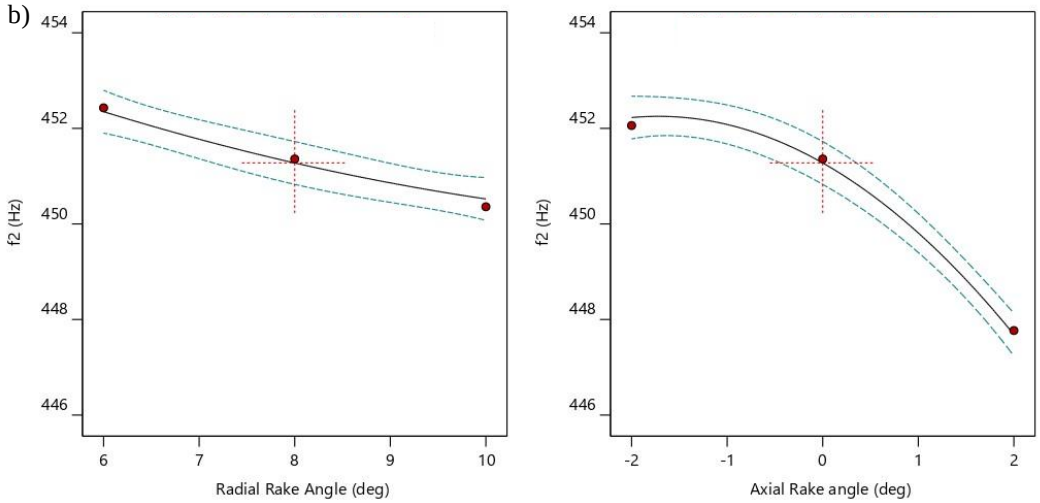
454
452
450
448
446
f2 (Hz)
6
7
8
9
10
Radial Rake Angle (deg)
-2
-1
0
1
2
Axial Rake angle (deg)

c)

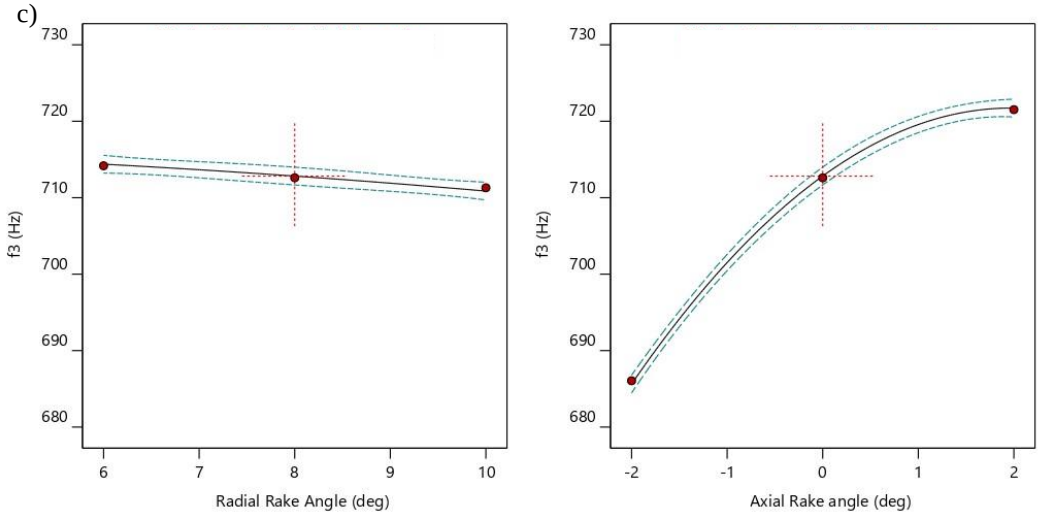
730
720
710
700
690
680
f3 (Hz)
6
7
8
9
10
Radial Rake Angle (deg)
-2
-1
0
1
2
Axial Rake angle (deg)

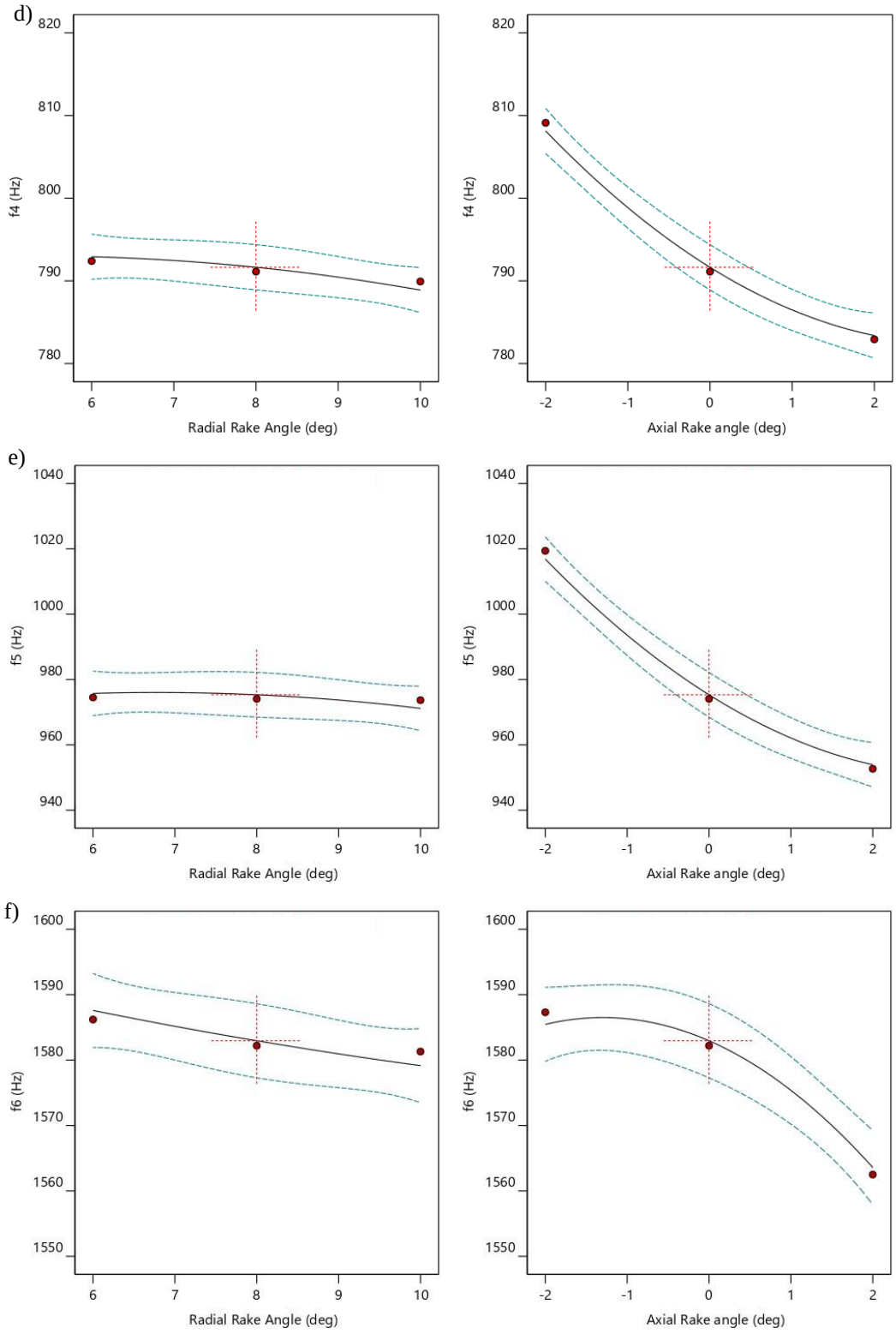


**Figure 5.14.** The variation of the natural frequencies with radial and axial rake angle of flat bottom drill; a) first, b) second, c) third, d) fourth, e) fifth, f) sixth modes.

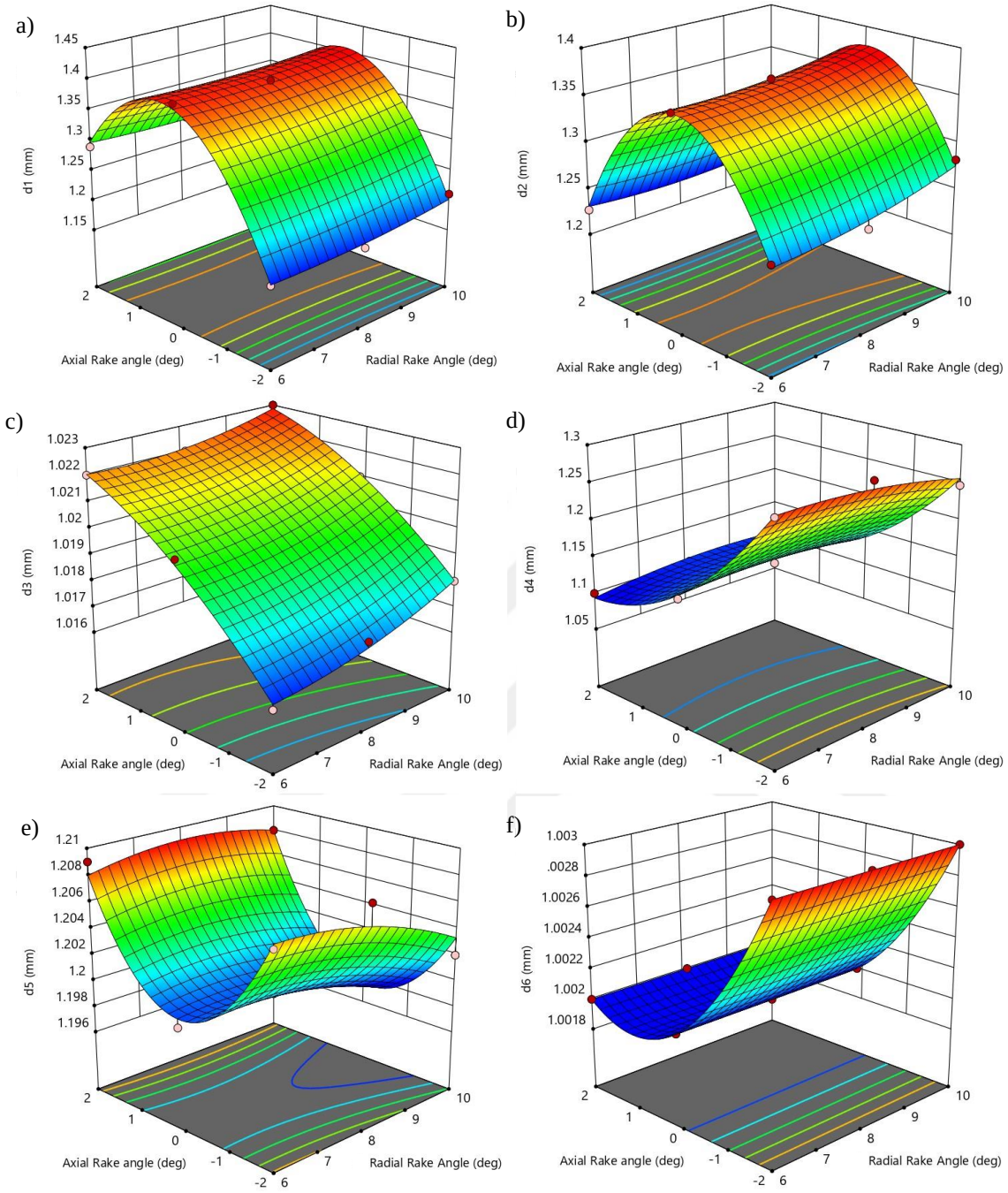


**Figure 5.15.** The variation of the natural frequencies with radial and axial rake angle of flat bottom drill; a) first, b) second, c) third, d) fourth, e) fifth, f) sixth modes.

**Table 5.8.** ANOVA results of first mode natural frequencies

| Source | Sum of Squares | df | Mean Square | F-value | p-value |
|---|---|---|---|---|---|

| | | | | | | |
|---|---|---|---|---|---|---|
| Mode I | 10.20 | 5 | 2.04 | 25.82 | 0.0114 | significant |
| A | 6.14 | 1 | 6.14 | 77.74 | 0.0031 | |
| B | 0.1504 | 1 | 0.1504 | 1.90 | 0.2615 | |
| AB | 0.3844 | 1 | 0.3844 | 4.87 | 0.1145 | |
| $A^2$ | 0.0983 | 1 | 0.0983 | 1.24 | 0.3460 | |
| $B^2$ | 3.42 | 1 | 3.42 | 43.34 | 0.0071 | |
| Residual | 0.2370 | 3 | 0.0790 | | | |
| Cor Total | 10.43 | 8 | | | | |

**Table 5.9.** ANOVA results of second mode natural frequencies

| Source | Sum of Squares | df | Mean Square | F-value | p-value | |
|---|---|---|---|---|---|---|
| Mode II | 39.64 | 5 | 7.93 | 222.47 | 0.0005 | significant |
| A | 5.01 | 1 | 5.01 | 140.45 | 0.0013 | |
| B | 30.92 | 1 | 30.92 | 867.59 | < 0.0001 | |
| AB | 0.1806 | 1 | 0.1806 | 5.07 | 0.1098 | |
| $A^2$ | 0.0512 | 1 | 0.0512 | 1.44 | 0.3167 | |

| | | | | | | |
|---|---|---|---|---|---|---|
| $B^2$ | 3.48 | 1 | 3.48 | 97.79 | 0.0022 | |
| Residual | 0.1069 | 3 | 0.0356 | | | |
| Cor Total | 39.75 | 8 | | | | |

**Table 5.10.** ANOVA results of third mode natural frequencies

| Source | Sum of Squares | df | Mean Square | F-value | p-value | |
|---|---|---|---|---|---|---|
| Mode III | 2142.03 | 5 | 428.41 | 1784.42 | < 0.0001 | significant |
| A | 18.55 | 1 | 18.55 | 77.27 | 0.0031 | |
| B | 1954.45 | 1 | 1954.45 | 8140.83 | < 0.0001 | |
| AB | 1.31 | 1 | 1.31 | 5.46 | 0.1015 | |
| $A^2$ | 0.0841 | 1 | 0.0841 | 0.3501 | 0.5957 | |
| $B^2$ | 167.63 | 1 | 167.63 | 698.22 | 0.0001 | |
| Residual | 0.7202 | 3 | 0.2401 | | | |
| Cor Total | 2142.75 | 8 | | | | |

**Table 5.11.** ANOVA results of fourth mode natural frequencies

| Source | Sum of Squares | df | Mean Square | F-value | p-value | |
|---|---|---|---|---|---|---|
| Mode IV | 2142.03 | 5 | 428.41 | 1784.42 | < 0.0001 | significant |
| A | 18.55 | 1 | 18.55 | 77.27 | 0.0031 | |
| B | 1954.45 | 1 | 1954.45 | 8140.83 | < 0.0001 | |
| AB | 1.31 | 1 | 1.31 | 5.46 | 0.1015 | |
| $A^2$ | 0.0841 | 1 | 0.0841 | 0.3501 | 0.5957 | |
| $B^2$ | 167.63 | 1 | 167.63 | 698.22 | 0.0001 | |
| Residual | 0.7202 | 3 | 0.2401 | | | |
| Cor Total | 2142.75 | 8 | | | | |

**Table 5.12.** ANOVA results of fifth mode natural frequencies

| Source | Sum of Squares | df | Mean Square | F-value | p-value | |
|---|---|---|---|---|---|---|
| Mode V | 2142.03 | 5 | 428.41 | 1784.42 | < 0.0001 | significant |
| A | 18.55 | 1 | 18.55 | 77.27 | 0.0031 | |
| B | 1954.45 | 1 | 1954.45 | 8140.83 | < 0.0001 | |
| AB | 1.31 | 1 | 1.31 | 5.46 | 0.1015 | |

| | | | | | |
|---|---|---|---|---|---|
| $A^2$ | 0.0841 | 1 | 0.0841 | 0.3501 | 0.5957 |
| $B^2$ | 167.63 | 1 | 167.63 | 698.22 | 0.0001 |
| Residual | 0.7202 | 3 | 0.2401 | | |
| Cor Total | 2142.75 | 8 | | | |

**Table 5.13.** ANOVA results of sixth mode natural frequencies

| Source | Sum of Squares | df | Mean Square | F-value | p-value | |
|---|---|---|---|---|---|---|
| Mode VI | 2142.03 | 5 | 428.41 | 1784.42 | < 0.0001 | significant |
| A | 18.55 | 1 | 18.55 | 77.27 | 0.0031 | |
| B | 1954.45 | 1 | 1954.45 | 8140.83 | < 0.0001 | |
| AB | 1.31 | 1 | 1.31 | 5.46 | 0.1015 | |
| $A^2$ | 0.0841 | 1 | 0.0841 | 0.3501 | 0.5957 | |
| $B^2$ | 167.63 | 1 | 167.63 | 698.22 | 0.0001 | |
| Residual | 0.7202 | 3 | 0.2401 | | | |
| Cor Total | 2142.75 | 8 | | | | |

**Table 5.14.** The quadratic order developed regression model for different shape modes of the designed flat bottom drills

| Mode No. | f1 | f2 | f3 | f4 | f5 | f6 |
|---|---|---|---|---|---|---|
| C | 371.006 | 457.490 | 716.587 | 787.822 | 954.488 | 1606.489 |
| A | -1.392 | -1.097 | -0.059 | 1.965 | 6.360 | -3.775 |
| B | 0.699 | -0.710 | 7.879 | -8.513 | -21.375 | -5.767 |
| AB | -0.078 | -0.053 | 0.143 | 0.291 | 0.704 | 0.038 |
| $A^2$ | 0.055 | 0.040 | -0.051 | -0.186 | -0.469 | 0.104 |
| $B^2$ | -0.327 | -0.330 | -2.289 | 1.029 | 2.516 | -2.108 |
| $R^2$ | 0.939 | 0.993 | 0.999 | 0.989 | 0.989 | 0.954 |

# 6. TESTS WITH DESIGNED FLAT BOTTOM DRILL CUTTING TOOLS

In this chapter, flat bottom drills have been designed by analyzing the geometrical inspection and performance evaluation tests of the reference cutting tools which has been explained in the previous chapter. Radial, axial rake angles as well the cutting-edge radius has been selected for a further investigation as the most significant influencing geometrical parameters in flat bottom drilling operation. The studied geometric parameters and studied levels for the parameters are illustrated in Table 6.1. The design process of the cutting tools was carried out in Tool Room, and they were manufactured from solid carbide with the given technical specifications in Table 6.2 using ANCA grinding machine as demonstrated in Figure 6.1 and 6.2. The geometry of the manufactured bottom drills was inspected using ZOLLER measuring device type Genius 3s and Keyence digital optical microscope as production assurance confirmation. It is noteworthy to mention that the tools which are manufactured in ANCA grinding machine have sharp cutting-edge radius (3-8 μm). Sharp tools are prone to chatter because of their lower level of contact during the cutting process. Therefore, they mostly are subjected to drag finishing. In this study, in order to obtain the desired cutting-edge radius, drag finishing operation was applied on the manufactured tools as shown in Figure 6.3. Afterwards, the cutting-edge radii of the tools were measured with Mitutoyo Contracer CV-2100M4.

**Table 6.1.** The geometric specification of the utilized cutting tools

| Parameter | Diameter (mm) | Helix angle (deg) | Radial rake angle (deg) | Axial rake angle (deg) | Cutting edge-radius (μm) |
|---|---|---|---|---|---|
| Flat Bottom Drill | 8 | 30 | 6 | -2 | 10 |
| | | | 8 | 0 | 15 |
| | | | 10 | 2 | 20 |

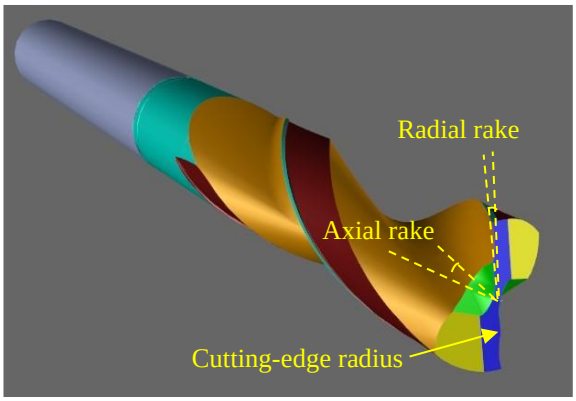


**Figure 6.1.** The designed flat bottom drill cutting tool

**Table 6.2.** Technical specifications of the utilized carbide material

| Grade | Classification | Co% | WC incl. doping | Density ($g/cm^3$) | Hardness HV30, ($Kg/mm^2$) | Tensile strength, (MPa) | Fracture Toughness $K_{IC}$, (MPa.m1/2) | Transverse rupture strength, ($N/mm^2$) | Average grain size, (μm) |
|---|---|---|---|---|---|---|---|---|---|
| DK500UF | K20-K30 | 12.0 | 88.0 | 14.05 | 1690 | 550 | 10.4 | 4200 | 0.5 |

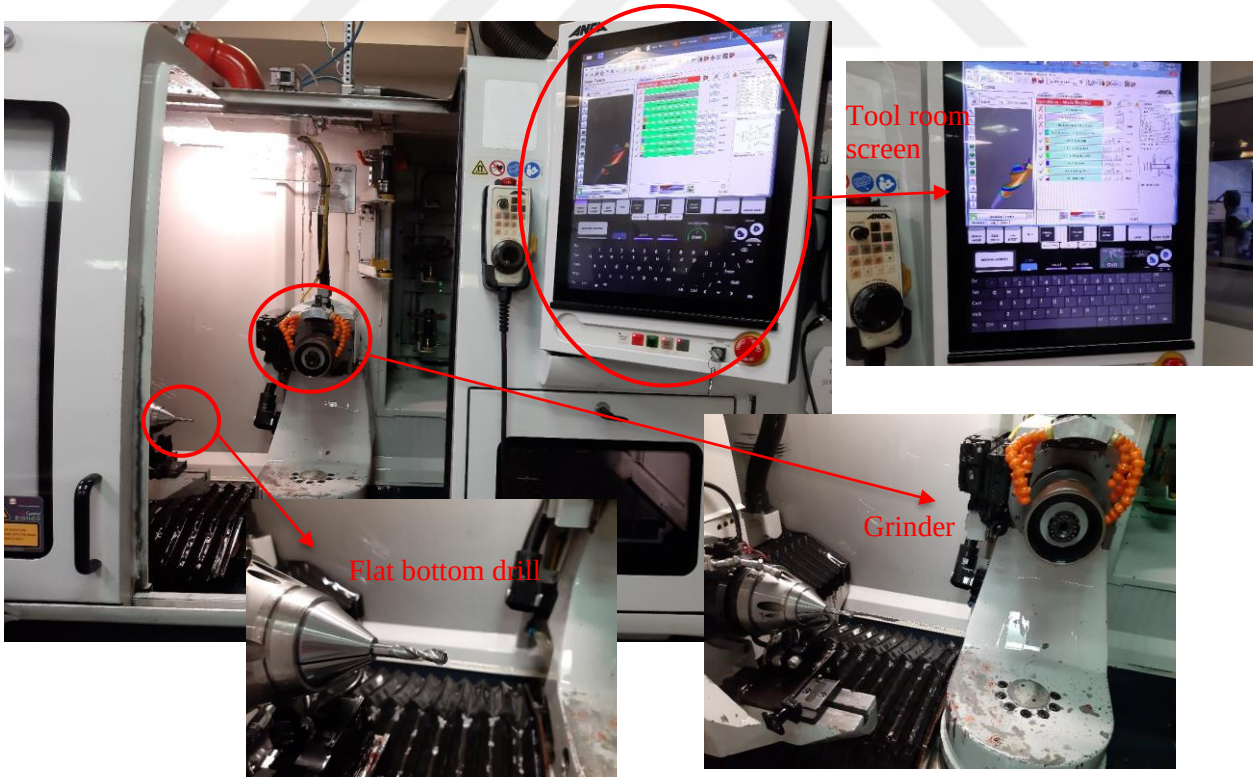


**Figure 6.2.** The process of the flat bottom drill design and its manufacturing




**Figure 6.3.** Drag finishing operation on the manufactured flat bottom drills

In order to evaluate the manufactured flat bottom drills, a full factorial design of experiments as demonstrated in Figure 6.5 were carried out on both extruded and forged-annealed leaded (CW617N), low-lead (CW511L), lead-free (CW724R) brass alloys under 90°, 60° and 45° of plunging angles as blind and through all holes. The used parameters in the experiments are given in Table 6.3. The cutting forces in thrust direction as well as the resultant one, the burr height at the hole entry and exit, the surface roughness at the hole bottom and wall, and dimensional accuracy in terms of diameter have been taken into consideration.

**Table 6.3.** The utilized test parameters for the experiments

| Material | Material Type | Hole Type | Angle | Parameter | Value |
|---|---|---|---|---|---|
| CW617N | Extruded Bar | Blind | 90° | $V_f$ , (mm/min) | 500.0 |
| CW724R | Forged+annealed | Through all | | $N$,(rpm) | 4000.0 |

| | | | |
|---|---|---|---|
| CW511L | | $V_c$ , (m/min) | 100.5 |
| | | $V_f$ , (mm/min) | 200.0 |
| | 45° | $N$,(rpm) | 3000.0 |
| | 60° | $V_c$ , (m/min) | 70.4 |

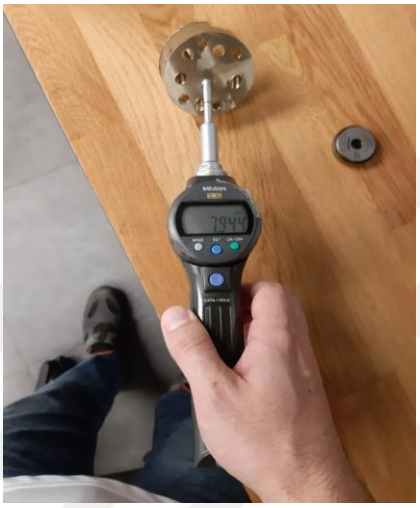

**Figure 6.4.** The utilized micrometer for measurement of the drilled holes diameter

a)

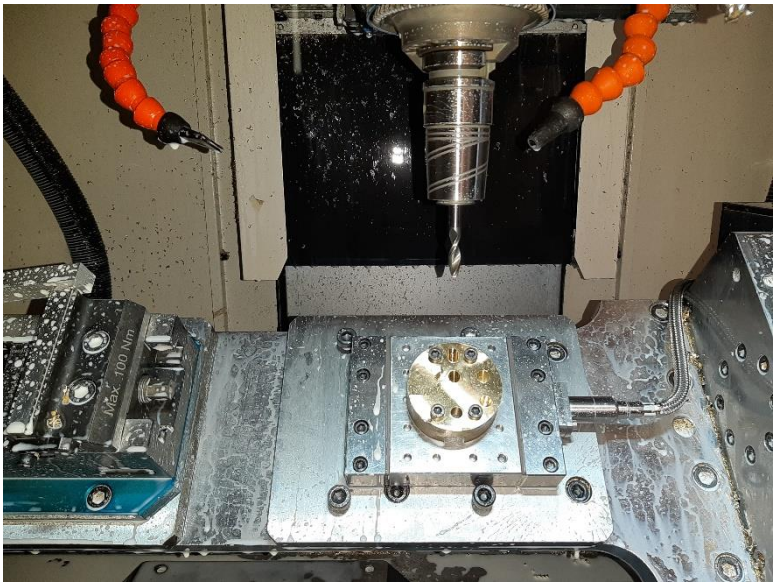

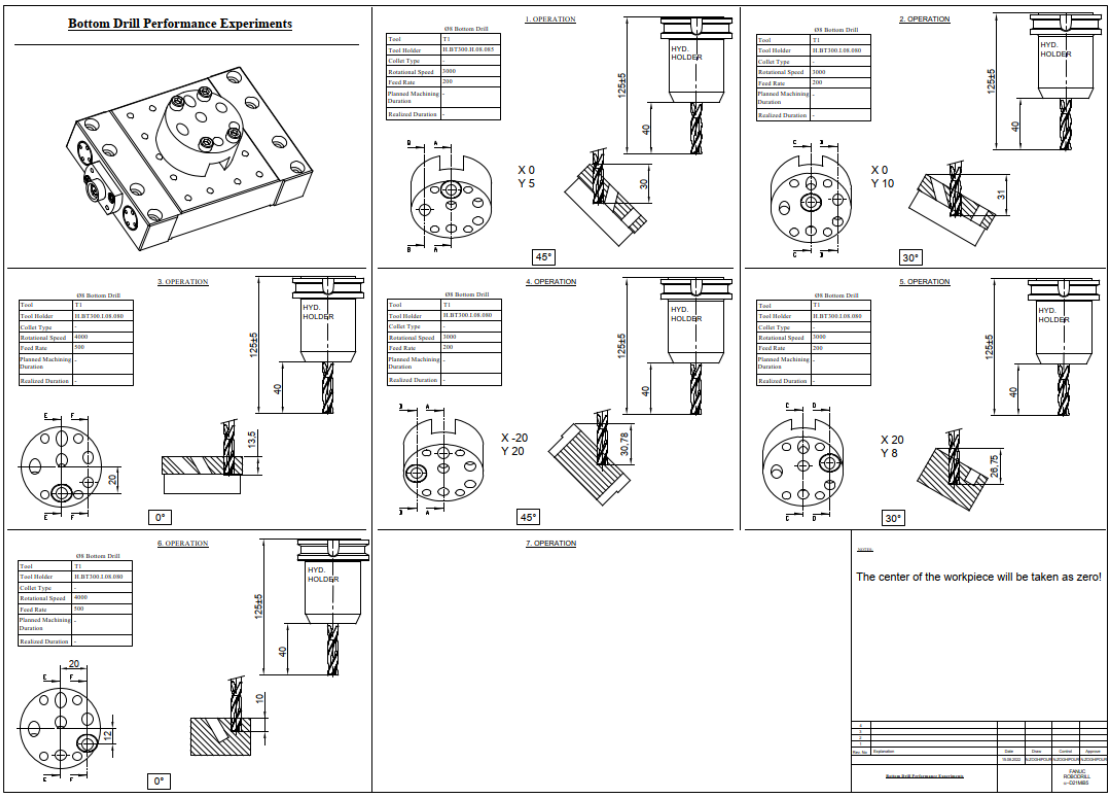
Bottom Drill Performance Experiments
1. OPERATION
2. OPERATION
3. OPERATION
4. OPERATION
5. OPERATION
6. OPERATION
7. OPERATION
HYD. HOLDER
X 0
Y 5
X 0
Y 10
X -20
Y 20
X 20
Y 8
45°
30°
0°
The center of the workpiece will be taken as zero!

b)

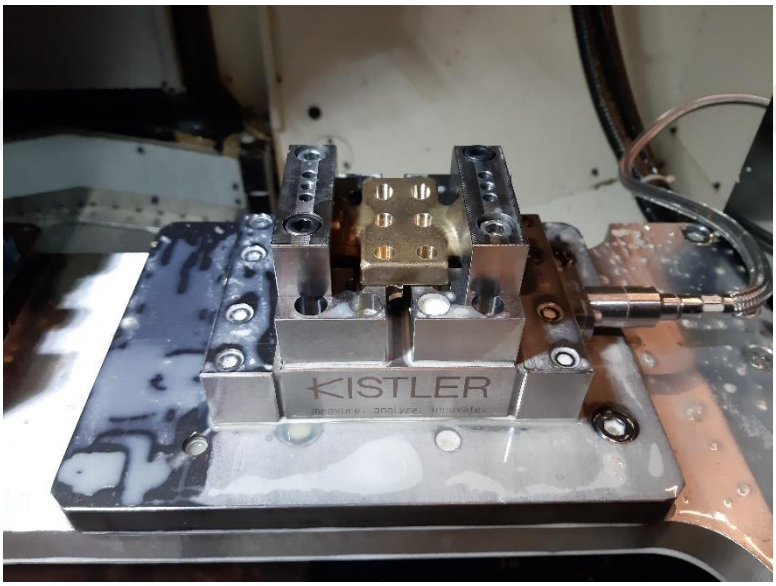
KISTLER

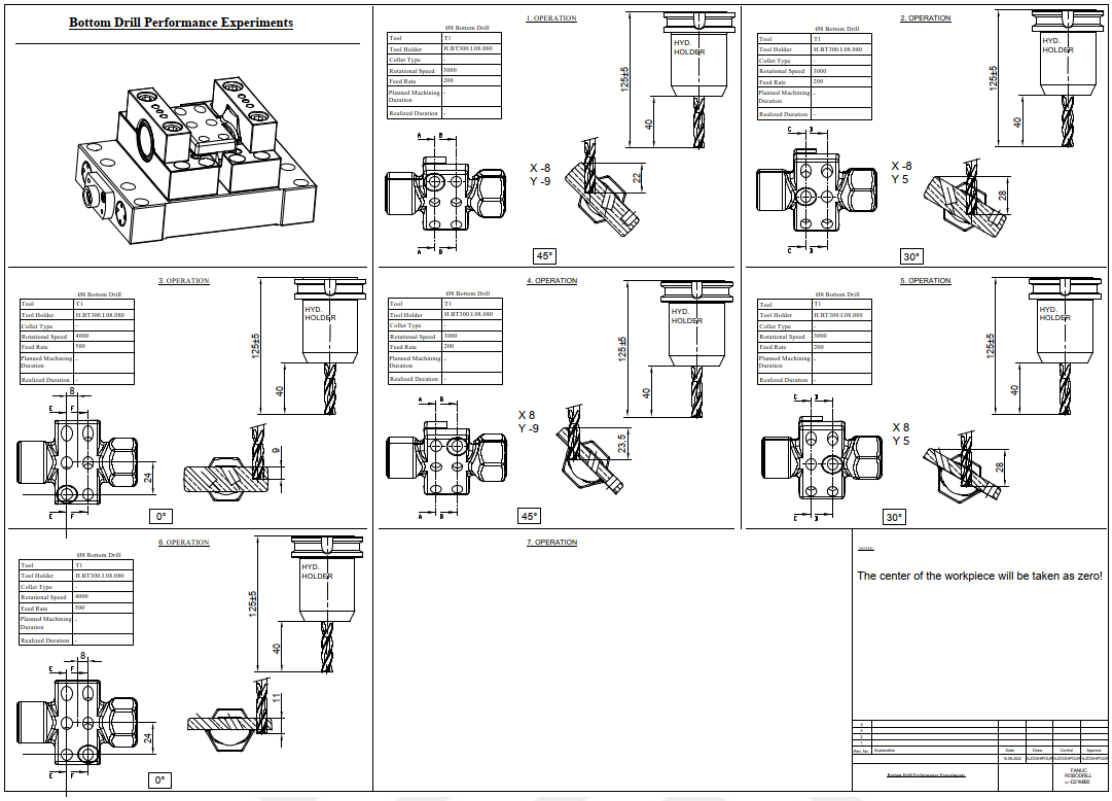


**Figure 6.5.** The used experimental and operational form setup in this study; a) extruded, b) forged-annealed specimens

The measurement results of the mentioned brass alloys for both extruded and forged-annealed specimens at various plunging angles are given in Table 6.4-21. The results have been discussed separately in this section.

**Table 6.4.** The measurement results for the extruded CW617N with 90° of plunging angle

| Run | PA, (°) | RRA, (°) | ARA, (°) | CER, (µm) | Fx, (N) | Fy, (N) | Fz, (N) | FR, (N) | BHEN, (µm) | BHEX, (µm) | Ra bottom , (µm) | Ra Wall, (µm) | Diameter, (mm) |
|---|---|---|---|---|---|---|---|---|---|---|---|---|---|
| 1 | 90 | 6 | -2 | 10 | 2.175 | 4.046 | 234.4 | 234.445 | 48.847 | 24.088 | 0.490 | 0.684 | 7.977 |
| 2 | 90 | 6 | 0 | 10 | 8.184 | 3.598 | 233.9 | 234.071 | 46.265 | 22.210 | 0.475 | 0.695 | 7.991 |
| 3 | 90 | 6 | 2 | 10 | 3.587 | 8.05 | 223.3 | 223.474 | 43.707 | 20.649 | 0.471 | 0.699 | 8.005 |
| 4 | 90 | 8 | -2 | 10 | 12.15 | 5.026 | 231.2 | 231.574 | 75.195 | 35.648 | 0.465 | 0.703 | 7.999 |
| 5 | 90 | 8 | 0 | 10 | 10.62 | 1.601 | 226 | 226.255 | 68.976 | 33.325 | 0.458 | 0.709 | 7.999 |
| 6 | 90 | 8 | 2 | 10 | 7.346 | 1.914 | 219.6 | 219.731 | 57.632 | 24.689 | 0.454 | 0.713 | 7.995 |
| 7 | 90 | 10 | -2 | 10 | 8.47 | 2.099 | 226.7 | 226.868 | 136.521 | 65.093 | 0.452 | 0.714 | 7.968 |
| 8 | 90 | 10 | 0 | 10 | 8.748 | 0.3517 | 223.7 | 223.871 | 101.057 | 46.636 | 0.450 | 0.716 | 7.946 |
| 9 | 90 | 10 | 2 | 10 | 7.119 | 7.967 | 201.4 | 201.683 | 81.923 | 38.526 | 0.430 | 0.734 | 7.966 |
| 10 | 90 | 6 | -2 | 15 | 5.172 | 3.549 | 282.2 | 282.270 | 66.058 | 29.914 | 0.419 | 0.744 | 7.951 |
| 11 | 90 | 6 | 0 | 15 | 2.66 | 21.6 | 271.1 | 271.972 | 62.467 | 28.179 | 0.416 | 0.747 | 7.953 |
| 12 | 90 | 6 | 2 | 15 | 10.04 | 14.79 | 265.4 | 266.001 | 59.011 | 25.360 | 0.412 | 0.751 | 7.975 |

| | | | | | | | | | | | | | |
|---|---|---|---|---|---|---|---|---|---|---|---|---|---|
| 13 | 90 | 8 | -2 | 15 | 8.597 | 0.7436 | 281.6 | 281.732 | 99.267 | 46.053 | 0.408 | 0.755 | 7.970 |
| 14 | 90 | 8 | 0 | 15 | 9.723 | 8.306 | 274 | 274.298 | 91.084 | 42.790 | 0.408 | 0.755 | 7.978 |
| 15 | 90 | 8 | 2 | 15 | 13.01 | 14.4 | 271.2 | 271.893 | 76.564 | 36.792 | 0.402 | 0.761 | 7.960 |
| 16 | 90 | 10 | -2 | 15 | 0.1446 | 9.777 | 265.7 | 265.880 | 183.371 | 85.449 | 0.402 | 0.761 | 7.939 |
| 17 | 90 | 10 | 0 | 15 | 10.65 | 29.01 | 265 | 266.796 | 135.377 | 64.484 | 0.401 | 0.762 | 7.945 |
| 18 | 90 | 10 | 2 | 15 | 13.81 | 3.755 | 262.2 | 262.590 | 110.562 | 51.818 | 0.398 | 0.766 | 7.954 |
| 19 | 90 | 6 | -2 | 20 | 13.97 | 8.605 | 337.8 | 338.198 | 95.542 | 43.306 | 0.369 | 0.798 | 7.972 |
| 20 | 90 | 6 | 0 | 20 | 6.382 | 14.8 | 315.5 | 315.911 | 92.120 | 43.311 | 0.368 | 0.799 | 7.981 |
| 21 | 90 | 6 | 2 | 20 | 34.67 | 30.31 | 312.2 | 315.578 | 86.979 | 42.120 | 0.364 | 0.804 | 7.984 |
| 22 | 90 | 8 | -2 | 20 | 4.305 | 22.4 | 336.2 | 336.973 | 134.485 | 63.052 | 0.362 | 0.806 | 7.974 |
| 23 | 90 | 8 | 0 | 20 | 12.65 | 32.7 | 327 | 328.874 | 125.231 | 59.276 | 0.361 | 0.807 | 7.962 |
| 24 | 90 | 8 | 2 | 20 | 1.856 | 13.76 | 294.6 | 294.927 | 107.362 | 48.352 | 0.360 | 0.808 | 7.943 |
| 25 | 90 | 10 | -2 | 20 | 9.83 | 16.44 | 315.4 | 315.981 | 232.787 | 107.013 | 0.358 | 0.811 | 7.931 |
| 26 | 90 | 10 | 0 | 20 | 8.994 | 17.02 | 314.4 | 314.989 | 176.855 | 76.240 | 0.358 | 0.811 | 7.934 |
| 27 | 90 | 10 | 2 | 20 | 2.773 | 6.731 | 313.6 | 313.684 | 63.957 | 47.905 | 0.337 | 0.837 | 7.940 |

**Table 6.5.** The measurement results for the extruded CW617N with 60° of plunging angle

| Run | PA, (°) | RRA, (°) | ARA, (°) | CER, (μm) | Fx, (N) | Fy, (N) | Fz, (N) | FR, (N) | BHEN, (μm) | BHEX, (μm) | Ra bottom , (μm) | Ra Wall, (μm) | Diameter, (mm) |
|---|---|---|---|---|---|---|---|---|---|---|---|---|---|
| 1 | 60 | 6 | -2 | 10 | 41.17 | 89.58 | 143.1 | 173.773 | 49.874 | 25.541 | 0.390 | 0.615 | 7.989 |
| 2 | 60 | 6 | 0 | 10 | 41.47 | 87.30 | 140.2 | 170.285 | 47.918 | 23.342 | 0.377 | 0.625 | 7.965 |
| 3 | 60 | 6 | 2 | 10 | 41.55 | 92.06 | 139.2 | 171.983 | 46.269 | 21.615 | 0.373 | 0.627 | 8.006 |
| 4 | 60 | 8 | -2 | 10 | 40.53 | 84.35 | 137.4 | 166.242 | 78.454 | 31.891 | 0.368 | 0.631 | 8.006 |
| 5 | 60 | 8 | 0 | 10 | 37.06 | 86.30 | 127.7 | 158.519 | 74.523 | 31.203 | 0.362 | 0.636 | 8.009 |
| 6 | 60 | 8 | 2 | 10 | 39.43 | 79.47 | 127.2 | 155.081 | 59.048 | 27.102 | 0.358 | 0.639 | 8.019 |
| 7 | 60 | 10 | -2 | 10 | 46.68 | 83.26 | 125.0 | 157.278 | 149.822 | 55.610 | 0.356 | 0.640 | 7.982 |
| 8 | 60 | 10 | 0 | 10 | 30.32 | 88.32 | 111.2 | 145.207 | 109.613 | 44.071 | 0.355 | 0.642 | 7.978 |
| 9 | 60 | 10 | 2 | 10 | 31.05 | 82.59 | 109.8 | 140.859 | 88.695 | 37.614 | 0.337 | 0.657 | 7.974 |
| 10 | 60 | 6 | -2 | 15 | 87.88 | 74.28 | 201.5 | 232.040 | 71.182 | 29.823 | 0.327 | 0.665 | 7.983 |
| 11 | 60 | 6 | 0 | 15 | 74.00 | 78.23 | 176.6 | 206.842 | 65.446 | 28.275 | 0.324 | 0.668 | 7.985 |
| 12 | 60 | 6 | 2 | 15 | 70.98 | 72.90 | 176.4 | 203.641 | 63.028 | 27.148 | 0.321 | 0.671 | 8.029 |
| 13 | 60 | 8 | -2 | 15 | 80.43 | 79.00 | 192.7 | 223.256 | 109.367 | 43.854 | 0.317 | 0.674 | 8.027 |
| 14 | 60 | 8 | 0 | 15 | 81.51 | 65.01 | 189.5 | 216.288 | 99.516 | 41.148 | 0.317 | 0.674 | 8.014 |
| 15 | 60 | 8 | 2 | 15 | 76.36 | 66.68 | 175.7 | 202.849 | 83.338 | 36.823 | 0.312 | 0.680 | 8.010 |
| 16 | 60 | 10 | -2 | 15 | 94.10 | 60.12 | 182.6 | 214.037 | 205.315 | 67.582 | 0.312 | 0.680 | 7.960 |
| 17 | 60 | 10 | 0 | 15 | 72.23 | 71.21 | 174.2 | 201.578 | 149.776 | 56.267 | 0.311 | 0.680 | 7.970 |
| 18 | 60 | 10 | 2 | 15 | 79.17 | 62.43 | 165.0 | 193.366 | 120.095 | 51.079 | 0.308 | 0.683 | 7.990 |
| 19 | 60 | 6 | -2 | 20 | 113.70 | 47.63 | 283.0 | 308.683 | 101.970 | 42.750 | 0.283 | 0.711 | 7.985 |
| 20 | 60 | 6 | 0 | 20 | 118.10 | 38.21 | 281.7 | 307.835 | 101.430 | 40.462 | 0.282 | 0.712 | 8.018 |
| 21 | 60 | 6 | 2 | 20 | 117.80 | 32.50 | 269.4 | 295.820 | 96.697 | 33.123 | 0.278 | 0.716 | 8.004 |
| 22 | 60 | 8 | -2 | 20 | 126.60 | 35.67 | 285.2 | 314.068 | 151.579 | 52.352 | 0.276 | 0.718 | 8.033 |
| 23 | 60 | 8 | 0 | 20 | 109.70 | 32.27 | 283.2 | 305.414 | 139.625 | 53.510 | 0.275 | 0.719 | 8.002 |
| 24 | 60 | 8 | 2 | 20 | 128.80 | 29.84 | 263.1 | 294.451 | 118.520 | 46.432 | 0.275 | 0.720 | 7.981 |

| | | | | | | | | | | | | | |
|---|---|---|---|---|---|---|---|---|---|---|---|---|---|
| 25 | 60 | 10 | -2 | 20 | 110.10 | 44.34 | 280.9 | 304.947 | 261.698 | 92.610 | 0.273 | 0.722 | 7.989 |
| 26 | 60 | 10 | 0 | 20 | 140.40 | 30.80 | 273.7 | 309.148 | 198.736 | 66.823 | 0.273 | 0.722 | 7.988 |
| 27 | 60 | 10 | 2 | 20 | 121.90 | 19.12 | 266.3 | 293.498 | 136.307 | 64.482 | 0.254 | 0.745 | 7.966 |

**Table 6.6.** The measurement results for the extruded CW617N with 45° of plunging angle

| Run | PA, (°) | RRA, (°) | ARA, (°) | CER, (μm) | Fx, (N) | Fy, (N) | Fz, (N) | FR, (N) | BHEN, (μm) | BHEX, (μm) | Ra bottom , (μm) | Ra Wall, (μm) | Diameter, (mm) |
|---|---|---|---|---|---|---|---|---|---|---|---|---|---|
| 1 | 45 | 6 | -2 | 10 | 44.28 | 112.8 | 126.1 | 174.888 | 30.085 | 12.121 | 0.360 | 0.598 | 7.992 |
| 2 | 45 | 6 | 0 | 10 | 42.42 | 109.8 | 116.6 | 165.684 | 28.683 | 11.636 | 0.351 | 0.608 | 7.998 |
| 3 | 45 | 6 | 2 | 10 | 34.23 | 110.5 | 110.7 | 160.114 | 27.295 | 10.950 | 0.348 | 0.611 | 8.009 |
| 4 | 45 | 8 | -2 | 10 | 43.87 | 103.1 | 118.5 | 163.084 | 44.385 | 17.739 | 0.345 | 0.615 | 8.006 |
| 5 | 45 | 8 | 0 | 10 | 45.44 | 99.09 | 115.6 | 158.893 | 41.010 | 16.580 | 0.341 | 0.620 | 8.002 |
| 6 | 45 | 8 | 2 | 10 | 32.99 | 94.08 | 102 | 142.630 | 34.853 | 14.068 | 0.338 | 0.623 | 8.027 |
| 7 | 45 | 10 | -2 | 10 | 39.66 | 98.39 | 106.3 | 150.177 | 77.644 | 26.518 | 0.337 | 0.625 | 7.974 |
| 8 | 45 | 10 | 0 | 10 | 50.75 | 93.47 | 106.1 | 150.231 | 58.417 | 23.440 | 0.336 | 0.626 | 7.977 |
| 9 | 45 | 10 | 2 | 10 | 35.63 | 93.06 | 96.19 | 138.500 | 48.037 | 19.095 | 0.324 | 0.642 | 7.972 |
| 10 | 45 | 6 | -2 | 15 | 89.78 | 91.98 | 203.4 | 240.608 | 39.426 | 17.055 | 0.317 | 0.651 | 7.995 |
| 11 | 45 | 6 | 0 | 15 | 84.15 | 91.37 | 180.4 | 219.029 | 37.477 | 15.532 | 0.315 | 0.653 | 7.973 |
| 12 | 45 | 6 | 2 | 15 | 72.29 | 91.1 | 179.8 | 214.133 | 35.602 | 15.587 | 0.313 | 0.656 | 7.980 |
| 13 | 45 | 8 | -2 | 15 | 80.03 | 97.45 | 186.5 | 225.130 | 57.446 | 24.032 | 0.311 | 0.660 | 8.033 |
| 14 | 45 | 8 | 0 | 15 | 50.98 | 117.1 | 183.4 | 223.488 | 53.007 | 22.299 | 0.311 | 0.660 | 8.005 |
| 15 | 45 | 8 | 2 | 15 | 92.49 | 74.36 | 157.4 | 197.126 | 45.128 | 19.852 | 0.307 | 0.665 | 8.034 |
| 16 | 45 | 10 | -2 | 15 | 86.43 | 82.51 | 178.9 | 215.135 | 103.027 | 33.243 | 0.307 | 0.665 | 7.971 |
| 17 | 45 | 10 | 0 | 15 | 82.35 | 82.68 | 179.3 | 213.930 | 77.024 | 26.094 | 0.306 | 0.665 | 7.982 |
| 18 | 45 | 10 | 2 | 15 | 79.7 | 71.88 | 170 | 201.044 | 63.571 | 26.773 | 0.305 | 0.668 | 7.972 |
| 19 | 45 | 6 | -2 | 20 | 123.9 | 83.53 | 299.5 | 334.707 | 55.425 | 23.239 | 0.287 | 0.693 | 7.991 |
| 20 | 45 | 6 | 0 | 20 | 119 | 90.58 | 278.4 | 316.026 | 53.569 | 20.443 | 0.287 | 0.694 | 8.021 |
| 21 | 45 | 6 | 2 | 20 | 137.2 | 61.59 | 276.4 | 314.665 | 50.780 | 19.996 | 0.284 | 0.698 | 8.035 |
| 22 | 45 | 8 | -2 | 20 | 129.5 | 73.01 | 302.7 | 337.236 | 76.541 | 27.398 | 0.283 | 0.700 | 8.034 |
| 23 | 45 | 8 | 0 | 20 | 137.1 | 62.91 | 292.5 | 329.105 | 71.525 | 26.304 | 0.282 | 0.701 | 8.045 |
| 24 | 45 | 8 | 2 | 20 | 124.5 | 64.1 | 272.3 | 306.197 | 61.836 | 24.296 | 0.282 | 0.702 | 8.029 |
| 25 | 45 | 10 | -2 | 20 | 141 | 66.34 | 295.2 | 333.804 | 129.785 | 50.251 | 0.281 | 0.703 | 8.016 |
| 26 | 45 | 10 | 0 | 20 | 132.1 | 70.17 | 286 | 322.754 | 99.498 | 34.074 | 0.281 | 0.703 | 8.005 |
| 27 | 45 | 10 | 2 | 20 | 146.9 | 45.59 | 285.9 | 324.649 | 82.992 | 33.894 | 0.268 | 0.724 | 8.006 |

**Table 6.7.** The measurement results for the extruded CW511L with 90° of plunging angle

| Run | PA, (°) | RRA, (°) | ARA, (°) | CER, (μm) | Fx, (N) | Fy, (N) | Fz, (N) | FR, (N) | BHEN, (μm) | BHEX, (μm) | Ra bottom , (μm) | Ra Wall, (μm) | Diameter, (mm) |
|---|---|---|---|---|---|---|---|---|---|---|---|---|---|
| 1 | 90 | 6 | -2 | 10 | 11.03 | 11.48 | 312.4 | 312.8054 | 395.326 | 165.638 | 1.044 | 1.355 | 9.121 |
| 2 | 90 | 6 | 0 | 10 | 2.357 | 14 | 330 | 330.3052 | 355.462 | 152.631 | 1.041 | 1.352 | 8.924 |
| 3 | 90 | 6 | 2 | 10 | 0.5592 | 9.076 | 325.7 | 325.8269 | 296.017 | 129.690 | 1.029 | 1.342 | 8.935 |

| | | | | | | | | | | | | | |
|---|---|---|---|---|---|---|---|---|---|---|---|---|---|
| 4 | 90 | 8 | -2 | 10 | 3.062 | 11.03 | 382.4 | 382.5713 | 428.683 | 177.718 | 1.025 | 1.338 | 8.891 |
| 5 | 90 | 8 | 0 | 10 | 10.25 | 3.166 | 359.1 | 359.2602 | 404.876 | 146.202 | 1.017 | 1.331 | 8.962 |
| 6 | 90 | 8 | 2 | 10 | 0.7638 | 6.855 | 343 | 343.0693 | 398.866 | 165.910 | 1.015 | 1.329 | 8.355 |
| 7 | 90 | 10 | -2 | 10 | 0.7455 | 9.295 | 353.2 | 353.3231 | 534.113 | 163.416 | 1.003 | 1.318 | 8.901 |
| 8 | 90 | 10 | 0 | 10 | 8.767 | 6.482 | 333.7 | 333.8781 | 513.016 | 161.083 | 1.002 | 1.318 | 8.811 |
| 9 | 90 | 10 | 2 | 10 | 2.133 | 8.115 | 323 | 323.109 | 439.657 | 167.084 | 1.000 | 1.316 | 8.766 |
| 10 | 90 | 6 | -2 | 15 | 4.65 | 1.992 | 413.3 | 413.361 | 407.589 | 165.648 | 0.984 | 1.302 | 7.936 |
| 11 | 90 | 6 | 0 | 15 | 7.997 | 0.6699 | 376.4 | 376.5655 | 409.774 | 170.078 | 0.952 | 1.274 | 8.797 |
| 12 | 90 | 6 | 2 | 15 | 8.63 | 13.05 | 415.2 | 415.5846 | 310.766 | 131.469 | 0.946 | 1.269 | 7.970 |
| 13 | 90 | 8 | -2 | 15 | 14.09 | 7.563 | 445.5 | 445.8469 | 441.188 | 184.407 | 0.946 | 1.269 | 8.241 |
| 14 | 90 | 8 | 0 | 15 | 4.822 | 1.902 | 392.6 | 392.6842 | 418.366 | 170.401 | 0.935 | 1.259 | 8.638 |
| 15 | 90 | 8 | 2 | 15 | 9.142 | 7.963 | 409.7 | 409.8793 | 412.641 | 172.636 | 0.930 | 1.255 | 8.493 |
| 16 | 90 | 10 | -2 | 15 | 2.435 | 1.018 | 390.8 | 390.8089 | 377.436 | 226.170 | 0.925 | 1.251 | 7.946 |
| 17 | 90 | 10 | 0 | 15 | 5.576 | 4.53 | 477.4 | 477.4541 | 528.997 | 216.630 | 0.923 | 1.249 | 8.123 |
| 18 | 90 | 10 | 2 | 15 | 12.2 | 12.46 | 466.3 | 466.626 | 271.226 | 187.497 | 0.914 | 1.241 | 8.065 |
| 19 | 90 | 6 | -2 | 20 | 6.59 | 10.1 | 405.7 | 405.8792 | 508.278 | 209.658 | 0.899 | 1.229 | 8.152 |
| 20 | 90 | 6 | 0 | 20 | 13.02 | 11.83 | 318.1 | 318.5861 | 458.445 | 191.038 | 0.899 | 1.229 | 8.206 |
| 21 | 90 | 6 | 2 | 20 | 15.4 | 0.3897 | 456.4 | 456.6599 | 382.036 | 157.085 | 0.893 | 1.224 | 7.970 |
| 22 | 90 | 8 | -2 | 20 | 4.234 | 6.575 | 469 | 469.0652 | 548.231 | 226.807 | 0.873 | 1.207 | 7.972 |
| 23 | 90 | 8 | 0 | 20 | 2.937 | 4.173 | 454.9 | 454.9286 | 519.237 | 213.834 | 0.873 | 1.207 | 7.978 |
| 24 | 90 | 8 | 2 | 20 | 5.287 | 9.588 | 447.6 | 447.7339 | 509.654 | 212.189 | 0.871 | 1.205 | 7.946 |
| 25 | 90 | 10 | -2 | 20 | 7.853 | 0.6217 | 495.4 | 495.4626 | 242.960 | 223.281 | 0.867 | 1.202 | 7.948 |
| 26 | 90 | 10 | 0 | 20 | 5.447 | 1.957 | 494.3 | 494.3339 | 604.409 | 247.544 | 0.855 | 1.192 | 7.945 |
| 27 | 90 | 10 | 2 | 20 | 7.301 | 5.479 | 469.8 | 469.8887 | 224.335 | 156.525 | 0.852 | 1.190 | 7.930 |

**Table 6.8.** The measurement results for the extruded CW511L with 60° of plunging angle

| Run | PA, (°) | RRA, (°) | ARA, (°) | CER, (µm) | Fx, (N) | Fy, (N) | Fz, (N) | FR, (N) | BHEN, (µm) | BHEX, (µm) | Ra bottom, (µm) | Ra Wall, (µm) | Diameter, (mm) |
|---|---|---|---|---|---|---|---|---|---|---|---|---|---|
| 1 | 60 | 6 | -2 | 10 | 69.24 | 163.1 | 246 | 303.170 | 348.223 | 138.109 | 0.827 | 0.931 | 8.016 |
| 2 | 60 | 6 | 0 | 10 | 18.74 | 48.76 | 248.8 | 254.225 | 315.177 | 126.838 | 0.824 | 0.932 | 8.263 |
| 3 | 60 | 6 | 2 | 10 | 35.35 | 151.5 | 242.5 | 288.111 | 265.894 | 111.580 | 0.815 | 0.934 | 8.007 |
| 4 | 60 | 8 | -2 | 10 | 62.01 | 168.8 | 251.4 | 309.096 | 375.873 | 147.097 | 0.812 | 0.935 | 8.007 |
| 5 | 60 | 8 | 0 | 10 | 50.25 | 166.8 | 236.5 | 293.734 | 356.139 | 124.525 | 0.805 | 0.936 | 8.030 |
| 6 | 60 | 8 | 2 | 10 | 54.71 | 164 | 235.7 | 292.307 | 351.157 | 136.533 | 0.804 | 0.937 | 7.999 |
| 7 | 60 | 10 | -2 | 10 | 62.51 | 169.7 | 236.4 | 297.642 | 463.254 | 134.501 | 0.794 | 0.939 | 7.979 |
| 8 | 60 | 10 | 0 | 10 | 67.73 | 160.1 | 281.4 | 330.765 | 445.769 | 133.754 | 0.794 | 0.939 | 7.993 |
| 9 | 60 | 10 | 2 | 10 | 43.38 | 161.6 | 241.4 | 293.718 | 384.969 | 138.107 | 0.792 | 0.940 | 7.984 |
| 10 | 60 | 6 | -2 | 15 | 134.6 | 106.5 | 317.6 | 361.011 | 358.388 | 135.527 | 0.779 | 0.943 | 7.991 |
| 11 | 60 | 6 | 0 | 15 | 130.9 | 121.8 | 310.5 | 358.302 | 360.199 | 141.360 | 0.754 | 0.951 | 8.005 |
| 12 | 60 | 6 | 2 | 15 | 123.6 | 114.8 | 287.3 | 333.163 | 278.122 | 113.244 | 0.750 | 0.952 | 8.026 |
| 13 | 60 | 8 | -2 | 15 | 96.5 | 144.4 | 314.7 | 359.444 | 386.237 | 164.924 | 0.750 | 0.952 | 8.003 |
| 14 | 60 | 8 | 0 | 15 | 125.9 | 101.8 | 301.5 | 342.223 | 367.321 | 141.112 | 0.741 | 0.955 | 8.017 |
| 15 | 60 | 8 | 2 | 15 | 97.64 | 126.6 | 297.1 | 337.386 | 362.575 | 144.092 | 0.737 | 0.956 | 8.023 |

| | | | | | | | | | | | | | |
|---|---|---|---|---|---|---|---|---|---|---|---|---|---|
| 16 | 60 | 10 | -2 | 15 | 115.9 | 127.6 | 298.6 | 344.785 | 304.872 | 190.797 | 0.733 | 0.958 | 7.981 |
| 17 | 60 | 10 | 0 | 15 | 129.7 | 120.7 | 286.1 | 336.517 | 459.014 | 180.535 | 0.731 | 0.958 | 7.999 |
| 18 | 60 | 10 | 2 | 15 | 110.2 | 124.2 | 278 | 323.811 | 240.942 | 153.712 | 0.724 | 0.961 | 7.980 |
| 19 | 60 | 6 | -2 | 20 | 165.1 | 85.42 | 435 | 473.053 | 441.843 | 171.447 | 0.713 | 0.965 | 7.995 |
| 20 | 60 | 6 | 0 | 20 | 176.2 | 61.15 | 425.5 | 464.582 | 400.541 | 152.221 | 0.713 | 0.965 | 7.997 |
| 21 | 60 | 6 | 2 | 20 | 172.1 | 60.51 | 414 | 452.411 | 337.206 | 128.353 | 0.708 | 0.967 | 7.982 |
| 22 | 60 | 8 | -2 | 20 | 163.7 | 75.87 | 430.5 | 466.781 | 474.954 | 180.714 | 0.692 | 0.974 | 8.017 |
| 23 | 60 | 8 | 0 | 20 | 149.5 | 68.07 | 424.6 | 455.268 | 450.926 | 174.375 | 0.692 | 0.974 | 8.016 |
| 24 | 60 | 8 | 2 | 20 | 179.5 | 73.56 | 392.9 | 438.180 | 255.010 | 171.438 | 0.691 | 0.974 | 7.986 |
| 25 | 60 | 10 | -2 | 20 | 162.6 | 87.11 | 434.4 | 471.943 | 225.043 | 180.011 | 0.687 | 0.976 | 7.955 |
| 26 | 60 | 10 | 0 | 20 | 169.1 | 87.53 | 430.9 | 471.096 | 521.509 | 194.824 | 0.678 | 0.980 | 7.952 |
| 27 | 60 | 10 | 2 | 20 | 177.4 | 56.34 | 417.6 | 457.203 | 163.225 | 146.527 | 0.676 | 0.981 | 7.940 |

**Table 6.9.** The measurement results for the extruded CW511L with 45° of plunging angle

| Run | PA, (°) | RRA, (°) | ARA, (°) | CER, (µm) | Fx, (N) | Fy, (N) | Fz, (N) | FR, (N) | BHEN, (µm) | BHEX, (µm) | Ra bottom, (µm) | Ra Wall, (µm) | Diameter, (mm) |
|---|---|---|---|---|---|---|---|---|---|---|---|---|---|
| 1 | 45 | 6 | -2 | 10 | 85.6 | 185.1 | 240 | 314.943 | 183.822 | 108.675 | 0.759 | 0.831 | 7.986 |
| 2 | 45 | 6 | 0 | 10 | 40.22 | 111.7 | 222.8 | 252.457 | 165.446 | 100.166 | 0.756 | 0.832 | 8.159 |
| 3 | 45 | 6 | 2 | 10 | 83.4 | 186.6 | 219.1 | 299.633 | 138.032 | 85.162 | 0.748 | 0.836 | 8.006 |
| 4 | 45 | 8 | -2 | 10 | 96.18 | 191.5 | 220.8 | 307.694 | 199.195 | 116.580 | 0.745 | 0.838 | 8.005 |
| 5 | 45 | 8 | 0 | 10 | 77.28 | 197.8 | 217.6 | 304.051 | 188.223 | 95.961 | 0.740 | 0.840 | 8.002 |
| 6 | 45 | 8 | 2 | 10 | 74.55 | 190.8 | 207.1 | 291.295 | 185.454 | 108.853 | 0.738 | 0.841 | 7.992 |
| 7 | 45 | 10 | -2 | 10 | 96.31 | 181.8 | 229.7 | 308.365 | 247.768 | 107.222 | 0.730 | 0.845 | 7.984 |
| 8 | 45 | 10 | 0 | 10 | 107.3 | 183.7 | 216.9 | 303.817 | 238.050 | 105.695 | 0.729 | 0.846 | 7.979 |
| 9 | 45 | 10 | 2 | 10 | 87.99 | 178.1 | 210.5 | 289.434 | 204.252 | 109.622 | 0.728 | 0.846 | 7.963 |
| 10 | 45 | 6 | -2 | 15 | 168 | 134.5 | 277.4 | 351.091 | 189.474 | 108.682 | 0.717 | 0.852 | 8.003 |
| 11 | 45 | 6 | 0 | 15 | 174.4 | 127.9 | 249.1 | 329.886 | 190.481 | 111.581 | 0.694 | 0.865 | 8.005 |
| 12 | 45 | 6 | 2 | 15 | 148.8 | 136.8 | 231 | 306.947 | 144.835 | 86.326 | 0.690 | 0.867 | 8.031 |
| 13 | 45 | 8 | -2 | 15 | 131.4 | 160.5 | 255.3 | 328.944 | 204.957 | 120.957 | 0.690 | 0.867 | 8.035 |
| 14 | 45 | 8 | 0 | 15 | 172.9 | 114.2 | 247.8 | 323.018 | 194.441 | 111.792 | 0.682 | 0.872 | 8.010 |
| 15 | 45 | 8 | 2 | 15 | 156.2 | 130.6 | 247.4 | 320.408 | 191.802 | 113.255 | 0.679 | 0.874 | 8.042 |
| 16 | 45 | 10 | -2 | 15 | 164.1 | 135.4 | 250.2 | 328.424 | 182.043 | 148.294 | 0.675 | 0.876 | 7.983 |
| 17 | 45 | 10 | 0 | 15 | 158.7 | 129 | 237.5 | 313.421 | 245.412 | 142.049 | 0.674 | 0.877 | 8.004 |
| 18 | 45 | 10 | 2 | 15 | 169.3 | 119.7 | 232.8 | 311.747 | 196.629 | 122.980 | 0.668 | 0.881 | 7.961 |
| 19 | 45 | 6 | -2 | 20 | 221.4 | 107.8 | 390.4 | 461.574 | 235.868 | 137.485 | 0.657 | 0.888 | 7.973 |
| 20 | 45 | 6 | 0 | 20 | 216 | 102.2 | 387.7 | 455.425 | 212.909 | 125.297 | 0.657 | 0.888 | 7.991 |
| 21 | 45 | 6 | 2 | 20 | 218.8 | 95.18 | 384.8 | 452.773 | 177.696 | 103.080 | 0.653 | 0.891 | 7.990 |
| 22 | 45 | 8 | -2 | 20 | 196.8 | 108.7 | 402.9 | 461.383 | 254.271 | 148.711 | 0.639 | 0.900 | 7.989 |
| 23 | 45 | 8 | 0 | 20 | 219.1 | 89.5 | 387.1 | 453.720 | 240.916 | 140.218 | 0.639 | 0.900 | 8.014 |
| 24 | 45 | 8 | 2 | 20 | 195.9 | 105.1 | 368.2 | 430.109 | 236.502 | 139.142 | 0.638 | 0.901 | 7.963 |
| 25 | 45 | 10 | -2 | 20 | 199.3 | 114.9 | 421.6 | 480.280 | 107.642 | 146.403 | 0.635 | 0.903 | 7.961 |
| 26 | 45 | 10 | 0 | 20 | 218.6 | 97.26 | 404.5 | 469.964 | 280.145 | 162.288 | 0.626 | 0.909 | 7.952 |
| 27 | 45 | 10 | 2 | 20 | 215.6 | 88.12 | 391.2 | 455.287 | 108.277 | 148.422 | 0.624 | 0.911 | 7.970 |

**Table 6.10.** The measurement results for the extruded CW724R with 90° of plunging angle

| Run | PA, (°) | RRA, (°) | ARA, (°) | CER, (µm) | Fx, (N) | Fy, (N) | Fz, (N) | FR, (N) | BHEN, (µm) | BHEX, (µm) | Ra bottom, (µm) | Ra Wall, (µm) | Diameter, (mm) |
|---|---|---|---|---|---|---|---|---|---|---|---|---|---|
| 1 | 90 | 6 | -2 | 10 | 6.632 | 8.894 | 324.6 | 324.790 | 37.387 | 20.240 | 0.523 | 0.660 | 7.985 |
| 2 | 90 | 6 | 0 | 10 | 8.109 | 0.1887 | 270.4 | 270.522 | 37.254 | 20.078 | 0.521 | 0.661 | 8.110 |
| 3 | 90 | 6 | 2 | 10 | 4.713 | 2.644 | 241.8 | 241.860 | 36.641 | 18.913 | 0.509 | 0.670 | 8.147 |
| 4 | 90 | 8 | -2 | 10 | 9.804 | 12.34 | 329.7 | 330.076 | 53.820 | 25.334 | 0.507 | 0.671 | 8.012 |
| 5 | 90 | 8 | 0 | 10 | 19.9 | 4.525 | 317.7 | 318.355 | 44.164 | 21.967 | 0.507 | 0.671 | 8.010 |
| 6 | 90 | 8 | 2 | 10 | 7.734 | 8.451 | 277.8 | 278.036 | 40.637 | 24.632 | 0.503 | 0.674 | 8.074 |
| 7 | 90 | 10 | -2 | 10 | 1.14 | 12 | 311.4 | 311.633 | 95.172 | 42.229 | 0.501 | 0.676 | 7.978 |
| 8 | 90 | 10 | 0 | 10 | 8.865 | 8.558 | 306.8 | 307.047 | 71.292 | 34.152 | 0.501 | 0.676 | 7.961 |
| 9 | 90 | 10 | 2 | 10 | 1.702 | 15.91 | 294.6 | 295.034 | 67.426 | 33.325 | 0.500 | 0.676 | 7.966 |
| 10 | 90 | 6 | -2 | 15 | 7.045 | 10.83 | 390.2 | 390.414 | 61.740 | 29.872 | 0.496 | 0.679 | 7.893 |
| 11 | 90 | 6 | 0 | 15 | 6.605 | 2.795 | 386.3 | 386.367 | 61.869 | 29.981 | 0.493 | 0.681 | 7.905 |
| 12 | 90 | 6 | 2 | 15 | 8.413 | 3.997 | 376.1 | 376.215 | 59.435 | 30.578 | 0.492 | 0.682 | 7.953 |
| 13 | 90 | 8 | -2 | 15 | 7.752 | 12.59 | 391.7 | 391.979 | 89.447 | 43.382 | 0.484 | 0.688 | 7.956 |
| 14 | 90 | 8 | 0 | 15 | 11.21 | 10.61 | 390.5 | 390.805 | 72.281 | 35.375 | 0.482 | 0.690 | 7.943 |
| 15 | 90 | 8 | 2 | 15 | 6.189 | 0.1148 | 379.3 | 379.351 | 66.154 | 33.291 | 0.481 | 0.691 | 7.964 |
| 16 | 90 | 10 | -2 | 15 | 9.968 | 11.45 | 378.5 | 378.804 | 159.576 | 71.793 | 0.479 | 0.692 | 7.943 |
| 17 | 90 | 10 | 0 | 15 | 3.099 | 5.271 | 367.4 | 367.451 | 119.174 | 55.415 | 0.473 | 0.697 | 7.949 |
| 18 | 90 | 10 | 2 | 15 | 12.65 | 1.694 | 364 | 364.224 | 112.523 | 52.545 | 0.469 | 0.700 | 7.947 |
| 19 | 90 | 6 | -2 | 20 | 6.237 | 6.694 | 399.0909 | 399.196 | 78.464 | 38.769 | 0.436 | 0.729 | 7.954 |
| 20 | 90 | 6 | 0 | 20 | 9.774 | 13.06 | 399.0909 | 399.424 | 78.742 | 39.453 | 0.431 | 0.733 | 7.970 |
| 21 | 90 | 6 | 2 | 20 | 0.5596 | 5.447 | 392.6364 | 392.675 | 75.054 | 34.152 | 0.422 | 0.742 | 7.965 |
| 22 | 90 | 8 | -2 | 20 | 3.213 | 13.04 | 413.3636 | 413.582 | 114.805 | 47.970 | 0.416 | 0.747 | 7.952 |
| 23 | 90 | 8 | 0 | 20 | 10.98 | 7.793 | 401.8182 | 402.044 | 92.210 | 41.458 | 0.413 | 0.750 | 7.979 |
| 24 | 90 | 8 | 2 | 20 | 3.992 | 6.522 | 372.0909 | 372.169 | 84.185 | 41.068 | 0.399 | 0.765 | 7.946 |
| 25 | 90 | 10 | -2 | 20 | 5.921 | 18.99 | 414.0909 | 414.568 | 205.319 | 94.281 | 0.386 | 0.778 | 7.920 |
| 26 | 90 | 10 | 0 | 20 | 7.719 | 4.762 | 397.5455 | 397.649 | 154.310 | 60.523 | 0.376 | 0.790 | 7.928 |
| 27 | 90 | 10 | 2 | 20 | 4.945 | 6.711 | 396.1818 | 396.270 | 114.285 | 42.999 | 0.345 | 0.827 | 7.931 |

**Table 6.11.** The measurement results for the extruded CW724R with 60° of plunging angle

| Run | PA, (°) | RRA, (°) | ARA, (°) | CER, (µm) | Fx, (N) | Fy, (N) | Fz, (N) | FR, (N) | BHEN, (µm) | BHEX, (µm) | Ra bottom, (µm) | Ra Wall, (µm) | Diameter, (mm) |
|---|---|---|---|---|---|---|---|---|---|---|---|---|---|
| 1 | 60 | 6 | -2 | 10 | 64.9 | 131 | 179.9 | 231.8125 | 55.937 | 24.289 | 0.374 | 0.627 | 7.991 |
| 2 | 60 | 6 | 0 | 10 | 41.82 | 128.7 | 178.3 | 223.8381 | 55.847 | 22.079 | 0.373 | 0.628 | 7.994 |
| 3 | 60 | 6 | 2 | 10 | 40.36 | 127.31 | 168.6 | 215.0877 | 55.432 | 21.736 | 0.365 | 0.634 | 7.999 |
| 4 | 60 | 8 | -2 | 10 | 68.08 | 116.1 | 188.2 | 231.3727 | 67.151 | 25.430 | 0.363 | 0.635 | 8.006 |
| 5 | 60 | 8 | 0 | 10 | 47.89 | 117.9 | 164.8 | 208.2136 | 60.545 | 25.940 | 0.363 | 0.635 | 8.012 |
| 6 | 60 | 8 | 2 | 10 | 45.6 | 117.1 | 162.2 | 205.1843 | 58.143 | 26.267 | 0.361 | 0.637 | 7.988 |

| | | | | | | | | | | | | | |
|---|---|---|---|---|---|---|---|---|---|---|---|---|---|
| 7 | 60 | 10 | -2 | 10 | 60.27 | 117.5 | 161.4 | 208.5394 | 95.651 | 36.825 | 0.359 | 0.638 | 7.986 |
| 8 | 60 | 10 | 0 | 10 | 75.2 | 109.3 | 160.9 | 208.5434 | 79.168 | 33.549 | 0.359 | 0.638 | 7.953 |
| 9 | 60 | 10 | 2 | 10 | 72.56 | 104.8 | 158.5 | 203.3968 | 76.504 | 33.604 | 0.359 | 0.639 | 7.977 |
| 10 | 60 | 6 | -2 | 15 | 174.9 | 48.6 | 279.3 | 333.1073 | 72.591 | 31.074 | 0.356 | 0.641 | 7.970 |
| 11 | 60 | 6 | 0 | 15 | 197.5 | 31.1 | 279 | 343.2411 | 72.679 | 30.089 | 0.354 | 0.642 | 7.972 |
| 12 | 60 | 6 | 2 | 15 | 161.4 | 54.51 | 256.3 | 307.7515 | 71.006 | 31.880 | 0.353 | 0.643 | 7.993 |
| 13 | 60 | 8 | -2 | 15 | 179.1 | 53.81 | 287.1 | 342.635 | 91.696 | 41.664 | 0.348 | 0.647 | 7.955 |
| 14 | 60 | 8 | 0 | 15 | 171.8 | 36.82 | 264.2 | 317.2894 | 79.850 | 36.829 | 0.346 | 0.648 | 7.990 |
| 15 | 60 | 8 | 2 | 15 | 167.1 | 27.6 | 258.4 | 308.9575 | 75.628 | 33.808 | 0.346 | 0.649 | 8.008 |
| 16 | 60 | 10 | -2 | 15 | 182.9 | 36.37 | 285.9 | 341.3415 | 140.199 | 66.802 | 0.344 | 0.650 | 7.961 |
| 17 | 60 | 10 | 0 | 15 | 182.9 | 31.98 | 280 | 335.9689 | 112.246 | 49.957 | 0.340 | 0.654 | 7.973 |
| 18 | 60 | 10 | 2 | 15 | 185.7 | 25.77 | 274.6 | 332.4962 | 107.646 | 50.472 | 0.338 | 0.656 | 7.972 |
| 19 | 60 | 6 | -2 | 20 | 193.6 | 21.48 | 342.1 | 393.6683 | 84.113 | 37.878 | 0.316 | 0.676 | 8.000 |
| 20 | 60 | 6 | 0 | 20 | 218.2 | 7.669 | 331.5 | 396.9412 | 84.305 | 40.514 | 0.312 | 0.679 | 8.018 |
| 21 | 60 | 6 | 2 | 20 | 208 | 10.01 | 328.1 | 388.605 | 81.761 | 34.370 | 0.306 | 0.685 | 7.969 |
| 22 | 60 | 8 | -2 | 20 | 216.6 | 12.1 | 334.4 | 398.6042 | 109.224 | 45.319 | 0.302 | 0.689 | 7.987 |
| 23 | 60 | 8 | 0 | 20 | 192 | 16.72 | 324.5 | 377.4173 | 93.604 | 41.084 | 0.300 | 0.691 | 8.022 |
| 24 | 60 | 8 | 2 | 20 | 202.8 | 2.153 | 316.1 | 375.5685 | 88.062 | 41.676 | 0.291 | 0.701 | 7.998 |
| 25 | 60 | 10 | -2 | 20 | 220.2 | 0.56223 | 346.3 | 410.3804 | 171.853 | 58.272 | 0.282 | 0.711 | 7.952 |
| 26 | 60 | 10 | 0 | 20 | 240 | 10.87 | 343.5 | 419.1783 | 136.556 | 56.276 | 0.275 | 0.719 | 7.933 |
| 27 | 60 | 10 | 2 | 20 | 212.8 | 15.35 | 342.1 | 403.1772 | 129.619 | 47.187 | 0.255 | 0.744 | 7.937 |

**Table 6.12.** The measurement results for the extruded CW724R with 45° of plunging angle

| Run | PA, (°) | RRA, (°) | ARA, (°) | CER, (μm) | Fx, (N) | Fy, (N) | Fz, (N) | FR, (N) | BHEN, (μm) | BHEX, (μm) | Ra bottom, (μm) | Ra Wall, (μm) | Diameter, (mm) |
|---|---|---|---|---|---|---|---|---|---|---|---|---|---|
| 1 | 45 | 6 | -2 | 10 | 104.9 | 119.6 | 192.4 | 249.652 | 34.494 | 17.871 | 0.339 | 0.623 | 7.986 |
| 2 | 45 | 6 | 0 | 10 | 61.16 | 139.1 | 173.9 | 230.934 | 34.377 | 17.023 | 0.338 | 0.624 | 7.990 |
| 3 | 45 | 6 | 2 | 10 | 82.3 | 127.3 | 165.7 | 224.578 | 33.841 | 16.391 | 0.331 | 0.633 | 8.012 |
| 4 | 45 | 8 | -2 | 10 | 37.34 | 123.3 | 188 | 227.906 | 48.943 | 21.587 | 0.329 | 0.635 | 8.002 |
| 5 | 45 | 8 | 0 | 10 | 77.37 | 126 | 176 | 229.865 | 40.442 | 18.451 | 0.329 | 0.635 | 7.966 |
| 6 | 45 | 8 | 2 | 10 | 88.63 | 108.8 | 172.6 | 222.449 | 37.344 | 20.011 | 0.327 | 0.638 | 7.994 |
| 7 | 45 | 10 | -2 | 10 | 94.35 | 108.9 | 176.5 | 227.845 | 85.517 | 33.231 | 0.326 | 0.639 | 7.980 |
| 8 | 45 | 10 | 0 | 10 | 95.58 | 107.2 | 171.8 | 223.925 | 64.374 | 29.068 | 0.326 | 0.639 | 7.974 |
| 9 | 45 | 10 | 2 | 10 | 89.12 | 96.62 | 162.8 | 209.241 | 60.956 | 26.302 | 0.325 | 0.640 | 7.977 |
| 10 | 45 | 6 | -2 | 15 | 206.3 | 85.27 | 230.7 | 321.019 | 55.932 | 24.976 | 0.323 | 0.643 | 8.009 |
| 11 | 45 | 6 | 0 | 15 | 203 | 87.07 | 269.5 | 348.454 | 56.046 | 25.150 | 0.321 | 0.645 | 8.021 |
| 12 | 45 | 6 | 2 | 15 | 169.6 | 93.08 | 265 | 328.105 | 53.897 | 26.916 | 0.321 | 0.646 | 8.033 |
| 13 | 45 | 8 | -2 | 15 | 191.4 | 99.23 | 279 | 352.593 | 80.444 | 33.243 | 0.316 | 0.652 | 8.047 |
| 14 | 45 | 8 | 0 | 15 | 178.7 | 88.08 | 262.5 | 329.542 | 65.249 | 29.591 | 0.315 | 0.654 | 8.022 |
| 15 | 45 | 8 | 2 | 15 | 195.7 | 71.28 | 251.8 | 326.776 | 59.831 | 28.567 | 0.314 | 0.655 | 8.002 |
| 16 | 45 | 10 | -2 | 15 | 184.8 | 80.16 | 269.2 | 336.222 | 142.673 | 55.744 | 0.313 | 0.656 | 8.010 |
| 17 | 45 | 10 | 0 | 15 | 197.1 | 72.35 | 267.7 | 340.215 | 106.802 | 46.700 | 0.310 | 0.661 | 7.990 |
| 18 | 45 | 10 | 2 | 15 | 202 | 64.13 | 249.8 | 327.592 | 100.901 | 45.585 | 0.307 | 0.664 | 8.010 |

| | | | | | | | | | | | | | |
|---|---|---|---|---|---|---|---|---|---|---|---|---|---|
| 19 | 45 | 6 | -2 | 20 | 258.5 | 78.1 | 320.9 | 419.403 | 70.719 | 31.890 | 0.288 | 0.692 | 7.956 |
| 20 | 45 | 6 | 0 | 20 | 252.6 | 83.72 | 317 | 413.890 | 70.965 | 32.906 | 0.285 | 0.697 | 8.009 |
| 21 | 45 | 6 | 2 | 20 | 251 | 82.13 | 314.5 | 410.678 | 67.702 | 28.582 | 0.280 | 0.705 | 7.995 |
| 22 | 45 | 8 | -2 | 20 | 248.3 | 81.94 | 313 | 407.843 | 102.926 | 40.557 | 0.276 | 0.710 | 7.960 |
| 23 | 45 | 8 | 0 | 20 | 266.5 | 71.59 | 312.8 | 417.123 | 82.892 | 34.604 | 0.275 | 0.713 | 8.013 |
| 24 | 45 | 8 | 2 | 20 | 253.6 | 64.88 | 307 | 403.449 | 75.783 | 35.587 | 0.266 | 0.726 | 7.980 |
| 25 | 45 | 10 | -2 | 20 | 274.5 | 62.71 | 325.9 | 430.690 | 183.322 | 52.690 | 0.259 | 0.739 | 7.961 |
| 26 | 45 | 10 | 0 | 20 | 305 | 46.43 | 323.2 | 446.810 | 137.996 | 47.233 | 0.253 | 0.749 | 7.952 |
| 27 | 45 | 10 | 2 | 20 | 269.8 | 48 | 316.5 | 418.651 | 129.093 | 40.507 | 0.235 | 0.782 | 7.950 |

**Table 6.13.** The measurement results for the forged CW617N with 90° of plunging angle

| Run | PA, (°) | RRA, (°) | ARA, (°) | CER, (μm) | Fx, (N) | Fy, (N) | Fz, (N) | FR, (N) | BHEN, (μm) | BHEX, (μm) | Ra bottom, (μm) | Ra Wall, (μm) | Diameter, (mm) |
|---|---|---|---|---|---|---|---|---|---|---|---|---|---|
| 1 | 90 | 6 | -2 | 10 | 7.442 | 2.854 | 255.356 | 255.480 | 41.305 | 17.198 | 0.427 | 0.737 | 7.972 |
| 2 | 90 | 6 | 0 | 10 | 3.996 | 8.414 | 248.876 | 249.050 | 38.873 | 15.645 | 0.414 | 0.750 | 7.980 |
| 3 | 90 | 6 | 2 | 10 | 8.542 | 7.365 | 231.488 | 231.763 | 36.470 | 14.365 | 0.410 | 0.753 | 8.010 |
| 4 | 90 | 8 | -2 | 10 | 8.13 | 7.381 | 259.136 | 259.369 | 66.386 | 26.980 | 0.405 | 0.758 | 7.980 |
| 5 | 90 | 8 | 0 | 10 | 1.043 | 4.84 | 255.356 | 255.404 | 60.433 | 24.991 | 0.399 | 0.765 | 7.984 |
| 6 | 90 | 8 | 2 | 10 | 11.81 | 0.5832 | 247.58 | 247.862 | 49.621 | 17.698 | 0.395 | 0.768 | 8.003 |
| 7 | 90 | 10 | -2 | 10 | 9.925 | 2.63 | 242.504 | 242.721 | 125.617 | 52.694 | 0.394 | 0.770 | 7.978 |
| 8 | 90 | 10 | 0 | 10 | 9.271 | 1.732 | 240.236 | 240.421 | 91.274 | 36.489 | 0.392 | 0.772 | 7.976 |
| 9 | 90 | 10 | 2 | 10 | 2.527 | 5.871 | 236.564 | 236.650 | 72.842 | 29.456 | 0.375 | 0.791 | 8.006 |
| 10 | 90 | 6 | -2 | 15 | 13.49 | 6.222 | 306.656 | 307.016 | 57.645 | 22.089 | 0.365 | 0.802 | 7.983 |
| 11 | 90 | 6 | 0 | 15 | 12.03 | 1.569 | 289.7 | 289.954 | 54.221 | 20.623 | 0.363 | 0.805 | 7.980 |
| 12 | 90 | 6 | 2 | 15 | 10.66 | 8.618 | 286.568 | 286.896 | 50.932 | 18.258 | 0.359 | 0.809 | 7.987 |
| 13 | 90 | 8 | -2 | 15 | 15.84 | 6.645 | 304.604 | 305.088 | 89.546 | 35.981 | 0.356 | 0.814 | 7.997 |
| 14 | 90 | 8 | 0 | 15 | 11.21 | 2.751 | 297.476 | 297.700 | 81.655 | 33.145 | 0.356 | 0.814 | 7.992 |
| 15 | 90 | 8 | 2 | 15 | 1.861 | 2.198 | 273.824 | 273.839 | 67.698 | 27.963 | 0.350 | 0.820 | 8.003 |
| 16 | 90 | 10 | -2 | 15 | 5.337 | 1.678 | 291.752 | 291.806 | 171.190 | 70.751 | 0.350 | 0.820 | 7.968 |
| 17 | 90 | 10 | 0 | 15 | 9.06 | 1.938 | 287 | 287.150 | 124.506 | 52.156 | 0.349 | 0.821 | 7.975 |
| 18 | 90 | 10 | 2 | 15 | 11.36 | 2.654 | 284.408 | 284.647 | 100.459 | 41.015 | 0.347 | 0.825 | 7.952 |
| 19 | 90 | 6 | -2 | 20 | 10.71 | 0.700 | 373.292 | 373.446 | 85.952 | 33.592 | 0.322 | 0.858 | 7.960 |
| 20 | 90 | 6 | 0 | 20 | 14.74 | 2.064 | 366.92 | 367.222 | 82.654 | 33.597 | 0.321 | 0.860 | 7.983 |
| 21 | 90 | 6 | 2 | 20 | 5.081 | 3.15 | 354.932 | 354.982 | 77.703 | 32.564 | 0.317 | 0.864 | 7.989 |
| 22 | 90 | 8 | -2 | 20 | 5.011 | 8.675 | 372.536 | 372.671 | 123.640 | 50.892 | 0.316 | 0.867 | 7.978 |
| 23 | 90 | 8 | 0 | 20 | 7.321 | 8.424 | 366.596 | 366.766 | 114.664 | 47.564 | 0.315 | 0.868 | 7.991 |
| 24 | 90 | 8 | 2 | 20 | 7.475 | 11.69 | 331.28 | 331.570 | 97.365 | 37.985 | 0.314 | 0.870 | 7.970 |
| 25 | 90 | 10 | -2 | 20 | 6.676 | 6.2 | 368.216 | 368.329 | 219.403 | 89.999 | 0.312 | 0.872 | 7.960 |
| 26 | 90 | 10 | 0 | 20 | 0.964 | 13.52 | 358.388 | 358.644 | 164.842 | 62.565 | 0.312 | 0.872 | 7.954 |
| 27 | 90 | 10 | 2 | 20 | 11.32 | 9.282 | 348.56 | 348.867 | 135.200 | 57.595 | 0.294 | 0.900 | 7.956 |

**Table 6.14.** The measurement results for the forged CW617N with 60° of plunging angle

| Run | PA, (°) | RRA, (°) | ARA, (°) | CER, (μm) | Fx, (N) | Fy, (N) | Fz, (N) | FR, (N) | BHEN, (μm) | BHEX, (μm) | Ra bottom, (μm) | Ra Wall, (μm) | Diameter, (mm) |
|---|---|---|---|---|---|---|---|---|---|---|---|---|---|
| 1 | 60 | 6 | -2 | 10 | 44.53 | 94.32 | 170.767 | 200.101 | 27.765 | 15.642 | 0.322 | 0.670 | 7.978 |
| 2 | 60 | 6 | 0 | 10 | 29.54 | 89.75 | 146.15 | 174.033 | 26.565 | 13.956 | 0.311 | 0.680 | 7.987 |
| 3 | 60 | 6 | 2 | 10 | 40.5 | 94.31 | 144.605 | 177.328 | 25.556 | 12.654 | 0.308 | 0.683 | 8.004 |
| 4 | 60 | 8 | -2 | 10 | 55 | 86.6 | 162.63 | 192.284 | 45.487 | 20.654 | 0.304 | 0.688 | 8.019 |
| 5 | 60 | 8 | 0 | 10 | 42.68 | 92.82 | 162.321 | 191.795 | 43.033 | 20.102 | 0.299 | 0.693 | 7.992 |
| 6 | 60 | 8 | 2 | 10 | 34.82 | 95.77 | 157.274 | 187.402 | 33.419 | 16.856 | 0.296 | 0.696 | 8.003 |
| 7 | 60 | 10 | -2 | 10 | 56.63 | 88.72 | 147.901 | 181.529 | 90.441 | 40.392 | 0.294 | 0.698 | 7.968 |
| 8 | 60 | 10 | 0 | 10 | 43.16 | 95.88 | 146.047 | 179.960 | 65.040 | 30.650 | 0.293 | 0.699 | 7.975 |
| 9 | 60 | 10 | 2 | 10 | 54 | 79.19 | 138.528 | 168.455 | 51.895 | 25.302 | 0.278 | 0.715 | 8.046 |
| 10 | 60 | 6 | -2 | 15 | 75.01 | 90.08 | 206.508 | 237.458 | 40.951 | 19.002 | 0.270 | 0.725 | 7.991 |
| 11 | 60 | 6 | 0 | 15 | 69.9 | 83.63 | 202.8 | 230.234 | 37.384 | 17.777 | 0.268 | 0.728 | 7.988 |
| 12 | 60 | 6 | 2 | 15 | 73.31 | 80.71 | 180.449 | 210.832 | 35.884 | 16.892 | 0.265 | 0.731 | 8.013 |
| 13 | 60 | 8 | -2 | 15 | 69.94 | 91.97 | 204.757 | 235.107 | 64.885 | 30.469 | 0.262 | 0.735 | 8.011 |
| 14 | 60 | 8 | 0 | 15 | 81.83 | 71.5 | 197.135 | 225.101 | 58.687 | 28.218 | 0.262 | 0.735 | 8.003 |
| 15 | 60 | 8 | 2 | 15 | 73.07 | 76.53 | 179.934 | 208.740 | 48.540 | 24.654 | 0.258 | 0.740 | 8.010 |
| 16 | 60 | 10 | -2 | 15 | 85.71 | 70.88 | 189.719 | 219.917 | 125.660 | 50.664 | 0.258 | 0.740 | 7.980 |
| 17 | 60 | 10 | 0 | 15 | 87.26 | 64.62 | 188.277 | 217.344 | 90.412 | 40.952 | 0.257 | 0.741 | 7.984 |
| 18 | 60 | 10 | 2 | 15 | 71.26 | 72.7 | 180.243 | 207.004 | 71.648 | 36.544 | 0.255 | 0.744 | 7.981 |
| 19 | 60 | 6 | -2 | 20 | 114.9 | 61.63 | 300.65 | 327.705 | 60.230 | 29.549 | 0.234 | 0.773 | 8.004 |
| 20 | 60 | 6 | 0 | 20 | 112.3 | 56.52 | 292.204 | 318.102 | 59.890 | 27.650 | 0.233 | 0.775 | 8.019 |
| 21 | 60 | 6 | 2 | 20 | 105.1 | 66.04 | 287.672 | 313.309 | 56.916 | 21.646 | 0.230 | 0.779 | 8.016 |
| 22 | 60 | 8 | -2 | 20 | 115.5 | 59.9 | 294.676 | 322.121 | 91.554 | 37.622 | 0.229 | 0.781 | 8.031 |
| 23 | 60 | 8 | 0 | 20 | 107.7 | 52.75 | 291.689 | 315.380 | 83.987 | 38.605 | 0.228 | 0.782 | 8.006 |
| 24 | 60 | 8 | 2 | 20 | 114.3 | 41.44 | 276.239 | 301.811 | 70.654 | 32.627 | 0.227 | 0.783 | 7.989 |
| 25 | 60 | 10 | -2 | 20 | 123.6 | 42.24 | 300.238 | 327.420 | 161.550 | 72.460 | 0.226 | 0.786 | 7.998 |
| 26 | 60 | 10 | 0 | 20 | 130.1 | 41.32 | 293.749 | 323.916 | 121.478 | 50.009 | 0.226 | 0.786 | 7.960 |
| 27 | 60 | 10 | 2 | 20 | 126.9 | 33.73 | 275.93 | 305.579 | 101.889 | 47.992 | 0.210 | 0.810 | 8.000 |

**Table 6.15.** The measurement results for the forged CW617N with 45° of plunging angle

| Run | PA, (°) | RRA, (°) | ARA, (°) | CER, (μm) | Fx, (N) | Fy, (N) | Fz, (N) | FR, (N) | BHEN, (μm) | BHEX, (μm) | Ra bottom, (μm) | Ra Wall, (μm) | Diameter, (mm) |
|---|---|---|---|---|---|---|---|---|---|---|---|---|---|
| 1 | 45 | 6 | -2 | 10 | 62.93 | 105.6 | 152.12 | 195.581 | 18.061 | 7.591 | 0.313 | 0.657 | 7.976 |
| 2 | 45 | 6 | 0 | 10 | 35.41 | 121.3 | 146.97 | 193.824 | 17.146 | 7.260 | 0.305 | 0.668 | 7.997 |

| | | | | | | | | | | | | | |
|---|---|---|---|---|---|---|---|---|---|---|---|---|---|
| 3 | 45 | 6 | 2 | 10 | 62.11 | 106.7 | 141.82 | 188.030 | 16.243 | 6.794 | 0.303 | 0.671 | 8.030 |
| 4 | 45 | 8 | -2 | 10 | 52.33 | 113.8 | 168.806 | 210.200 | 27.491 | 11.503 | 0.300 | 0.675 | 8.044 |
| 5 | 45 | 8 | 0 | 10 | 56.16 | 110.5 | 152.017 | 196.146 | 25.253 | 10.687 | 0.296 | 0.680 | 7.988 |
| 6 | 45 | 8 | 2 | 10 | 36.97 | 116.4 | 151.708 | 194.759 | 21.187 | 8.933 | 0.294 | 0.683 | 8.013 |
| 7 | 45 | 10 | -2 | 10 | 61.73 | 105.8 | 145.734 | 190.375 | 49.762 | 17.777 | 0.293 | 0.685 | 8.007 |
| 8 | 45 | 10 | 0 | 10 | 74.56 | 99.74 | 136.67 | 184.894 | 36.849 | 15.562 | 0.292 | 0.686 | 8.007 |
| 9 | 45 | 10 | 2 | 10 | 49.94 | 97 | 126.679 | 167.184 | 29.919 | 12.462 | 0.281 | 0.702 | 7.986 |
| 10 | 45 | 6 | -2 | 15 | 78.83 | 106.7 | 214.847 | 252.504 | 24.205 | 11.021 | 0.276 | 0.711 | 7.974 |
| 11 | 45 | 6 | 0 | 15 | 90.36 | 93.17 | 204.444 | 242.163 | 22.917 | 9.952 | 0.274 | 0.714 | 7.978 |
| 12 | 45 | 6 | 2 | 15 | 87.76 | 87.31 | 198.47 | 233.912 | 21.680 | 9.991 | 0.272 | 0.717 | 8.005 |
| 13 | 45 | 8 | -2 | 15 | 79.14 | 111.2 | 220.306 | 259.158 | 36.199 | 15.987 | 0.270 | 0.720 | 7.999 |
| 14 | 45 | 8 | 0 | 15 | 86.55 | 88.6 | 198.573 | 234.034 | 33.232 | 14.745 | 0.270 | 0.720 | 7.992 |
| 15 | 45 | 8 | 2 | 15 | 72.75 | 88.59 | 194.762 | 225.993 | 27.984 | 13.000 | 0.267 | 0.725 | 8.003 |
| 16 | 45 | 10 | -2 | 15 | 76.93 | 88.77 | 198.573 | 230.715 | 66.897 | 22.651 | 0.267 | 0.725 | 7.978 |
| 17 | 45 | 10 | 0 | 15 | 83.39 | 82.1 | 195.586 | 227.921 | 49.344 | 20.471 | 0.266 | 0.726 | 7.976 |
| 18 | 45 | 10 | 2 | 15 | 98.03 | 78.19 | 192.393 | 229.648 | 40.303 | 17.961 | 0.265 | 0.729 | 7.978 |
| 19 | 45 | 6 | -2 | 20 | 128.3 | 88.43 | 316.302 | 352.601 | 34.848 | 15.418 | 0.250 | 0.755 | 8.030 |
| 20 | 45 | 6 | 0 | 20 | 127.8 | 92.4 | 311.461 | 349.111 | 33.608 | 13.420 | 0.249 | 0.755 | 8.035 |
| 21 | 45 | 6 | 2 | 20 | 121.3 | 95.72 | 307.65 | 344.273 | 31.746 | 13.102 | 0.247 | 0.759 | 8.032 |
| 22 | 45 | 8 | -2 | 20 | 121.87 | 96.54 | 314.654 | 350.969 | 49.019 | 18.412 | 0.246 | 0.761 | 8.044 |
| 23 | 45 | 8 | 0 | 20 | 131.9 | 87.84 | 277.574 | 319.626 | 45.644 | 17.622 | 0.246 | 0.762 | 8.046 |
| 24 | 45 | 8 | 2 | 20 | 115.7 | 75.77 | 254.605 | 289.743 | 39.139 | 16.177 | 0.245 | 0.763 | 8.019 |
| 25 | 45 | 10 | -2 | 20 | 128.2 | 75.46 | 325.881 | 358.228 | 85.026 | 35.110 | 0.244 | 0.765 | 8.020 |
| 26 | 45 | 10 | 0 | 20 | 138.1 | 73.24 | 324.748 | 360.412 | 64.511 | 23.256 | 0.244 | 0.765 | 7.975 |
| 27 | 45 | 10 | 2 | 20 | 135.1 | 76.62 | 305.796 | 342.977 | 53.365 | 25.125 | 0.233 | 0.785 | 8.016 |

**Table 6.16.** The measurement results for the forged CW511L with 90° of plunging angle

| Run | PA, (°) | RRA, (°) | ARA, (°) | CER, (μm) | Fx, (N) | Fy, (N) | Fz, (N) | FR, (N) | BHEN, (μm) | BHEX, (μm) | Ra bottom, (μm) | Ra Wall, (μm) | Diameter, (mm) |
|---|---|---|---|---|---|---|---|---|---|---|---|---|---|
| 1 | 90 | 6 | -2 | 10 | 8.927 | 1.293 | 410.184 | 410.283 | 378.480 | 142.651 | 0.908 | 1.236 | 8.498 |
| 2 | 90 | 6 | 0 | 10 | 3.696 | 9.522 | 396.036 | 396.168 | 339.420 | 130.942 | 0.905 | 1.234 | 8.196 |
| 3 | 90 | 6 | 2 | 10 | 11.26 | 1.946 | 387.936 | 388.104 | 281.220 | 110.323 | 0.895 | 1.225 | 8.397 |
| 4 | 90 | 8 | -2 | 10 | 3.262 | 6.74 | 465.48 | 465.540 | 411.180 | 153.536 | 0.891 | 1.222 | 8.373 |
| 5 | 90 | 8 | 0 | 10 | 3.931 | 1.892 | 453.6 | 453.621 | 387.840 | 125.159 | 0.884 | 1.216 | 8.164 |
| 6 | 90 | 8 | 2 | 10 | 1.96 | 1.972 | 443.556 | 443.565 | 381.950 | 142.896 | 0.883 | 1.215 | 8.659 |
| 7 | 90 | 10 | -2 | 10 | 2.201 | 10.87 | 435.564 | 435.705 | 514.600 | 140.650 | 0.872 | 1.206 | 8.326 |
| 8 | 90 | 10 | 0 | 10 | 1.897 | 5.816 | 417.42 | 417.465 | 493.898 | 138.549 | 0.871 | 1.206 | 8.492 |
| 9 | 90 | 10 | 2 | 10 | 7.975 | 4.389 | 391.5 | 391.606 | 421.940 | 143.954 | 0.869 | 1.204 | 8.665 |
| 10 | 90 | 6 | -2 | 15 | 11.01 | 3.152 | 535.032 | 535.155 | 390.500 | 142.660 | 0.856 | 1.193 | 8.998 |
| 11 | 90 | 6 | 0 | 15 | 3.928 | 3.303 | 512.244 | 512.270 | 392.642 | 146.651 | 0.828 | 1.171 | 8.863 |
| 12 | 90 | 6 | 2 | 15 | 1.093 | 11.55 | 473.364 | 473.506 | 295.654 | 111.920 | 0.823 | 1.166 | 8.836 |
| 13 | 90 | 8 | -2 | 15 | 5.626 | 1.041 | 550.584 | 550.614 | 423.441 | 159.567 | 0.823 | 1.166 | 8.910 |

| | | | | | | | | | | | | | |
|---|---|---|---|---|---|---|---|---|---|---|---|---|---|
| 14 | 90 | 8 | 0 | 15 | 5.095 | 7.159 | 467.748 | 467.831 | 401.065 | 146.942 | 0.813 | 1.159 | 8.905 |
| 15 | 90 | 8 | 2 | 15 | 2.122 | 4.282 | 491.94 | 491.963 | 395.452 | 148.956 | 0.809 | 1.155 | 8.244 |
| 16 | 90 | 10 | -2 | 15 | 7.887 | 1.256 | 488.268 | 488.333 | 360.948 | 197.269 | 0.804 | 1.152 | 8.064 |
| 17 | 90 | 10 | 0 | 15 | 0.446 | 9.311 | 486.216 | 486.305 | 509.580 | 188.651 | 0.803 | 1.151 | 8.297 |
| 18 | 90 | 10 | 2 | 15 | 0.074 | 5.077 | 451.548 | 451.577 | 256.970 | 162.354 | 0.795 | 1.145 | 8.142 |
| 19 | 90 | 6 | -2 | 20 | 12.03 | 4.293 | 507.6 | 507.761 | 489.250 | 182.354 | 0.782 | 1.135 | 8.194 |
| 20 | 90 | 6 | 0 | 20 | 0.587 | 9.503 | 485.676 | 485.769 | 440.365 | 165.548 | 0.782 | 1.135 | 8.178 |
| 21 | 90 | 6 | 2 | 20 | 3.931 | 6.791 | 455.868 | 455.936 | 365.455 | 134.950 | 0.777 | 1.131 | 8.189 |
| 22 | 90 | 8 | -2 | 20 | 13.44 | 3.048 | 571.86 | 572.026 | 528.456 | 197.845 | 0.759 | 1.118 | 8.146 |
| 23 | 90 | 8 | 0 | 20 | 1.913 | 3.776 | 542.268 | 542.285 | 500.003 | 186.125 | 0.759 | 1.118 | 7.985 |
| 24 | 90 | 8 | 2 | 20 | 10.7 | 8.741 | 520.02 | 520.204 | 490.600 | 184.640 | 0.758 | 1.116 | 8.635 |
| 25 | 90 | 10 | -2 | 20 | 5.816 | 1.974 | 545.184 | 545.219 | 229.340 | 194.659 | 0.754 | 1.114 | 7.949 |
| 26 | 90 | 10 | 0 | 20 | 12.38 | 2.133 | 505.224 | 505.380 | 583.600 | 216.590 | 0.744 | 1.106 | 8.868 |
| 27 | 90 | 10 | 2 | 20 | 6.146 | 6.751 | 475.632 | 475.720 | 230.684 | 197.446 | 0.741 | 1.104 | 7.954 |

**Table 6.17.** The measurement results for the forged CW511L with 60° of plunging angle

| Run | PA, (°) | RRA, (°) | ARA, (°) | CER, (µm) | Fx, (N) | Fy, (N) | Fz, (N) | FR, (N) | BHEN, (µm) | BHEX, (µm) | Ra bottom, (µm) | Ra Wall, (µm) | Diameter, (mm) |
|---|---|---|---|---|---|---|---|---|---|---|---|---|---|
| 1 | 60 | 6 | -2 | 10 | 33.6 | 130.6 | 280.405 | 311.147 | 216.744 | 112.661 | 0.708 | 0.967 | 8.008 |
| 2 | 60 | 6 | 0 | 10 | 6.7771 | 42.35 | 271.771 | 275.134 | 195.652 | 102.657 | 0.706 | 0.968 | 8.023 |
| 3 | 60 | 6 | 2 | 10 | 35.48 | 91.88 | 269.482 | 286.917 | 164.224 | 89.156 | 0.698 | 0.971 | 8.057 |
| 4 | 60 | 8 | -2 | 10 | 59.35 | 142.2 | 281.862 | 321.231 | 234.402 | 120.654 | 0.695 | 0.972 | 8.057 |
| 5 | 60 | 8 | 0 | 10 | 49.87 | 154.1 | 271.355 | 316.018 | 221.799 | 100.607 | 0.690 | 0.975 | 8.038 |
| 6 | 60 | 8 | 2 | 10 | 6.044 | 71.77 | 269.586 | 279.041 | 218.618 | 111.261 | 0.689 | 0.975 | 8.052 |
| 7 | 60 | 10 | -2 | 10 | 47.42 | 156.2 | 275.620 | 320.333 | 290.249 | 109.456 | 0.681 | 0.979 | 8.011 |
| 8 | 60 | 10 | 0 | 10 | 55.4 | 165.2 | 271.459 | 322.568 | 279.070 | 108.793 | 0.680 | 0.979 | 8.001 |
| 9 | 60 | 10 | 2 | 10 | 29.68 | 90.01 | 263.968 | 280.468 | 240.213 | 112.659 | 0.679 | 0.980 | 7.998 |
| 10 | 60 | 6 | -2 | 15 | 123 | 94 | 366.188 | 397.566 | 223.235 | 110.367 | 0.668 | 0.985 | 7.970 |
| 11 | 60 | 6 | 0 | 15 | 110.8 | 107.5 | 358.064 | 389.926 | 224.392 | 115.551 | 0.646 | 0.996 | 7.985 |
| 12 | 60 | 6 | 2 | 15 | 101.1 | 102.8 | 331.515 | 361.513 | 172.018 | 90.626 | 0.642 | 0.998 | 8.007 |
| 13 | 60 | 8 | -2 | 15 | 101.8 | 121.3 | 362.870 | 395.918 | 241.023 | 136.542 | 0.642 | 0.998 | 8.007 |
| 14 | 60 | 8 | 0 | 15 | 98.67 | 110.5 | 347.765 | 378.003 | 228.940 | 115.330 | 0.635 | 1.002 | 7.986 |
| 15 | 60 | 8 | 2 | 15 | 114.4 | 100.1 | 342.73 | 374.928 | 225.909 | 117.980 | 0.632 | 1.004 | 8.005 |
| 16 | 60 | 10 | -2 | 15 | 106.9 | 111.1 | 344.446 | 377.378 | 189.077 | 159.664 | 0.628 | 1.006 | 7.971 |
| 17 | 60 | 10 | 0 | 15 | 112.3 | 102.4 | 330.142 | 363.443 | 287.538 | 150.485 | 0.627 | 1.006 | 7.979 |
| 18 | 60 | 10 | 2 | 15 | 120.1 | 106.9 | 320.873 | 358.902 | 148.329 | 126.545 | 0.621 | 1.010 | 7.975 |
| 19 | 60 | 6 | -2 | 20 | 129.7 | 81.41 | 500.533 | 523.434 | 276.560 | 142.365 | 0.611 | 1.016 | 7.981 |
| 20 | 60 | 6 | 0 | 20 | 124.2 | 62.09 | 489.662 | 508.969 | 250.162 | 125.216 | 0.611 | 1.016 | 8.008 |
| 21 | 60 | 6 | 2 | 20 | 123.6 | 66.97 | 476.502 | 496.806 | 209.711 | 104.000 | 0.607 | 1.018 | 8.039 |

| | | | | | | | | | | | | | |
|---|---|---|---|---|---|---|---|---|---|---|---|---|---|
| 22 | 60 | 8 | -2 | 20 | 140.4 | 59.27 | 495.383 | 518.295 | 297.731 | 150.645 | 0.593 | 1.027 | 8.018 |
| 23 | 60 | 8 | 0 | 20 | 135.2 | 57.9 | 488.632 | 510.287 | 282.367 | 144.980 | 0.593 | 1.027 | 8.011 |
| 24 | 60 | 8 | 2 | 20 | 130.2 | 65.24 | 452.356 | 475.221 | 157.289 | 142.357 | 0.592 | 1.028 | 7.981 |
| 25 | 60 | 10 | -2 | 20 | 145.1 | 81.38 | 499.846 | 526.804 | 138.209 | 150.017 | 0.589 | 1.030 | 7.963 |
| 26 | 60 | 10 | 0 | 20 | 143.6 | 50.82 | 495.841 | 518.712 | 327.509 | 163.268 | 0.581 | 1.035 | 7.980 |
| 27 | 60 | 10 | 2 | 20 | 148.2 | 44.78 | 480.621 | 504.941 | 98.934 | 152.147 | 0.579 | 1.036 | 7.987 |

**Table 6.18.** The measurement results for the forged CW511L with 45° of plunging angle

| Run | PA, (°) | RRA, (°) | ARA, (°) | CER, (μm) | Fx, (N) | Fy, (N) | Fz, (N) | FR, (N) | BHEN, (μm) | BHEX, (μm) | Ra bottom, (μm) | Ra Wall, (μm) | Diameter, (mm) |
|---|---|---|---|---|---|---|---|---|---|---|---|---|---|
| 1 | 45 | 6 | -2 | 10 | 71.24 | 189.8 | 266.565 | 334.897 | 121.745 | 78.434 | 0.682 | 0.872 | 8.039 |
| 2 | 45 | 6 | 0 | 10 | 28.33 | 107.1 | 249.673 | 273.148 | 109.245 | 72.100 | 0.680 | 0.874 | 8.034 |
| 3 | 45 | 6 | 2 | 10 | 56.13 | 180.2 | 224.438 | 293.249 | 90.621 | 60.945 | 0.672 | 0.878 | 8.065 |
| 4 | 45 | 8 | -2 | 10 | 78.84 | 172.7 | 258.737 | 320.914 | 132.209 | 84.323 | 0.670 | 0.880 | 8.052 |
| 5 | 45 | 8 | 0 | 10 | 93.21 | 178.5 | 236.283 | 310.451 | 124.740 | 68.971 | 0.665 | 0.883 | 8.050 |
| 6 | 45 | 8 | 2 | 10 | 59.85 | 157.6 | 219.391 | 276.681 | 122.855 | 78.567 | 0.664 | 0.884 | 8.061 |
| 7 | 45 | 10 | -2 | 10 | 84.68 | 178.3 | 241.536 | 311.931 | 165.303 | 77.352 | 0.656 | 0.889 | 8.023 |
| 8 | 45 | 10 | 0 | 10 | 110 | 183 | 226.807 | 311.497 | 158.678 | 76.215 | 0.655 | 0.889 | 8.031 |
| 9 | 45 | 10 | 2 | 10 | 66.78 | 173.2 | 217.434 | 285.894 | 135.652 | 79.139 | 0.654 | 0.890 | 7.997 |
| 10 | 45 | 6 | -2 | 15 | 137.7 | 119 | 278.204 | 332.445 | 125.591 | 78.439 | 0.644 | 0.897 | 7.972 |
| 11 | 45 | 6 | 0 | 15 | 151 | 126.4 | 271.303 | 335.236 | 126.276 | 80.598 | 0.624 | 0.911 | 7.979 |
| 12 | 45 | 6 | 2 | 15 | 125.6 | 124.7 | 264.196 | 318.002 | 95.240 | 61.809 | 0.620 | 0.914 | 8.012 |
| 13 | 45 | 8 | -2 | 15 | 126.7 | 148.4 | 284.59 | 345.061 | 136.132 | 87.586 | 0.620 | 0.914 | 8.018 |
| 14 | 45 | 8 | 0 | 15 | 127.2 | 128.8 | 279.852 | 333.296 | 128.972 | 80.756 | 0.613 | 0.919 | 8.000 |
| 15 | 45 | 8 | 2 | 15 | 116 | 135.7 | 261.621 | 316.727 | 127.176 | 81.845 | 0.610 | 0.921 | 8.008 |
| 16 | 45 | 10 | -2 | 15 | 133.6 | 131.5 | 285.62 | 341.643 | 120.534 | 107.983 | 0.607 | 0.924 | 7.971 |
| 17 | 45 | 10 | 0 | 15 | 139.2 | 122 | 272.745 | 329.622 | 163.697 | 103.320 | 0.606 | 0.925 | 7.970 |
| 18 | 45 | 10 | 2 | 15 | 151.8 | 117.6 | 270.685 | 331.879 | 130.461 | 89.094 | 0.600 | 0.929 | 7.975 |
| 19 | 45 | 6 | -2 | 20 | 175.6 | 112.9 | 561.5397 | 599.090 | 157.191 | 99.914 | 0.591 | 0.937 | 8.001 |
| 20 | 45 | 6 | 0 | 20 | 157.2 | 95.004 | 557.624 | 587.096 | 141.548 | 90.821 | 0.591 | 0.937 | 8.015 |
| 21 | 45 | 6 | 2 | 20 | 174.3 | 96.69 | 553.4184 | 588.219 | 117.577 | 74.268 | 0.587 | 0.940 | 8.028 |
| 22 | 45 | 8 | -2 | 20 | 171.1 | 89.8 | 579.6677 | 611.027 | 169.737 | 108.294 | 0.574 | 0.950 | 8.022 |
| 23 | 45 | 8 | 0 | 20 | 152.8 | 100.1 | 556.7539 | 585.955 | 160.632 | 101.954 | 0.574 | 0.950 | 8.020 |
| 24 | 45 | 8 | 2 | 20 | 147.4 | 104.8 | 529.3444 | 559.388 | 157.623 | 101.150 | 0.573 | 0.952 | 7.991 |
| 25 | 45 | 10 | -2 | 20 | 163 | 121 | 606.7872 | 639.844 | 70.020 | 106.571 | 0.571 | 0.954 | 7.984 |
| 26 | 45 | 10 | 0 | 20 | 184.6 | 79.19 | 581.9881 | 615.677 | 187.383 | 118.435 | 0.563 | 0.960 | 7.987 |
| 27 | 45 | 10 | 2 | 20 | 178.6 | 79.4 | 562.6999 | 595.679 | 70.450 | 108.078 | 0.561 | 0.962 | 7.999 |

**Table 6.19.** The measurement results for the forged CW724R with 90° of plunging angle

| Run | PA, (°) | RRA, (°) | ARA, (°) | CER, (μm) | Fx, (N) | Fy, (N) | Fz, (N) | FR, (N) | BHEN, (μm) | BHEX, (μm) | Ra bottom, | Ra Wall, | Diameter, (mm) |
|---|---|---|---|---|---|---|---|---|---|---|---|---|---|

| | | | | | | | | | | | (µm) | (µm) | |
|---|---|---|---|---|---|---|---|---|---|---|---|---|---|
| 1 | 90 | 6 | -2 | 10 | 14.69 | 4.392 | 355.364 | 355.695 | 30.569 | 14.032 | 0.422 | 0.742 | 7.956 |
| 2 | 90 | 6 | 0 | 10 | 3.997 | 0.2506 | 348.128 | 348.151 | 30.445 | 13.900 | 0.420 | 0.743 | 7.967 |
| 3 | 90 | 6 | 2 | 10 | 10.34 | 0.2202 | 291.104 | 291.288 | 29.876 | 12.956 | 0.411 | 0.753 | 7.986 |
| 4 | 90 | 8 | -2 | 10 | 2.073 | 6.771 | 366.38 | 366.448 | 46.005 | 18.236 | 0.409 | 0.754 | 7.964 |
| 5 | 90 | 8 | 0 | 10 | 5.485 | 1.299 | 353.744 | 353.789 | 36.899 | 15.445 | 0.409 | 0.754 | 7.946 |
| 6 | 90 | 8 | 2 | 10 | 7.482 | 8.055 | 306.872 | 307.069 | 33.597 | 17.651 | 0.406 | 0.757 | 7.965 |
| 7 | 90 | 10 | -2 | 10 | 11.03 | 8.321 | 344.888 | 345.165 | 85.595 | 32.658 | 0.404 | 0.759 | 7.954 |
| 8 | 90 | 10 | 0 | 10 | 9.123 | 8.195 | 333.224 | 333.450 | 62.648 | 25.698 | 0.404 | 0.759 | 7.962 |
| 9 | 90 | 10 | 2 | 10 | 10.57 | 7.656 | 320.48 | 320.746 | 58.952 | 24.991 | 0.403 | 0.760 | 7.948 |
| 10 | 90 | 6 | -2 | 15 | 4.811 | 10.09 | 454.4 | 454.537 | 53.528 | 22.054 | 0.400 | 0.763 | 7.956 |
| 11 | 90 | 6 | 0 | 15 | 10.41 | 0.1006 | 424.268 | 424.396 | 53.651 | 22.146 | 0.398 | 0.766 | 7.963 |
| 12 | 90 | 6 | 2 | 15 | 9.287 | 8.123 | 414.656 | 414.840 | 51.335 | 22.652 | 0.397 | 0.767 | 7.989 |
| 13 | 90 | 8 | -2 | 15 | 0.718 | 4.935 | 441.98 | 442.008 | 80.079 | 33.658 | 0.391 | 0.773 | 7.985 |
| 14 | 90 | 8 | 0 | 15 | 6.925 | 1.422 | 437.552 | 437.609 | 63.595 | 26.746 | 0.389 | 0.775 | 7.980 |
| 15 | 90 | 8 | 2 | 15 | 7.947 | 0.3962 | 409.688 | 409.765 | 57.737 | 24.962 | 0.388 | 0.776 | 7.988 |
| 16 | 90 | 10 | -2 | 15 | 2.5 | 6.27 | 415.844 | 415.899 | 148.021 | 58.621 | 0.387 | 0.778 | 7.956 |
| 17 | 90 | 10 | 0 | 15 | 7.209 | 0.9141 | 400.292 | 400.358 | 108.795 | 44.169 | 0.382 | 0.783 | 7.958 |
| 18 | 90 | 10 | 2 | 15 | 7.873 | 0.2895 | 398.888 | 398.966 | 102.356 | 41.652 | 0.379 | 0.787 | 7.954 |
| 19 | 90 | 6 | -2 | 20 | 2.129 | 5.188 | 495.656 | 495.688 | 69.521 | 29.666 | 0.352 | 0.818 | 7.945 |
| 20 | 90 | 6 | 0 | 20 | 8.475 | 5.644 | 484.964 | 485.071 | 69.788 | 30.256 | 0.348 | 0.823 | 7.971 |
| 21 | 90 | 6 | 2 | 20 | 13.99 | 2.912 | 474.056 | 474.271 | 66.251 | 25.698 | 0.341 | 0.833 | 7.969 |
| 22 | 90 | 8 | -2 | 20 | 5.223 | 1.459 | 497.276 | 497.306 | 104.565 | 37.652 | 0.336 | 0.839 | 7.974 |
| 23 | 90 | 8 | 0 | 20 | 5.583 | 11.54 | 478.268 | 478.440 | 82.740 | 31.990 | 0.333 | 0.842 | 7.969 |
| 24 | 90 | 8 | 2 | 20 | 0.6445 | 6.973 | 440.684 | 440.740 | 75.016 | 31.652 | 0.322 | 0.858 | 7.943 |
| 25 | 90 | 10 | -2 | 20 | 9.429 | 11.28 | 493.604 | 493.823 | 192.590 | 78.623 | 0.312 | 0.873 | 7.944 |
| 26 | 90 | 10 | 0 | 20 | 7.499 | 0.4164 | 476.972 | 477.031 | 142.900 | 48.662 | 0.304 | 0.885 | 7.938 |
| 27 | 90 | 10 | 2 | 20 | 14.78 | 3.287 | 475.892 | 476.133 | 133.156 | 43.326 | 0.279 | 0.925 | 7.943 |

**Table 6.20.** The measurement results for the forged CW724R with 60° of plunging angle

| Run | PA, (°) | RRA, (°) | ARA, (°) | CER, (µm) | Fx, (N) | Fy, (N) | Fz, (N) | FR, (N) | BHEN, (µm) | BHEX, (µm) | Ra bottom, (µm) | Ra Wall, (µm) | Diameter, (mm) |
|---|---|---|---|---|---|---|---|---|---|---|---|---|---|
| 1 | 60 | 6 | -2 | 10 | 77.97 | 109.3 | 196.908 | 238.325 | 31.497 | 14.678 | 0.310 | 0.682 | 7.985 |
| 2 | 60 | 6 | 0 | 10 | 42.86 | 124.7 | 193.268 | 233.965 | 31.441 | 13.002 | 0.309 | 0.683 | 7.985 |
| 3 | 60 | 6 | 2 | 10 | 66.95 | 114.3 | 179.644 | 223.201 | 31.185 | 12.745 | 0.302 | 0.690 | 7.983 |
| 4 | 60 | 8 | -2 | 10 | 76.66 | 101.5 | 185.988 | 225.323 | 38.443 | 15.556 | 0.301 | 0.691 | 7.990 |
| 5 | 60 | 8 | 0 | 10 | 63.37 | 109.9 | 184.012 | 223.504 | 34.346 | 15.951 | 0.301 | 0.691 | 7.964 |
| 6 | 60 | 8 | 2 | 10 | 73.72 | 105 | 176.108 | 217.885 | 32.860 | 16.205 | 0.299 | 0.693 | 7.954 |
| 7 | 60 | 10 | -2 | 10 | 64.97 | 111 | 186.612 | 226.641 | 56.259 | 24.656 | 0.297 | 0.694 | 7.982 |
| 8 | 60 | 10 | 0 | 10 | 80.97 | 105.4 | 183.18 | 226.319 | 45.933 | 21.990 | 0.297 | 0.694 | 7.985 |
| 9 | 60 | 10 | 2 | 10 | 65.02 | 102.7 | 159.572 | 200.594 | 44.269 | 22.034 | 0.297 | 0.695 | 7.982 |
| 10 | 60 | 6 | -2 | 15 | 170.6 | 39.91 | 341.78 | 384.071 | 41.829 | 19.999 | 0.295 | 0.697 | 7.987 |
| 11 | 60 | 6 | 0 | 15 | 167.8 | 32.75 | 330.652 | 372.237 | 41.884 | 19.213 | 0.293 | 0.699 | 7.991 |

| | | | | | | | | | | | | | |
|---|---|---|---|---|---|---|---|---|---|---|---|---|---|
| 12 | 60 | 6 | 2 | 15 | 153 | 53.15 | 307.356 | 347.421 | 40.842 | 20.645 | 0.293 | 0.700 | 8.012 |
| 13 | 60 | 8 | -2 | 15 | 157.3 | 46.53 | 336.268 | 374.145 | 53.777 | 28.646 | 0.288 | 0.704 | 8.007 |
| 14 | 60 | 8 | 0 | 15 | 144.5 | 36.91 | 322.124 | 354.974 | 46.359 | 24.659 | 0.287 | 0.706 | 8.031 |
| 15 | 60 | 8 | 2 | 15 | 160.8 | 24.08 | 306.42 | 346.886 | 43.723 | 22.199 | 0.286 | 0.706 | 8.030 |
| 16 | 60 | 10 | -2 | 15 | 176 | 25.72 | 324.828 | 370.339 | 84.350 | 49.991 | 0.285 | 0.707 | 7.985 |
| 17 | 60 | 10 | 0 | 15 | 168.5 | 25.91 | 301.428 | 346.298 | 66.699 | 35.595 | 0.282 | 0.711 | 7.982 |
| 18 | 60 | 10 | 2 | 15 | 159 | 25.3 | 299.244 | 339.806 | 63.801 | 36.030 | 0.280 | 0.714 | 7.956 |
| 19 | 60 | 6 | -2 | 20 | 190.3 | 22.78 | 457.012 | 495.573 | 49.025 | 25.519 | 0.262 | 0.736 | 7.999 |
| 20 | 60 | 6 | 0 | 20 | 170.1 | 27.5 | 453.268 | 484.915 | 49.146 | 27.693 | 0.259 | 0.739 | 8.012 |
| 21 | 60 | 6 | 2 | 20 | 172.7 | 26.62 | 440.06 | 473.484 | 47.554 | 22.655 | 0.254 | 0.746 | 8.017 |
| 22 | 60 | 8 | -2 | 20 | 185.4 | 22.97 | 450.148 | 487.375 | 64.795 | 31.694 | 0.250 | 0.750 | 8.014 |
| 23 | 60 | 8 | 0 | 20 | 178.5 | 25.44 | 445.676 | 480.767 | 54.974 | 28.165 | 0.249 | 0.752 | 8.020 |
| 24 | 60 | 8 | 2 | 20 | 181 | 10.33 | 425.916 | 462.895 | 51.498 | 28.656 | 0.241 | 0.763 | 7.989 |
| 25 | 60 | 10 | -2 | 20 | 199.8 | 4.295 | 454.932 | 496.892 | 104.407 | 42.664 | 0.234 | 0.773 | 7.991 |
| 26 | 60 | 10 | 0 | 20 | 212.6 | 4.134 | 440.996 | 489.585 | 82.046 | 40.959 | 0.228 | 0.781 | 7.991 |
| 27 | 60 | 10 | 2 | 20 | 191.8 | 5.513 | 437.46 | 477.691 | 77.661 | 36.261 | 0.211 | 0.809 | 7.980 |

**Table 6.21.** The measurement results for the forged CW724R with 45° of plunging angle

| Run | PA, (°) | RRA, (°) | ARA, (°) | CER, (μm) | Fx, (N) | Fy, (N) | Fz, (N) | FR, (N) | BHEN, (μm) | BHEX, (μm) | Ra bottom, (μm) | Ra Wall, (μm) | Diameter, (mm) |
|---|---|---|---|---|---|---|---|---|---|---|---|---|---|
| 1 | 45 | 6 | -2 | 10 | 100.1 | 116.7 | 193.033 | 246.781 | 20.952 | 11.596 | 0.274 | 0.714 | 7.986 |
| 2 | 45 | 6 | 0 | 10 | 65.87 | 135.1 | 181.085 | 235.335 | 20.875 | 10.998 | 0.273 | 0.715 | 7.963 |
| 3 | 45 | 6 | 2 | 10 | 88.4 | 122.5 | 173.154 | 229.789 | 20.522 | 10.554 | 0.268 | 0.724 | 7.979 |
| 4 | 45 | 8 | -2 | 10 | 94.65 | 113.6 | 193.033 | 243.157 | 30.522 | 14.236 | 0.267 | 0.726 | 7.958 |
| 5 | 45 | 8 | 0 | 10 | 81.2 | 124.7 | 187.986 | 239.755 | 24.876 | 12.006 | 0.267 | 0.726 | 7.966 |
| 6 | 45 | 8 | 2 | 10 | 78.86 | 118.3 | 184.484 | 232.912 | 22.829 | 13.113 | 0.265 | 0.729 | 7.991 |
| 7 | 45 | 10 | -2 | 10 | 102.5 | 103.8 | 189.222 | 238.926 | 55.068 | 22.642 | 0.264 | 0.730 | 7.982 |
| 8 | 45 | 10 | 0 | 10 | 109 | 104.3 | 182.012 | 236.406 | 40.841 | 19.620 | 0.264 | 0.730 | 7.975 |
| 9 | 45 | 10 | 2 | 10 | 94.46 | 93.47 | 179.437 | 223.287 | 38.549 | 17.621 | 0.263 | 0.731 | 7.985 |
| 10 | 45 | 6 | -2 | 15 | 170.9 | 102.7 | 349.799 | 402.633 | 35.186 | 16.666 | 0.261 | 0.734 | 7.972 |
| 11 | 45 | 6 | 0 | 15 | 165.6 | 91.95 | 319.62 | 371.531 | 35.263 | 16.791 | 0.260 | 0.737 | 7.975 |
| 12 | 45 | 6 | 2 | 15 | 169.5 | 97.35 | 311.689 | 367.909 | 33.827 | 18.064 | 0.260 | 0.738 | 7.982 |
| 13 | 45 | 8 | -2 | 15 | 173.2 | 105.5 | 339.293 | 395.282 | 51.648 | 22.651 | 0.256 | 0.744 | 8.018 |
| 14 | 45 | 8 | 0 | 15 | 177.4 | 87.14 | 326.418 | 381.593 | 41.428 | 19.999 | 0.255 | 0.746 | 7.992 |
| 15 | 45 | 8 | 2 | 15 | 176.5 | 78.92 | 314.779 | 369.414 | 37.796 | 19.257 | 0.254 | 0.746 | 8.000 |
| 16 | 45 | 10 | -2 | 15 | 182.6 | 77.6 | 326.933 | 382.426 | 93.772 | 39.158 | 0.253 | 0.748 | 7.958 |
| 17 | 45 | 10 | 0 | 15 | 178.1 | 76.54 | 322.195 | 376.015 | 69.452 | 32.498 | 0.251 | 0.753 | 7.956 |
| 18 | 45 | 10 | 2 | 15 | 188.6 | 66.81 | 313.852 | 372.205 | 65.460 | 31.679 | 0.249 | 0.756 | 7.956 |
| 19 | 45 | 6 | -2 | 20 | 216.1 | 103.6 | 471.751 | 529.132 | 45.102 | 21.667 | 0.233 | 0.785 | 8.014 |
| 20 | 45 | 6 | 0 | 20 | 228 | 96.03 | 466.086 | 527.676 | 45.268 | 22.406 | 0.231 | 0.790 | 8.034 |
| 21 | 45 | 6 | 2 | 20 | 214.5 | 103.5 | 463.305 | 520.936 | 43.075 | 19.268 | 0.227 | 0.798 | 8.033 |
| 22 | 45 | 8 | -2 | 20 | 207.1 | 105.7 | 476.592 | 530.286 | 66.829 | 27.991 | 0.224 | 0.804 | 8.030 |
| 23 | 45 | 8 | 0 | 20 | 227.6 | 97.97 | 471.648 | 532.777 | 53.298 | 23.642 | 0.222 | 0.806 | 8.040 |

| | | | | | | | | | | | | | |
|---|---|---|---|---|---|---|---|---|---|---|---|---|---|
| 24 | 45 | 8 | 2 | 20 | 224.5 | 80.24 | 439.512 | 500.010 | 48.509 | 24.359 | 0.216 | 0.820 | 7.999 |
| 25 | 45 | 10 | -2 | 20 | 232.2 | 80.02 | 486.48 | 544.961 | 121.405 | 36.906 | 0.210 | 0.833 | 7.993 |
| 26 | 45 | 10 | 0 | 20 | 235.8 | 83.74 | 480.094 | 541.391 | 90.597 | 32.890 | 0.205 | 0.843 | 7.998 |
| 27 | 45 | 10 | 2 | 20 | 230.3 | 71.63 | 451.151 | 511.572 | 84.556 | 27.955 | 0.190 | 0.877 | 8.003 |

### 6.1. Evaluation of the cutting forces:

As experimental and analytical studies were conducted for both vertical and inclined drilling condition, the outcomes for the resultant forces have been discussed. However, the measured cutting forces in X, Y, Z directions and resultant ones for both extruded and forged+annealed specimens of the studied brass alloys in different plunging angles are demonstrated in Figure 6.6 to Figure 6.39.

Considering the extruded specimens, the highest cutting force in X direction was measured as 140.401, 179.514, 240.004, 146.924, 221.466 and 305.413 N in 60° and 45° of inclined plunging for CW617N, CW511L and CW724R, respectively. However, the lowest values for the mentioned brass alloys were 30.32, 18.745, 40.364, 32.992, 40.22, 37.345 N, respectively. Considering the forged+annealed workpieces, the highest cutting force in X direction was measured as 130.101, 148.205, 212.632, 138.109, 184.606 and 235.8 N in 60° and 45° of inclined plunging for CW617N, CW511L and CW724R, respectively. However, the lowest values for the mentioned brass alloys were 29.54, 6.044, 42.869, 3235.41, 28.331, 65.874 N, respectively.

Considering the extruded specimens, the highest cutting force in Y direction was measured as 92.061, 169.705, 131, 117.102, 197.803 and 46.43 N in 60° and 45° of inclined plunging for CW617N, CW511L and CW724R, respectively. However, the lowest values for the mentioned brass alloys were 19.124, 48.765, 0.52, 45.59, 88.127, 46.432 N, respectively. Considering the forged+annealed workpieces, the highest cutting force in Y direction was measured as 95.88, 165.238, 124.703, 121.305, 189.8 and 135.101 N in 60° and 45° of inclined plunging for CW617N, CW511L and CW724R, respectively. However, the lowest values for the mentioned brass alloys were 33.73, 42.35, 4.134, 73.241, 79.196, 66.81 N, respectively.

Considering the extruded specimens, the highest cutting force in Z direction was measured as 337.800, 495.400 and 414.091 N in vertical plunging for CW617N, CW511L

and CW724R, respectively. In 60° and 45° of inclined plunging conditions, these values were 285.200, 435.000, 346.300, 302.700, 421.600, 325.900 N for the same materials. The lowest cutting force in Z direction was measured as 201.42, 312.405 and 241.831 N in vertical plunging for CW617N, CW511L and CW724R, respectively. In 60° and 45° of inclined plunging conditions, these values were 109.89, 235.7, 158.5, 96.19, 207.1, 162.87 N for the same materials. Considering the forged+annealed specimens, the highest cutting force in Z direction was measured as 373.292, 571.860 and 497.276 N in vertical plunging for CW617N, CW511L and CW724R, respectively. In 60° and 45° of inclined plunging conditions, these values were 300.650, 500.533, 457.012, 325.881, 606.787, 486.480 N for the same materials. The lowest cutting force in Z direction was measured as 231.488, 387.936 and 291.104 N in vertical plunging for CW617N, CW511L and CW724R, respectively. In 60° and 45° of inclined plunging conditions, these values were 138.528, 263.969, 159.572, 126.679, 217.434, 173.154 N for the same materials.

Considering the extruded specimens, the highest resultant force was measured as 338.198, 495.463 and 414.568 N in vertical plunging for CW617N, CW511L and CW724R, respectively. In 60° and 45° of inclined plunging conditions, these values were 314.068, 473.053, 419.178, 337.236, 480.280, 446.810 N for the same materials. The lowest resultant force was measured as 201.683, 312.805 and 241.860 N in vertical plunging for CW617N, CW511L and CW724R, respectively. In 60° and 45° of inclined plunging conditions, these values were 140.859, 254.225, 203.397, 138.500, 252.457, 209.241 N for the same materials. Considering the forged+annealed specimens, the highest resultant force was measured as 373.446, 572.026 and 497.306 N in vertical plunging for CW617N, CW511L and CW724R, respectively. In 60° and 45° of inclined plunging conditions, these values were 327.705, 526.805, 496.892, 360.412, 639.844, 544.961 N for the same materials. The lowest resultant force was measured as 231.763, 388.104 and 291.288 N in vertical plunging for CW617N, CW511L and CW724R, respectively. In 60° and 45° of inclined plunging conditions, these values were 168.455, 275.135, 200.594, 1167.184, 273.148, 223.287 N for the same materials. It is seen that in all the cases, the highest cutting forces belongs to CW511L, while the lowest values are for CW617N. The same results were also reported by several authors [39]. It is evident that the existence of the lead element in the chemical composition of the alloys seriously reduces the cutting forces. On the other hand, low chip breakability of CW511L as

compared to the other investigated materials in this study has resulted in higher cutting forces. Furthermore, it is seen that the cutting forces in the forged+annealed specimens are higher than the extruded ones due to the increase in the β phase percentage and higher micro hardness. Coming to the geometric parameters of the designed flat bottom drill, a reduction in the cutting forces is observed with the increase in the radial and axial rake angles. Increasing the radial rake angle improves the chip distraction and its removal through the tool flute channels. Negative axial rake angle might be useful in chip breaking by applying higher moments on the chips. However, they are not popular in deep cuts due the poor chip distraction. Positive axial rake angle leads the chip toward the tool's flute channels. Increasing the cutting edge-radius intensifies the cutting forces because of the boosting contact area between cutting tool and workpiece [39, 40].

The obtained experimental measurements have been compared with the developed analytical model results for both extruded and forged+annealed specimens as demonstrated in Figure 6.6 to 6.39. Although simplifications in the cutting tool geometry have been utilized in developing of the analytical model, it is seen that it has a good level of accuracy in predicting the cutting forces in different directions. The highest model error is for CW511L material in 90° of plunging angle. But it can be said that the lack of tool ability in the cutting and chip breaking as well as chip distract has led to higher recorded experimental results. Therefore, considering that the analytical model does not include such issues, it seems that the model can give a satisfactory level of accuracy and application in industrial fields.

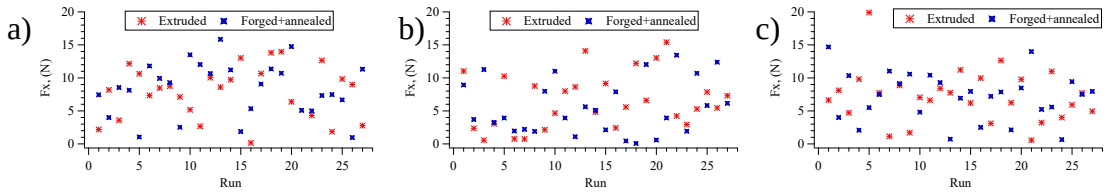


**Figure 6.6.** The measured forces in X direction (Fx) with 90° of plunging angle; a) CW617N, b) CW511L, c) CW724R

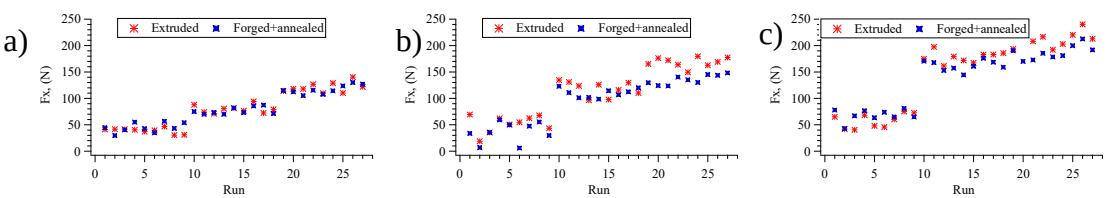

**Figure 6.7.** The measured forces in X direction (Fx) with 60° of plunging angle; a) CW617N, b) CW511L, c) CW724R

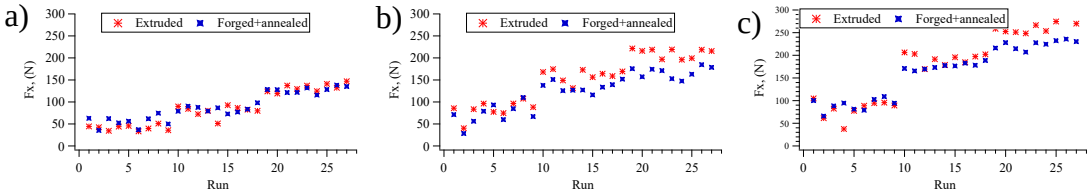


**Figure 6.8.** The measured forces in X direction (Fx) with 45° of plunging angle; a) CW617N, b) CW511L, c) CW724R

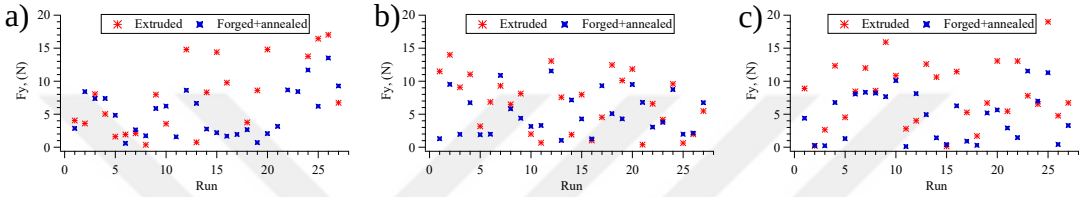


**Figure 6.9.** The measured forces in Y direction (Fy) with 90° of plunging angle; a) CW617N, b) CW511L, c) CW724R

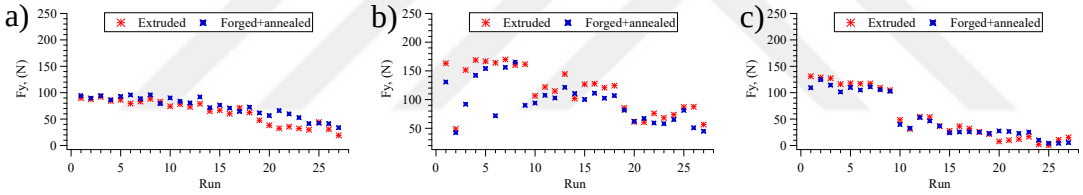


**Figure 6.10.** The measured forces in Y direction (Fy) with 60° of plunging angle; a) CW617N, b) CW511L, c) CW724R

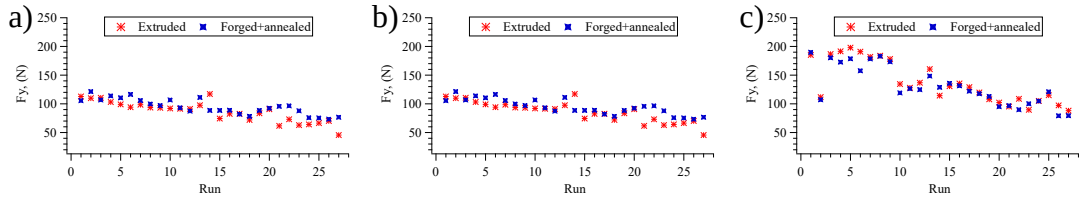


**Figure 6.11.** The measured forces in Y direction (Fy) with 45° of plunging angle; a) CW617N, b) CW511L, c) CW724R

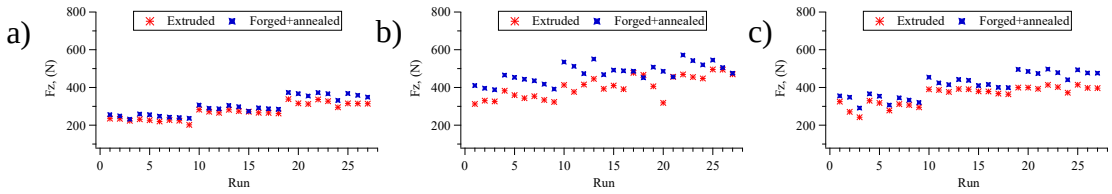

**Figure 6.12.** The measured forces in Z direction (Fz) with 90° of plunging angle; a) CW617N, b) CW511L, c) CW724R

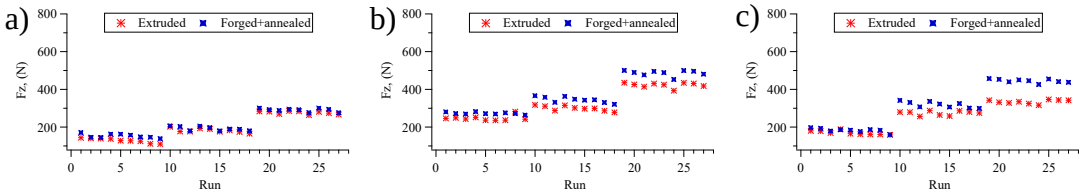


**Figure 6.13.** The measured forces in Z direction (Fz) with 60° of plunging angle; a) CW617N, b) CW511L, c) CW724R

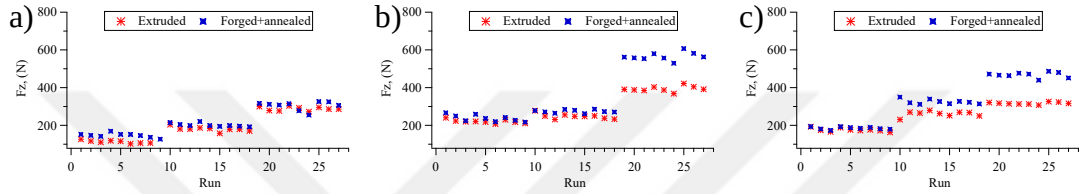


**Figure 6.14.** The measured forces in Z direction (Fz) with 45° of plunging angle; a) CW617N, b) CW511L, c) CW724R

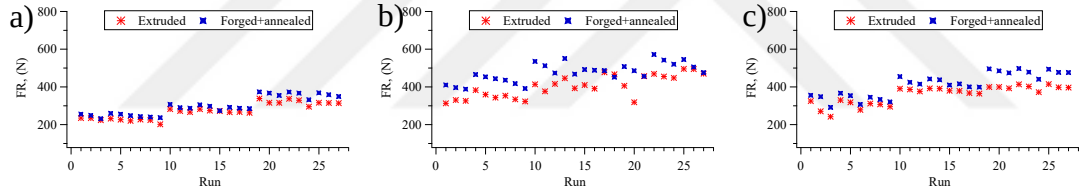


**Figure 6.15.** The measured resultant cutting forces (FR) with 90° of plunging angle; a) CW617N, b) CW511L, c) CW724R

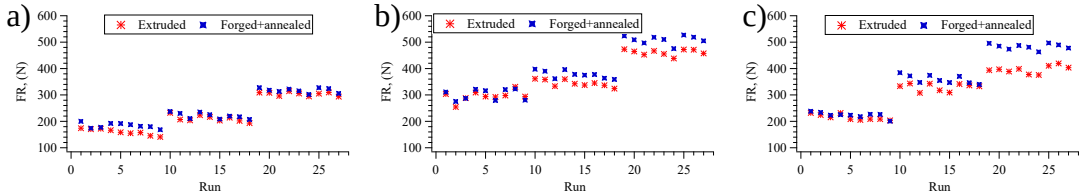


**Figure 6.16.** The measured resultant cutting forces (FR) with 60° of plunging angle; a) CW617N, b) CW511L, c) CW724R

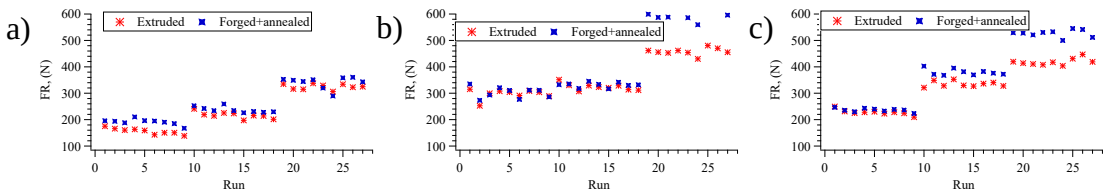

**Figure 6.17.** The measured resultant cutting forces (FR) with 45° of plunging angle; a) CW617N, b) CW511L, c) CW724R

### 6.1.1. Determination of the cutting force coefficients

In order to determine the cutting force coefficients, oblique cutting experiments have been carried out by turning tests using CNMG-120408 carbide insert on Doosan Puma GT2100 CNC turn machine with 18 kW power and maximum spindle speed of 4500 rpm as shown in Figure 6.17. Various feeds of 0.10, 0.15, 0.20, 0.25, 0.30 mm/rev and cutting speeds 200, 225, 250, 275, 300 m/min have been used during the experiments. The same experiments have been performed with flat bottom drill for all the materials. Parameters such chip ratio, friction and shear angle have been measured/calculated by Equations 6.1- and deployed in the developed mechanistic model. Thereafter, the cutting coefficients were calculated by Equations 6.4-6.

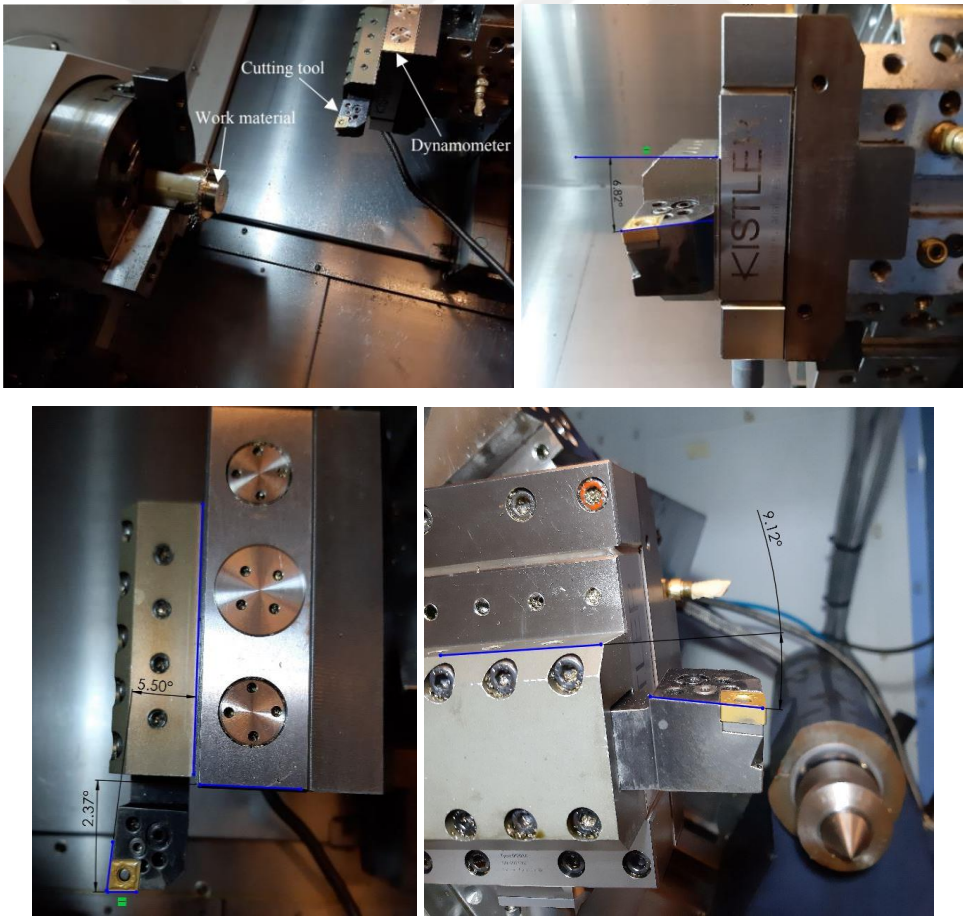


**Figure 6.18.** Oblique cutting tests setup

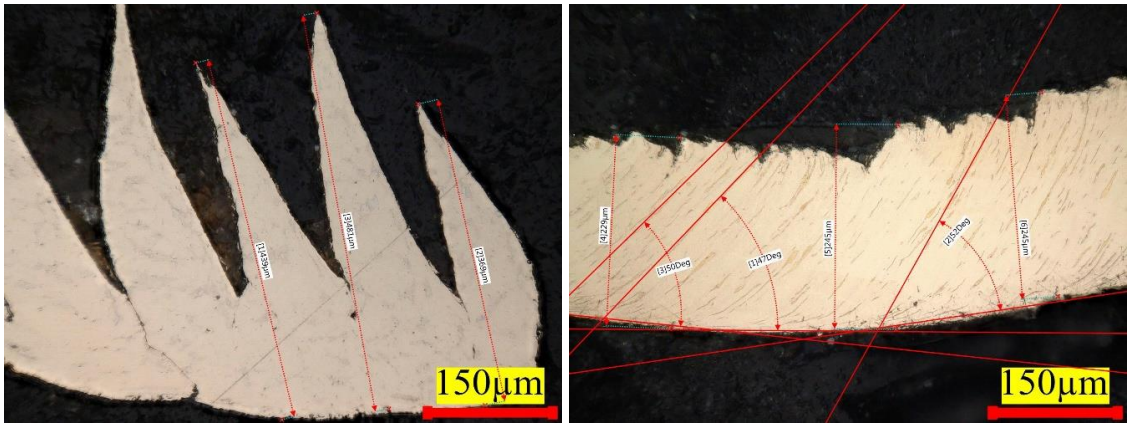


**Figure 6.19.** The generated chips; a) CW724R; $f_t$= 0.2, $V_c$=250, b) CW511L; $f_t$ =0.25, $V_c$ =250

$$r_c = \frac{h}{h_c} \tag{6.1}$$

$$\beta_a = \alpha_r + \tan^{-1}(\frac{F_f}{F_t}) \tag{6.2}$$

$$\phi_c = \frac{\pi}{4} - \frac{\beta_a - \alpha_r}{2} \tag{6.3}$$

$$K_f(h) = \alpha_f . h^{p_f} + \beta_f . h^{q_f} \tag{6.4}$$

$$K_r(h) = \alpha_r . h^{p_f} + \beta_r . h^{q_f} \tag{6.5}$$

$$K_t(h) = \alpha_t . h^{p_f} + \beta_t . h^{q_f} \tag{6.6}$$

**Table 6.22.** The specific cutting forces in flat bottom drilling

| | Parameter | **α** | **p** | **β** | **q** |
|---|---|---|---|---|---|
| CW617N | $K_f$ | 226.16 | -0.006 | 39.11 | 0.5701 |
| | $K_r$ | 3.353 | 0.4176 | 1.68 | -0.5304 |
| | $K_t$ | 10.523 | 0.1517 | -1.93 | 0.020 |
| CW511L | $K_f$ | 465.89 | -0.012 | 80.567 | 1.174 |
| | $K_r$ | 6.907 | 0.86 | 3.461 | -1.093 |

| | | | | | |
|---|---|---|---|---|---|
| | $K_t$ | 21.677 | 0.313 | -3.976 | 0.041 |
| | $K_f$ | 357.333 | -0.009 | 61.794 | 0.901 |
| CW724R | $K_r$ | 5.298 | 0.66 | 2.654 | -0.838 |
| | $K_t$ | 16.626 | 0.24 | -3.049 | 0.032 |

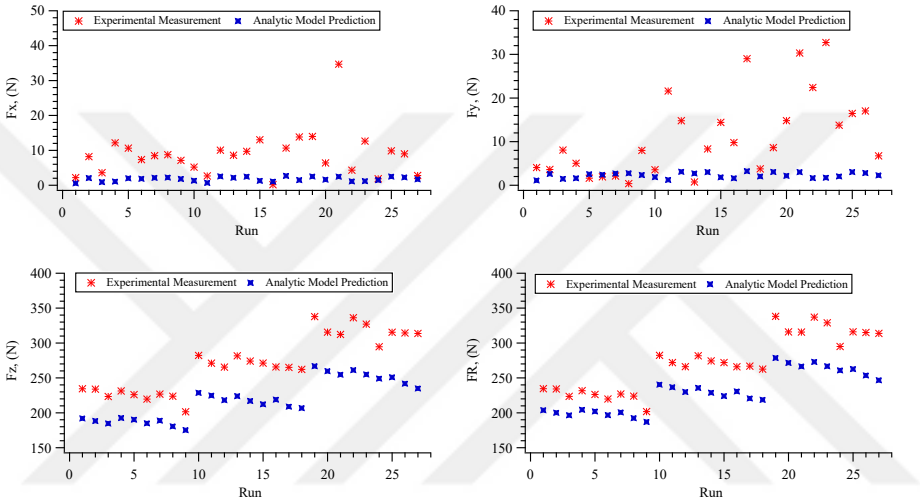


**Figure 6.20.** Comparison between experimental measurements and analytical model prediction for cutting forces of extruded CW617N with 90° of plunging angle

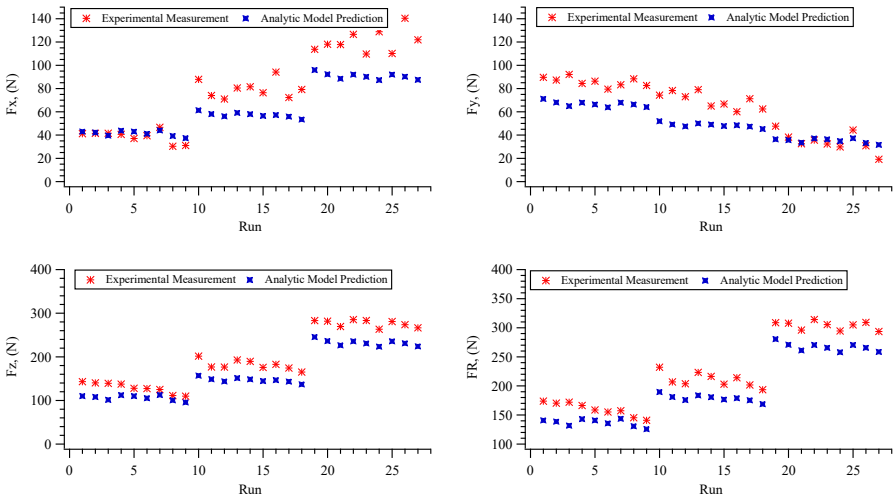


**Figure 6.21.** Comparison between experimental measurements and analytical model prediction for cutting forces of extruded CW617N with 60° of plunging angle

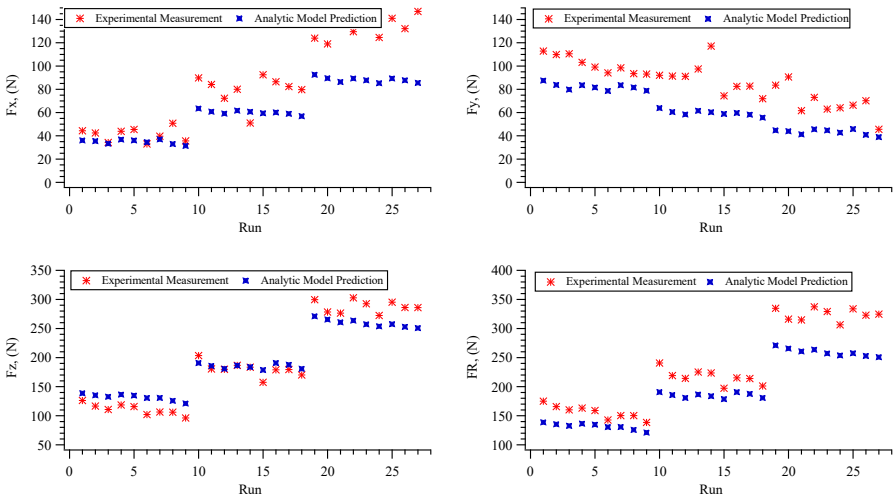


**Figure 6.22.** Comparison between experimental measurements and analytical model prediction for cutting forces of extruded CW617N with 45° of plunging angle

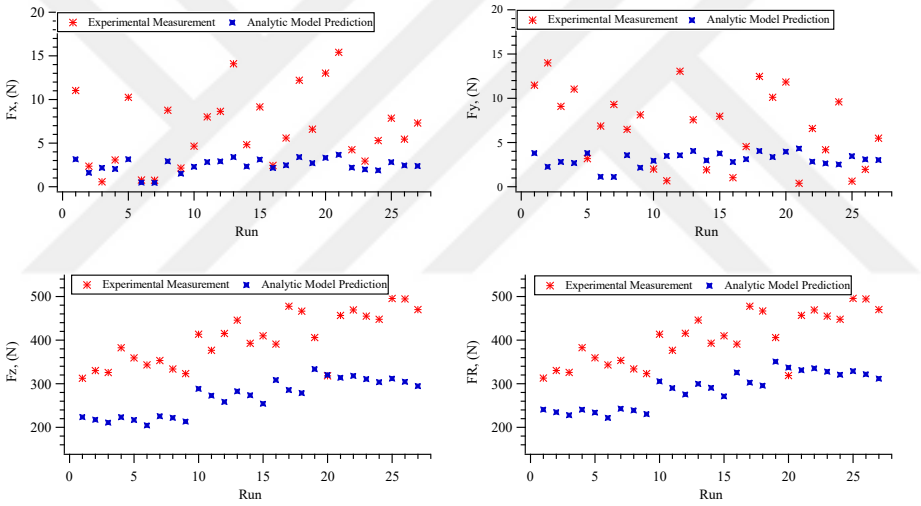


**Figure 6.23.** Comparison between experimental measurements and analytical model prediction for cutting forces of extruded CW511L with 90° of plunging angle

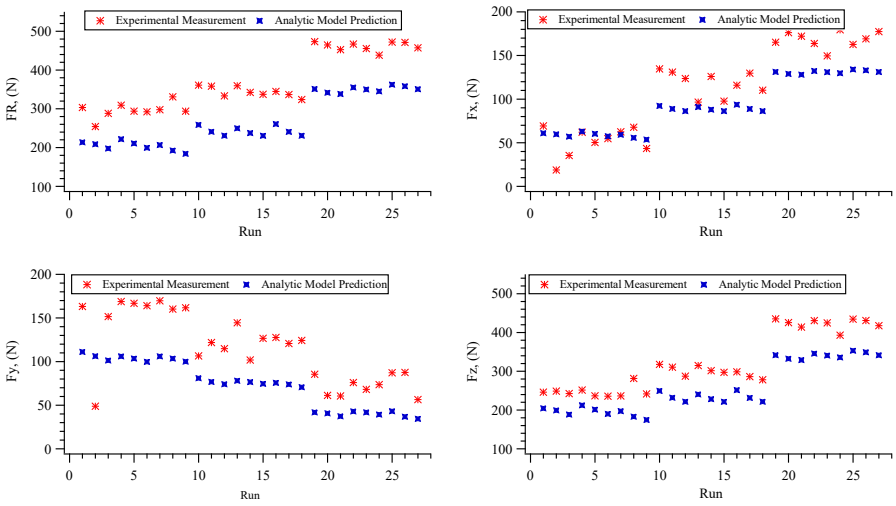


**Figure 6.24.** Comparison between experimental measurements and analytical model prediction for cutting forces of extruded CW511L with 60° of plunging angle

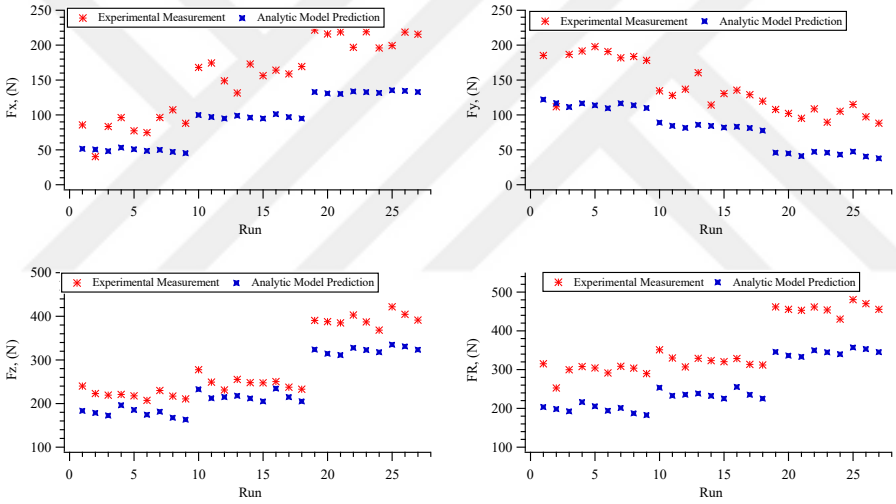


**Figure 6.25.** Comparison between experimental measurements and analytical model prediction for cutting forces of extruded CW511L with 45° of plunging angle

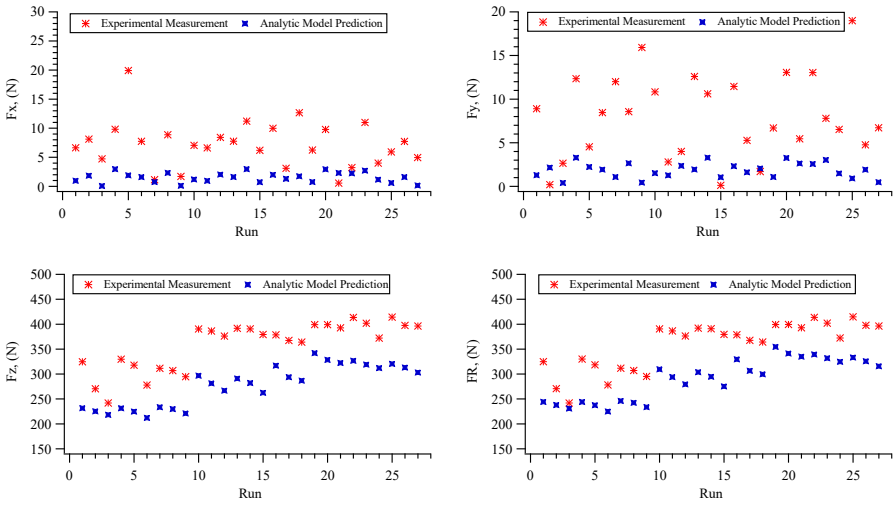


**Figure 6.26.** Comparison between experimental measurements and analytical model prediction for cutting forces of extruded CW724R with 90° of plunging angle

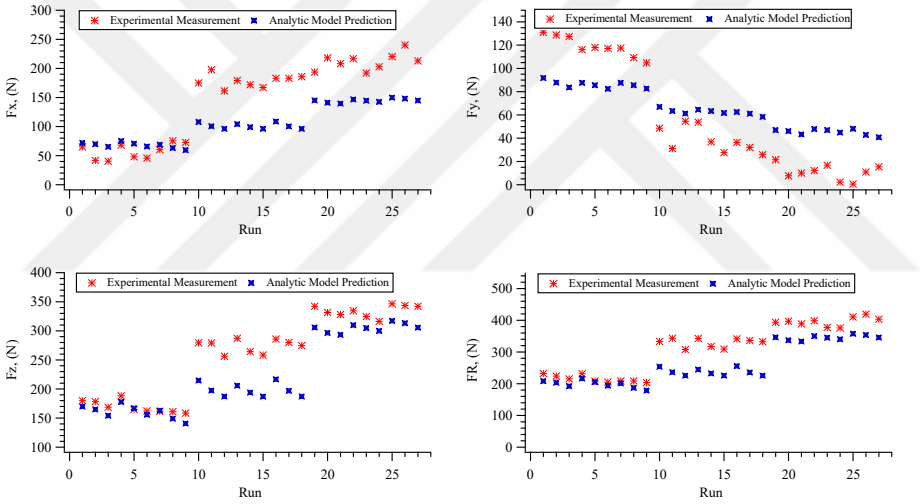


**Figure 6.27.** Comparison between experimental measurements and analytical model prediction for cutting forces of extruded CW724R with 60° of plunging angle

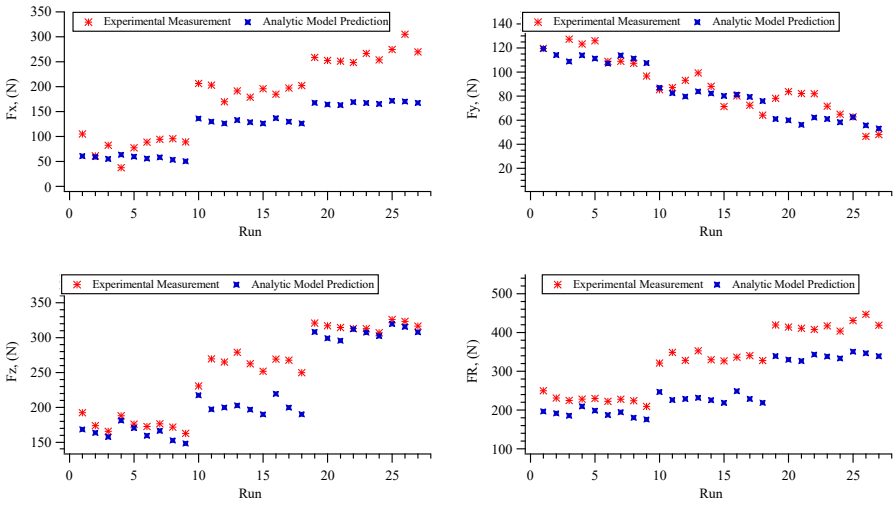


**Figure 6.28.** Comparison between experimental measurements and analytical model prediction for cutting forces of extruded CW724R with 45° of plunging angle

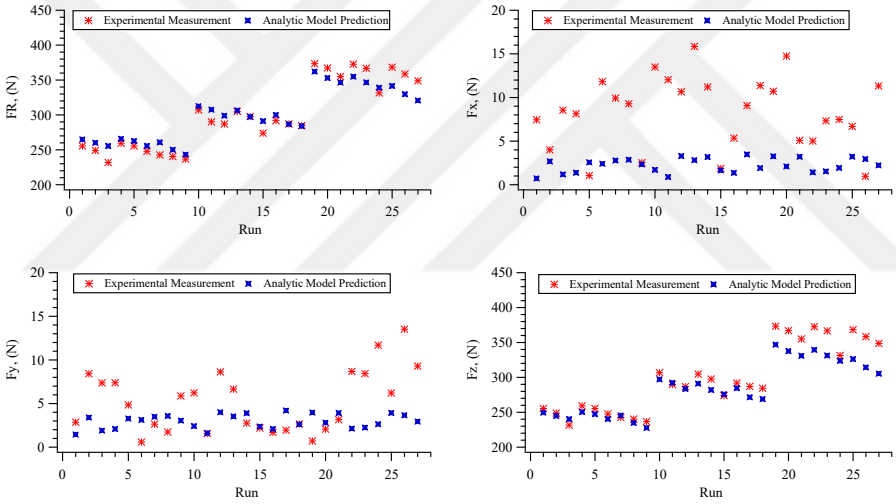


**Figure 6.29.** Comparison between experimental measurements and analytical model prediction for cutting forces of forged+annealed CW617N with 90° of plunging angle

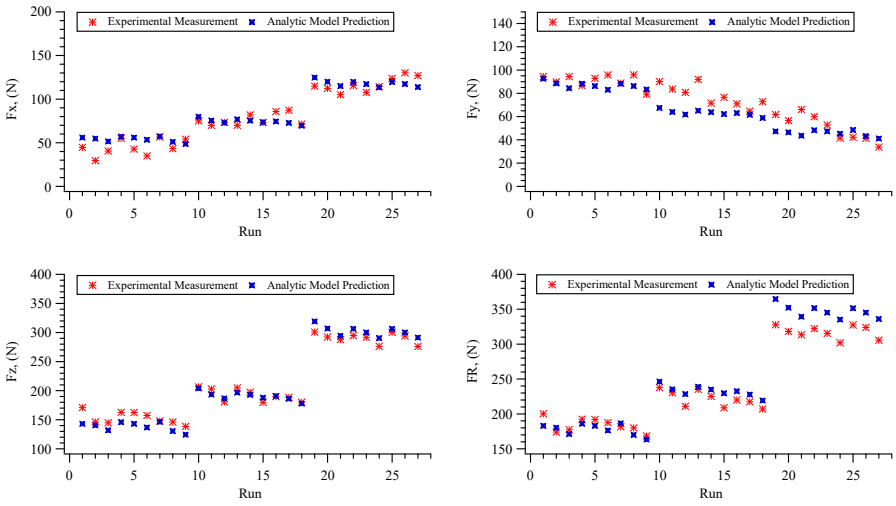


**Figure 6.30.** Comparison between experimental measurements and analytical model prediction for cutting forces of forged+annealed CW617N with 60° of plunging angle

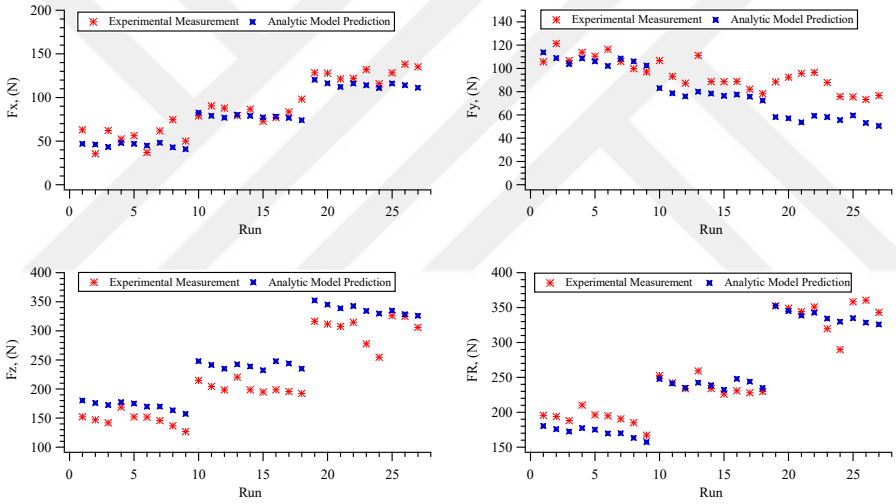


**Figure 6.31.** Comparison between experimental measurements and analytical model prediction for cutting forces of forged+annealed CW617N with 45° of plunging angle

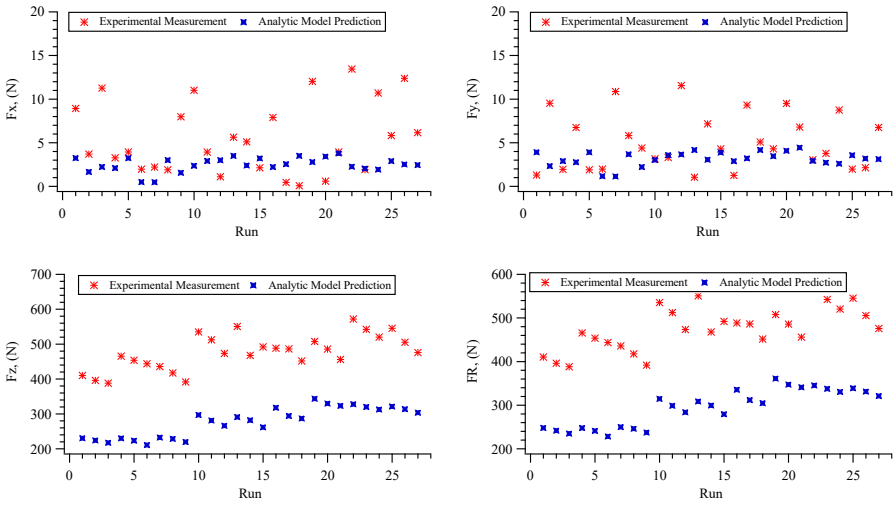


**Figure 6.32.** Comparison between experimental measurements and analytical model prediction for cutting forces of forged+annealed CW511L with 90° of plunging angle

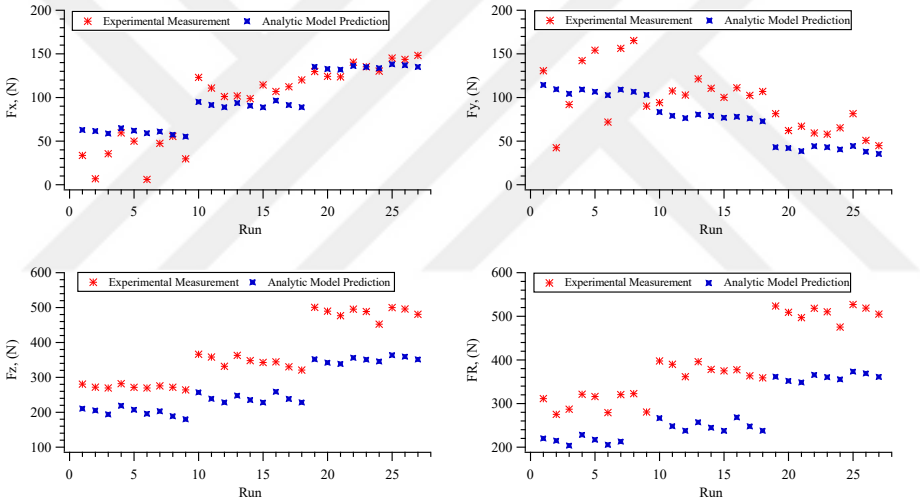


**Figure 6.33.** Comparison between experimental measurements and analytical model prediction for cutting forces of forged+annealed CW511L with 60° of plunging angle

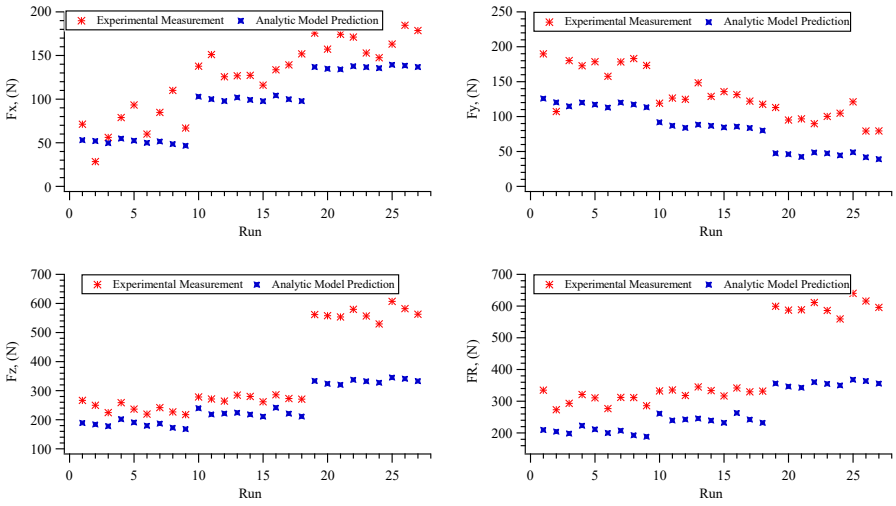


**Figure 6.34.** Comparison between experimental measurements and analytical model prediction for cutting forces of forged+annealed CW511L with 45° of plunging angle

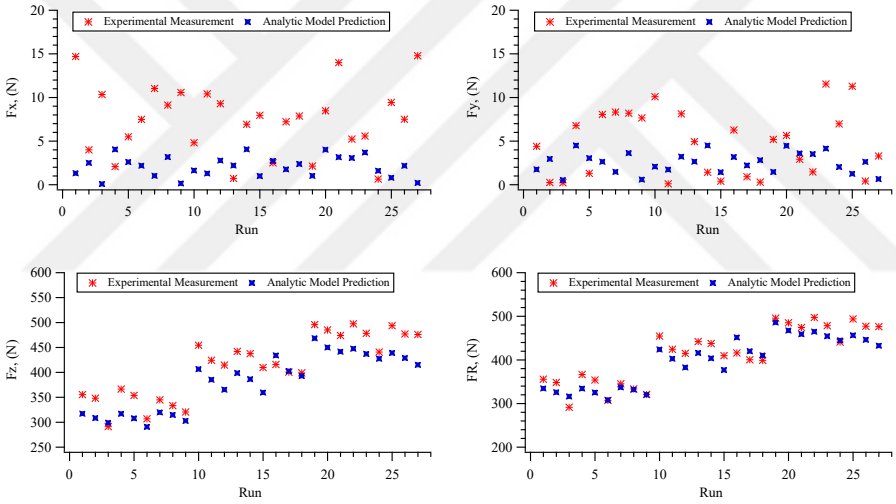


**Figure 6.35.** Comparison between experimental measurements and analytical model prediction for cutting forces of forged+annealed CW724R with 90° of plunging angle

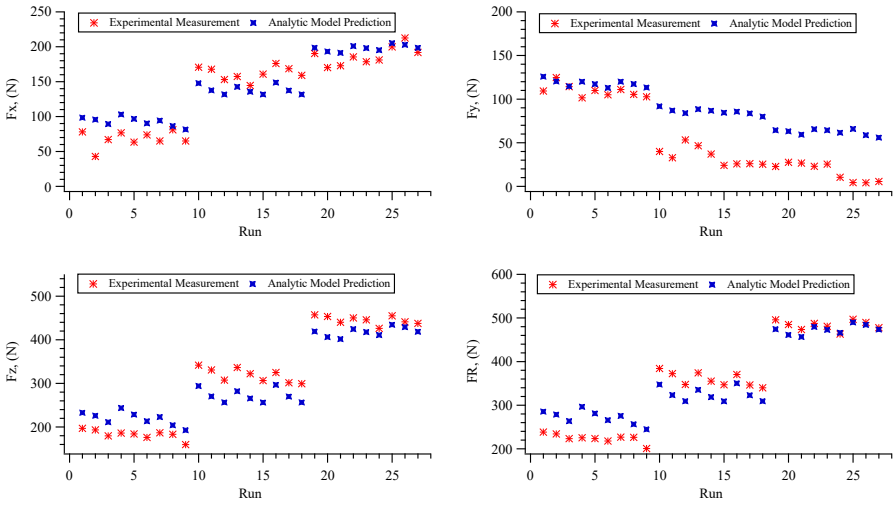


**Figure 6.36.** Comparison between experimental measurements and analytical model prediction for cutting forces of forged+annealed CW724R with 60° of plunging angle

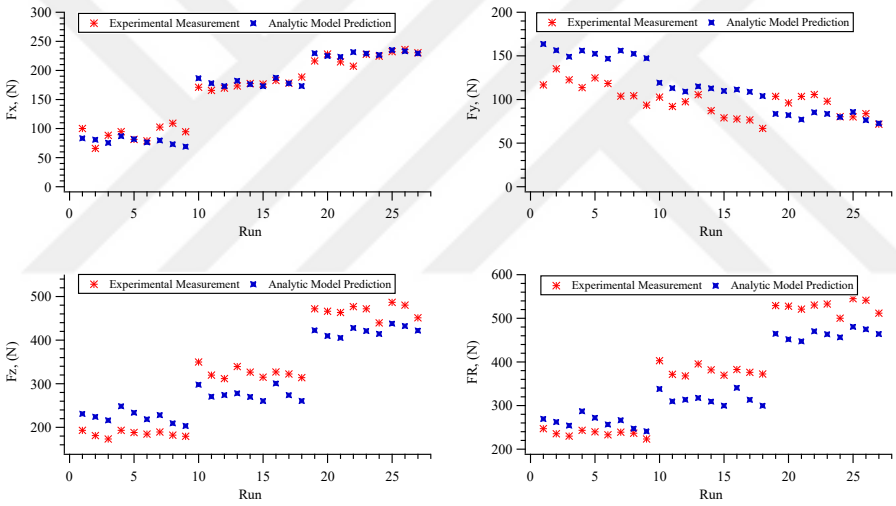


**Figure 6.37.** Comparison between experimental measurements and analytical model prediction for cutting forces of forged+annealed CW724R with 45° of plunging angle

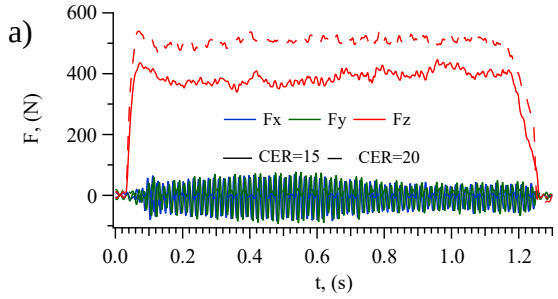

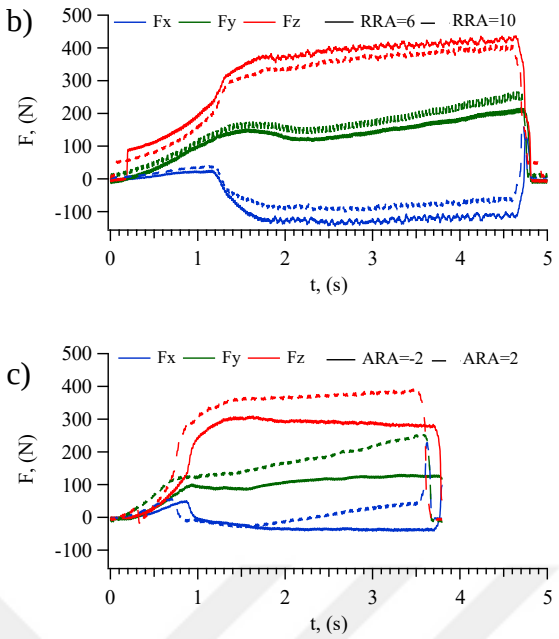


**Figure 6.38.** The measured cutting forces of blind flat bottom drilling; a) forged+annealed CW511L at 90° of plunging angle in constant RRA=10° and ARA=-2°, b) forged+annealed CW511L at 45° of plunging angle in constant CER=20 µm and ARA=-2°, c) forged+annealed CW724 at 60° of plunging angle in constant RRA=10° and CER=20 µm

### 6.2. Evaluation of the formed burr heights:

The measured average burr heights from four points of the drilled holes at tool entry and exit are demonstrated in Figure 6.40 to Figure 6.45. In plunging with 90°, the highest measured entry burr heights of the drilled holes were 107.013, 247.544, and 94.281 µm for extruded CW617N, CW511L and CW724R, respectively. For forged+annealed CW617N, CW511L and CW724R, these values were measured as 89.999, 216.590, 78.623 µm, respectively. The lowest measured values were 20.649, 129.690, 18.913 µm for extruded CW617N, CW511L and CW724R, respectively. For forged+annealed CW617N, CW511L and CW724R, these values were measured as 14.365, 110.323, 12.956 µm, respectively. In plunging with 60°, the highest measured entry burr heights of the drilled holes were 92.610, 194.824, and 66.802 µm for extruded CW617N, CW511L and CW724R, respectively. For forged+annealed CW617N, CW511L and CW724R, these values were measured as 72.460, 163.268, 49.991 µm, respectively. The lowest measured values were 21.615, 111.580, 217.736 µm for extruded CW617N,

CW511L and CW724R, respectively. For forged+annealed CW617N, CW511L and CW724R, these values were measured as 12.654, 89.156, 12.745 µm, respectively. In plunging with 45°, the highest measured entry burr heights of the drilled holes were 50.251, 162.288, and 55.744 µm for extruded CW617N, CW511L and CW724R, respectively. For forged+annealed CW617N, CW511L and CW724R, these values were measured as 89.999, 216.590, 78.623 µm, respectively. The lowest measured values were 20.649, 129.690, 18.913 µm for extruded CW617N, CW511L and CW724R, respectively. For forged+annealed CW617N, CW511L and CW724R, these values were measured as 10.950, 85.162, 16.391 µm, respectively. It is seen that the highest burr sizes belong to CW511L. The lower chip breakability, yield strength and generated higher cutting forces of these alloys is the main reason for the swelling and tumefaction. Higher cutting forces and contact area results in more tumefaction on the hole entry and exit. This idea is also confirmed with the results of the lower impact fracture and toughness obtainments for the same material. The same approach is also valid when considering the differences of the formed burr heights in extruded and forged+annealed specimens. On the other hand, the highest yield strength and fracture toughness was measured for CW724R. Subsequently, the lowest burr height at both entry and exit of the holes was measured for this material. Moreover, uniform, and smoother burrs have formed by decreasing the plunging angle.

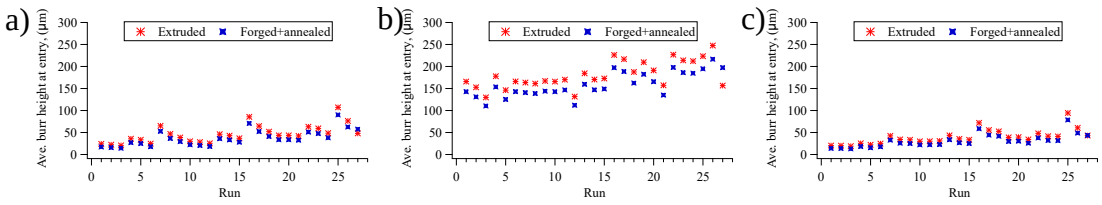


**Figure 6.39.** The measured burr heights at hole entry (BHEN) with 90° of plunging angle; a) CW617N, b) CW511L, c) CW724R

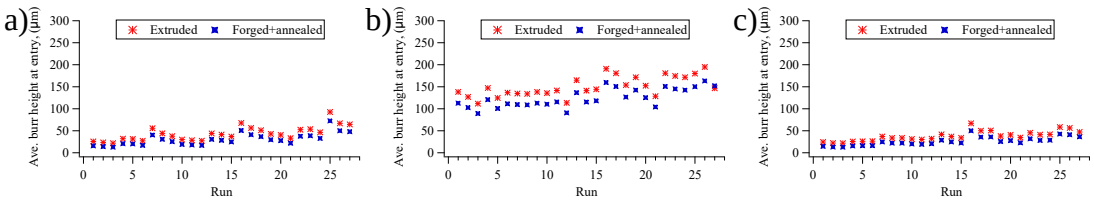


**Figure 6.40.** The measured burr heights at hole entry (BHEN) with 60° of plunging angle; a) CW617N, b) CW511L, c) CW724R

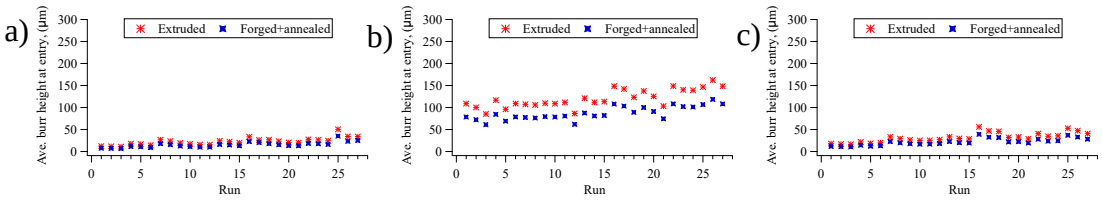


**Figure 6.41.** The measured burr heights at hole entry (BHEN) with 45° of plunging angle; a) CW617N, b) CW511L, c) CW724R

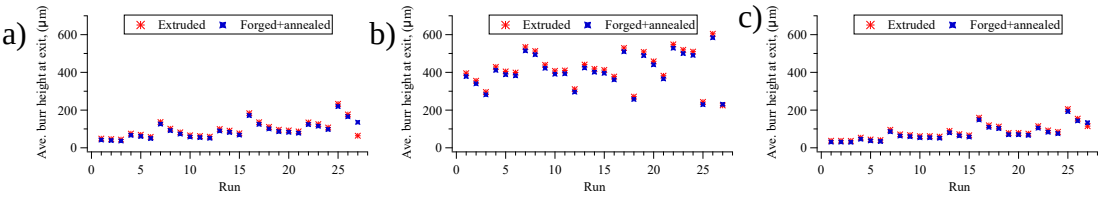


**Figure 6.42.** The measured burr heights at hole exit (BHEX) with 90° of plunging angle; a) CW617N, b) CW511L, c) CW724R

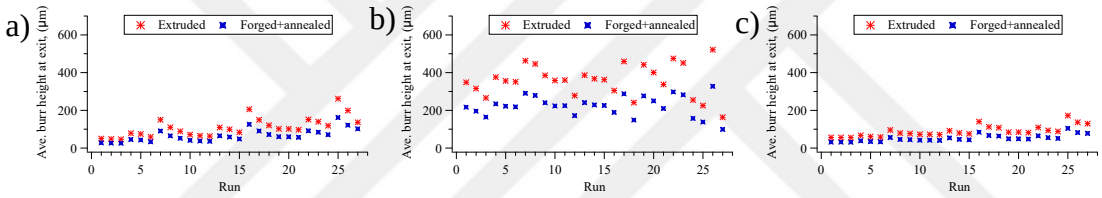


**Figure 6.43.** The measured burr heights at hole exit (BHEX) with 60° of plunging angle; a) CW617N, b) CW511L, c) CW724R

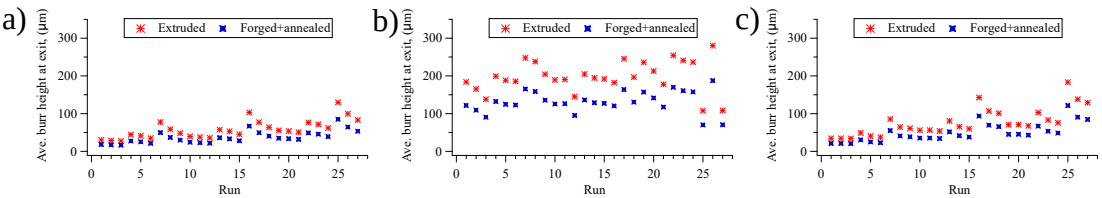


**Figure 6.44.** The measured burr heights at hole exit (BHEX) with 45° of plunging angle; a) CW617N, b) CW511L, c) CW724R

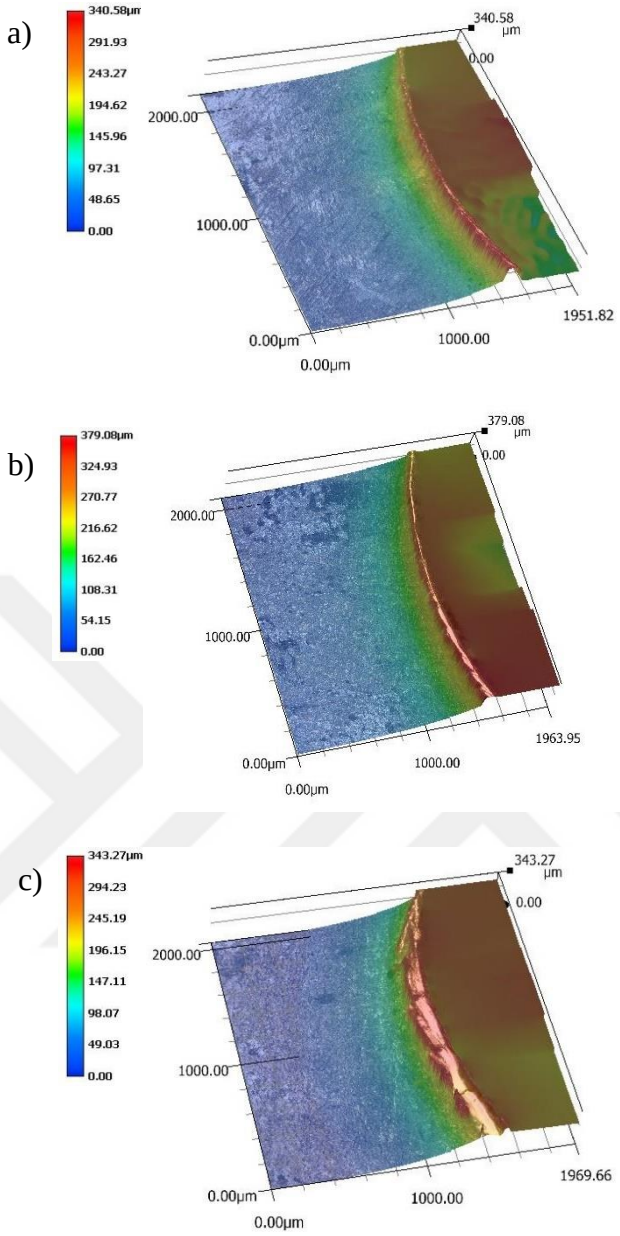


**Figure 6.45.** The images of the formed entry burrs on hot forged+annealed; a) CW617N, b) CW511L, c) CW724R specimens.

### 6.3. Evaluation of the surface quality:

The measured average surface roughness from the drilled holes' wall and bottom at different plunging angles are demonstrated in Figure 6.46 to Figure 6.52. In plunging with 90°, the highest measured Ra on the drilled holes wall values were 0.837, 1.355, and 0.827 µm for extruded CW617N, CW511L and CW724R, respectively. For forged+annealed CW617N, CW511L and CW724R, these values were measured as

0.900, 1.236, 0.925 μm, respectively. The lowest measured values were 0.684, 1.190 and 0.660 μm for extruded CW617N, CW511L and CW724R, respectively. For forged+annealed CW617N, CW511L and CW724R, these values were measured as 0.737, 1.104, 0.742 μm, respectively. In plunging with 60°, the highest measured Ra on the drilled holes wall values were 0.745, 0.981, and 0.744 μm for extruded CW617N, CW511L and CW724R, respectively. For forged+annealed CW617N, CW511L and CW724R, these values were measured as 0.810, 1.036, 0.809 μm, respectively. The lowest measured values were 0.615, 0.931 and 0.627 μm for extruded CW617N, CW511L and CW724R, respectively. For forged+annealed CW617N, CW511L and CW724R, these values were measured as 0.670, 0.967, 0.682 μm, respectively. In plunging with 45°, the highest measured Ra on the drilled holes wall values were 0.724, 0.911, and 0.782 μm for extruded CW617N, CW511L and CW724R, respectively. For forged+annealed CW617N, CW511L and CW724R, these values were measured as 0.785, 0.962 0.877 μm, respectively. The lowest measured values were 0.598, 0.831 and 0.623 μm for extruded CW617N, CW511L and CW724R, respectively. For forged+annealed CW617N, CW511L and CW724R, these values were measured as 0.657, 0.872, 0.714 μm, respectively.

In plunging with 90°, the highest measured Ra on the drilled holes bottom values were 0.490, 1.044 and 0.523 μm for extruded CW617N, CW511L and CW724R, respectively. For forged+annealed CW617N, CW511L and CW724R, these values were measured as 0.427, 0.908, 0.422 μm, respectively. The lowest measured values were 0.337, 0.852 and 0.345 μm for extruded CW617N, CW511L and CW724R, respectively. For forged+annealed CW617N, CW511L and CW724R, these values were measured as 0.294, 0.741, 0.279 μm, respectively. In plunging with 60°, the highest measured Ra on the drilled holes bottom values were 0.390, 0.827 and 0.374 μm for extruded CW617N, CW511L and CW724R, respectively. For forged+annealed CW617N, CW511L and CW724R, these values were measured as 0.322, 0.708, 0.310 μm, respectively. The lowest measured values were 0.254, 0.676 and 0.255 μm for extruded CW617N, CW511L and CW724R, respectively. For forged+annealed CW617N, CW511L and CW724R, these values were measured as 0.210, 0.579, 0.211 μm, respectively. In plunging with 45°, the highest measured Ra on the drilled holes bottom values were 0.360, 0.759, and 0.339 μm for extruded CW617N, CW511L and CW724R, respectively. For

forged+annealed CW617N, CW511L and CW724R, these values were measured as 0.313, 0.682 0.274 µm, respectively. The lowest measured values were 0.268, 0.624 and 0.235 µm for extruded CW617N, CW511L and CW724R, respectively. For forged+annealed CW617N, CW511L and CW724R, these values were measured as 0.233, 0.561, 0.190 µm, respectively. It is seen that the forged+annealed specimens have demonstrated better surface quality as compared to extruded ones due to the lower plastic deformation properties and higher hardness. Moreover, an increasing trend in surface quality with the intensifying radial, axial rake angles and cutting edge-radius was determined. The highest radial and axial rake angles improve the chip breakage and its distraction from the hole. Higher cutting edge-radius on the flat bottom drill results in less vibration and excessive undesired tool motions leading to over cut and chatter by increasing the contact area between the cutter and workpiece. Subsequently, enhanced surface quality on the drilled holes is achieved. The surface topography images of the drilled holes on the extruded brass alloys are shown in Figure 6.53. Inhomogeneities on the surface of the CW617N is seen which might be due to the low solubility of Lead and segregation in the entire microstructure and grain boundaries [1].

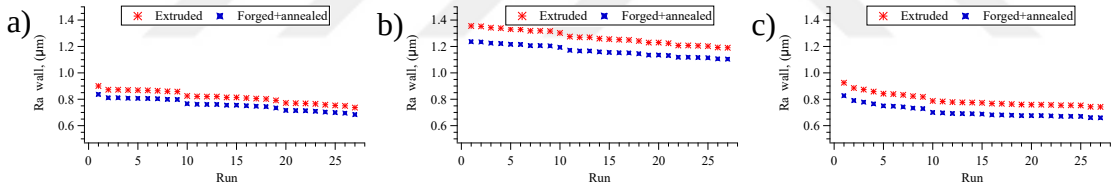


**Figure 6.46.** The measured surface roughness at hole wall with 90° of plunging angle; a) CW617N, b) CW511L, c) CW724R

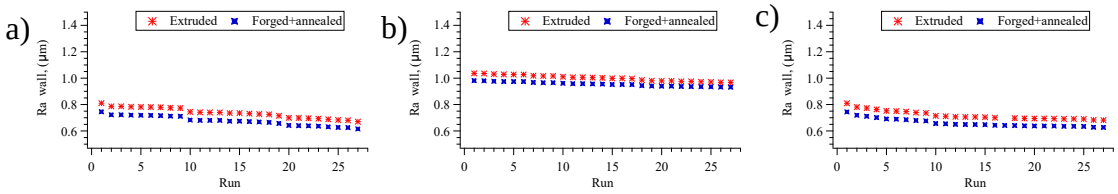


**Figure 6.47.** The measured surface roughness at hole wall with 60° of plunging angle; a) CW617N, b) CW511L, c) CW724R

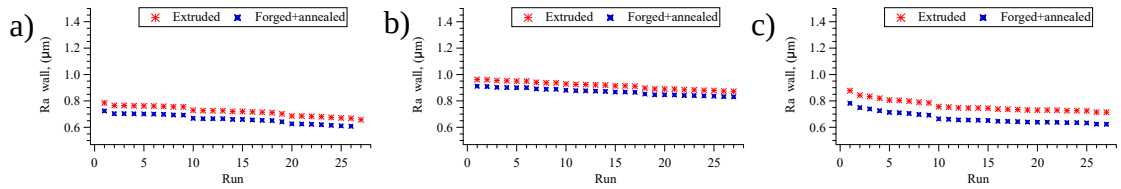


**Figure 6.48.** The measured surface roughness at hole wall with 45° of plunging angle; a) CW617N, b) CW511L, c) CW724R

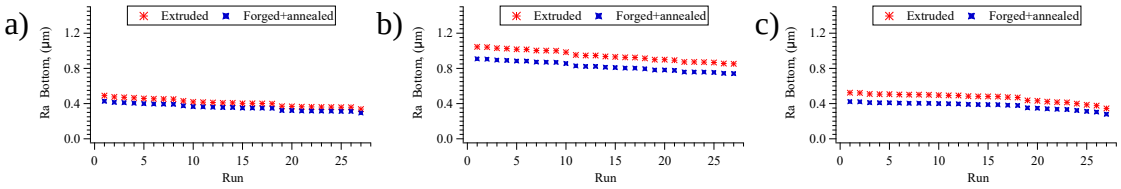


**Figure 6.49.** The measured surface roughness at hole bottom with 90° of plunging angle; a) CW617N, b) CW511L, c) CW724R

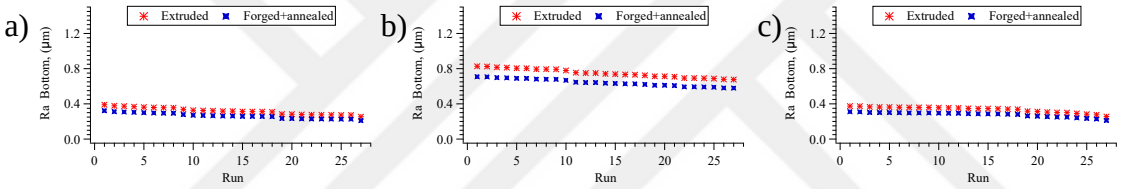


**Figure 6.50.** The measured surface roughness at hole bottom with 60° of plunging angle; a) CW617N, b) CW511L, c) CW724R

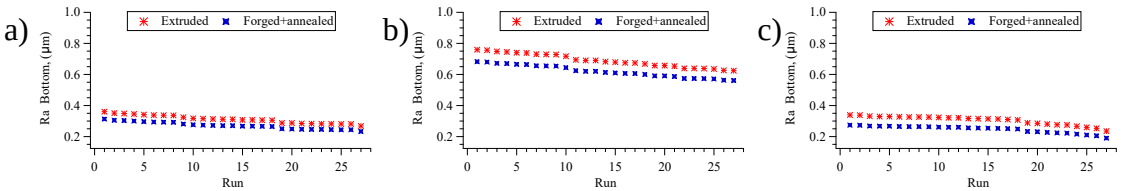


**Figure 6.51.** The measured surface roughness at hole bottom with 45° of plunging angle; a) CW617N, b) CW511L, c) CW724R

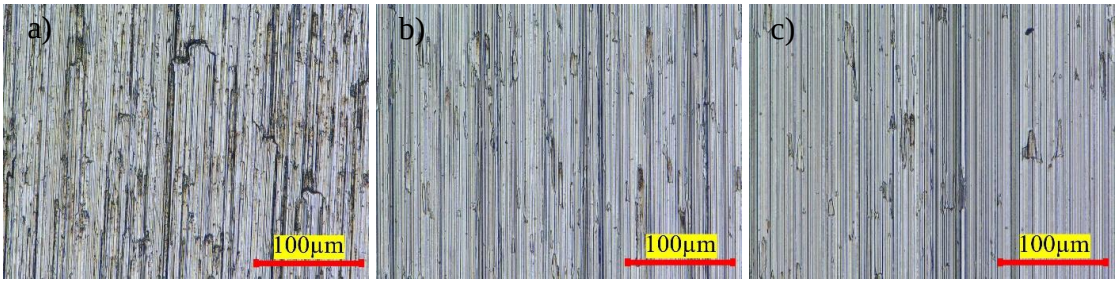

**Figure 6.52.** Surface topography images of the drilled holes on extruded; a) CW617N, b) CW511L, c) CW724R

### 6.4. Evaluation of the dimensional accuracy:

The dimensional accuracies of the generated hole diameter are demonstrated in Figure 6.53 to Figure 6.55. A tolerance range of ±0.1 mm has been considered for the Ø8 mm diameter. It is seen that the holes diameter with 90° of plunging angle are mostly in the tolerance excluding CW511L material. The low chip breakability of this alloy has resulted in incapsulating the generated chips to the cutting tool and over cut on the hole diameter. However, with the increase in the cutting-edge radius a reduction was observed on the dimension and entering the defined tolerance range which can be attributed to the reduction in the chatter and tool vibration. In plunging with 90°, the highest measured values were 8.005, 9.121 and 8.174 mm for extruded CW617N, CW511L and CW724R, respectively. For forged+annealed CW617N, CW511L and CW724R, these values were measured as 8.010, 8.998, 7.989 mm, respectively. The lowest measured values were 7.931, 7.930 and 7.893 mm for extruded CW617N, CW511L and CW724R, respectively. For forged+annealed CW617N, CW511L and CW724R, these values were measured as 7.952, 7.949, 7.938 mm, respectively. Almost all of the diameter dimensions were in the tolerance range in inclined drilling. In plunging with 60°, the highest measured values were 8.033, 8.263 and 8.022 mm for extruded CW617N, CW511L and CW724R, respectively. For forged+annealed CW617N, CW511L and CW724R, these values were measured as 8.046, 8.057, 8.031 mm, respectively. The lowest measured values were 7.960, 7.940 and 7.933 mm for extruded CW617N, CW511L and CW724R, respectively. For forged+annealed CW617N, CW511L and CW724R, these values were measured as 7.960, 7.963, 7.954 mm, respectively. In plunging with 45°, the highest measured values were 8.045, 8.159 and 8.047 mm for extruded CW617N, CW511L and CW724R, respectively. For forged+annealed CW617N, CW511L and CW724R, these values were measured as 8.046, 8.065, 8.040 mm, respectively. The lowest measured values were 7.971, 7.952 and 7.950 mm for extruded CW617N, CW511L and CW724R, respectively. For forged+annealed CW617N, CW511L and CW724R, these values were measured as 7.974, 7.970, 7.956 mm, respectively. It is seen that all the out of dimensional tolerance holes were generated using flat bottom drills having either the lowest radial rake angle or

cutting edge-radius. These results confirm the justification for lower chip removal ability of the designed tools in lower radial rake angles and generated chip wraps and incapsulates and experiment observations. No obvious prevailing differences in the penetrated holes diameter was observed between extruded and forged+annealed specimens.

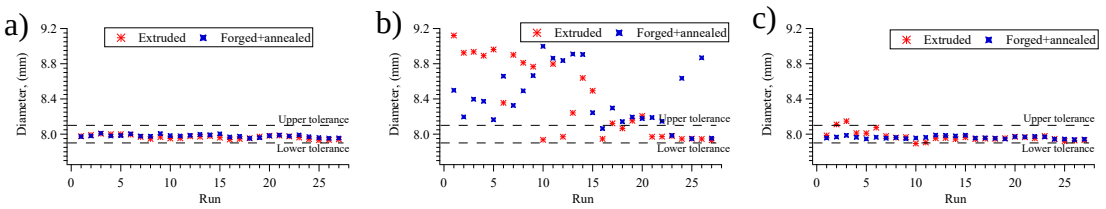


**Figure 6.53.** The measured hole diameter with 90° of plunging angle; a) CW617N, b) CW511L, c) CW724R

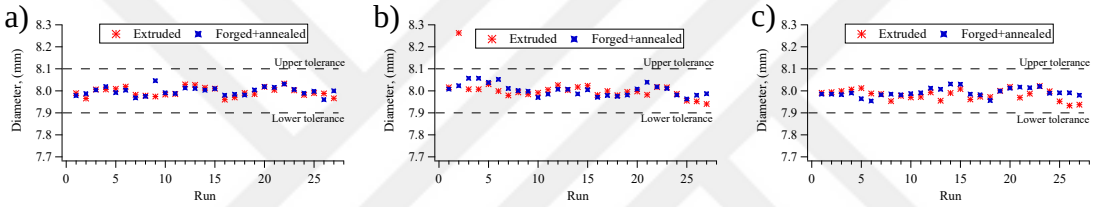


**Figure 6.54.** The measured hole diameter with 60° of plunging angle; a) CW617N, b) CW511L, c) CW724R

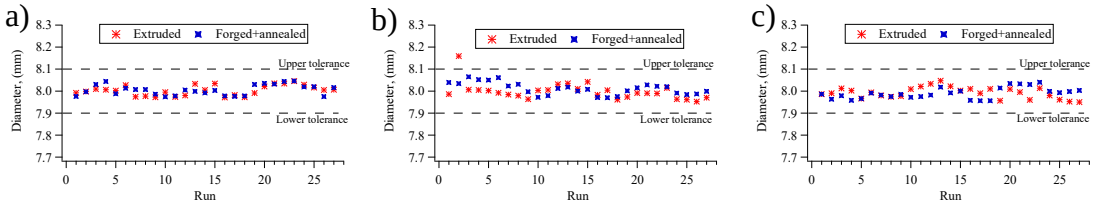


**Figure 6.55.** The measured hole diameter with 45° of plunging angle; a) CW617N, b) CW511L, c) CW724R

## 6.5. Analysis of variance (ANOVA) for the obtained results

ANOVA has been employed as a statistical technique for inspection of the designed cutting tool geometric parameters on the machining responses. The significance of the statistic model was assessed and illustrated by the F-values and P-values of ANOVA results. P-values less than 0.0500 indicate model terms are significant. In this case there are no significant model terms. Values greater than 0.1000 indicate the model terms are not significant. Furthermore, polynomial regression models have been developed with the

purpose of prediction of the machining response with corresponding confidences ($R^2$). The analysis results are given in Tables 6.23 to 6.202, respectively. Meanwhile, the variation of the corresponding machining responses is displayed in 3D surface plot formats.

**Table 6.23.** The ANOVA results for measured forces in X direction (Fx) during drilling of extruded CW617N with 90° of plunging angle

| Source | Sum of Squares | df | Mean Square | F-value | p-value |
|---|---|---|---|---|---|
| **Model** | 984.26 | 22 | 44.74 | 1.73 | 0.3195 |
| A-Radial rake angle | 54.44 | 1 | 54.44 | 2.1 | 0.2209 |
| B-Axial rake angle | 10.62 | 1 | 10.62 | 0.4097 | 0.5569 |
| C-Edge radius | 39.37 | 1 | 39.37 | 1.52 | 0.2854 |
| AB | 19.35 | 1 | 19.35 | 0.7461 | 0.4364 |
| AC | 1.05 | 1 | 1.05 | 0.0404 | 0.8504 |
| BC | 1.39 | 1 | 1.39 | 0.0535 | 0.8285 |
| $A^2$ | 52.02 | 1 | 52.02 | 2.01 | 0.2296 |
| $B^2$ | 7.12 | 1 | 7.12 | 0.2746 | 0.628 |
| $C^2$ | 3.09 | 1 | 3.09 | 0.1191 | 0.7474 |
| ABC | 78.09 | 1 | 78.09 | 3.01 | 0.1577 |
| $A^2B$ | 39.94 | 1 | 39.94 | 1.54 | 0.2824 |
| $A^2C$ | 103.18 | 1 | 103.18 | 3.98 | 0.1168 |
| $AB^2$ | 68.89 | 1 | 68.89 | 2.66 | 0.1785 |
| $AC^2$ | 37.01 | 1 | 37.01 | 1.43 | 0.2982 |
| $B^2C$ | 18.22 | 1 | 18.22 | 0.7025 | 0.4491 |
| $BC^2$ | 43.21 | 1 | 43.21 | 1.67 | 0.2663 |
| $A^2B^2$ | 31.11 | 1 | 31.11 | 1.2 | 0.3349 |
| $A^2BC$ | 3.28 | 1 | 3.28 | 0.1265 | 0.7401 |
| $A^2C^2$ | 30.52 | 1 | 30.52 | 1.18 | 0.339 |
| $AB^2C$ | 104 | 1 | 104 | 4.01 | 0.1158 |
| $ABC^2$ | 96.46 | 1 | 96.46 | 3.72 | 0.126 |
| $B^2C^2$ | 1.41 | 1 | 1.41 | 0.0542 | 0.8273 |
| **Residual** | 103.73 | 4 | 25.93 | | |
| **Cor Total** | 1087.99 | 26 | | | |

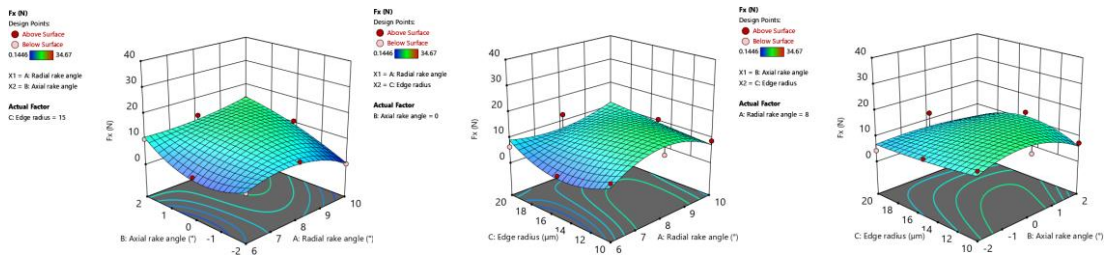

**Figure 6.56.** 3D surface plot of the measured forces in X direction (Fx) variation during drilling of extruded CW617N with 90° of plunging angle with respect to the studied

cutting tool geometry

**Table 6.24.** The ANOVA results for measured forces in Y direction (Fy) during drilling of extruded CW617N with 90° of plunging angle

| Source | Sum of Squares | df | Mean Square | F-value | p-value |
|---|---|---|---|---|---|
| **Model** | 1956.1 | 22 | 88.91 | 1.07 | 0.5384 |
| A-Radial rake angle | 20.7 | 1 | 20.7 | 0.2487 | 0.6442 |
| B-Axial rake angle | 12.36 | 1 | 12.36 | 0.1485 | 0.7196 |
| C-Edge radius | 586.51 | 1 | 586.51 | 7.05 | 0.0567 |
| AB | 74.5 | 1 | 74.5 | 0.8954 | 0.3976 |
| AC | 7.47 | 1 | 7.47 | 0.0898 | 0.7794 |
| BC | 7.64 | 1 | 7.64 | 0.0918 | 0.777 |
| $A^2$ | 44.36 | 1 | 44.36 | 0.5332 | 0.5057 |
| $B^2$ | 162.95 | 1 | 162.95 | 1.96 | 0.2343 |
| $C^2$ | 5.16 | 1 | 5.16 | 0.062 | 0.8156 |
| ABC | 138.43 | 1 | 138.43 | 1.66 | 0.2666 |
| $A^2B$ | 15.05 | 1 | 15.05 | 0.1809 | 0.6925 |
| $A^2C$ | 77.57 | 1 | 77.57 | 0.9322 | 0.389 |
| $AB^2$ | 34.71 | 1 | 34.71 | 0.4171 | 0.5536 |
| $AC^2$ | 16.01 | 1 | 16.01 | 0.1924 | 0.6836 |
| $B^2C$ | 66.14 | 1 | 66.14 | 0.7948 | 0.423 |
| $BC^2$ | 21.21 | 1 | 21.21 | 0.2549 | 0.6402 |
| $A^2B^2$ | 0.0675 | 1 | 0.0675 | 0.0008 | 0.9786 |
| $A^2BC$ | 7.24 | 1 | 7.24 | 0.087 | 0.7827 |
| $A^2C^2$ | 103.93 | 1 | 103.93 | 1.25 | 0.3263 |
| $AB^2C$ | 25.31 | 1 | 25.31 | 0.3042 | 0.6106 |
| $ABC^2$ | 1.03 | 1 | 1.03 | 0.0124 | 0.9167 |
| $B^2C^2$ | 153.7 | 1 | 153.7 | 1.85 | 0.2457 |
| **Residual** | 332.84 | 4 | 83.21 | | |
| **Cor Total** | 2288.93 | 26 | | | |

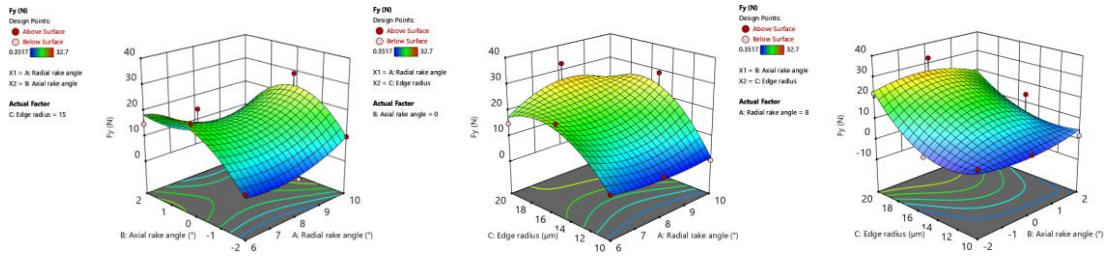

**Figure 6.57.** 3D surface plot of the measured forces in Y direction (Fy) variation during drilling of extruded CW617N with 90° of plunging angle with respect to the studied cutting tool geometry

**Table 6.25.** The ANOVA results for measured forces in Z direction (Fz) during drilling of extruded CW617N with 90° of plunging angle

| Source | Sum of Squares | df | Mean Square | F-value | p-value | |
|---|---|---|---|---|---|---|
| **Model** | 41554.8 | 6 | 6925.8 | 153.54 | < 0.0001 | significant |
| A-Radial rake angle | 427.29 | 1 | 427.29 | 9.47 | 0.0059 | |
| B-Axial rake angle | 1211.96 | 1 | 1211.96 | 26.87 | < 0.0001 | |
| C-Edge radius | 39809 | 1 | 39809 | 882.52 | < 0.0001 | |
| AB | 43.7 | 1 | 43.7 | 0.9688 | 0.3367 | |
| AC | 26.11 | 1 | 26.11 | 0.5788 | 0.4557 | |
| BC | 36.75 | 1 | 36.75 | 0.8147 | 0.3775 | |
| **Residual** | 902.17 | 20 | 45.11 | | | |
| **Cor Total** | 42457 | 26 | | | | |

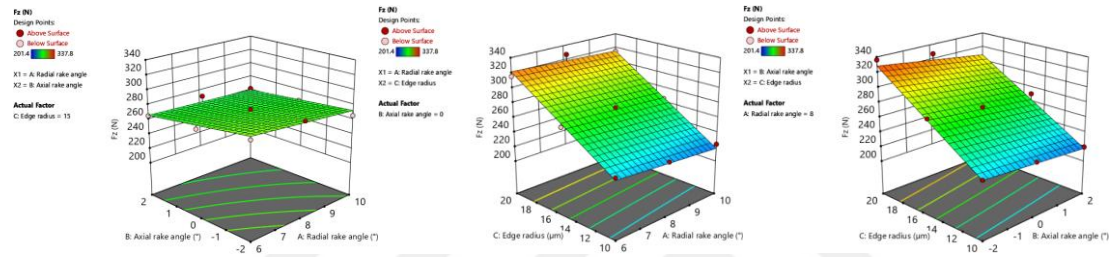

**Figure 6.58.** 3D surface plot of the measured forces in Z direction (Fz) variation during drilling of extruded CW617N with 90° of plunging angle with respect to the studied cutting tool geometry

**Table 6.26.** The ANOVA results for measured resultant forces (FR) during drilling of extruded CW617N with 90° of plunging angle

| Source | Sum of Squares | df | Mean Square | F-value | p-value | |
|---|---|---|---|---|---|---|
| **Model** | 42117.9 | 6 | 7019.65 | 148.11 | < 0.0001 | significant |
| A-Radial rake angle | 445.79 | 1 | 445.79 | 9.41 | 0.0061 | |
| B-Axial rake angle | 1157.73 | 1 | 1157.73 | 24.43 | < 0.0001 | |
| C-Edge radius | 40436.4 | 1 | 40436.4 | 853.16 | < 0.0001 | |
| AB | 30.37 | 1 | 30.37 | 0.6407 | 0.4329 | |
| AC | 17.6 | 1 | 17.6 | 0.3714 | 0.5491 | |
| BC | 29.97 | 1 | 29.97 | 0.6323 | 0.4358 | |
| **Residual** | 947.92 | 20 | 47.4 | | | |
| **Cor Total** | 43065.8 | 26 | | | | |

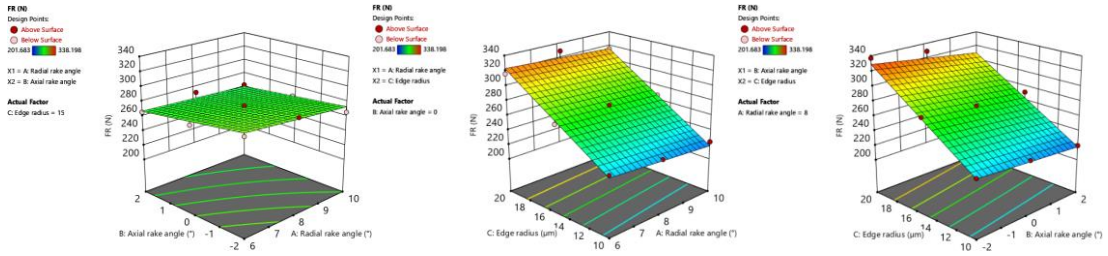

**Figure 6.59.** 3D surface plot of the measured resultant forces variation during drilling of extruded CW617N with 90° of plunging angle with respect to the studied cutting tool geometry

**Table 6.27.** The ANOVA results for measured burr heights at hole entry (BHEN) during drilling of extruded CW617N with 90° of plunging angle

| Source | Sum of Squares | df | Mean Square | F-value | p-value | |
|---|---|---|---|---|---|---|
| **Model** | 48873.9 | 6 | 8145.66 | 33.07 | < 0.0001 | significant |
| A-Radial rake angle | 21453.4 | 1 | 21453.4 | 87.1 | < 0.0001 | |
| B-Axial rake angle | 8208.2 | 1 | 8208.2 | 33.32 | < 0.0001 | |
| C-Edge radius | 11511.4 | 1 | 11511.4 | 46.73 | < 0.0001 | |
| AB | 6324.53 | 1 | 6324.53 | 25.68 | < 0.0001 | |
| AC | 27.84 | 1 | 27.84 | 0.113 | 0.7402 | |
| BC | 1348.59 | 1 | 1348.59 | 5.48 | 0.0298 | |
| **Residual** | 4926.28 | 20 | 246.31 | | | |
| **Cor Total** | 53800.2 | 26 | | | | |

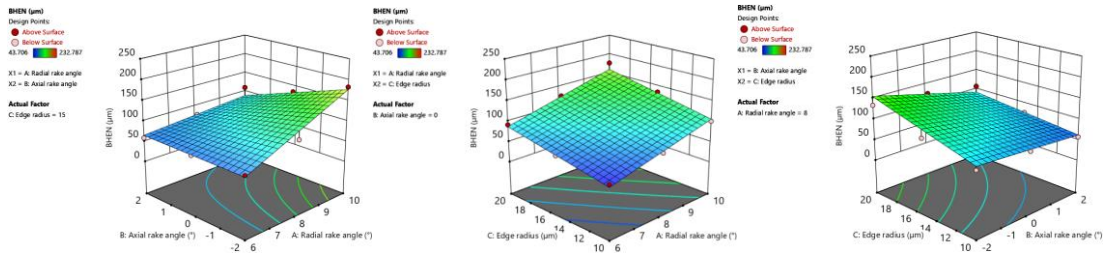

**Figure 6.60.** 3D surface plot of the measured burr heights at hole entry (BHEN) variation during drilling of extruded CW617N with 90° of plunging angle with respect to the studied cutting tool geometry

**Table 6.28.** The ANOVA results for measured burr heights at hole exit (BHEX) during drilling of extruded CW617N with 90° of plunging angle

| Source | Sum of Squares | df | Mean Square | F-value | p-value | |
|---|---|---|---|---|---|---|
| **Model** | 10438.2 | 6 | 1739.71 | 61.95 | < 0.0001 | significant |
| A-Radial rake angle | 5135.2 | 1 | 5135.2 | 182.87 | < 0.0001 | |
| B-Axial rake angle | 1483.44 | 1 | 1483.44 | 52.83 | < 0.0001 | |

| | | | | | |
|---|---|---|---|---|---|
| C-Edge radius | 2681.9 | 1 | 2681.9 | 95.51 | < 0.0001 |
| AB | 1010.76 | 1 | 1010.76 | 35.99 | < 0.0001 |
| AC | 30.44 | 1 | 30.44 | 1.08 | 0.3103 |
| BC | 96.5 | 1 | 96.5 | 3.44 | 0.0786 |
| **Residual** | 561.62 | 20 | 28.08 | | |
| **Cor Total** | 10999.9 | 26 | | | |

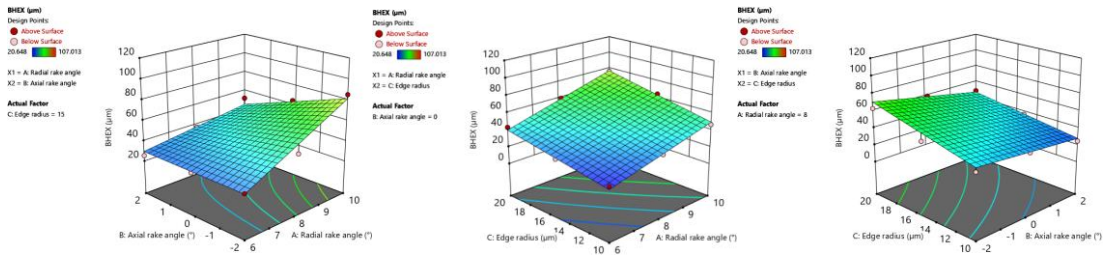

**Figure 6.61.** 3D surface plot of the measured burr heights at hole exit (BHEX) variation during drilling of extruded CW617N with 90° of plunging angle with respect to the studied cutting tool geometry

**Table 6.29.** The ANOVA results for measured surface roughness at hole bottom (Ra) during drilling of extruded CW617N with 90° of plunging angle

| Source | Sum of Squares | df | Mean Square | F-value | p-value | |
|---|---|---|---|---|---|---|
| **Model** | 0.0488 | 6 | 0.0081 | 320.99 | < 0.0001 | significant |
| A-Radial rake angle | 0.0022 | 1 | 0.0022 | 85.9 | < 0.0001 | |
| B-Axial rake angle | 0.0005 | 1 | 0.0005 | 20.61 | 0.0002 | |
| C-Edge radius | 0.0458 | 1 | 0.0458 | 1806.38 | < 0.0001 | |
| AB | 0 | 1 | 0 | 0.8413 | 0.3699 | |
| AC | 0.0003 | 1 | 0.0003 | 10.31 | 0.0044 | |
| BC | 0 | 1 | 0 | 1.89 | 0.1841 | |
| **Residual** | 0.0005 | 20 | 0 | | | |
| **Cor Total** | 0.0493 | 26 | | | | |

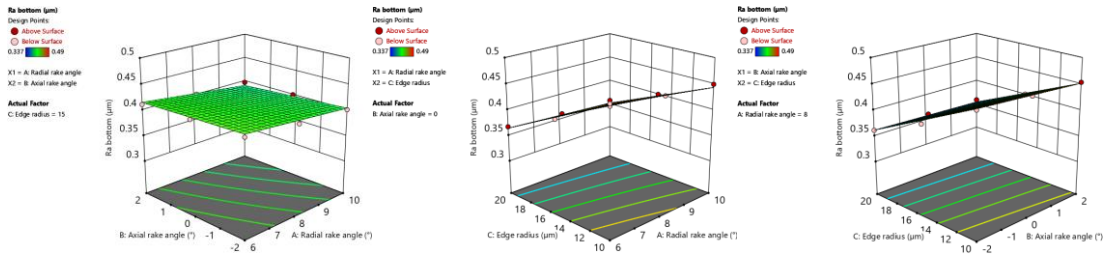

**Figure 6.62.** 3D surface plot of the measured surface roughness at hole bottom (Ra) variation during drilling of extruded CW617N with 90° of plunging angle with respect to the studied cutting tool geometry

**Table 6.30.** The ANOVA results for measured surface roughness at hole wall (Ra) during drilling of extruded CW617N with 90° of plunging angle

| Source | Sum of Squares | df | Mean Square | F-value | p-value | |
|---|---|---|---|---|---|---|
| **Model** | 0.0488 | 6 | 0.0081 | 301 | < 0.0001 | significant |
| A-Radial rake angle | 0.0021 | 1 | 0.0021 | 76.55 | < 0.0001 | |
| B-Axial rake angle | 0.0005 | 1 | 0.0005 | 19.34 | 0.0003 | |
| C-Edge radius | 0.0461 | 1 | 0.0461 | 1705.67 | < 0.0001 | |
| AB | 0 | 1 | 0 | 1.63 | 0.2162 | |
| AC | 0.0001 | 1 | 0.0001 | 2.59 | 0.123 | |
| BC | 5.33E-06 | 1 | 5.33E-06 | 0.1973 | 0.6617 | |
| **Residual** | 0.0005 | 20 | 0 | | | |
| **Cor Total** | 0.0494 | 26 | | | | |

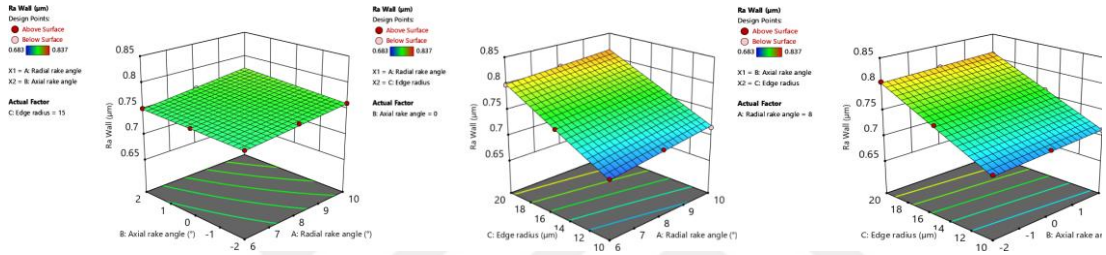

**Figure 6.63.** 3D surface plot of the measured surface roughness at hole wall (Ra) variation during drilling of extruded CW617N with 90° of plunging angle with respect to the studied cutting tool geometry

**Table 6.31.** The ANOVA results for measured diameter variation during drilling of extruded CW617N with 90° of plunging angle

| Source | Sum of Squares | df | Mean Square | F-value | p-value | |
|---|---|---|---|---|---|---|
| **Model** | 0.0113 | 16 | 0.0007 | 13.62 | < 0.0001 | significant |
| A-Radial rake angle | 0.0003 | 1 | 0.0003 | 5.3 | 0.0442 | |
| B-Axial rake angle | 0.0001 | 1 | 0.0001 | 1.7 | 0.2213 | |
| C-Edge radius | 0.001 | 1 | 0.001 | 18.57 | 0.0015 | |
| AB | 0.0001 | 1 | 0.0001 | 2.84 | 0.1227 | |
| AC | 0.0001 | 1 | 0.0001 | 2.45 | 0.1485 | |
| BC | 0.0001 | 1 | 0.0001 | 1.65 | 0.2279 | |
| $A^2$ | 0.0011 | 1 | 0.0011 | 22.02 | 0.0009 | |
| $B^2$ | 0 | 1 | 0 | 0.2238 | 0.6463 | |
| $C^2$ | 0.0009 | 1 | 0.0009 | 16.86 | 0.0021 | |
| ABC | 0.0001 | 1 | 0.0001 | 1.76 | 0.2139 | |
| $A^2B$ | 0.0009 | 1 | 0.0009 | 16.64 | 0.0022 | |
| $A^2C$ | 0.0004 | 1 | 0.0004 | 7.35 | 0.0219 | |
| $AB^2$ | 0 | 1 | 0 | 0.6209 | 0.449 | |
| $AC^2$ | 0.0006 | 1 | 0.0006 | 10.98 | 0.0078 | |
| $B^2C$ | 0.0001 | 1 | 0.0001 | 1.24 | 0.292 | |

| | | | | | |
|---|---|---|---|---|---|
| $BC^2$ | 0.0001 | 1 | 0.0001 | 1.14 | 0.3114 |
| **Residual** | 0.0005 | 10 | 0.0001 | | |
| **Cor Total** | 0.0118 | 26 | | | |

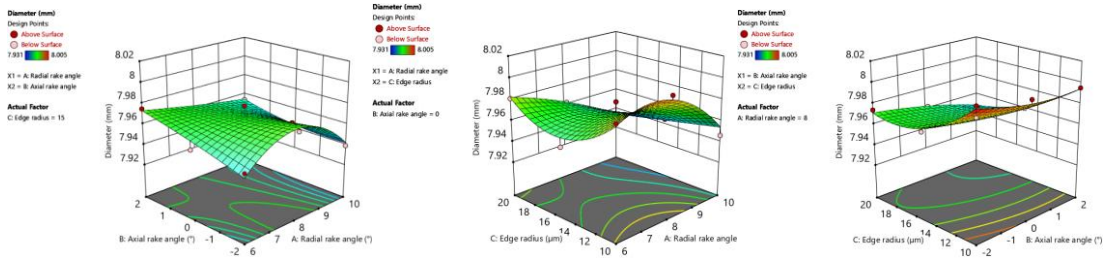

**Figure 6.64.** 3D surface plot of the measured hole diameter variation during drilling of extruded CW617N with 90° of plunging angle with respect to the studied cutting tool geometry

**Table 6.32.** The developed regression model for drilling of extruded CW617N with 90° of plunging angle

| Extruded CW617N 90 | Fx | Fy | Fz | FR | BHEN | BHEX | Ra bottom | Ra Wall | Diameter |
|---|---|---|---|---|---|---|---|---|---|
| | 12.07 | 15.59 | 271.31 | 271.87 | 98.49 | 46.38 | 0.4092 | 0.757 | 7.97 |
| A | 3.89 | 2.4 | -4.87 | -4.98 | 34.52 | 16.89 | -0.011 | 0.0107 | -0.0087 |
| B | 1.72 | 1.85 | -8.21 | -8.02 | -21.35 | -9.08 | -0.0054 | 0.0054 | -0.0049 |
| C | -3.31 | 12.76 | 47.03 | 47.4 | 25.29 | 12.21 | -0.0504 | 0.0506 | -0.0163 |
| AB | 2.2 | -4.32 | 1.91 | 1.59 | -22.96 | -9.18 | -0.0013 | 0.0019 | -0.0035 |
| AC | 0.512 | 1.37 | 1.47 | 1.21 | 1.52 | 1.59 | 0.0047 | -0.0024 | -0.0033 |
| BC | 0.5887 | -1.38 | -1.75 | -1.58 | -10.6 | -2.84 | 0.002 | -0.0007 | -0.0027 |
| $A^2$ | -6.58 | 6.08 | 0 | 0 | 0 | 0 | 0 | 0 | -0.0138 |
| $B^2$ | -2.44 | -11.65 | 0 | 0 | 0 | 0 | 0 | 0 | 0.0014 |
| $C^2$ | -1.6 | -2.07 | 0 | 0 | 0 | 0 | 0 | 0 | 0.0121 |
| ABC | -3.12 | -4.16 | 0 | 0 | 0 | 0 | 0 | 0 | 0.0034 |
| $A^2B$ | 3.16 | 1.94 | 0 | 0 | 0 | 0 | 0 | 0 | 0.0147 |
| $A^2C$ | 5.08 | -4.4 | 0 | 0 | 0 | 0 | 0 | 0 | 0.0098 |
| $AB^2$ | -4.15 | -2.95 | 0 | 0 | 0 | 0 | 0 | 0 | 0.0028 |
| $AC^2$ | -3.04 | -2 | 0 | 0 | 0 | 0 | 0 | 0 | -0.0119 |
| $B^2C$ | 2.13 | -4.07 | 0 | 0 | 0 | 0 | 0 | 0 | -0.004 |
| $BC^2$ | -3.29 | -2.3 | 0 | 0 | 0 | 0 | 0 | 0 | -0.0038 |
| $A^2B^2$ | 4.83 | -0.225 | 0 | 0 | 0 | 0 | 0 | 0 | 0 |
| $A^2BC$ | 1.11 | 1.65 | 0 | 0 | 0 | 0 | 0 | 0 | 0 |
| $A^2C^2$ | 4.78 | -8.83 | 0 | 0 | 0 | 0 | 0 | 0 | 0 |
| $AB^2C$ | -6.25 | -3.08 | 0 | 0 | 0 | 0 | 0 | 0 | 0 |
| $ABC^2$ | -6.01 | 0.622 | 0 | 0 | 0 | 0 | 0 | 0 | 0 |
| $B^2C^2$ | -1.03 | 10.74 | 0 | 0 | 0 | 0 | 0 | 0 | 0 |
| **Regression confidence $R^2$** | 0.904 | 0.854 | 0.978 | 0.978 | 0.908 | 0.948 | 0.989 | 0.989 | 0.956 |

**Table 6.33.** The ANOVA results for measured forces in X direction (Fx) during drilling of extruded CW617N with 60° of plunging angle

| Source | Sum of Squares | df | Mean Square | F-value | p-value | |
|---|---|---|---|---|---|---|
| **Model** | 30559 | 6 | 5093.16 | 88.72 | < 0.0001 | significant |
| A-Radial rake angle | 20.69 | 1 | 20.69 | 0.3605 | 0.555 | |
| B-Axial rake angle | 64.79 | 1 | 64.79 | 1.13 | 0.3007 | |
| C-Edge radius | 30244.9 | 1 | 30244.9 | 526.88 | < 0.0001 | |
| AB | 3.35 | 1 | 3.35 | 0.0584 | 0.8116 | |
| AC | 126.36 | 1 | 126.36 | 2.2 | 0.1535 | |
| BC | 98.9 | 1 | 98.9 | 1.72 | 0.2042 | |
| **Residual** | 1148.08 | 20 | 57.4 | | | |
| **Cor Total** | 31707.1 | 26 | | | | |

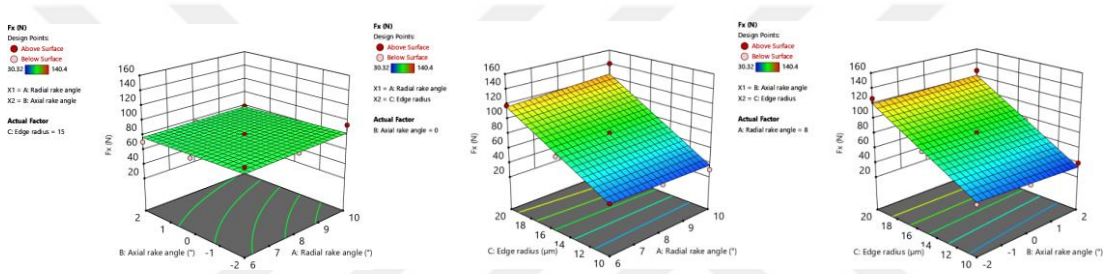

**Figure 6.65.** 3D surface plot of the measured forces in X direction (Fx) variation during drilling of extruded CW617N with 60° of plunging angle with respect to the studied cutting tool geometry

**Table 6.34.** The ANOVA results for measured forces in Y direction (Fy) during drilling of extruded CW617N with 60° of plunging angle

| Source | Sum of Squares | df | Mean Square | F-value | p-value | |
|---|---|---|---|---|---|---|
| **Model** | 13159.5 | 9 | 1462.16 | 67.05 | < 0.0001 | significant |
| A-Radial rake angle | 276.12 | 1 | 276.12 | 12.66 | 0.0024 | |
| B-Axial rake angle | 204.29 | 1 | 204.29 | 9.37 | 0.0071 | |
| C-Edge radius | 11901.7 | 1 | 11901.7 | 545.77 | < 0.0001 | |
| AB | 7.6 | 1 | 7.6 | 0.3485 | 0.5627 | |
| AC | 7.22 | 1 | 7.22 | 0.3312 | 0.5725 | |
| BC | 154.87 | 1 | 154.87 | 7.1 | 0.0163 | |
| $A^2$ | 26.32 | 1 | 26.32 | 1.21 | 0.2873 | |
| $B^2$ | 7.03 | 1 | 7.03 | 0.3222 | 0.5777 | |
| $C^2$ | 574.35 | 1 | 574.35 | 26.34 | < 0.0001 | |
| **Residual** | 370.72 | 17 | 21.81 | | | |
| **Cor Total** | 13530.2 | 26 | | | | |

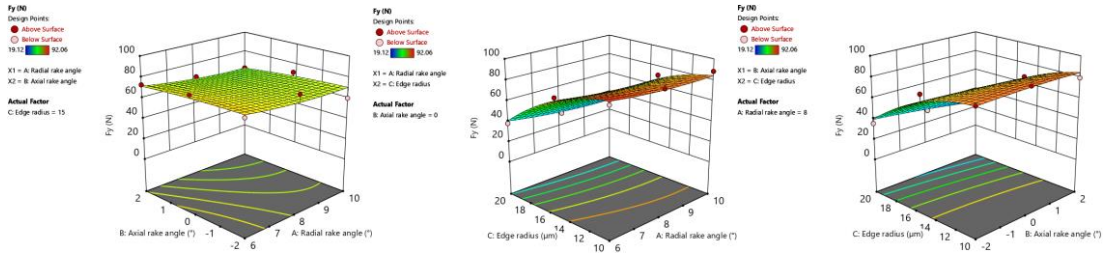

**Figure 6.66.** 3D surface plot of the measured forces in Y direction (Fy) variation during drilling of extruded CW617N with 60° of plunging angle with respect to the studied cutting tool geometry

**Table 6.35.** The ANOVA results for measured forces in Z direction (Fz) during drilling of extruded CW617N with 60° of plunging angle

| Source | Sum of Squares | df | Mean Square | F-value | p-value | |
|---|---|---|---|---|---|---|
| **Model** | 1.03E+05 | 9 | 11406.1 | 488.65 | < 0.0001 | significant |
| A-Radial rake angle | 832.32 | 1 | 832.32 | 35.66 | < 0.0001 | |
| B-Axial rake angle | 1078.03 | 1 | 1078.03 | 46.18 | < 0.0001 | |
| C-Edge radius | 97637.81 | 1 | 97637.8 | 4182.93 | < 0.0001 | |
| AB | 1.92 | 1 | 1.92 | 0.0823 | 0.7777 | |
| AC | 333.91 | 1 | 333.91 | 14.31 | 0.0015 | |
| BC | 36.75 | 1 | 36.75 | 1.57 | 0.2265 | |
| $A^2$ | 74.91 | 1 | 74.91 | 3.21 | 0.091 | |
| $B^2$ | 1.04 | 1 | 1.04 | 0.0446 | 0.8352 | |
| $C^2$ | 2658.61 | 1 | 2658.61 | 113.9 | < 0.0001 | |
| **Residual** | 396.81 | 17 | 23.34 | | | |
| **Cor Total** | 1.03E+05 | 26 | | | | |

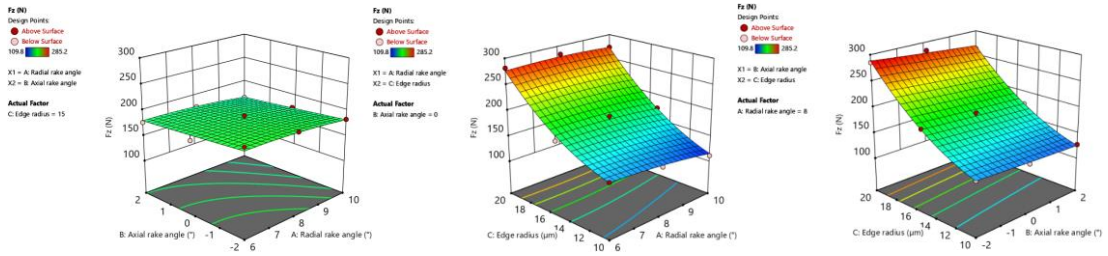

**Figure 6.67.** 3D surface plot of the measured forces in Z direction (Fz) variation during drilling of extruded CW617N with 60° of plunging angle with respect to the studied cutting tool geometry

**Table 6.36.** The ANOVA results for measured resultant forces (FR) during drilling of extruded CW617N with 60° of plunging angle

| Source | Sum of Squares | df | Mean Square | F-value | p-value |
|---|---|---|---|---|---|

| | | | | | | |
|---|---|---|---|---|---|---|
| **Model** | 98119.03 | 9 | 10902.1 | 418.25 | < 0.0001 | significant |
| A-Radial rake angle | 684.31 | 1 | 684.31 | 26.25 | < 0.0001 | |
| B-Axial rake angle | 1132.54 | 1 | 1132.54 | 43.45 | < 0.0001 | |
| C-Edge radius | 93115.88 | 1 | 93115.9 | 3572.29 | < 0.0001 | |
| AB | 2.51 | 1 | 2.51 | 0.0962 | 0.7602 | |
| AC | 384.79 | 1 | 384.79 | 14.76 | 0.0013 | |
| BC | 17.67 | 1 | 17.67 | 0.6777 | 0.4218 | |
| $A^2$ | 31.92 | 1 | 31.92 | 1.22 | 0.2839 | |
| $B^2$ | 0.2451 | 1 | 0.2451 | 0.0094 | 0.9239 | |
| $C^2$ | 2749.18 | 1 | 2749.18 | 105.47 | < 0.0001 | |
| **Residual** | 443.13 | 17 | 26.07 | | | |
| **Cor Total** | 98562.16 | 26 | | | | |

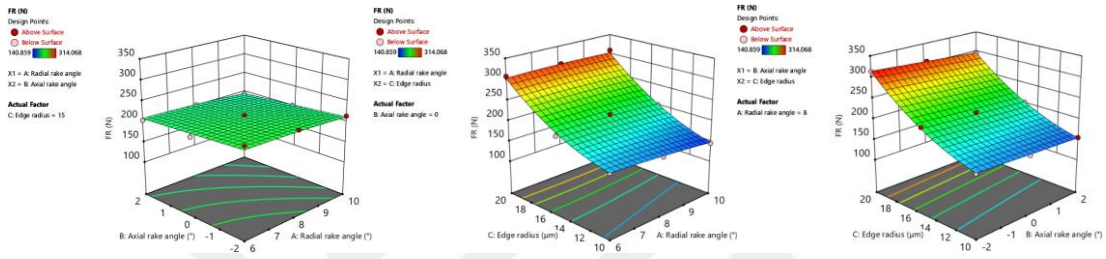

**Figure 6.68.** 3D surface plot of the measured resultant forces variation during drilling of extruded CW617N with 60° of plunging angle with respect to the studied cutting tool geometry

**Table 6.37.** The ANOVA results for measured burr heights at hole entry (BHEN) during drilling of extruded CW617N with 60° of plunging angle

| Source | Sum of Squares | df | Mean Square | F-value | p-value | |
|---|---|---|---|---|---|---|
| **Model** | 68919.65 | 9 | 7657.74 | 95.73 | < 0.0001 | significant |
| A-Radial rake angle | 33475.42 | 1 | 33475.4 | 418.49 | < 0.0001 | |
| B-Axial rake angle | 7493.46 | 1 | 7493.46 | 93.68 | < 0.0001 | |
| C-Edge radius | 20156.83 | 1 | 20156.8 | 251.99 | < 0.0001 | |
| AB | 5406.23 | 1 | 5406.23 | 67.59 | < 0.0001 | |
| AC | 714.17 | 1 | 714.17 | 8.93 | 0.0083 | |
| BC | 527.82 | 1 | 527.82 | 6.6 | 0.0199 | |
| $A^2$ | 1030.83 | 1 | 1030.83 | 12.89 | 0.0023 | |
| $B^2$ | 6.07 | 1 | 6.07 | 0.0758 | 0.7864 | |
| $C^2$ | 108.82 | 1 | 108.82 | 1.36 | 0.2596 | |
| **Residual** | 1359.83 | 17 | 79.99 | | | |
| **Cor Total** | 70279.48 | 26 | | | | |

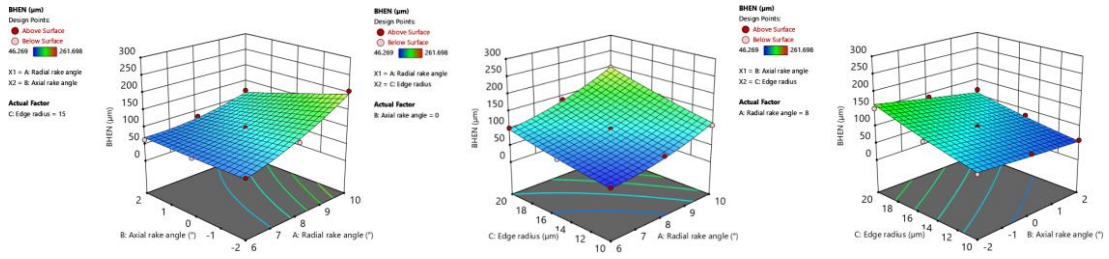

**Figure 6.69.** 3D surface plot of the measured burr heights at hole entry (BHEN) variation during drilling of extruded CW617N with 60° of plunging angle with respect to the studied cutting tool geometry

**Table 6.38.** The ANOVA results for measured burr heights at hole exit (BHEX) during drilling of extruded CW617N with 60° of plunging angle

| Source | Sum of Squares | df | Mean Square | F-value | p-value | |
|---|---|---|---|---|---|---|
| **Model** | 6972.91 | 9 | 774.77 | 63.05 | < 0.0001 | significant |
| A-Radial rake angle | 3873.74 | 1 | 3873.74 | 315.23 | < 0.0001 | |
| B-Axial rake angle | 518.38 | 1 | 518.38 | 42.18 | < 0.0001 | |
| C-Edge radius | 2102.96 | 1 | 2102.96 | 171.13 | < 0.0001 | |
| AB | 179.39 | 1 | 179.39 | 14.6 | 0.0014 | |
| AC | 138.61 | 1 | 138.61 | 11.28 | 0.0037 | |
| BC | 23.97 | 1 | 23.97 | 1.95 | 0.1805 | |
| $A^2$ | 117.31 | 1 | 117.31 | 9.55 | 0.0066 | |
| $B^2$ | 5.5 | 1 | 5.5 | 0.4472 | 0.5126 | |
| $C^2$ | 13.04 | 1 | 13.04 | 1.06 | 0.3174 | |
| **Residual** | 208.91 | 17 | 12.29 | | | |
| **Cor Total** | 7181.82 | 26 | | | | |

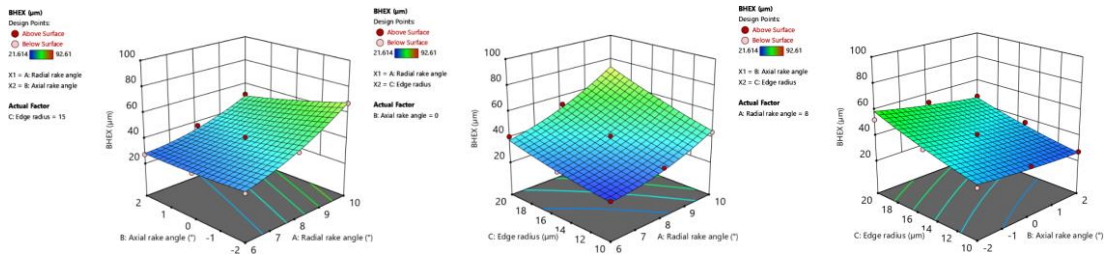

**Figure 6.70.** 3D surface plot of the measured burr heights at hole exit (BHEX) variation during drilling of extruded CW617N with 60° of plunging angle with respect to the studied cutting tool geometry

**Table 6.39.** The ANOVA results for measured surface roughness at hole bottom (Ra) during drilling of extruded CW617N with 60° of plunging angle

| Source | Sum of Squares | df | Mean Square | F-value | p-value | |
|---|---|---|---|---|---|---|
| **Model** | 0.0387 | 6 | 0.0064 | 322.74 | < 0.0001 | significant |

| | | | | | |
|---|---|---|---|---|---|
| A-Radial rake angle | 0.0017 | 1 | 0.0017 | 87.09 | < 0.0001 |
| B-Axial rake angle | 0.0004 | 1 | 0.0004 | 21.04 | 0.0002 |
| C-Edge radius | 0.0363 | 1 | 0.0363 | 1814.94 | < 0.0001 |
| AB | 0 | 1 | 0 | 0.7047 | 0.4111 |
| AC | 0.0002 | 1 | 0.0002 | 10.42 | 0.0042 |
| BC | 0 | 1 | 0 | 2.21 | 0.1531 |
| **Residual** | 0.0004 | 20 | 0 | | |
| **Cor Total** | 0.0391 | 26 | | | |

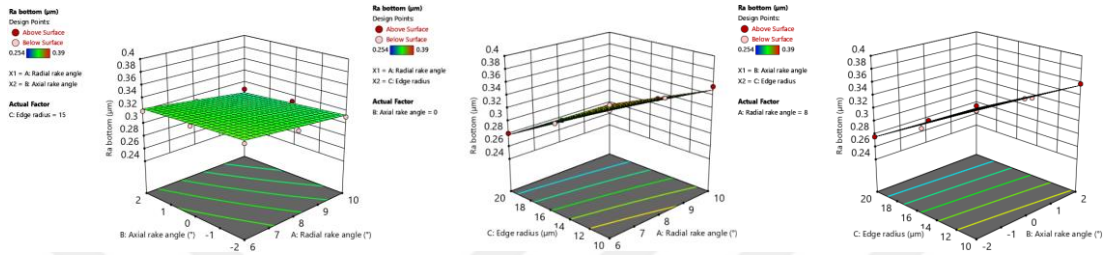

**Figure 6.71.** 3D surface plot of the measured surface roughness at hole bottom (Ra) variation during drilling of extruded CW617N with 60° of plunging angle with respect to the studied cutting tool geometry

**Table 6.40.** The ANOVA results for measured surface roughness at hole wall (Ra) during drilling of extruded CW617N with 60° of plunging angle

| Source | Sum of Squares | df | Mean Square | F-value | p-value | |
|---|---|---|---|---|---|---|
| **Model** | 0.0347 | 6 | 0.0058 | 281.86 | < 0.0001 | significant |
| A-Radial rake angle | 0.0014 | 1 | 0.0014 | 70.12 | < 0.0001 | |
| B-Axial rake angle | 0.0004 | 1 | 0.0004 | 17.75 | 0.0004 | |
| C-Edge radius | 0.0329 | 1 | 0.0329 | 1599.82 | < 0.0001 | |
| AB | 0 | 1 | 0 | 1.79 | 0.196 | |
| AC | 0 | 1 | 0 | 1.62 | 0.2173 | |
| BC | 1.33E-06 | 1 | 1.333E-06 | 0.0649 | 0.8015 | |
| **Residual** | 0.0004 | 20 | 0 | | | |
| **Cor Total** | 0.0351 | 26 | | | | |

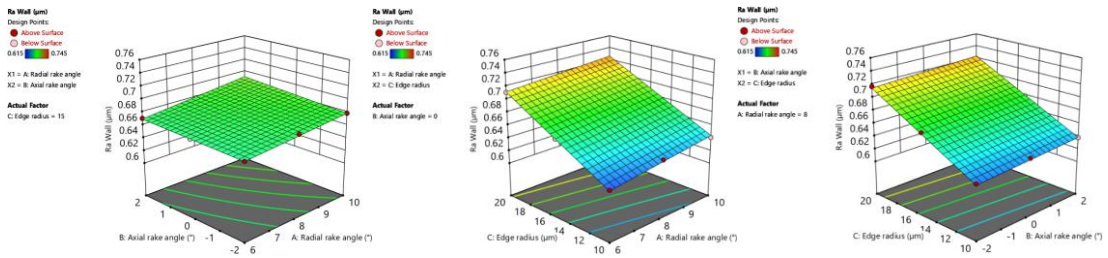

**Figure 6.72.** 3D surface plot of the measured surface roughness at hole wall (Ra) variation during drilling of extruded CW617N with 60° of plunging angle with respect to the studied cutting tool geometry

**Table 6.41.** The ANOVA results for measured hole diameter during drilling of extruded CW617N with 60° of plunging angle

| Source | Sum of Squares | df | Mean Square | F-value | p-value | |
|---|---|---|---|---|---|---|
| **Model** | 0.0093 | 16 | 0.0006 | 3.25 | 0.032 | significant |
| A-Radial rake angle | 0.0003 | 1 | 0.0003 | 1.59 | 0.2353 | |
| B-Axial rake angle | 2.84E-06 | 1 | 2.844E-06 | 0.0159 | 0.902 | |
| C-Edge radius | 0.0001 | 1 | 0.0001 | 0.3598 | 0.562 | |
| AB | 0.0006 | 1 | 0.0006 | 3.22 | 0.103 | |
| AC | 0.0001 | 1 | 0.0001 | 0.6747 | 0.4306 | |
| BC | 0.0005 | 1 | 0.0005 | 2.84 | 0.1227 | |
| $A^2$ | 0.0036 | 1 | 0.0036 | 20.19 | 0.0012 | |
| $B^2$ | 0.0001 | 1 | 0.0001 | 0.584 | 0.4624 | |
| $C^2$ | 0 | 1 | 0 | 0.1831 | 0.6778 | |
| ABC | 0 | 1 | 0 | 0.2025 | 0.6623 | |
| $A^2B$ | 0.001 | 1 | 0.001 | 5.8 | 0.0368 | |
| $A^2C$ | 0.0002 | 1 | 0.0002 | 1.32 | 0.2776 | |
| $AB^2$ | 0.0001 | 1 | 0.0001 | 0.7851 | 0.3964 | |
| $AC^2$ | 0.0001 | 1 | 0.0001 | 0.6379 | 0.443 | |
| $B^2C$ | 0.0005 | 1 | 0.0005 | 2.63 | 0.1358 | |
| $BC^2$ | 0.0006 | 1 | 0.0006 | 3.6 | 0.0871 | |
| **Residual** | 0.0018 | 10 | 0.0002 | | | |
| **Cor Total** | 0.0111 | 26 | | | | |

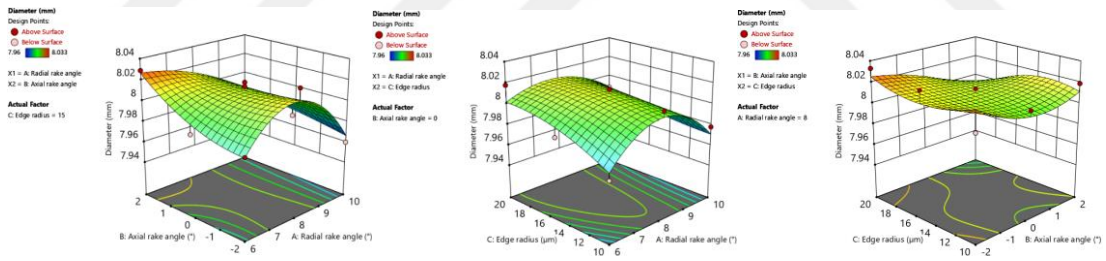


**Figure 6.73.** 3D surface plot of the measured hole diameter variation during drilling of extruded CW617N with 60° of plunging angle with respect to the studied cutting tool geometry

**Table 6.42.** The developed regression model for drilling of extruded CW617N with 60° of plunging angle

| Extruded CW617N 60 | Fx | Fy | Fz | FR | BHEN | BHEX | Ra bottom | Ra Wall | Diameter |
|---|---|---|---|---|---|---|---|---|---|
| | 79.74 | 69.31 | 183.66 | 211.84 | 98.04 | 38.86 | 0.3179 | 0.6762 | 8.01 |
| A | 1.07 | -3.92 | -6.8 | -6.17 | 43.12 | 14.67 | -0.0098 | 0.0089 | -0.0089 |
| B | -1.9 | -3.37 | -7.74 | -7.93 | -20.4 | -5.37 | -0.0048 | 0.0045 | -0.0009 |
| C | 40.99 | -25.71 | 73.65 | 71.92 | 33.46 | 10.81 | -0.0449 | 0.0427 | 0.0042 |
| AB | -0.5283 | -0.7958 | -0.4 | -0.4572 | -21.23 | -3.87 | -0.0011 | 0.0017 | -0.0069 |

| | | | | | | | | | |
|---|---|---|---|---|---|---|---|---|---|
| AC | 3.24 | -0.7758 | 5.27 | 5.66 | 7.71 | 3.4 | 0.0042 | -0.0017 | -0.0032 |
| BC | 2.87 | -3.59 | -1.75 | -1.21 | -6.63 | -1.41 | 0.0019 | -0.0003 | -0.0065 |
| $A^2$ | 0 | 2.09 | -3.53 | -2.31 | 13.11 | 4.42 | 0 | 0 | -0.0245 |
| $B^2$ | 0 | -1.08 | 0.4167 | 0.2021 | 1.01 | 0.9571 | 0 | 0 | 0.0042 |
| $C^2$ | 0 | -9.78 | 21.05 | 21.41 | 4.26 | 1.47 | 0 | 0 | -0.0023 |
| ABC | 0 | 0 | 0 | 0 | 0 | 0 | 0 | 0 | -0.0021 |
| $A^2B$ | 0 | 0 | 0 | 0 | 0 | 0 | 0 | 0 | 0.0161 |
| $A^2C$ | 0 | 0 | 0 | 0 | 0 | 0 | 0 | 0 | 0.0077 |
| $AB^2$ | 0 | 0 | 0 | 0 | 0 | 0 | 0 | 0 | -0.0059 |
| $AC^2$ | 0 | 0 | 0 | 0 | 0 | 0 | 0 | 0 | 0.0053 |
| $B^2C$ | 0 | 0 | 0 | 0 | 0 | 0 | 0 | 0 | -0.0108 |
| $BC^2$ | 0 | 0 | 0 | 0 | 0 | 0 | 0 | 0 | -0.0127 |
| **Regression confidence $R^2$** | 0.963 | 0.972 | 0.996 | 0.995 | 0.98 | 0.97 | 0.989 | 0.988 | 0.838 |

**Table 6.43.** The ANOVA results for measured forces in X direction (Fx) during drilling of extruded CW617N with 45° of plunging angle

| Source | Sum of Squares | df | Mean Square | F-value | p-value | |
|---|---|---|---|---|---|---|
| **Model** | 37919.9 | 6 | 6319.98 | 61.89 | < 0.0001 | significant |
| A-Radial rake angle | 124.14 | 1 | 124.14 | 1.22 | 0.2833 | |
| B-Axial rake angle | 28.18 | 1 | 28.18 | 0.2759 | 0.6052 | |
| C-Edge radius | 37531.61 | 1 | 37531.6 | 367.55 | < 0.0001 | |
| AB | 7.33 | 1 | 7.33 | 0.0718 | 0.7915 | |
| AC | 100.86 | 1 | 100.86 | 0.9877 | 0.3322 | |
| BC | 127.79 | 1 | 127.79 | 1.25 | 0.2765 | |
| **Residual** | 2042.29 | 20 | 102.11 | | | |
| **Cor Total** | 39962.19 | 26 | | | | |

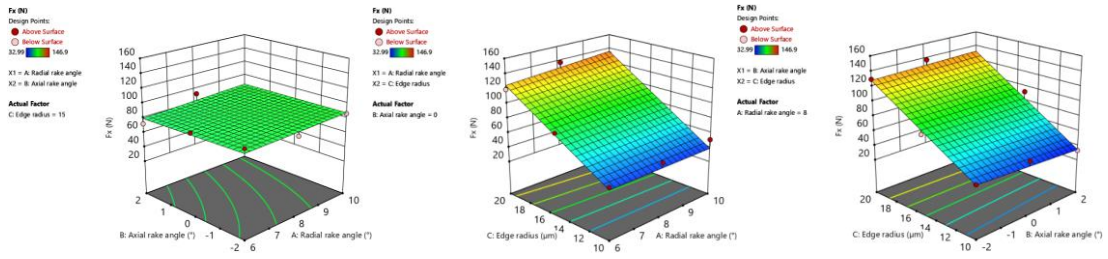

**Figure 6.74.** 3D surface plot of the measured forces in X direction (Fx) variation during drilling of extruded CW617N with 45° of plunging angle with respect to the studied cutting tool geometry

**Table 6.44.** The ANOVA results for measured forces in Y direction (Fy) during drilling of extruded CW617N with 45° of plunging angle

| Source | Sum of Squares | df | Mean Square | F-value | p-value | |
|---|---|---|---|---|---|---|
| **Model** | 7021.48 | 9 | 780.16 | 10.45 | < 0.0001 | significant |

| | | | | | |
|---|---|---|---|---|---|
| A-Radial rake angle | 1075.86 | 1 | 1075.86 | 14.41 | 0.0014 |
| B-Axial rake angle | 587.67 | 1 | 587.67 | 7.87 | 0.0122 |
| C-Edge radius | 4883.03 | 1 | 4883.03 | 65.41 | < 0.0001 |
| AB | 11.19 | 1 | 11.19 | 0.15 | 0.7034 |
| AC | 2.45 | 1 | 2.45 | 0.0328 | 0.8584 |
| BC | 101.79 | 1 | 101.79 | 1.36 | 0.259 |
| $A^2$ | 9.85 | 1 | 9.85 | 0.1319 | 0.7209 |
| $B^2$ | 262.11 | 1 | 262.11 | 3.51 | 0.0782 |
| $C^2$ | 87.53 | 1 | 87.53 | 1.17 | 0.294 |
| **Residual** | 1269.02 | 17 | 74.65 | | |
| **Cor Total** | 8290.5 | 26 | | | |

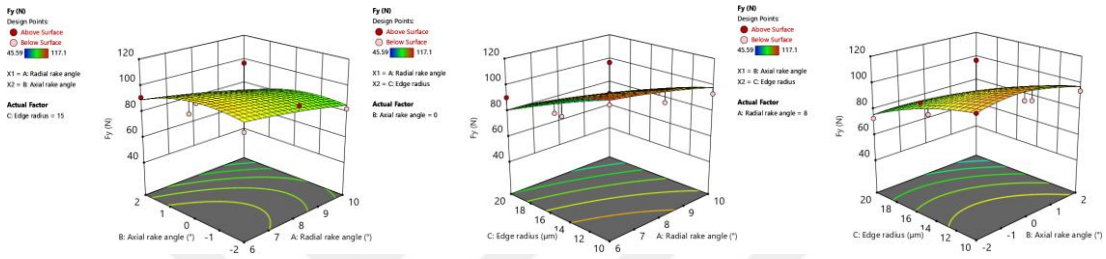

**Figure 6.75.** 3D surface plot of the measured forces in Y direction (Fy) variation during drilling of extruded CW617N with 45° of plunging angle with respect to the studied cutting tool geometry

**Table 6.45.** The ANOVA results for measured forces in Z direction (Fz) during drilling of extruded CW617N with 45° of plunging angle

| Source | Sum of Squares | df | Mean Square | F-value | p-value | |
|---|---|---|---|---|---|---|
| **Model** | 1.45E+05 | 9 | 16116.6 | 460.69 | < 0.0001 | significant |
| A-Radial rake angle | 252.45 | 1 | 252.45 | 7.22 | 0.0156 | |
| B-Axial rake angle | 1538.46 | 1 | 1538.46 | 43.98 | < 0.0001 | |
| C-Edge radius | 1.41E+05 | 1 | 1.41E+05 | 4018.8 | < 0.0001 | |
| AB | 95.15 | 1 | 95.15 | 2.72 | 0.1175 | |
| AC | 276.58 | 1 | 276.58 | 7.91 | 0.012 | |
| BC | 36.02 | 1 | 36.02 | 1.03 | 0.3245 | |
| $A^2$ | 3.32 | 1 | 3.32 | 0.0949 | 0.7618 | |
| $B^2$ | 1.44 | 1 | 1.44 | 0.0411 | 0.8418 | |
| $C^2$ | 2252.86 | 1 | 2252.86 | 64.4 | < 0.0001 | |
| **Residual** | 594.73 | 17 | 34.98 | | | |
| **Cor Total** | 1.46E+05 | 26 | | | | |

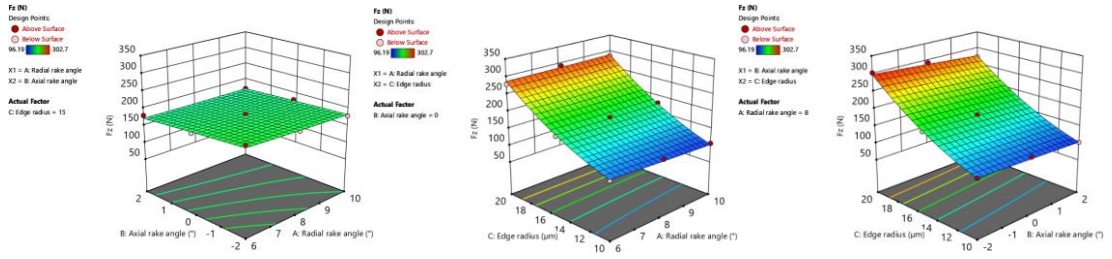

**Figure 6.76.** 3D surface plot of the measured forces in Z direction (Fz) variation during drilling of extruded CW617N with 45° of plunging angle with respect to the studied cutting tool geometry

**Table 6.46.** The ANOVA results for measured resultant forces (FR) during drilling of extruded CW617N with 45° of plunging angle

| Source | Sum of Squares | df | Mean Square | F-value | p-value | |
|---|---|---|---|---|---|---|
| **Model** | 1.34E+05 | 9 | 14843.48 | 467.38 | < 0.0001 | significant |
| A-Radial rake angle | 446.3 | 1 | 446.3 | 14.05 | 0.0016 | |
| B-Axial rake angle | 1715.26 | 1 | 1715.26 | 54.01 | < 0.0001 | |
| C-Edge radius | 1.28E+05 | 1 | 1.28E+05 | 4014.73 | < 0.0001 | |
| AB | 57.94 | 1 | 57.94 | 1.82 | 0.1945 | |
| AC | 501.63 | 1 | 501.63 | 15.8 | 0.001 | |
| BC | 14.81 | 1 | 14.81 | 0.4663 | 0.5039 | |
| $A^2$ | 10.94 | 1 | 10.94 | 0.3443 | 0.5651 | |
| $B^2$ | 11.07 | 1 | 11.07 | 0.3487 | 0.5626 | |
| $C^2$ | 3330.66 | 1 | 3330.66 | 104.87 | < 0.0001 | |
| **Residual** | 539.9 | 17 | 31.76 | | | |
| **Cor Total** | 1.34E+05 | 26 | | | | |

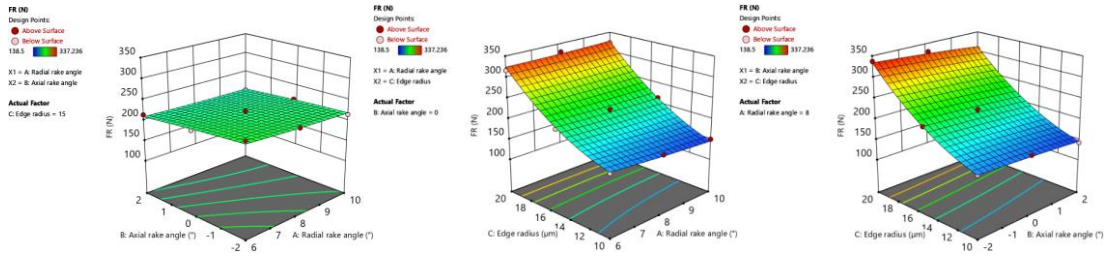

**Figure 6.77.** 3D surface plot of the measured resultant forces variation during drilling of extruded CW617N with 45° of plunging angle with respect to the studied cutting tool geometry

**Table 6.47.** The ANOVA results for measured burr heights at hole entry (BHEN) during drilling of extruded CW617N with 45° of plunging angle

| Source | Sum of Squares | df | Mean Square | F-value | p-value | |
|---|---|---|---|---|---|---|
| **Model** | 15863.03 | 9 | 1762.56 | 149.46 | < 0.0001 | significant |

| | | | | | |
|---|---|---|---|---|---|
| A-Radial rake angle | 8092.27 | 1 | 8092.27 | 686.21 | < 0.0001 |
| B-Axial rake angle | 1488.26 | 1 | 1488.26 | 126.2 | < 0.0001 |
| C-Edge radius | 4722.05 | 1 | 4722.05 | 400.42 | < 0.0001 |
| AB | 911.72 | 1 | 911.72 | 77.31 | < 0.0001 |
| AC | 247.22 | 1 | 247.22 | 20.96 | 0.0003 |
| BC | 48.86 | 1 | 48.86 | 4.14 | 0.0577 |
| $A^2$ | 298.12 | 1 | 298.12 | 25.28 | 0.0001 |
| $B^2$ | 10.17 | 1 | 10.17 | 0.8626 | 0.366 |
| $C^2$ | 44.36 | 1 | 44.36 | 3.76 | 0.0692 |
| **Residual** | 200.48 | 17 | 11.79 | | |
| **Cor Total** | 16063.5 | 26 | | | |

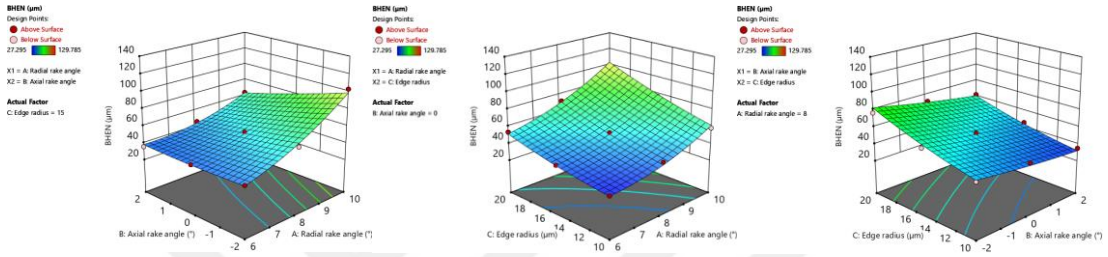

**Figure 6.78.** 3D surface plot of the measured burr heights at hole entry (BHEN) variation during drilling of extruded CW617N with 45° of plunging angle with respect to the studied cutting tool geometry

**Table 6.48.** The ANOVA results for measured burr heights at hole exit (BHEX) during drilling of extruded CW617N with 45° of plunging angle

| Source | Sum of Squares | df | Mean Square | F-value | p-value | |
|---|---|---|---|---|---|---|
| **Model** | 1754.23 | 6 | 292.37 | 44.97 | < 0.0001 | significant |
| A-Radial rake angle | 893.56 | 1 | 893.56 | 137.45 | < 0.0001 | |
| B-Axial rake angle | 123.16 | 1 | 123.16 | 18.95 | 0.0003 | |
| C-Edge radius | 644.94 | 1 | 644.94 | 99.21 | < 0.0001 | |
| AB | 49.48 | 1 | 49.48 | 7.61 | 0.0121 | |
| AC | 34 | 1 | 34 | 5.23 | 0.0332 | |
| BC | 9.08 | 1 | 9.08 | 1.4 | 0.2512 | |
| **Residual** | 130.02 | 20 | 6.5 | | | |
| **Cor Total** | 1884.24 | 26 | | | | |

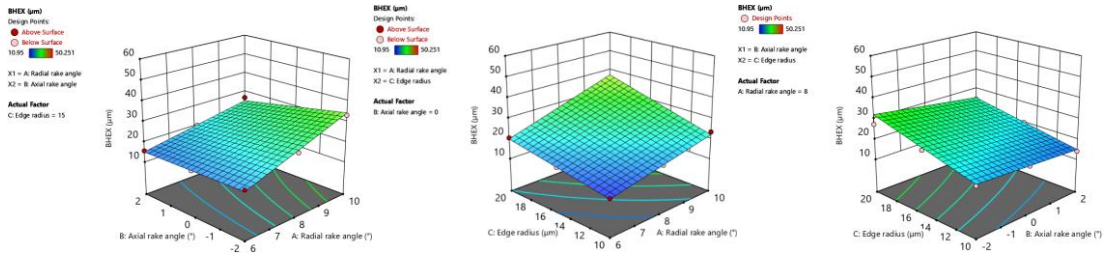

**Figure 6.79.** 3D surface plot of the measured burr heights at hole exit (BHEX) variation

during drilling of extruded CW617N with 45° of plunging angle with respect to the studied cutting tool geometry

**Table 6.49.** The ANOVA results for measured surface roughness at hole bottom (Ra) during drilling of extruded CW617N with 45° of plunging angle

| Source | Sum of Squares | df | Mean Square | F-value | p-value | |
|---|---|---|---|---|---|---|
| **Model** | 0.0175 | 6 | 0.0029 | 347.92 | < 0.0001 | significant |
| A-Radial rake angle | 0.0008 | 1 | 0.0008 | 94 | < 0.0001 | |
| B-Axial rake angle | 0.0002 | 1 | 0.0002 | 22.33 | 0.0001 | |
| C-Edge radius | 0.0164 | 1 | 0.0164 | 1957.18 | < 0.0001 | |
| AB | 0 | 1 | 0 | 1.2 | 0.2854 | |
| AC | 0.0001 | 1 | 0.0001 | 10.84 | 0.0036 | |
| BC | 0 | 1 | 0 | 1.95 | 0.1777 | |
| **Residual** | 0.0002 | 20 | 8.37E-06 | | | |
| **Cor Total** | 0.0176 | 26 | | | | |

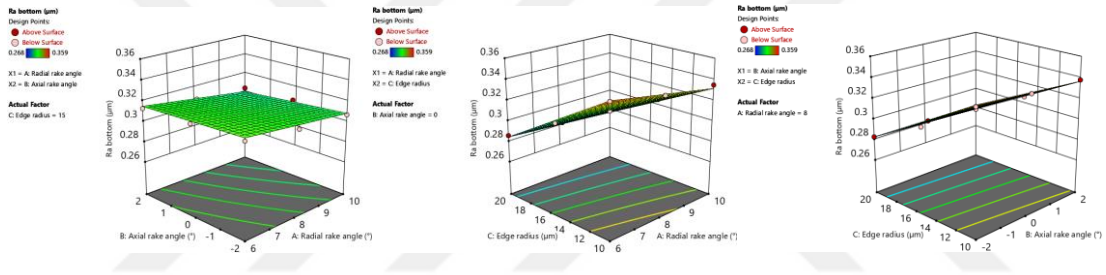

**Figure 6.80.** 3D surface plot of the measured surface roughness at hole bottom (Ra) variation during drilling of extruded CW617N with 45° of plunging angle with respect to the studied cutting tool geometry

**Table 6.50.** The ANOVA results for measured surface roughness at hole wall (Ra) during drilling of extruded CW617N with 45° of plunging angle

| Source | Sum of Squares | df | Mean Square | F-value | p-value | |
|---|---|---|---|---|---|---|
| **Model** | 0.033 | 6 | 0.0055 | 336.59 | < 0.0001 | significant |
| A-Radial rake angle | 0.0014 | 1 | 0.0014 | 84.85 | < 0.0001 | |
| B-Axial rake angle | 0.0003 | 1 | 0.0003 | 20.68 | 0.0002 | |
| C-Edge radius | 0.0312 | 1 | 0.0312 | 1906.87 | < 0.0001 | |
| AB | 0 | 1 | 0 | 1.47 | 0.2389 | |
| AC | 0.0001 | 1 | 0.0001 | 4.9 | 0.0386 | |
| BC | 0 | 1 | 0 | 0.7342 | 0.4017 | |
| **Residual** | 0.0003 | 20 | 0 | | | |
| **Cor Total** | 0.0333 | 26 | | | | |

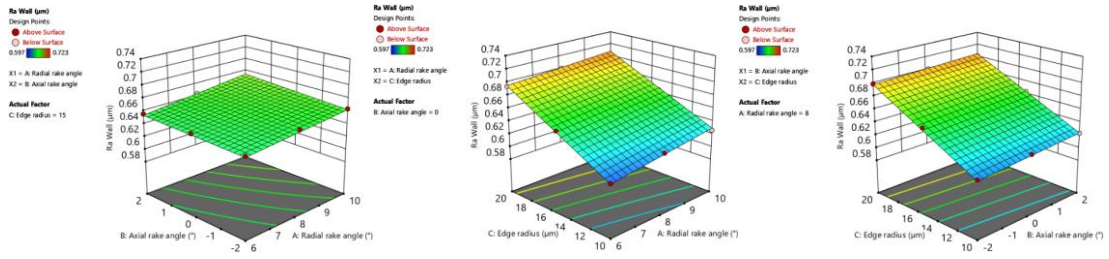

**Figure 6.81.** 3D surface plot of the measured surface roughness at hole wall (Ra) variation during drilling of extruded CW617N with 45° of plunging angle with respect to the studied cutting tool geometry

**Table 6.51.** The ANOVA results for measured hole diameter during drilling of extruded CW617N with 45° of plunging angle

| Source | Sum of Squares | df | Mean Square | F-value | p-value | |
|---|---|---|---|---|---|---|
| **Model** | 0.0113 | 9 | 0.0013 | 7.71 | 0.0002 | significant |
| A-Radial rake angle | 0.0008 | 1 | 0.0008 | 4.82 | 0.0423 | |
| B-Axial rake angle | 0.0002 | 1 | 0.0002 | 0.9199 | 0.3509 | |
| C-Edge radius | 0.0028 | 1 | 0.0028 | 17.22 | 0.0007 | |
| AB | 0.0003 | 1 | 0.0003 | 1.66 | 0.2151 | |
| AC | 0.0003 | 1 | 0.0003 | 1.6 | 0.2229 | |
| BC | 4.08E-06 | 1 | 4.08E-06 | 0.025 | 0.8762 | |
| $A^2$ | 0.0058 | 1 | 0.0058 | 35.69 | < 0.0001 | |
| $B^2$ | 0.0001 | 1 | 0.0001 | 0.4083 | 0.5314 | |
| $C^2$ | 0.0011 | 1 | 0.0011 | 7.03 | 0.0168 | |
| **Residual** | 0.0028 | 17 | 0.0002 | | | |
| **Cor Total** | 0.0141 | 26 | | | | |

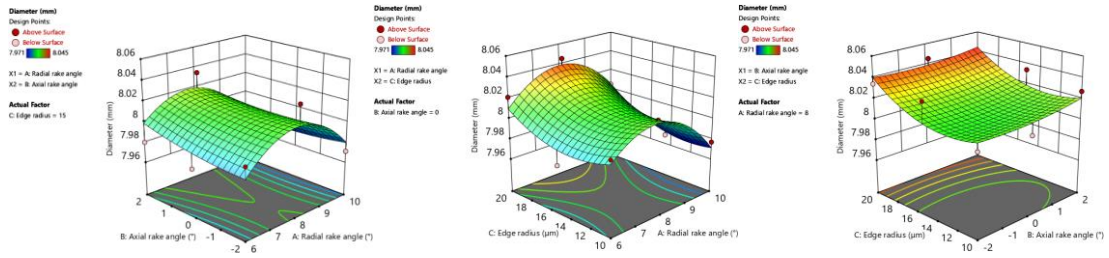

**Figure 6.82.** 3D surface plot of the measured hole diameter variation during drilling of extruded CW617N with 45° of plunging angle with respect to the studied cutting tool geometry

**Table 6.52.** The developed regression model for drilling of extruded CW617N with 45° of plunging angle

| Extruded CW617N 45 | Fx | Fy | Fz | FR | BHEN | BHEX | Ra bottom | Ra Wall | Diameter |
|---|---|---|---|---|---|---|---|---|---|
| | 84.4 | 94.2 | 179.73 | 216.63 | 51.29 | 22.69 | 0.3109 | 0.6598 | 8.01 |

| | | | | | | | | | |
|---|---|---|---|---|---|---|---|---|---|
| A | 2.63 | -7.73 | -3.74 | -4.98 | 21.2 | 7.05 | -0.0066 | 0.0088 | -0.0066 |
| B | -1.25 | -5.71 | -9.24 | -9.76 | -9.09 | -2.62 | -0.0032 | 0.0043 | 0.0029 |
| C | 45.66 | -16.47 | 88.38 | 84.16 | 16.2 | 5.99 | -0.0302 | 0.0416 | 0.0125 |
| AB | 0.7817 | -0.9658 | 2.82 | 2.2 | -8.72 | -2.03 | -0.0009 | 0.0014 | -0.0048 |
| AC | 2.9 | -0.4517 | 4.8 | 6.47 | 4.54 | 1.68 | 0.0027 | -0.0026 | 0.0047 |
| BC | 3.26 | -2.91 | -1.73 | -1.11 | -2.02 | -0.8697 | 0.0012 | -0.001 | -0.0006 |
| $A^2$ | 0 | -1.28 | 0.7439 | 1.35 | 7.05 | 0 | 0 | 0 | -0.0312 |
| $B^2$ | 0 | -6.61 | -0.4894 | -1.36 | 1.3 | 0 | 0 | 0 | 0.0033 |
| $C^2$ | 0 | -3.82 | 19.38 | 23.56 | 2.72 | 0 | 0 | 0 | 0.0138 |
| **Regression confidence $R^2$** | 0.948 | 0.846 | 0.995 | 0.996 | 0.987 | 0.931 | 0.99 | 0.99 | 0.803 |

**Table 6.53.** The ANOVA results for measured forces in X direction (Fx) during drilling of extruded CW511L with 90° of plunging angle

| Source | Sum of Squares | df | Mean Square | F-value | p-value |
|---|---|---|---|---|---|
| **Model** | 384.7 | 22 | 17.49 | 0.916 | 0.6149 |
| A-Radial rake angle | 0.1626 | 1 | 0.1626 | 0.0085 | 0.9309 |
| B-Axial rake angle | 0.0131 | 1 | 0.0131 | 0.0007 | 0.9804 |
| C-Edge radius | 12.22 | 1 | 12.22 | 0.6402 | 0.4685 |
| AB | 8.37 | 1 | 8.37 | 0.4383 | 0.5441 |
| AC | 48.88 | 1 | 48.88 | 2.56 | 0.1848 |
| BC | 2.81 | 1 | 2.81 | 0.1471 | 0.7209 |
| $A^2$ | 4.78 | 1 | 4.78 | 0.2506 | 0.643 |
| $B^2$ | 9.63 | 1 | 9.63 | 0.5045 | 0.5167 |
| $C^2$ | 5.75 | 1 | 5.75 | 0.3014 | 0.6122 |
| ABC | 56.29 | 1 | 56.29 | 2.95 | 0.1611 |
| $A^2B$ | 17.79 | 1 | 17.79 | 0.9319 | 0.389 |
| $A^2C$ | 30.72 | 1 | 30.72 | 1.61 | 0.2734 |
| $AB^2$ | 1.37 | 1 | 1.37 | 0.0718 | 0.802 |
| $AC^2$ | 5.9 | 1 | 5.9 | 0.3092 | 0.6078 |
| $B^2C$ | 22.27 | 1 | 22.27 | 1.17 | 0.3409 |
| $BC^2$ | 10.74 | 1 | 10.74 | 0.5627 | 0.4949 |
| $A^2B^2$ | 0.5812 | 1 | 0.5812 | 0.0304 | 0.87 |
| $A^2BC$ | 4.72 | 1 | 4.72 | 0.2471 | 0.6452 |
| $A^2C^2$ | 30.48 | 1 | 30.48 | 1.6 | 0.275 |
| $AB^2C$ | 37.1 | 1 | 37.1 | 1.94 | 0.2357 |
| $ABC^2$ | 3.43 | 1 | 3.43 | 0.1797 | 0.6934 |
| $B^2C^2$ | 22.52 | 1 | 22.52 | 1.18 | 0.3385 |
| **Residual** | 76.36 | 4 | 19.09 | | |
| **Cor Total** | 461.05 | 26 | | | |

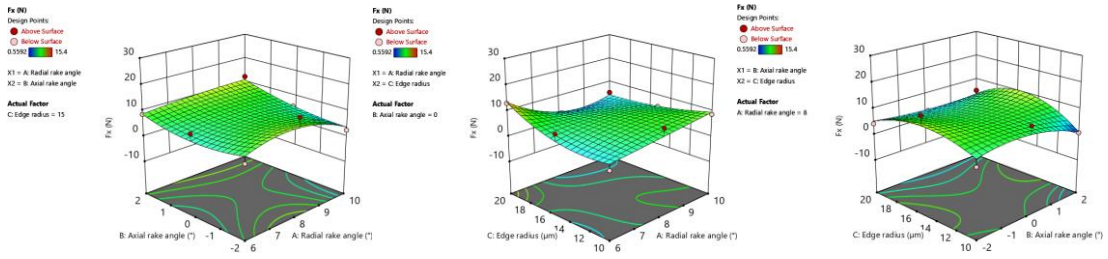

**Figure 6.83.** 3D surface plot of the measured forces in X direction (Fx) variation during drilling of extruded CW511L with 90° of plunging angle with respect to the studied cutting tool geometry

**Table 6.54.** The ANOVA results for measured forces in Y direction (Fy) during drilling of extruded CW511L with 90° of plunging angle

| Source | Sum of Squares | df | Mean Square | F-value | p-value |
|---|---|---|---|---|---|
| **Model** | 398.17 | 22 | 18.1 | 1.01 | 0.5645 |
| A-Radial rake angle | 1.36 | 1 | 1.36 | 0.0763 | 0.796 |
| B-Axial rake angle | 31.34 | 1 | 31.34 | 1.76 | 0.2558 |
| C-Edge radius | 1.02 | 1 | 1.02 | 0.0571 | 0.8229 |
| AB | 0.0369 | 1 | 0.0369 | 0.0021 | 0.9659 |
| AC | 1.39 | 1 | 1.39 | 0.0777 | 0.7943 |
| BC | 12.92 | 1 | 12.92 | 0.7236 | 0.4429 |
| $A^2$ | 11.06 | 1 | 11.06 | 0.6194 | 0.4753 |
| $B^2$ | 80.66 | 1 | 80.66 | 4.52 | 0.1007 |
| $C^2$ | 20.22 | 1 | 20.22 | 1.13 | 0.3472 |
| ABC | 22.26 | 1 | 22.26 | 1.25 | 0.3267 |
| $A^2B$ | 6.75 | 1 | 6.75 | 0.3781 | 0.5719 |
| $A^2C$ | 19.71 | 1 | 19.71 | 1.1 | 0.3526 |
| $AB^2$ | 8.96 | 1 | 8.96 | 0.5021 | 0.5177 |
| $AC^2$ | 24.2 | 1 | 24.2 | 1.36 | 0.309 |
| $B^2C$ | 3.82 | 1 | 3.82 | 0.2138 | 0.6678 |
| $BC^2$ | 85.25 | 1 | 85.25 | 4.78 | 0.0942 |
| $A^2B^2$ | 31.2 | 1 | 31.2 | 1.75 | 0.2567 |
| $A^2BC$ | 10.2 | 1 | 10.2 | 0.5713 | 0.4918 |
| $A^2C^2$ | 0.6415 | 1 | 0.6415 | 0.0359 | 0.8589 |
| $AB^2C$ | 0.5008 | 1 | 0.5008 | 0.0281 | 0.8751 |
| $ABC^2$ | 9.4 | 1 | 9.4 | 0.5269 | 0.5081 |
| $B^2C^2$ | 27.3 | 1 | 27.3 | 1.53 | 0.2839 |
| **Residual** | 71.4 | 4 | 17.85 | | |
| **Cor Total** | 469.58 | 26 | | | |

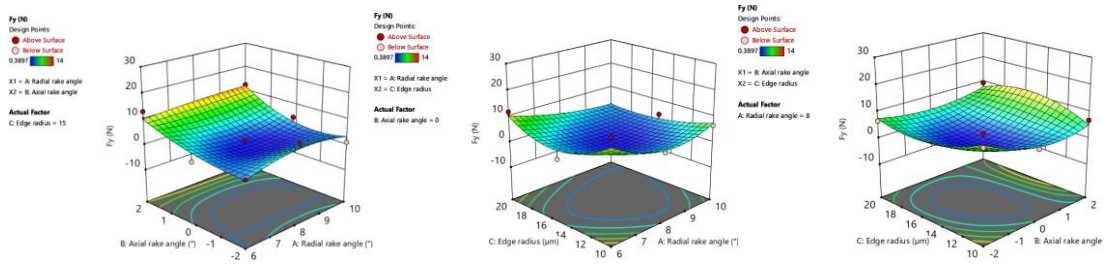

**Figure 6.84.** 3D surface plot of the measured forces in Y direction (Fy) variation during drilling of extruded CW511L with 90° of plunging angle with respect to the studied cutting tool geometry

**Table 6.55.** The ANOVA results for measured forces in Z direction (Fz) during drilling of extruded CW511L with 90° of plunging angle

| Source | Sum of Squares | df | Mean Square | F-value | p-value | |
|---|---|---|---|---|---|---|
| **Model** | 82132.48 | 16 | 5133.28 | 5.1 | 0.0063 | significant |
| A-Radial rake angle | 6762.77 | 1 | 6762.77 | 6.72 | 0.0268 | |
| B-Axial rake angle | 264.13 | 1 | 264.13 | 0.2626 | 0.6194 | |
| C-Edge radius | 4633.97 | 1 | 4633.97 | 4.61 | 0.0574 | |
| AB | 178.33 | 1 | 178.33 | 0.1773 | 0.6826 | |
| AC | 4700.52 | 1 | 4700.52 | 4.67 | 0.0559 | |
| BC | 300 | 1 | 300 | 0.2983 | 0.5969 | |
| $A^2$ | 1162.23 | 1 | 1162.23 | 1.16 | 0.3076 | |
| $B^2$ | 1169.66 | 1 | 1169.66 | 1.16 | 0.3062 | |
| $C^2$ | 4654.11 | 1 | 4654.11 | 4.63 | 0.0569 | |
| ABC | 134.48 | 1 | 134.48 | 0.1337 | 0.7222 | |
| $A^2B$ | 2161.94 | 1 | 2161.94 | 2.15 | 0.1733 | |
| $A^2C$ | 213.65 | 1 | 213.65 | 0.2124 | 0.6547 | |
| $AB^2$ | 4267.57 | 1 | 4267.57 | 4.24 | 0.0664 | |
| $AC^2$ | 107.81 | 1 | 107.81 | 0.1072 | 0.7501 | |
| $B^2C$ | 1286.42 | 1 | 1286.42 | 1.28 | 0.2844 | |
| $BC^2$ | 512.27 | 1 | 512.27 | 0.5094 | 0.4917 | |
| **Residual** | 10056.6 | 10 | 1005.66 | | | |
| **Cor Total** | 92189.08 | 26 | | | | |

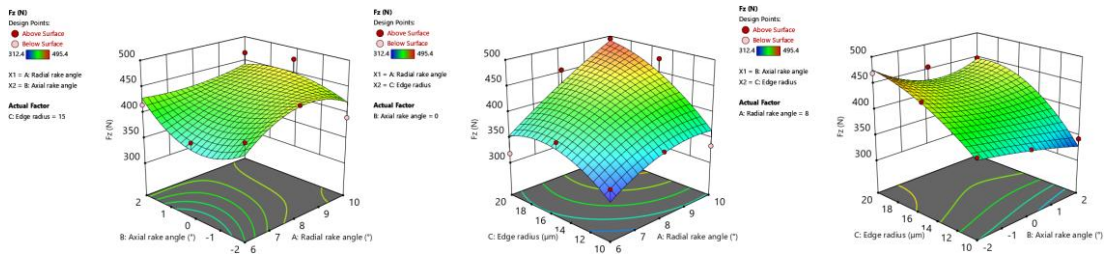

**Figure 6.85.** 3D surface plot of the measured forces in Z direction (Fz) variation during drilling of extruded CW511L with 90° of plunging angle with respect to the studied

cutting tool geometry

**Table 6.56.** The ANOVA results for measured resultant forces (FR) during drilling of extruded CW511L with 90° of plunging angle

| Source | Sum of Squares | df | Mean Square | F-value | p-value | |
|---|---|---|---|---|---|---|
| **Model** | 82022.43 | 16 | 5126.4 | 5.11 | 0.0063 | significant |
| A-Radial rake angle | 6750.48 | 1 | 6750.48 | 6.73 | 0.0268 | |
| B-Axial rake angle | 261.59 | 1 | 261.59 | 0.2608 | 0.6206 | |
| C-Edge radius | 4626.89 | 1 | 4626.89 | 4.61 | 0.0573 | |
| AB | 176.31 | 1 | 176.31 | 0.1758 | 0.6839 | |
| AC | 4688.16 | 1 | 4688.16 | 4.67 | 0.0559 | |
| BC | 305.73 | 1 | 305.73 | 0.3048 | 0.593 | |
| $A^2$ | 1153.89 | 1 | 1153.89 | 1.15 | 0.3087 | |
| $B^2$ | 1171.43 | 1 | 1171.43 | 1.17 | 0.3052 | |
| $C^2$ | 4646.95 | 1 | 4646.95 | 4.63 | 0.0568 | |
| ABC | 137.11 | 1 | 137.11 | 0.1367 | 0.7193 | |
| $A^2B$ | 2172.44 | 1 | 2172.44 | 2.17 | 0.1719 | |
| $A^2C$ | 214.67 | 1 | 214.67 | 0.214 | 0.6535 | |
| $AB^2$ | 4253.59 | 1 | 4253.59 | 4.24 | 0.0665 | |
| $AC^2$ | 103.96 | 1 | 103.96 | 0.1037 | 0.7541 | |
| $B^2C$ | 1286.11 | 1 | 1286.11 | 1.28 | 0.2839 | |
| $BC^2$ | 521.1 | 1 | 521.1 | 0.5196 | 0.4875 | |
| **Residual** | 10029.75 | 10 | 1002.97 | | | |
| **Cor Total** | 92052.18 | 26 | | | | |

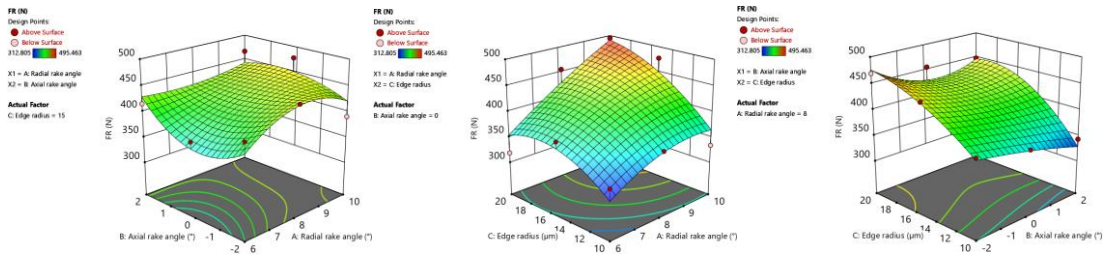

**Figure 6.86.** 3D surface plot of the measured resultant forces variation during drilling of extruded CW511L with 90° of plunging angle with respect to the studied cutting tool geometry

**Table 6.57.** The ANOVA results for measured burr heights at hole entry (BHEN) during drilling of extruded CW511L with 90° of plunging angle

| Source | Sum of Squares | df | Mean Square | F-value | p-value |
|---|---|---|---|---|---|
| **Model** | 1.92E+05 | 16 | 12013.47 | 2.51 | 0.072 |
| A-Radial rake angle | 16116.29 | 1 | 16116.29 | 3.36 | 0.0966 |
| B-Axial rake angle | 1337.54 | 1 | 1337.54 | 0.279 | 0.6089 |
| C-Edge radius | 33205.88 | 1 | 33205.88 | 6.93 | 0.0251 |

| | | | | | |
|---|---|---|---|---|---|
| AB | 885.55 | 1 | 885.55 | 0.1847 | 0.6765 |
| AC | 42844.99 | 1 | 42844.99 | 8.94 | 0.0136 |
| BC | 134.25 | 1 | 134.25 | 0.028 | 0.8704 |
| $A^2$ | 15121.74 | 1 | 15121.74 | 3.15 | 0.1061 |
| $B^2$ | 31111.78 | 1 | 31111.78 | 6.49 | 0.029 |
| $C^2$ | 6837.37 | 1 | 6837.37 | 1.43 | 0.2599 |
| ABC | 1320.08 | 1 | 1320.08 | 0.2754 | 0.6112 |
| $A^2B$ | 3359.81 | 1 | 3359.81 | 0.7008 | 0.4221 |
| $A^2C$ | 17890.09 | 1 | 17890.09 | 3.73 | 0.0822 |
| $AB^2$ | 30962.18 | 1 | 30962.18 | 6.46 | 0.0293 |
| $AC^2$ | 113.3 | 1 | 113.3 | 0.0236 | 0.8809 |
| $B^2C$ | 13403.62 | 1 | 13403.62 | 2.8 | 0.1255 |
| $BC^2$ | 87.53 | 1 | 87.53 | 0.0183 | 0.8952 |
| **Residual** | 47939.14 | 10 | 4793.91 | | |
| **Cor Total** | 2.40E+05 | 26 | | | |

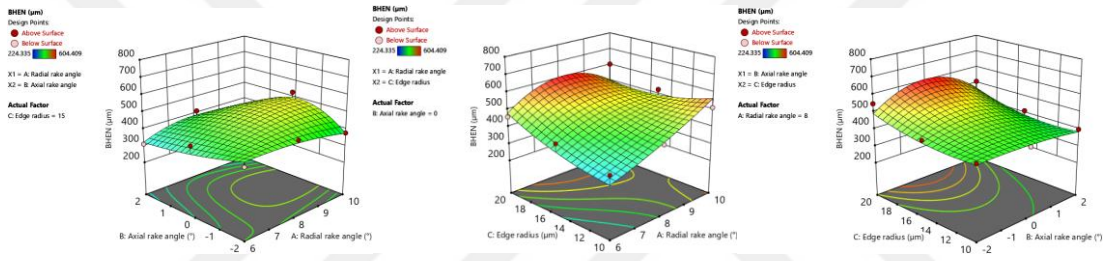

**Figure 6.87.** 3D surface plot of the measured burr heights at hole entry (BHEN) variation during drilling of extruded CW511L with 90° of plunging angle with respect to the studied cutting tool geometry

**Table 6.58.** The ANOVA results for measured burr heights at hole exit (BHEX) during drilling of extruded CW511L with 90° of plunging angle

| Source | Sum of Squares | df | Mean Square | F-value | p-value | |
|---|---|---|---|---|---|---|
| **Model** | 21926.79 | 16 | 1370.42 | 4.71 | 0.0085 | significant |
| A-Radial rake angle | 3331.13 | 1 | 3331.13 | 11.46 | 0.0069 | |
| B-Axial rake angle | 124.37 | 1 | 124.37 | 0.4279 | 0.5278 | |
| C-Edge radius | 4809.39 | 1 | 4809.39 | 16.55 | 0.0023 | |
| AB | 36.54 | 1 | 36.54 | 0.1257 | 0.7303 | |
| AC | 56.1 | 1 | 56.1 | 0.193 | 0.6698 | |
| BC | 672.89 | 1 | 672.89 | 2.31 | 0.1591 | |
| $A^2$ | 258.04 | 1 | 258.04 | 0.8877 | 0.3683 | |
| $B^2$ | 249.42 | 1 | 249.42 | 0.8581 | 0.3761 | |
| $C^2$ | 5.65 | 1 | 5.65 | 0.0194 | 0.8919 | |
| ABC | 361.8 | 1 | 361.8 | 1.24 | 0.2907 | |
| $A^2B$ | 609 | 1 | 609 | 2.1 | 0.1784 | |
| $A^2C$ | 179.62 | 1 | 179.62 | 0.6179 | 0.45 | |
| $AB^2$ | 94.2 | 1 | 94.2 | 0.3241 | 0.5817 | |

| | | | | | |
|---|---|---|---|---|---|
| $AC^2$ | 1260.39 | 1 | 1260.39 | 4.34 | 0.0639 |
| $B^2C$ | 792.5 | 1 | 792.5 | 2.73 | 0.1297 |
| $BC^2$ | 2.15 | 1 | 2.15 | 0.0074 | 0.9332 |
| **Residual** | 2906.77 | 10 | 290.68 | | |
| **Cor Total** | 24833.55 | 26 | | | |

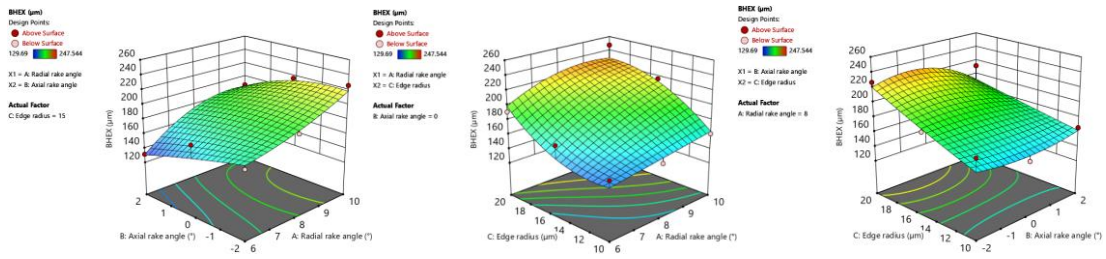

**Figure 6.88.** 3D surface plot of the measured burr heights at hole exit (BHEX) variation during drilling of extruded CW511L with 90° of plunging angle with respect to the studied cutting tool geometry

**Table 6.59.** The ANOVA results for measured surface roughness at hole bottom (Ra) during drilling of extruded CW511L with 90° of plunging angle

| Source | Sum of Squares | df | Mean Square | F-value | p-value | |
|---|---|---|---|---|---|---|
| **Model** | 0.101 | 9 | 0.0112 | 335.89 | < 0.0001 | significant |
| A-Radial rake angle | 0.0067 | 1 | 0.0067 | 199.1 | < 0.0001 | |
| B-Axial rake angle | 0.0007 | 1 | 0.0007 | 22.38 | 0.0002 | |
| C-Edge radius | 0.093 | 1 | 0.093 | 2784.77 | < 0.0001 | |
| AB | 0.0001 | 1 | 0.0001 | 2.25 | 0.1524 | |
| AC | 5.33E-06 | 1 | 5.33E-06 | 0.1597 | 0.6944 | |
| BC | 2.08E-06 | 1 | 2.08E-06 | 0.0624 | 0.8058 | |
| $A^2$ | 0.0001 | 1 | 0.0001 | 1.86 | 0.1899 | |
| $B^2$ | 8.96E-06 | 1 | 8.96E-06 | 0.2683 | 0.6111 | |
| $C^2$ | 0.0004 | 1 | 0.0004 | 12.14 | 0.0028 | |
| **Residual** | 0.0006 | 17 | 0 | | | |
| **Cor Total** | 0.1015 | 26 | | | | |

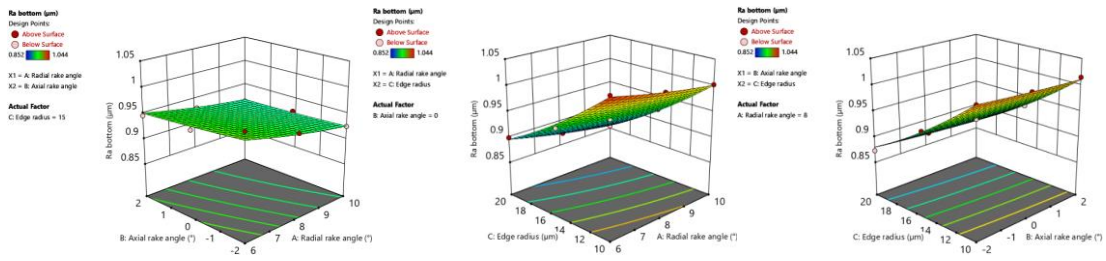

**Figure 6.89.** 3D surface plot of the measured surface roughness at hole bottom (Ra) variation during drilling of extruded CW511L with 90° of plunging angle with respect to the studied cutting tool geometry

**Table 6.60.** The ANOVA results for measured surface roughness at hole wall (Ra) during drilling of extruded CW511L with 90° of plunging angle

| Source | Sum of Squares | df | Mean Square | F-value | p-value | |
|---|---|---|---|---|---|---|
| **Model** | 0.075 | 9 | 0.0083 | 338.04 | < 0.0001 | significant |
| A-Radial rake angle | 0.0049 | 1 | 0.0049 | 198.88 | < 0.0001 | |
| B-Axial rake angle | 0.0006 | 1 | 0.0006 | 23.46 | 0.0002 | |
| C-Edge radius | 0.0689 | 1 | 0.0689 | 2798.06 | < 0.0001 | |
| AB | 0.0001 | 1 | 0.0001 | 2.47 | 0.1348 | |
| AC | 3.33E-07 | 1 | 3.33E-07 | 0.0135 | 0.9088 | |
| BC | 3.00E-06 | 1 | 3.00E-06 | 0.1218 | 0.7314 | |
| $A^2$ | 0 | 1 | 0 | 1.66 | 0.2148 | |
| $B^2$ | 7.41E-06 | 1 | 7.41E-06 | 0.3006 | 0.5906 | |
| $C^2$ | 0.0004 | 1 | 0.0004 | 17.36 | 0.0006 | |
| **Residual** | 0.0004 | 17 | 0 | | | |
| **Cor Total** | 0.0754 | 26 | | | | |

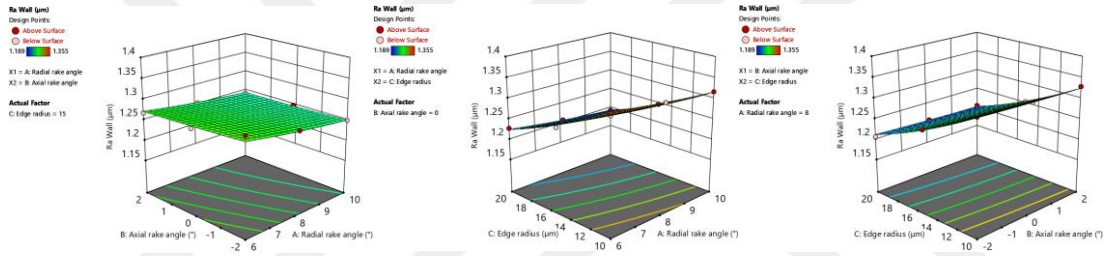

**Figure 6.90.** 3D surface plot of the measured surface roughness at hole wall (Ra) variation during drilling of extruded CW511L with 90° of plunging angle with respect to the studied cutting tool geometry

**Table 6.61.** The ANOVA results for measured hole diameter during drilling of extruded CW511L with 90° of plunging angle

| Source | Sum of Squares | df | Mean Square | F-value | p-value | |
|---|---|---|---|---|---|---|
| **Model** | 3.83 | 9 | 0.4254 | 8.37 | 0.0001 | significant |
| A-Radial rake angle | 0.138 | 1 | 0.138 | 2.72 | 0.1177 | |
| B-Axial rake angle | 0.0255 | 1 | 0.0255 | 0.5026 | 0.488 | |
| C-Edge radius | 3.22 | 1 | 3.22 | 63.46 | < 0.0001 | |
| AB | 0.0075 | 1 | 0.0075 | 0.1476 | 0.7056 | |
| AC | 7.50E-07 | 1 | 7.50E-07 | 0 | 0.997 | |
| BC | 0.0332 | 1 | 0.0332 | 0.653 | 0.4302 | |
| $A^2$ | 0.0047 | 1 | 0.0047 | 0.0933 | 0.7637 | |
| $B^2$ | 0.1932 | 1 | 0.1932 | 3.8 | 0.0679 | |
| $C^2$ | 0.2011 | 1 | 0.2011 | 3.96 | 0.063 | |
| **Residual** | 0.8639 | 17 | 0.0508 | | | |
| **Cor Total** | 4.69 | 26 | | | | |

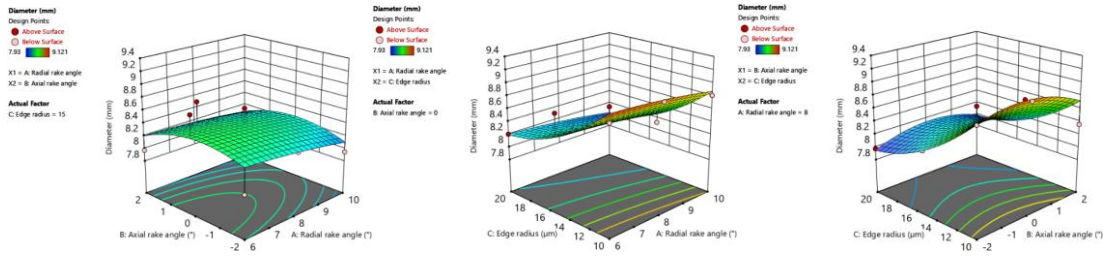

**Figure 6.91.** 3D surface plot of the measured hole diameter variation during drilling of extruded CW511L with 90° of plunging angle with respect to the studied cutting tool geometry

**Table 6.62.** The developed regression model for drilling of extruded CW511L with 90° of plunging angle

| Extruded CW511L 90 | Fx | Fy | Fz | FR | BHEN | BHEX | Ra bottom | Ra Wall | Diameter |
|---|---|---|---|---|---|---|---|---|---|
| | 7.46 | 0.3437 | 420.8 | 420.91 | 479.03 | 189.22 | 0.9365 | 1.26 | 8.38 |
| A | 0.2125 | -0.6152 | 43.34 | 43.3 | 66.91 | 30.42 | -0.0192 | -0.0165 | -0.0876 |
| B | 0.0603 | 2.95 | -8.57 | -8.52 | -19.28 | -5.88 | -0.0064 | -0.0057 | -0.0377 |
| C | -1.84 | 0.532 | 35.88 | 35.85 | 96.04 | 36.55 | -0.0719 | -0.0619 | -0.4233 |
| AB | 1.45 | 0.096 | -3.86 | -3.83 | 8.59 | 1.74 | 0.0025 | 0.0022 | 0.025 |
| AC | -3.5 | -0.5887 | 19.79 | 19.77 | -59.75 | 2.16 | -0.0007 | 0.0002 | -0.0003 |
| BC | 0.8378 | 1.8 | 5 | 5.05 | 3.34 | -7.49 | 0.0004 | 0.0005 | 0.0526 |
| $A^2$ | -2 | 3.04 | -13.92 | -13.87 | -50.2 | -6.56 | 0.0032 | 0.0026 | -0.0281 |
| $B^2$ | 2.83 | 8.2 | 13.96 | 13.97 | -72.01 | -6.45 | 0.0012 | 0.0011 | -0.1794 |
| $C^2$ | -2.19 | 4.1 | -27.85 | -27.83 | 33.76 | 0.9701 | 0.0082 | 0.0084 | 0.1831 |
| ABC | -2.65 | 1.67 | -4.1 | -4.14 | 12.85 | -6.72 | 0 | 0 | 0 |
| $A^2B$ | 2.11 | 1.3 | 23.25 | 23.3 | -28.98 | -12.34 | 0 | 0 | 0 |
| $A^2C$ | 2.77 | -2.22 | 7.31 | 7.33 | -66.88 | -6.7 | 0 | 0 | 0 |
| $AB^2$ | -0.5853 | 1.5 | -32.66 | -32.61 | -87.98 | -4.85 | 0 | 0 | 0 |
| $AC^2$ | -1.21 | -2.46 | 5.19 | 5.1 | 5.32 | -17.75 | 0 | 0 | 0 |
| $B^2C$ | 2.36 | -0.9768 | 17.93 | 17.93 | -57.89 | -14.08 | 0 | 0 | 0 |
| $BC^2$ | -1.64 | -4.62 | -11.32 | -11.41 | 4.68 | -0.7325 | 0 | 0 | 0 |
| $A^2B^2$ | -0.6602 | -4.84 | 0 | 0 | 0 | 0 | 0 | 0 | 0 |
| $A^2BC$ | 1.33 | -1.96 | 0 | 0 | 0 | 0 | 0 | 0 | 0 |
| $A^2C^2$ | 4.78 | 0.6936 | 0 | 0 | 0 | 0 | 0 | 0 | 0 |
| $AB^2C$ | 3.73 | 0.4334 | 0 | 0 | 0 | 0 | 0 | 0 | 0 |
| $ABC^2$ | -1.13 | 1.88 | 0 | 0 | 0 | 0 | 0 | 0 | 0 |
| $B^2C^2$ | -4.11 | -4.52 | 0 | 0 | 0 | 0 | 0 | 0 | 0 |
| **Regression confidence $R^2$** | 0.834 | 0.847 | 0.89 | 0.891 | 0.8 | 0.883 | 0.994 | 0.994 | 0.815 |

**Table 6.63.** The ANOVA results for measured forces in X direction (Fx) during drilling of extruded CW511L with 60° of plunging angle

| Source | Sum of Squares | df | Mean Square | F-value | p-value | |
|---|---|---|---|---|---|---|
| **Model** | 62601.83 | 6 | 10433.64 | 55.54 | < 0.0001 | significant |
| A-Radial rake angle | 8.95 | 1 | 8.95 | 0.0476 | 0.8295 | |
| B-Axial rake angle | 81.41 | 1 | 81.41 | 0.4334 | 0.5178 | |
| C-Edge radius | 61399.42 | 1 | 61399.42 | 326.87 | < 0.0001 | |
| AB | 64.68 | 1 | 64.68 | 0.3443 | 0.5639 | |
| AC | 248.34 | 1 | 248.34 | 1.32 | 0.2638 | |
| BC | 799.03 | 1 | 799.03 | 4.25 | 0.0524 | |
| **Residual** | 3756.86 | 20 | 187.84 | | | |
| **Cor Total** | 66358.69 | 26 | | | | |

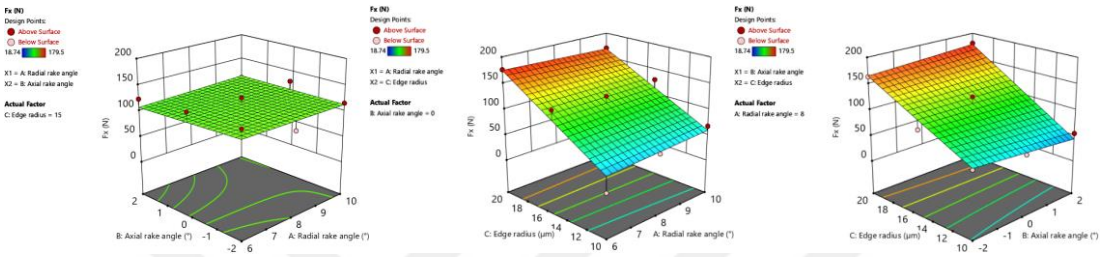

**Figure 6.92.** 3D surface plot of the measured forces in X direction (Fx) variation during drilling of extruded CW511L with 60° of plunging angle with respect to the studied cutting tool geometry

**Table 6.64.** The ANOVA results for measured forces in Y direction (Fy) during drilling of extruded CW511L with 60° of plunging angle

| Source | Sum of Squares | df | Mean Square | F-value | p-value | |
|---|---|---|---|---|---|---|
| **Model** | 36850.59 | 16 | 2303.16 | 4.52 | 0.01 | significant |
| A-Radial rake angle | 1114.57 | 1 | 1114.57 | 2.19 | 0.1699 | |
| B-Axial rake angle | 3.62 | 1 | 3.62 | 0.0071 | 0.9345 | |
| C-Edge radius | 4329.59 | 1 | 4329.59 | 8.5 | 0.0154 | |
| AB | 16.47 | 1 | 16.47 | 0.0323 | 0.8609 | |
| AC | 903.76 | 1 | 903.76 | 1.77 | 0.2124 | |
| BC | 93.47 | 1 | 93.47 | 0.1835 | 0.6775 | |
| $A^2$ | 543.91 | 1 | 543.91 | 1.07 | 0.3258 | |
| $B^2$ | 1538.03 | 1 | 1538.03 | 3.02 | 0.1129 | |
| $C^2$ | 515.72 | 1 | 515.72 | 1.01 | 0.338 | |
| ABC | 10.95 | 1 | 10.95 | 0.0215 | 0.8863 | |
| $A^2B$ | 11.86 | 1 | 11.86 | 0.0233 | 0.8818 | |
| $A^2C$ | 604.34 | 1 | 604.34 | 1.19 | 0.3016 | |
| $AB^2$ | 1450.59 | 1 | 1450.59 | 2.85 | 0.1224 | |
| $AC^2$ | 240.97 | 1 | 240.97 | 0.4731 | 0.5072 | |
| $B^2C$ | 1369.86 | 1 | 1369.86 | 2.69 | 0.1321 | |
| $BC^2$ | 89.27 | 1 | 89.27 | 0.1753 | 0.6843 | |
| **Residual** | 5093.54 | 10 | 509.35 | | | |
| **Cor Total** | 41944.13 | 26 | | | | |

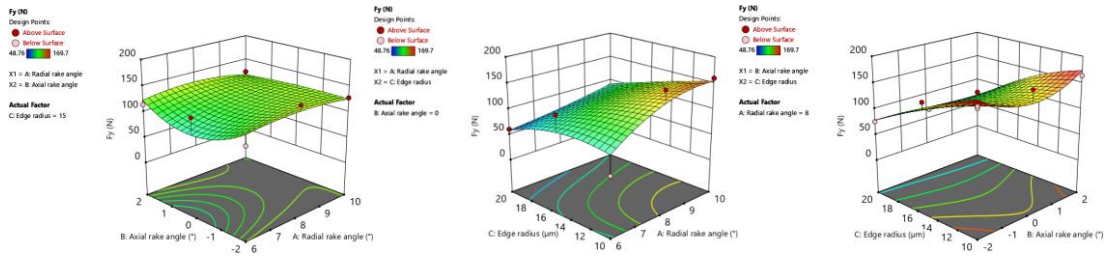

**Figure 6.93.** 3D surface plot of the measured forces in Y direction (Fy) variation during drilling of extruded CW511L with 60° of plunging angle with respect to the studied cutting tool geometry

**Table 6.65.** The ANOVA results for measured forces in Z direction (Fz) during drilling of extruded CW511L with 60° of plunging angle

| Source | Sum of Squares | df | Mean Square | F-value | p-value | |
|---|---|---|---|---|---|---|
| **Model** | 1.49E+05 | 9 | 16599.6 | 118.66 | < 0.0001 | significant |
| A-Radial rake angle | 27.88 | 1 | 27.88 | 0.1993 | 0.6609 | |
| B-Axial rake angle | 1388.64 | 1 | 1388.64 | 9.93 | 0.0058 | |
| C-Edge radius | 1.40E+05 | 1 | 1.40E+05 | 998.1 | < 0.0001 | |
| AB | 41.81 | 1 | 41.81 | 0.2989 | 0.5917 | |
| AC | 15.19 | 1 | 15.19 | 0.1086 | 0.7458 | |
| BC | 312.12 | 1 | 312.12 | 2.23 | 0.1536 | |
| $A^2$ | 71.65 | 1 | 71.65 | 0.5122 | 0.4839 | |
| $B^2$ | 268.89 | 1 | 268.89 | 1.92 | 0.1835 | |
| $C^2$ | 7649.32 | 1 | 7649.32 | 54.68 | < 0.0001 | |
| **Residual** | 2378.07 | 17 | 139.89 | | | |
| **Cor Total** | 1.52E+05 | 26 | | | | |

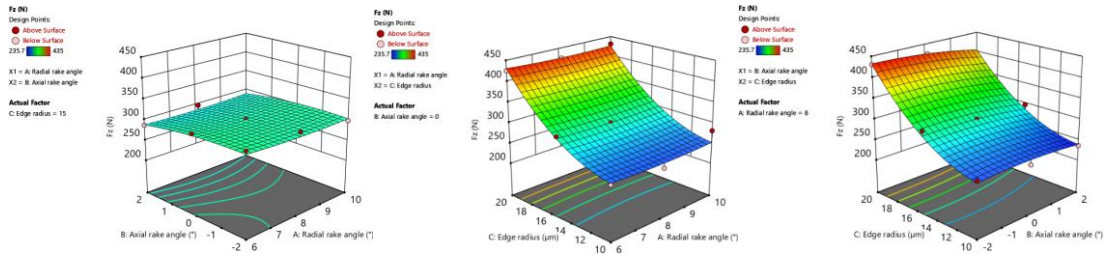

**Figure 6.94.** 3D surface plot of the measured forces in Z direction (Fz) variation during drilling of extruded CW511L with 60° of plunging angle with respect to the studied cutting tool geometry

**Table 6.66.** The ANOVA results for measured resultant forces (FR) during drilling of extruded CW511L with 60° of plunging angle

| Source | Sum of Squares | df | Mean Square | F-value | p-value |
|---|---|---|---|---|---|

| | | | | | | |
|---|---|---|---|---|---|---|
| **Model** | 1.32E+05 | 9 | 14698.42 | 71.8 | < 0.0001 | significant |
| A-Radial rake angle | 86.47 | 1 | 86.47 | 0.4224 | 0.5244 | |
| B-Axial rake angle | 1617.54 | 1 | 1617.54 | 7.9 | 0.012 | |
| C-Edge radius | 1.23E+05 | 1 | 1.23E+05 | 600.64 | < 0.0001 | |
| AB | 47.65 | 1 | 47.65 | 0.2327 | 0.6356 | |
| AC | 367.67 | 1 | 367.67 | 1.8 | 0.1978 | |
| BC | 66.33 | 1 | 66.33 | 0.324 | 0.5767 | |
| $A^2$ | 13.17 | 1 | 13.17 | 0.0643 | 0.8028 | |
| $B^2$ | 1.93 | 1 | 1.93 | 0.0094 | 0.9238 | |
| $C^2$ | 7118.56 | 1 | 7118.56 | 34.77 | < 0.0001 | |
| **Residual** | 3480.34 | 17 | 204.73 | | | |
| **Cor Total** | 1.36E+05 | 26 | | | | |

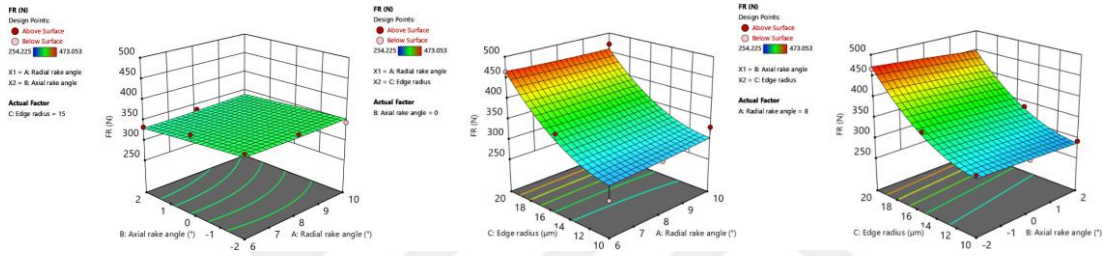

**Figure 6.95.** 3D surface plot of the measured resultant forces variation during drilling of extruded CW511L with 60° of plunging angle with respect to the studied cutting tool geometry

**Table 6.67.** The ANOVA results for measured burr heights at hole entry (BHEN) during drilling of extruded CW511L with 60° of plunging angle

| Source | Sum of Squares | df | Mean Square | F-value | p-value | |
|---|---|---|---|---|---|---|
| **Model** | 1.55E+05 | 16 | 9695.7 | 2.88 | 0.0473 | significant |
| A-Radial rake angle | 10507.86 | 1 | 10507.86 | 3.12 | 0.1078 | |
| B-Axial rake angle | 3596.72 | 1 | 3596.72 | 1.07 | 0.3258 | |
| C-Edge radius | 13371.98 | 1 | 13371.98 | 3.97 | 0.0743 | |
| AB | 332.84 | 1 | 332.84 | 0.0988 | 0.7597 | |
| AC | 33550.25 | 1 | 33550.25 | 9.96 | 0.0102 | |
| BC | 3369.12 | 1 | 3369.12 | 1 | 0.3409 | |
| $A^2$ | 3686.87 | 1 | 3686.87 | 1.09 | 0.3202 | |
| $B^2$ | 33024.07 | 1 | 33024.07 | 9.8 | 0.0107 | |
| $C^2$ | 2158.02 | 1 | 2158.02 | 0.6405 | 0.4421 | |
| ABC | 187.94 | 1 | 187.94 | 0.0558 | 0.8181 | |
| $A^2B$ | 118.73 | 1 | 118.73 | 0.0352 | 0.8548 | |
| $A^2C$ | 3013.28 | 1 | 3013.28 | 0.8943 | 0.3666 | |
| $AB^2$ | 24970.33 | 1 | 24970.33 | 7.41 | 0.0215 | |
| $AC^2$ | 171.82 | 1 | 171.82 | 0.051 | 0.8259 | |
| $B^2C$ | 17950.12 | 1 | 17950.12 | 5.33 | 0.0436 | |

| | | | | | | |
|---|---|---|---|---|---|---|
| $BC^2$ | 1547.29 | 1 | 1547.29 | 0.4592 | 0.5134 | |
| **Residual** | 33692.39 | 10 | 3369.24 | | | |
| **Cor Total** | 1.89E+05 | 26 | | | | |

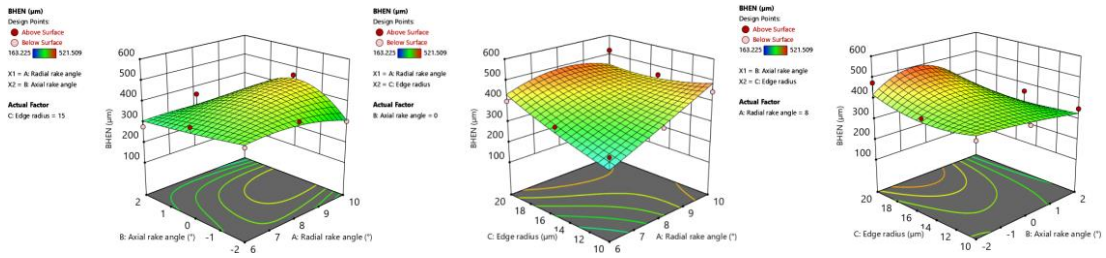

**Figure 6.96.** 3D surface plot of the measured burr heights at hole entry (BHEN) variation during drilling of extruded CW511L with 60° of plunging angle with respect to the studied cutting tool geometry

**Table 6.68.** The ANOVA results for measured burr heights at hole exit (BHEX) during drilling of extruded CW511L with 60° of plunging angle

| Source | Sum of Squares | df | Mean Square | F-value | p-value | |
|---|---|---|---|---|---|---|
| **Model** | 12666.34 | 16 | 791.65 | 5.63 | 0.0043 | significant |
| A-Radial rake angle | 2119.27 | 1 | 2119.27 | 15.08 | 0.003 | |
| B-Axial rake angle | 295.48 | 1 | 295.48 | 2.1 | 0.1777 | |
| C-Edge radius | 2301.86 | 1 | 2301.86 | 16.38 | 0.0023 | |
| AB | 51.85 | 1 | 51.85 | 0.3689 | 0.5571 | |
| AC | 130.06 | 1 | 130.06 | 0.9255 | 0.3587 | |
| BC | 228.53 | 1 | 228.53 | 1.63 | 0.2311 | |
| $A^2$ | 178.48 | 1 | 178.48 | 1.27 | 0.2861 | |
| $B^2$ | 50.79 | 1 | 50.79 | 0.3614 | 0.5611 | |
| $C^2$ | 29.12 | 1 | 29.12 | 0.2072 | 0.6587 | |
| ABC | 52.66 | 1 | 52.66 | 0.3747 | 0.5541 | |
| $A^2B$ | 166.95 | 1 | 166.95 | 1.19 | 0.3013 | |
| $A^2C$ | 59.42 | 1 | 59.42 | 0.4228 | 0.5302 | |
| $AB^2$ | 28.43 | 1 | 28.43 | 0.2023 | 0.6625 | |
| $AC^2$ | 808.93 | 1 | 808.93 | 5.76 | 0.0374 | |
| $B^2C$ | 278 | 1 | 278 | 1.98 | 0.1899 | |
| $BC^2$ | 46.83 | 1 | 46.83 | 0.3332 | 0.5765 | |
| **Residual** | 1405.4 | 10 | 140.54 | | | |
| **Cor Total** | 14071.73 | 26 | | | | |

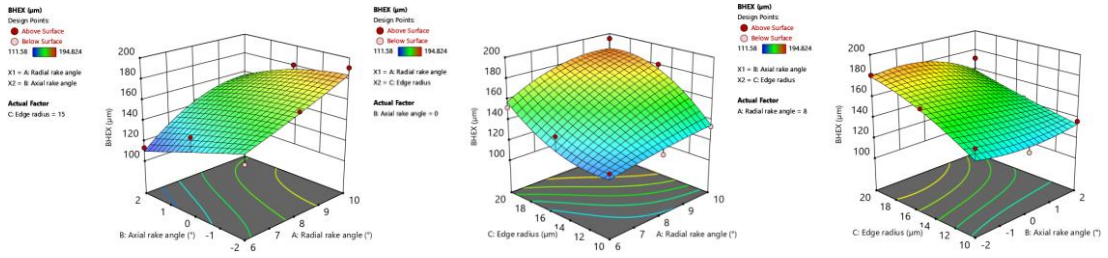

**Figure 6.97.** 3D surface plot of the measured burr heights at hole exit (BHEX) variation during drilling of extruded CW511L with 60° of plunging angle with respect to the studied cutting tool geometry

**Table 6.69.** The ANOVA results for measured surface roughness at hole bottom (Ra) during drilling of extruded CW511L with 60° of plunging angle

| Source | Sum of Squares | df | Mean Square | F-value | p-value | |
|---|---|---|---|---|---|---|
| **Model** | 0.0623 | 9 | 0.0069 | 338.79 | < 0.0001 | significant |
| A-Radial rake angle | 0.004 | 1 | 0.004 | 198.08 | < 0.0001 | |
| B-Axial rake angle | 0.0005 | 1 | 0.0005 | 23.5 | 0.0002 | |
| C-Edge radius | 0.0575 | 1 | 0.0575 | 2810.34 | < 0.0001 | |
| AB | 0 | 1 | 0 | 2.35 | 0.1439 | |
| AC | 3.00E-06 | 1 | 3.00E-06 | 0.1467 | 0.7064 | |
| BC | 7.50E-07 | 1 | 7.50E-07 | 0.0367 | 0.8504 | |
| $A^2$ | 0 | 1 | 0 | 2.09 | 0.1668 | |
| $B^2$ | 4.17E-06 | 1 | 4.17E-06 | 0.2038 | 0.6574 | |
| $C^2$ | 0.0003 | 1 | 0.0003 | 12.4 | 0.0026 | |
| **Residual** | 0.0003 | 17 | 0 | | | |
| **Cor Total** | 0.0627 | 26 | | | | |

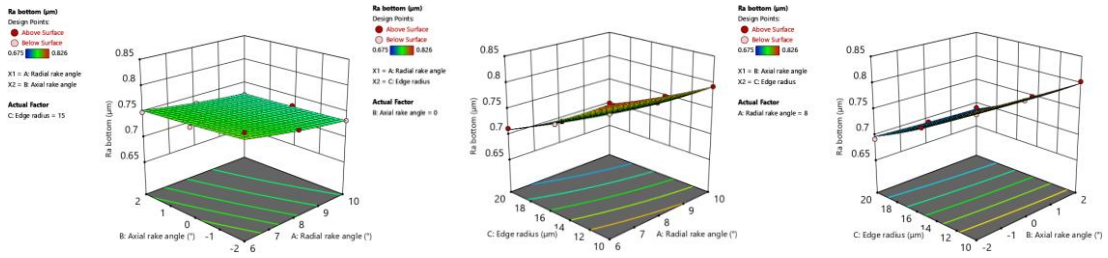

**Figure 6.98.** 3D surface plot of the measured surface roughness at hole bottom (Ra) variation during drilling of extruded CW511L with 60° of plunging angle with respect to the studied cutting tool geometry

**Table 6.70.** The ANOVA results for measured surface roughness at hole wall (Ra) during drilling of extruded CW511L with 60° of plunging angle

| Source | Sum of Squares | df | Mean Square | F-value | p-value | |
|---|---|---|---|---|---|---|
| **Model** | 0.0068 | 6 | 0.0011 | 472.54 | < 0.0001 | significant |

| | | | | | |
|---|---|---|---|---|---|
| A-Radial rake angle | 0.0005 | 1 | 0.0005 | 191.39 | < 0.0001 |
| B-Axial rake angle | 0.0001 | 1 | 0.0001 | 22.21 | 0.0001 |
| C-Edge radius | 0.0063 | 1 | 0.0063 | 2609.31 | < 0.0001 |
| AB | 1.33E-06 | 1 | 1.33E-06 | 0.5547 | 0.4651 |
| AC | 0 | 1 | 0 | 11.23 | 0.0032 |
| BC | 1.33E-06 | 1 | 1.33E-06 | 0.5547 | 0.4651 |
| **Residual** | 0 | 20 | 2.40E-06 | | |
| **Cor Total** | 0.0069 | 26 | | | |

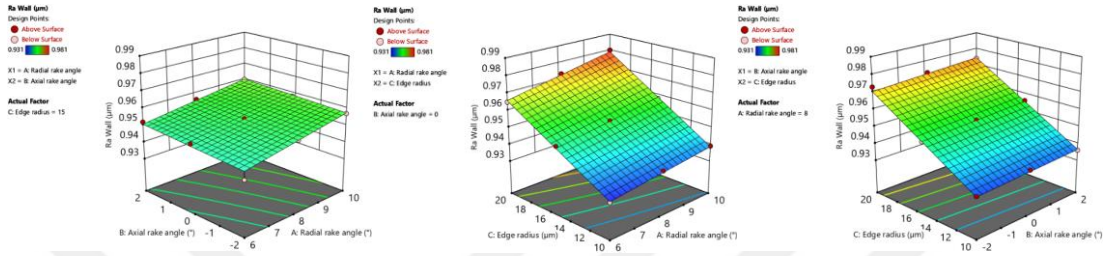

**Figure 6.99.** 3D surface plot of the measured surface roughness at hole wall (Ra) variation during drilling of extruded CW511L with 60° of plunging angle with respect to the studied cutting tool geometry

**Table 6.71.** The ANOVA results for measured hole diameter during drilling of extruded CW511L with 60° of plunging angle

| Source | Sum of Squares | df | Mean Square | F-value | p-value |
|---|---|---|---|---|---|
| **Model** | 0.0738 | 22 | 0.0034 | 1.66 | 0.3342 |
| A-Radial rake angle | 0.0044 | 1 | 0.0044 | 2.19 | 0.2131 |
| B-Axial rake angle | 0.0002 | 1 | 0.0002 | 0.0821 | 0.7887 |
| C-Edge radius | 0.0037 | 1 | 0.0037 | 1.83 | 0.2476 |
| AB | 0.0003 | 1 | 0.0003 | 0.1608 | 0.7089 |
| AC | 0.0127 | 1 | 0.0127 | 6.28 | 0.0663 |
| BC | 0.0001 | 1 | 0.0001 | 0.0656 | 0.8104 |
| $A^2$ | 0 | 1 | 0 | 0.0142 | 0.9108 |
| $B^2$ | 0.0003 | 1 | 0.0003 | 0.1503 | 0.718 |
| $C^2$ | 0.0008 | 1 | 0.0008 | 0.3991 | 0.5619 |
| ABC | 0 | 1 | 0 | 0.0159 | 0.9058 |
| $A^2B$ | 0 | 1 | 0 | 0.0221 | 0.8891 |
| $A^2C$ | 0.0042 | 1 | 0.0042 | 2.06 | 0.2241 |
| $AB^2$ | 0.0055 | 1 | 0.0055 | 2.72 | 0.1746 |
| $AC^2$ | 0.0031 | 1 | 0.0031 | 1.53 | 0.284 |
| $B^2C$ | 0.0077 | 1 | 0.0077 | 3.8 | 0.1231 |
| $BC^2$ | 0.0009 | 1 | 0.0009 | 0.4417 | 0.5427 |
| $A^2B^2$ | 0.0015 | 1 | 0.0015 | 0.7352 | 0.4395 |
| $A^2BC$ | 0 | 1 | 0 | 0.01 | 0.9251 |
| $A^2C^2$ | 0.0002 | 1 | 0.0002 | 0.1191 | 0.7474 |
| $AB^2C$ | 0.0093 | 1 | 0.0093 | 4.61 | 0.0984 |

| | | | | | |
|---|---|---|---|---|---|
| $ABC^2$ | 0.0003 | 1 | 0.0003 | 0.1459 | 0.7219 |
| $B^2C^2$ | 0.0029 | 1 | 0.0029 | 1.44 | 0.297 |
| **Residual** | 0.0081 | 4 | 0.002 | | |
| **Cor Total** | 0.0818 | 26 | | | |

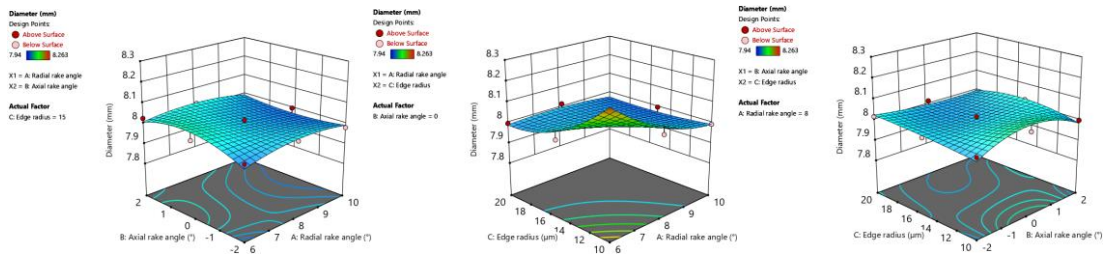

**Figure 6.100.** 3D surface plot of the measured hole diameter variation during drilling of extruded CW511L with 60° of plunging angle with respect to the studied cutting tool geometry

**Table 6.72.** The developed regression model for drilling of extruded CW511L with 60° of plunging angle

| Extruded CW511L 60 | Fx | Fy | Fz | FR | BHEN | BHEX | Ra bottom | Ra Wall | Diameter |
|---|---|---|---|---|---|---|---|---|---|
| | 112.74 | 116.61 | 301.2 | 343.46 | 412.39 | 157.28 | 0.7416 | 0.9537 | 8 |
| A | 0.705 | 17.6 | -1.24 | 2.19 | 54.03 | 24.26 | -0.015 | 0.0051 | -0.035 |
| B | -2.13 | -1 | -8.78 | -9.48 | -31.61 | -9.06 | -0.0052 | 0.0017 | 0.0068 |
| C | 58.4 | -34.68 | 88.07 | 82.65 | 60.95 | 25.29 | -0.0565 | 0.0187 | -0.032 |
| AB | 2.32 | -1.17 | 1.87 | 1.99 | 5.27 | 2.08 | 0.002 | -0.0003 | -0.009 |
| AC | -4.55 | -8.68 | -1.13 | -5.54 | -52.88 | 3.29 | -0.0005 | 0.0015 | 0.0562 |
| BC | 8.16 | -2.79 | -5.1 | -2.35 | -16.76 | -4.36 | 0.0002 | 0.0003 | -0.0057 |
| $A^2$ | 0 | -9.52 | 3.46 | 1.48 | -24.79 | -5.45 | 0.0027 | 0 | 0.0049 |
| $B^2$ | 0 | 16.01 | -6.69 | -0.5669 | -74.19 | -2.91 | 0.0008 | 0 | 0.0159 |
| $C^2$ | 0 | -9.27 | 35.71 | 34.44 | 18.96 | -2.2 | 0.0065 | 0 | 0.0259 |
| ABC | 0 | -1.17 | 0 | 0 | 4.85 | -2.57 | 0 | 0 | -0.002 |
| $A^2B$ | 0 | -1.72 | 0 | 0 | 5.45 | -6.46 | 0 | 0 | 0.0033 |
| $A^2C$ | 0 | 12.29 | 0 | 0 | -27.45 | -3.85 | 0 | 0 | -0.0322 |
| $AB^2$ | 0 | -19.04 | 0 | 0 | -79.01 | -2.67 | 0 | 0 | 0.037 |
| $AC^2$ | 0 | 7.76 | 0 | 0 | 6.55 | -14.22 | 0 | 0 | -0.0277 |
| $B^2C$ | 0 | -18.51 | 0 | 0 | -66.99 | -8.34 | 0 | 0 | 0.0438 |
| $BC^2$ | 0 | -4.72 | 0 | 0 | -19.67 | 3.42 | 0 | 0 | -0.0149 |
| $A^2B^2$ | 0 | 0 | 0 | 0 | 0 | 0 | 0 | 0 | -0.0333 |
| $A^2BC$ | 0 | 0 | 0 | 0 | 0 | 0 | 0 | 0 | 0.0027 |
| $A^2C^2$ | 0 | 0 | 0 | 0 | 0 | 0 | 0 | 0 | 0.0134 |
| $AB^2C$ | 0 | 0 | 0 | 0 | 0 | 0 | 0 | 0 | -0.059 |
| $ABC^2$ | 0 | 0 | 0 | 0 | 0 | 0 | 0 | 0 | 0.0105 |
| $B^2C^2$ | 0 | 0 | 0 | 0 | 0 | 0 | 0 | 0 | -0.0466 |
| **Regression confidence $R^2$** | 0.943 | 0.878 | 0.984 | 0.974 | 0.821 | 0.9 | 0.994 | 0.993 | 0.901 |

**Table 6.73.** The ANOVA results for measured forces in X direction (Fx) during drilling of extruded CW511L with 45° of plunging angle

| Source | Sum of Squares | df | Mean Square | F-value | p-value | |
|---|---|---|---|---|---|---|
| **Model** | 75225.45 | 6 | 12537.58 | 50.75 | < 0.0001 | significant |
| A-Radial rake angle | 203.89 | 1 | 203.89 | 0.8252 | 0.3745 | |
| B-Axial rake angle | 4.06 | 1 | 4.06 | 0.0164 | 0.8993 | |
| C-Edge radius | 73813.78 | 1 | 73813.78 | 298.76 | < 0.0001 | |
| AB | 115.2 | 1 | 115.2 | 0.4663 | 0.5025 | |
| AC | 920.15 | 1 | 920.15 | 3.72 | 0.0679 | |
| BC | 168.38 | 1 | 168.38 | 0.6815 | 0.4188 | |
| **Residual** | 4941.3 | 20 | 247.06 | | | |
| **Cor Total** | 80166.75 | 26 | | | | |

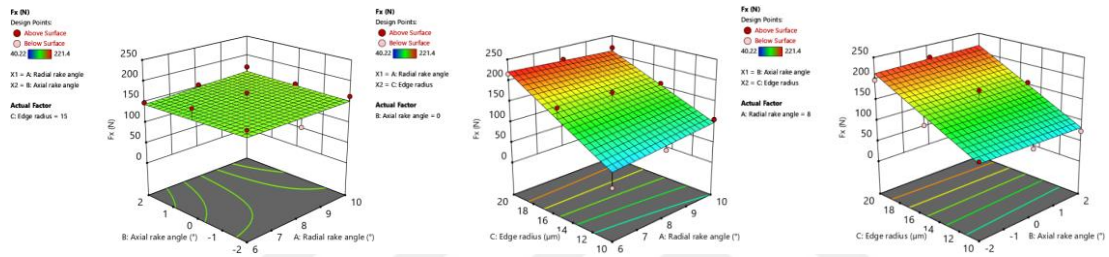

**Figure 6.101.** 3D surface plot of the measured forces in X direction (Fx) variation during drilling of extruded CW511L with 45° of plunging angle with respect to the studied cutting tool geometry

**Table 6.74.** The ANOVA results for measured forces in Y direction (Fy) during drilling of extruded CW511L with 45° of plunging angle

| Source | Sum of Squares | df | Mean Square | F-value | p-value | |
|---|---|---|---|---|---|---|
| **Model** | 30177.12 | 9 | 3353.01 | 12.43 | < 0.0001 | significant |
| A-Radial rake angle | 89.78 | 1 | 89.78 | 0.3328 | 0.5716 | |
| B-Axial rake angle | 442.04 | 1 | 442.04 | 1.64 | 0.2177 | |
| C-Edge radius | 27093.26 | 1 | 27093.26 | 100.42 | < 0.0001 | |
| AB | 116.31 | 1 | 116.31 | 0.4311 | 0.5202 | |
| AC | 353.17 | 1 | 353.17 | 1.31 | 0.2684 | |
| BC | 134 | 1 | 134 | 0.4967 | 0.4905 | |
| $A^2$ | 483.84 | 1 | 483.84 | 1.79 | 0.1981 | |
| $B^2$ | 1108.67 | 1 | 1108.67 | 4.11 | 0.0586 | |
| $C^2$ | 356.05 | 1 | 356.05 | 1.32 | 0.2665 | |
| **Residual** | 4586.38 | 17 | 269.79 | | | |
| **Cor Total** | 34763.5 | 26 | | | | |

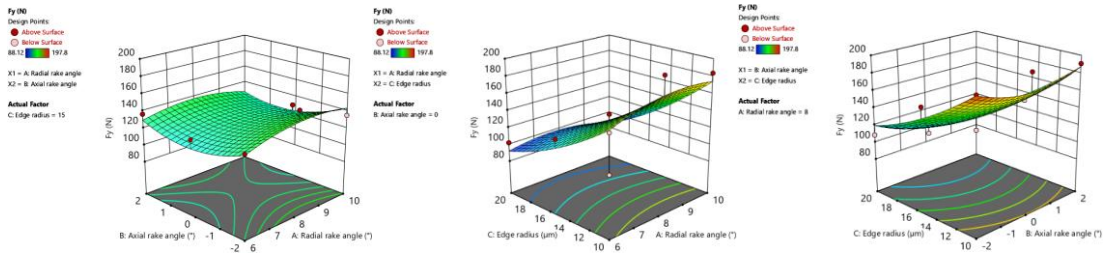

**Figure 6.102.** 3D surface plot of the measured forces in Y direction (Fy) variation during drilling of extruded CW511L with 45° of plunging angle with respect to the studied cutting tool geometry

**Table 6.75.** The ANOVA results for measured forces in Z direction (Fz) during drilling of extruded CW511L with 45° of plunging angle

| Source | Sum of Squares | df | Mean Square | F-value | p-value | |
|---|---|---|---|---|---|---|
| **Model** | 1.58E+05 | 9 | 17560.98 | 236 | < 0.0001 | significant |
| A-Radial rake angle | 3.04 | 1 | 3.04 | 0.0409 | 0.8422 | |
| B-Axial rake angle | 2138.58 | 1 | 2138.58 | 28.74 | < 0.0001 | |
| C-Edge radius | 1.34E+05 | 1 | 1.34E+05 | 1802.74 | < 0.0001 | |
| AB | 2.9 | 1 | 2.9 | 0.039 | 0.8458 | |
| AC | 522.72 | 1 | 522.72 | 7.02 | 0.0168 | |
| BC | 23.8 | 1 | 23.8 | 0.3199 | 0.5791 | |
| $A^2$ | 146.03 | 1 | 146.03 | 1.96 | 0.1792 | |
| $B^2$ | 27.31 | 1 | 27.31 | 0.367 | 0.5527 | |
| $C^2$ | 21039.68 | 1 | 21039.68 | 282.75 | < 0.0001 | |
| **Residual** | 1264.99 | 17 | 74.41 | | | |
| **Cor Total** | 1.59E+05 | 26 | | | | |

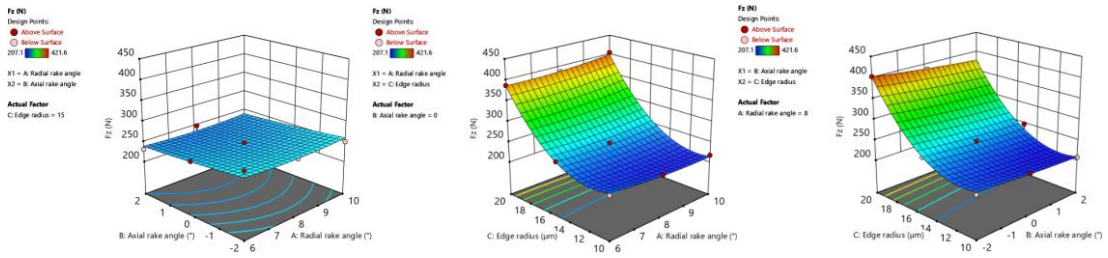

**Figure 6.103.** 3D surface plot of the measured forces in Z direction (Fz) variation during drilling of extruded CW511L with 45° of plunging angle with respect to the studied cutting tool geometry

**Table 6.76.** The ANOVA results for measured resultant forces (FR) during drilling of extruded CW511L with 45° of plunging angle

| Source | Sum of Squares | df | Mean Square | F-value | p-value | |
|---|---|---|---|---|---|---|
| **Model** | 1.36E+05 | 9 | 15113.39 | 74.63 | < 0.0001 | significant |

| | | | | | |
|---|---|---|---|---|---|
| A-Radial rake angle | 72.03 | 1 | 72.03 | 0.3557 | 0.5588 |
| B-Axial rake angle | 1902.71 | 1 | 1902.71 | 9.4 | 0.007 |
| C-Edge radius | 1.17E+05 | 1 | 1.17E+05 | 575.85 | < 0.0001 |
| AB | 4.88 | 1 | 4.88 | 0.0241 | 0.8784 |
| AC | 0.115 | 1 | 0.115 | 0.0006 | 0.9813 |
| BC | 17.35 | 1 | 17.35 | 0.0857 | 0.7733 |
| $A^2$ | 36.22 | 1 | 36.22 | 0.1788 | 0.6777 |
| $B^2$ | 146.08 | 1 | 146.08 | 0.7214 | 0.4075 |
| $C^2$ | 17224.49 | 1 | 17224.49 | 85.05 | < 0.0001 |
| **Residual** | 3442.72 | 17 | 202.51 | | |
| **Cor Total** | 1.40E+05 | 26 | | | |

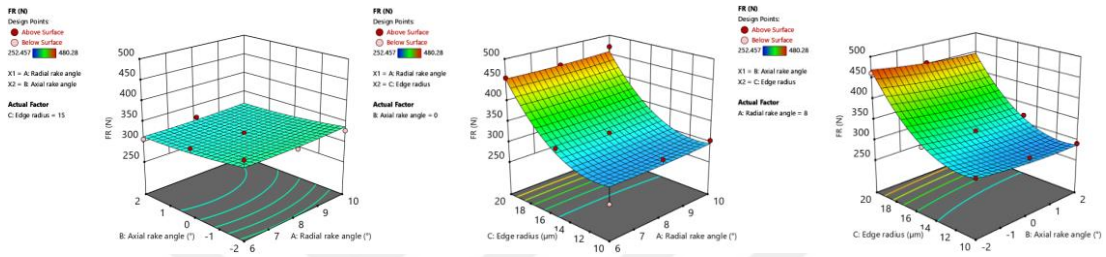

**Figure 6.104.** 3D surface plot of the measured resultant forces variation during drilling of extruded CW511L with 45° of plunging angle with respect to the studied cutting tool geometry

**Table 6.77.** The ANOVA results for measured burr heights at hole entry (BHEN) during drilling of extruded CW511L with 45° of plunging angle

| Source | Sum of Squares | df | Mean Square | F-value | p-value |
|---|---|---|---|---|---|
| **Model** | 44089.92 | 22 | 2004.09 | 3.61 | 0.1105 |
| A-Radial rake angle | 5609.62 | 1 | 5609.62 | 10.09 | 0.0336 |
| B-Axial rake angle | 19.66 | 1 | 19.66 | 0.0354 | 0.86 |
| C-Edge radius | 7097.28 | 1 | 7097.28 | 12.77 | 0.0233 |
| AB | 876.88 | 1 | 876.88 | 1.58 | 0.2774 |
| AC | 7.21 | 1 | 7.21 | 0.013 | 0.9148 |
| BC | 4.06 | 1 | 4.06 | 0.0073 | 0.936 |
| $A^2$ | 918.57 | 1 | 918.57 | 1.65 | 0.2679 |
| $B^2$ | 78.74 | 1 | 78.74 | 0.1417 | 0.7257 |
| $C^2$ | 708.04 | 1 | 708.04 | 1.27 | 0.3221 |
| ABC | 399.51 | 1 | 399.51 | 0.7189 | 0.4442 |
| $A^2B$ | 212.98 | 1 | 212.98 | 0.3833 | 0.5694 |
| $A^2C$ | 3853.69 | 1 | 3853.69 | 6.93 | 0.058 |
| $AB^2$ | 4730.17 | 1 | 4730.17 | 8.51 | 0.0433 |
| $AC^2$ | 442.59 | 1 | 442.59 | 0.7965 | 0.4226 |
| $B^2C$ | 2893.9 | 1 | 2893.9 | 5.21 | 0.0846 |
| $BC^2$ | 234.79 | 1 | 234.79 | 0.4225 | 0.5511 |
| $A^2B^2$ | 3317.68 | 1 | 3317.68 | 5.97 | 0.0709 |

| | | | | | |
|---|---|---|---|---|---|
| $A^2BC$ | 66.09 | 1 | 66.09 | 0.1189 | 0.7476 |
| $A^2C^2$ | 542.99 | 1 | 542.99 | 0.9772 | 0.3789 |
| $AB^2C$ | 4188.99 | 1 | 4188.99 | 7.54 | 0.0516 |
| $ABC^2$ | 137.13 | 1 | 137.13 | 0.2468 | 0.6454 |
| $B^2C^2$ | 46.34 | 1 | 46.34 | 0.0834 | 0.7871 |
| **Residual** | 2222.75 | 4 | 555.69 | | |
| **Cor Total** | 46312.67 | 26 | | | |

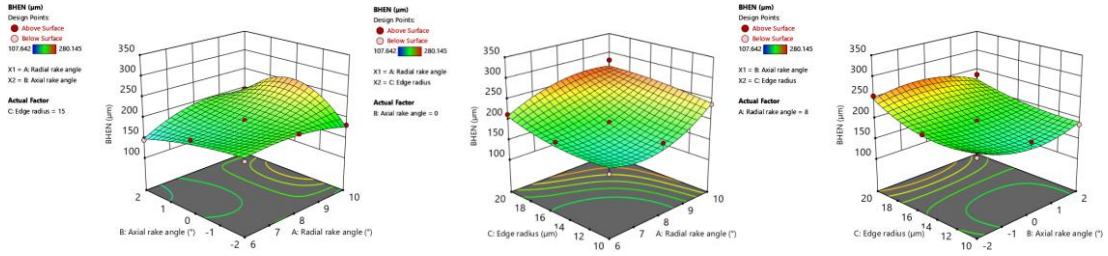

**Figure 6.105.** 3D surface plot of the measured burr heights at hole entry (BHEN) variation during drilling of extruded CW511L with 45° of plunging angle with respect to the studied cutting tool geometry

**Table 6.78.** The ANOVA results for measured burr heights at hole exit (BHEX) during drilling of extruded CW511L with 45° of plunging angle

| Source | Sum of Squares | df | Mean Square | F-value | p-value | |
|---|---|---|---|---|---|---|
| **Model** | 9817.51 | 6 | 1636.25 | 24.17 | < 0.0001 | significant |
| A-Radial rake angle | 2850.67 | 1 | 2850.67 | 42.1 | < 0.0001 | |
| B-Axial rake angle | 884.35 | 1 | 884.35 | 13.06 | 0.0017 | |
| C-Edge radius | 5446.53 | 1 | 5446.53 | 80.44 | < 0.0001 | |
| AB | 293.83 | 1 | 293.83 | 4.34 | 0.0503 | |
| AC | 327.79 | 1 | 327.79 | 4.84 | 0.0397 | |
| BC | 14.34 | 1 | 14.34 | 0.2117 | 0.6504 | |
| **Residual** | 1354.18 | 20 | 67.71 | | | |
| **Cor Total** | 11171.69 | 26 | | | | |

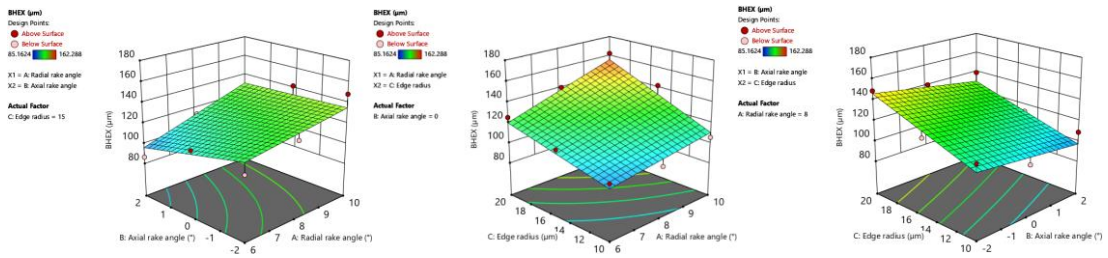

**Figure 6.106.** 3D surface plot of the measured burr heights at hole exit (BHEX) variation during drilling of extruded CW511L with 45° of plunging angle with respect to the studied cutting tool geometry

**Table 6.79.** The ANOVA results for measured surface roughness at hole bottom (Ra) during drilling of extruded CW511L with 45° of plunging angle

| Source | Sum of Squares | df | Mean Square | F-value | p-value | |
|---|---|---|---|---|---|---|
| **Model** | 0.0495 | 9 | 0.0055 | 344.65 | < 0.0001 | significant |
| A-Radial rake angle | 0.0033 | 1 | 0.0033 | 207.08 | < 0.0001 | |
| B-Axial rake angle | 0.0004 | 1 | 0.0004 | 22.82 | 0.0002 | |
| C-Edge radius | 0.0456 | 1 | 0.0456 | 2855.08 | < 0.0001 | |
| AB | 0 | 1 | 0 | 2.3 | 0.1477 | |
| AC | 2.08E-06 | 1 | 2.08E-06 | 0.1304 | 0.7224 | |
| BC | 7.50E-07 | 1 | 7.50E-07 | 0.047 | 0.831 | |
| $A^2$ | 0 | 1 | 0 | 2.05 | 0.1708 | |
| $B^2$ | 4.17E-06 | 1 | 4.17E-06 | 0.2609 | 0.6161 | |
| $C^2$ | 0.0002 | 1 | 0.0002 | 12.06 | 0.0029 | |
| **Residual** | 0.0003 | 17 | 0 | | | |
| **Cor Total** | 0.0498 | 26 | | | | |

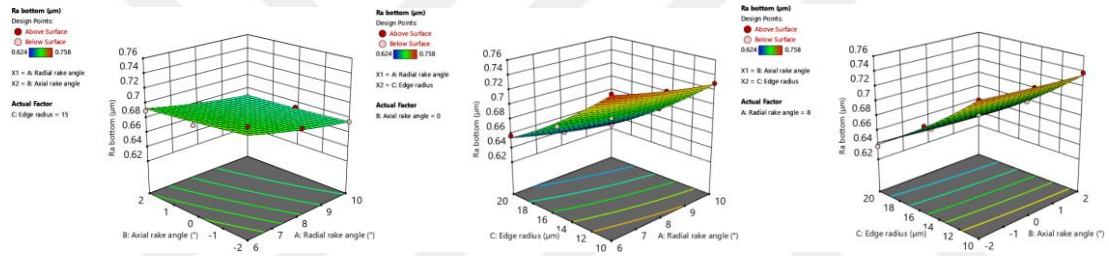

**Figure 6.107.** 3D surface plot of the measured surface roughness at hole bottom (Ra) variation during drilling of extruded CW511L with 45° of plunging angle with respect to the studied cutting tool geometry

**Table 6.80.** The ANOVA results for measured surface roughness at hole wall (Ra) during drilling of extruded CW511L with 45° of plunging angle

| Source | Sum of Squares | df | Mean Square | F-value | p-value | |
|---|---|---|---|---|---|---|
| **Model** | 0.0173 | 6 | 0.0029 | 472.28 | < 0.0001 | significant |
| A-Radial rake angle | 0.0011 | 1 | 0.0011 | 186.55 | < 0.0001 | |
| B-Axial rake angle | 0.0001 | 1 | 0.0001 | 20.15 | 0.0002 | |
| C-Edge radius | 0.016 | 1 | 0.016 | 2620.92 | < 0.0001 | |
| AB | 6.75E-06 | 1 | 6.75E-06 | 1.11 | 0.305 | |
| AC | 0 | 1 | 0 | 4.94 | 0.0379 | |
| BC | 0 | 1 | 0 | 0 | 1 | |
| **Residual** | 0.0001 | 20 | 6.09E-06 | | | |
| **Cor Total** | 0.0174 | 26 | | | | |

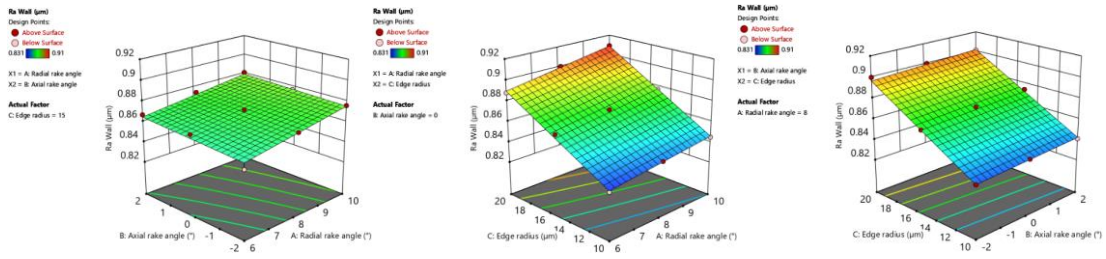

**Figure 6.108.** 3D surface plot of the measured surface roughness at hole wall (Ra) variation during drilling of extruded CW511L with 45° of plunging angle with respect to the studied cutting tool geometry

**Table 6.81.** The ANOVA results for measured hole diameter during drilling of extruded CW511L with 45° of plunging angle

| Source | Sum of Squares | df | Mean Square | F-value | p-value |
|---|---|---|---|---|---|
| **Model** | 0.0407 | 25 | 0.0016 | 16.74 | 0.1911 |
| A-Radial rake angle | 5.00E-07 | 1 | 5.00E-07 | 0.0051 | 0.9545 |
| B-Axial rake angle | 0 | 1 | 0 | 0.2517 | 0.704 |
| C-Edge radius | 0.0001 | 1 | 0.0001 | 0.7397 | 0.5478 |
| AB | 0.0006 | 1 | 0.0006 | 6.42 | 0.2393 |
| AC | 0.005 | 1 | 0.005 | 51.06 | 0.0885 |
| BC | 0 | 1 | 0 | 0.4341 | 0.6291 |
| $A^2$ | 0.0002 | 1 | 0.0002 | 2.27 | 0.3733 |
| $B^2$ | 0.0005 | 1 | 0.0005 | 5.15 | 0.2642 |
| $C^2$ | 0.0001 | 1 | 0.0001 | 1.25 | 0.465 |
| ABC | 0.0001 | 1 | 0.0001 | 1.4 | 0.4469 |
| $A^2B$ | 5.33E-06 | 1 | 5.33E-06 | 0.0548 | 0.8536 |
| $A^2C$ | 0.004 | 1 | 0.004 | 41.06 | 0.0986 |
| $AB^2$ | 0.0006 | 1 | 0.0006 | 6.63 | 0.2358 |
| $AC^2$ | 0.0039 | 1 | 0.0039 | 40.31 | 0.0994 |
| $B^2C$ | 0.0004 | 1 | 0.0004 | 4.08 | 0.2928 |
| $BC^2$ | 0.0002 | 1 | 0.0002 | 2.4 | 0.3646 |
| $A^2B^2$ | 0.0009 | 1 | 0.0009 | 9.56 | 0.1991 |
| $A^2BC$ | 0.0001 | 1 | 0.0001 | 1.2 | 0.4707 |
| $A^2C^2$ | 0.0012 | 1 | 0.0012 | 12.19 | 0.1776 |
| $AB^2C$ | 0.003 | 1 | 0.003 | 30.97 | 0.1132 |
| $ABC^2$ | 0.0001 | 1 | 0.0001 | 1.11 | 0.4829 |
| $B^2C^2$ | 0.0018 | 1 | 0.0018 | 18.92 | 0.1439 |
| $A^2B^2C$ | 0.0032 | 1 | 0.0032 | 33.29 | 0.1093 |
| $A^2BC^2$ | 0.0002 | 1 | 0.0002 | 2.02 | 0.3903 |
| $AB^2C^2$ | 0.004 | 1 | 0.004 | 41.15 | 0.0985 |
| **Residual** | 0.0001 | 1 | 0.0001 | | |
| **Cor Total** | 0.0408 | 26 | | | |

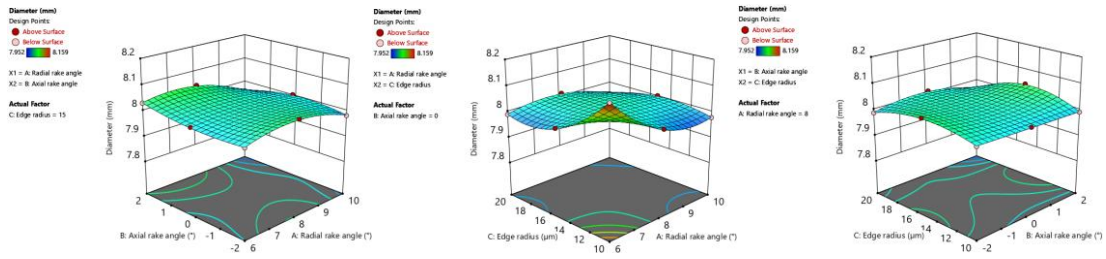

**Figure 6.109.** 3D surface plot of the measured hole diameter variation during drilling of extruded CW511L with 45° of plunging angle with respect to the studied cutting tool geometry

**Table 6.82.** The developed regression model for drilling of extruded CW511L with 45° of plunging angle

| Extruded CW511L 45 | Fx | Fy | Fz | FR | BHEN | BHEX | Ra bottom | Ra Wall | Diameter |
|---|---|---|---|---|---|---|---|---|---|
| | 151.63 | 128.99 | 242.9 | 318.84 | 191.67 | 120.55 | 0.6829 | 0.8694 | 8.02 |
| A | 3.37 | 2.23 | -0.4111 | 2 | 39.47 | 12.58 | -0.0136 | 0.0079 | -0.0005 |
| B | -0.475 | -4.96 | -10.9 | -10.28 | -2.34 | -7.01 | -0.0045 | 0.0026 | 0.0035 |
| C | 64.04 | -38.8 | 86.33 | 80.49 | 44.4 | 17.39 | -0.0503 | 0.0298 | 0.006 |
| AB | 3.1 | -3.11 | 0.4917 | 0.6379 | 14.81 | 4.95 | 0.0017 | -0.0008 | -0.0125 |
| AC | -8.76 | -5.43 | 6.6 | 0.0979 | -1.34 | 5.23 | -0.0004 | 0.0016 | 0.0353 |
| BC | 3.75 | -3.34 | -1.41 | -1.2 | -1.01 | -1.09 | 0.0002 | 0 | -0.0032 |
| $A^2$ | 0 | -8.98 | 4.93 | 2.46 | 27.67 | 0 | 0.0023 | 0 | -0.0136 |
| $B^2$ | 0 | 13.59 | 2.13 | 4.93 | 8.1 | 0 | 0.0008 | 0 | 0.0204 |
| $C^2$ | 0 | 7.7 | 59.22 | 53.58 | 24.29 | 0 | 0.0057 | 0 | -0.0101 |
| ABC | 0 | 0 | 0 | 0 | 7.07 | 0 | 0 | 0 | 0.0041 |
| $A^2B$ | 0 | 0 | 0 | 0 | -7.3 | 0 | 0 | 0 | -0.002 |
| $A^2C$ | 0 | 0 | 0 | 0 | -31.04 | 0 | 0 | 0 | -0.0547 |
| $AB^2$ | 0 | 0 | 0 | 0 | -34.39 | 0 | 0 | 0 | -0.022 |
| $AC^2$ | 0 | 0 | 0 | 0 | -10.52 | 0 | 0 | 0 | -0.0542 |
| $B^2C$ | 0 | 0 | 0 | 0 | -26.9 | 0 | 0 | 0 | -0.0172 |
| $BC^2$ | 0 | 0 | 0 | 0 | -7.66 | 0 | 0 | 0 | -0.0132 |
| $A^2B^2$ | 0 | 0 | 0 | 0 | -49.88 | 0 | 0 | 0 | -0.0264 |
| $A^2BC$ | 0 | 0 | 0 | 0 | 4.98 | 0 | 0 | 0 | 0.0066 |
| $A^2C^2$ | 0 | 0 | 0 | 0 | -20.18 | 0 | 0 | 0 | 0.0298 |
| $AB^2C$ | 0 | 0 | 0 | 0 | -39.63 | 0 | 0 | 0 | -0.0336 |
| $ABC^2$ | 0 | 0 | 0 | 0 | -7.17 | 0 | 0 | 0 | 0.0064 |
| $B^2C^2$ | 0 | 0 | 0 | 0 | -5.9 | 0 | 0 | 0 | -0.0372 |
| $A^2B^2C$ | 0 | 0 | 0 | 0 | 0 | 0 | 0 | 0 | 0.0604 |
| $A^2BC^2$ | 0 | 0 | 0 | 0 | 0 | 0 | 0 | 0 | 0.0149 |
| $AB^2C^2$ | 0 | 0 | 0 | 0 | 0 | 0 | 0 | 0 | 0.0671 |
| **Regression confidence $R^2$** | 0.938 | 0.868 | 0.992 | 0.975 | 0.952 | 0.878 | 0.994 | 0.993 | 0.997 |

**Table 6.83.** The ANOVA results for measured forces in X direction (Fx) during drilling

of extruded CW724R with 90° of plunging angle

| Source | Sum of Squares | df | Mean Square | F-value | p-value |
|---|---|---|---|---|---|
| **Model** | 392.23 | 22 | 17.83 | 2.77 | 0.1662 |
| A-Radial rake angle | 0.021 | 1 | 0.021 | 0.0033 | 0.9572 |
| B-Axial rake angle | 0.3627 | 1 | 0.3627 | 0.0564 | 0.824 |
| C-Edge radius | 50.93 | 1 | 50.93 | 7.92 | 0.0481 |
| AB | 0.4316 | 1 | 0.4316 | 0.0671 | 0.8084 |
| AC | 1.98 | 1 | 1.98 | 0.3071 | 0.609 |
| BC | 2.03 | 1 | 2.03 | 0.3155 | 0.6043 |
| $A^2$ | 23.79 | 1 | 23.79 | 3.7 | 0.1268 |
| $B^2$ | 6.54 | 1 | 6.54 | 1.02 | 0.3705 |
| $C^2$ | 45.18 | 1 | 45.18 | 7.02 | 0.057 |
| ABC | 0.6163 | 1 | 0.6163 | 0.0958 | 0.7724 |
| $A^2B$ | 0.0848 | 1 | 0.0848 | 0.0132 | 0.9141 |
| $A^2C$ | 50.18 | 1 | 50.18 | 7.8 | 0.0492 |
| $AB^2$ | 4.23 | 1 | 4.23 | 0.6572 | 0.463 |
| $AC^2$ | 4.72 | 1 | 4.72 | 0.7344 | 0.4398 |
| $B^2C$ | 2.75 | 1 | 2.75 | 0.4271 | 0.5491 |
| $BC^2$ | 5.66 | 1 | 5.66 | 0.8801 | 0.4013 |
| $A^2B^2$ | 48.77 | 1 | 48.77 | 7.58 | 0.0512 |
| $A^2BC$ | 5.04 | 1 | 5.04 | 0.783 | 0.4262 |
| $A^2C^2$ | 14.73 | 1 | 14.73 | 2.29 | 0.2048 |
| $AB^2C$ | 13.79 | 1 | 13.79 | 2.14 | 0.2169 |
| $ABC^2$ | 0.8643 | 1 | 0.8643 | 0.1344 | 0.7325 |
| $B^2C^2$ | 82.65 | 1 | 82.65 | 12.85 | 0.0231 |
| **Residual** | 25.73 | 4 | 6.43 | | |
| **Cor Total** | 417.96 | 26 | | | |

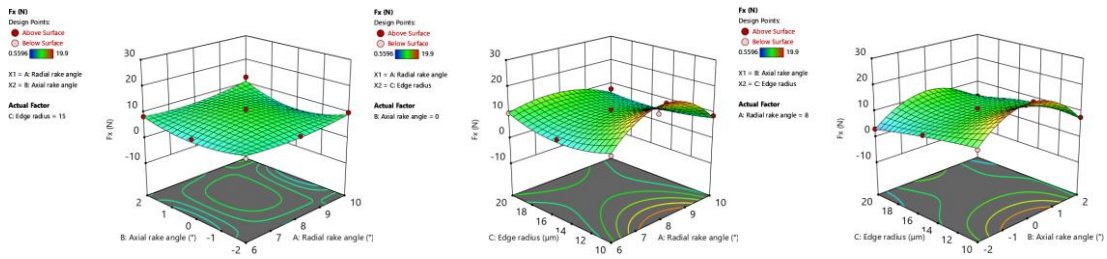

**Figure 6.110.** 3D surface plot of the measured forces in X direction (Fx) variation during drilling of extruded CW724R with 90° of plunging angle with respect to the studied cutting tool geometry

**Table 6.84.** The ANOVA results for measured forces in Y direction (Fy) during drilling of extruded CW724R with 90° of plunging angle

| Source | Sum of Squares | df | Mean Square | F-value | p-value | |
|---|---|---|---|---|---|---|
| **Model** | 488.24 | 16 | 30.51 | 2.85 | 0.0486 | significant |

| | | | | | |
|---|---|---|---|---|---|
| A-Radial rake angle | 4.8 | 1 | 4.8 | 0.4485 | 0.5182 |
| B-Axial rake angle | 112.23 | 1 | 112.23 | 10.49 | 0.0089 |
| C-Edge radius | 12.57 | 1 | 12.57 | 1.18 | 0.3037 |
| AB | 1.2 | 1 | 1.2 | 0.1122 | 0.7445 |
| AC | 31.62 | 1 | 31.62 | 2.96 | 0.1163 |
| BC | 15.9 | 1 | 15.9 | 1.49 | 0.2506 |
| $A^2$ | 2.7 | 1 | 2.7 | 0.2525 | 0.6262 |
| $B^2$ | 34.55 | 1 | 34.55 | 3.23 | 0.1025 |
| $C^2$ | 26.5 | 1 | 26.5 | 2.48 | 0.1465 |
| ABC | 56.14 | 1 | 56.14 | 5.25 | 0.0449 |
| $A^2B$ | 4.92 | 1 | 4.92 | 0.4601 | 0.513 |
| $A^2C$ | 0.3195 | 1 | 0.3195 | 0.0299 | 0.8662 |
| $AB^2$ | 14.89 | 1 | 14.89 | 1.39 | 0.2653 |
| $AC^2$ | 22.43 | 1 | 22.43 | 2.1 | 0.1781 |
| $B^2C$ | 21.04 | 1 | 21.04 | 1.97 | 0.191 |
| $BC^2$ | 28.19 | 1 | 28.19 | 2.64 | 0.1355 |
| **Residual** | 106.94 | 10 | 10.69 | | |
| **Cor Total** | 595.18 | 26 | | | |

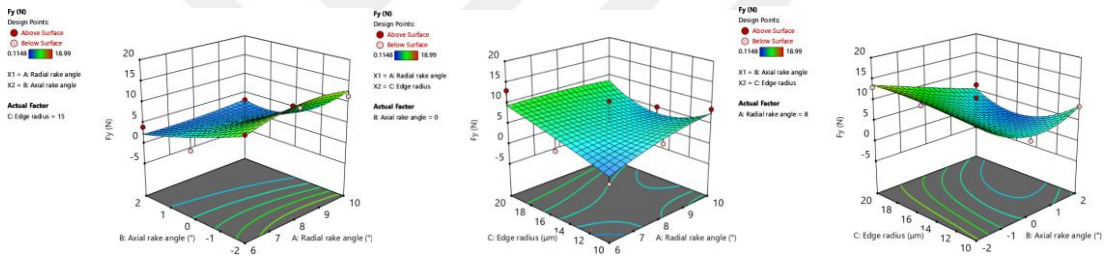

**Figure 6.111.** 3D surface plot of the measured forces in Y direction (Fy) variation during drilling of extruded CW724R with 90° of plunging angle with respect to the studied cutting tool geometry

**Table 6.85.** The ANOVA results for measured forces in Z direction (Fz) during drilling of extruded CW724R with 90° of plunging angle

| Source | Sum of Squares | df | Mean Square | F-value | p-value | |
|---|---|---|---|---|---|---|
| **Model** | 57859.35 | 9 | 6428.82 | 32.4 | < 0.0001 | significant |
| A-Radial rake angle | 140.56 | 1 | 140.56 | 0.7085 | 0.4116 | |
| B-Axial rake angle | 3701.91 | 1 | 3701.91 | 18.66 | 0.0005 | |
| C-Edge radius | 46117.77 | 1 | 46117.77 | 232.45 | < 0.0001 | |
| AB | 244.31 | 1 | 244.31 | 1.23 | 0.2826 | |
| AC | 290.08 | 1 | 290.08 | 1.46 | 0.2431 | |
| BC | 614.38 | 1 | 614.38 | 3.1 | 0.0964 | |
| $A^2$ | 348.64 | 1 | 348.64 | 1.76 | 0.2025 | |
| $B^2$ | 14.47 | 1 | 14.47 | 0.0729 | 0.7904 | |
| $C^2$ | 6387.23 | 1 | 6387.23 | 32.19 | < 0.0001 | |
| **Residual** | 3372.81 | 17 | 198.4 | | | |

| | | |
|---|---|---|
| **Cor Total** | 61232.16 | 26 |

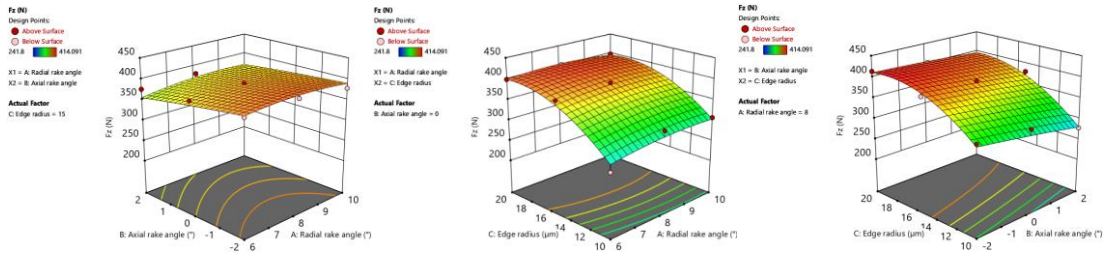

**Figure 6.112.** 3D surface plot of the measured forces in Z direction (Fz) variation during drilling of extruded CW724R with 90° of plunging angle with respect to the studied cutting tool geometry

**Table 6.86.** The ANOVA results for measured resultant forces (FR) during drilling of extruded CW724R with 90° of plunging angle

| Source | Sum of Squares | df | Mean Square | F-value | p-value | |
|---|---|---|---|---|---|---|
| **Model** | 57787.89 | 9 | 6420.88 | 32.04 | < 0.0001 | significant |
| A-Radial rake angle | 145.74 | 1 | 145.74 | 0.7273 | 0.4056 | |
| B-Axial rake angle | 3732.73 | 1 | 3732.73 | 18.63 | 0.0005 | |
| C-Edge radius | 46028.06 | 1 | 46028.06 | 229.7 | < 0.0001 | |
| AB | 244.54 | 1 | 244.54 | 1.22 | 0.2847 | |
| AC | 293.54 | 1 | 293.54 | 1.46 | 0.2427 | |
| BC | 606.85 | 1 | 606.85 | 3.03 | 0.0999 | |
| $A^2$ | 356 | 1 | 356 | 1.78 | 0.2002 | |
| $B^2$ | 14.99 | 1 | 14.99 | 0.0748 | 0.7878 | |
| $C^2$ | 6365.44 | 1 | 6365.44 | 31.77 | < 0.0001 | |
| **Residual** | 3406.52 | 17 | 200.38 | | | |
| **Cor Total** | 61194.41 | 26 | | | | |

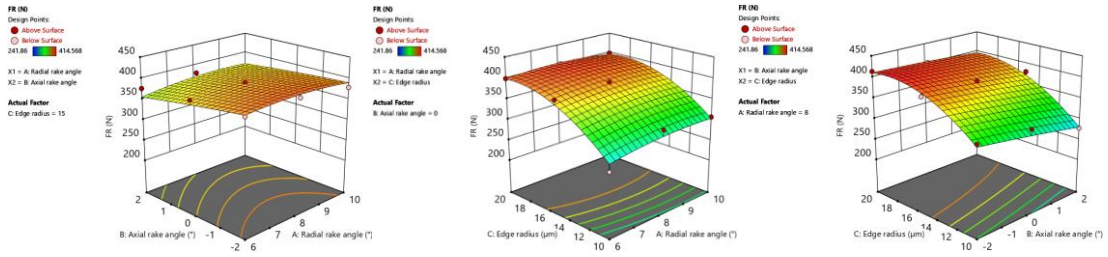

**Figure 6.113.** 3D surface plot of the measured resultant forces variation during drilling of extruded CW724R with 90° of plunging angle with respect to the studied cutting tool geometry

**Table 6.87.** The ANOVA results for measured burr heights at hole entry (BHEN) during drilling of extruded CW724R with 90° of plunging angle

| Source | Sum of Squares | df | Mean Square | F-value | p-value | |
|---|---|---|---|---|---|---|
| **Model** | 42135.05 | 9 | 4681.67 | 82.31 | < 0.0001 | significant |
| A-Radial rake angle | 18208.27 | 1 | 18208.27 | 320.13 | < 0.0001 | |
| B-Axial rake angle | 3183.74 | 1 | 3183.74 | 55.98 | < 0.0001 | |
| C-Edge radius | 14653.77 | 1 | 14653.77 | 257.64 | < 0.0001 | |
| AB | 2116.62 | 1 | 2116.62 | 37.21 | < 0.0001 | |
| AC | 1181.02 | 1 | 1181.02 | 20.76 | 0.0003 | |
| BC | 579.53 | 1 | 579.53 | 10.19 | 0.0053 | |
| $A^2$ | 1782.63 | 1 | 1782.63 | 31.34 | < 0.0001 | |
| $B^2$ | 148.27 | 1 | 148.27 | 2.61 | 0.1248 | |
| $C^2$ | 281.2 | 1 | 281.2 | 4.94 | 0.04 | |
| **Residual** | 966.92 | 17 | 56.88 | | | |
| **Cor Total** | 43101.97 | 26 | | | | |

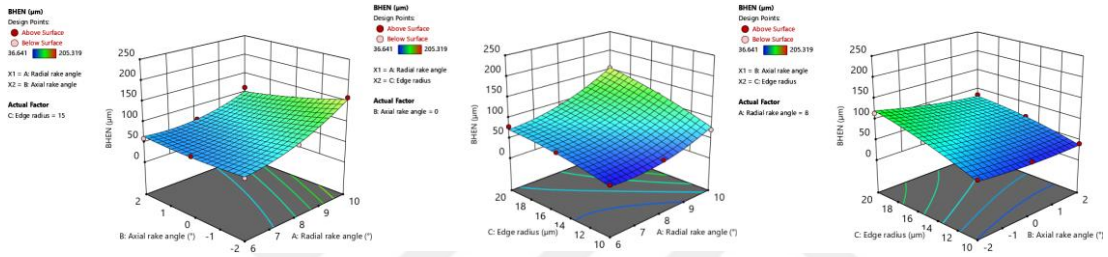

**Figure 6.114.** 3D surface plot of the measured burr heights at hole entry (BHEN) variation during drilling of extruded CW724R with 90° of plunging angle with respect to the studied cutting tool geometry

**Table 6.88.** The ANOVA results for measured burr heights at hole exit (BHEX) during drilling of extruded CW724R with 90° of plunging angle

| Source | Sum of Squares | df | Mean Square | F-value | p-value | |
|---|---|---|---|---|---|---|
| **Model** | 6842.12 | 9 | 760.24 | 26.11 | < 0.0001 | significant |
| A-Radial rake angle | 2818.08 | 1 | 2818.08 | 96.77 | < 0.0001 | |
| B-Axial rake angle | 582.21 | 1 | 582.21 | 19.99 | 0.0003 | |
| C-Edge radius | 2217.82 | 1 | 2217.82 | 76.16 | < 0.0001 | |
| AB | 458.74 | 1 | 458.74 | 15.75 | 0.001 | |
| AC | 101.84 | 1 | 101.84 | 3.5 | 0.0788 | |
| BC | 224.21 | 1 | 224.21 | 7.7 | 0.013 | |
| $A^2$ | 268.2 | 1 | 268.2 | 9.21 | 0.0075 | |
| $B^2$ | 43.69 | 1 | 43.69 | 1.5 | 0.2373 | |
| $C^2$ | 127.33 | 1 | 127.33 | 4.37 | 0.0519 | |
| **Residual** | 495.07 | 17 | 29.12 | | | |
| **Cor Total** | 7337.19 | 26 | | | | |

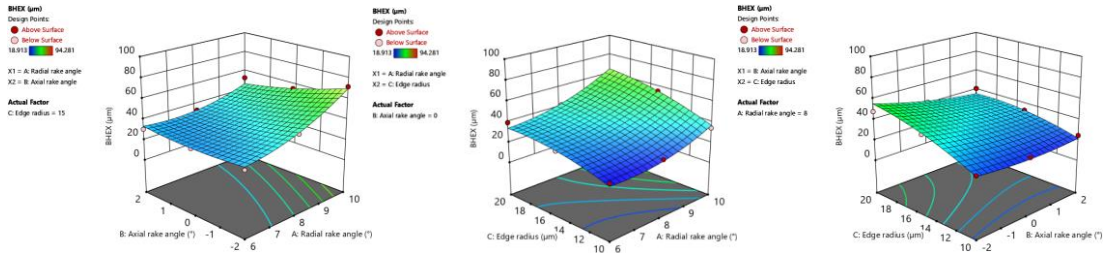

**Figure 6.115.** 3D surface plot of the measured burr heights at hole exit (BHEX) variation during drilling of extruded CW724R with 90° of plunging angle with respect to the studied cutting tool geometry

**Table 6.89.** The ANOVA results for measured surface roughness at hole bottom (Ra) during drilling of extruded CW724R with 90° of plunging angle

| Source | Sum of Squares | df | Mean Square | F-value | p-value | |
|---|---|---|---|---|---|---|
| **Model** | 0.0618 | 9 | 0.0069 | 119.09 | < 0.0001 | significant |
| A-Radial rake angle | 0.0048 | 1 | 0.0048 | 82.76 | < 0.0001 | |
| B-Axial rake angle | 0.0006 | 1 | 0.0006 | 11.24 | 0.0038 | |
| C-Edge radius | 0.0499 | 1 | 0.0499 | 866.38 | < 0.0001 | |
| AB | 0 | 1 | 0 | 0.5784 | 0.4574 | |
| AC | 0.0014 | 1 | 0.0014 | 24.82 | 0.0001 | |
| BC | 0.0002 | 1 | 0.0002 | 4.06 | 0.06 | |
| $A^2$ | 0 | 1 | 0 | 0.3088 | 0.5857 | |
| $B^2$ | 0 | 1 | 0 | 0.68 | 0.421 | |
| $C^2$ | 0.0047 | 1 | 0.0047 | 80.98 | < 0.0001 | |
| **Residual** | 0.001 | 17 | 0.0001 | | | |
| **Cor Total** | 0.0627 | 26 | | | | |

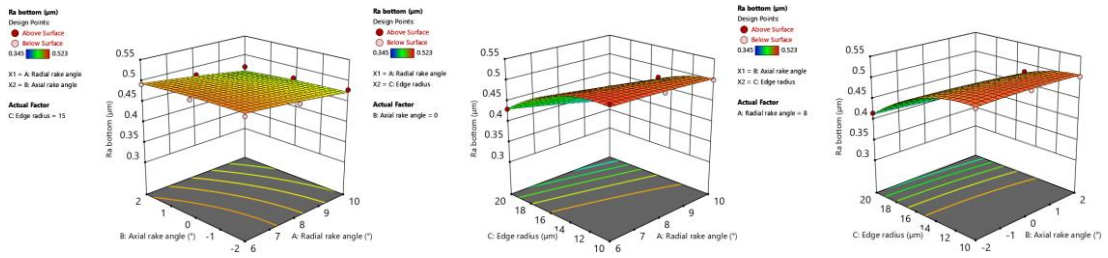

**Figure 6.116.** 3D surface plot of the measured surface roughness at hole bottom (Ra) variation during drilling of extruded CW724R with 90° of plunging angle with respect to the studied cutting tool geometry

**Table 6.90.** The ANOVA results for measured surface roughness at hole wall (Ra) during drilling of extruded CW724R with 90° of plunging angle

| Source | Sum of Squares | df | Mean Square | F-value | p-value | |
|---|---|---|---|---|---|---|
| **Model** | 0.0495 | 9 | 0.0055 | 72.5 | < 0.0001 | significant |

| | | | | | |
|---|---|---|---|---|---|
| A-Radial rake angle | 0.0041 | 1 | 0.0041 | 54.56 | < 0.0001 |
| B-Axial rake angle | 0.0006 | 1 | 0.0006 | 7.92 | 0.012 |
| C-Edge radius | 0.0377 | 1 | 0.0377 | 497.05 | < 0.0001 |
| AB | 0.0001 | 1 | 0.0001 | 1.12 | 0.3038 |
| AC | 0.002 | 1 | 0.002 | 26.38 | < 0.0001 |
| BC | 0.0004 | 1 | 0.0004 | 4.64 | 0.0459 |
| $A^2$ | 0.0001 | 1 | 0.0001 | 0.6854 | 0.4192 |
| $B^2$ | 0 | 1 | 0 | 0.61 | 0.4455 |
| $C^2$ | 0.0045 | 1 | 0.0045 | 59.55 | < 0.0001 |
| **Residual** | 0.0013 | 17 | 0.0001 | | |
| **Cor Total** | 0.0508 | 26 | | | |

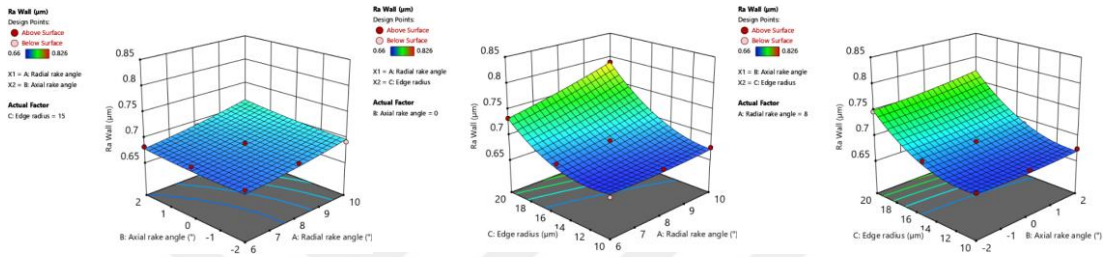

**Figure 6.117.** 3D surface plot of the measured surface roughness at hole wall (Ra) variation during drilling of extruded CW724R with 90° of plunging angle with respect to the studied cutting tool geometry

**Table 6.91.** The ANOVA results for measured hole diameter during drilling of extruded CW724R with 90° of plunging angle

| Source | Sum of Squares | df | Mean Square | F-value | p-value | |
|---|---|---|---|---|---|---|
| **Model** | 0.0824 | 16 | 0.0051 | 16.31 | < 0.0001 | significant |
| A-Radial rake angle | 0.0004 | 1 | 0.0004 | 1.17 | 0.3056 | |
| B-Axial rake angle | 0.0001 | 1 | 0.0001 | 0.4106 | 0.5361 | |
| C-Edge radius | 0.0036 | 1 | 0.0036 | 11.48 | 0.0069 | |
| AB | 0.0044 | 1 | 0.0044 | 13.97 | 0.0039 | |
| AC | 0.0043 | 1 | 0.0043 | 13.6 | 0.0042 | |
| BC | 0.0032 | 1 | 0.0032 | 10.14 | 0.0097 | |
| $A^2$ | 0.0013 | 1 | 0.0013 | 4.18 | 0.0681 | |
| $B^2$ | 0 | 1 | 0 | 0.0338 | 0.8578 | |
| $C^2$ | 0.0144 | 1 | 0.0144 | 45.64 | < 0.0001 | |
| ABC | 0.0038 | 1 | 0.0038 | 11.99 | 0.0061 | |
| $A^2B$ | 0.0003 | 1 | 0.0003 | 1.03 | 0.3349 | |
| $A^2C$ | 0 | 1 | 0 | 0.1479 | 0.7086 | |
| $AB^2$ | 0.0002 | 1 | 0.0002 | 0.5918 | 0.4595 | |
| $AC^2$ | 0.0108 | 1 | 0.0108 | 34.16 | 0.0002 | |
| $B^2C$ | 0.0002 | 1 | 0.0002 | 0.6509 | 0.4386 | |
| $BC^2$ | 0.0002 | 1 | 0.0002 | 0.621 | 0.449 | |
| **Residual** | 0.0032 | 10 | 0.0003 | | | |

| | | |
|---|---|---|
| **Cor Total** | 0.0855 | 26 |

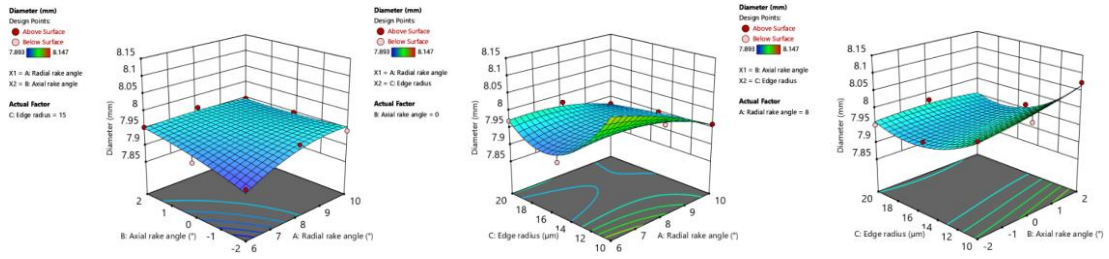

**Figure 6.118.** 3D surface plot of the measured hole diameter variation during drilling of extruded CW724R with 90° of plunging angle with respect to the studied cutting tool geometry

**Table 6.92.** The developed regression model for drilling of extruded CW724R with 90° of plunging angle

| Extruded CW724R 90 | Fx | Fy | Fz | FR | BHEN | BHEX | Ra bottom | Ra Wall | Diameter |
|---|---|---|---|---|---|---|---|---|---|
| | 9.94 | 5.44 | 386.56 | 386.81 | 74.33 | 36.21 | 0.4861 | 0.6847 | 7.95 |
| A | -0.0764 | -1.15 | 2.79 | 2.85 | 31.81 | 12.51 | -0.0163 | 0.0152 | 0.0101 |
| B | 0.3174 | -5.58 | -14.34 | -14.4 | -13.3 | -5.69 | -0.006 | 0.0058 | 0.006 |
| C | -3.76 | 1.87 | 50.62 | 50.57 | 28.53 | 11.1 | -0.0527 | 0.0458 | -0.0317 |
| AB | 0.3285 | -0.3163 | 4.51 | 4.51 | -13.28 | -6.18 | -0.0017 | 0.0027 | -0.0192 |
| AC | -0.7027 | -1.62 | -4.92 | -4.95 | 9.92 | 2.91 | -0.0109 | 0.0129 | 0.0189 |
| BC | 0.7122 | -1.15 | 7.16 | 7.11 | -6.95 | -4.32 | -0.0044 | 0.0054 | -0.0163 |
| $A^2$ | -4.45 | -0.6709 | -7.62 | -7.7 | 17.24 | 6.69 | -0.0017 | 0.0029 | -0.0148 |
| $B^2$ | -2.33 | 2.4 | -1.55 | -1.58 | 4.97 | 2.7 | -0.0026 | 0.0028 | -0.0013 |
| $C^2$ | 6.14 | 2.1 | -32.63 | -32.57 | -6.85 | -4.61 | -0.0279 | 0.0274 | 0.049 |
| ABC | 0.2776 | -2.65 | 0 | 0 | 0 | 0 | 0 | 0 | 0.0218 |
| $A^2B$ | 0.1456 | 1.11 | 0 | 0 | 0 | 0 | 0 | 0 | 0.009 |
| $A^2C$ | 3.54 | 0.2826 | 0 | 0 | 0 | 0 | 0 | 0 | -0.0034 |
| $AB^2$ | 1.03 | 1.93 | 0 | 0 | 0 | 0 | 0 | 0 | 0.0068 |
| $AC^2$ | -1.09 | 2.37 | 0 | 0 | 0 | 0 | 0 | 0 | -0.0519 |
| $B^2C$ | 0.8287 | -2.29 | 0 | 0 | 0 | 0 | 0 | 0 | -0.0072 |
| $BC^2$ | -1.19 | 0 | 0 | 0 | 0 | 0 | 0 | 0 | 0.007 |
| $A^2B^2$ | 6.05 | 0 | 0 | 0 | 0 | 0 | 0 | 0 | 0 |
| $A^2BC$ | -1.37 | 0 | 0 | 0 | 0 | 0 | 0 | 0 | 0 |
| $A^2C^2$ | -3.32 | 0 | 0 | 0 | 0 | 0 | 0 | 0 | 0 |
| $AB^2C$ | 2.27 | 0 | 0 | 0 | 0 | 0 | 0 | 0 | 0 |
| $ABC^2$ | 0.5693 | 0 | 0 | 0 | 0 | 0 | 0 | 0 | 0 |
| $B^2C^2$ | -7.87 | 0 | 0 | 0 | 0 | 0 | 0 | 0 | 0 |
| **Regression confidence $R^2$** | 0.938 | 0.82 | 0.944 | 0.944 | 0.977 | 0.932 | 0.984 | 0.974 | 0.963 |

**Table 6.93.** The ANOVA results for measured forces in X direction (Fx) during drilling of extruded CW724R with 60° of plunging angle

| Source | Sum of Squares | df | Mean Square | F-value | p-value | |
|---|---|---|---|---|---|---|
| **Model** | 1.20E+05 | 9 | 13363.47 | 99.4 | < 0.0001 | significant |
| A-Radial rake angle | 965.8 | 1 | 965.8 | 7.18 | 0.0158 | |
| B-Axial rake angle | 229.19 | 1 | 229.19 | 1.7 | 0.2091 | |
| C-Edge radius | 1.07E+05 | 1 | 1.07E+05 | 795.54 | < 0.0001 | |
| AB | 81.8 | 1 | 81.8 | 0.6084 | 0.4461 | |
| AC | 5.01 | 1 | 5.01 | 0.0372 | 0.8493 | |
| BC | 65.01 | 1 | 65.01 | 0.4835 | 0.4962 | |
| $A^2$ | 423.75 | 1 | 423.75 | 3.15 | 0.0937 | |
| $B^2$ | 111.95 | 1 | 111.95 | 0.8326 | 0.3743 | |
| $C^2$ | 11432.52 | 1 | 11432.52 | 85.03 | < 0.0001 | |
| **Residual** | 2285.57 | 17 | 134.45 | | | |
| **Cor Total** | 1.23E+05 | 26 | | | | |

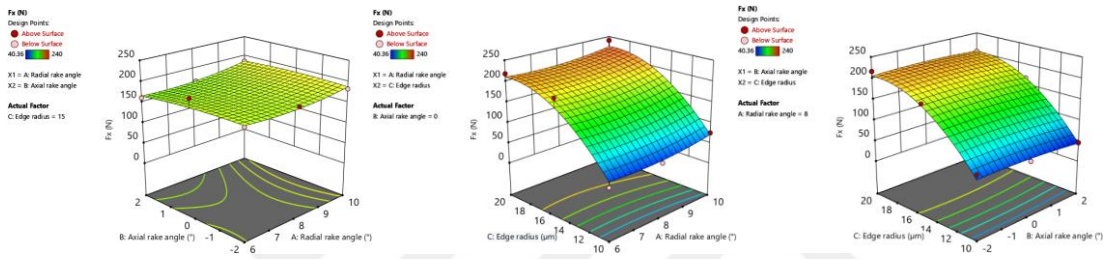

**Figure 6.119.** 3D surface plot of the measured forces in X direction (Fx) variation during drilling of extruded CW724R with 60° of plunging angle with respect to the studied cutting tool geometry

**Table 6.94.** The ANOVA results for measured forces in Y direction (Fy) during drilling of extruded CW724R with 60° of plunging angle

| Source | Sum of Squares | df | Mean Square | F-value | p-value | |
|---|---|---|---|---|---|---|
| **Model** | 57721.24 | 9 | 6413.47 | 113.27 | < 0.0001 | significant |
| A-Radial rake angle | 646.52 | 1 | 646.52 | 11.42 | 0.0036 | |
| B-Axial rake angle | 155.58 | 1 | 155.58 | 2.75 | 0.1157 | |
| C-Edge radius | 52573.98 | 1 | 52573.98 | 928.48 | < 0.0001 | |
| AB | 0.0454 | 1 | 0.0454 | 0.0008 | 0.9778 | |
| AC | 154.32 | 1 | 154.32 | 2.73 | 0.1171 | |
| BC | 6.4 | 1 | 6.4 | 0.113 | 0.7409 | |
| $A^2$ | 2.79 | 1 | 2.79 | 0.0493 | 0.827 | |
| $B^2$ | 29.64 | 1 | 29.64 | 0.5235 | 0.4792 | |
| $C^2$ | 4151.97 | 1 | 4151.97 | 73.33 | < 0.0001 | |
| **Residual** | 962.6 | 17 | 56.62 | | | |
| **Cor Total** | 58683.84 | 26 | | | | |

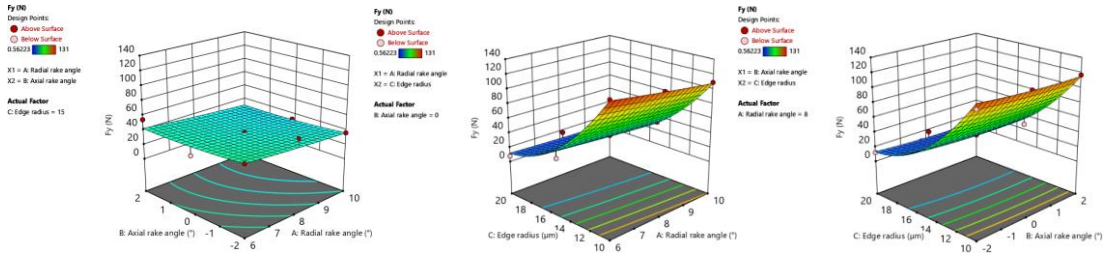

**Figure 6.120.** 3D surface plot of the measured forces in Y direction (Fy) variation during drilling of extruded CW724R with 60° of plunging angle with respect to the studied cutting tool geometry

**Table 6.95.** The ANOVA results for measured forces in Z direction (Fz) during drilling of extruded CW724R with 60° of plunging angle

| Source | Sum of Squares | df | Mean Square | F-value | p-value | |
|---|---|---|---|---|---|---|
| **Model** | 1.27E+05 | 9 | 14156.39 | 260.55 | < 0.0001 | significant |
| A-Radial rake angle | 5.67 | 1 | 5.67 | 0.1043 | 0.7507 | |
| B-Axial rake angle | 1084.23 | 1 | 1084.23 | 19.95 | 0.0003 | |
| C-Edge radius | 1.23E+05 | 1 | 1.23E+05 | 2257.24 | < 0.0001 | |
| AB | 74.5 | 1 | 74.5 | 1.37 | 0.2578 | |
| AC | 483.87 | 1 | 483.87 | 8.91 | 0.0083 | |
| BC | 1.14 | 1 | 1.14 | 0.021 | 0.8865 | |
| $A^2$ | 172.45 | 1 | 172.45 | 3.17 | 0.0927 | |
| $B^2$ | 4.8 | 1 | 4.8 | 0.0883 | 0.7699 | |
| $C^2$ | 2936.36 | 1 | 2936.36 | 54.04 | < 0.0001 | |
| **Residual** | 923.67 | 17 | 54.33 | | | |
| **Cor Total** | 1.28E+05 | 26 | | | | |

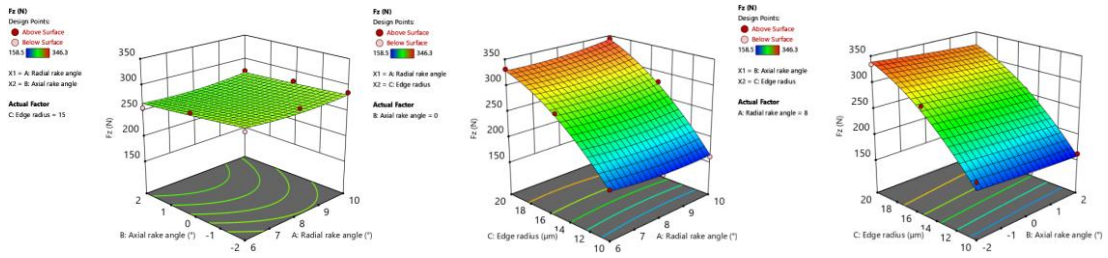

**Figure 6.121.** 3D surface plot of the measured forces in Z direction (Fz) variation during drilling of extruded CW724R with 60° of plunging angle with respect to the studied cutting tool geometry

**Table 6.96.** The ANOVA results for measured resultant forces (FR) during drilling of extruded CW724R with 60° of plunging angle

| Source | Sum of Squares | df | Mean Square | F-value | p-value | |
|---|---|---|---|---|---|---|
| **Model** | 1.53E+05 | 9 | 17037.62 | 205.52 | < 0.0001 | significant |

| | | | | | |
|---|---|---|---|---|---|
| A-Radial rake angle | 46.62 | 1 | 46.62 | 0.5624 | 0.4635 |
| B-Axial rake angle | 1270.69 | 1 | 1270.69 | 15.33 | 0.0011 |
| C-Edge radius | 1.47E+05 | 1 | 1.47E+05 | 1775.19 | < 0.0001 |
| AB | 56.13 | 1 | 56.13 | 0.6771 | 0.422 |
| AC | 897.53 | 1 | 897.53 | 10.83 | 0.0043 |
| BC | 13.55 | 1 | 13.55 | 0.1635 | 0.691 |
| $A^2$ | 513.93 | 1 | 513.93 | 6.2 | 0.0234 |
| $B^2$ | 16.2 | 1 | 16.2 | 0.1954 | 0.664 |
| $C^2$ | 3361.43 | 1 | 3361.43 | 40.55 | < 0.0001 |
| **Residual** | 1409.29 | 17 | 82.9 | | |
| **Cor Total** | 1.55E+05 | 26 | | | |

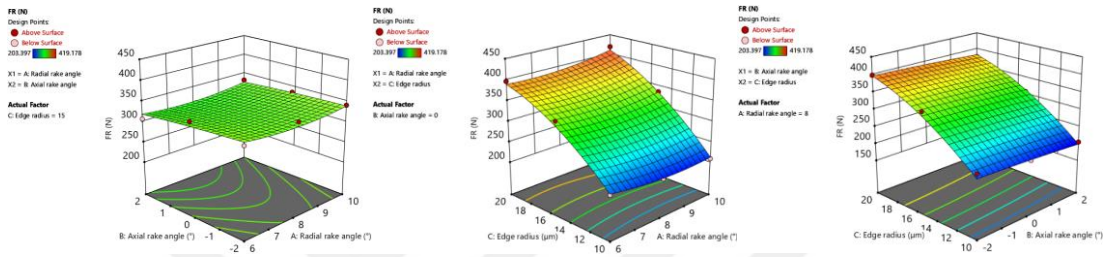

**Figure 6.122.** 3D surface plot of the measured resultant forces variation during drilling of extruded CW724R with 60° of plunging angle with respect to the studied cutting tool geometry

**Table 6.97.** The ANOVA results for measured burr heights at hole entry (BHEN) during drilling of extruded CW724R with 60° of plunging angle

| Source | Sum of Squares | df | Mean Square | F-value | p-value | |
|---|---|---|---|---|---|---|
| **Model** | 21471.39 | 9 | 2385.71 | 124.02 | < 0.0001 | significant |
| A-Radial rake angle | 9603.46 | 1 | 9603.46 | 499.24 | < 0.0001 | |
| B-Axial rake angle | 1161.8 | 1 | 1161.8 | 60.4 | < 0.0001 | |
| C-Edge radius | 7800.76 | 1 | 7800.76 | 405.52 | < 0.0001 | |
| AB | 667.35 | 1 | 667.35 | 34.69 | < 0.0001 | |
| AC | 896.77 | 1 | 896.77 | 46.62 | < 0.0001 | |
| BC | 114.61 | 1 | 114.61 | 5.96 | 0.0259 | |
| $A^2$ | 1025.32 | 1 | 1025.32 | 53.3 | < 0.0001 | |
| $B^2$ | 126.39 | 1 | 126.39 | 6.57 | 0.0202 | |
| $C^2$ | 74.93 | 1 | 74.93 | 3.9 | 0.0649 | |
| **Residual** | 327.02 | 17 | 19.24 | | | |
| **Cor Total** | 21798.41 | 26 | | | | |

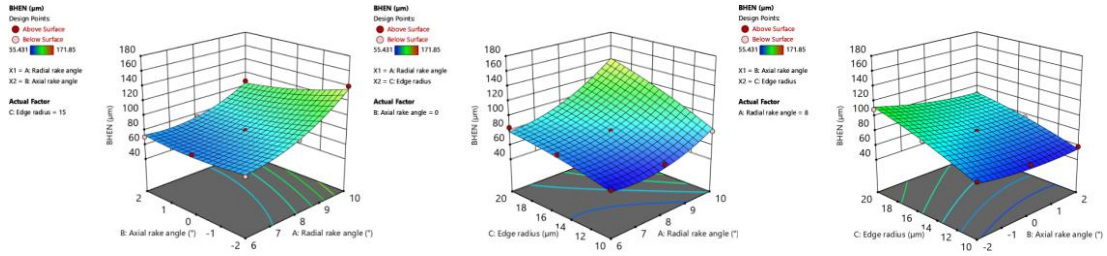

**Figure 6.123.** 3D surface plot of the measured burr heights at hole entry (BHEN) variation during drilling of extruded CW724R with 60° of plunging angle with respect to the studied cutting tool geometry

**Table 6.98.** The ANOVA results for measured burr heights at hole exit (BHEX) during drilling of extruded CW724R with 60° of plunging angle

| Source | Sum of Squares | df | Mean Square | F-value | p-value | |
|---|---|---|---|---|---|---|
| **Model** | 3163.58 | 9 | 351.51 | 23.17 | < 0.0001 | significant |
| A-Radial rake angle | 1405.12 | 1 | 1405.12 | 92.61 | < 0.0001 | |
| B-Axial rake angle | 120.4 | 1 | 120.4 | 7.94 | 0.0119 | |
| C-Edge radius | 1298.1 | 1 | 1298.1 | 85.55 | < 0.0001 | |
| AB | 53.69 | 1 | 53.69 | 3.54 | 0.0772 | |
| AC | 14.29 | 1 | 14.29 | 0.942 | 0.3454 | |
| BC | 14.74 | 1 | 14.74 | 0.9713 | 0.3382 | |
| $A^2$ | 92.88 | 1 | 92.88 | 6.12 | 0.0242 | |
| $B^2$ | 4.69 | 1 | 4.69 | 0.3092 | 0.5854 | |
| $C^2$ | 159.66 | 1 | 159.66 | 10.52 | 0.0048 | |
| **Residual** | 257.94 | 17 | 15.17 | | | |
| **Cor Total** | 3421.52 | 26 | | | | |

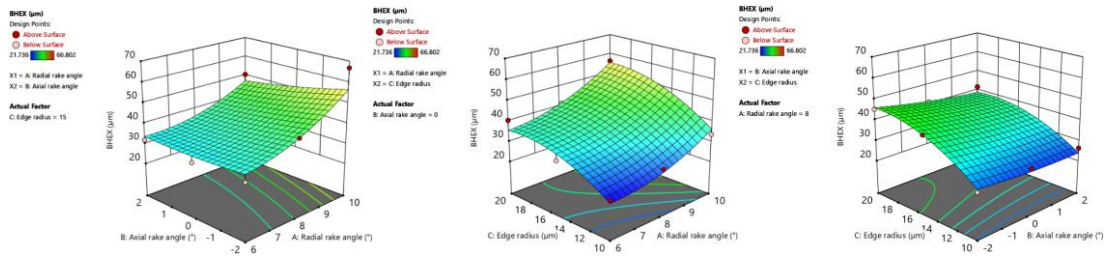

**Figure 6.124.** 3D surface plot of the measured burr heights at hole exit (BHEX) variation during drilling of extruded CW724R with 60° of plunging angle with respect to the studied cutting tool geometry

**Table 6.99.** The ANOVA results for measured surface roughness at hole bottom (Ra) during drilling of extruded CW724R with 60° of plunging angle

| Source | Sum of Squares | df | Mean Square | F-value | p-value | |
|---|---|---|---|---|---|---|
| **Model** | 0.0277 | 9 | 0.0031 | 119.05 | < 0.0001 | significant |

| | | | | | |
|---|---|---|---|---|---|
| A-Radial rake angle | 0.0021 | 1 | 0.0021 | 81.74 | < 0.0001 |
| B-Axial rake angle | 0.0003 | 1 | 0.0003 | 11.29 | 0.0037 |
| C-Edge radius | 0.0223 | 1 | 0.0223 | 863.39 | < 0.0001 |
| AB | 0 | 1 | 0 | 0.6717 | 0.4238 |
| AC | 0.0007 | 1 | 0.0007 | 26.38 | < 0.0001 |
| BC | 0.0001 | 1 | 0.0001 | 4.35 | 0.0523 |
| $A^2$ | 9.84E-06 | 1 | 9.84E-06 | 0.3809 | 0.5453 |
| $B^2$ | 0 | 1 | 0 | 0.7322 | 0.4041 |
| $C^2$ | 0.0021 | 1 | 0.0021 | 82.48 | < 0.0001 |
| **Residual** | 0.0004 | 17 | 0 | | |
| **Cor Total** | 0.0281 | 26 | | | |

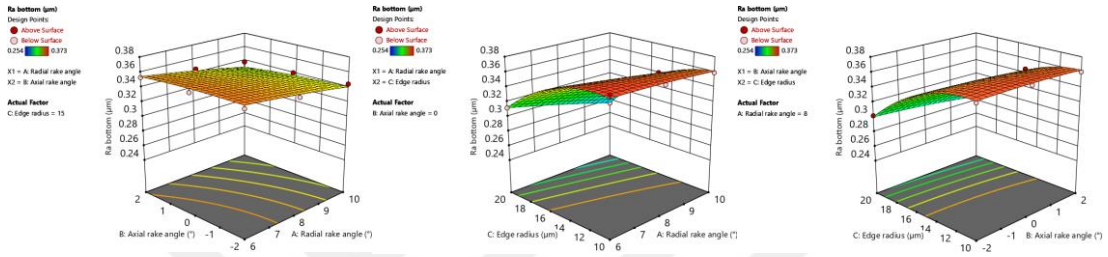

**Figure 6.125.** 3D surface plot of the measured surface roughness at hole bottom (Ra) variation during drilling of extruded CW724R with 60° of plunging angle with respect to the studied cutting tool geometry

**Table 6.100.** The ANOVA results for measured surface roughness at hole wall (Ra) during drilling of extruded CW724R with 60° of plunging angle

| Source | Sum of Squares | df | Mean Square | F-value | p-value | |
|---|---|---|---|---|---|---|
| **Model** | 0.0251 | 9 | 0.0028 | 73.85 | < 0.0001 | significant |
| A-Radial rake angle | 0.0021 | 1 | 0.0021 | 55.96 | < 0.0001 | |
| B-Axial rake angle | 0.0003 | 1 | 0.0003 | 7.63 | 0.0133 | |
| C-Edge radius | 0.0193 | 1 | 0.0193 | 510.54 | < 0.0001 | |
| AB | 0 | 1 | 0 | 0.883 | 0.3605 | |
| AC | 0.0009 | 1 | 0.0009 | 24.34 | 0.0001 | |
| BC | 0.0002 | 1 | 0.0002 | 4.27 | 0.0543 | |
| $A^2$ | 0 | 1 | 0 | 0.6716 | 0.4239 | |
| $B^2$ | 0 | 1 | 0 | 0.5671 | 0.4617 | |
| $C^2$ | 0.0023 | 1 | 0.0023 | 59.75 | < 0.0001 | |
| **Residual** | 0.0006 | 17 | 0 | | | |
| **Cor Total** | 0.0257 | 26 | | | | |

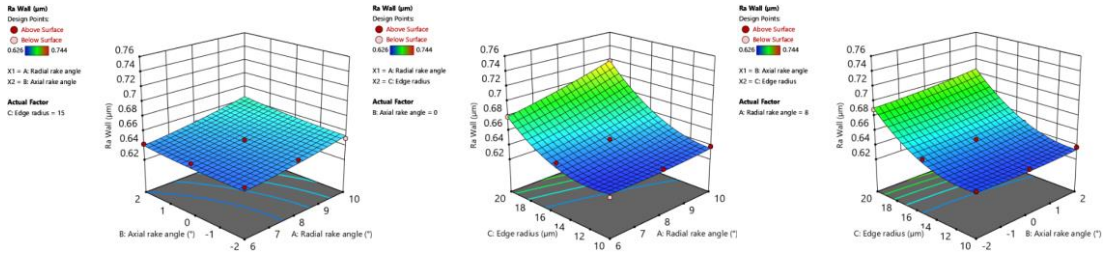

**Figure 6.126.** 3D surface plot of the measured surface roughness at hole wall (Ra) variation during drilling of extruded CW724R with 60° of plunging angle with respect to the studied cutting tool geometry

**Table 6.101.** The ANOVA results for measured hole diameter during drilling of extruded CW724R with 60° of plunging angle

| Source | Sum of Squares | df | Mean Square | F-value | p-value | |
|---|---|---|---|---|---|---|
| **Model** | 0.0121 | 16 | 0.0008 | 3.4 | 0.0276 | significant |
| A-Radial rake angle | 0.0004 | 1 | 0.0004 | 1.99 | 0.1885 | |
| B-Axial rake angle | 0.0015 | 1 | 0.0015 | 6.67 | 0.0273 | |
| C-Edge radius | 0.0002 | 1 | 0.0002 | 0.9074 | 0.3633 | |
| AB | 0 | 1 | 0 | 0.0631 | 0.8067 | |
| AC | 0.0008 | 1 | 0.0008 | 3.51 | 0.0903 | |
| BC | 0 | 1 | 0 | 0.0956 | 0.7635 | |
| $A^2$ | 0.0027 | 1 | 0.0027 | 12.11 | 0.0059 | |
| $B^2$ | 0.0001 | 1 | 0.0001 | 0.5995 | 0.4567 | |
| $C^2$ | 0.0003 | 1 | 0.0003 | 1.49 | 0.2502 | |
| ABC | 0.0001 | 1 | 0.0001 | 0.61 | 0.4529 | |
| $A^2B$ | 0.0003 | 1 | 0.0003 | 1.37 | 0.2686 | |
| $A^2C$ | 0.0002 | 1 | 0.0002 | 1.08 | 0.3239 | |
| $AB^2$ | 0.0004 | 1 | 0.0004 | 1.59 | 0.236 | |
| $AC^2$ | 0.0009 | 1 | 0.0009 | 3.81 | 0.0794 | |
| $B^2C$ | 0.0005 | 1 | 0.0005 | 2.17 | 0.1716 | |
| $BC^2$ | 0.0014 | 1 | 0.0014 | 6.47 | 0.0292 | |
| **Residual** | 0.0022 | 10 | 0.0002 | | | |
| **Cor Total** | 0.0144 | 26 | | | | |

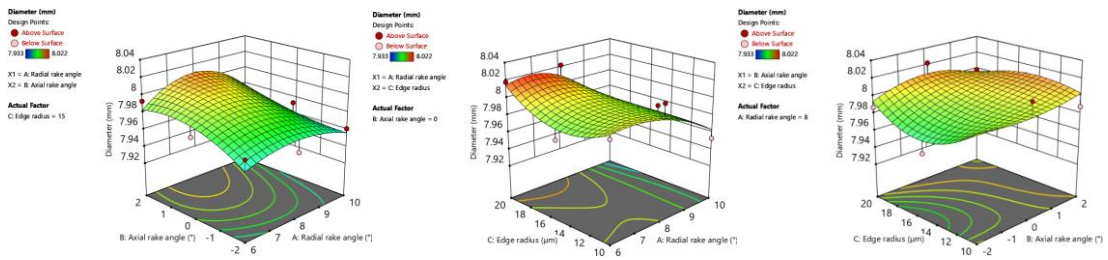

**Figure 6.127.** 3D surface plot of the measured hole diameter variation during drilling of extruded CW724R with 60° of plunging angle with respect to the studied cutting tool

geometry

**Table 6.102.** The developed regression model for drilling of extruded CW724R with 60° of plunging angle

| Extruded CW724R 60 | Fx | Fy | Fz | FR | BHEN | BHEX | Ra bottom | Ra Wall | Diameter |
|---|---|---|---|---|---|---|---|---|---|
| | 175.42 | 36.57 | 269.7 | 324.12 | 79.73 | 38.18 | 0.3493 | 0.6446 | 7.99 |
| A | 7.33 | -5.99 | 0.5611 | 1.61 | 23.1 | 8.84 | -0.0108 | 0.0108 | -0.0111 |
| B | -3.57 | -2.94 | -7.76 | -8.4 | -8.03 | -2.59 | -0.004 | 0.004 | 0.0203 |
| C | 77.08 | -54.04 | 82.54 | 90.42 | 20.82 | 8.49 | -0.0352 | 0.0327 | 0.0075 |
| AB | 2.61 | 0.0615 | 2.49 | 2.16 | -7.46 | -2.12 | -0.0012 | 0.0017 | -0.0011 |
| AC | -0.6458 | 3.59 | 6.35 | 8.65 | 8.64 | 1.09 | -0.0075 | 0.0087 | -0.0081 |
| BC | 2.33 | 0.7301 | 0.3083 | 1.06 | -3.09 | -1.11 | -0.0031 | 0.0037 | -0.0013 |
| $A^2$ | 8.4 | 0.682 | 5.36 | 9.25 | 13.07 | 3.93 | -0.0013 | 0.0021 | -0.0212 |
| $B^2$ | -4.32 | 2.22 | 0.8944 | -1.64 | 4.59 | 0.8843 | -0.0018 | 0.0019 | -0.0047 |
| $C^2$ | -43.65 | 26.31 | -22.12 | -23.67 | -3.53 | -5.16 | -0.0188 | 0.0194 | 0.0074 |
| ABC | 0 | 0 | 0 | 0 | 0 | 0 | 0 | 0 | 0.0041 |
| $A^2B$ | 0 | 0 | 0 | 0 | 0 | 0 | 0 | 0 | -0.0087 |
| $A^2C$ | 0 | 0 | 0 | 0 | 0 | 0 | 0 | 0 | -0.0077 |
| $AB^2$ | 0 | 0 | 0 | 0 | 0 | 0 | 0 | 0 | 0.0094 |
| $AC^2$ | 0 | 0 | 0 | 0 | 0 | 0 | 0 | 0 | -0.0146 |
| $B^2C$ | 0 | 0 | 0 | 0 | 0 | 0 | 0 | 0 | -0.011 |
| $BC^2$ | 0 | 0 | 0 | 0 | 0 | 0 | 0 | 0 | -0.019 |
| **Regression confidence $R^2$** | 0.981 | 0.983 | 0.992 | 0.99 | 0.985 | 0.924 | 0.984 | 0.975 | 0.844 |

**Table 6.103.** The ANOVA results for measured forces in X direction (Fx) during drilling of extruded CW724R with 45° of plunging angle

| Source | Sum of Squares | df | Mean Square | F-value | p-value | |
|---|---|---|---|---|---|---|
| **Model** | 1.56E+05 | 9 | 17331.82 | 66.59 | < 0.0001 | significant |
| A-Radial rake angle | 839 | 1 | 839 | 3.22 | 0.0904 | |
| B-Axial rake angle | 0.1028 | 1 | 0.1028 | 0.0004 | 0.9844 | |
| C-Edge radius | 1.51E+05 | 1 | 1.51E+05 | 580.44 | < 0.0001 | |
| AB | 457.2 | 1 | 457.2 | 1.76 | 0.2026 | |
| AC | 266.12 | 1 | 266.12 | 1.02 | 0.3261 | |
| BC | 76.81 | 1 | 76.81 | 0.2951 | 0.594 | |
| $A^2$ | 950.29 | 1 | 950.29 | 3.65 | 0.073 | |
| $B^2$ | 95.68 | 1 | 95.68 | 0.3676 | 0.5523 | |
| $C^2$ | 2225.3 | 1 | 2225.3 | 8.55 | 0.0095 | |
| **Residual** | 4424.71 | 17 | 260.28 | | | |
| **Cor Total** | 1.60E+05 | 26 | | | | |

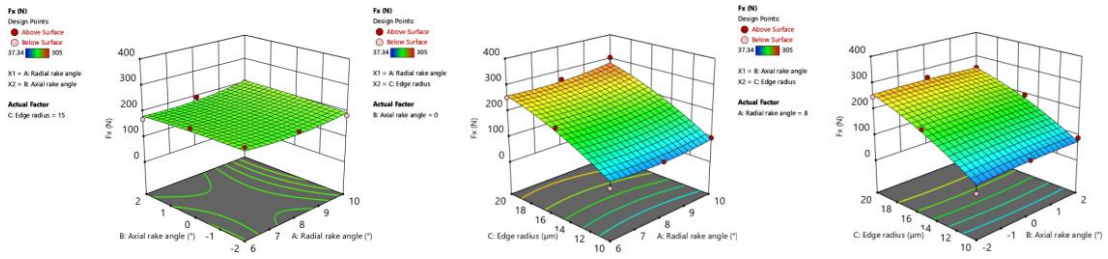

**Figure 6.128.** 3D surface plot of the measured forces in X direction (Fx) variation during drilling of extruded CW724R with 45° of plunging angle with respect to the studied cutting tool geometry

**Table 6.104.** The ANOVA results for measured forces in Y direction (Fy) during drilling of extruded CW724R with 45° of plunging angle

| Source | Sum of Squares | df | Mean Square | F-value | p-value | |
|---|---|---|---|---|---|---|
| **Model** | 14669.76 | 9 | 1629.97 | 39.6 | < 0.0001 | significant |
| A-Radial rake angle | 2423.7 | 1 | 2423.7 | 58.88 | < 0.0001 | |
| B-Axial rake angle | 382.63 | 1 | 382.63 | 9.3 | 0.0073 | |
| C-Edge radius | 10624.93 | 1 | 10624.93 | 258.12 | < 0.0001 | |
| AB | 326.15 | 1 | 326.15 | 7.92 | 0.0119 | |
| AC | 15.26 | 1 | 15.26 | 0.3706 | 0.5507 | |
| BC | 6.25 | 1 | 6.25 | 0.1518 | 0.7016 | |
| $A^2$ | 144.48 | 1 | 144.48 | 3.51 | 0.0783 | |
| $B^2$ | 42.05 | 1 | 42.05 | 1.02 | 0.3263 | |
| $C^2$ | 704.31 | 1 | 704.31 | 17.11 | 0.0007 | |
| **Residual** | 699.76 | 17 | 41.16 | | | |
| **Cor Total** | 15369.52 | 26 | | | | |

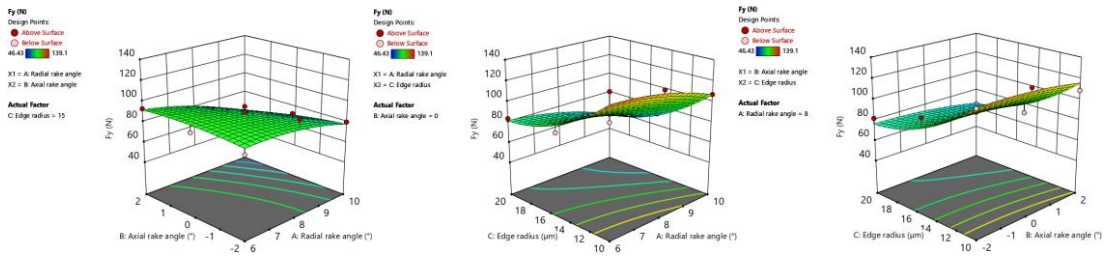

**Figure 6.129.** 3D surface plot of the measured forces in Y direction (Fy) variation during drilling of extruded CW724R with 45° of plunging angle with respect to the studied cutting tool geometry

**Table 6.105.** The ANOVA results for measured forces in Z direction (Fz) during drilling of extruded CW724R with 45° of plunging angle

| Source | Sum of Squares | df | Mean Square | F-value | p-value | |
|---|---|---|---|---|---|---|
| **Model** | 91868.32 | 9 | 10207.59 | 96.72 | < 0.0001 | significant |

| | | | | | |
|---|---|---|---|---|---|
| A-Radial rake angle | 10.58 | 1 | 10.58 | 0.1002 | 0.7554 |
| B-Axial rake angle | 449 | 1 | 449 | 4.25 | 0.0548 |
| C-Edge radius | 89760.85 | 1 | 89760.85 | 850.5 | < 0.0001 |
| AB | 159.14 | 1 | 159.14 | 1.51 | 0.2362 |
| AC | 96.9 | 1 | 96.9 | 0.9181 | 0.3514 |
| BC | 96.33 | 1 | 96.33 | 0.9128 | 0.3528 |
| $A^2$ | 2.85 | 1 | 2.85 | 0.027 | 0.8715 |
| $B^2$ | 41.78 | 1 | 41.78 | 0.3959 | 0.5376 |
| $C^2$ | 1250.89 | 1 | 1250.89 | 11.85 | 0.0031 |
| **Residual** | 1794.17 | 17 | 105.54 | | |
| **Cor Total** | 93662.49 | 26 | | | |

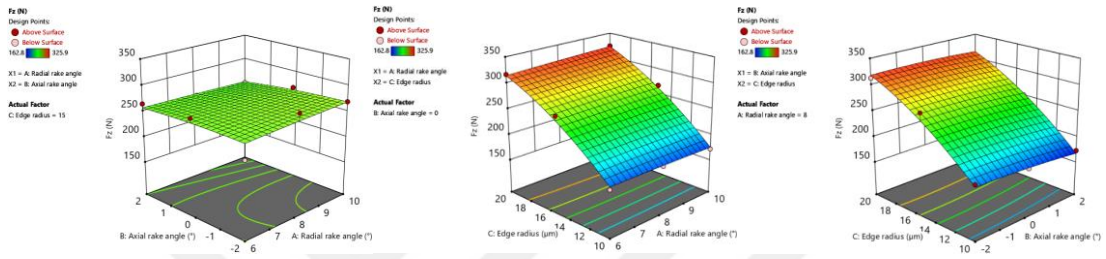

**Figure 6.130.** 3D surface plot of the measured forces in Z direction (Fz) variation during drilling of extruded CW724R with 45° of plunging angle with respect to the studied cutting tool geometry

**Table 6.106.** The ANOVA results for measured resultant forces (FR) during drilling of extruded CW724R with 45° of plunging angle

| Source | Sum of Squares | df | Mean Square | F-value | p-value | |
|---|---|---|---|---|---|---|
| **Model** | 1.67E+05 | 9 | 18591.41 | 225.02 | < 0.0001 | significant |
| A-Radial rake angle | 11.65 | 1 | 11.65 | 0.1409 | 0.712 | |
| B-Axial rake angle | 574.08 | 1 | 574.08 | 6.95 | 0.0173 | |
| C-Edge radius | 1.65E+05 | 1 | 1.65E+05 | 1994.22 | < 0.0001 | |
| AB | 13.15 | 1 | 13.15 | 0.1591 | 0.6949 | |
| AC | 773.31 | 1 | 773.31 | 9.36 | 0.0071 | |
| BC | 47.91 | 1 | 47.91 | 0.5799 | 0.4568 | |
| $A^2$ | 98.17 | 1 | 98.17 | 1.19 | 0.2909 | |
| $B^2$ | 252.75 | 1 | 252.75 | 3.06 | 0.0983 | |
| $C^2$ | 786.67 | 1 | 786.67 | 9.52 | 0.0067 | |
| **Residual** | 1404.56 | 17 | 82.62 | | | |
| **Cor Total** | 1.69E+05 | 26 | | | | |

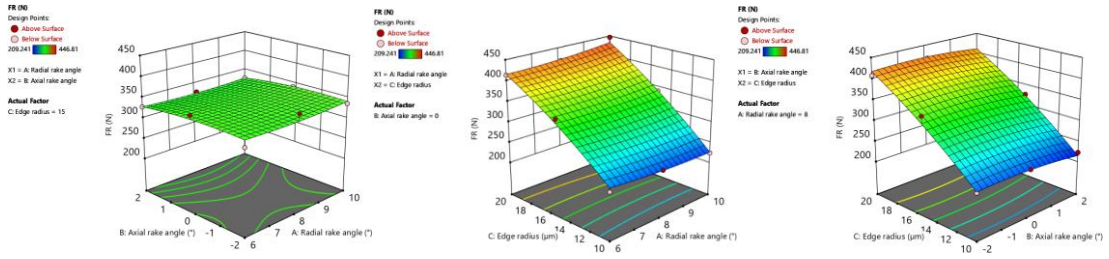

**Figure 6.131.** 3D surface plot of the measured resultant forces variation during drilling of extruded CW724R with 45° of plunging angle with respect to the studied cutting tool geometry

**Table 6.107.** The ANOVA results for measured burr heights at hole entry (BHEN) during drilling of extruded CW724R with 45° of plunging angle

| Source | Sum of Squares | df | Mean Square | F-value | p-value | |
|---|---|---|---|---|---|---|
| **Model** | 35375.26 | 9 | 3930.58 | 123.97 | < 0.0001 | significant |
| A-Radial rake angle | 15821.96 | 1 | 15821.96 | 499.04 | < 0.0001 | |
| B-Axial rake angle | 1914.2 | 1 | 1914.2 | 60.38 | < 0.0001 | |
| C-Edge radius | 12859.33 | 1 | 12859.33 | 405.59 | < 0.0001 | |
| AB | 1099.33 | 1 | 1099.33 | 34.67 | < 0.0001 | |
| AC | 1471.69 | 1 | 1471.69 | 46.42 | < 0.0001 | |
| BC | 188.63 | 1 | 188.63 | 5.95 | 0.026 | |
| $A^2$ | 1687.81 | 1 | 1687.81 | 53.23 | < 0.0001 | |
| $B^2$ | 208.2 | 1 | 208.2 | 6.57 | 0.0202 | |
| $C^2$ | 124.11 | 1 | 124.11 | 3.91 | 0.0643 | |
| **Residual** | 538.99 | 17 | 31.71 | | | |
| **Cor Total** | 35914.24 | 26 | | | | |

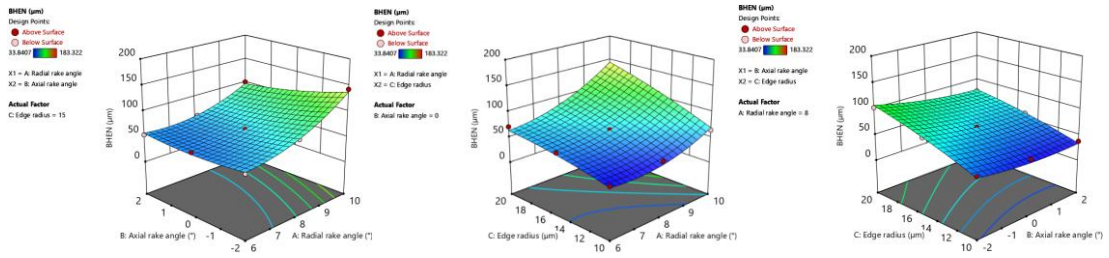

**Figure 6.132.** 3D surface plot of the measured burr heights at hole entry (BHEN) variation during drilling of extruded CW724R with 45° of plunging angle with respect to the studied cutting tool geometry

**Table 6.108.** The ANOVA results for measured burr heights at hole exit (BHEX) during drilling of extruded CW724R with 45° of plunging angle

| Source | Sum of Squares | df | Mean Square | F-value | p-value | |
|---|---|---|---|---|---|---|
| **Model** | 2936.24 | 9 | 326.25 | 36.28 | < 0.0001 | significant |

| | | | | | |
|---|---|---|---|---|---|
| A-Radial rake angle | 1340.88 | 1 | 1340.88 | 149.11 | < 0.0001 |
| B-Axial rake angle | 104.34 | 1 | 104.34 | 11.6 | 0.0034 |
| C-Edge radius | 1161.94 | 1 | 1161.94 | 129.21 | < 0.0001 |
| AB | 58.18 | 1 | 58.18 | 6.47 | 0.021 |
| AC | 7.9 | 1 | 7.9 | 0.8784 | 0.3618 |
| BC | 9.15 | 1 | 9.15 | 1.02 | 0.3274 |
| $A^2$ | 102.43 | 1 | 102.43 | 11.39 | 0.0036 |
| $B^2$ | 6.53 | 1 | 6.53 | 0.7265 | 0.4059 |
| $C^2$ | 144.9 | 1 | 144.9 | 16.11 | 0.0009 |
| **Residual** | 152.87 | 17 | 8.99 | | |
| **Cor Total** | 3089.12 | 26 | | | |

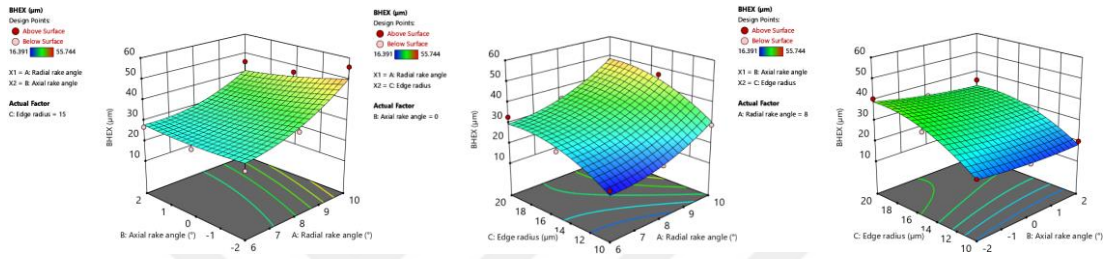

**Figure 6.133.** 3D surface plot of the measured burr heights at hole exit (BHEX) variation during drilling of extruded CW724R with 45° of plunging angle with respect to the studied cutting tool geometry

**Table 6.109.** The ANOVA results for measured surface roughness at hole bottom (Ra) during drilling of extruded CW724R with 45° of plunging angle

| Source | Sum of Squares | df | Mean Square | F-value | p-value | |
|---|---|---|---|---|---|---|
| **Model** | 0.0212 | 9 | 0.0024 | 117.41 | < 0.0001 | significant |
| A-Radial rake angle | 0.0016 | 1 | 0.0016 | 82.04 | < 0.0001 | |
| B-Axial rake angle | 0.0002 | 1 | 0.0002 | 11.01 | 0.0041 | |
| C-Edge radius | 0.0171 | 1 | 0.0171 | 851.11 | < 0.0001 | |
| AB | 0 | 1 | 0 | 0.5033 | 0.4877 | |
| AC | 0.0005 | 1 | 0.0005 | 24.66 | 0.0001 | |
| BC | 0.0001 | 1 | 0.0001 | 4.26 | 0.0546 | |
| $A^2$ | 8.96E-06 | 1 | 8.96E-06 | 0.4474 | 0.5126 | |
| $B^2$ | 0 | 1 | 0 | 0.5777 | 0.4576 | |
| $C^2$ | 0.0016 | 1 | 0.0016 | 82.09 | < 0.0001 | |
| **Residual** | 0.0003 | 17 | 0 | | | |
| **Cor Total** | 0.0215 | 26 | | | | |

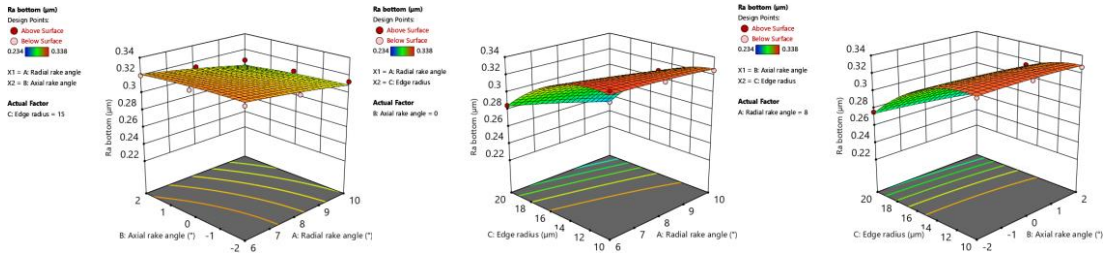

**Figure 6.134.** 3D surface plot of the measured surface roughness at hole bottom (Ra) variation during drilling of extruded CW724R with 45° of plunging angle with respect to the studied cutting tool geometry

**Table 6.110.** The ANOVA results for measured surface roughness at hole wall (Ra) during drilling of extruded CW724R with 45° of plunging angle

| Source | Sum of Squares | df | Mean Square | F-value | p-value | |
|---|---|---|---|---|---|---|
| **Model** | 0.0468 | 9 | 0.0052 | 83.87 | < 0.0001 | significant |
| A-Radial rake angle | 0.0038 | 1 | 0.0038 | 62.01 | < 0.0001 | |
| B-Axial rake angle | 0.0006 | 1 | 0.0006 | 8.96 | 0.0082 | |
| C-Edge radius | 0.0364 | 1 | 0.0364 | 586.73 | < 0.0001 | |
| AB | 0.0001 | 1 | 0.0001 | 0.8405 | 0.3721 | |
| AC | 0.0016 | 1 | 0.0016 | 25.98 | < 0.0001 | |
| BC | 0.0003 | 1 | 0.0003 | 4.52 | 0.0484 | |
| $A^2$ | 0 | 1 | 0 | 0.6051 | 0.4473 | |
| $B^2$ | 0 | 1 | 0 | 0.5271 | 0.4777 | |
| $C^2$ | 0.004 | 1 | 0.004 | 64.61 | < 0.0001 | |
| **Residual** | 0.0011 | 17 | 0.0001 | | | |
| **Cor Total** | 0.0478 | 26 | | | | |

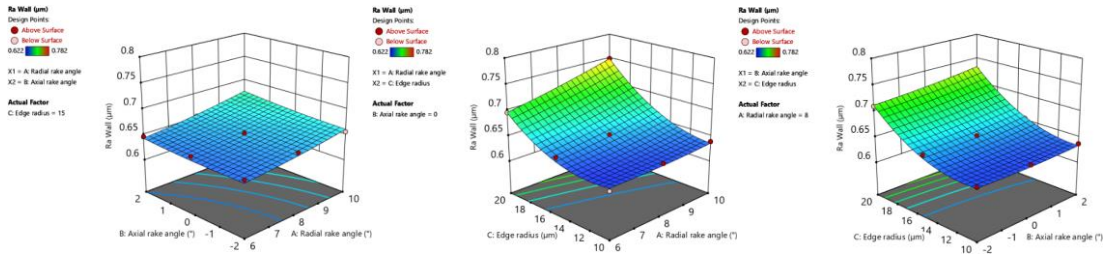

**Figure 6.135.** 3D surface plot of the measured surface roughness at hole wall (Ra) variation during drilling of extruded CW724R with 45° of plunging angle with respect to the studied cutting tool geometry

**Table 6.111.** The ANOVA results for measured hole diameter during drilling of extruded CW724R with 45° of plunging angle

| Source | Sum of Squares | df | Mean Square | F-value | p-value | |
|---|---|---|---|---|---|---|
| **Model** | 0.015 | 16 | 0.0009 | 5.02 | 0.0068 | significant |

| | | | | | |
|---|---|---|---|---|---|
| A-Radial rake angle | 0.0008 | 1 | 0.0008 | 4.13 | 0.0695 |
| B-Axial rake angle | 0.0005 | 1 | 0.0005 | 2.47 | 0.1473 |
| C-Edge radius | 0.0005 | 1 | 0.0005 | 2.61 | 0.137 |
| AB | 0.0009 | 1 | 0.0009 | 4.72 | 0.055 |
| AC | 0.0001 | 1 | 0.0001 | 0.7114 | 0.4187 |
| BC | 0.0001 | 1 | 0.0001 | 0.4842 | 0.5024 |
| $A^2$ | 0.0005 | 1 | 0.0005 | 2.44 | 0.1497 |
| $B^2$ | 1.85E-06 | 1 | 1.85E-06 | 0.0099 | 0.9228 |
| $C^2$ | 0.0074 | 1 | 0.0074 | 39.34 | < 0.0001 |
| ABC | 0.0001 | 1 | 0.0001 | 0.2941 | 0.5995 |
| $A^2B$ | 0.0006 | 1 | 0.0006 | 2.95 | 0.1168 |
| $A^2C$ | 0.0002 | 1 | 0.0002 | 0.9017 | 0.3647 |
| $AB^2$ | 0.0003 | 1 | 0.0003 | 1.63 | 0.23 |
| $AC^2$ | 0.0001 | 1 | 0.0001 | 0.3415 | 0.5719 |
| $B^2C$ | 0.0016 | 1 | 0.0016 | 8.32 | 0.0162 |
| $BC^2$ | 0.0003 | 1 | 0.0003 | 1.63 | 0.23 |
| **Residual** | 0.0019 | 10 | 0.0002 | | |
| **Cor Total** | 0.0169 | 26 | | | |

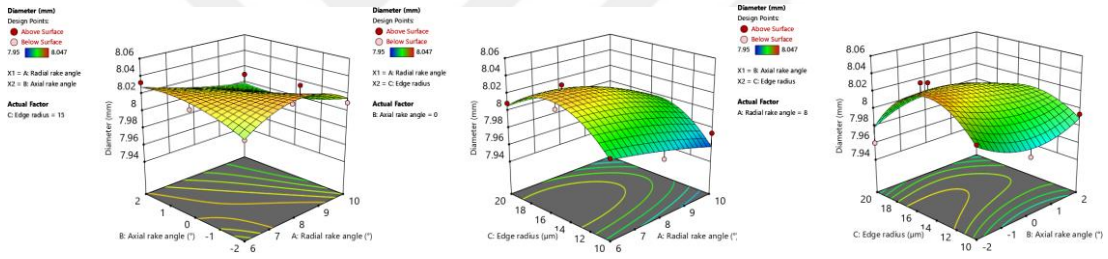

**Figure 6.136.** 3D surface plot of the measured hole diameter variation during drilling of extruded CW724R with 45° of plunging angle with respect to the studied cutting tool geometry

**Table 6.112.** The developed regression model for drilling of extruded CW724R with 45° of plunging angle

| Extruded CW724R 45 | Fx | Fy | Fz | FR | BHEN | BHEX | Ra bottom | Ra Wall | Diameter |
|---|---|---|---|---|---|---|---|---|---|
| | 186.34 | 87.33 | 262.8 | 336.13 | 65.09 | 31.71 | 0.317 | 0.6493 | 8.02 |
| A | 6.83 | -11.6 | 0.7667 | 0.8043 | 29.65 | 8.63 | -0.0096 | 0.0146 | -0.0147 |
| B | 0.0756 | -4.61 | -4.99 | -5.65 | -10.31 | -2.41 | -0.0035 | 0.0056 | -0.0113 |
| C | 91.61 | -24.3 | 70.62 | 95.67 | 26.73 | 8.03 | -0.0308 | 0.0449 | 0.0117 |
| AB | 6.17 | -5.21 | -3.64 | -1.05 | -9.57 | -2.2 | -0.0009 | 0.0021 | -0.0086 |
| AC | 4.71 | -1.13 | 2.84 | 8.03 | 11.07 | 0.8113 | -0.0064 | 0.0116 | -0.0033 |
| BC | -2.53 | -0.7217 | 2.83 | 2 | -3.96 | -0.873 | -0.0027 | 0.0048 | 0.0027 |
| $A^2$ | 12.58 | -4.91 | -0.6889 | 4.05 | 16.77 | 4.13 | -0.0012 | 0.0025 | -0.0087 |
| $B^2$ | -3.99 | -2.65 | -2.64 | -6.49 | 5.89 | 1.04 | -0.0014 | 0.0023 | -0.0006 |
| $C^2$ | -19.26 | 10.83 | -14.44 | -11.45 | -4.55 | -4.91 | -0.0166 | 0.0258 | -0.0351 |
| ABC | 0 | 0 | 0 | 0 | 0 | 0 | 0 | 0 | -0.0026 |

| | | | | | | | | | |
|---|---|---|---|---|---|---|---|---|---|
| $A^2B$ | 0 | 0 | 0 | 0 | 0 | 0 | 0 | 0 | 0.0118 |
| $A^2C$ | 0 | 0 | 0 | 0 | 0 | 0 | 0 | 0 | -0.0065 |
| $AB^2$ | 0 | 0 | 0 | 0 | 0 | 0 | 0 | 0 | 0.0088 |
| $AC^2$ | 0 | 0 | 0 | 0 | 0 | 0 | 0 | 0 | -0.004 |
| $B^2C$ | 0 | 0 | 0 | 0 | 0 | 0 | 0 | 0 | -0.0197 |
| $BC^2$ | 0 | 0 | 0 | 0 | 0 | 0 | 0 | 0 | 0.0088 |
| **Regression confidence $R^2$** | 0.972 | 0.954 | 0.98 | 0.991 | 0.985 | 0.95 | 0.984 | 0.978 | 0.889 |

**Table 6.113.** The ANOVA results for measured forces in X direction (Fx) during drilling of forged CW617N with 90° of plunging angle

| Source | Sum of Squares | df | Mean Square | F-value | p-value |
|---|---|---|---|---|---|
| **Model** | 420.08 | 25 | 16.8 | 1.93 | 0.5213 |
| A-Radial rake angle | 4.41 | 1 | 4.41 | 0.5075 | 0.6059 |
| B-Axial rake angle | 97.71 | 1 | 97.71 | 11.24 | 0.1845 |
| C-Edge radius | 19.71 | 1 | 19.71 | 2.27 | 0.3732 |
| AB | 19.59 | 1 | 19.59 | 2.25 | 0.374 |
| AC | 90.73 | 1 | 90.73 | 10.44 | 0.1911 |
| BC | 0.3697 | 1 | 0.3697 | 0.0425 | 0.8705 |
| $A^2$ | 3.64 | 1 | 3.64 | 0.419 | 0.6343 |
| $B^2$ | 0.0027 | 1 | 0.0027 | 0.0003 | 0.9888 |
| $C^2$ | 25.62 | 1 | 25.62 | 2.95 | 0.3357 |
| ABC | 44.04 | 1 | 44.04 | 5.07 | 0.2661 |
| $A^2B$ | 80.87 | 1 | 80.87 | 9.31 | 0.2017 |
| $A^2C$ | 8.53 | 1 | 8.53 | 0.9818 | 0.5029 |
| $AB^2$ | 0.1908 | 1 | 0.1908 | 0.022 | 0.9064 |
| $AC^2$ | 0.5463 | 1 | 0.5463 | 0.0629 | 0.8436 |
| $B^2C$ | 33.37 | 1 | 33.37 | 3.84 | 0.3004 |
| $BC^2$ | 96.91 | 1 | 96.91 | 11.15 | 0.1852 |
| $A^2B^2$ | 3.35 | 1 | 3.35 | 0.3851 | 0.6464 |
| $A^2BC$ | 2.5 | 1 | 2.5 | 0.2876 | 0.6866 |
| $A^2C^2$ | 0.0177 | 1 | 0.0177 | 0.002 | 0.9712 |
| $AB^2C$ | 80.07 | 1 | 80.07 | 9.21 | 0.2026 |
| $ABC^2$ | 10.57 | 1 | 10.57 | 1.22 | 0.4688 |
| $B^2C^2$ | 9.53 | 1 | 9.53 | 1.1 | 0.4853 |
| $A^2B^2C$ | 22.78 | 1 | 22.78 | 2.62 | 0.3523 |
| $A^2BC^2$ | 93.1 | 1 | 93.1 | 10.71 | 0.1888 |
| $AB^2C^2$ | 4.86 | 1 | 4.86 | 0.5589 | 0.5913 |
| **Residual** | 8.69 | 1 | 8.69 | | |
| **Cor Total** | 428.77 | 26 | | | |

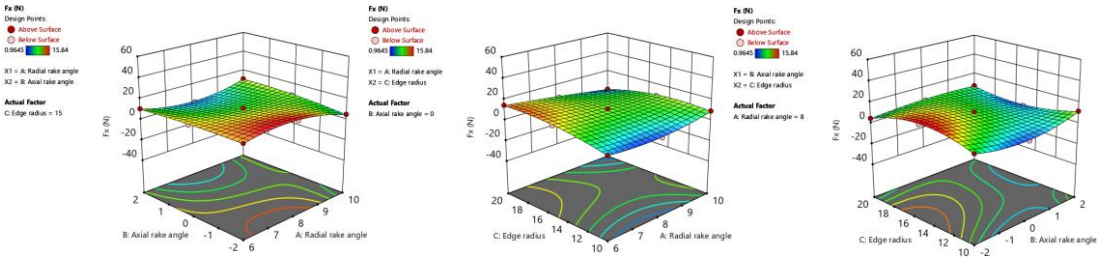

**Figure 6.137.** 3D surface plot of the measured forces in X direction (Fx) variation during drilling of forged CW617N with 90° of plunging angle with respect to the studied cutting tool geometry

**Table 6.114.** The ANOVA results for measured forces in Y direction (Fy) during drilling of forged CW617N with 90° of plunging angle

| Source | Sum of Squares | df | Mean Square | F-value | p-value |
|---|---|---|---|---|---|
| **Model** | 307.05 | 22 | 13.96 | 3.28 | 0.1286 |
| A-Radial rake angle | 4.24 | 1 | 4.24 | 0.9959 | 0.3748 |
| B-Axial rake angle | 14.67 | 1 | 14.67 | 3.45 | 0.137 |
| C-Edge radius | 31.19 | 1 | 31.19 | 7.33 | 0.0537 |
| AB | 0.5041 | 1 | 0.5041 | 0.1184 | 0.7481 |
| AC | 82.25 | 1 | 82.25 | 19.31 | 0.0117 |
| BC | 24.07 | 1 | 24.07 | 5.65 | 0.0762 |
| $A^2$ | 0.3709 | 1 | 0.3709 | 0.0871 | 0.7826 |
| $B^2$ | 12.47 | 1 | 12.47 | 2.93 | 0.1622 |
| $C^2$ | 35.44 | 1 | 35.44 | 8.32 | 0.0448 |
| ABC | 0.4522 | 1 | 0.4522 | 0.1062 | 0.7608 |
| $A^2B$ | 30.46 | 1 | 30.46 | 7.15 | 0.0555 |
| $A^2C$ | 18.66 | 1 | 18.66 | 4.38 | 0.1044 |
| $AB^2$ | 3.29 | 1 | 3.29 | 0.7722 | 0.4292 |
| $AC^2$ | 33.96 | 1 | 33.96 | 7.98 | 0.0476 |
| $B^2C$ | 0.7031 | 1 | 0.7031 | 0.1651 | 0.7053 |
| $BC^2$ | 3.77 | 1 | 3.77 | 0.8855 | 0.4 |
| $A^2B^2$ | 1.23 | 1 | 1.23 | 0.2893 | 0.6192 |
| $A^2BC$ | 19.88 | 1 | 19.88 | 4.67 | 0.0968 |
| $A^2C^2$ | 3.13 | 1 | 3.13 | 0.7351 | 0.4396 |
| $AB^2C$ | 21.9 | 1 | 21.9 | 5.14 | 0.0859 |
| $ABC^2$ | 0.202 | 1 | 0.202 | 0.0474 | 0.8382 |
| $B^2C^2$ | 16.81 | 1 | 16.81 | 3.95 | 0.1179 |
| **Residual** | 17.03 | 4 | 4.26 | | |
| **Cor Total** | 324.08 | 26 | | | |

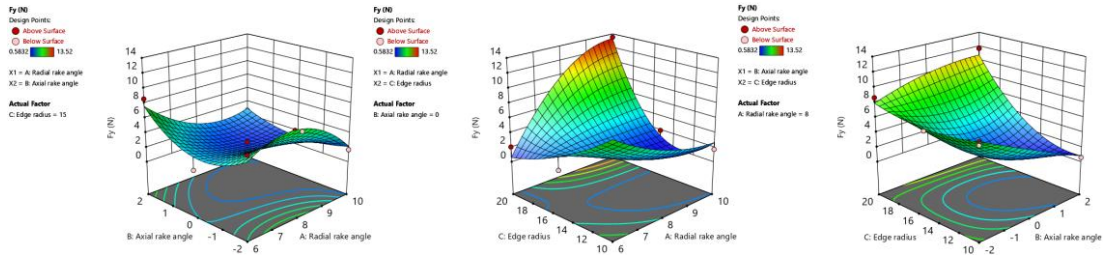

**Figure 6.138.** 3D surface plot of the measured forces in Y direction (Fy) variation during drilling of forged CW617N with 90° of plunging angle with respect to the studied cutting tool geometry

**Table 6.115.** The ANOVA results for measured forces in Z direction (Fz) during drilling of forged CW617N with 90° of plunging angle

| Source | Sum of Squares | df | Mean Square | F-value | p-value | |
|---|---|---|---|---|---|---|
| **Model** | 61291.1 | 9 | 6810.12 | 145.86 | < 0.0001 | significant |
| A-Radial rake angle | 175.22 | 1 | 175.22 | 3.75 | 0.0695 | |
| B-Axial rake angle | 1777.03 | 1 | 1777.03 | 38.06 | < 0.0001 | |
| C-Edge radius | 58211.5 | 1 | 58211.5 | 1246.78 | < 0.0001 | |
| AB | 71.91 | 1 | 71.91 | 1.54 | 0.2314 | |
| AC | 1.06 | 1 | 1.06 | 0.0227 | 0.8821 | |
| BC | 119.75 | 1 | 119.75 | 2.56 | 0.1277 | |
| $A^2$ | 38.1 | 1 | 38.1 | 0.8161 | 0.379 | |
| $B^2$ | 49.77 | 1 | 49.77 | 1.07 | 0.3163 | |
| $C^2$ | 846.81 | 1 | 846.81 | 18.14 | 0.0005 | |
| **Residual** | 793.72 | 17 | 46.69 | | | |
| **Cor Total** | 62084.8 | 26 | | | | |

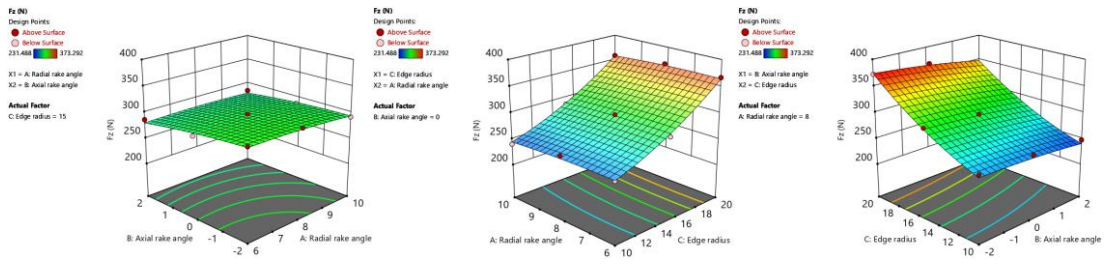

**Figure 6.139.** 3D surface plot of the measured forces in Z direction (Fz) variation during drilling of forged CW617N with 90° of plunging angle with respect to the studied cutting tool geometry

**Table 6.116.** The ANOVA results for measured resultant forces (FR) during drilling of forged CW617N with 90° of plunging angle

| Source | Sum of Squares | df | Mean Square | F-value | p-value | |
|---|---|---|---|---|---|---|
| **Model** | 61304.4 | 9 | 6811.6 | 145.37 | < 0.0001 | significant |

| | | | | | |
|---|---|---|---|---|---|
| A-Radial rake angle | 177.81 | 1 | 177.81 | 3.79 | 0.0681 |
| B-Axial rake angle | 1777.03 | 1 | 1777.03 | 37.92 | < 0.0001 |
| C-Edge radius | 58228.8 | 1 | 58228.8 | 1242.66 | < 0.0001 |
| AB | 73.07 | 1 | 73.07 | 1.56 | 0.2287 |
| AC | 0.9128 | 1 | 0.9128 | 0.0195 | 0.8906 |
| BC | 118.63 | 1 | 118.63 | 2.53 | 0.13 |
| $A^2$ | 38.33 | 1 | 38.33 | 0.8179 | 0.3784 |
| $B^2$ | 49.34 | 1 | 49.34 | 1.05 | 0.3192 |
| $C^2$ | 840.4 | 1 | 840.4 | 17.93 | 0.0006 |
| **Residual** | 796.59 | 17 | 46.86 | | |
| **Cor Total** | 62101 | 26 | | | |

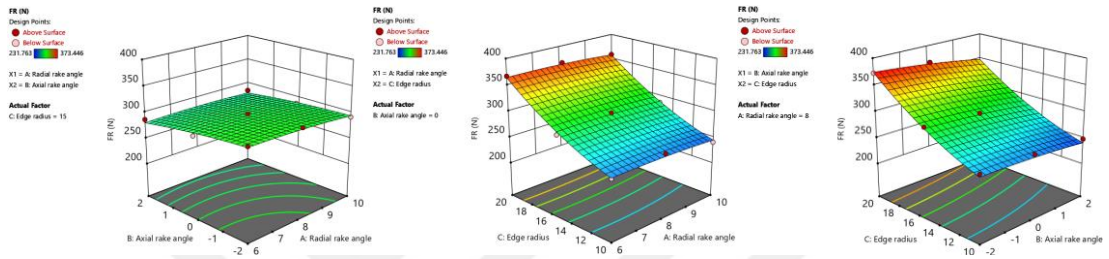


**Figure 6.140.** 3D surface plot of the measured resultant forces variation during drilling of forged CW617N with 90° of plunging angle with respect to the studied cutting tool geometry

**Table 6.117.** The ANOVA results for measured burr heights at hole entry (BHEN) during drilling of forged CW617N with 90° of plunging angle

| Source | Sum of Squares | df | Mean Square | F-value | p-value | |
|---|---|---|---|---|---|---|
| **Model** | 50439.7 | 9 | 5604.41 | 145.46 | < 0.0001 | significant |
| A-Radial rake angle | 25657 | 1 | 25657 | 665.91 | < 0.0001 | |
| B-Axial rake angle | 4749.65 | 1 | 4749.65 | 123.27 | < 0.0001 | |
| C-Edge radius | 14941.6 | 1 | 14941.6 | 387.8 | < 0.0001 | |
| AB | 2942.56 | 1 | 2942.56 | 76.37 | < 0.0001 | |
| AC | 834.19 | 1 | 834.19 | 21.65 | 0.0002 | |
| BC | 163.93 | 1 | 163.93 | 4.25 | 0.0548 | |
| $A^2$ | 971.74 | 1 | 971.74 | 25.22 | 0.0001 | |
| $B^2$ | 33.81 | 1 | 33.81 | 0.8775 | 0.362 | |
| $C^2$ | 145.17 | 1 | 145.17 | 3.77 | 0.069 | |
| **Residual** | 655 | 17 | 38.53 | | | |
| **Cor Total** | 51094.7 | 26 | | | | |

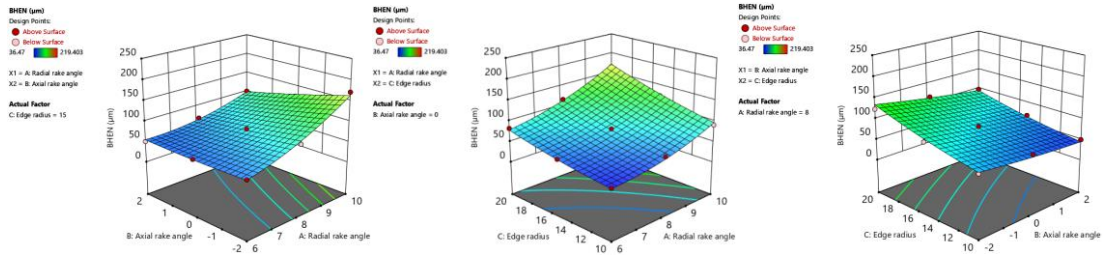

**Figure 6.141.** 3D surface plot of the measured burr heights at hole entry (BHEN) variation during drilling of forged CW617N with 90° of plunging angle with respect to the studied cutting tool geometry

**Table 6.118.** The ANOVA results for measured burr heights at hole exit (BHEX) during drilling of forged CW617N with 90° of plunging angle

| Source | Sum of Squares | df | Mean Square | F-value | p-value | |
|---|---|---|---|---|---|---|
| **Model** | 8660.62 | 9 | 962.29 | 91.37 | < 0.0001 | significant |
| A-Radial rake angle | 4505.82 | 1 | 4505.82 | 427.84 | < 0.0001 | |
| B-Axial rake angle | 844.29 | 1 | 844.29 | 80.17 | < 0.0001 | |
| C-Edge radius | 2469.57 | 1 | 2469.57 | 234.49 | < 0.0001 | |
| AB | 502.93 | 1 | 502.93 | 47.75 | < 0.0001 | |
| AC | 126.59 | 1 | 126.59 | 12.02 | 0.0029 | |
| BC | 10.06 | 1 | 10.06 | 0.955 | 0.3422 | |
| $A^2$ | 164.51 | 1 | 164.51 | 15.62 | 0.001 | |
| $B^2$ | 10.25 | 1 | 10.25 | 0.9731 | 0.3377 | |
| $C^2$ | 26.61 | 1 | 26.61 | 2.53 | 0.1304 | |
| **Residual** | 179.04 | 17 | 10.53 | | | |
| **Cor Total** | 8839.66 | 26 | | | | |

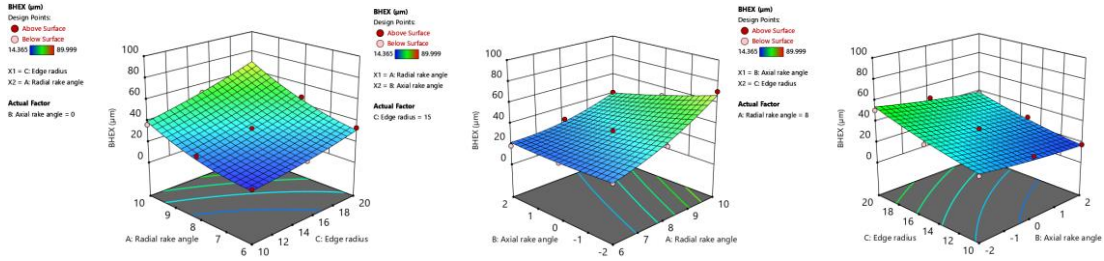

**Figure 6.142.** 3D surface plot of the measured burr heights at hole exit (BHEX) variation during drilling of forged CW617N with 90° of plunging angle with respect to the studied cutting tool geometry

**Table 6.119.** The ANOVA results for measured surface roughness at hole bottom (Ra) during drilling of forged CW617N with 90° of plunging angle

| Source | Sum of Squares | df | Mean Square | F-value | p-value | |
|---|---|---|---|---|---|---|
| **Model** | 0.0368 | 6 | 0.0061 | 320.99 | < 0.0001 | significant |

| | | | | | |
|---|---|---|---|---|---|
| A-Radial rake angle | 0.0016 | 1 | 0.0016 | 85.9 | < 0.0001 |
| B-Axial rake angle | 0.0004 | 1 | 0.0004 | 20.61 | 0.0002 |
| C-Edge radius | 0.0345 | 1 | 0.0345 | 1806.38 | < 0.0001 |
| AB | 0 | 1 | 0 | 0.8413 | 0.3699 |
| AC | 0.0002 | 1 | 0.0002 | 10.31 | 0.0044 |
| BC | 0 | 1 | 0 | 1.89 | 0.1841 |
| **Residual** | 0.0004 | 20 | 0 | | |
| **Cor Total** | 0.0371 | 26 | | | |

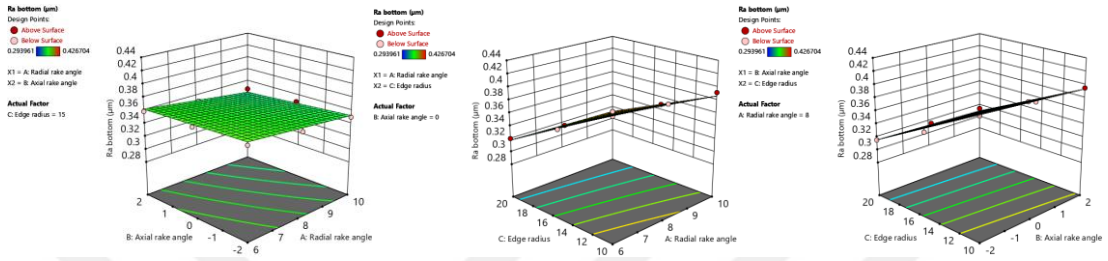


**Figure 6.143.** 3D surface plot of the measured surface roughness at hole bottom (Ra) variation during drilling of forged CW617N with 90° of plunging angle with respect to the studied cutting tool geometry

**Table 6.120.** The ANOVA results for measured surface roughness at hole wall (Ra) during drilling of forged CW617N with 90° of plunging angle

| Source | Sum of Squares | df | Mean Square | F-value | p-value | |
|---|---|---|---|---|---|---|
| **Model** | 0.055 | 6 | 0.0092 | 315.58 | < 0.0001 | significant |
| A-Radial rake angle | 0.0023 | 1 | 0.0023 | 79.66 | < 0.0001 | |
| B-Axial rake angle | 0.0006 | 1 | 0.0006 | 19.76 | 0.0002 | |
| C-Edge radius | 0.0519 | 1 | 0.0519 | 1789.24 | < 0.0001 | |
| AB | 0 | 1 | 0 | 1.63 | 0.2163 | |
| AC | 0.0001 | 1 | 0.0001 | 2.86 | 0.1066 | |
| BC | 8.88E-06 | 1 | 8.88E-06 | 0.3059 | 0.5863 | |
| **Residual** | 0.0006 | 20 | 0 | | | |
| **Cor Total** | 0.0555 | 26 | | | | |

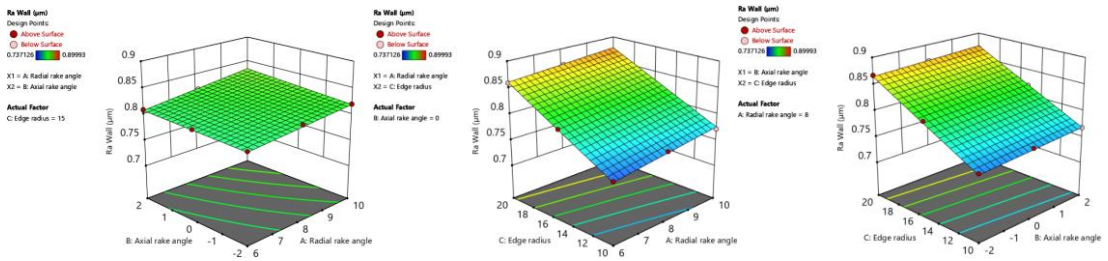


**Figure 6.144.** 3D surface plot of the measured surface roughness at hole wall (Ra) variation during drilling of forged CW617N with 90° of plunging angle with respect to the studied cutting tool geometry

**Table 6.121.** The ANOVA results for measured hole diameter during drilling of forged CW617N with 90° of plunging angle

| Source | Sum of Squares | df | Mean Square | F-value | p-value | |
|---|---|---|---|---|---|---|
| **Model** | 0.0056 | 16 | 0.0004 | 3.87 | 0.0176 | significant |
| A-Radial rake angle | 0.0003 | 1 | 0.0003 | 3.13 | 0.1074 | |
| B-Axial rake angle | 0 | 1 | 0 | 0.3695 | 0.5568 | |
| C-Edge radius | 8.71E-06 | 1 | 8.71E-06 | 0.0958 | 0.7633 | |
| AB | 0.0003 | 1 | 0.0003 | 3.64 | 0.0856 | |
| AC | 0.0003 | 1 | 0.0003 | 3.3 | 0.0994 | |
| BC | 0.0004 | 1 | 0.0004 | 4.75 | 0.0543 | |
| $A^2$ | 0.001 | 1 | 0.001 | 10.49 | 0.0089 | |
| $B^2$ | 8.96E-06 | 1 | 8.96E-06 | 0.0985 | 0.76 | |
| $C^2$ | 0 | 1 | 0 | 0.3942 | 0.5442 | |
| ABC | 0.0001 | 1 | 0.0001 | 0.727 | 0.4138 | |
| $A^2B$ | 0 | 1 | 0 | 0.4181 | 0.5325 | |
| $A^2C$ | 0.0001 | 1 | 0.0001 | 1.25 | 0.2895 | |
| $AB^2$ | 6.94E-07 | 1 | 6.94E-07 | 0.0076 | 0.9321 | |
| $AC^2$ | 0.0001 | 1 | 0.0001 | 0.6462 | 0.4402 | |
| $B^2C$ | 0.0003 | 1 | 0.0003 | 3.83 | 0.0788 | |
| $BC^2$ | 0.0004 | 1 | 0.0004 | 4.25 | 0.0662 | |
| **Residual** | 0.0009 | 10 | 0.0001 | | | |
| **Cor Total** | 0.0065 | 26 | | | | |

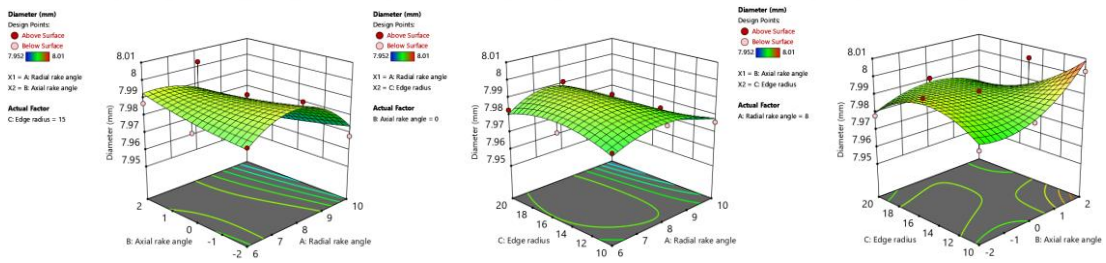


**Figure 6.145.** 3D surface plot of the measured hole diameter variation during drilling of forged CW617N with 90° of plunging angle with respect to the studied cutting tool geometry

**Table 6.122.** The developed regression model for drilling of forged CW617N with 90° of plunging angle

| Forged CW617N 90 | Fx | Fy | Fz | FR | BHEN | BHEX | Ra bottom | Ra Wall | Diameter |
|---|---|---|---|---|---|---|---|---|---|
| | 9.61 | 1.72 | 294.93 | 295.16 | 78.58 | 31.41 | 0.3566 | 0.8158 | 7.99 |
| A | -1.48 | -1.09 | -3.12 | -3.14 | 37.75 | 15.82 | -0.0095 | 0.0113 | -0.0089 |
| B | -6.99 | -2.02 | -9.94 | -9.94 | -16.24 | -6.85 | -0.0047 | 0.0056 | -0.0031 |
| C | 3.14 | 2.94 | 56.87 | 56.88 | 28.81 | 11.71 | -0.0438 | 0.0537 | 0.0016 |
| AB | 2.21 | -0.355 | 2.45 | 2.47 | -15.66 | -6.47 | -0.0012 | 0.002 | -0.0053 |

| | | | | | | | | | |
|---|---|---|---|---|---|---|---|---|---|
| AC | -4.76 | 4.53 | -0.297 | -0.2758 | 8.34 | 3.25 | 0.004 | -0.0026 | -0.005 |
| BC | -0.304 | 2.45 | -3.16 | -3.14 | -3.7 | -0.9155 | 0.0017 | -0.0009 | -0.006 |
| $A^2$ | 1.74 | 0.556 | -2.52 | -2.53 | 12.73 | 5.24 | 0 | 0 | -0.0126 |
| $B^2$ | 0.0475 | 3.22 | -2.88 | -2.87 | 2.37 | 1.31 | 0 | 0 | 0.0012 |
| $C^2$ | -4.62 | 5.43 | 11.88 | 11.83 | 4.92 | 2.11 | 0 | 0 | -0.0024 |
| ABC | 2.35 | 0.2378 | 0 | 0 | 0 | 0 | 0 | 0 | -0.0029 |
| $A^2B$ | 7.79 | 2.76 | 0 | 0 | 0 | 0 | 0 | 0 | 0.0031 |
| $A^2C$ | -2.53 | -2.16 | 0 | 0 | 0 | 0 | 0 | 0 | -0.0053 |
| $AB^2$ | -0.3783 | -0.9067 | 0 | 0 | 0 | 0 | 0 | 0 | -0.0004 |
| $AC^2$ | -0.6401 | 2.91 | 0 | 0 | 0 | 0 | 0 | 0 | 0.0038 |
| $B^2C$ | -5 | -0.4193 | 0 | 0 | 0 | 0 | 0 | 0 | -0.0093 |
| $BC^2$ | 8.53 | 0.9709 | 0 | 0 | 0 | 0 | 0 | 0 | 0.0098 |
| $A^2B^2$ | -1.58 | -0.9612 | 0 | 0 | 0 | 0 | 0 | 0 | 0 |
| $A^2BC$ | 0.9681 | -2.73 | 0 | 0 | 0 | 0 | 0 | 0 | 0 |
| $A^2C^2$ | 0.1154 | -1.53 | 0 | 0 | 0 | 0 | 0 | 0 | 0 |
| $AB^2C$ | 5.48 | -2.87 | 0 | 0 | 0 | 0 | 0 | 0 | 0 |
| $ABC^2$ | -1.99 | 0.2753 | 0 | 0 | 0 | 0 | 0 | 0 | 0 |
| $B^2C^2$ | 2.67 | -3.55 | 0 | 0 | 0 | 0 | 0 | 0 | 0 |
| $A^2B^2C$ | 5.06 | 0 | 0 | 0 | 0 | 0 | 0 | 0 | 0 |
| $A^2BC^2$ | -10.23 | 0 | 0 | 0 | 0 | 0 | 0 | 0 | 0 |
| $AB^2C^2$ | 2.34 | 0 | 0 | 0 | 0 | 0 | 0 | 0 | 0 |
| **Regression confidence $R^2$** | 0.979 | 0.947 | 0.987 | 0.987 | 0.986 | 0.979 | 0.989 | 0.989 | 0.861 |

**Table 6.123.** The ANOVA results for measured forces in X direction (Fx) during drilling of forged CW617N with 60° of plunging angle

| Source | Sum of Squares | df | Mean Square | F-value | p-value | |
|---|---|---|---|---|---|---|
| **Model** | 24493 | 9 | 2721.45 | 67.57 | < 0.0001 | significant |
| A-Radial rake angle | 716.06 | 1 | 716.06 | 17.78 | 0.0006 | |
| B-Axial rake angle | 125.66 | 1 | 125.66 | 3.12 | 0.0953 | |
| C-Edge radius | 23439 | 1 | 23439 | 581.93 | < 0.0001 | |
| AB | 0.2552 | 1 | 0.2552 | 0.0063 | 0.9375 | |
| AC | 6.87 | 1 | 6.87 | 0.1706 | 0.6848 | |
| BC | 30.53 | 1 | 30.53 | 0.7579 | 0.3961 | |
| $A^2$ | 54.06 | 1 | 54.06 | 1.34 | 0.2627 | |
| $B^2$ | 11.7 | 1 | 11.7 | 0.2906 | 0.5968 | |
| $C^2$ | 108.89 | 1 | 108.89 | 2.7 | 0.1185 | |
| **Residual** | 684.72 | 17 | 40.28 | | | |
| **Cor Total** | 25177.8 | 26 | | | | |

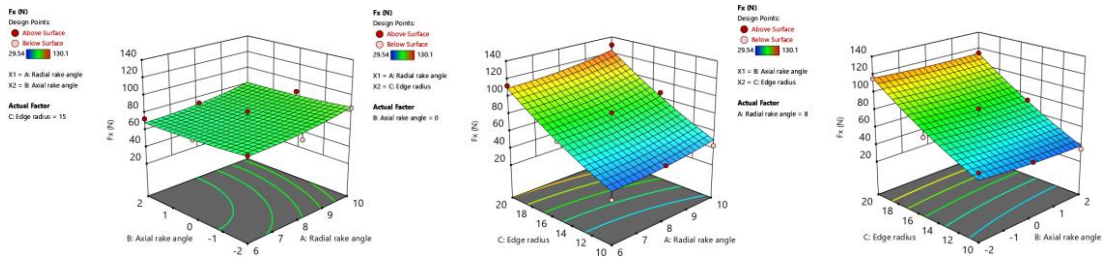

**Figure 6.146.** 3D surface plot of the measured forces in X direction (Fx) variation during drilling of forged CW617N with 60° of plunging angle with respect to the studied cutting tool geometry

**Table 6.124.** The ANOVA results for measured forces in Y direction (Fy) during drilling of forged CW617N with 60° of plunging angle

| Source | Sum of Squares | df | Mean Square | F-value | p-value | |
|---|---|---|---|---|---|---|
| **Model** | 8933.9 | 9 | 992.66 | 28.49 | < 0.0001 | significant |
| A-Radial rake angle | 906.1 | 1 | 906.1 | 26.01 | < 0.0001 | |
| B-Axial rake angle | 117.15 | 1 | 117.15 | 3.36 | 0.0843 | |
| C-Edge radius | 7271.78 | 1 | 7271.78 | 208.73 | < 0.0001 | |
| AB | 10.55 | 1 | 10.55 | 0.3027 | 0.5893 | |
| AC | 228.03 | 1 | 228.03 | 6.55 | 0.0204 | |
| BC | 41.03 | 1 | 41.03 | 1.18 | 0.293 | |
| $A^2$ | 19.31 | 1 | 19.31 | 0.5542 | 0.4668 | |
| $B^2$ | 15.77 | 1 | 15.77 | 0.4526 | 0.5101 | |
| $C^2$ | 324.18 | 1 | 324.18 | 9.31 | 0.0072 | |
| **Residual** | 592.25 | 17 | 34.84 | | | |
| **Cor Total** | 9526.14 | 26 | | | | |

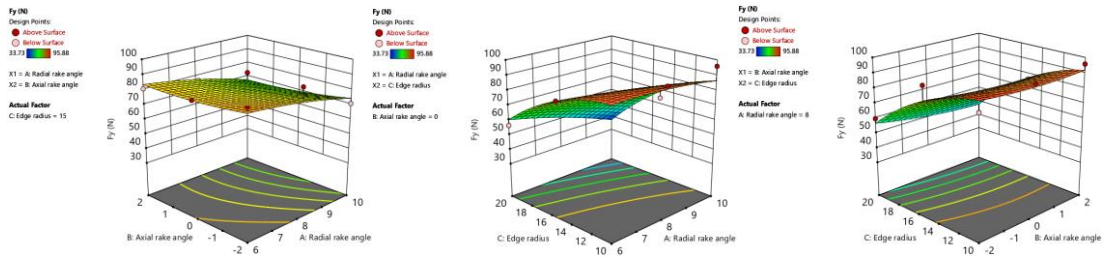

**Figure 6.147.** 3D surface plot of the measured forces in Y direction (Fy) variation during drilling of forged CW617N with 60° of plunging angle with respect to the studied cutting tool geometry

**Table 6.125.** The ANOVA results for measured forces in Z direction (Fz) during drilling of forged CW617N with 60° of plunging angle

| Source | Sum of Squares | df | Mean Square | F-value | p-value | |
|---|---|---|---|---|---|---|
| **Model** | 92018.51 | 9 | 10224.28 | 255 | < 0.0001 | significant |

| | | | | | |
|---|---|---|---|---|---|
| A-Radial rake angle | 281.42 | 1 | 281.42 | 7.02 | 0.0169 |
| B-Axial rake angle | 1368.9 | 1 | 1368.9 | 34.14 | < 0.0001 |
| C-Edge radius | 84985.2 | 1 | 84985.2 | 2119.56 | < 0.0001 |
| AB | 40.49 | 1 | 40.49 | 1.01 | 0.329 |
| AC | 28.33 | 1 | 28.33 | 0.7065 | 0.4123 |
| BC | 18.33 | 1 | 18.33 | 0.4572 | 0.508 |
| $A^2$ | 68.62 | 1 | 68.62 | 1.71 | 0.2082 |
| $B^2$ | 32.7 | 1 | 32.7 | 0.8156 | 0.3791 |
| $C^2$ | 5194.51 | 1 | 5194.51 | 129.55 | < 0.0001 |
| **Residual** | 681.63 | 17 | 40.1 | | |
| **Cor Total** | 92700.13 | 26 | | | |

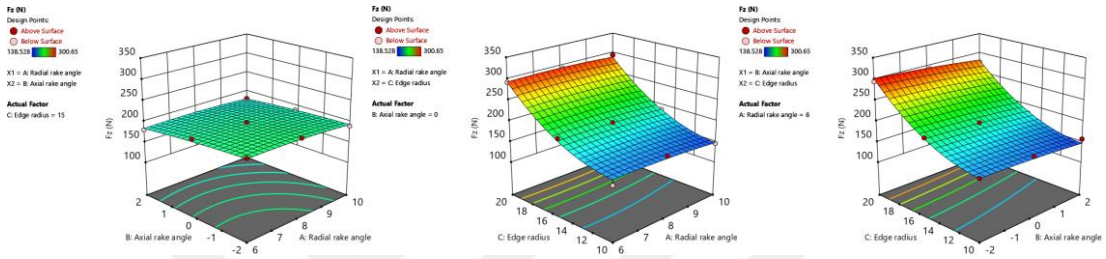

**Figure 6.148.** 3D surface plot of the measured forces in Z direction (Fz) variation during drilling of forged CW617N with 60° of plunging angle with respect to the studied cutting tool geometry

**Table 6.126.** The ANOVA results for measured resultant forces (FR) during drilling of forged CW617N with 60° of plunging angle

| Source | Sum of Squares | df | Mean Square | F-value | p-value | |
|---|---|---|---|---|---|---|
| **Model** | 87209.3 | 9 | 9689.93 | 223.95 | < 0.0001 | significant |
| A-Radial rake angle | 186.75 | 1 | 186.75 | 4.32 | 0.0532 | |
| B-Axial rake angle | 1479.39 | 1 | 1479.39 | 34.19 | < 0.0001 | |
| C-Edge radius | 80328 | 1 | 80328 | 1856.47 | < 0.0001 | |
| AB | 21.25 | 1 | 21.25 | 0.491 | 0.4929 | |
| AC | 31.1 | 1 | 31.1 | 0.7187 | 0.4083 | |
| BC | 20.85 | 1 | 20.85 | 0.4819 | 0.4969 | |
| $A^2$ | 28.53 | 1 | 28.53 | 0.6594 | 0.428 | |
| $B^2$ | 14.13 | 1 | 14.13 | 0.3266 | 0.5751 | |
| $C^2$ | 5099.37 | 1 | 5099.37 | 117.85 | < 0.0001 | |
| **Residual** | 735.58 | 17 | 43.27 | | | |
| **Cor Total** | 87944.9 | 26 | | | | |

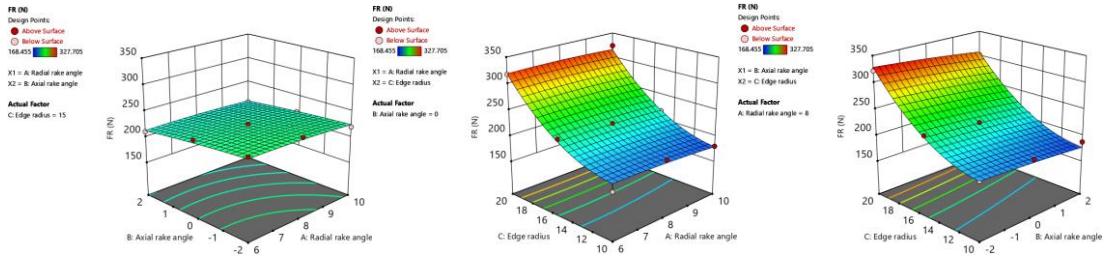

**Figure 6.149.** 3D surface plot of the measured resultant forces variation during drilling of forged CW617N with 60° of plunging angle with respect to the studied cutting tool geometry

**Table 6.127.** The ANOVA results for measured burr heights at hole entry (BHEN) during drilling of forged CW617N with 60° of plunging angle

| Source | Sum of Squares | df | Mean Square | F-value | p-value | |
|---|---|---|---|---|---|---|
| **Model** | 28665.63 | 9 | 3185.07 | 160.25 | < 0.0001 | significant |
| A-Radial rake angle | 14386.15 | 1 | 14386.15 | 723.82 | < 0.0001 | |
| B-Axial rake angle | 2499.76 | 1 | 2499.76 | 125.77 | < 0.0001 | |
| C-Edge radius | 8842.15 | 1 | 8842.15 | 444.88 | < 0.0001 | |
| AB | 1671.56 | 1 | 1671.56 | 84.1 | < 0.0001 | |
| AC | 538.56 | 1 | 538.56 | 27.1 | < 0.0001 | |
| BC | 80.35 | 1 | 80.35 | 4.04 | 0.0605 | |
| $A^2$ | 539.36 | 1 | 539.36 | 27.14 | < 0.0001 | |
| $B^2$ | 18.93 | 1 | 18.93 | 0.9524 | 0.3428 | |
| $C^2$ | 88.8 | 1 | 88.8 | 4.47 | 0.0496 | |
| **Residual** | 337.88 | 17 | 19.88 | | | |
| **Cor Total** | 29003.51 | 26 | | | | |

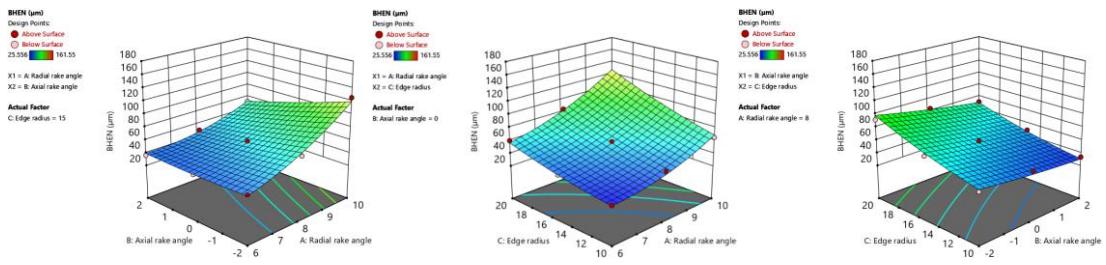

**Figure 6.150.** 3D surface plot of the measured burr heights at hole entry (BHEN) variation during drilling of forged CW617N with 60° of plunging angle with respect to the studied cutting tool geometry

**Table 6.128.** The ANOVA results for measured burr heights at hole exit (BHEX) during drilling of forged CW617N with 60° of plunging angle

| Source | Sum of Squares | df | Mean Square | F-value | p-value | |
|---|---|---|---|---|---|---|
| **Model** | 4899.5 | 9 | 544.39 | 59.5 | < 0.0001 | significant |

| | | | | | |
|---|---|---|---|---|---|
| A-Radial rake angle | 2693.71 | 1 | 2693.71 | 294.39 | < 0.0001 |
| B-Axial rake angle | 367.09 | 1 | 367.09 | 40.12 | < 0.0001 |
| C-Edge radius | 1457.14 | 1 | 1457.14 | 159.25 | < 0.0001 |
| AB | 137.88 | 1 | 137.88 | 15.07 | 0.0012 |
| AC | 117.34 | 1 | 117.34 | 12.82 | 0.0023 |
| BC | 20 | 1 | 20 | 2.19 | 0.1576 |
| $A^2$ | 91.05 | 1 | 91.05 | 9.95 | 0.0058 |
| $B^2$ | 4.61 | 1 | 4.61 | 0.5041 | 0.4873 |
| $C^2$ | 10.69 | 1 | 10.69 | 1.17 | 0.2949 |
| **Residual** | 155.55 | 17 | 9.15 | | |
| **Cor Total** | 5055.05 | 26 | | | |

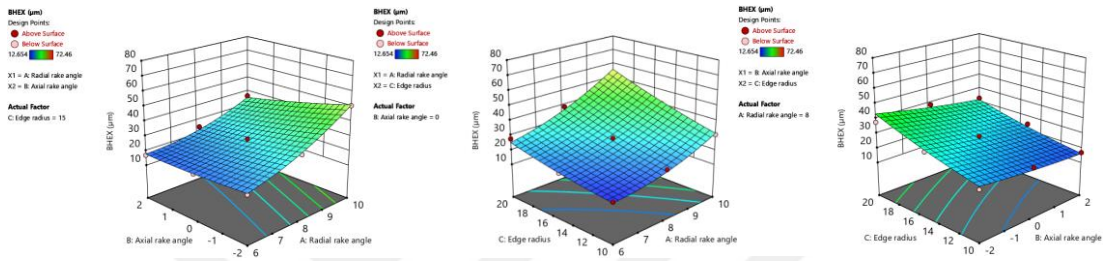


**Figure 6.151.** 3D surface plot of the measured burr heights at hole exit (BHEX) variation during drilling of forged CW617N with 60° of plunging angle with respect to the studied cutting tool geometry

**Table 6.129.** The ANOVA results for measured surface roughness at hole bottom (Ra) during drilling of forged CW617N with 60° of plunging angle

| Source | Sum of Squares | df | Mean Square | F-value | p-value | |
|---|---|---|---|---|---|---|
| **Model** | 0.0261 | 6 | 0.0044 | 320.99 | < 0.0001 | significant |
| A-Radial rake angle | 0.0012 | 1 | 0.0012 | 85.9 | < 0.0001 | |
| B-Axial rake angle | 0.0003 | 1 | 0.0003 | 20.61 | 0.0002 | |
| C-Edge radius | 0.0245 | 1 | 0.0245 | 1806.38 | < 0.0001 | |
| AB | 0 | 1 | 0 | 0.8413 | 0.3699 | |
| AC | 0.0001 | 1 | 0.0001 | 10.31 | 0.0044 | |
| BC | 0 | 1 | 0 | 1.89 | 0.1841 | |
| **Residual** | 0.0003 | 20 | 0 | | | |
| **Cor Total** | 0.0264 | 26 | | | | |

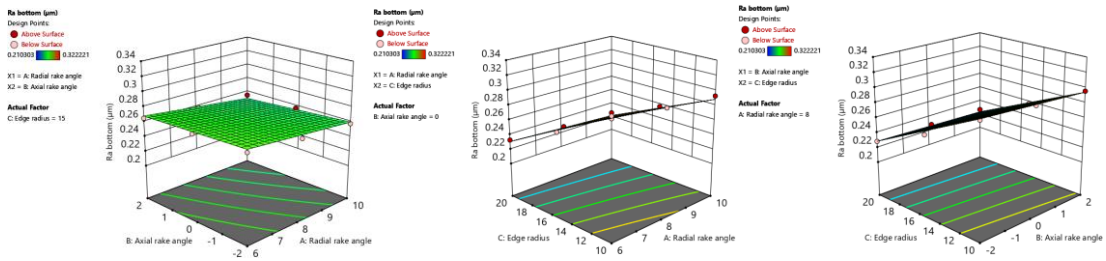


**Figure 6.152.** 3D surface plot of the measured surface roughness at hole bottom (Ra)

variation during drilling of forged CW617N with 60° of plunging angle with respect to the studied cutting tool geometry

**Table 6.130.** The ANOVA results for measured surface roughness at hole wall (Ra) during drilling of forged CW617N with 60° of plunging angle

| Source | Sum of Squares | df | Mean Square | F-value | p-value | |
|---|---|---|---|---|---|---|
| **Model** | 0.0408 | 6 | 0.0068 | 300.87 | < 0.0001 | significant |
| A-Radial rake angle | 0.0017 | 1 | 0.0017 | 75.6 | < 0.0001 | |
| B-Axial rake angle | 0.0004 | 1 | 0.0004 | 18.85 | 0.0003 | |
| C-Edge radius | 0.0386 | 1 | 0.0386 | 1706.73 | < 0.0001 | |
| AB | 0 | 1 | 0 | 1.67 | 0.2108 | |
| AC | 0 | 1 | 0 | 2.16 | 0.1569 | |
| BC | 4.38E-06 | 1 | 4.38E-06 | 0.1939 | 0.6644 | |
| **Residual** | 0.0005 | 20 | 0 | | | |
| **Cor Total** | 0.0413 | 26 | | | | |

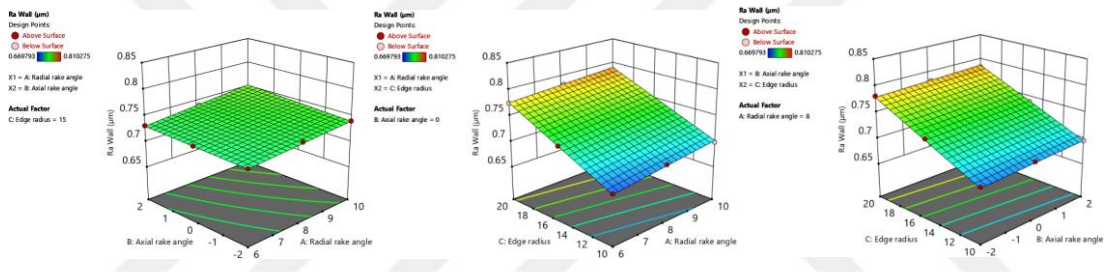

**Figure 6.153.** 3D surface plot of the measured surface roughness at hole wall (Ra) variation during drilling of forged CW617N with 60° of plunging angle with respect to the studied cutting tool geometry

**Table 6.131.** The ANOVA results for measured hole diameter during drilling of forged CW617N with 60° of plunging angle

| Source | Sum of Squares | df | Mean Square | F-value | p-value |
|---|---|---|---|---|---|
| **Model** | 0.008 | 16 | 0.0005 | 2.73 | 0.0556 |
| A-Radial rake angle | 0.0007 | 1 | 0.0007 | 4.06 | 0.0717 |
| B-Axial rake angle | 0.0004 | 1 | 0.0004 | 2.27 | 0.1628 |
| C-Edge radius | 0.0001 | 1 | 0.0001 | 0.3708 | 0.5562 |
| AB | 0 | 1 | 0 | 0.2016 | 0.663 |
| AC | 0.0009 | 1 | 0.0009 | 4.66 | 0.0562 |
| BC | 0.0011 | 1 | 0.0011 | 6.15 | 0.0325 |
| $A^2$ | 0.001 | 1 | 0.001 | 5.66 | 0.0387 |
| $B^2$ | 0.0008 | 1 | 0.0008 | 4.65 | 0.0564 |
| $C^2$ | 0.0001 | 1 | 0.0001 | 0.5413 | 0.4788 |
| ABC | 0.0005 | 1 | 0.0005 | 2.64 | 0.1356 |
| $A^2B$ | 0.0019 | 1 | 0.0019 | 10.22 | 0.0095 |

| | | | | | |
|---|---|---|---|---|---|
| $A^2C$ | 6.25E-06 | 1 | 6.25E-06 | 0.0343 | 0.8568 |
| $AB^2$ | 0.0004 | 1 | 0.0004 | 2.09 | 0.1793 |
| $AC^2$ | 0 | 1 | 0 | 0.1659 | 0.6923 |
| $B^2C$ | 0 | 1 | 0 | 0.2688 | 0.6154 |
| $BC^2$ | 7.11E-06 | 1 | 7.11E-06 | 0.039 | 0.8474 |
| **Residual** | 0.0018 | 10 | 0.0002 | | |
| **Cor Total** | 0.0098 | 26 | | | |

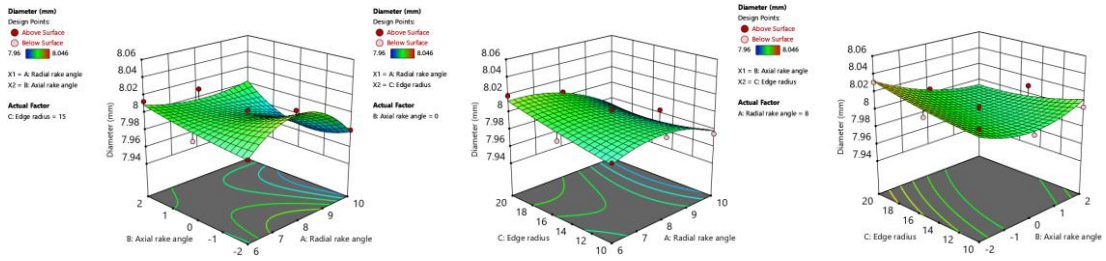


**Figure 6.154.** 3D surface plot of the measured hole diameter variation during drilling of forged CW617N with 60° of plunging angle with respect to the studied cutting tool geometry

**Table 6.132.** The developed regression model for drilling of forged CW617N with 60° of plunging angle

| Forged CW617N 60 | Fx | Fy | Fz | FR | BHEN | BHEX | Ra bottom | Ra Wall | Diameter |
|---|---|---|---|---|---|---|---|---|---|
| | 73.43 | 78.18 | 196.01 | 223.78 | 56.28 | 26.28 | 0.2631 | 0.7369 | 8 |
| A | 6.31 | -7.09 | -3.95 | -3.22 | 28.27 | 12.23 | -0.008 | 0.0097 | -0.0143 |
| B | -2.64 | -2.55 | -8.72 | -9.07 | -11.78 | -4.52 | -0.0039 | 0.0049 | -0.0107 |
| C | 36.09 | -20.1 | 68.71 | 66.8 | 22.16 | 9 | -0.0369 | 0.0463 | 0.0043 |
| AB | 0.1458 | -0.9375 | 1.84 | 1.33 | -11.8 | -3.39 | -0.001 | 0.0018 | 0.0017 |
| AC | 0.7567 | -4.36 | 1.54 | 1.61 | 6.7 | 3.13 | 0.0034 | -0.002 | -0.0084 |
| BC | 1.59 | -1.85 | -1.24 | -1.32 | -2.59 | -1.29 | 0.0015 | -0.0006 | -0.0097 |
| $A^2$ | 3 | -1.79 | -3.38 | -2.18 | 9.48 | 3.9 | 0 | 0 | -0.0131 |
| $B^2$ | 1.4 | 1.62 | -2.33 | -1.53 | 1.78 | 0.8768 | 0 | 0 | 0.0119 |
| $C^2$ | 4.26 | -7.35 | 29.42 | 29.15 | 3.85 | 1.33 | 0 | 0 | 0.0041 |
| ABC | 0 | 0 | 0 | 0 | 0 | 0 | 0 | 0 | -0.0077 |
| $A^2B$ | 0 | 0 | 0 | 0 | 0 | 0 | 0 | 0 | 0.0216 |
| $A^2C$ | 0 | 0 | 0 | 0 | 0 | 0 | 0 | 0 | 0.0013 |
| $AB^2$ | 0 | 0 | 0 | 0 | 0 | 0 | 0 | 0 | 0.0098 |

| | | | | | | | | | |
|---|---|---|---|---|---|---|---|---|---|
| $AC^2$ | 0 | 0 | 0 | 0 | 0 | 0 | 0 | 0 | 0.0028 |
| $B^2C$ | 0 | 0 | 0 | 0 | 0 | 0 | 0 | 0 | -0.0035 |
| $BC^2$ | 0 | 0 | 0 | 0 | 0 | 0 | 0 | 0 | 0.0013 |
| **Regression confidence $R^2$** | 0.972 | 0.937 | 0.992 | 0.991 | 0.988 | 0.969 | 0.989 | 0.989 | 0.813 |

**Table 6.133.** The ANOVA results for measured forces in X direction (Fx) during drilling of forged CW617N with 45° of plunging angle

| Source | Sum of Squares | df | Mean Square | F-value | p-value | |
|---|---|---|---|---|---|---|
| **Model** | 24127.3 | 6 | 4021.22 | 35.2 | < 0.0001 | significant |
| A-Radial rake angle | 145.52 | 1 | 145.52 | 1.27 | 0.2724 | |
| B-Axial rake angle | 6.24 | 1 | 6.24 | 0.0546 | 0.8176 | |
| C-Edge radius | 23917 | 1 | 23917 | 209.34 | < 0.0001 | |
| AB | 19 | 1 | 19 | 0.1663 | 0.6877 | |
| AC | 0.264 | 1 | 0.264 | 0.0023 | 0.9621 | |
| BC | 39.24 | 1 | 39.24 | 0.3435 | 0.5644 | |
| **Residual** | 2284.94 | 20 | 114.25 | | | |
| **Cor Total** | 26412.3 | 26 | | | | |

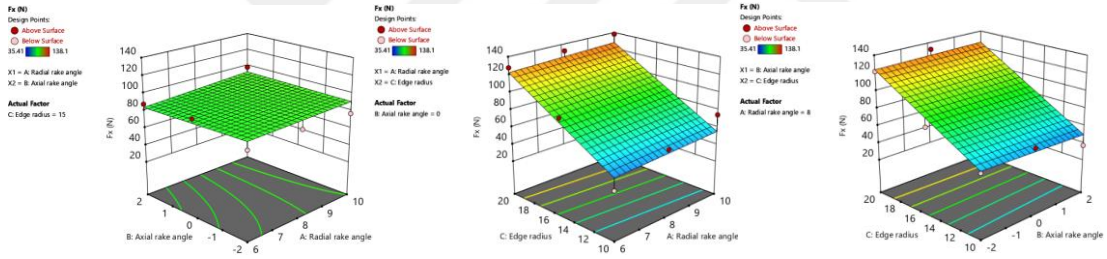

**Figure 6.155.** 3D surface plot of the measured forces in X direction (Fx) variation during drilling of forged CW617N with 45° of plunging angle with respect to the studied cutting tool geometry

**Table 6.134.** The ANOVA results for measured forces in Y direction (Fy) during drilling of forged CW617N with 45° of plunging angle

| Source | Sum of Squares | df | Mean Square | F-value | p-value | |
|---|---|---|---|---|---|---|
| **Model** | 4039.14 | 9 | 448.79 | 9.6 | < 0.0001 | significant |
| A-Radial rake angle | 805.48 | 1 | 805.48 | 17.22 | 0.0007 | |
| B-Axial rake angle | 272.22 | 1 | 272.22 | 5.82 | 0.0274 | |
| C-Edge radius | 2563.76 | 1 | 2563.76 | 54.81 | < 0.0001 | |
| AB | 4.34 | 1 | 4.34 | 0.0929 | 0.7643 | |
| AC | 33.9 | 1 | 33.9 | 0.7248 | 0.4064 | |
| BC | 4.34 | 1 | 4.34 | 0.0929 | 0.7643 | |
| $A^2$ | 201.18 | 1 | 201.18 | 4.3 | 0.0536 | |
| $B^2$ | 5.24 | 1 | 5.24 | 0.112 | 0.742 | |

| | | | | | |
|---|---|---|---|---|---|
| $C^2$ | 148.67 | 1 | 148.67 | 3.18 | 0.0925 |
| **Residual** | 795.14 | 17 | 46.77 | | |
| **Cor Total** | 4834.28 | 26 | | | |

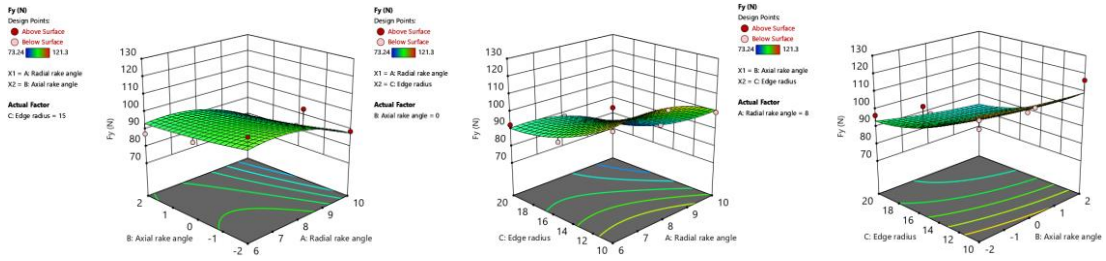

**Figure 6.156.** 3D surface plot of the measured forces in Y direction (Fy) variation during drilling of forged CW617N with 45° of plunging angle with respect to the studied cutting tool geometry

**Table 6.135.** The ANOVA results for measured forces in Z direction (Fz) during drilling of forged CW617N with 45° of plunging angle

| Source | Sum of Squares | df | Mean Square | F-value | p-value | |
|---|---|---|---|---|---|---|
| **Model** | 1.17E+05 | 9 | 13029.12 | 59.68 | < 0.0001 | significant |
| A-Radial rake angle | 98.11 | 1 | 98.11 | 0.4494 | 0.5116 | |
| B-Axial rake angle | 1867.42 | 1 | 1867.42 | 8.55 | 0.0095 | |
| C-Edge radius | 1.11E+05 | 1 | 1.11E+05 | 510.35 | < 0.0001 | |
| AB | 8.32 | 1 | 8.32 | 0.0381 | 0.8475 | |
| AC | 232.66 | 1 | 232.66 | 1.07 | 0.3164 | |
| BC | 149.34 | 1 | 149.34 | 0.6841 | 0.4196 | |
| $A^2$ | 118.92 | 1 | 118.92 | 0.5447 | 0.4706 | |
| $B^2$ | 22.71 | 1 | 22.71 | 0.104 | 0.751 | |
| $C^2$ | 3349.43 | 1 | 3349.43 | 15.34 | 0.0011 | |
| **Residual** | 3711.26 | 17 | 218.31 | | | |
| **Cor Total** | 1.21E+05 | 26 | | | | |

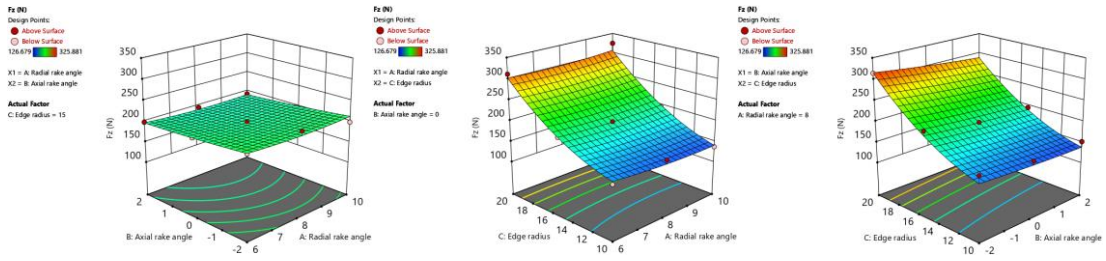

**Figure 6.157.** 3D surface plot of the measured forces in Z direction (Fz) variation during drilling of forged CW617N with 45° of plunging angle with respect to the studied cutting tool geometry

**Table 6.136.** The ANOVA results for measured resultant forces (FR) during drilling of

forged CW617N with 45° of plunging angle

| Source | Sum of Squares | df | Mean Square | F-value | p-value | |
|---|---|---|---|---|---|---|
| **Model** | 1.08E+05 | 9 | 12031.32 | 55.98 | < 0.0001 | significant |
| A-Radial rake angle | 197.63 | 1 | 197.63 | 0.9196 | 0.351 | |
| B-Axial rake angle | 1877.02 | 1 | 1877.02 | 8.73 | 0.0089 | |
| C-Edge radius | 1.01E+05 | 1 | 1.01E+05 | 469 | < 0.0001 | |
| AB | 2.12 | 1 | 2.12 | 0.0098 | 0.9221 | |
| AC | 213.49 | 1 | 213.49 | 0.9934 | 0.3329 | |
| BC | 124.3 | 1 | 124.3 | 0.5784 | 0.4574 | |
| $A^2$ | 127.87 | 1 | 127.87 | 0.595 | 0.4511 | |
| $B^2$ | 0.0065 | 1 | 0.0065 | 0 | 0.9957 | |
| $C^2$ | 4946.64 | 1 | 4946.64 | 23.02 | 0.0002 | |
| **Residual** | 3653.5 | 17 | 214.91 | | | |
| **Cor Total** | 1.12E+05 | 26 | | | | |

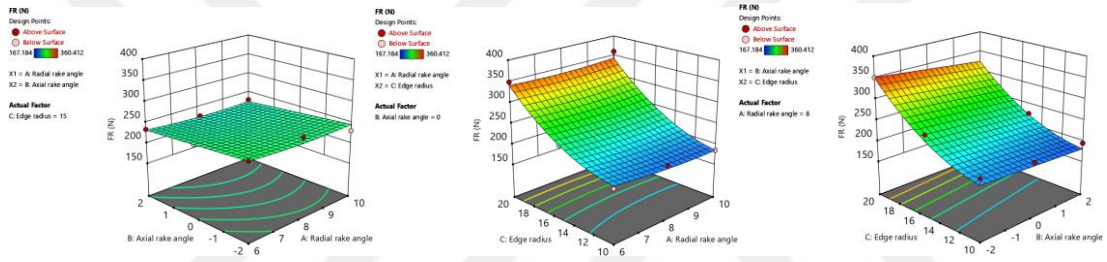


**Figure 6.158.** 3D surface plot of the measured resultant forces variation during drilling of forged CW617N with 45° of plunging angle with respect to the studied cutting tool geometry

**Table 6.137.** The ANOVA results for measured burr heights at hole entry (BHEN) during drilling of forged CW617N with 45° of plunging angle

| Source | Sum of Squares | df | Mean Square | F-value | p-value | |
|---|---|---|---|---|---|---|
| **Model** | 7130.96 | 9 | 792.33 | 145.46 | < 0.0001 | significant |
| A-Radial rake angle | 3627.28 | 1 | 3627.28 | 665.91 | < 0.0001 | |
| B-Axial rake angle | 671.49 | 1 | 671.49 | 123.27 | < 0.0001 | |
| C-Edge radius | 2112.39 | 1 | 2112.39 | 387.8 | < 0.0001 | |
| AB | 416.01 | 1 | 416.01 | 76.37 | < 0.0001 | |
| AC | 117.93 | 1 | 117.93 | 21.65 | 0.0002 | |
| BC | 23.18 | 1 | 23.18 | 4.25 | 0.0548 | |
| $A^2$ | 137.38 | 1 | 137.38 | 25.22 | 0.0001 | |
| $B^2$ | 4.78 | 1 | 4.78 | 0.8775 | 0.362 | |
| $C^2$ | 20.52 | 1 | 20.52 | 3.77 | 0.069 | |
| **Residual** | 92.6 | 17 | 5.45 | | | |
| **Cor Total** | 7223.56 | 26 | | | | |

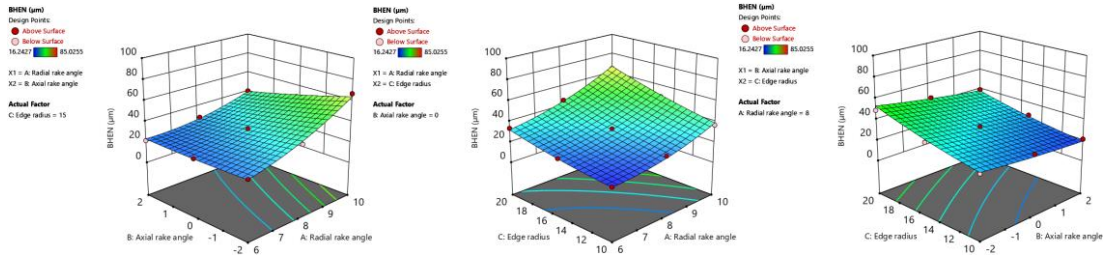

**Figure 6.159.** 3D surface plot of the measured burr heights at hole entry (BHEN) variation during drilling of forged CW617N with 45° of plunging angle with respect to the studied cutting tool geometry

**Table 6.138.** The ANOVA results for measured burr heights at hole exit (BHEX) during drilling of forged CW617N with 45° of plunging angle

| Source | Sum of Squares | df | Mean Square | F-value | p-value | |
|---|---|---|---|---|---|---|
| **Model** | 963.13 | 6 | 160.52 | 46.36 | < 0.0001 | significant |
| A-Radial rake angle | 510.15 | 1 | 510.15 | 147.33 | < 0.0001 | |
| B-Axial rake angle | 56.62 | 1 | 56.62 | 16.35 | 0.0006 | |
| C-Edge radius | 347.36 | 1 | 347.36 | 100.32 | < 0.0001 | |
| AB | 20.93 | 1 | 20.93 | 6.04 | 0.0232 | |
| AC | 25.22 | 1 | 25.22 | 7.28 | 0.0138 | |
| BC | 2.86 | 1 | 2.86 | 0.8247 | 0.3746 | |
| **Residual** | 69.25 | 20 | 3.46 | | | |
| **Cor Total** | 1032.38 | 26 | | | | |

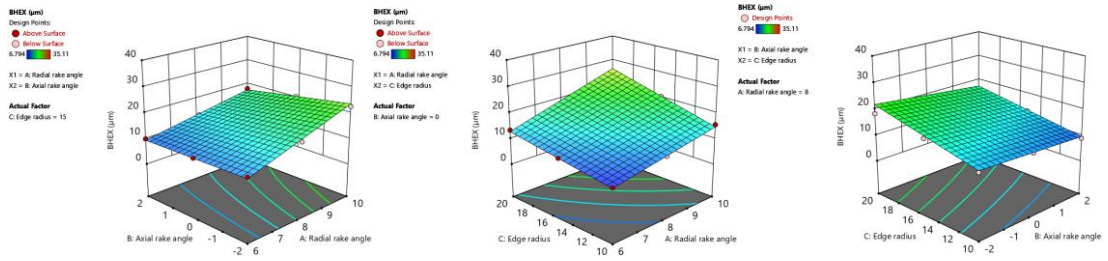

**Figure 6.160.** 3D surface plot of the measured burr heights at hole exit (BHEX) variation during drilling of forged CW617N with 45° of plunging angle with respect to the studied cutting tool geometry

**Table 6.139.** The ANOVA results for measured surface roughness at hole bottom (Ra) during drilling of forged CW617N with 45° of plunging angle

| Source | Sum of Squares | df | Mean Square | F-value | p-value | |
|---|---|---|---|---|---|---|
| **Model** | 0.0131 | 6 | 0.0022 | 320.99 | < 0.0001 | significant |
| A-Radial rake angle | 0.0006 | 1 | 0.0006 | 85.9 | < 0.0001 | |
| B-Axial rake angle | 0.0001 | 1 | 0.0001 | 20.61 | 0.0002 | |
| C-Edge radius | 0.0123 | 1 | 0.0123 | 1806.38 | < 0.0001 | |

| | | | | | |
|---|---|---|---|---|---|
| AB | 5.74E-06 | 1 | 5.74E-06 | 0.8413 | 0.3699 |
| AC | 0.0001 | 1 | 0.0001 | 10.31 | 0.0044 |
| BC | 0 | 1 | 0 | 1.89 | 0.1841 |
| **Residual** | 0.0001 | 20 | 6.82E-06 | | |
| **Cor Total** | 0.0133 | 26 | | | |

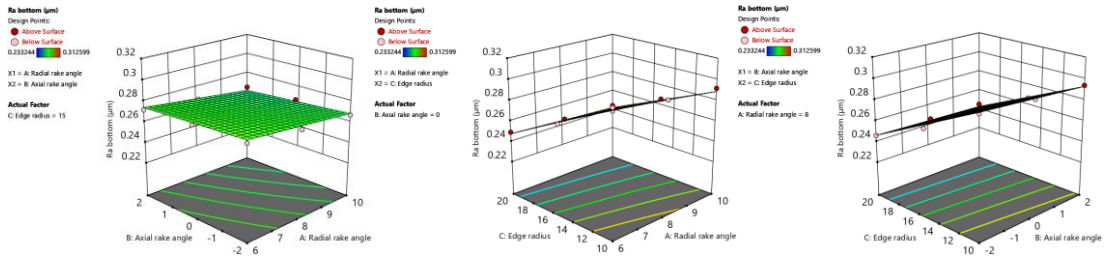

**Figure 6.161.** 3D surface plot of the measured surface roughness at hole bottom (Ra) variation during drilling of forged CW617N with 45° of plunging angle with respect to the studied cutting tool geometry

**Table 6.140.** The ANOVA results for measured surface roughness at hole wall (Ra) during drilling of forged CW617N with 45° of plunging angle

| Source | Sum of Squares | df | Mean Square | F-value | p-value | |
|---|---|---|---|---|---|---|
| **Model** | 0.0342 | 6 | 0.0057 | 341.44 | < 0.0001 | significant |
| A-Radial rake angle | 0.0015 | 1 | 0.0015 | 87.86 | < 0.0001 | |
| B-Axial rake angle | 0.0004 | 1 | 0.0004 | 21.51 | 0.0002 | |
| C-Edge radius | 0.0322 | 1 | 0.0322 | 1931.73 | < 0.0001 | |
| AB | 0 | 1 | 0 | 1.41 | 0.2482 | |
| AC | 0.0001 | 1 | 0.0001 | 5.36 | 0.0313 | |
| BC | 0 | 1 | 0 | 0.7753 | 0.389 | |
| **Residual** | 0.0003 | 20 | 0 | | | |
| **Cor Total** | 0.0345 | 26 | | | | |

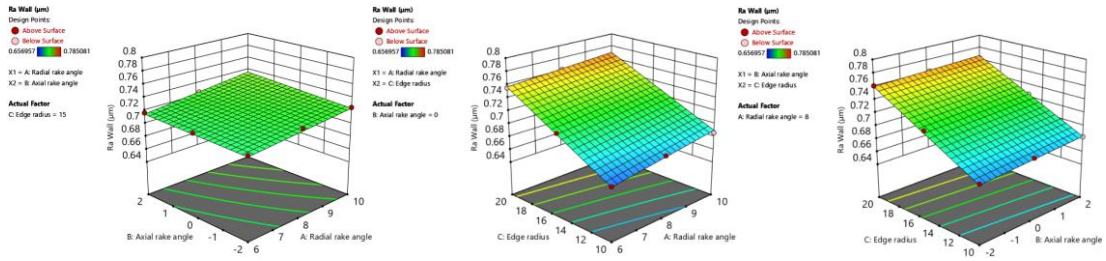

**Figure 6.162.** 3D surface plot of the measured surface roughness at hole wall (Ra) variation during drilling of forged CW617N with 45° of plunging angle with respect to the studied cutting tool geometry

**Table 6.141.** The ANOVA results for measured hole diameter during drilling of forged CW617N with 45° of plunging angle

| Source | Sum of Squares | df | Mean Square | F-value | p-value | |
|---|---|---|---|---|---|---|
| **Model** | 0.0125 | 16 | 0.0008 | 3.27 | 0.0312 | significant |
| A-Radial rake angle | 0.0002 | 1 | 0.0002 | 0.6382 | 0.4429 | |
| B-Axial rake angle | 0 | 1 | 0 | 0.1735 | 0.6858 | |
| C-Edge radius | 0.0005 | 1 | 0.0005 | 2.16 | 0.1728 | |
| AB | 0.001 | 1 | 0.001 | 4.39 | 0.0627 | |
| AC | 0.0006 | 1 | 0.0006 | 2.41 | 0.1517 | |
| BC | 0.0001 | 1 | 0.0001 | 0.2941 | 0.5995 | |
| $A^2$ | 0.0016 | 1 | 0.0016 | 6.81 | 0.0261 | |
| $B^2$ | 0.0005 | 1 | 0.0005 | 2.14 | 0.1741 | |
| $C^2$ | 0.0046 | 1 | 0.0046 | 19.35 | 0.0013 | |
| ABC | 0.0006 | 1 | 0.0006 | 2.5 | 0.1451 | |
| $A^2B$ | 0.0008 | 1 | 0.0008 | 3.21 | 0.1034 | |
| $A^2C$ | 0 | 1 | 0 | 0.0617 | 0.8089 | |
| $AB^2$ | 0 | 1 | 0 | 0.2056 | 0.6599 | |
| $AC^2$ | 0 | 1 | 0 | 0.1773 | 0.6826 | |
| $B^2C$ | 0 | 1 | 0 | 0.0617 | 0.8089 | |
| $BC^2$ | 0.0003 | 1 | 0.0003 | 1.05 | 0.3292 | |
| **Residual** | 0.0024 | 10 | 0.0002 | | | |
| **Cor Total** | 0.0149 | 26 | | | | |

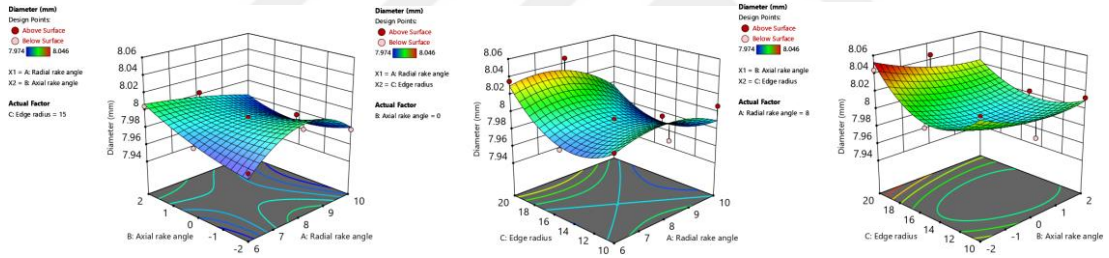


**Figure 6.163.** 3D surface plot of the measured hole diameter variation during drilling of forged CW617N with 45° of plunging angle with respect to the studied cutting tool geometry

**Table 6.142.** The developed regression model for drilling of forged CW617N with 45° of plunging angle

| Forged CW617N 45 | Fx | Fy | Fz | FR | BHEN | BHEX | Ra bottom | Ra Wall | Diameter |
|---|---|---|---|---|---|---|---|---|---|
| | 88.67 | 94.86 | 197.73 | 234.24 | 32.08 | 15.26 | 0.2707 | 0.7209 | 7.99 |
| A | 2.84 | -6.69 | -2.33 | -3.31 | 14.2 | 5.32 | -0.0057 | 0.009 | -0.0065 |
| B | -0.5889 | -3.89 | -10.19 | -10.21 | -6.11 | -1.77 | -0.0028 | 0.0045 | -0.0034 |
| C | 36.45 | -11.93 | 78.67 | 74.83 | 10.83 | 4.39 | -0.0262 | 0.0423 | 0.0119 |

| | | | | | | | | | |
|---|---|---|---|---|---|---|---|---|---|
| AB | 1.26 | -0.6017 | -0.8326 | -0.4199 | -5.89 | -1.32 | -0.0007 | 0.0014 | -0.0093 |
| AC | -0.1483 | -1.68 | 4.4 | 4.22 | 3.13 | 1.45 | 0.0024 | -0.0027 | -0.0069 |
| BC | 1.81 | -0.6017 | -3.53 | -3.22 | -1.39 | -0.4878 | 0.001 | -0.001 | -0.0024 |
| $A^2$ | 0 | -5.79 | 4.45 | 4.62 | 4.79 | 0 | 0 | 0 | -0.0164 |
| $B^2$ | 0 | 0.9344 | 1.95 | 0.0329 | 0.8926 | 0 | 0 | 0 | 0.0092 |
| $C^2$ | 0 | 4.98 | 23.63 | 28.71 | 1.85 | 0 | 0 | 0 | 0.0277 |
| ABC | 0 | 0 | 0 | 0 | 0 | 0 | 0 | 0 | 0.0086 |
| $A^2B$ | 0 | 0 | 0 | 0 | 0 | 0 | 0 | 0 | 0.0138 |
| $A^2C$ | 0 | 0 | 0 | 0 | 0 | 0 | 0 | 0 | -0.0019 |
| $AB^2$ | 0 | 0 | 0 | 0 | 0 | 0 | 0 | 0 | 0.0035 |
| $AC^2$ | 0 | 0 | 0 | 0 | 0 | 0 | 0 | 0 | -0.0032 |
| $B^2C$ | 0 | 0 | 0 | 0 | 0 | 0 | 0 | 0 | -0.0019 |
| $BC^2$ | 0 | 0 | 0 | 0 | 0 | 0 | 0 | 0 | -0.0079 |
| **Regression confidence $R^2$** | 0.913 | 0.835 | 0.969 | 0.967 | 0.987 | 0.932 | 0.989 | 0.99 | 0.839 |

**Table 6.143.** The ANOVA results for measured forces in X direction (Fx) during drilling of forged CW511L with 90° of plunging angle

| Source | Sum of Squares | df | Mean Square | F-value | p-value |
|---|---|---|---|---|---|
| **Model** | 432.65 | 25 | 17.31 | 1.72 | 0.5467 |
| A-Radial rake angle | 6.06 | 1 | 6.06 | 0.6033 | 0.5796 |
| B-Axial rake angle | 6.14 | 1 | 6.14 | 0.6111 | 0.5776 |
| C-Edge radius | 2.04 | 1 | 2.04 | 0.2027 | 0.7307 |
| AB | 1.11 | 1 | 1.11 | 0.1102 | 0.796 |
| AC | 46.18 | 1 | 46.18 | 4.6 | 0.2778 |
| BC | 0.517 | 1 | 0.517 | 0.0515 | 0.858 |
| $A^2$ | 0.1227 | 1 | 0.1227 | 0.0122 | 0.9299 |
| $B^2$ | 2.24 | 1 | 2.24 | 0.2232 | 0.719 |
| $C^2$ | 0.2066 | 1 | 0.2066 | 0.0206 | 0.9093 |
| ABC | 3.11 | 1 | 3.11 | 0.3096 | 0.6768 |
| $A^2B$ | 9.58 | 1 | 9.58 | 0.9536 | 0.5076 |
| $A^2C$ | 10.85 | 1 | 10.85 | 1.08 | 0.4877 |
| $AB^2$ | 0.6632 | 1 | 0.6632 | 0.066 | 0.8399 |
| $AC^2$ | 23.96 | 1 | 23.96 | 2.38 | 0.3658 |
| $B^2C$ | 43.91 | 1 | 43.91 | 4.37 | 0.284 |
| $BC^2$ | 0.7331 | 1 | 0.7331 | 0.073 | 0.832 |
| $A^2B^2$ | 0.0376 | 1 | 0.0376 | 0.0037 | 0.9611 |
| $A^2BC$ | 7.04 | 1 | 7.04 | 0.701 | 0.5563 |
| $A^2C^2$ | 0.7382 | 1 | 0.7382 | 0.0735 | 0.8315 |
| $AB^2C$ | 18.67 | 1 | 18.67 | 1.86 | 0.4029 |

| | | | | | |
|---|---|---|---|---|---|
| $ABC^2$ | 2.45 | 1 | 2.45 | 0.2435 | 0.7082 |
| $B^2C^2$ | 4.12 | 1 | 4.12 | 0.4101 | 0.6374 |
| $A^2B^2C$ | 55.3 | 1 | 55.3 | 5.5 | 0.2565 |
| $A^2BC^2$ | 12.39 | 1 | 12.39 | 1.23 | 0.4667 |
| $AB^2C^2$ | 21.82 | 1 | 21.82 | 2.17 | 0.3795 |
| **Residual** | 10.05 | 1 | 10.05 | | |
| **Cor Total** | 442.69 | 26 | | | |

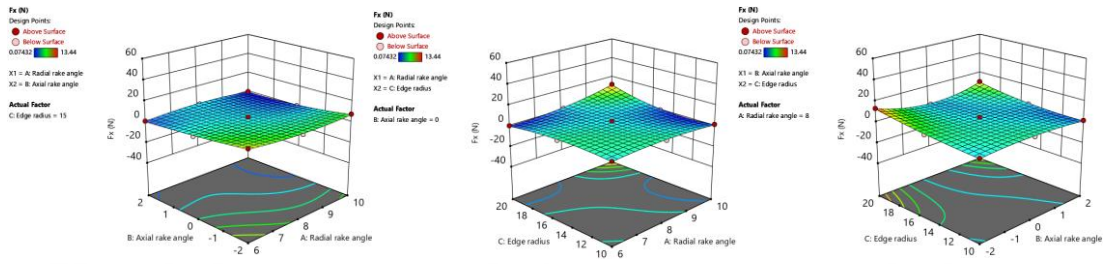

**Figure 6.164.** 3D surface plot of the measured forces in X direction (Fx) variation during drilling of forged CW511L with 90° of plunging angle with respect to the studied cutting tool geometry

**Table 6.144.** The ANOVA results for measured forces in Y direction (Fy) during drilling of forged CW511L with 90° of plunging angle

| Source | Sum of Squares | df | Mean Square | F-value | p-value |
|---|---|---|---|---|---|
| **Model** | 249.46 | 25 | 9.98 | 0.5687 | 0.8032 |
| A-Radial rake angle | 18.05 | 1 | 18.05 | 1.03 | 0.4955 |
| B-Axial rake angle | 5.25 | 1 | 5.25 | 0.2993 | 0.6813 |
| C-Edge radius | 1.77 | 1 | 1.77 | 0.1011 | 0.804 |
| AB | 5.24 | 1 | 5.24 | 0.2985 | 0.6817 |
| AC | 3.36 | 1 | 3.36 | 0.1913 | 0.7375 |
| BC | 27.36 | 1 | 27.36 | 1.56 | 0.4299 |
| $A^2$ | 7.92 | 1 | 7.92 | 0.4511 | 0.6235 |
| $B^2$ | 1.39 | 1 | 1.39 | 0.0794 | 0.8252 |
| $C^2$ | 0.9822 | 1 | 0.9822 | 0.056 | 0.8521 |
| ABC | 11.08 | 1 | 11.08 | 0.6312 | 0.5726 |
| $A^2B$ | 2.74 | 1 | 2.74 | 0.1563 | 0.7603 |
| $A^2C$ | 4.65 | 1 | 4.65 | 0.265 | 0.6973 |
| $AB^2$ | 34.63 | 1 | 34.63 | 1.97 | 0.3938 |
| $AC^2$ | 44.44 | 1 | 44.44 | 2.53 | 0.3572 |
| $B^2C$ | 0.0398 | 1 | 0.0398 | 0.0023 | 0.9697 |
| $BC^2$ | 2.57 | 1 | 2.57 | 0.1467 | 0.7672 |
| $A^2B^2$ | 3.77 | 1 | 3.77 | 0.2148 | 0.7237 |
| $A^2BC$ | 2.55 | 1 | 2.55 | 0.1452 | 0.7683 |
| $A^2C^2$ | 0.1815 | 1 | 0.1815 | 0.0103 | 0.9355 |
| $AB^2C$ | 2.07 | 1 | 2.07 | 0.1181 | 0.7893 |
| $ABC^2$ | 0.7701 | 1 | 0.7701 | 0.0439 | 0.8685 |

| | | | | | |
|---|---|---|---|---|---|
| $B^2C^2$ | 3.67 | 1 | 3.67 | 0.209 | 0.727 |
| $A^2B^2C$ | 1.42 | 1 | 1.42 | 0.0807 | 0.8238 |
| $A^2BC^2$ | 1.96 | 1 | 1.96 | 0.1117 | 0.7947 |
| $AB^2C^2$ | 73.17 | 1 | 73.17 | 4.17 | 0.2899 |
| **Residual** | 17.55 | 1 | 17.55 | | |
| **Cor Total** | 267.01 | 26 | | | |

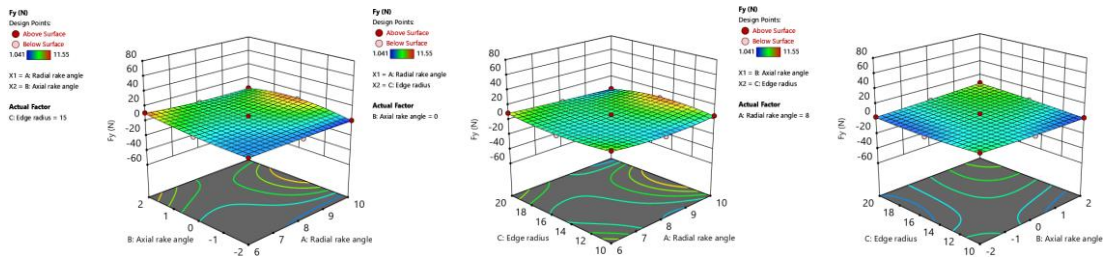

**Figure 6.165.** 3D surface plot of the measured forces in Y direction (Fy) variation during drilling of forged CW511L with 90° of plunging angle with respect to the studied cutting tool geometry

**Table 6.145.** The ANOVA results for measured forces in Z direction (Fz) during drilling of forged CW511L with 90° of plunging angle

| Source | Sum of Squares | df | Mean Square | F-value | p-value | |
|---|---|---|---|---|---|---|
| **Model** | 59424.96 | 9 | 6602.77 | 15.77 | < 0.0001 | significant |
| A-Radial rake angle | 59.1 | 1 | 59.1 | 0.1411 | 0.7118 | |
| B-Axial rake angle | 9725.1 | 1 | 9725.1 | 23.22 | 0.0002 | |
| C-Edge radius | 36275.25 | 1 | 36275.25 | 86.63 | < 0.0001 | |
| AB | 17.98 | 1 | 17.98 | 0.0429 | 0.8383 | |
| AC | 58.82 | 1 | 58.82 | 0.1405 | 0.7125 | |
| BC | 600.5 | 1 | 600.5 | 1.43 | 0.2475 | |
| $A^2$ | 7911.37 | 1 | 7911.37 | 18.89 | 0.0004 | |
| $B^2$ | 86.28 | 1 | 86.28 | 0.206 | 0.6556 | |
| $C^2$ | 4690.57 | 1 | 4690.57 | 11.2 | 0.0038 | |
| **Residual** | 7118.82 | 17 | 418.75 | | | |
| **Cor Total** | 66543.79 | 26 | | | | |

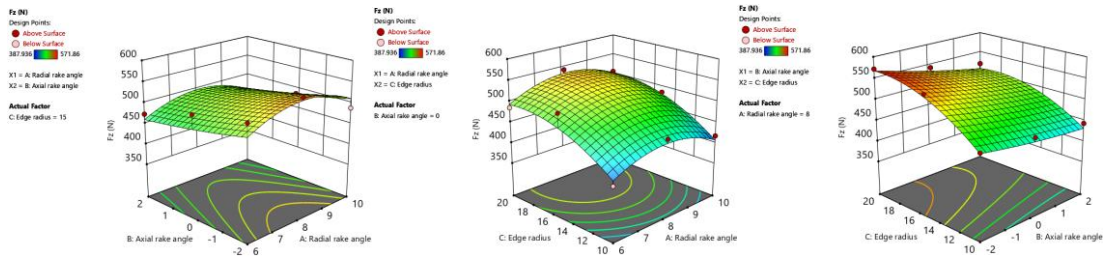

**Figure 6.166.** 3D surface plot of the measured forces in Z direction (Fz) variation during drilling of forged CW511L with 90° of plunging angle with respect to the studied

cutting tool geometry

**Table 6.146.** The ANOVA results for measured resultant forces (FR) during drilling of forged CW511L with 90° of plunging angle

| Source | Sum of Squares | df | Mean Square | F-value | p-value | |
|---|---|---|---|---|---|---|
| **Model** | 59421.05 | 9 | 6602.34 | 15.78 | < 0.0001 | significant |
| A-Radial rake angle | 58.17 | 1 | 58.17 | 0.139 | 0.7139 | |
| B-Axial rake angle | 9728.08 | 1 | 9728.08 | 23.25 | 0.0002 | |
| C-Edge radius | 36291.87 | 1 | 36291.87 | 86.73 | < 0.0001 | |
| AB | 18.01 | 1 | 18.01 | 0.043 | 0.8381 | |
| AC | 59.11 | 1 | 59.11 | 0.1412 | 0.7117 | |
| BC | 600.57 | 1 | 600.57 | 1.44 | 0.2474 | |
| $A^2$ | 7897.3 | 1 | 7897.3 | 18.87 | 0.0004 | |
| $B^2$ | 87.22 | 1 | 87.22 | 0.2084 | 0.6538 | |
| $C^2$ | 4680.72 | 1 | 4680.72 | 11.19 | 0.0038 | |
| **Residual** | 7113.72 | 17 | 418.45 | | | |
| **Cor Total** | 66534.77 | 26 | | | | |

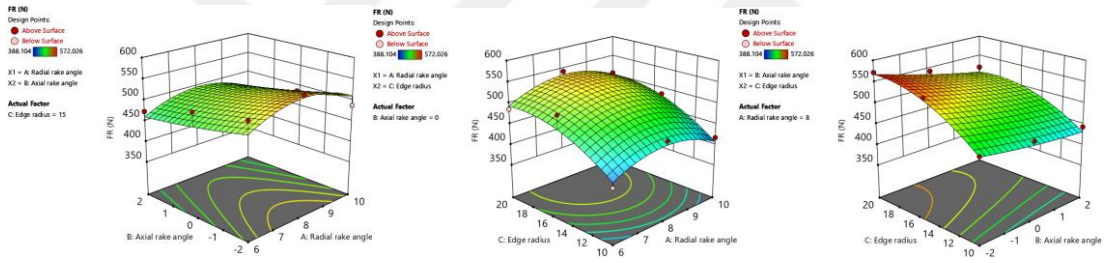

**Figure 6.167.** 3D surface plot of the measured resultant forces variation during drilling of forged CW511L with 90° of plunging angle with respect to the studied cutting tool geometry

**Table 6.147.** The ANOVA results for measured burr heights at hole entry (BHEN) during drilling of forged CW511L with 90° of plunging angle

| Source | Sum of Squares | df | Mean Square | F-value | p-value |
|---|---|---|---|---|---|
| **Model** | 1.79E+05 | 16 | 11192.1 | 2.52 | 0.0711 |
| A-Radial rake angle | 14989.42 | 1 | 14989.4 | 3.37 | 0.0962 |
| B-Axial rake angle | 1435.16 | 1 | 1435.16 | 0.3228 | 0.5825 |
| C-Edge radius | 31191.18 | 1 | 31191.2 | 7.02 | 0.0244 |
| AB | 1212.17 | 1 | 1212.17 | 0.2726 | 0.6129 |
| AC | 38847.22 | 1 | 38847.2 | 8.74 | 0.0144 |
| BC | 288.54 | 1 | 288.54 | 0.0649 | 0.8041 |
| $A^2$ | 13869.73 | 1 | 13869.7 | 3.12 | 0.1078 |
| $B^2$ | 28967.88 | 1 | 28967.9 | 6.52 | 0.0287 |
| $C^2$ | 7021.88 | 1 | 7021.88 | 1.58 | 0.2374 |

| | | | | | |
|---|---|---|---|---|---|
| ABC | 1816.21 | 1 | 1816.21 | 0.4085 | 0.5371 |
| $A^2B$ | 2863.05 | 1 | 2863.05 | 0.6439 | 0.4409 |
| $A^2C$ | 16343.15 | 1 | 16343.2 | 3.68 | 0.0842 |
| $AB^2$ | 28638.74 | 1 | 28638.7 | 6.44 | 0.0295 |
| $AC^2$ | 188.92 | 1 | 188.92 | 0.0425 | 0.8408 |
| $B^2C$ | 12144.22 | 1 | 12144.2 | 2.73 | 0.1294 |
| $BC^2$ | 152.81 | 1 | 152.81 | 0.0344 | 0.8566 |
| $A^3$ | 0 | 0 | | | |
| $B^3$ | 0 | 0 | | | |
| $C^3$ | 0 | 0 | | | |
| **Residual** | 44462 | 10 | 4446.2 | | |
| **Cor Total** | 2.24E+05 | 26 | | | |

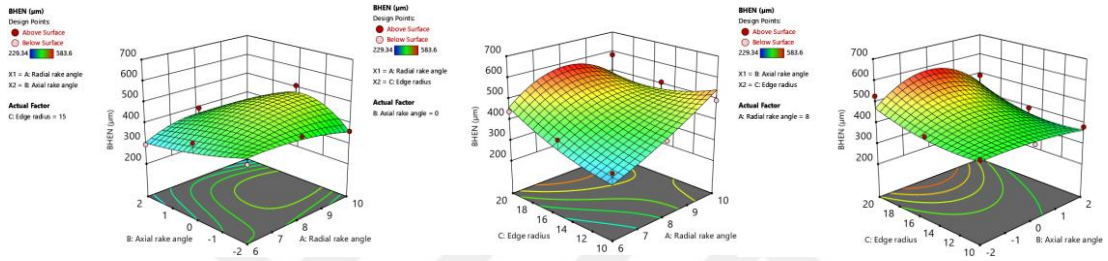


**Figure 6.168.** 3D surface plot of the measured burr heights at hole entry (BHEN) variation during drilling of forged CW511L with 90° of plunging angle with respect to the studied cutting tool geometry

**Table 6.148.** The ANOVA results for measured burr heights at hole exit (BHEX) during drilling of forged CW511L with 90° of plunging angle

| Source | Sum of Squares | df | Mean Square | F-value | p-value | |
|---|---|---|---|---|---|---|
| **Model** | 18641.4 | 6 | 3106.9 | 24.17 | < 0.0001 | significant |
| A-Radial rake angle | 5412.26 | 1 | 5412.26 | 42.1 | < 0.0001 | |
| B-Axial rake angle | 1677.21 | 1 | 1677.21 | 13.05 | 0.0017 | |
| C-Edge radius | 10343.9 | 1 | 10343.9 | 80.47 | < 0.0001 | |
| AB | 555.53 | 1 | 555.53 | 4.32 | 0.0507 | |
| AC | 625.05 | 1 | 625.05 | 4.86 | 0.0393 | |
| BC | 27.48 | 1 | 27.48 | 0.2137 | 0.6488 | |
| **Residual** | 2570.95 | 20 | 128.55 | | | |
| **Cor Total** | 21212.4 | 26 | | | | |

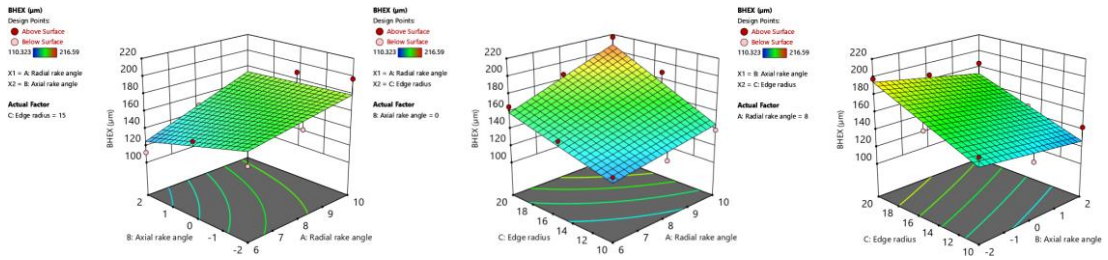

**Figure 6.169.** 3D surface plot of the measured burr heights at hole exit (BHEX) variation during drilling of forged CW511L with 90° of plunging angle with respect to the studied cutting tool geometry

**Table 6.149.** The ANOVA results for measured surface roughness at hole bottom (Ra) during drilling of forged CW511L with 90° of plunging angle

| Source | Sum of Squares | df | Mean Square | F-value | p-value | |
|---|---|---|---|---|---|---|
| **Model** | 0.076 | 9 | 0.0084 | 335.89 | < 0.0001 | significant |
| A-Radial rake angle | 0.005 | 1 | 0.005 | 199.1 | < 0.0001 | |
| B-Axial rake angle | 0.0006 | 1 | 0.0006 | 22.38 | 0.0002 | |
| C-Edge radius | 0.07 | 1 | 0.07 | 2784.77 | < 0.0001 | |
| AB | 0.0001 | 1 | 0.0001 | 2.25 | 0.1524 | |
| AC | 4.02E-06 | 1 | 4.02E-06 | 0.1597 | 0.6944 | |
| BC | 1.57E-06 | 1 | 1.57E-06 | 0.0624 | 0.8058 | |
| $A^2$ | 0 | 1 | 0 | 1.86 | 0.1899 | |
| $B^2$ | 6.75E-06 | 1 | 6.75E-06 | 0.2683 | 0.6111 | |
| $C^2$ | 0.0003 | 1 | 0.0003 | 12.14 | 0.0028 | |
| **Residual** | 0.0004 | 17 | 0 | | | |
| **Cor Total** | 0.0764 | 26 | | | | |

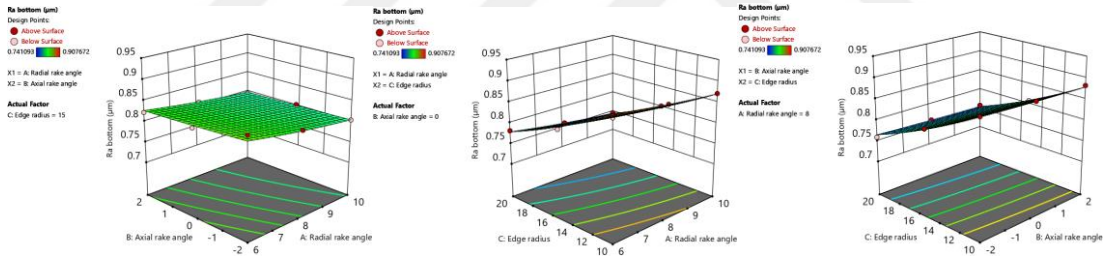


**Figure 6.170.** 3D surface plot of the measured surface roughness at hole bottom (Ra) variation during drilling of forged CW511L with 90° of plunging angle with respect to the studied cutting tool geometry

**Table 6.150.** The ANOVA results for measured surface roughness at hole wall (Ra) during drilling of forged CW511L with 90° of plunging angle

| Source | Sum of Squares | df | Mean Square | F-value | p-value | |
|---|---|---|---|---|---|---|
| **Model** | 0.0478 | 9 | 0.0053 | 335.5 | < 0.0001 | significant |
| A-Radial rake angle | 0.0031 | 1 | 0.0031 | 197.48 | < 0.0001 | |
| B-Axial rake angle | 0.0004 | 1 | 0.0004 | 22.45 | 0.0002 | |
| C-Edge radius | 0.044 | 1 | 0.044 | 2776.83 | < 0.0001 | |
| AB | 0 | 1 | 0 | 2.58 | 0.1263 | |
| AC | 4.26E-07 | 1 | 4.26E-07 | 0.0269 | 0.8717 | |
| BC | 2.38E-06 | 1 | 2.38E-06 | 0.1504 | 0.7029 | |
| $A^2$ | 0 | 1 | 0 | 1.93 | 0.1824 | |

| | | | | | |
|---|---|---|---|---|---|
| $B^2$ | 4.30E-06 | 1 | 4.30E-06 | 0.2713 | 0.6092 |
| $C^2$ | 0.0003 | 1 | 0.0003 | 17.79 | 0.0006 |
| **Residual** | 0.0003 | 17 | 0 | | |
| **Cor Total** | 0.0481 | 26 | | | |

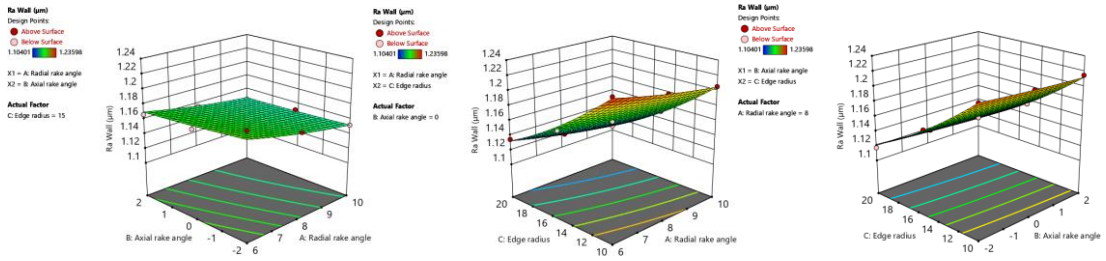

**Figure 6.171.** 3D surface plot of the measured surface roughness at hole wall (Ra) variation during drilling of forged CW511L with 90° of plunging angle with respect to the studied cutting tool geometry

**Table 6.151.** The ANOVA results for measured hole diameter during drilling of forged CW511L with 90° of plunging angle

| Source | Sum of Squares | df | Mean Square | F-value | p-value |
|---|---|---|---|---|---|
| **Model** | 2.29 | 22 | 0.1041 | 0.8245 | 0.6663 |
| A-Radial rake angle | 0.1546 | 1 | 0.1546 | 1.22 | 0.3306 |
| B-Axial rake angle | 0.0531 | 1 | 0.0531 | 0.4204 | 0.5521 |
| C-Edge radius | 0.0094 | 1 | 0.0094 | 0.0743 | 0.7987 |
| AB | 0.0144 | 1 | 0.0144 | 0.114 | 0.7526 |
| AC | 0.0388 | 1 | 0.0388 | 0.3073 | 0.6089 |
| BC | 0.0103 | 1 | 0.0103 | 0.0816 | 0.7894 |
| $A^2$ | 0.0011 | 1 | 0.0011 | 0.0086 | 0.9308 |
| $B^2$ | 0.0009 | 1 | 0.0009 | 0.0069 | 0.9377 |
| $C^2$ | 0.2713 | 1 | 0.2713 | 2.15 | 0.2166 |
| ABC | 0.0231 | 1 | 0.0231 | 0.183 | 0.6908 |
| $A^2B$ | 0.0001 | 1 | 0.0001 | 0.0009 | 0.9775 |
| $A^2C$ | 0.0041 | 1 | 0.0041 | 0.0321 | 0.8665 |
| $AB^2$ | 0.2259 | 1 | 0.2259 | 1.79 | 0.252 |
| $AC^2$ | 0.6917 | 1 | 0.6917 | 5.48 | 0.0794 |
| $B^2C$ | 0.1355 | 1 | 0.1355 | 1.07 | 0.3587 |
| $BC^2$ | 0.1754 | 1 | 0.1754 | 1.39 | 0.3039 |
| $A^2B^2$ | 0.1005 | 1 | 0.1005 | 0.7955 | 0.4228 |
| $A^2BC$ | 0.0173 | 1 | 0.0173 | 0.1368 | 0.7302 |
| $A^2C^2$ | 0.0306 | 1 | 0.0306 | 0.2423 | 0.6483 |
| $AB^2C$ | 0.0775 | 1 | 0.0775 | 0.6138 | 0.4771 |
| $ABC^2$ | 0 | 1 | 0 | 0.0003 | 0.9871 |
| $B^2C^2$ | 0.0405 | 1 | 0.0405 | 0.3206 | 0.6015 |
| **Residual** | 0.5052 | 4 | 0.1263 | | |
| **Cor Total** | 2.8 | 26 | | | |

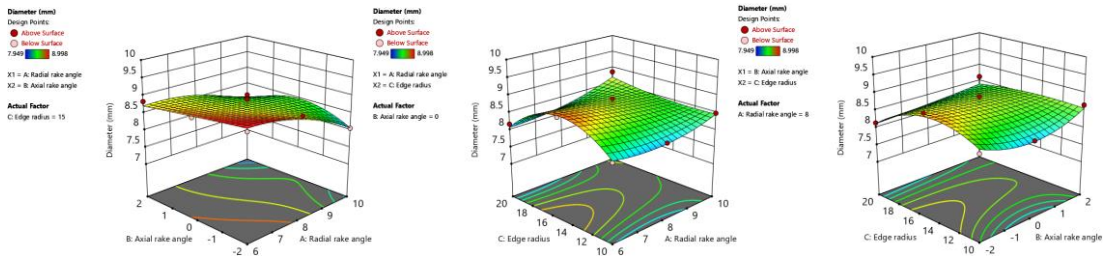

**Figure 6.172.** 3D surface plot of the measured hole diameter variation during drilling of forged CW511L with 90° of plunging angle with respect to the studied cutting tool geometry

**Table 6.152.** The developed regression model for drilling of forged CW511L with 90° of plunging angle

| Forged CW511L 90 | Fx | Fy | Fz | FR | BHEN | BHEX | Ra bottom | Ra Wall | Diameter |
|---|---|---|---|---|---|---|---|---|---|
| | 3.37 | 4.88 | 516.9 | 516.93 | 459.07 | 159.03 | 0.8144 | 1.16 | 8.67 |
| A | -1.74 | 3 | 1.81 | 1.8 | 64.53 | 17.34 | -0.0167 | -0.0132 | -0.2072 |
| B | -1.75 | 1.62 | -23.24 | -23.25 | -19.97 | -9.65 | -0.0056 | -0.0044 | -0.1214 |
| C | -1.01 | 0.942 | 44.89 | 44.9 | 93.08 | 23.97 | -0.0624 | -0.0494 | 0.0511 |
| AB | 0.5261 | -1.14 | -1.22 | -1.23 | 10.05 | 6.8 | 0.0022 | 0.0018 | 0.06 |
| AC | 3.4 | -0.916 | 2.21 | 2.22 | -56.9 | 7.22 | -0.0006 | 0.0002 | 0.0985 |
| BC | -0.3595 | 2.62 | -7.07 | -7.07 | 4.9 | -1.51 | 0.0004 | 0.0004 | 0.0507 |
| $A^2$ | -0.3198 | 2.57 | -36.31 | -36.28 | -48.08 | 0 | 0.0028 | 0.0023 | 0.03 |
| $B^2$ | 1.37 | -1.08 | 3.79 | 3.81 | -69.48 | 0 | 0.0011 | 0.0008 | 0.027 |
| $C^2$ | 0.4149 | -0.9047 | -27.96 | -27.93 | 34.21 | 0 | 0.0071 | 0.0069 | -0.4755 |
| ABC | 0.6235 | 1.18 | 0 | 0 | 15.07 | 0 | 0 | 0 | -0.0537 |
| $A^2B$ | -2.68 | 1.43 | 0 | 0 | -26.75 | 0 | 0 | 0 | -0.0053 |
| $A^2C$ | 2.85 | -1.87 | 0 | 0 | -63.92 | 0 | 0 | 0 | -0.0318 |
| $AB^2$ | 0.7053 | -5.1 | 0 | 0 | -84.61 | 0 | 0 | 0 | -0.2377 |
| $AC^2$ | 4.24 | -5.77 | 0 | 0 | 6.87 | 0 | 0 | 0 | 0.4158 |
| $B^2C$ | 5.74 | -0.1728 | 0 | 0 | -55.1 | 0 | 0 | 0 | -0.1841 |
| $BC^2$ | 0.741 | -1.39 | 0 | 0 | 6.18 | 0 | 0 | 0 | 0.2094 |

| | | | | | | | | | |
|---|---|---|---|---|---|---|---|---|---|
| | 5 | | | | | | | | |
| $A^2B^2$ | 0.168 | -1.68 | 0 | 0 | 0 | 0 | 0 | 0 | -0.2745 |
| $A^2BC$ | -1.62 | -0.9774 | 0 | 0 | 0 | 0 | 0 | 0 | -0.0805 |
| $A^2C^2$ | 0.7441 | -0.3689 | 0 | 0 | 0 | 0 | 0 | 0 | 0.1515 |
| $AB^2C$ | -2.65 | -0.8814 | 0 | 0 | 0 | 0 | 0 | 0 | -0.1705 |
| $ABC^2$ | 0.9577 | 0.5374 | 0 | 0 | 0 | 0 | 0 | 0 | -0.0038 |
| $B^2C^2$ | 1.76 | 1.66 | 0 | 0 | 0 | 0 | 0 | 0 | 0.1742 |
| $A^2B^2C$ | -7.89 | 1.26 | 0 | 0 | 0 | 0 | 0 | 0 | 0 |
| $A^2BC^2$ | 3.73 | -1.48 | 0 | 0 | 0 | 0 | 0 | 0 | 0 |
| $AB^2C^2$ | -4.95 | 9.07 | 0 | 0 | 0 | 0 | 0 | 0 | 0 |
| **Regression confidence $R^2$** | 0.977 | 0.934 | 0.893 | 0.893 | 0.801 | 0.878 | 0.994 | 0.994 | 0.819 |

**Table 6.153.** The ANOVA results for measured forces in X direction (Fx) during drilling of forged CW511L with 60° of plunging angle

| Source | Sum of Squares | df | Mean Square | F-value | p-value | |
|---|---|---|---|---|---|---|
| **Model** | 49633.1 | 9 | 5514.79 | 33.3 | < 0.0001 | significant |
| A-Radial rake angle | 805.92 | 1 | 805.92 | 4.87 | 0.0414 | |
| B-Axial rake angle | 342.05 | 1 | 342.05 | 2.07 | 0.1688 | |
| C-Edge radius | 44658.5 | 1 | 44658.5 | 269.69 | < 0.0001 | |
| AB | 50.76 | 1 | 50.76 | 0.3065 | 0.587 | |
| AC | 0.6335 | 1 | 0.6335 | 0.0038 | 0.9514 | |
| BC | 261.02 | 1 | 261.02 | 1.58 | 0.2263 | |
| $A^2$ | 11.66 | 1 | 11.66 | 0.0704 | 0.794 | |
| $B^2$ | 9.32 | 1 | 9.32 | 0.0563 | 0.8153 | |
| $C^2$ | 3493.2 | 1 | 3493.2 | 21.1 | 0.0003 | |
| **Residual** | 2815.08 | 17 | 165.59 | | | |
| **Cor Total** | 52448.2 | 26 | | | | |

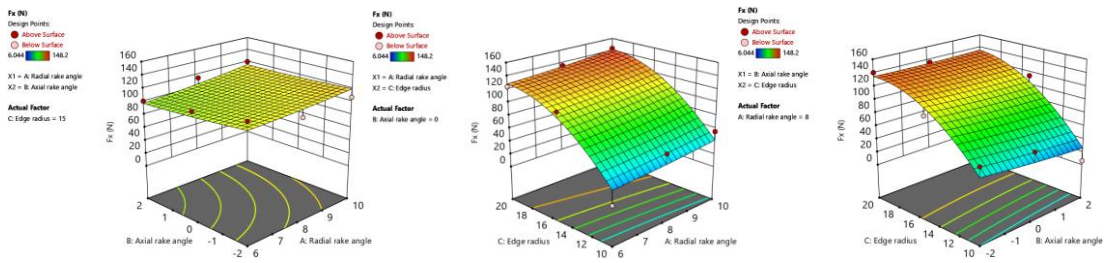


**Figure 6.173.** 3D surface plot of the measured forces in X direction (Fx) variation during drilling of forged CW511L with 60° of plunging angle with respect to the studied cutting tool geometry

**Table 6.154.** The ANOVA results for measured forces in Y direction (Fy) during drilling of forged CW511L with 60° of plunging angle

| Source | Sum of Squares | df | Mean Square | F-value | p-value | |
|---|---|---|---|---|---|---|
| **Model** | 25395.2 | 16 | 1587.2 | 2.89 | 0.0468 | significant |
| A-Radial rake angle | 632.29 | 1 | 632.29 | 1.15 | 0.3086 | |
| B-Axial rake angle | 54.09 | 1 | 54.09 | 0.0984 | 0.7602 | |
| C-Edge radius | 4767.67 | 1 | 4767.67 | 8.68 | 0.0146 | |
| AB | 326.88 | 1 | 326.88 | 0.5949 | 0.4584 | |
| AC | 2702.1 | 1 | 2702.1 | 4.92 | 0.0509 | |
| BC | 1414.19 | 1 | 1414.19 | 2.57 | 0.1397 | |
| $A^2$ | 108.01 | 1 | 108.01 | 0.1966 | 0.6669 | |
| $B^2$ | 2.75 | 1 | 2.75 | 0.005 | 0.945 | |
| $C^2$ | 1655.91 | 1 | 1655.91 | 3.01 | 0.1132 | |
| ABC | 3.52 | 1 | 3.52 | 0.0064 | 0.9377 | |
| $A^2B$ | 11.08 | 1 | 11.08 | 0.0202 | 0.8899 | |
| $A^2C$ | 189.2 | 1 | 189.2 | 0.3443 | 0.5703 | |
| $AB^2$ | 1005.42 | 1 | 1005.42 | 1.83 | 0.2059 | |
| $AC^2$ | 181.76 | 1 | 181.76 | 0.3308 | 0.5779 | |
| $B^2C$ | 267.16 | 1 | 267.16 | 0.4862 | 0.5015 | |
| $BC^2$ | 973.54 | 1 | 973.54 | 1.77 | 0.2127 | |
| **Residual** | 5494.52 | 10 | 549.45 | | | |
| **Cor Total** | 30889.7 | 26 | | | | |

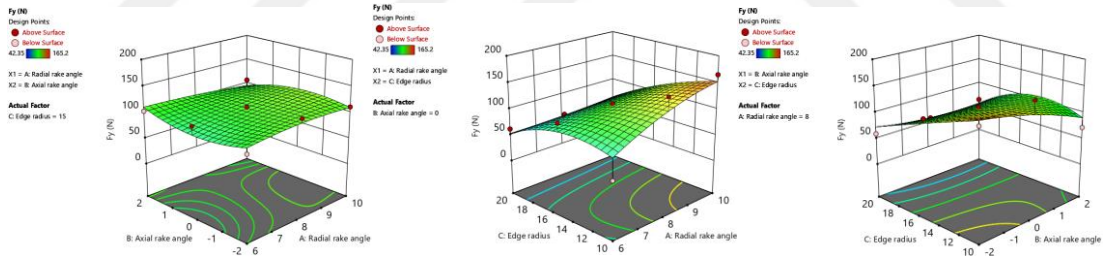

**Figure 6.174.** 3D surface plot of the measured forces in Y direction (Fy) variation during drilling of forged CW511L with 60° of plunging angle with respect to the studied cutting tool geometry

**Table 6.155.** The ANOVA results for measured forces in Z direction (Fz) during drilling of forged CW511L with 60° of plunging angle

| Source | Sum of Squares | df | Mean Square | F-value | p-value | |
|---|---|---|---|---|---|---|
| **Model** | 2.16E+05 | 9 | 23954.71 | 306.51 | < 0.0001 | significant |
| A-Radial rake angle | 208.79 | 1 | 208.79 | 2.67 | 0.1205 | |
| B-Axial rake angle | 2211.55 | 1 | 2211.55 | 28.3 | < 0.0001 | |
| C-Edge radius | 2.06E+05 | 1 | 2.06E+05 | 2631.09 | < 0.0001 | |
| AB | 19.2 | 1 | 19.2 | 0.2456 | 0.6265 | |

| | | | | | |
|---|---|---|---|---|---|
| AC | 34.08 | 1 | 34.08 | 0.4361 | 0.5179 |
| BC | 220.44 | 1 | 220.44 | 2.82 | 0.1113 |
| $A^2$ | 0.0642 | 1 | 0.0642 | 0.0008 | 0.9775 |
| $B^2$ | 22.16 | 1 | 22.16 | 0.2835 | 0.6013 |
| $C^2$ | 7249.98 | 1 | 7249.98 | 92.77 | < 0.0001 |
| **Residual** | 1328.59 | 17 | 78.15 | | |
| **Cor Total** | 2.17E+05 | 26 | | | |

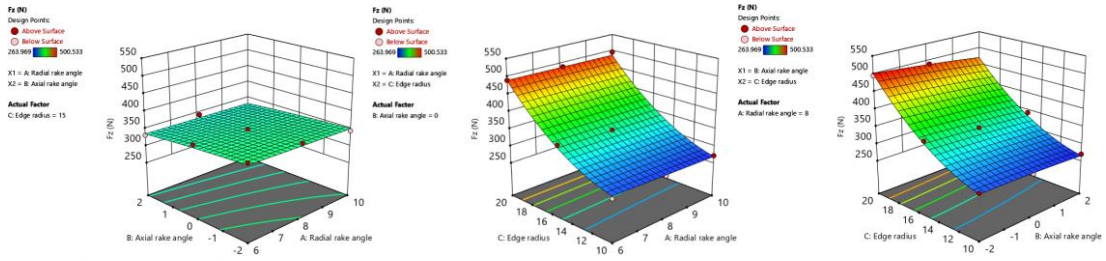

**Figure 6.175.** 3D surface plot of the measured forces in Z direction (Fz) variation during drilling of forged CW511L with 60° of plunging angle with respect to the studied cutting tool geometry

**Table 6.156.** The ANOVA results for measured resultant forces (FR) during drilling of forged CW511L with 60° of plunging angle

| Source | Sum of Squares | df | Mean Square | F-value | p-value | |
|---|---|---|---|---|---|---|
| **Model** | 2.03E+05 | 9 | 22597.84 | 140.64 | < 0.0001 | significant |
| A-Radial rake angle | 27.23 | 1 | 27.23 | 0.1694 | 0.6857 | |
| B-Axial rake angle | 4151.73 | 1 | 4151.73 | 25.84 | < 0.0001 | |
| C-Edge radius | 1.94E+05 | 1 | 1.94E+05 | 1209.86 | < 0.0001 | |
| AB | 3.75 | 1 | 3.75 | 0.0233 | 0.8804 | |
| AC | 69.7 | 1 | 69.7 | 0.4338 | 0.5189 | |
| BC | 18.05 | 1 | 18.05 | 0.1124 | 0.7416 | |
| $A^2$ | 3.09 | 1 | 3.09 | 0.0192 | 0.8913 | |
| $B^2$ | 56.58 | 1 | 56.58 | 0.3521 | 0.5607 | |
| $C^2$ | 4651.3 | 1 | 4651.3 | 28.95 | < 0.0001 | |
| **Residual** | 2731.55 | 17 | 160.68 | | | |
| **Cor Total** | 2.06E+05 | 26 | | | | |

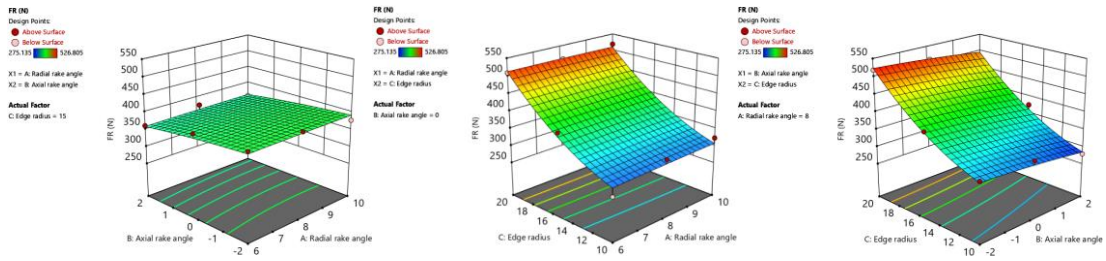

**Figure 6.176.** 3D surface plot of the measured resultant forces variation during drilling

of forged CW511L with 60° of plunging angle with respect to the studied cutting tool geometry

**Table 6.157.** The ANOVA results for measured burr heights at hole entry (BHEN) during drilling of forged CW511L with 60° of plunging angle

| Source | Sum of Squares | df | Mean Square | F-value | p-value | |
|---|---|---|---|---|---|---|
| **Model** | 63187.2 | 16 | 3949.2 | 2.88 | 0.0474 | significant |
| A-Radial rake angle | 4287.69 | 1 | 4287.69 | 3.12 | 0.1076 | |
| B-Axial rake angle | 1466.3 | 1 | 1466.3 | 1.07 | 0.3258 | |
| C-Edge radius | 5456.19 | 1 | 5456.19 | 3.97 | 0.0742 | |
| AB | 136.88 | 1 | 136.88 | 0.0997 | 0.7587 | |
| AC | 13648 | 1 | 13648 | 9.94 | 0.0103 | |
| BC | 1370.13 | 1 | 1370.13 | 0.9979 | 0.3414 | |
| $A^2$ | 1497.11 | 1 | 1497.11 | 1.09 | 0.321 | |
| $B^2$ | 13454.7 | 1 | 13454.7 | 9.8 | 0.0107 | |
| $C^2$ | 884.27 | 1 | 884.27 | 0.644 | 0.4409 | |
| ABC | 78.7 | 1 | 78.7 | 0.0573 | 0.8156 | |
| $A^2B$ | 49.08 | 1 | 49.08 | 0.0357 | 0.8538 | |
| $A^2C$ | 1227.37 | 1 | 1227.37 | 0.8939 | 0.3667 | |
| $AB^2$ | 10177.6 | 1 | 10177.6 | 7.41 | 0.0215 | |
| $AC^2$ | 70.93 | 1 | 70.93 | 0.0517 | 0.8248 | |
| $B^2C$ | 7311.7 | 1 | 7311.7 | 5.33 | 0.0437 | |
| $BC^2$ | 631.26 | 1 | 631.26 | 0.4598 | 0.5131 | |
| **Residual** | 13730.1 | 10 | 1373.01 | | | |
| **Cor Total** | 76917.3 | 26 | | | | |

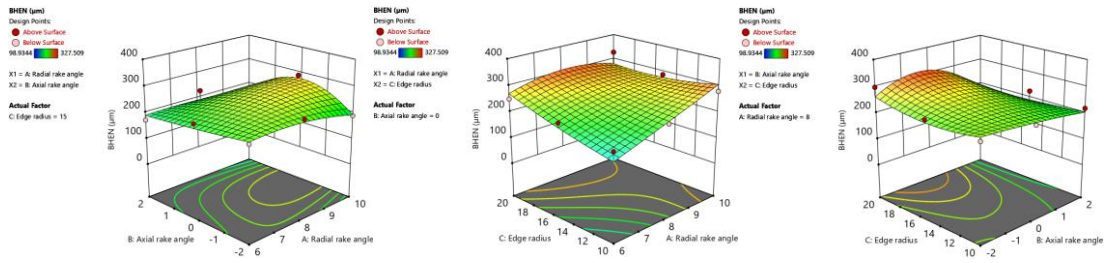


**Figure 6.177.** 3D surface plot of the measured burr heights at hole entry (BHEN) variation during drilling of forged CW511L with 60° of plunging angle with respect to the studied cutting tool geometry

**Table 6.158.** The ANOVA results for measured burr heights at hole exit (BHEX) during drilling of forged CW511L with 60° of plunging angle

| Source | Sum of Squares | df | Mean Square | F-value | p-value | |
|---|---|---|---|---|---|---|
| **Model** | 10267.66 | 6 | 1711.28 | 20.53 | < 0.0001 | significant |
| A-Radial rake angle | 3211.61 | 1 | 3211.61 | 38.53 | < 0.0001 | |

| | | | | | |
|---|---|---|---|---|---|
| B-Axial rake angle | 1178.39 | 1 | 1178.39 | 14.14 | 0.0012 |
| C-Edge radius | 5239.16 | 1 | 5239.16 | 62.85 | < 0.0001 |
| AB | 241.43 | 1 | 241.43 | 2.9 | 0.1043 |
| AC | 378.75 | 1 | 378.75 | 4.54 | 0.0456 |
| BC | 18.32 | 1 | 18.32 | 0.2198 | 0.6443 |
| **Residual** | 1667.25 | 20 | 83.36 | | |
| **Cor Total** | 11934.92 | 26 | | | |

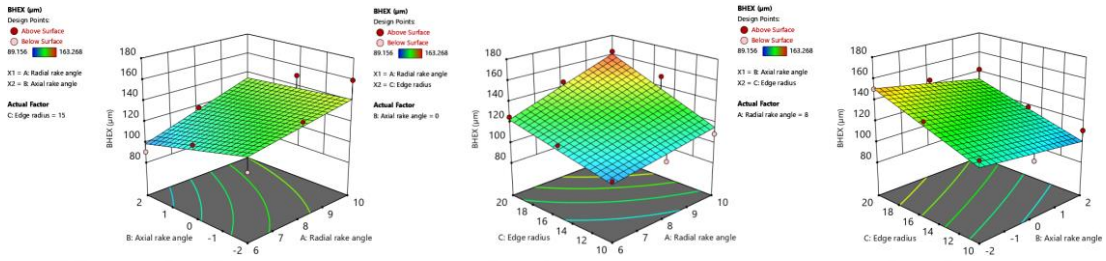

**Figure 6.178.** 3D surface plot of the measured burr heights at hole exit (BHEX) variation during drilling of forged CW511L with 60° of plunging angle with respect to the studied cutting tool geometry

**Table 6.159.** The ANOVA results for measured surface roughness at hole bottom (Ra) during drilling of forged CW511L with 60° of plunging angle

| Source | Sum of Squares | df | Mean Square | F-value | p-value | |
|---|---|---|---|---|---|---|
| **Model** | 0.0456 | 9 | 0.0051 | 335.89 | < 0.0001 | significant |
| A-Radial rake angle | 0.003 | 1 | 0.003 | 199.1 | < 0.0001 | |
| B-Axial rake angle | 0.0003 | 1 | 0.0003 | 22.38 | 0.0002 | |
| C-Edge radius | 0.042 | 1 | 0.042 | 2784.77 | < 0.0001 | |
| AB | 0 | 1 | 0 | 2.25 | 0.1524 | |
| AC | 2.41E-06 | 1 | 2.41E-06 | 0.1597 | 0.6944 | |
| BC | 9.40E-07 | 1 | 9.40E-07 | 0.0624 | 0.8058 | |
| $A^2$ | 0 | 1 | 0 | 1.86 | 0.1899 | |
| $B^2$ | 4.05E-06 | 1 | 4.05E-06 | 0.2683 | 0.6111 | |
| $C^2$ | 0.0002 | 1 | 0.0002 | 12.14 | 0.0028 | |
| **Residual** | 0.0003 | 17 | 0 | | | |
| **Cor Total** | 0.0458 | 26 | | | | |

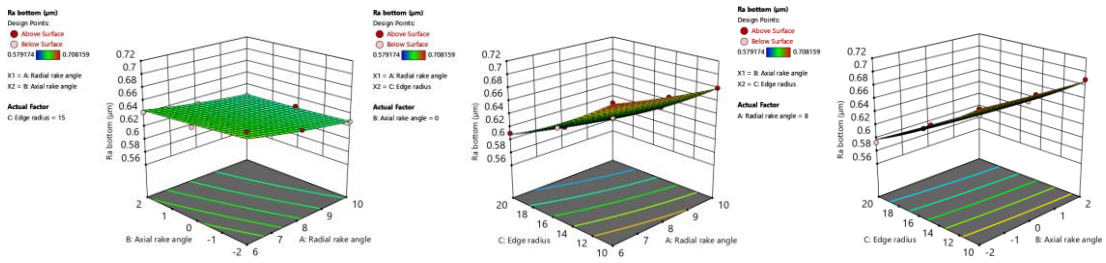

**Figure 6.179.** 3D surface plot of the measured surface roughness at hole bottom (Ra)

variation during drilling of forged CW511L with 60° of plunging angle with respect to the studied cutting tool geometry

**Table 6.160.** The ANOVA results for measured surface roughness at hole wall (Ra) during drilling of forged CW511L with 60° of plunging angle

| Source | Sum of Squares | df | Mean Square | F-value | p-value | |
|---|---|---|---|---|---|---|
| **Model** | 0.0131 | 6 | 0.0022 | 526.87 | < 0.0001 | significant |
| A-Radial rake angle | 0.0009 | 1 | 0.0009 | 213.02 | < 0.0001 | |
| B-Axial rake angle | 0.0001 | 1 | 0.0001 | 22.85 | 0.0001 | |
| C-Edge radius | 0.0121 | 1 | 0.0121 | 2916.55 | < 0.0001 | |
| AB | 4.74E-06 | 1 | 4.74E-06 | 1.14 | 0.2974 | |
| AC | 0 | 1 | 0 | 7.56 | 0.0124 | |
| BC | 4.25E-07 | 1 | 4.25E-07 | 0.1026 | 0.7521 | |
| **Residual** | 0.0001 | 20 | 4.14E-06 | | | |
| **Cor Total** | 0.0132 | 26 | | | | |

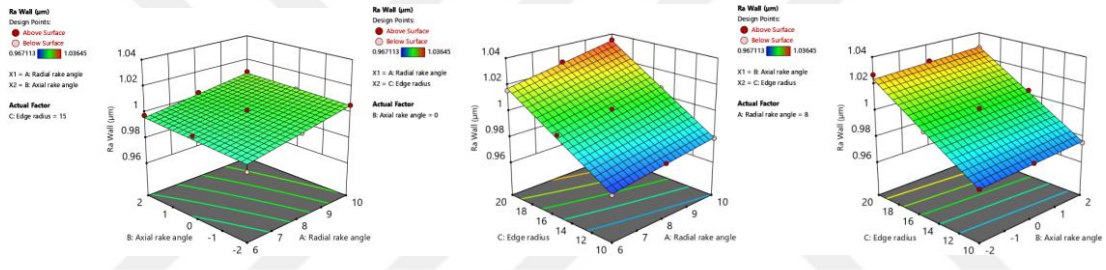

**Figure 6.180.** 3D surface plot of the measured surface roughness at hole wall (Ra) variation during drilling of forged CW511L with 60° of plunging angle with respect to the studied cutting tool geometry

**Table 6.161.** The ANOVA results for measured hole diameter during drilling of forged CW511L with 60° of plunging angle

| Source | Sum of Squares | df | Mean Square | F-value | p-value | |
|---|---|---|---|---|---|---|
| **Model** | 0.018 | 16 | 0.0011 | 10.85 | 0.0003 | significant |
| A-Radial rake angle | 0 | 1 | 0 | 0.4666 | 0.5101 | |
| B-Axial rake angle | 0.0002 | 1 | 0.0002 | 1.81 | 0.2082 | |
| C-Edge radius | 0.0012 | 1 | 0.0012 | 11.18 | 0.0075 | |
| AB | 0.0014 | 1 | 0.0014 | 13.37 | 0.0044 | |
| AC | 0 | 1 | 0 | 0.3214 | 0.5833 | |
| BC | 0 | 1 | 0 | 0.1575 | 0.6998 | |
| $A^2$ | 0.0025 | 1 | 0.0025 | 24.05 | 0.0006 | |
| $B^2$ | 0.0001 | 1 | 0.0001 | 0.7543 | 0.4055 | |
| $C^2$ | 0.0036 | 1 | 0.0036 | 35.04 | 0.0001 | |
| ABC | 0.0001 | 1 | 0.0001 | 0.9448 | 0.354 | |
| $A^2B$ | 0.0017 | 1 | 0.0017 | 16.34 | 0.0024 | |

| | | | | | |
|---|---|---|---|---|---|
| $A^2C$ | 0.0005 | 1 | 0.0005 | 4.81 | 0.0531 |
| $AB^2$ | 0.0001 | 1 | 0.0001 | 0.5423 | 0.4784 |
| $AC^2$ | 0.0003 | 1 | 0.0003 | 2.79 | 0.126 |
| $B^2C$ | 0.0002 | 1 | 0.0002 | 2.07 | 0.1804 |
| $BC^2$ | 1.11E-07 | 1 | 1.11E-07 | 0.0011 | 0.9745 |
| **Residual** | 0.001 | 10 | 0.0001 | | |
| **Cor Total** | 0.0191 | 26 | | | |

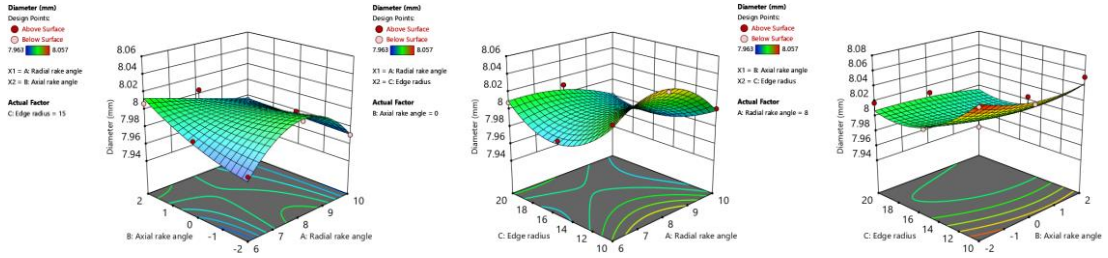

**Figure 6.181.** 3D surface plot of the measured hole diameter variation during drilling of forged CW511L with 60° of plunging angle with respect to the studied cutting tool geometry

**Table 6.162.** The developed regression model for drilling of forged CW511L with 60° of plunging angle

| Forged CW511L 60 | Fx | Fy | Fz | FR | BHEN | BHEX | Ra bottom | Ra Wall | Diameter |
|---|---|---|---|---|---|---|---|---|---|
| | 108.14 | 108.67 | 346.17 | 380.03 | 257.71 | 124.67 | 0.6359 | 1.00 | 8.00 |
| A | 6.69 | 13.25 | -3.41 | 1.23 | 34.51 | 13.36 | -0.0129 | 0.007 | -0.0037 |
| B | -4.36 | -3.88 | -11.08 | -15.19 | -20.18 | -8.09 | -0.0043 | 0.0023 | -0.0072 |
| C | 49.81 | -36.39 | 106.88 | 103.92 | 38.93 | 17.06 | -0.0483 | 0.0259 | -0.0179 |
| AB | 2.06 | -5.22 | 1.26 | 0.5589 | 3.38 | 4.49 | 0.0017 | -0.0006 | -0.0108 |
| AC | 0.2298 | -15.01 | 1.69 | -2.41 | -33.72 | 5.62 | -0.0004 | 0.0016 | -0.0017 |
| BC | 4.66 | 10.86 | -4.29 | 1.23 | -10.69 | -1.24 | 0.0003 | 0.0002 | 0.0012 |
| $A^2$ | 1.39 | -4.24 | 0.1035 | -0.7179 | -15.8 | 0 | 0.0022 | 0 | -0.0204 |
| $B^2$ | 1.25 | 0.6772 | -1.92 | -3.07 | -47.35 | 0 | 0.0008 | 0 | 0.0036 |
| $C^2$ | -24.13 | -16.61 | 34.76 | 27.84 | 12.14 | 0 | 0.0055 | 0 | 0.0246 |
| ABC | 0 | 0.6638 | 0 | 0 | 3.14 | 0 | 0 | 0 | 0.0035 |

| | | | | | | | | | |
|---|---|---|---|---|---|---|---|---|---|
| $A^2B$ | 0 | 1.66 | 0 | 0 | 3.5 | 0 | 0 | 0 | 0.0206 |
| $A^2C$ | 0 | 6.88 | 0 | 0 | -17.52 | 0 | 0 | 0 | 0.0112 |
| $AB^2$ | 0 | -15.85 | 0 | 0 | -50.44 | 0 | 0 | 0 | -0.0037 |
| $AC^2$ | 0 | 6.74 | 0 | 0 | 4.21 | 0 | 0 | 0 | -0.0085 |
| $B^2C$ | 0 | 8.17 | 0 | 0 | -42.75 | 0 | 0 | 0 | -0.0073 |
| $BC^2$ | 0 | -15.6 | 0 | 0 | -12.56 | 0 | 0 | 0 | -0.0002 |
| $A^2B^2$ | 0 | 0 | 0 | 0 | 0 | 0 | 0 | 0 | 0 |
| $A^2BC$ | 0 | 0 | 0 | 0 | 0 | 0 | 0 | 0 | 0 |
| $A^2C^2$ | 0 | 0 | 0 | 0 | 0 | 0 | 0 | 0 | 0 |
| $AB^2C$ | 0 | 0 | 0 | 0 | 0 | 0 | 0 | 0 | 0 |
| $ABC^2$ | 0 | 0 | 0 | 0 | 0 | 0 | 0 | 0 | 0 |
| $B^2C^2$ | 0 | 0 | 0 | 0 | 0 | 0 | 0 | 0 | 0 |
| $A^2B^2C$ | 0 | 0 | 0 | 0 | 0 | 0 | 0 | 0 | 0 |
| $A^2BC^2$ | 0 | 0 | 0 | 0 | 0 | 0 | 0 | 0 | 0 |
| $AB^2C^2$ | 0 | 0 | 0 | 0 | 0 | 0 | 0 | 0 | 0 |
| **Regression confidence $R^2$** | 0.946 | 0.822 | 0.993 | 0.986 | 0.821 | 0.86 | 0.994 | 0.993 | 0.945 |

**Table 6.163.** The ANOVA results for measured forces in X direction (Fx) during drilling of forged CW511L with 45° of plunging angle

| Source | Sum of Squares | df | Mean Square | F-value | p-value | |
|---|---|---|---|---|---|---|
| **Model** | 42862.13 | 6 | 7143.69 | 24 | < 0.0001 | significant |
| A-Radial rake angle | 1014.9 | 1 | 1014.9 | 3.41 | 0.0797 | |
| B-Axial rake angle | 242 | 1 | 242 | 0.813 | 0.378 | |
| C-Edge radius | 40663.82 | 1 | 40663.82 | 136.61 | < 0.0001 | |
| AB | 164.35 | 1 | 164.35 | 0.5521 | 0.4661 | |
| AC | 625.83 | 1 | 625.83 | 2.1 | 0.1626 | |
| BC | 151.23 | 1 | 151.23 | 0.5081 | 0.4842 | |
| **Residual** | 5953.33 | 20 | 297.67 | | | |
| **Cor Total** | 48815.46 | 26 | | | | |

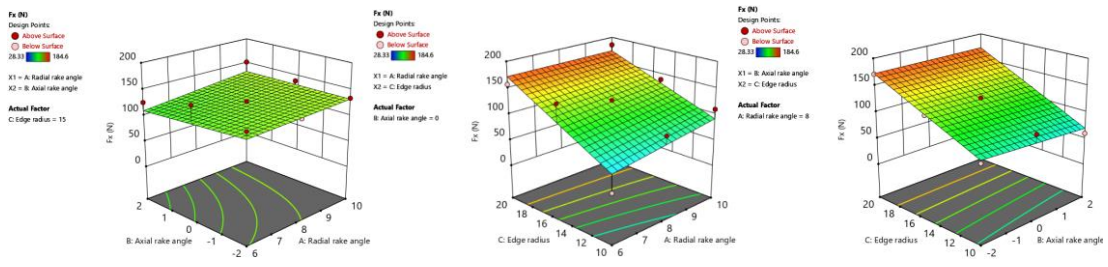

**Figure 6.182.** 3D surface plot of the measured forces in X direction (Fx) variation during drilling of forged CW511L with 45° of plunging angle with respect to the studied cutting tool geometry

**Table 6.164.** The ANOVA results for measured forces in Y direction (Fy) during

drilling of forged CW511L with 45° of plunging angle

| Source | Sum of Squares | df | Mean Square | F-value | p-value | |
|---|---|---|---|---|---|---|
| **Model** | 25142 | 9 | 2793.56 | 9.31 | < 0.0001 | significant |
| A-Radial rake angle | 61.96 | 1 | 61.96 | 0.2064 | 0.6554 | |
| B-Axial rake angle | 485.78 | 1 | 485.78 | 1.62 | 0.2205 | |
| C-Edge radius | 22863.49 | 1 | 22863.49 | 76.16 | < 0.0001 | |
| AB | 136.62 | 1 | 136.62 | 0.4551 | 0.509 | |
| AC | 565.87 | 1 | 565.87 | 1.88 | 0.1876 | |
| BC | 14.11 | 1 | 14.11 | 0.047 | 0.831 | |
| $A^2$ | 170.01 | 1 | 170.01 | 0.5663 | 0.462 | |
| $B^2$ | 690.53 | 1 | 690.53 | 2.3 | 0.1477 | |
| $C^2$ | 153.64 | 1 | 153.64 | 0.5118 | 0.4841 | |
| **Residual** | 5103.55 | 17 | 300.21 | | | |
| **Cor Total** | 30245.55 | 26 | | | | |

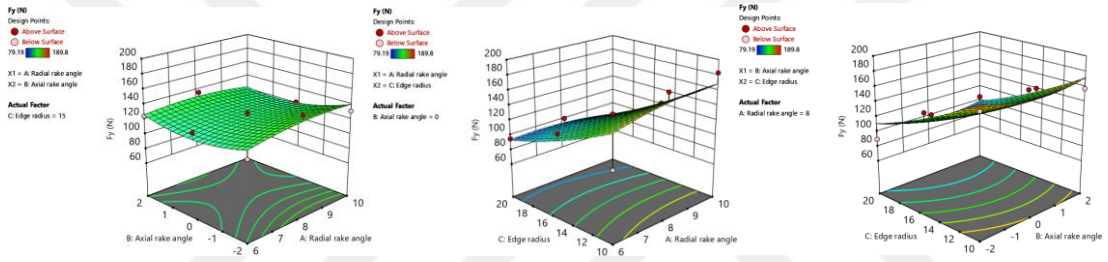

**Figure 6.183.** 3D surface plot of the measured forces in Y direction (Fy) variation during drilling of forged CW511L with 45° of plunging angle with respect to the studied cutting tool geometry

**Table 6.165.** The ANOVA results for measured forces in Z direction (Fz) during drilling of forged CW511L with 45° of plunging angle

| Source | Sum of Squares | df | Mean Square | F-value | p-value | |
|---|---|---|---|---|---|---|
| **Model** | 5.86E+05 | 9 | 65109.83 | 819.42 | < 0.0001 | significant |
| A-Radial rake angle | 85.98 | 1 | 85.98 | 1.08 | 0.3128 | |
| B-Axial rake angle | 3756.1 | 1 | 3756.1 | 47.27 | < 0.0001 | |
| C-Edge radius | 4.83E+05 | 1 | 4.83E+05 | 6080.29 | < 0.0001 | |
| AB | 29.67 | 1 | 29.67 | 0.3734 | 0.5493 | |
| AC | 1491.69 | 1 | 1491.69 | 18.77 | 0.0005 | |
| BC | 0.7717 | 1 | 0.7717 | 0.0097 | 0.9227 | |
| $A^2$ | 120.85 | 1 | 120.85 | 1.52 | 0.2343 | |
| $B^2$ | 0.0032 | 1 | 0.0032 | 0 | 0.995 | |
| $C^2$ | 97372.26 | 1 | 97372.26 | 1225.45 | < 0.0001 | |
| **Residual** | 1350.8 | 17 | 79.46 | | | |
| **Cor Total** | 5.87E+05 | 26 | | | | |

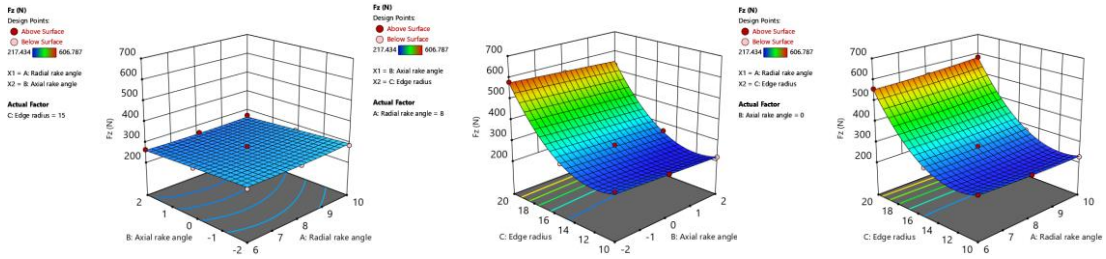

**Figure 6.184.** 3D surface plot of the measured forces in Z direction (Fz) variation during drilling of forged CW511L with 45° of plunging angle with respect to the studied cutting tool geometry

**Table 6.166.** The ANOVA results for measured resultant forces (FR) during drilling of forged CW511L with 45° of plunging angle

| Source | Sum of Squares | df | Mean Square | F-value | p-value | |
|---|---|---|---|---|---|---|
| **Model** | 4.84E+05 | 9 | 53735.49 | 304.79 | < 0.0001 | significant |
| A-Radial rake angle | 581.23 | 1 | 581.23 | 3.3 | 0.0871 | |
| B-Axial rake angle | 4084.14 | 1 | 4084.14 | 23.17 | 0.0002 | |
| C-Edge radius | 3.94E+05 | 1 | 3.94E+05 | 2235.18 | < 0.0001 | |
| AB | 14.09 | 1 | 14.09 | 0.0799 | 0.7808 | |
| AC | 394.07 | 1 | 394.07 | 2.24 | 0.1532 | |
| BC | 2.29 | 1 | 2.29 | 0.013 | 0.9106 | |
| $A^2$ | 208.26 | 1 | 208.26 | 1.18 | 0.2923 | |
| $B^2$ | 27.61 | 1 | 27.61 | 0.1566 | 0.6972 | |
| $C^2$ | 84239.04 | 1 | 84239.04 | 477.81 | < 0.0001 | |
| **Residual** | 2997.15 | 17 | 176.3 | | | |
| **Cor Total** | 4.87E+05 | 26 | | | | |

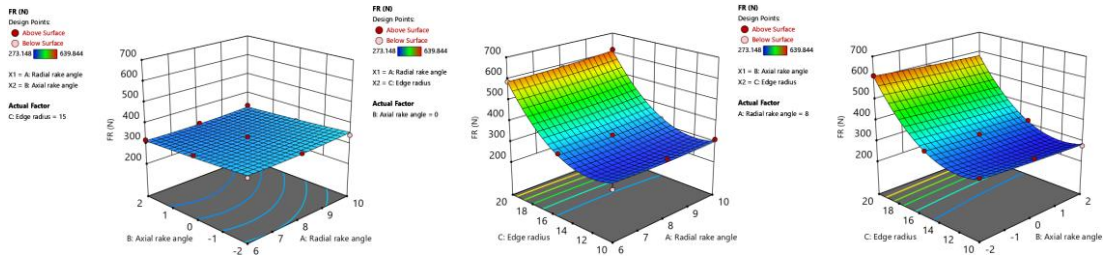

**Figure 6.185.** 3D surface plot of the measured resultant forces variation during drilling of forged CW511L with 45° of plunging angle with respect to the studied cutting tool geometry

**Table 6.167.** The ANOVA results for measured burr heights at hole entry (BHEN) during drilling of forged CW511L with 45° of plunging angle

| Source | Sum of Squares | df | Mean Square | F-value | p-value |
|---|---|---|---|---|---|
| **Model** | 20411.59 | 22 | 927.8 | 3.61 | 0.1104 |

| | | | | | |
|---|---|---|---|---|---|
| A-Radial rake angle | 2599.35 | 1 | 2599.35 | 10.11 | 0.0335 |
| B-Axial rake angle | 9.09 | 1 | 9.09 | 0.0354 | 0.86 |
| C-Edge radius | 3290 | 1 | 3290 | 12.8 | 0.0232 |
| AB | 405.57 | 1 | 405.57 | 1.58 | 0.2775 |
| AC | 3.24 | 1 | 3.24 | 0.0126 | 0.9161 |
| BC | 1.9 | 1 | 1.9 | 0.0074 | 0.9355 |
| $A^2$ | 425.84 | 1 | 425.84 | 1.66 | 0.2675 |
| $B^2$ | 36.37 | 1 | 36.37 | 0.1415 | 0.7259 |
| $C^2$ | 328.18 | 1 | 328.18 | 1.28 | 0.3217 |
| ABC | 185.98 | 1 | 185.98 | 0.7234 | 0.4429 |
| $A^2B$ | 98.45 | 1 | 98.45 | 0.383 | 0.5695 |
| $A^2C$ | 1784.41 | 1 | 1784.41 | 6.94 | 0.0579 |
| $AB^2$ | 2192.13 | 1 | 2192.13 | 8.53 | 0.0432 |
| $AC^2$ | 203.59 | 1 | 203.59 | 0.7919 | 0.4238 |
| $B^2C$ | 1339.38 | 1 | 1339.38 | 5.21 | 0.0845 |
| $BC^2$ | 109.08 | 1 | 109.08 | 0.4243 | 0.5503 |
| $A^2B^2$ | 1536.49 | 1 | 1536.49 | 5.98 | 0.0708 |
| $A^2BC$ | 30.62 | 1 | 30.62 | 0.1191 | 0.7474 |
| $A^2C^2$ | 251.05 | 1 | 251.05 | 0.9765 | 0.379 |
| $AB^2C$ | 1938.45 | 1 | 1938.45 | 7.54 | 0.0516 |
| $ABC^2$ | 63.5 | 1 | 63.5 | 0.247 | 0.6453 |
| $B^2C^2$ | 21.3 | 1 | 21.3 | 0.0829 | 0.7878 |
| **Residual** | 1028.3 | 4 | 257.07 | | |
| **Cor Total** | 21439.89 | 26 | | | |

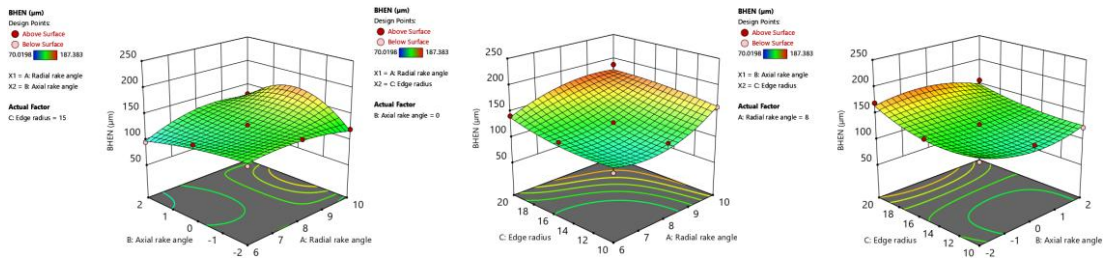

**Figure 6.186.** 3D surface plot of the measured burr heights at hole entry (BHEN) variation during drilling of forged CW511L with 45° of plunging angle with respect to the studied cutting tool geometry

**Table 6.168.** The ANOVA results for measured burr heights at hole exit (BHEX) during drilling of forged CW511L with 45° of plunging angle

| Source | Sum of Squares | df | Mean Square | F-value | p-value | |
|---|---|---|---|---|---|---|
| **Model** | 5455.98 | 6 | 909.33 | 24.17 | < 0.0001 | significant |
| A-Radial rake angle | 1584.07 | 1 | 1584.07 | 42.1 | < 0.0001 | |
| B-Axial rake angle | 490.89 | 1 | 490.89 | 13.05 | 0.0017 | |
| C-Edge radius | 3027.45 | 1 | 3027.45 | 80.47 | < 0.0001 | |
| AB | 162.59 | 1 | 162.59 | 4.32 | 0.0507 | |

| | | | | | |
|---|---|---|---|---|---|
| AC | 182.94 | 1 | 182.94 | 4.86 | 0.0393 |
| BC | 8.04 | 1 | 8.04 | 0.2137 | 0.6488 |
| **Residual** | 752.47 | 20 | 37.62 | | |
| **Cor Total** | 6208.45 | 26 | | | |

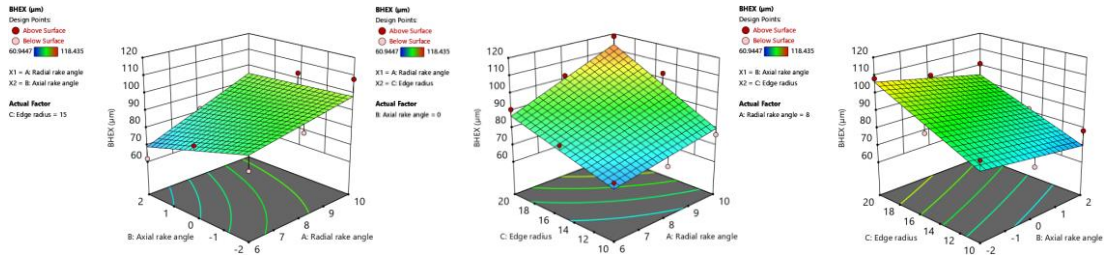


**Figure 6.187.** 3D surface plot of the measured burr heights at hole exit (BHEX) variation during drilling of forged CW511L with 45° of plunging angle with respect to the studied cutting tool geometry

**Table 6.169.** The ANOVA results for measured surface roughness at hole bottom (Ra) during drilling of forged CW511L with 45° of plunging angle

| Source | Sum of Squares | df | Mean Square | F-value | p-value | |
|---|---|---|---|---|---|---|
| **Model** | 0.0398 | 9 | 0.0044 | 335.89 | < 0.0001 | significant |
| A-Radial rake angle | 0.0026 | 1 | 0.0026 | 199.1 | < 0.0001 | |
| B-Axial rake angle | 0.0003 | 1 | 0.0003 | 22.38 | 0.0002 | |
| C-Edge radius | 0.0366 | 1 | 0.0366 | 2784.77 | < 0.0001 | |
| AB | 0 | 1 | 0 | 2.25 | 0.1524 | |
| AC | 2.10E-06 | 1 | 2.10E-06 | 0.1597 | 0.6944 | |
| BC | 8.20E-07 | 1 | 8.20E-07 | 0.0624 | 0.8058 | |
| $A^2$ | 0 | 1 | 0 | 1.86 | 0.1899 | |
| $B^2$ | 3.53E-06 | 1 | 3.53E-06 | 0.2683 | 0.6111 | |
| $C^2$ | 0.0002 | 1 | 0.0002 | 12.14 | 0.0028 | |
| **Residual** | 0.0002 | 17 | 0 | | | |
| **Cor Total** | 0.04 | 26 | | | | |

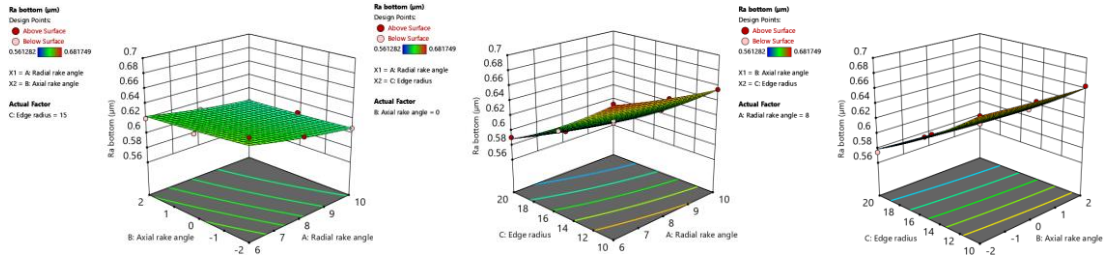


**Figure 6.188.** 3D surface plot of the measured surface roughness at hole bottom (Ra) variation during drilling of forged CW511L with 45° of plunging angle with respect to the studied cutting tool geometry

**Table 6.170.** The ANOVA results for measured surface roughness at hole wall (Ra) during drilling of forged CW511L with 45° of plunging angle

| Source | Sum of Squares | df | Mean Square | F-value | p-value | |
|---|---|---|---|---|---|---|
| **Model** | 0.0219 | 6 | 0.0037 | 486.86 | < 0.0001 | significant |
| A-Radial rake angle | 0.0015 | 1 | 0.0015 | 195.9 | < 0.0001 | |
| B-Axial rake angle | 0.0002 | 1 | 0.0002 | 21.29 | 0.0002 | |
| C-Edge radius | 0.0202 | 1 | 0.0202 | 2698.52 | < 0.0001 | |
| AB | 9.97E-06 | 1 | 9.97E-06 | 1.33 | 0.2625 | |
| AC | 0 | 1 | 0 | 4.08 | 0.0569 | |
| BC | 1.79E-07 | 1 | 1.79E-07 | 0.0239 | 0.8787 | |
| **Residual** | 0.0001 | 20 | 7.50E-06 | | | |
| **Cor Total** | 0.0221 | 26 | | | | |

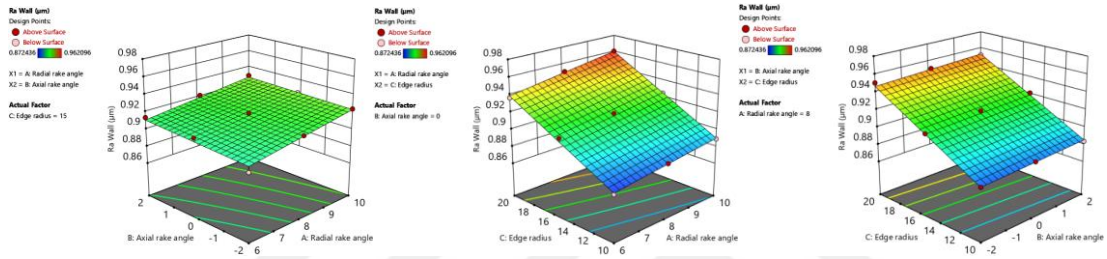

**Figure 6.189.** 3D surface plot of the measured surface roughness at hole wall (Ra) variation during drilling of forged CW511L with 45° of plunging angle with respect to the studied cutting tool geometry

**Table 6.171.** The ANOVA results for measured hole diameter during drilling of forged CW511L with 45° of plunging angle

| Source | Sum of Squares | df | Mean Square | F-value | p-value | |
|---|---|---|---|---|---|---|
| **Model** | 0.0175 | 9 | 0.0019 | 11.17 | < 0.0001 | significant |
| A-Radial rake angle | 0.0024 | 1 | 0.0024 | 13.83 | 0.0017 | |
| B-Axial rake angle | 0.0002 | 1 | 0.0002 | 0.9318 | 0.3479 | |
| C-Edge radius | 0.0052 | 1 | 0.0052 | 29.73 | < 0.0001 | |
| AB | 0.0008 | 1 | 0.0008 | 4.79 | 0.0428 | |
| AC | 0 | 1 | 0 | 0.081 | 0.7794 | |
| BC | 3.33E-07 | 1 | 3.33E-07 | 0.0019 | 0.9656 | |
| $A^2$ | 0.0024 | 1 | 0.0024 | 13.96 | 0.0016 | |
| $B^2$ | 0 | 1 | 0 | 0.2254 | 0.641 | |
| $C^2$ | 0.0064 | 1 | 0.0064 | 36.95 | < 0.0001 | |
| **Residual** | 0.003 | 17 | 0.0002 | | | |
| **Cor Total** | 0.0204 | 26 | | | | |

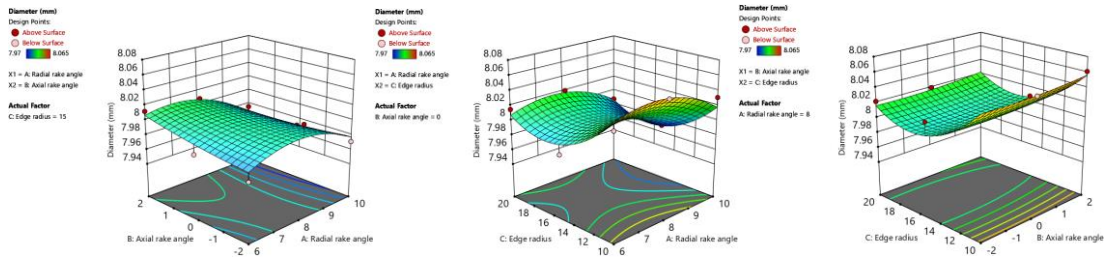


**Figure 6.190.** 3D surface plot of the measured hole diameter variation during drilling of forged CW511L with 45° of plunging angle with respect to the studied cutting tool geometry

**Table 6.172.** The developed regression model for drilling of forged CW511L with 45° of plunging angle

| Forged CW511L 45 | Fx | Fy | Fz | FR | BHEN | BHEX | Ra bottom | Ra Wall | Diameter |
|---|---|---|---|---|---|---|---|---|---|
| | 124.54 | 124.63 | 271.31 | 326.19 | 127.09 | 87.29 | 0.6143 | 0.9161 | 8.00 |
| A | 7.51 | 1.86 | 2.19 | 5.68 | 26.87 | 9.38 | -0.0121 | 0.009 | -0.0116 |
| B | -3.67 | -5.19 | -14.45 | -15.06 | -1.59 | -5.22 | -0.004 | 0.003 | 0.003 |
| C | 47.53 | -35.64 | 163.83 | 147.96 | 30.23 | 12.97 | -0.0451 | 0.0335 | -0.0169 |
| AB | 3.7 | -3.37 | -1.57 | -1.08 | 10.07 | 3.68 | 0.0016 | -0.0009 | -0.0083 |
| AC | -7.22 | -6.87 | 11.15 | 5.73 | -0.8994 | 3.9 | -0.0004 | 0.0016 | 0.0011 |
| BC | 3.55 | -1.08 | 0.2536 | 0.437 | -0.6901 | -0.8186 | 0.0003 | 0.0001 | 0.0002 |
| $A^2$ | 0 | -5.32 | 4.49 | 5.89 | 18.84 | 0 | 0.002 | 0 | -0.0201 |
| $B^2$ | 0 | 10.73 | 0.0231 | 2.15 | 5.51 | 0 | 0.0008 | 0 | 0.0026 |
| $C^2$ | 0 | 5.06 | 127.39 | 118.49 | 16.54 | 0 | 0.0052 | 0 | 0.0327 |
| ABC | 0 | 0 | 0 | 0 | 4.82 | 0 | 0 | 0 | 0 |
| $A^2B$ | 0 | 0 | 0 | 0 | -4.96 | 0 | 0 | 0 | 0 |
| $A^2C$ | 0 | 0 | 0 | 0 | -21.12 | 0 | 0 | 0 | 0 |
| $AB^2$ | 0 | 0 | 0 | 0 | -23.41 | 0 | 0 | 0 | 0 |
| $AC^2$ | 0 | 0 | 0 | 0 | -7.13 | 0 | 0 | 0 | 0 |
| $B^2C$ | 0 | 0 | 0 | 0 | -18.3 | 0 | 0 | 0 | 0 |
| $BC^2$ | 0 | 0 | 0 | 0 | -5.22 | 0 | 0 | 0 | 0 |
| $A^2B^2$ | 0 | 0 | 0 | 0 | -33.95 | 0 | 0 | 0 | 0 |
| $A^2BC$ | 0 | 0 | 0 | 0 | 3.39 | 0 | 0 | 0 | 0 |
| $A^2C^2$ | 0 | 0 | 0 | 0 | -13.72 | 0 | 0 | 0 | 0 |

| | | | | | | | | | |
|---|---|---|---|---|---|---|---|---|---|
| $AB^2C$ | 0 | 0 | 0 | 0 | -26.96 | 0 | 0 | 0 | 0 |
| $ABC^2$ | 0 | 0 | 0 | 0 | -4.88 | 0 | 0 | 0 | 0 |
| $B^2C^2$ | 0 | 0 | 0 | 0 | -4.00 | 0 | 0 | 0 | 0 |
| **Regression confidence $R^2$** | 0.878 | 0.831 | 0.977 | 0.993 | 0.952 | 0.878 | 0.994 | 0.993 | 0.855 |

**Table 6.173.** The ANOVA results for measured forces in X direction (Fx) during drilling of forged CW724R with 90° of plunging angle

| Source | Sum of Squares | df | Mean Square | F-value | p-value |
|---|---|---|---|---|---|
| **Model** | 389.55 | 22 | 17.71 | 4.58 | 0.0746 |
| A-Radial rake angle | 4.36 | 1 | 4.36 | 1.13 | 0.348 |
| B-Axial rake angle | 22.6 | 1 | 22.6 | 5.85 | 0.0729 |
| C-Edge radius | 0.2918 | 1 | 0.2918 | 0.0755 | 0.7971 |
| AB | 0.2012 | 1 | 0.2012 | 0.052 | 0.8307 |
| AC | 9.31 | 1 | 9.31 | 2.41 | 0.1957 |
| BC | 24.94 | 1 | 24.94 | 6.45 | 0.064 |
| $A^2$ | 0.3047 | 1 | 0.3047 | 0.0788 | 0.7928 |
| $B^2$ | 29.77 | 1 | 29.77 | 7.7 | 0.0501 |
| $C^2$ | 17.14 | 1 | 17.14 | 4.43 | 0.103 |
| ABC | 13.52 | 1 | 13.52 | 3.5 | 0.1348 |
| $A^2B$ | 1.04 | 1 | 1.04 | 0.2702 | 0.6306 |
| $A^2C$ | 0.3867 | 1 | 0.3867 | 0.1 | 0.7676 |
| $AB^2$ | 0.0258 | 1 | 0.0258 | 0.0067 | 0.9389 |
| $AC^2$ | 14.27 | 1 | 14.27 | 3.69 | 0.1271 |
| $B^2C$ | 7.02 | 1 | 7.02 | 1.82 | 0.2492 |
| $BC^2$ | 12.16 | 1 | 12.16 | 3.15 | 0.1508 |
| $A^2B^2$ | 16.18 | 1 | 16.18 | 4.19 | 0.1102 |
| $A^2BC$ | 73.49 | 1 | 73.49 | 19.01 | 0.0121 |
| $A^2C^2$ | 15.76 | 1 | 15.76 | 4.08 | 0.1136 |
| $AB^2C$ | 23.45 | 1 | 23.45 | 6.07 | 0.0695 |
| $ABC^2$ | 0.8118 | 1 | 0.8118 | 0.21 | 0.6706 |
| $B^2C^2$ | 26.96 | 1 | 26.96 | 6.97 | 0.0575 |
| **Residual** | 15.46 | 4 | 3.87 | | |
| **Cor Total** | 405.01 | 26 | | | |

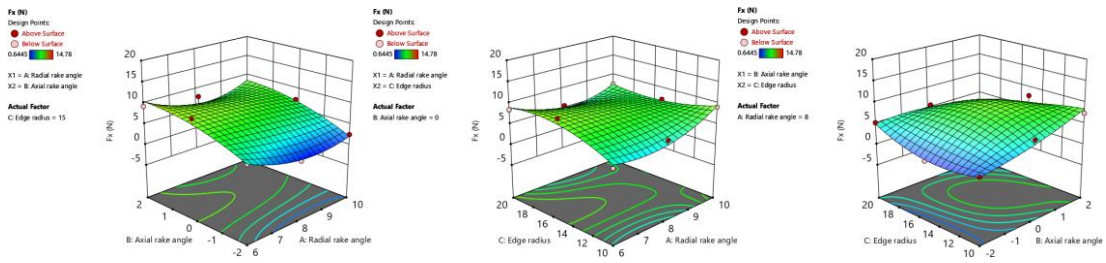

**Figure 6.191.** 3D surface plot of the measured forces in X direction (Fx) variation during drilling of forged CW724R with 90° of plunging angle with respect to the

studied cutting tool geometry

**Table 6.174.** The ANOVA results for measured forces in Y direction (Fy) during drilling of forged CW724R with 90° of plunging angle

| Source | Sum of Squares | df | Mean Square | F-value | p-value |
|---|---|---|---|---|---|
| **Model** | 357.8 | 25 | 14.31 | 11.42 | 0.2303 |
| A-Radial rake angle | 0.3309 | 1 | 0.3309 | 0.264 | 0.6978 |
| B-Axial rake angle | 10.3 | 1 | 10.3 | 8.22 | 0.2137 |
| C-Edge radius | 52.44 | 1 | 52.44 | 41.84 | 0.0976 |
| AB | 4.03 | 1 | 4.03 | 3.21 | 0.324 |
| AC | 43.38 | 1 | 43.38 | 34.61 | 0.1072 |
| BC | 4.47 | 1 | 4.47 | 3.57 | 0.3099 |
| $A^2$ | 4.08E-07 | 1 | 4.08E-07 | 3.26E-07 | 0.9996 |
| $B^2$ | 5.59 | 1 | 5.59 | 4.46 | 0.2816 |
| $C^2$ | 41.94 | 1 | 41.94 | 33.46 | 0.109 |
| ABC | 10.63 | 1 | 10.63 | 8.49 | 0.2105 |
| $A^2B$ | 0.1064 | 1 | 0.1064 | 0.0849 | 0.8195 |
| $A^2C$ | 43.58 | 1 | 43.58 | 34.77 | 0.1069 |
| $AB^2$ | 14.7 | 1 | 14.7 | 11.73 | 0.1809 |
| $AC^2$ | 0.099 | 1 | 0.099 | 0.079 | 0.8256 |
| $B^2C$ | 60.19 | 1 | 60.19 | 48.03 | 0.0912 |
| $BC^2$ | 21 | 1 | 21 | 16.76 | 0.1525 |
| $A^2B^2$ | 12.58 | 1 | 12.58 | 10.03 | 0.1947 |
| $A^2BC$ | 8.04 | 1 | 8.04 | 6.42 | 0.2394 |
| $A^2C^2$ | 14.08 | 1 | 14.08 | 11.23 | 0.1846 |
| $AB^2C$ | 19.16 | 1 | 19.16 | 15.29 | 0.1594 |
| $ABC^2$ | 1.41 | 1 | 1.41 | 1.12 | 0.4813 |
| $B^2C^2$ | 13.82 | 1 | 13.82 | 11.03 | 0.1862 |
| $A^2B^2C$ | 51.01 | 1 | 51.01 | 40.7 | 0.099 |
| $A^2BC^2$ | 13.31 | 1 | 13.31 | 10.62 | 0.1895 |
| $AB^2C^2$ | 21.08 | 1 | 21.08 | 16.82 | 0.1523 |
| **Residual** | 1.25 | 1 | 1.25 | | |
| **Cor Total** | 359.05 | 26 | | | |

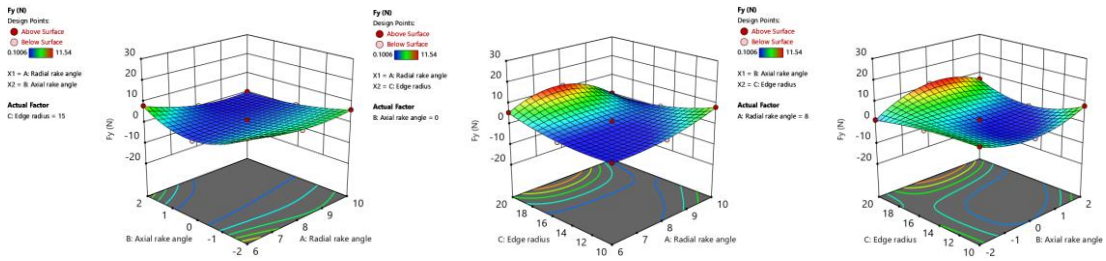

**Figure 6.192.** 3D surface plot of the measured forces in Y direction (Fy) variation during drilling of forged CW724R with 90° of plunging angle with respect to the studied cutting tool geometry

**Table 6.175.** The ANOVA results for measured forces in Z direction (Fz) during drilling of forged CW724R with 90° of plunging angle

| Source | Sum of Squares | df | Mean Square | F-value | p-value | |
|---|---|---|---|---|---|---|
| **Model** | 1.01E+05 | 6 | 16772.3 | 77.37 | < 0.0001 | significant |
| A-Radial rake angle | 378.24 | 1 | 378.24 | 1.74 | 0.2014 | |
| B-Axial rake angle | 6163.16 | 1 | 6163.16 | 28.43 | < 0.0001 | |
| C-Edge radius | 93483.15 | 1 | 93483.2 | 431.23 | < 0.0001 | |
| AB | 368.83 | 1 | 368.83 | 1.7 | 0.2069 | |
| AC | 12.41 | 1 | 12.41 | 0.0573 | 0.8133 | |
| BC | 227.7 | 1 | 227.7 | 1.05 | 0.3177 | |
| **Residual** | 4335.61 | 20 | 216.78 | | | |
| **Cor Total** | 1.05E+05 | 26 | | | | |

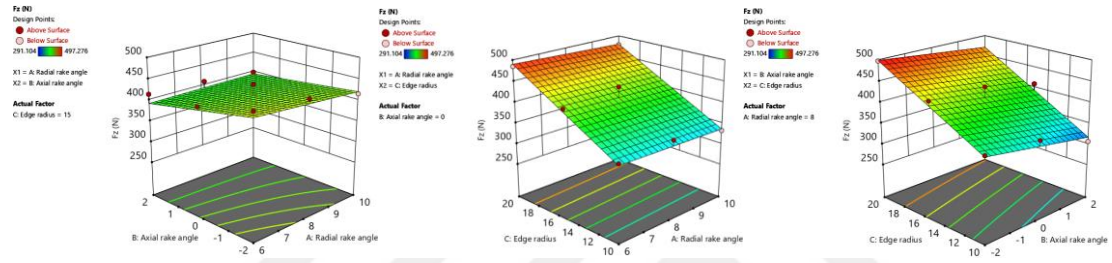

**Figure 6.193.** 3D surface plot of the measured forces in Z direction (Fz) variation during drilling of forged CW724R with 90° of plunging angle with respect to the studied cutting tool geometry

**Table 6.176.** The ANOVA results for measured resultant forces (FR) during drilling of forged CW724R with 90° of plunging angle

| Source | Sum of Squares | df | Mean Square | F-value | p-value | |
|---|---|---|---|---|---|---|
| **Model** | 1.01E+05 | 6 | 16758.7 | 77.5 | < 0.0001 | significant |
| A-Radial rake angle | 376.9 | 1 | 376.9 | 1.74 | 0.2017 | |
| B-Axial rake angle | 6151.32 | 1 | 6151.32 | 28.45 | < 0.0001 | |
| C-Edge radius | 93413.17 | 1 | 93413.2 | 431.98 | < 0.0001 | |
| AB | 368.29 | 1 | 368.29 | 1.7 | 0.2067 | |
| AC | 12.55 | 1 | 12.55 | 0.058 | 0.8121 | |
| BC | 229.98 | 1 | 229.98 | 1.06 | 0.3147 | |
| **Residual** | 4324.88 | 20 | 216.24 | | | |
| **Cor Total** | 1.05E+05 | 26 | | | | |

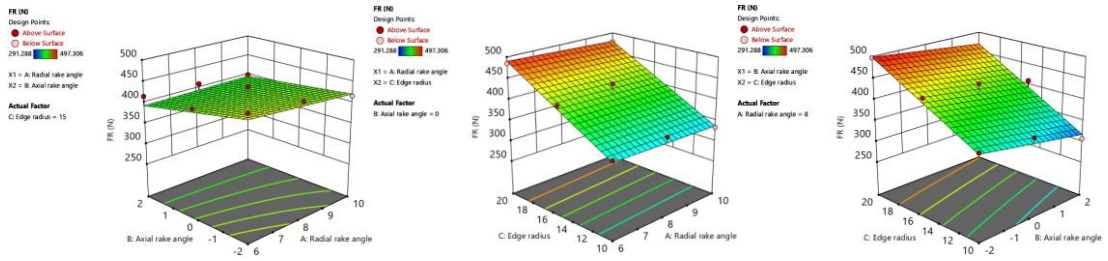

**Figure 6.194.** 3D surface plot of the measured resultant forces variation during drilling of forged CW724R with 90° of plunging angle with respect to the studied cutting tool geometry

**Table 6.177.** The ANOVA results for measured burr heights at hole entry (BHEN) during drilling of forged CW724R with 90° of plunging angle

| Source | Sum of Squares | df | Mean Square | F-value | p-value | |
|---|---|---|---|---|---|---|
| **Model** | 41836.98 | 9 | 4648.55 | 121.08 | < 0.0001 | significant |
| A-Radial rake angle | 18692.05 | 1 | 18692.1 | 486.88 | < 0.0001 | |
| B-Axial rake angle | 2271.31 | 1 | 2271.31 | 59.16 | < 0.0001 | |
| C-Edge radius | 15134.57 | 1 | 15134.6 | 394.22 | < 0.0001 | |
| AB | 1314.32 | 1 | 1314.32 | 34.23 | < 0.0001 | |
| AC | 1795.39 | 1 | 1795.39 | 46.77 | < 0.0001 | |
| BC | 229.77 | 1 | 229.77 | 5.98 | 0.0256 | |
| $A^2$ | 2010.7 | 1 | 2010.7 | 52.37 | < 0.0001 | |
| $B^2$ | 248.44 | 1 | 248.44 | 6.47 | 0.021 | |
| $C^2$ | 140.43 | 1 | 140.43 | 3.66 | 0.0728 | |
| **Residual** | 652.65 | 17 | 38.39 | | | |
| **Cor Total** | 42489.63 | 26 | | | | |

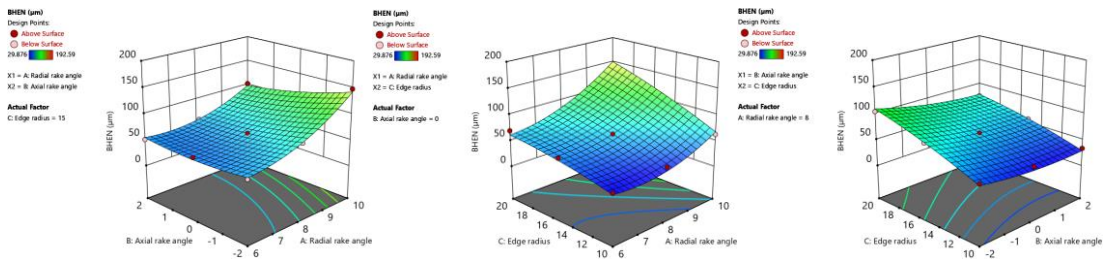

**Figure 6.195.** 3D surface plot of the measured burr heights at hole entry (BHEN) variation during drilling of forged CW724R with 90° of plunging angle with respect to the studied cutting tool geometry

**Table 6.178.** The ANOVA results for measured burr heights at hole exit (BHEX) during drilling of forged CW724R with 90° of plunging angle

| Source | Sum of Squares | df | Mean Square | F-value | p-value | |
|---|---|---|---|---|---|---|
| **Model** | 5409.34 | 9 | 601.04 | 34.98 | < 0.0001 | significant |

| | | | | | |
|---|---|---|---|---|---|
| A-Radial rake angle | 2335.63 | 1 | 2335.63 | 135.92 | < 0.0001 |
| B-Axial rake angle | 352.54 | 1 | 352.54 | 20.52 | 0.0003 |
| C-Edge radius | 1839.37 | 1 | 1839.37 | 107.04 | < 0.0001 |
| AB | 256.57 | 1 | 256.57 | 14.93 | 0.0012 |
| AC | 150.75 | 1 | 150.75 | 8.77 | 0.0087 |
| BC | 107.62 | 1 | 107.62 | 6.26 | 0.0228 |
| $A^2$ | 248.22 | 1 | 248.22 | 14.45 | 0.0014 |
| $B^2$ | 51.46 | 1 | 51.46 | 2.99 | 0.1016 |
| $C^2$ | 67.17 | 1 | 67.17 | 3.91 | 0.0645 |
| **Residual** | 292.13 | 17 | 17.18 | | |
| **Cor Total** | 5701.47 | 26 | | | |

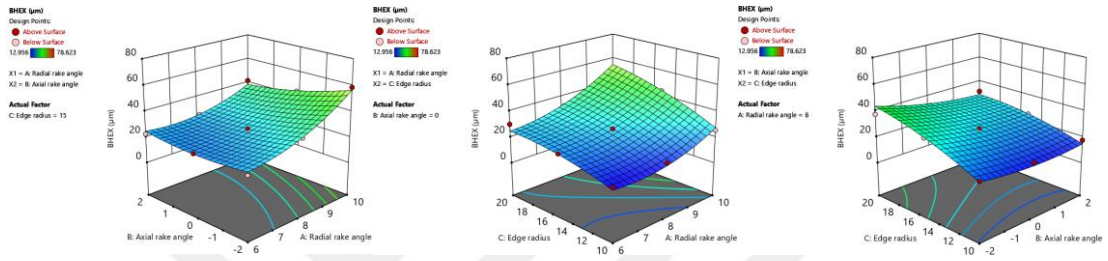


**Figure 6.196.** 3D surface plot of the measured burr heights at hole exit (BHEX) variation during drilling of forged CW724R with 90° of plunging angle with respect to the studied cutting tool geometry

**Table 6.179.** The ANOVA results for measured surface roughness at hole bottom (Ra) during drilling of forged CW724R with 90° of plunging angle

| Source | Sum of Squares | df | Mean Square | F-value | p-value | |
|---|---|---|---|---|---|---|
| **Model** | 0.04 | 9 | 0.0044 | 119.09 | < 0.0001 | significant |
| A-Radial rake angle | 0.0031 | 1 | 0.0031 | 82.76 | < 0.0001 | |
| B-Axial rake angle | 0.0004 | 1 | 0.0004 | 11.24 | 0.0038 | |
| C-Edge radius | 0.0323 | 1 | 0.0323 | 866.38 | < 0.0001 | |
| AB | 0 | 1 | 0 | 0.5784 | 0.4574 | |
| AC | 0.0009 | 1 | 0.0009 | 24.82 | 0.0001 | |
| BC | 0.0002 | 1 | 0.0002 | 4.06 | 0.06 | |
| $A^2$ | 0 | 1 | 0 | 0.3088 | 0.5857 | |
| $B^2$ | 0 | 1 | 0 | 0.68 | 0.421 | |
| $C^2$ | 0.003 | 1 | 0.003 | 80.98 | < 0.0001 | |
| **Residual** | 0.0006 | 17 | 0 | | | |
| **Cor Total** | 0.0406 | 26 | | | | |

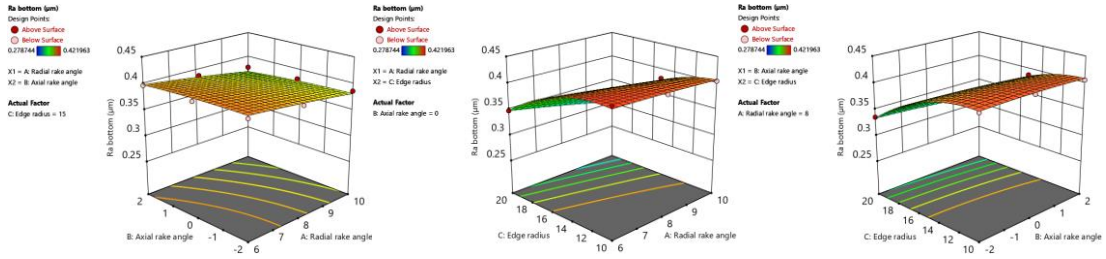

**Figure 6.197.** 3D surface plot of the measured surface roughness at hole bottom (Ra) variation during drilling of forged CW724R with 90° of plunging angle with respect to the studied cutting tool geometry

**Table 6.180.** The ANOVA results for measured surface roughness at hole wall (Ra) during drilling of forged CW724R with 90° of plunging angle

| Source | Sum of Squares | df | Mean Square | F-value | p-value | |
|---|---|---|---|---|---|---|
| **Model** | 0.0605 | 9 | 0.0067 | 74.65 | < 0.0001 | significant |
| A-Radial rake angle | 0.005 | 1 | 0.005 | 55.99 | < 0.0001 | |
| B-Axial rake angle | 0.0007 | 1 | 0.0007 | 8.21 | 0.0107 | |
| C-Edge radius | 0.0464 | 1 | 0.0464 | 514.7 | < 0.0001 | |
| AB | 0.0001 | 1 | 0.0001 | 1.03 | 0.3254 | |
| AC | 0.0023 | 1 | 0.0023 | 26.03 | < 0.0001 | |
| BC | 0.0004 | 1 | 0.0004 | 4.57 | 0.0473 | |
| $A^2$ | 0.0001 | 1 | 0.0001 | 0.6598 | 0.4279 | |
| $B^2$ | 0.0001 | 1 | 0.0001 | 0.5654 | 0.4624 | |
| $C^2$ | 0.0054 | 1 | 0.0054 | 60.09 | < 0.0001 | |
| **Residual** | 0.0015 | 17 | 0.0001 | | | |
| **Cor Total** | 0.0621 | 26 | | | | |

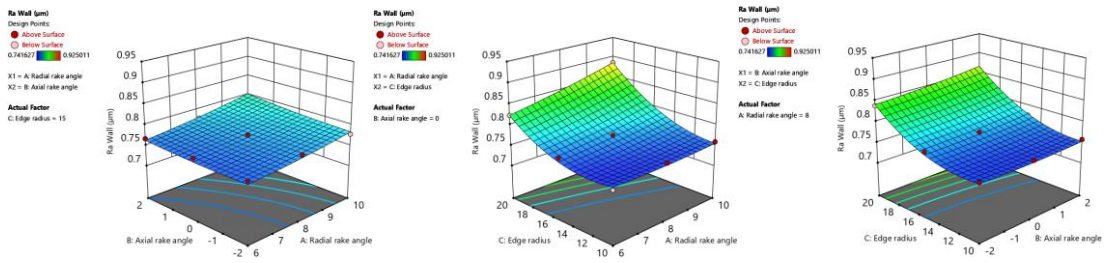

**Figure 6.198.** 3D surface plot of the measured surface roughness at hole wall (Ra) variation during drilling of forged CW724R with 90° of plunging angle with respect to the studied cutting tool geometry

**Table 6.181.** The ANOVA results for measured hole diameter during drilling of forged CW724R with 90° of plunging angle

| Source | Sum of Squares | df | Mean Square | F-value | p-value | |
|---|---|---|---|---|---|---|
| **Model** | 0.0037 | 9 | 0.0004 | 3.36 | 0.0151 | significant |

| | | | | | |
|---|---|---|---|---|---|
| A-Radial rake angle | 0.0012 | 1 | 0.0012 | 9.49 | 0.0068 |
| B-Axial rake angle | 0.0001 | 1 | 0.0001 | 1.17 | 0.2936 |
| C-Edge radius | 0.0002 | 1 | 0.0002 | 1.22 | 0.2845 |
| AB | 0.0008 | 1 | 0.0008 | 6.24 | 0.023 |
| AC | 0 | 1 | 0 | 0.1524 | 0.7011 |
| BC | 0.0001 | 1 | 0.0001 | 0.7376 | 0.4024 |
| $A^2$ | 0.0005 | 1 | 0.0005 | 4.3 | 0.0536 |
| $B^2$ | 2.24E-06 | 1 | 2.24E-06 | 0.0182 | 0.8942 |
| $C^2$ | 0.0008 | 1 | 0.0008 | 6.89 | 0.0177 |
| **Residual** | 0.0021 | 17 | 0.0001 | | |
| **Cor Total** | 0.0058 | 26 | | | |

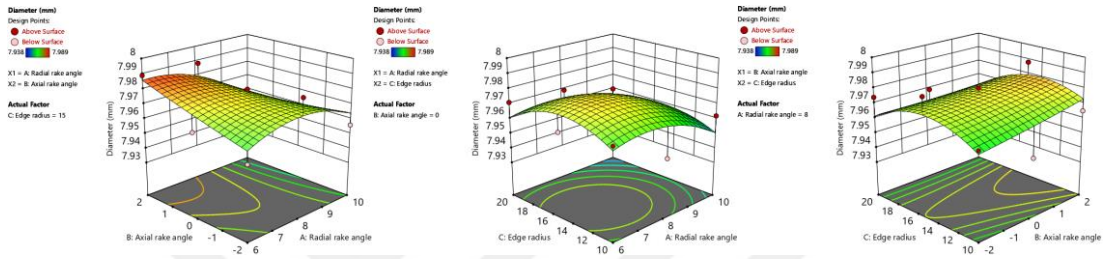

**Figure 6.199.** 3D surface plot of the measured hole diameter variation during drilling of forged CW724R with 90° of plunging angle with respect to the studied cutting tool geometry

**Table 6.182.** The developed regression model for drilling of forged CW724R with 90° of plunging angle

| Forged CW724R 90 | Fx | Fy | Fz | FR | BHEN | BHEX | Ra bottom | Ra Wall | Diameter |
|---|---|---|---|---|---|---|---|---|---|
| | 8.52 | 0.8126 | 412.41 | 412.54 | 63.41 | 26.72 | 0.3923 | 0.7702 | 7.98 |
| A | -1.1 | 0.4068 | -4.58 | -4.58 | 32.22 | 11.39 | -0.0131 | 0.0167 | -0.0081 |
| B | 2.51 | -2.27 | -18.5 | -18.49 | -11.23 | -4.43 | -0.0048 | 0.0064 | 0.0028 |
| C | 0.2847 | 5.12 | 72.07 | 72.04 | 29 | 10.11 | -0.0424 | 0.0508 | -0.0029 |
| AB | 0.2242 | -1 | 5.54 | 5.54 | -10.47 | -4.62 | -0.0013 | 0.0028 | -0.008 |
| AC | -1.53 | -3.29 | -1.02 | -1.02 | 12.23 | 3.54 | -0.0088 | 0.014 | -0.0013 |
| BC | -2.5 | 1.06 | 4.36 | 4.38 | -4.38 | -2.99 | -0.0036 | 0.0059 | -0.0028 |
| $A^2$ | -0.5039 | -0.0006 | 0 | 0 | 18.31 | 6.43 | -0.0014 | 0.0031 | -0.0094 |

| | | | | | | | | | |
|---|---|---|---|---|---|---|---|---|---|
| $B^2$ | -4.98 | 2.16 | 0 | 0 | 6.43 | 2.93 | -0.0021 | 0.0029 | 0.0006 |
| $C^2$ | -3.78 | 5.91 | 0 | 0 | -4.84 | -3.35 | -0.0224 | 0.03 | -0.0119 |
| ABC | -1.3 | -1.15 | 0 | 0 | 0 | 0 | 0 | 0 | 0 |
| $A^2B$ | 0.511 | 0.2825 | 0 | 0 | 0 | 0 | 0 | 0 | 0 |
| $A^2C$ | 0.3109 | -5.72 | 0 | 0 | 0 | 0 | 0 | 0 | 0 |
| $AB^2$ | -0.0802 | -3.32 | 0 | 0 | 0 | 0 | 0 | 0 | 0 |
| $AC^2$ | 1.89 | 0.2724 | 0 | 0 | 0 | 0 | 0 | 0 | 0 |
| $B^2C$ | -1.32 | -6.72 | 0 | 0 | 0 | 0 | 0 | 0 | 0 |
| $BC^2$ | -1.74 | 3.97 | 0 | 0 | 0 | 0 | 0 | 0 | 0 |
| $A^2B^2$ | 3.48 | 3.07 | 0 | 0 | 0 | 0 | 0 | 0 | 0 |
| $A^2BC$ | 5.25 | -1.74 | 0 | 0 | 0 | 0 | 0 | 0 | 0 |
| $A^2C^2$ | 3.44 | -3.25 | 0 | 0 | 0 | 0 | 0 | 0 | 0 |
| $AB^2C$ | 2.97 | 2.68 | 0 | 0 | 0 | 0 | 0 | 0 | 0 |
| $ABC^2$ | -0.5518 | 0.7271 | 0 | 0 | 0 | 0 | 0 | 0 | 0 |
| $B^2C^2$ | 4.5 | -3.22 | 0 | 0 | 0 | 0 | 0 | 0 | 0 |
| $A^2B^2C$ | 0 | 7.58 | 0 | 0 | 0 | 0 | 0 | 0 | 0 |
| $A^2BC^2$ | 0 | -3.87 | 0 | 0 | 0 | 0 | 0 | 0 | 0 |
| $AB^2C^2$ | 0 | 4.87 | 0 | 0 | 0 | 0 | 0 | 0 | 0 |
| **Regression confidence $R^2$** | 0.961 | 0.996 | 0.958 | 0.958 | 0.984 | 0.948 | 0.984 | 0.975 | 0.84 |

**Table 6.183.** The ANOVA results for measured forces in X direction (Fx) during drilling of forged CW724R with 60° of plunging angle

| Source | Sum of Squares | df | Mean Square | F-value | p-value | |
|---|---|---|---|---|---|---|
| **Model** | 24493 | 9 | 2721.45 | 67.57 | < 0.0001 | significant |
| A-Radial rake angle | 716.06 | 1 | 716.06 | 17.78 | 0.0006 | |
| B-Axial rake angle | 125.66 | 1 | 125.66 | 3.12 | 0.0953 | |
| C-Edge radius | 23439 | 1 | 23439 | 581.93 | < 0.0001 | |
| AB | 0.2552 | 1 | 0.2552 | 0.0063 | 0.9375 | |
| AC | 6.87 | 1 | 6.87 | 0.1706 | 0.6848 | |
| BC | 30.53 | 1 | 30.53 | 0.7579 | 0.3961 | |
| $A^2$ | 54.06 | 1 | 54.06 | 1.34 | 0.2627 | |
| $B^2$ | 11.7 | 1 | 11.7 | 0.2906 | 0.5968 | |
| $C^2$ | 108.89 | 1 | 108.89 | 2.7 | 0.1185 | |
| **Residual** | 684.72 | 17 | 40.28 | | | |
| **Cor Total** | 25177.8 | 26 | | | | |

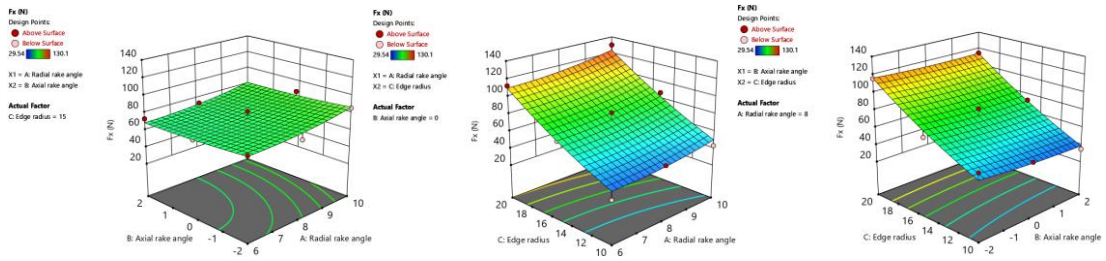

**Figure 6.200.** 3D surface plot of the measured forces in X direction (Fx) variation during drilling of forged CW724R with 60° of plunging angle with respect to the studied cutting tool geometry

**Table 6.184.** The ANOVA results for measured forces in Y direction (Fy) during drilling of forged CW724R with 60° of plunging angle

| Source | Sum of Squares | df | Mean Square | F-value | p-value | |
|---|---|---|---|---|---|---|
| **Model** | 8933.9 | 9 | 992.66 | 28.49 | < 0.0001 | significant |
| A-Radial rake angle | 906.1 | 1 | 906.1 | 26.01 | < 0.0001 | |
| B-Axial rake angle | 117.15 | 1 | 117.15 | 3.36 | 0.0843 | |
| C-Edge radius | 7271.78 | 1 | 7271.78 | 208.73 | < 0.0001 | |
| AB | 10.55 | 1 | 10.55 | 0.3027 | 0.5893 | |
| AC | 228.03 | 1 | 228.03 | 6.55 | 0.0204 | |
| BC | 41.03 | 1 | 41.03 | 1.18 | 0.293 | |
| $A^2$ | 19.31 | 1 | 19.31 | 0.5542 | 0.4668 | |
| $B^2$ | 15.77 | 1 | 15.77 | 0.4526 | 0.5101 | |
| $C^2$ | 324.18 | 1 | 324.18 | 9.31 | 0.0072 | |
| **Residual** | 592.25 | 17 | 34.84 | | | |
| **Cor Total** | 9526.14 | 26 | | | | |

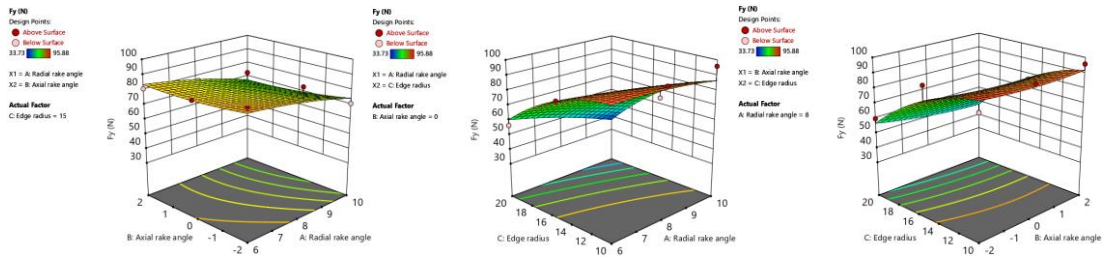

**Figure 6.201.** 3D surface plot of the measured forces in Y direction (Fy) variation during drilling of forged CW724R with 60° of plunging angle with respect to the studied cutting tool geometry

**Table 6.185.** The ANOVA results for measured forces in Z direction (Fz) during drilling of forged CW724R with 60° of plunging angle

| Source | Sum of Squares | df | Mean Square | F-value | p-value | |
|---|---|---|---|---|---|---|
| **Model** | 92018.51 | 9 | 10224.28 | 255 | < 0.0001 | significant |

| | | | | | |
|---|---|---|---|---|---|
| A-Radial rake angle | 281.42 | 1 | 281.42 | 7.02 | 0.0169 |
| B-Axial rake angle | 1368.9 | 1 | 1368.9 | 34.14 | < 0.0001 |
| C-Edge radius | 84985.2 | 1 | 84985.2 | 2119.56 | < 0.0001 |
| AB | 40.49 | 1 | 40.49 | 1.01 | 0.329 |
| AC | 28.33 | 1 | 28.33 | 0.7065 | 0.4123 |
| BC | 18.33 | 1 | 18.33 | 0.4572 | 0.508 |
| $A^2$ | 68.62 | 1 | 68.62 | 1.71 | 0.2082 |
| $B^2$ | 32.7 | 1 | 32.7 | 0.8156 | 0.3791 |
| $C^2$ | 5194.51 | 1 | 5194.51 | 129.55 | < 0.0001 |
| **Residual** | 681.63 | 17 | 40.1 | | |
| **Cor Total** | 92700.13 | 26 | | | |

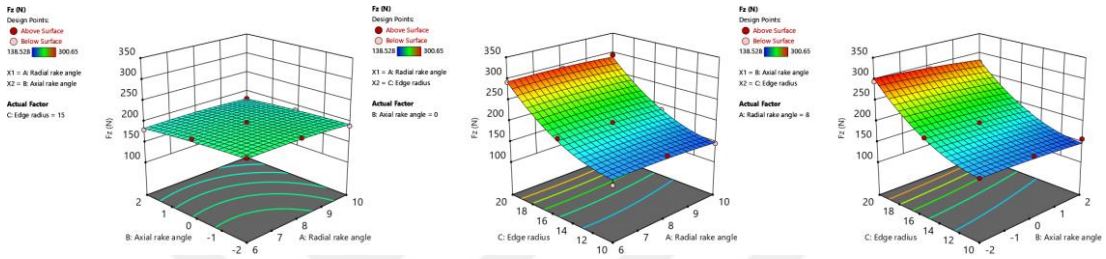

**Figure 6.202.** 3D surface plot of the measured forces in Z direction (Fz) variation during drilling of forged CW724R with 60° of plunging angle with respect to the studied cutting tool geometry

**Table 6.186.** The ANOVA results for measured resultant forces (FR) during drilling of forged CW724R with 60° of plunging angle

| Source | Sum of Squares | df | Mean Square | F-value | p-value | |
|---|---|---|---|---|---|---|
| **Model** | 87209.34 | 9 | 9689.93 | 223.95 | < 0.0001 | significant |
| A-Radial rake angle | 186.75 | 1 | 186.75 | 4.32 | 0.0532 | |
| B-Axial rake angle | 1479.39 | 1 | 1479.39 | 34.19 | < 0.0001 | |
| C-Edge radius | 80327.96 | 1 | 80327.96 | 1856.47 | < 0.0001 | |
| AB | 21.25 | 1 | 21.25 | 0.491 | 0.4929 | |
| AC | 31.1 | 1 | 31.1 | 0.7187 | 0.4083 | |
| BC | 20.85 | 1 | 20.85 | 0.4819 | 0.4969 | |
| $A^2$ | 28.53 | 1 | 28.53 | 0.6594 | 0.428 | |
| $B^2$ | 14.13 | 1 | 14.13 | 0.3266 | 0.5751 | |
| $C^2$ | 5099.37 | 1 | 5099.37 | 117.85 | < 0.0001 | |
| **Residual** | 735.58 | 17 | 43.27 | | | |
| **Cor Total** | 87944.92 | 26 | | | | |

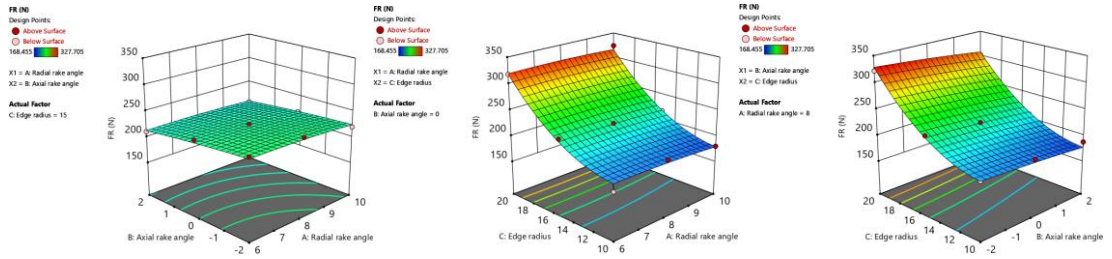


**Figure 6.203.** 3D surface plot of the measured resultant forces variation during drilling of forged CW724R with 60° of plunging angle with respect to the studied cutting tool geometry

**Table 6.187.** The ANOVA results for measured burr heights at hole entry (BHEN) during drilling of forged CW724R with 60° of plunging angle

| Source | Sum of Squares | df | Mean Square | F-value | p-value | |
|---|---|---|---|---|---|---|
| **Model** | 28665.6 | 9 | 3185.07 | 160.25 | < 0.0001 | significant |
| A-Radial rake angle | 14386.2 | 1 | 14386.2 | 723.82 | < 0.0001 | |
| B-Axial rake angle | 2499.76 | 1 | 2499.76 | 125.77 | < 0.0001 | |
| C-Edge radius | 8842.15 | 1 | 8842.15 | 444.88 | < 0.0001 | |
| AB | 1671.56 | 1 | 1671.56 | 84.1 | < 0.0001 | |
| AC | 538.56 | 1 | 538.56 | 27.1 | < 0.0001 | |
| BC | 80.35 | 1 | 80.35 | 4.04 | 0.0605 | |
| $A^2$ | 539.36 | 1 | 539.36 | 27.14 | < 0.0001 | |
| $B^2$ | 18.93 | 1 | 18.93 | 0.9524 | 0.3428 | |
| $C^2$ | 88.8 | 1 | 88.8 | 4.47 | 0.0496 | |
| **Residual** | 337.88 | 17 | 19.88 | | | |
| **Cor Total** | 29003.5 | 26 | | | | |

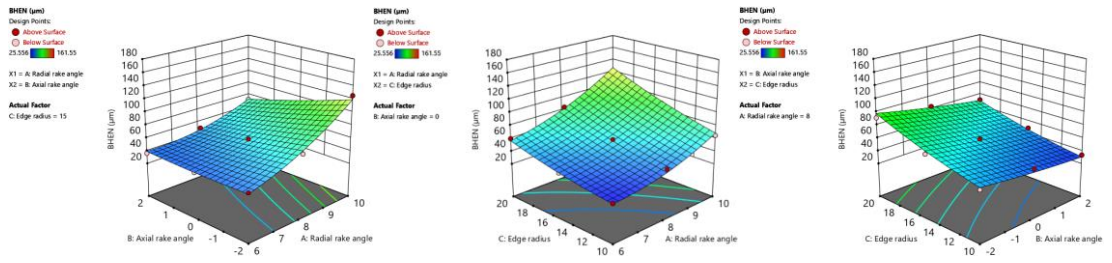


**Figure 6.204.** 3D surface plot of the measured burr heights at hole entry (BHEN) variation during drilling of forged CW724R with 60° of plunging angle with respect to the studied cutting tool geometry

**Table 6.188.** The ANOVA results for measured burr heights at hole exit (BHEX) during drilling of forged CW724R with 60° of plunging angle

| Source | Sum of Squares | df | Mean Square | F-value | p-value | |
|---|---|---|---|---|---|---|
| **Model** | 28665.6 | 9 | 3185.07 | 160.25 | < 0.0001 | significant |

| | | | | | |
|---|---|---|---|---|---|
| A-Radial rake angle | 14386.2 | 1 | 14386.2 | 723.82 | < 0.0001 |
| B-Axial rake angle | 2499.76 | 1 | 2499.76 | 125.77 | < 0.0001 |
| C-Edge radius | 8842.15 | 1 | 8842.15 | 444.88 | < 0.0001 |
| AB | 1671.56 | 1 | 1671.56 | 84.1 | < 0.0001 |
| AC | 538.56 | 1 | 538.56 | 27.1 | < 0.0001 |
| BC | 80.35 | 1 | 80.35 | 4.04 | 0.0605 |
| $A^2$ | 539.36 | 1 | 539.36 | 27.14 | < 0.0001 |
| $B^2$ | 18.93 | 1 | 18.93 | 0.9524 | 0.3428 |
| $C^2$ | 88.8 | 1 | 88.8 | 4.47 | 0.0496 |
| **Residual** | 337.88 | 17 | 19.88 | | |
| **Cor Total** | 29003.5 | 26 | | | |

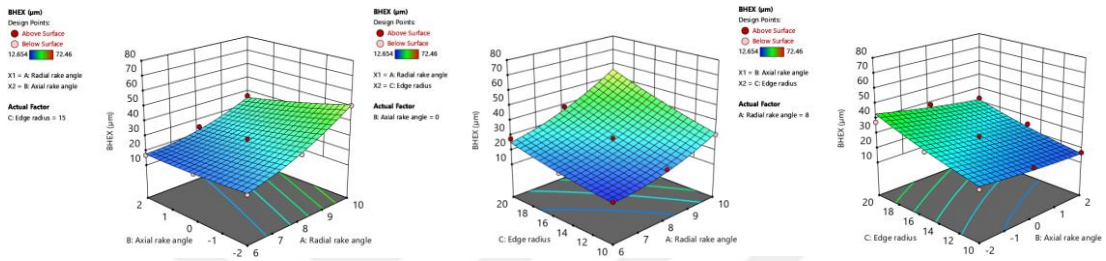


**Figure 6.205.** 3D surface plot of the measured burr heights at hole exit (BHEX) variation during drilling of forged CW724R with 60° of plunging angle with respect to the studied cutting tool geometry

**Table 6.189.** The ANOVA results for measured surface roughness at hole bottom (Ra) during drilling of forged CW724R with 60° of plunging angle

| Source | Sum of Squares | df | Mean Square | F-value | p-value | |
|---|---|---|---|---|---|---|
| **Model** | 0.0261 | 6 | 0.0044 | 320.99 | < 0.0001 | significant |
| A-Radial rake angle | 0.0012 | 1 | 0.0012 | 85.9 | < 0.0001 | |
| B-Axial rake angle | 0.0003 | 1 | 0.0003 | 20.61 | 0.0002 | |
| C-Edge radius | 0.0245 | 1 | 0.0245 | 1806.38 | < 0.0001 | |
| AB | 0 | 1 | 0 | 0.8413 | 0.3699 | |
| AC | 0.0001 | 1 | 0.0001 | 10.31 | 0.0044 | |
| BC | 0 | 1 | 0 | 1.89 | 0.1841 | |
| **Residual** | 0.0003 | 20 | 0 | | | |
| **Cor Total** | 0.0264 | 26 | | | | |

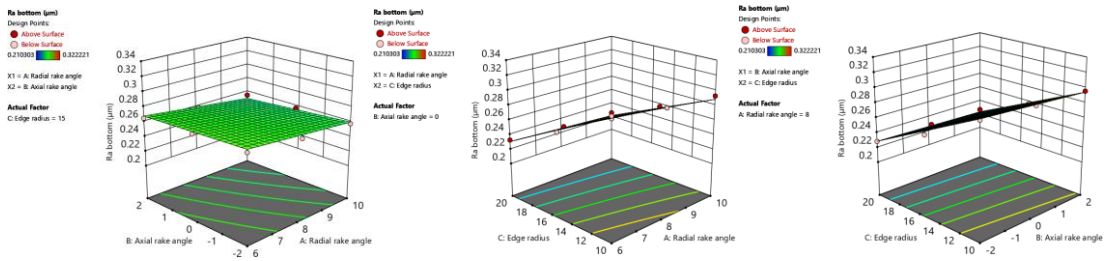


**Figure 6.206.** 3D surface plot of the measured surface roughness at hole bottom (Ra)

variation during drilling of forged CW724R with 60° of plunging angle with respect to the studied cutting tool geometry

**Table 6.190.** The ANOVA results for measured surface roughness at hole wall (Ra) during drilling of forged CW724R with 60° of plunging angle

| Source | Sum of Squares | df | Mean Square | F-value | p-value | |
|---|---|---|---|---|---|---|
| **Model** | 0.0408 | 6 | 0.0068 | 300.87 | < 0.0001 | significant |
| A-Radial rake angle | 0.0017 | 1 | 0.0017 | 75.6 | < 0.0001 | |
| B-Axial rake angle | 0.0004 | 1 | 0.0004 | 18.85 | 0.0003 | |
| C-Edge radius | 0.0386 | 1 | 0.0386 | 1706.73 | < 0.0001 | |
| AB | 0 | 1 | 0 | 1.67 | 0.2108 | |
| AC | 0 | 1 | 0 | 2.16 | 0.1569 | |
| BC | 4.38E-06 | 1 | 4.38E-06 | 0.1939 | 0.6644 | |
| **Residual** | 0.0005 | 20 | 0 | | | |
| **Cor Total** | 0.0413 | 26 | | | | |

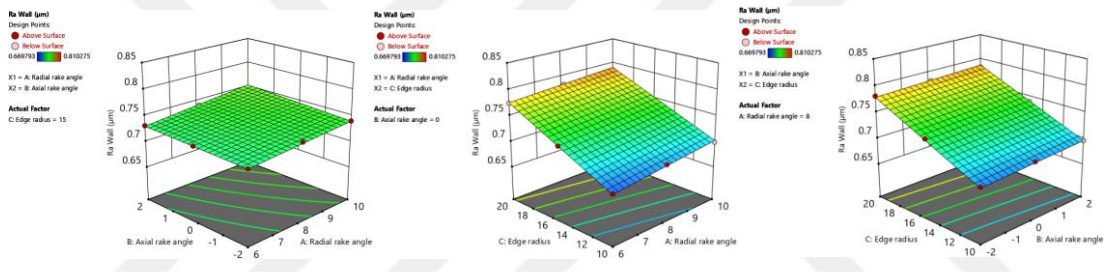

**Figure 6.207.** 3D surface plot of the measured surface roughness at hole wall (Ra) variation during drilling of forged CW724R with 60° of plunging angle with respect to the studied cutting tool geometry

**Table 6.191.** The ANOVA results for measured hole diameter during drilling of forged CW724R with 60° of plunging angle

| Source | Sum of Squares | df | Mean Square | F-value | p-value |
|---|---|---|---|---|---|
| **Model** | 0.008 | 16 | 0.0005 | 2.73 | 0.0556 |
| A-Radial rake angle | 0.0007 | 1 | 0.0007 | 4.06 | 0.0717 |
| B-Axial rake angle | 0.0004 | 1 | 0.0004 | 2.27 | 0.1628 |
| C-Edge radius | 0.0001 | 1 | 0.0001 | 0.3708 | 0.5562 |
| AB | 0 | 1 | 0 | 0.2016 | 0.663 |
| AC | 0.0009 | 1 | 0.0009 | 4.66 | 0.0562 |
| BC | 0.0011 | 1 | 0.0011 | 6.15 | 0.0325 |
| $A^2$ | 0.001 | 1 | 0.001 | 5.66 | 0.0387 |
| $B^2$ | 0.0008 | 1 | 0.0008 | 4.65 | 0.0564 |
| $C^2$ | 0.0001 | 1 | 0.0001 | 0.5413 | 0.4788 |
| ABC | 0.0005 | 1 | 0.0005 | 2.64 | 0.1356 |
| $A^2B$ | 0.0019 | 1 | 0.0019 | 10.22 | 0.0095 |

| | | | | | |
|---|---|---|---|---|---|
| $A^2C$ | 6.25E-06 | 1 | 6.25E-06 | 0.0343 | 0.8568 |
| $AB^2$ | 0.0004 | 1 | 0.0004 | 2.09 | 0.1793 |
| $AC^2$ | 0 | 1 | 0 | 0.1659 | 0.6923 |
| $B^2C$ | 0 | 1 | 0 | 0.2688 | 0.6154 |
| $BC^2$ | 7.11E-06 | 1 | 7.11E-06 | 0.039 | 0.8474 |
| **Residual** | 0.0018 | 10 | 0.0002 | | |
| **Cor Total** | 0.0098 | 26 | | | |

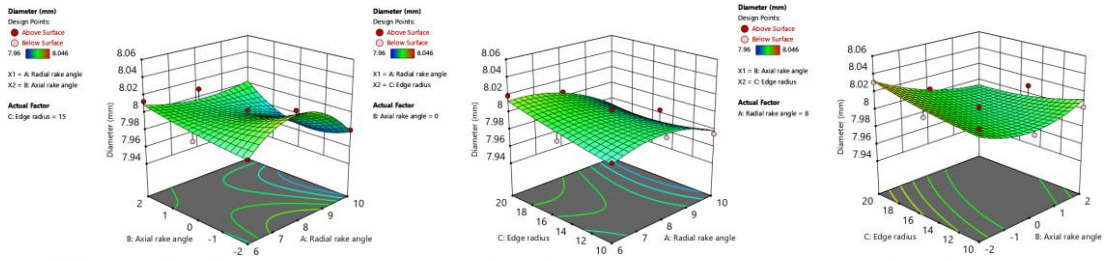


**Figure 6.208.** 3D surface plot of the measured hole diameter variation during drilling of forged CW724R with 60° of plunging angle with respect to the studied cutting tool geometry

**Table 6.192.** The developed regression model for drilling of forged CW724R with 60° of plunging angle

| Forged CW724R 60 | Fx | Fy | Fz | FR | BHEN | BHEX | Ra bottom | Ra Wall | Diameter |
|---|---|---|---|---|---|---|---|---|---|
| | 73.43 | 78.18 | 196.01 | 223.78 | 56.28 | 26.28 | 0.2631 | 0.7369 | 8.00 |
| A | 6.31 | -7.09 | -3.95 | -3.22 | 28.27 | 12.23 | -0.008 | 0.0097 | -0.0143 |
| B | -2.64 | -2.55 | -8.72 | -9.07 | -11.78 | -4.52 | -0.0039 | 0.0049 | -0.0107 |
| C | 36.09 | -20.1 | 68.71 | 66.8 | 22.16 | 9.00 | -0.0369 | 0.0463 | 0.0043 |
| AB | 0.1458 | -0.9375 | 1.84 | 1.33 | -11.8 | -3.39 | -0.001 | 0.0018 | 0.0017 |
| AC | 0.7567 | -4.36 | 1.54 | 1.61 | 6.7 | 3.13 | 0.0034 | -0.002 | -0.0084 |
| BC | 1.59 | -1.85 | -1.24 | -1.32 | -2.59 | -1.29 | 0.0015 | -0.0006 | -0.0097 |
| $A^2$ | 3.00 | -1.79 | -3.38 | -2.18 | 9.48 | 3.9 | 0 | 0 | -0.0131 |
| $B^2$ | 1.4 | 1.62 | -2.33 | -1.53 | 1.78 | 0.8768 | 0 | 0 | 0.0119 |
| $C^2$ | 4.26 | -7.35 | 29.42 | 29.15 | 3.85 | 1.33 | 0 | 0 | 0.0041 |
| ABC | 0 | 0 | 0 | 0 | 0 | 0 | 0 | 0 | -0.0077 |
| $A^2B$ | 0 | 0 | 0 | 0 | 0 | 0 | 0 | 0 | 0.0216 |
| $A^2C$ | 0 | 0 | 0 | 0 | 0 | 0 | 0 | 0 | 0.0013 |
| $AB^2$ | 0 | 0 | 0 | 0 | 0 | 0 | 0 | 0 | 0.0098 |

| | | | | | | | | | |
|---|---|---|---|---|---|---|---|---|---|
| $AC^2$ | 0 | 0 | 0 | 0 | 0 | 0 | 0 | 0 | 0.0028 |
| $B^2C$ | 0 | 0 | 0 | 0 | 0 | 0 | 0 | 0 | -0.0035 |
| $BC^2$ | 0 | 0 | 0 | 0 | 0 | 0 | 0 | 0 | 0.0013 |
| **Regression confidence $R^2$** | 0.972 | 0.937 | 0.992 | 0.991 | 0.988 | 0.969 | 0.989 | 0.989 | 0.813 |

**Table 6.193.** The ANOVA results for measured forces in X direction (Fx) during drilling of forged CW724R with 45° of plunging angle

| Source | Sum of Squares | df | Mean Square | F-value | p-value | |
|---|---|---|---|---|---|---|
| **Model** | 83597.8 | 9 | 9288.64 | 136.58 | < 0.0001 | significant |
| A-Radial rake angle | 1006.36 | 1 | 1006.36 | 14.8 | 0.0013 | |
| B-Axial rake angle | 10.47 | 1 | 10.47 | 0.154 | 0.6996 | |
| C-Edge radius | 80141.4 | 1 | 80141.4 | 1178.39 | < 0.0001 | |
| AB | 9.65 | 1 | 9.65 | 0.1419 | 0.7111 | |
| AC | 11.78 | 1 | 11.78 | 0.1732 | 0.6825 | |
| BC | 203.61 | 1 | 203.61 | 2.99 | 0.1017 | |
| $A^2$ | 151.7 | 1 | 151.7 | 2.23 | 0.1536 | |
| $B^2$ | 1.14 | 1 | 1.14 | 0.0167 | 0.8987 | |
| $C^2$ | 2061.65 | 1 | 2061.65 | 30.31 | < 0.0001 | |
| **Residual** | 1156.16 | 17 | 68.01 | | | |
| **Cor Total** | 84753.9 | 26 | | | | |

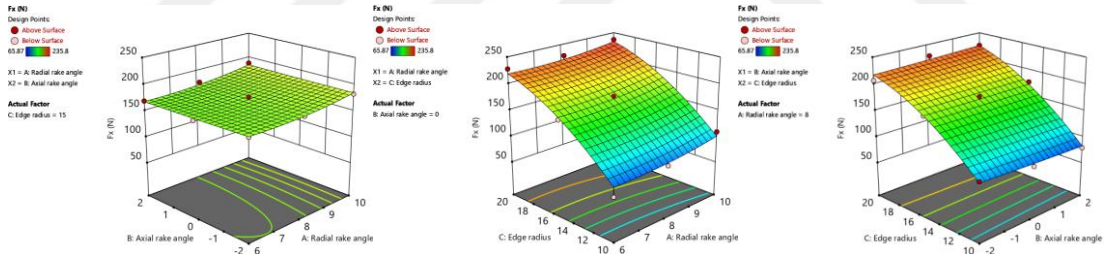


**Figure 6.209.** 3D surface plot of the measured forces in X direction (Fx) variation during drilling of forged CW724R with 45° of plunging angle with respect to the studied cutting tool geometry

**Table 6.194.** The ANOVA results for measured forces in Y direction (Fy) during drilling of forged CW724R with 45° of plunging angle

| Source | Sum of Squares | df | Mean Square | F-value | p-value | |
|---|---|---|---|---|---|---|
| **Model** | 7174.06 | 9 | 797.12 | 18.77 | < 0.0001 | significant |
| A-Radial rake angle | 2485.6 | 1 | 2485.6 | 58.53 | < 0.0001 | |
| B-Axial rake angle | 325.12 | 1 | 325.12 | 7.66 | 0.0132 | |
| C-Edge radius | 2450.93 | 1 | 2450.93 | 57.71 | < 0.0001 | |
| AB | 74.3 | 1 | 74.3 | 1.75 | 0.2034 | |
| AC | 2.08 | 1 | 2.08 | 0.0489 | 0.8277 | |

| | | | | | |
|---|---|---|---|---|---|
| BC | 97.01 | 1 | 97.01 | 2.28 | 0.149 |
| $A^2$ | 173.52 | 1 | 173.52 | 4.09 | 0.0593 |
| $B^2$ | 52.02 | 1 | 52.02 | 1.22 | 0.2838 |
| $C^2$ | 1513.47 | 1 | 1513.47 | 35.64 | < 0.0001 |
| **Residual** | 721.94 | 17 | 42.47 | | |
| **Cor Total** | 7896 | 26 | | | |

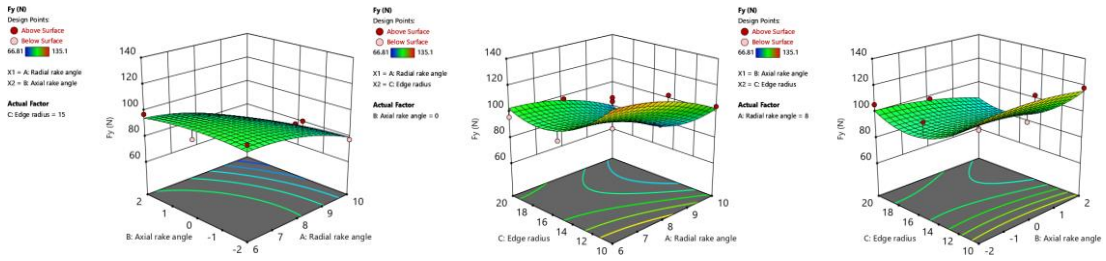

**Figure 6.210.** 3D surface plot of the measured forces in Y direction (Fy) variation during drilling of forged CW724R with 45° of plunging angle with respect to the studied cutting tool geometry

**Table 6.195.** The ANOVA results for measured forces in Z direction (Fz) during drilling of forged CW724R with 45° of plunging angle

| Source | Sum of Squares | df | Mean Square | F-value | p-value | |
|---|---|---|---|---|---|---|
| **Model** | 3.62E+05 | 6 | 60266.29 | 1142.87 | < 0.0001 | significant |
| A-Radial rake angle | 0.191 | 1 | 0.191 | 0.0036 | 0.9526 | |
| B-Axial rake angle | 2107.58 | 1 | 2107.58 | 39.97 | < 0.0001 | |
| C-Edge radius | 3.59E+05 | 1 | 3.59E+05 | 6814.01 | < 0.0001 | |
| AB | 5.66 | 1 | 5.66 | 0.1073 | 0.7466 | |
| AC | 14.48 | 1 | 14.48 | 0.2747 | 0.606 | |
| BC | 151.53 | 1 | 151.53 | 2.87 | 0.1056 | |
| **Residual** | 1054.65 | 20 | 52.73 | | | |
| **Cor Total** | 3.63E+05 | 26 | | | | |

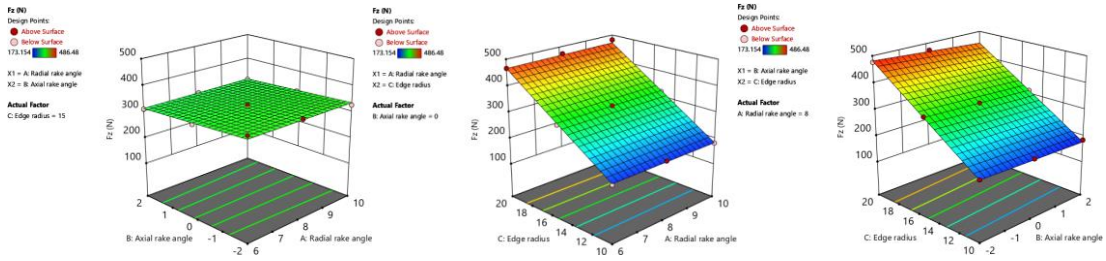

**Figure 6.211.** 3D surface plot of the measured forces in Z direction (Fz) variation during drilling of forged CW724R with 45° of plunging angle with respect to the studied cutting tool geometry

**Table 6.196.** The ANOVA results for measured resultant forces (FR) during drilling of

forged CW724R with 45° of plunging angle

| Source | Sum of Squares | df | Mean Square | F-value | p-value | |
|---|---|---|---|---|---|---|
| **Model** | 3.81E+05 | 6 | 63536.95 | 1179.84 | < 0.0001 | significant |
| A-Radial rake angle | 1.14 | 1 | 1.14 | 0.0212 | 0.8857 | |
| B-Axial rake angle | 1912.73 | 1 | 1912.73 | 35.52 | < 0.0001 | |
| C-Edge radius | 3.79E+05 | 1 | 3.79E+05 | 7040.49 | < 0.0001 | |
| AB | 0.0366 | 1 | 0.0366 | 0.0007 | 0.9795 | |
| AC | 93.33 | 1 | 93.33 | 1.73 | 0.2029 | |
| BC | 70.02 | 1 | 70.02 | 1.3 | 0.2676 | |
| **Residual** | 1077.04 | 20 | 53.85 | | | |
| **Cor Total** | 3.82E+05 | 26 | | | | |

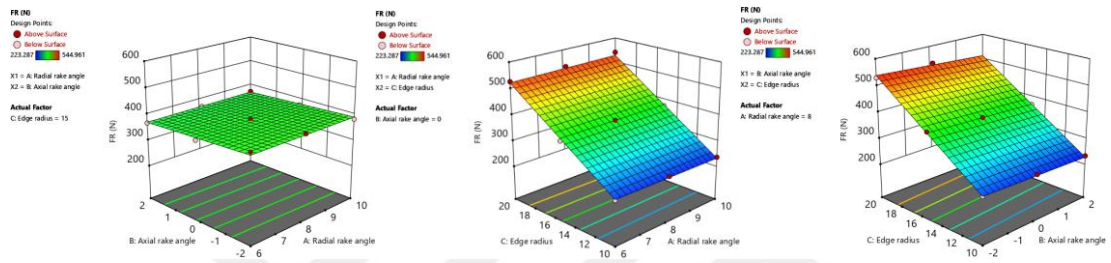

**Figure 6.212.** 3D surface plot of the measured resultant forces variation during drilling of forged CW724R with 45° of plunging angle with respect to the studied cutting tool geometry

**Table 6.197.** The ANOVA results for measured burr heights at hole entry (BHEN) during drilling of forged CW724R with 45° of plunging angle

| Source | Sum of Squares | df | Mean Square | F-value | p-value | |
|---|---|---|---|---|---|---|
| **Model** | 16082.1 | 9 | 1786.9 | 121.08 | < 0.0001 | significant |
| A-Radial rake angle | 7185.22 | 1 | 7185.22 | 486.88 | < 0.0001 | |
| B-Axial rake angle | 873.09 | 1 | 873.09 | 59.16 | < 0.0001 | |
| C-Edge radius | 5817.73 | 1 | 5817.73 | 394.22 | < 0.0001 | |
| AB | 505.22 | 1 | 505.22 | 34.23 | < 0.0001 | |
| AC | 690.15 | 1 | 690.15 | 46.77 | < 0.0001 | |
| BC | 88.32 | 1 | 88.32 | 5.98 | 0.0256 | |
| $A^2$ | 772.91 | 1 | 772.91 | 52.37 | < 0.0001 | |
| $B^2$ | 95.5 | 1 | 95.5 | 6.47 | 0.021 | |
| $C^2$ | 53.98 | 1 | 53.98 | 3.66 | 0.0728 | |
| **Residual** | 250.88 | 17 | 14.76 | | | |
| **Cor Total** | 16333 | 26 | | | | |

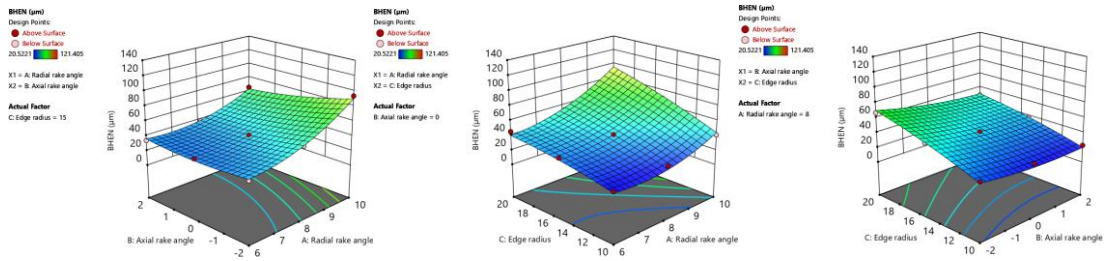

**Figure 6.213.** 3D surface plot of the measured burr heights at hole entry (BHEN) variation during drilling of forged CW724R with 45° of plunging angle with respect to the studied cutting tool geometry

**Table 6.198.** The ANOVA results for measured burr heights at hole exit (BHEX) during drilling of forged CW724R with 45° of plunging angle

| Source | Sum of Squares | df | Mean Square | F-value | p-value | |
|---|---|---|---|---|---|---|
| **Model** | 1549.24 | 9 | 172.14 | 35.4 | < 0.0001 | significant |
| A-Radial rake angle | 708.87 | 1 | 708.87 | 145.78 | < 0.0001 | |
| B-Axial rake angle | 55.63 | 1 | 55.63 | 11.44 | 0.0035 | |
| C-Edge radius | 608.98 | 1 | 608.98 | 125.24 | < 0.0001 | |
| AB | 31.39 | 1 | 31.39 | 6.46 | 0.0211 | |
| AC | 4.91 | 1 | 4.91 | 1.01 | 0.3291 | |
| BC | 5.06 | 1 | 5.06 | 1.04 | 0.3218 | |
| $A^2$ | 54.95 | 1 | 54.95 | 11.3 | 0.0037 | |
| $B^2$ | 3.47 | 1 | 3.47 | 0.713 | 0.4102 | |
| $C^2$ | 75.98 | 1 | 75.98 | 15.63 | 0.001 | |
| **Residual** | 82.66 | 17 | 4.86 | | | |
| **Cor Total** | 1631.91 | 26 | | | | |

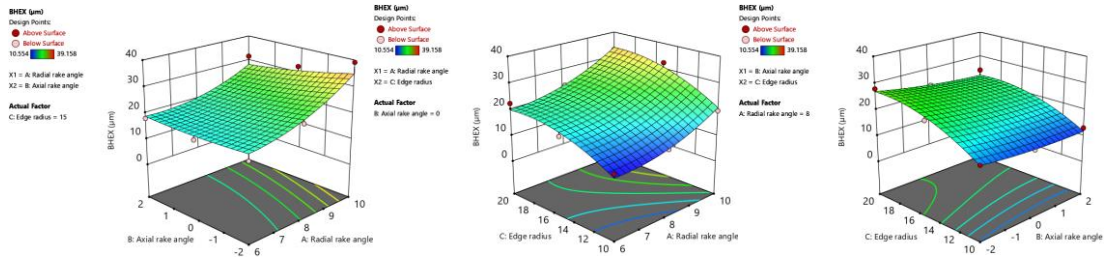

**Figure 6.214.** 3D surface plot of the measured burr heights at hole exit (BHEX) variation during drilling of forged CW724R with 45° of plunging angle with respect to the studied cutting tool geometry

**Table 6.199.** The ANOVA results for measured surface roughness at hole bottom (Ra) during drilling of forged CW724R with 45° of plunging angle

| Source | Sum of Squares | df | Mean Square | F-value | p-value | |
|---|---|---|---|---|---|---|
| **Model** | 0.0137 | 9 | 0.0015 | 119.09 | < 0.0001 | significant |

| | | | | | |
|---|---|---|---|---|---|
| A-Radial rake angle | 0.0011 | 1 | 0.0011 | 82.76 | < 0.0001 |
| B-Axial rake angle | 0.0001 | 1 | 0.0001 | 11.24 | 0.0038 |
| C-Edge radius | 0.0111 | 1 | 0.0111 | 866.38 | < 0.0001 |
| AB | 7.39E-06 | 1 | 7.39E-06 | 0.5784 | 0.4574 |
| AC | 0.0003 | 1 | 0.0003 | 24.82 | 0.0001 |
| BC | 0.0001 | 1 | 0.0001 | 4.06 | 0.06 |
| $A^2$ | 3.95E-06 | 1 | 3.95E-06 | 0.3088 | 0.5857 |
| $B^2$ | 8.69E-06 | 1 | 8.69E-06 | 0.68 | 0.421 |
| $C^2$ | 0.001 | 1 | 0.001 | 80.98 | < 0.0001 |
| **Residual** | 0.0002 | 17 | 0 | | |
| **Cor Total** | 0.0139 | 26 | | | |

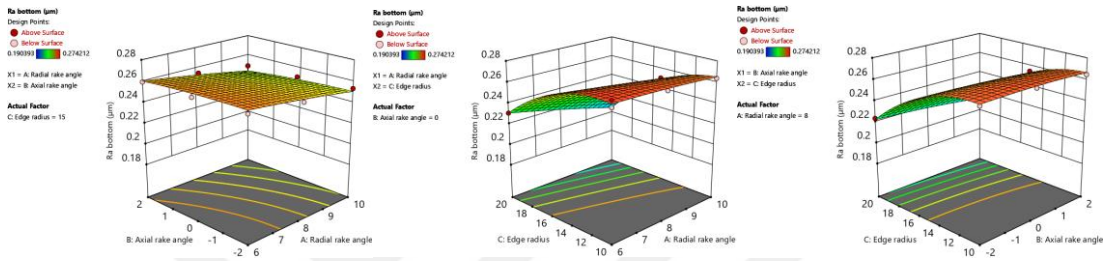

**Figure 6.215.** 3D surface plot of the measured surface roughness at hole bottom (Ra) variation during drilling of forged CW724R with 45° of plunging angle with respect to the studied cutting tool geometry

**Table 6.200.** The ANOVA results for measured surface roughness at hole wall (Ra) during drilling of forged CW724R with 45° of plunging angle

| Source | Sum of Squares | df | Mean Square | F-value | p-value | |
|---|---|---|---|---|---|---|
| **Model** | 0.0491 | 9 | 0.0055 | 85.25 | < 0.0001 | significant |
| A-Radial rake angle | 0.004 | 1 | 0.004 | 62.51 | < 0.0001 | |
| B-Axial rake angle | 0.0006 | 1 | 0.0006 | 8.96 | 0.0082 | |
| C-Edge radius | 0.0382 | 1 | 0.0382 | 597.85 | < 0.0001 | |
| AB | 0.0001 | 1 | 0.0001 | 0.9017 | 0.3556 | |
| AC | 0.0017 | 1 | 0.0017 | 25.9 | < 0.0001 | |
| BC | 0.0003 | 1 | 0.0003 | 4.46 | 0.0497 | |
| $A^2$ | 0 | 1 | 0 | 0.5613 | 0.464 | |
| $B^2$ | 0 | 1 | 0 | 0.5942 | 0.4514 | |
| $C^2$ | 0.0042 | 1 | 0.0042 | 65.55 | < 0.0001 | |
| **Residual** | 0.0011 | 17 | 0.0001 | | | |
| **Cor Total** | 0.0502 | 26 | | | | |

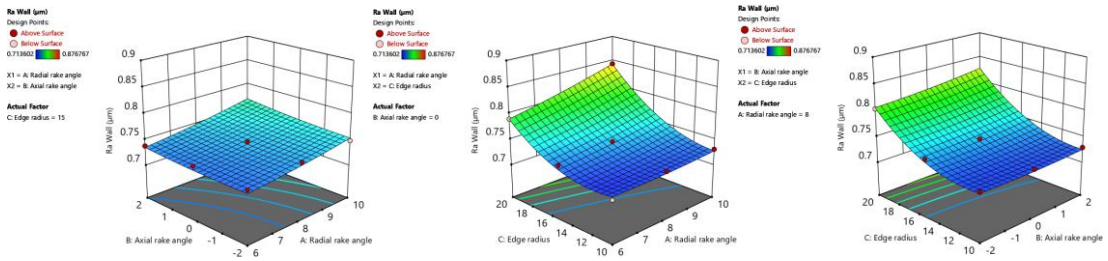

**Figure 6.216.** 3D surface plot of the measured surface roughness at hole wall (Ra) variation during drilling of forged CW724R with 45° of plunging angle with respect to the studied cutting tool geometry

**Table 6.201.** The ANOVA results for measured hole diameter during drilling of forged CW724R with 45° of plunging angle

| Source | Sum of Squares | df | Mean Square | F-value | p-value |
|---|---|---|---|---|---|
| **Model** | 0.0132 | 16 | 0.0008 | 2.55 | 0.0687 |
| A-Radial rake angle | 0.0003 | 1 | 0.0003 | 1.04 | 0.3314 |
| B-Axial rake angle | 0.0001 | 1 | 0.0001 | 0.3096 | 0.5902 |
| C-Edge radius | 0.0041 | 1 | 0.0041 | 12.66 | 0.0052 |
| AB | 9.90E-06 | 1 | 9.90E-06 | 0.0306 | 0.8646 |
| AC | 0.0009 | 1 | 0.0009 | 2.64 | 0.1356 |
| BC | 0.0001 | 1 | 0.0001 | 0.2462 | 0.6305 |
| $A^2$ | 0.0011 | 1 | 0.0011 | 3.41 | 0.0944 |
| $B^2$ | 0 | 1 | 0 | 0.0958 | 0.7632 |
| $C^2$ | 0.0018 | 1 | 0.0018 | 5.54 | 0.0404 |
| ABC | 0 | 1 | 0 | 0.1411 | 0.715 |
| $A^2B$ | 0.0001 | 1 | 0.0001 | 0.362 | 0.5608 |
| $A^2C$ | 0.0003 | 1 | 0.0003 | 0.91 | 0.3626 |
| $AB^2$ | 2.34E-07 | 1 | 2.34E-07 | 0.0007 | 0.9791 |
| $AC^2$ | 0.0001 | 1 | 0.0001 | 0.1748 | 0.6847 |
| $B^2C$ | 0.0006 | 1 | 0.0006 | 1.8 | 0.2089 |
| $BC^2$ | 0.0001 | 1 | 0.0001 | 0.189 | 0.6729 |
| **Residual** | 0.0032 | 10 | 0.0003 | | |
| **Cor Total** | 0.0164 | 26 | | | |

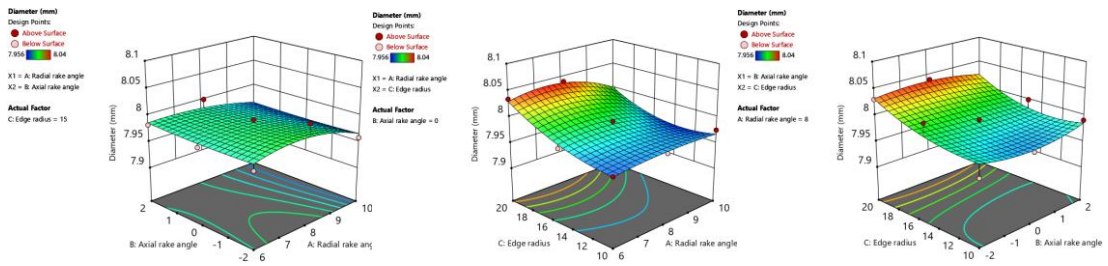

**Figure 6.217.** 3D surface plot of the measured hole diameter variation during drilling of forged CW724R with 45° of plunging angle with respect to the studied cutting tool

geometry

**Table 6.202.** The developed regression model for drilling of forged CW724R with 45° of plunging angle

| Forged CW724R 45 | Fx | Fy | Fz | FR | BHEN | BHEX | Ra bottom | Ra Wall | Diameter |
|---|---|---|---|---|---|---|---|---|---|
| | 172.18 | 92.72 | 325.73 | 380.89 | 41.31 | 21.56 | 0.2568 | 0.7414 | 7.99 |
| A | 7.48 | -11.75 | 0.103 | -0.2518 | 19.98 | 6.28 | -0.0077 | 0.0149 | -0.0097 |
| B | -0.7628 | -4.25 | -10.82 | -10.31 | -6.96 | -1.76 | -0.0028 | 0.0056 | -0.0053 |
| C | 66.73 | -11.67 | 141.29 | 145.13 | 17.98 | 5.82 | -0.0248 | 0.0461 | 0.0337 |
| AB | 0.8967 | -2.49 | 0.6867 | 0.0552 | -6.49 | -1.62 | -0.0008 | 0.0022 | -0.0009 |
| AC | -0.9908 | 0.4158 | 1.1 | 2.79 | 7.58 | 0.6396 | -0.0051 | 0.0117 | -0.0084 |
| BC | 4.12 | -2.84 | -3.55 | -2.42 | -2.71 | -0.6497 | -0.0021 | 0.0049 | -0.0026 |
| $A^2$ | 5.03 | -5.38 | 0 | 0 | 11.35 | 3.03 | -0.0008 | 0.0024 | -0.0136 |
| $B^2$ | 0.435 | -2.94 | 0 | 0 | 3.99 | 0.7602 | -0.0012 | 0.0025 | 0.0023 |
| $C^2$ | -18.54 | 15.88 | 0 | 0 | -3.00 | -3.56 | -0.0131 | 0.0264 | 0.0173 |
| ABC | 0 | 0 | 0 | 0 | 0 | 0 | 0 | 0 | -0.0024 |
| $A^2B$ | 0 | 0 | 0 | 0 | 0 | 0 | 0 | 0 | 0.0054 |
| $A^2C$ | 0 | 0 | 0 | 0 | 0 | 0 | 0 | 0 | -0.0086 |
| $AB^2$ | 0 | 0 | 0 | 0 | 0 | 0 | 0 | 0 | -0.0002 |
| $AC^2$ | 0 | 0 | 0 | 0 | 0 | 0 | 0 | 0 | 0.0038 |
| $B^2C$ | 0 | 0 | 0 | 0 | 0 | 0 | 0 | 0 | -0.0121 |
| $BC^2$ | 0 | 0 | 0 | 0 | 0 | 0 | 0 | 0 | 0.0039 |
| **Regression confidence $R^2$** | 0.986 | 0.908 | 0.997 | 0.997 | 0.984 | 0.949 | 0.984 | 0.978 | 0.802 |

## 6.6. Evaluation of the surface and sub-surface microhardness

The variation of the surface and sub-surface microhardness after 90° of flat bottom drilling operation for extruded specimens are demonstrated in Figure 6.218. The highest hardness value was measured as 112.7, 152.9 and 164 HV at 15 μm distance from the

machined surface with the tool having radial rake of 10°, axial rake of -2° and 20 µm of cutting-edge radius for the CW617N, CW511L and CW724L, respectively. However, the lowest microhardness variation was measured as 97.5, 136.8 and 147.6 HV for machined surfaces by the tool having radial rake of 6°, axial rake of -2° and 20 µm of cutting-edge radius of CW617N, CW511L and CW724L, respectively. It is clear that the hardness has improved with intensifying radial rake angle and cutting-edge radius in comparison to the unmachined surface for CW617N, CW511L, and CW724, respectively. But when the axial rake angle increases, the microhardness diminishes. The general observation that hardening happens under all cutting conditions shows that the material's surface has undergone significant strain hardening accomplished by plastic deformation. In addition, due of the increased tool-to-material contact area, friction created, and increased material flow on the tool's rake face, as well as their effects, the hardness of the machined surface increases with increasing cutting-edge radius and radial rake angle [1, 39]. Increased mechanical work and energy during the cutting process as a result of increasing the cutting-edge radius and radial rake angle eventually leads to an accelerated rate of work hardening on the specimen's surface and subsurface [1, 39]. Lower contact between the machined surface and the tool rake face is obtained by negative axial rake angle due to the chip breaking enhancement.

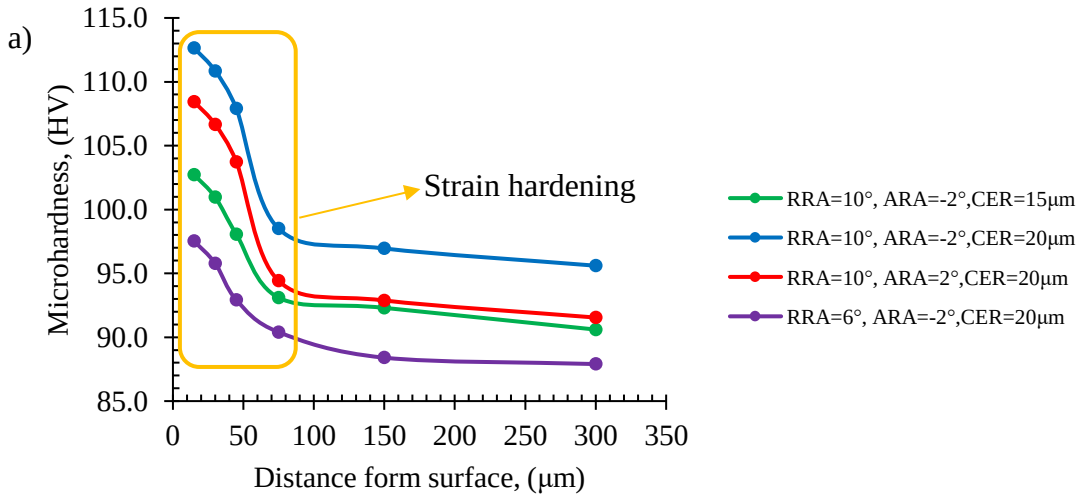

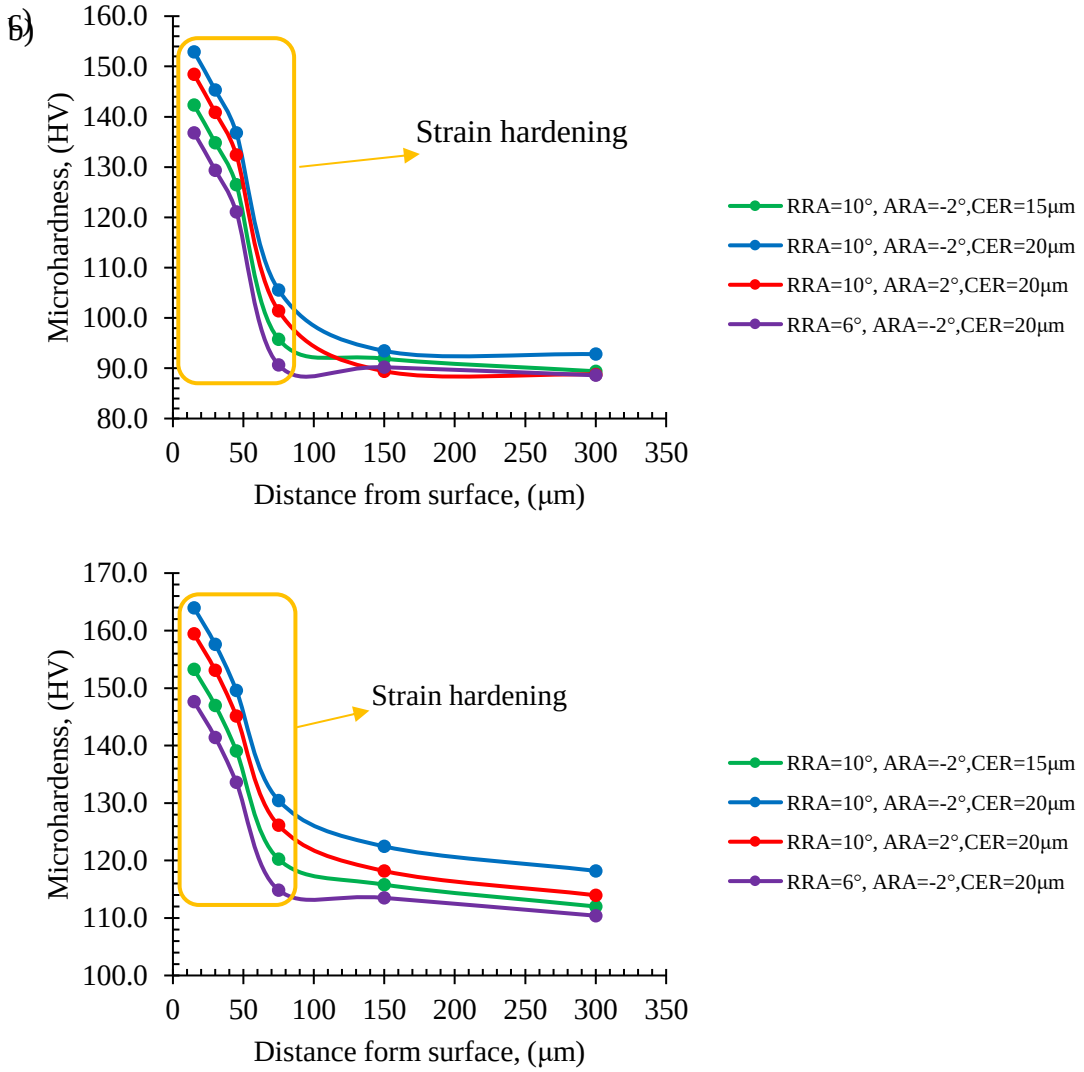


**Figure 6.218.** Measured surface and sub-surface microhardness of the extruded specimens; a) CW617N, b) CW511L, c) CW724R

Based upon the obtained results from the experiments, it has attempted to choose the optimized geometry of the flat bottom drill which concludes in the higher machined product quality. Therefore, the cutting tool with the radial and axial rake angles of 10°, 2° and 20 µm of edge radius has been selected to be utilized in vertical and inclined blind or through all hole drilling processes.

In Figure 6.219, the SEM images of the machined surface and sub-surfaces are displayed. The harsh surface and sub-surface deformations, imperfections, and twinning have been shaped in the brass alloys CW511L and CW724R as a result of the stain hardening and plastic deformation during machining. In comparison to CW724R, CW511L has a

substantially higher number and thickness of deformation twins. On the other hand, CW617N's machined surface is smooth, and no twinning or sub-surface deformation was seen. Therefore, it can be deduced that an increase in the twin numbers and its density causes the strain-hardening rate to increase, which is consistent with the measurements that were made.

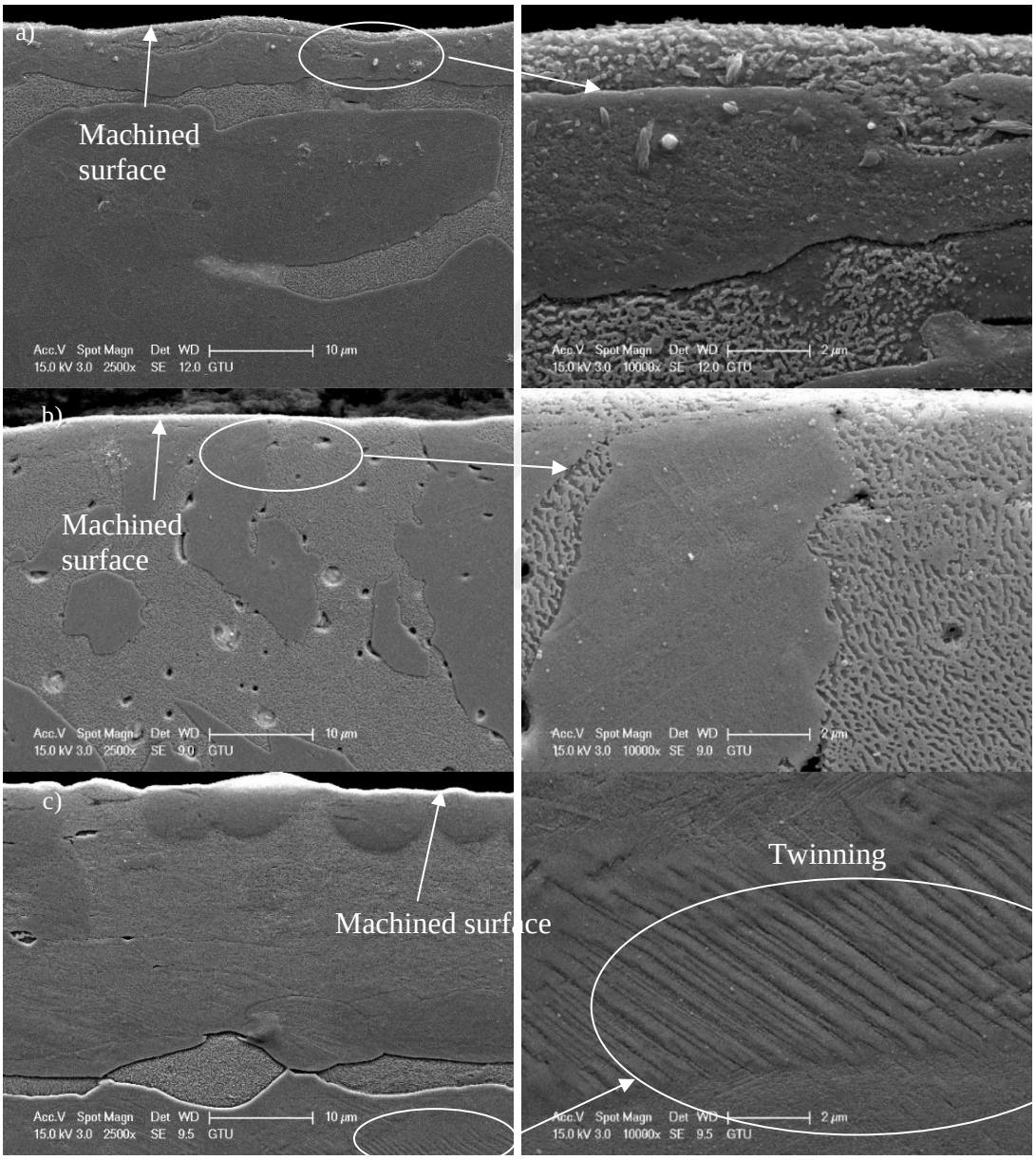

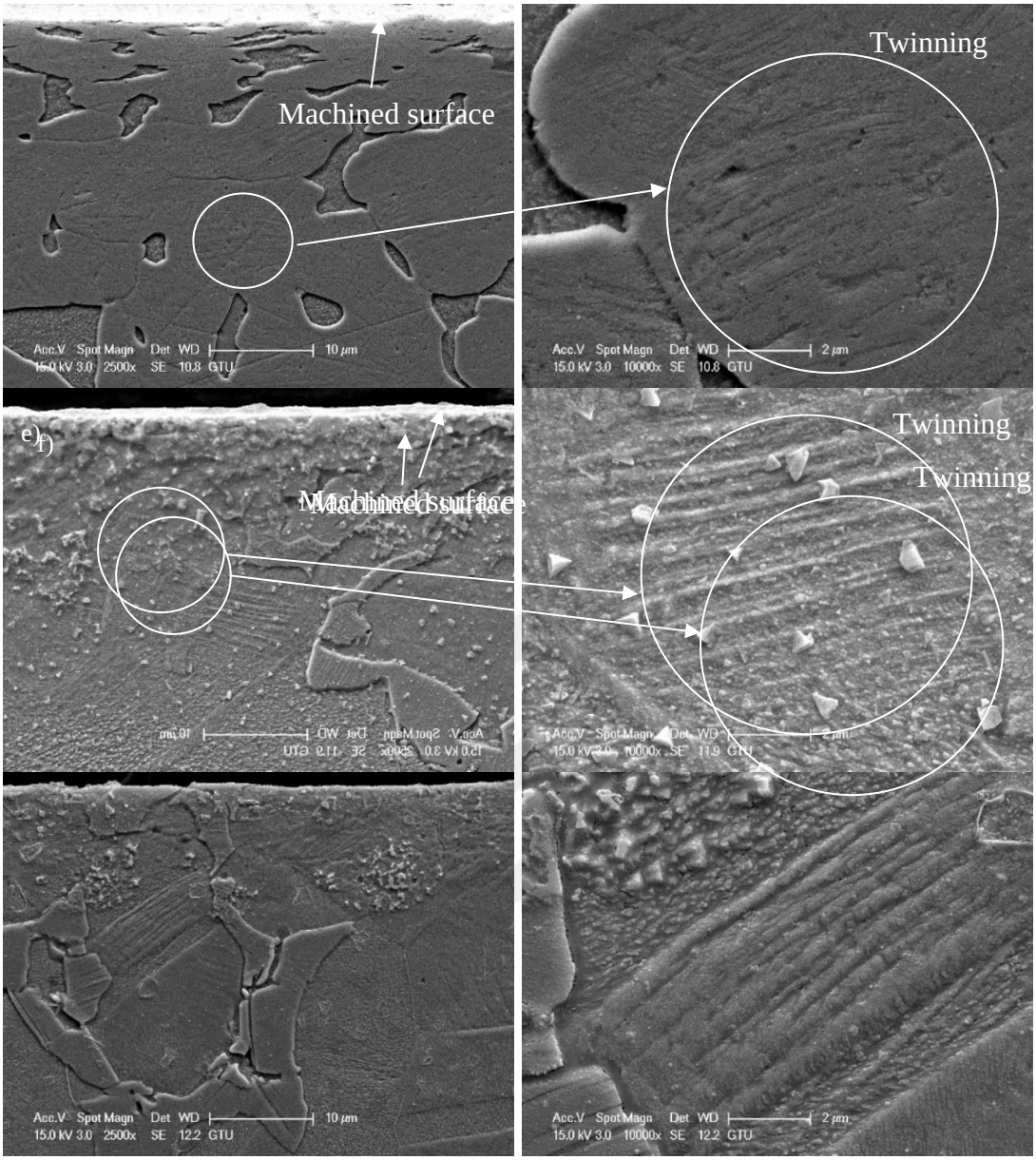


**Figure 6.219.** The SEM images of the deformation on the sub-surfaces of the machined holes; a) extruded CW617N, b) forged CW617N, c) extruded CW511L, d) forged+annealed CW511L, e) extruded CW724R, f) forged CW724R

# 7. EVALUATION OF DIFFERENT COATINGS ON THE MACHINABILITY OF THE MANUFACTURED TOOLS

In this chapter, an ANCA grinding machine has been used to manufacture a flat bottom drill with optimum geometrical features based on the findings of the previous chapter 6's results. The tools were put through drag finishing to create a cutting-edge radius of 17 μm in preparation for the PVD (physical vapor deposition) coating that will be applied to them. Tools were coated with three different industrial coatings for non-ferrous materials, including brass alloys, and their performance was compared to that of uncoated carbide flat bottom drills. The machining parameters and conditions were the same as those described in chapter 6. Below is a description of the coatings in more detail:

**Raptor:** This coating utilizes a ZrN-based cover coating together with a multi-layer structure of TiN and TiAlN. It is appropriate for drilling and milling operations on carbon, free-cutting, and low alloy steels. Table 7.1 provides an illustration of the coating's technical parameters. The coatings were carried out by Gühring Turkey.

**Table 7.1.** Technical specifications of Raptor coating

| Structure | Color | Hardness (HV 0.05) | Application Temperature | Coating Material |
|---|---|---|---|---|
| multi-layered, graded | pale gold | 3300 | < 1470°F | TiN/TiAIN based with ZrN cover coating |

**AlTiCN:** AlTiCN, also known as aluminum titanium carbo nitride, is a chemical mixture of the element’s aluminum, titanium, carbon, and nitrogen. This coating has a very good heat and oxidation resistance. This is partially caused by the 38 Gigapascal nanohardness (GPa). As a result, the coating system continues to be stable even at greater cutting temperatures and speeds. The Kapco company applied this coating.

**Table 7.2.** Technical specifications of AlTiCN coating

| Color | Friction Coefficient (steel) | Hardness (HV 0.05) | Application Temperature | Application |
|---|---|---|---|---|
| Pink | 0.3 | 3500 | < 1450°F | High Strength Steel, Stainless |

**CrN:** Precision metal parts frequently receive the thin film coating of chromium nitride,

which is exceedingly durable and inert. In situations with high temperatures, chrome nitride is the best option due to its higher thermal resistance than titanium nitride. Due to its resilience at sharp edges and corners, this type of coating is suitable for applications involving high temperatures, sliding wear, and wear resistance on precision components. Despite having qualities that are similar to those of TiN, this coating is superior to TiN due to its higher temperature resistance, inertness and stability, extremely strong adhesion—molecular bond to substrate metal, uniform coating with no buildup on the edges, resistance to most chemicals, metallic chrome appearance, anti-oxidization, and environmentally friendly process.

**Table 7.3.** Technical specifications of CrN coating

| Color | Friction Coefficient (steel) | Hardness (HV 0.05) | Application Temperature | Adhesion, Scratch |
|---|---|---|---|---|
| Silver | 0.4 | 1750 | < 1300°F | > 3.0 kgf on hard steel substrates |

**Table 7.4.** Obtained results extruded CW617N at 90° of plunging angle

| Run | Coating | Fx, (N) | Fy, (N) | Fz, (N) | FR, (N) | BHEN, (µm) | BHEX, (µm) | Ra bottom, (µm) | Ra Wall, (µm) | Diameter, (mm) |
|---|---|---|---|---|---|---|---|---|---|---|
| 1 | Uncoated | 11.03 | 8.376 | 233.8 | 234.2 | 141.635 | 76.453 | 0.39 | 0.85 | 8.003 |
| 2 | Raptor | 1.649 | 14.5 | 314.6 | 314.9 | 131.698 | 79.498 | 0.36 | 0.85 | 7.985 |
| 3 | AlTiCN | 5.221 | 10.3 | 305.3 | 305.5 | 116.87 | 75.941 | 0.31 | 0.78 | 7.997 |
| 4 | CrN | 13.26 | 4.227 | 348.8 | 349.0 | 96.466 | 51.564 | 0.34 | 0.74 | 8 |

**Table 7.5.** Obtained results extruded CW617N at 60° of plunging angle

| Run | Coating | Fx, (N) | Fy, (N) | Fz, (N) | FR, (N) | BHEN, (µm) | BHEX, (µm) | Ra bottom, (µm) | Ra Wall, (µm) | Diameter, (mm) |
|---|---|---|---|---|---|---|---|---|---|---|
| 1 | Uncoated | 39.7 | 34.57 | 183.4 | 190.8 | 127.875 | 76.456 | 0.34 | 0.95 | 8.014 |
| 2 | Raptor | 111.6 | 17.01 | 262.1 | 285.3 | 95.546 | 68.977 | 0.28 | 0.84 | 7.999 |
| 3 | AlTiCN | 100.6 | 6.605 | 256.9 | 275.9 | 84.999 | 63.796 | 0.23 | 0.78 | 8.054 |
| 4 | CrN | 45.85 | 8.828 | 272.9 | 276.8 | 78.932 | 54.565 | 0.22 | 0.67 | 8.006 |

**Table 7.6.** Obtained results extruded CW617N at 45° of plunging angle

| Run | Coating | Fx, (N) | Fy, (N) | Fz, (N) | FR, (N) | BHEN, (µm) | BHEX, (µm) | Ra bottom, (µm) | Ra Wall, (µm) | Diameter, (mm) |
|---|---|---|---|---|---|---|---|---|---|---|

| | | | | | | | | | | |
|---|---|---|---|---|---|---|---|---|---|---|
| 1 | Uncoated | 74.34 | 58.57 | 169.6 | 194.2 | 72.649 | 39.154 | 0.31 | 0.89 | 8.004 |
| 2 | Raptor | 104.7 | 40.45 | 273.5 | 295.6 | 65.595 | 37.944 | 0.28 | 0.84 | 8.012 |
| 3 | AlTiCN | 101.2 | 106.2 | 222.7 | 266.6 | 60.621 | 33.561 | 0.3 | 0.79 | 8.004 |
| 4 | CrN | 88.42 | 87.56 | 293.9 | 319.1 | 59.49 | 27.477 | 0.28 | 0.75 | 8.014 |

**Table 7.7.** Obtained results extruded CW511L at 90° of plunging angle

| Run | Coating | Fx, (N) | Fy, (N) | Fz, (N) | FR, (N) | BHEN, (µm) | BHEX, (µm) | Ra bottom, (µm) | Ra Wall, (µm) | Diameter, (mm) |
|---|---|---|---|---|---|---|---|---|---|---|
| 1 | Uncoated | 6.233 | 6.293 | 367.9 | 368.0 | 278.374 | 234.587 | 0.74 | 1.23 | 8.007 |
| 2 | Raptor | 11.47 | 19.87 | 427.9 | 428.5 | 324.655 | 204.571 | 0.69 | 1.02 | 7.994 |
| 3 | AlTiCN | 10.3 | 20.4 | 405.7 | 406.3 | 312.585 | 196.548 | 0.67 | 0.99 | 7.98 |
| 4 | CrN | 1.75 | 13.71 | 472.3 | 472.5 | 197.462 | 172.489 | 0.63 | 0.92 | 7.998 |

**Table 7.8.** Obtained results extruded CW511L at 60° of plunging angle

| Run | Coating | Fx, (N) | Fy, (N) | Fz, (N) | FR, (N) | BHEN, (µm) | BHEX, (µm) | Ra bottom, (µm) | Ra Wall, (µm) | Diameter, (mm) |
|---|---|---|---|---|---|---|---|---|---|---|
| 1 | Uncoated | 119.4 | 40.16 | 236.1 | 267.6 | 190.762 | 176..59 | 0.65 | 1.05 | 8.004 |
| 2 | Raptor | 132 | 70 | 277 | 314.7 | 178.956 | 220.87 | 0.61 | 1.05 | 8.004 |
| 3 | AlTiCN | 112.2 | 58.1 | 250.4 | 280.4 | 153.269 | 197.952 | 0.62 | 1.07 | 8.008 |
| 4 | CrN | 88.79 | 6.514 | 298.2 | 311.2 | 103.659 | 120.356 | 0.53 | 0.98 | 8.014 |

**Table 7.9.** Obtained results extruded CW511L at 45° of plunging angle

| Run | Coating | Fx, (N) | Fy, (N) | Fz, (N) | FR, (N) | BHEN, (µm) | BHEX, (µm) | Ra bottom, (µm) | Ra Wall, (µm) | Diameter, (mm) |
|---|---|---|---|---|---|---|---|---|---|---|
| 1 | Uncoated | 118.3 | 67.24 | 259.2 | 292.7 | 90.783 | 138.498 | 0.63 | 1.12 | 8.012 |
| 2 | Raptor | 142.3 | 91.02 | 313.5 | 356.1 | 148.955 | 126.458 | 0.59 | 1.02 | 8.014 |
| 3 | AlTiCN | 35.6 | 89.5 | 306.7 | 321.4 | 138.566 | 114.952 | 0.57 | 1.05 | 8.007 |
| 4 | CrN | 137 | 45.01 | 323.4 | 354.0 | 69.594 | 88.594 | 0.48 | 1.03 | 8.002 |

**Table 7.10.** Obtained results extruded CW724R at 90° of plunging angle

| Run | Coating | Fx, (N) | Fy, (N) | Fz, (N) | FR, (N) | BHEN, (µm) | BHEX, (µm) | Ra bottom, (µm) | Ra Wall, (µm) | Diameter, (mm) |
|---|---|---|---|---|---|---|---|---|---|---|
| 1 | Uncoated | 4.918 | 1.591 | 363.2 | 363.2 | 149.595 | 69.549 | 0.31 | 0.98 | 8.009 |
| 2 | Raptor | 9.433 | 9.669 | 420.4 | 420.6 | 127.659 | 55.949 | 0.27 | 0.93 | 7.998 |
| 3 | AlTiCN | 5.056 | 5.386 | 411.3 | 411.3 | 130.89 | 46.194 | 0.22 | 0.81 | 8.003 |
| 4 | CrN | 17.23 | 1.228 | 432.2 | 432.5 | 110 | 39.852 | 0.23 | 0.76 | 7.991 |

**Table 7.11.** Obtained results extruded CW724R at 60° of plunging angle

| Run | Coating | Fx, (N) | Fy, (N) | Fz, (N) | FR, (N) | BHEN, (µm) | BHEX, (µm) | Ra bottom, (µm) | Ra Wall, (µm) | Diameter, (mm) |
|---|---|---|---|---|---|---|---|---|---|---|
| 1 | Uncoated | 143 | 35.911 | 305.2 | 338.9 | 98.327 | 57.454 | 0.23 | 0.98 | 8.003 |
| 2 | Raptor | 11.3 | 118.8 | 354.2 | 373.7 | 79.454 | 50.941 | 0.26 | 0.86 | 8.014 |
| 3 | AlTiCN | 8.75 | 112.6 | 330.2 | 348.9 | 78.345 | 45.487 | 0.19 | 0.75 | 8.01 |
| 4 | CrN | 128.5 | 3.467 | 387.7 | 408.4 | 69.443 | 40.493 | 0.16 | 0.75 | 7.987 |

**Table 7.12.** Obtained results extruded CW724R at 45° of plunging angle

| Run | Coating | Fx, (N) | Fy, (N) | Fz, (N) | FR, (N) | BHEN, (µm) | BHEX, (µm) | Ra bottom, (µm) | Ra Wall, (µm) | Diameter, (mm) |
|---|---|---|---|---|---|---|---|---|---|---|
| 1 | Uncoated | 161.5 | 42.25 | 347.2 | 385.2 | 99.492 | 47.659 | 0.29 | 0.95 | 8.005 |
| 2 | Raptor | 173.8 | 94.83 | 376.4 | 425.2 | 91.651 | 42.659 | 0.24 | 0.86 | 8.012 |
| 3 | AlTiCN | 150.3 | 93.45 | 359.8 | 400.9 | 89.492 | 38.1622 | 0.24 | 0.86 | 8.003 |
| 4 | CrN | 107.3 | 30.09 | 381.1 | 397.0 | 82.952 | 39.549 | 0.21 | 0.76 | 8.013 |

**Table 7.13.** Obtained results forged+annealed CW617N at 90° of plunging angle

| Run | Coating | Fx, (N) | Fy, (N) | Fz, (N) | FR, (N) | BHEN, (µm) | BHEX, (µm) | Ra bottom, (µm) | Ra Wall, (µm) | Diameter, (mm) |
|---|---|---|---|---|---|---|---|---|---|---|
| 1 | Uncoated | 4.265 | 1.02 | 257.4 | 257.4 | 143.983 | 88.946 | 0.360 | 0.830 | 7.991 |
| 2 | Raptor | 13.79 | 16.55 | 318.4 | 319.1 | 127.654 | 70.354 | 0.34 | 0.79 | 7.982 |
| 3 | AlTiCN | 3.976 | 7.87 | 310.2 | 310.3 | 113.582 | 69.752 | 0.28 | 0.75 | 7.991 |
| 4 | CrN | 7.888 | 11.96 | 324 | 324.3 | 89.61 | 43.292 | 0.33 | 0.71 | 8.002 |

**Table 7.14.** Obtained results forged+annealed CW617N at 60° of plunging angle

| Run | Coating | Fx, (N) | Fy, (N) | Fz, (N) | FR, (N) | BHEN, (µm) | BHEX, (µm) | Ra bottom, (µm) | Ra Wall, (µm) | Diameter, (mm) |
|---|---|---|---|---|---|---|---|---|---|---|
| 1 | Uncoated | 63.67 | 49 | 200.6 | 216.0 | 115.633 | 66.378 | 0.230 | 0.910 | 7.995 |
| 2 | Raptor | 58.35 | 60.56 | 267.7 | 280.5 | 90.456 | 65.325 | 0.24 | 0.87 | 7.984 |
| 3 | AlTiCN | 118.2 | 8.426 | 260.1 | 285.8 | 79.799 | 58.457 | 0.21 | 0.73 | 7.992 |
| 4 | CrN | 84.81 | 23.56 | 275.9 | 289.6 | 74.582 | 47.615 | 0.19 | 0.69 | 7.997 |

**Table 7.15.** Obtained results forged+annealed CW617N at 45° of plunging angle

| Run | Coating | Fx, (N) | Fy, (N) | Fz, (N) | FR, (N) | BHEN, (µm) | BHEX, (µm) | Ra bottom, (µm) | Ra Wall, (µm) | Diameter, (mm) |
|---|---|---|---|---|---|---|---|---|---|---|
| 1 | Uncoated | 127.4 | 66.62 | 226.3 | 268.1 | 67.678 | 34.575 | 0.270 | 0.830 | 8.001 |
| 2 | Raptor | 112.8 | 81.99 | 274.6 | 307.9 | 62.65 | 33.758 | 0.25 | 0.8 | 8.006 |
| 3 | AlTiCN | 151.9 | 79.72 | 258.1 | 309.9 | 58.92 | 28.945 | 0.25 | 0.78 | 7.999 |
| 4 | CrN | 140.3 | 58.3 | 286.6 | 324.3 | 57.046 | 26.906 | 0.23 | 0.72 | 8.009 |

**Table 7.16.** Obtained results forged+annealed CW511L at 90° of plunging angle

| Run | Coating | Fx, (N) | Fy, (N) | Fz, (N) | FR, (N) | BHEN, (µm) | BHEX, (µm) | Ra bottom, (µm) | Ra Wall, (µm) | Diameter, (mm) |
|---|---|---|---|---|---|---|---|---|---|---|
| 1 | Uncoated | 4.647 | 9.785 | 401.9 | 402.0 | 260.563 | 215.675 | 0.690 | 1.010 | 7.964 |
| 2 | Raptor | 6.672 | 5.13 | 479.9 | 479.9 | 315.89 | 196.341 | 0.65 | 0.94 | 7.984 |
| 3 | AlTiCN | 6.842 | 8.028 | 446.2 | 446.3 | 296.262 | 180.391 | 0.61 | 0.92 | 7.976 |
| 4 | CrN | 11.169 | 5.362 | 523.4 | 523.5 | 180.648 | 165.877 | 0.56 | 0.87 | 7.98 |

**Table 7.17.** Obtained results forged+annealed CW511L at 60° of plunging angle

| Run | Coating | Fx, (N) | Fy, (N) | Fz, (N) | FR, (N) | BHEN, (µm) | BHEX, (µm) | Ra bottom, (µm) | Ra Wall, (µm) | Diameter, (mm) |
|---|---|---|---|---|---|---|---|---|---|---|
| 1 | Uncoated | 143.3 | 29.29 | 311.6 | 344.2 | 199.13 | 168.658 | 0.620 | 1.000 | 7.986 |
| 2 | Raptor | 69.99 | 127.48 | 349.8 | 378.8 | 172.659 | 215.65 | 0.57 | 0.97 | 8.002 |
| 3 | AlTiCN | 113.4 | 127.5 | 337.9 | 378.5 | 147.765 | 190.873 | 0.56 | 0.91 | 8 |
| 4 | CrN | 90.78 | 104.1 | 359.2 | 384.8 | 99.125 | 114.942 | 0.48 | 0.89 | 7.999 |

**Table 7.18.** Obtained results forged+annealed CW511L at 45° of plunging angle

| Run | Coating | Fx, (N) | Fy, (N) | Fz, (N) | FR, (N) | BHEN, (µm) | BHEX, (µm) | Ra bottom, (µm) | Ra Wall, (µm) | Diameter, (mm) |
|---|---|---|---|---|---|---|---|---|---|---|
| 1 | Uncoated | 130.7 | 84.04 | 310.5 | 347.2 | 86.987 | 131.546 | 0.580 | 1.050 | 8.002 |
| 2 | Raptor | 143.1 | 180 | 322.3 | 395.9 | 143.594 | 116.549 | 0.55 | 1.01 | 8.001 |
| 3 | AlTiCN | 162.1 | 189 | 314.6 | 401.2 | 131.154 | 104.529 | 0.52 | 0.99 | 7.998 |
| 4 | CrN | 187.5 | 139.8 | 359.8 | 429.1 | 61.037 | 82.374 | 0.42 | 0.97 | 7.992 |

**Table 7.19.** Obtained results forged+annealed CW724R at 90° of plunging angle

| Run | Coating | Fx, (N) | Fy, (N) | Fz, (N) | FR, (N) | BHEN, (µm) | BHEX, (µm) | Ra bottom, (µm) | Ra Wall, (µm) | Diameter, (mm) |
|---|---|---|---|---|---|---|---|---|---|---|
| 1 | Uncoated | 16.11 | 16.1 | 389.9 | 390.5 | 145.3 | 59.48 | 0.260 | 0.900 | 7.995 |
| 2 | Raptor | 5.42 | 10.86 | 423 | 423.1 | 120.74 | 42.654 | 0.24 | 0.87 | 8.002 |
| 3 | AlTiCN | 9.142 | 2.54 | 417.5 | 417.6 | 117.98 | 37.489 | 0.23 | 0.75 | 8.009 |
| 4 | CrN | 8.731 | 5.999 | 434.8 | 434.9 | 102.748 | 34.018 | 0.19 | 0.71 | 8.015 |

**Table 7.20.** Obtained results forged+annealed CW724R at 60° of plunging angle

| Run | Coating | Fx, (N) | Fy, (N) | Fz, (N) | FR, (N) | BHEN, (µm) | BHEX, (µm) | Ra bottom, (µm) | Ra Wall, (µm) | Diameter, (mm) |
|---|---|---|---|---|---|---|---|---|---|---|

| | | | | | | | | | | |
|---|---|---|---|---|---|---|---|---|---|---|
| 1 | Uncoated | 149.7 | 47.58 | 361.2 | 393.8 | 88.74 | 51.365 | 0.190 | 0.780 | 7.991 |
| 2 | Raptor | 126.2 | 29.85 | 388.5 | 409.5 | 73.666 | 46.902 | 0.16 | 0.75 | 7.998 |
| 3 | AlTiCN | 184.9 | 15.82 | 364.6 | 409.1 | 69.45 | 39.54 | 0.15 | 0.72 | 7.992 |
| 4 | CrN | 104.3 | 12.29 | 381.1 | 395.3 | 64.814 | 33.775 | 0.14 | 0.63 | 7.997 |

**Table 7.21.** Obtained results forged+annealed CW724R at 45° of plunging angle

| Run | Coating | Fx, (N) | Fy, (N) | Fz, (N) | FR, (N) | BHEN, (µm) | BHEX, (µm) | Ra bottom, (µm) | Ra Wall, (µm) | Diameter, (mm) |
|---|---|---|---|---|---|---|---|---|---|---|
| 1 | Uncoated | 163.2 | 13.28 | 360.5 | 395.9 | 93.478 | 40.302 | 0.210 | 0.890 | 8.001 |
| 2 | Raptor | 195 | 106.1 | 366.4 | 428.4 | 85.641 | 36.555 | 0.19 | 0.81 | 8 |
| 3 | AlTiCN | 149.8 | 73.13 | 361.8 | 398.3 | 81.902 | 33.4 | 0.18 | 0.79 | 8.002 |
| 4 | CrN | 146.5 | 62.57 | 395.6 | 426.4 | 76.634 | 31.5 | 0.17 | 0.7 | 8.004 |

Due to the increase in cutting-edge radii, it can be seen that the coatings applied have increased the cutting forces in all directions. Additionally, since the manufactured flat bottom drills were all polished before being coated, the tools' surface roughness may not be smooth, and the friction coefficient may have been increased. The burr heights and surface roughness values in the bottom and wall of the drilled holes have improved as a result of this increase. As a result, tools with CrN coatings applied at all plunging angles and workpiece material types have demonstrated the best performance. Figure 7.1 illustrates 3D topographic images of the drill holes on extruded CW511L for various coated flat bottom drills. It is noteworthy to mention that no obvious change in the surface and sub-surface microhardness was observed with respect to the cutting tools coating material.

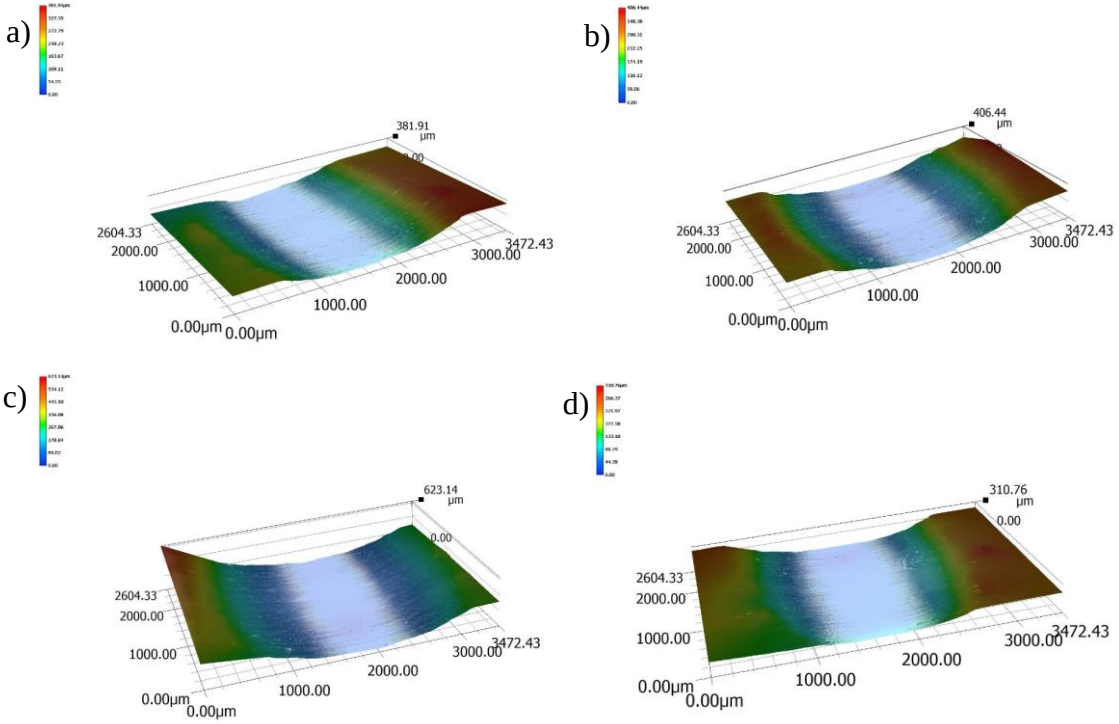


**Figure 7.1.** 3D topography images of the drilled holes on extruded CW511L; a) uncoated, b) raptor, c) AlTiCN, d) CrN

# 8. APPLICATION OF ARTIFICIAL INTELLIGENCE AND POLYNOMIAL REGRESSION MODELS IN PREDICTION OF THE PRODUCT QUALITY

It is well known that both the new industrial revolution and the new technology revolution are gathering steam. This new era is characterized by the quick development and fusion of new AI technologies with Internet technologies, new generations of information and materials technologies, and other technologies. This will allow for the game-changing transformation of models, means, and ecosystems in terms of their application to the national economy, well-being, and national security. Intelligent manufacturing is a new approach to manufacturing and the technological means through which major manufacturing technologies, including design, production, testing, and integration, as well as new information and communication technology, are applied. Three factors, including application technology, industry, and application impact, may be taken into account when evaluating the integrated application of AI in the field of intelligent manufacturing. It has been attempted to develop and implement AI models within this concept to predict the quality of the generated parts in this chapter.

## 8.1. Fuzzy Logic Modeling

Fuzzy logic has a wide range of applications for many reasons because of its capacity to behave in a manner comparable to human judgments. As shown in Figure 8.1, a fuzzy logic system consists of the following steps:

- Fuzzification, in which the membership functions (MFs) or crisp data are transformed into fuzzy data;

- Fuzzy Inference, in which the membership functions and control rules used to generate the fuzzy output are combined. The output of a fuzzy controller is created by fuzzifying the inputs and outputs using these membership functions.

- Defuzzification, in which the output is converted to a crisp variable using various techniques.

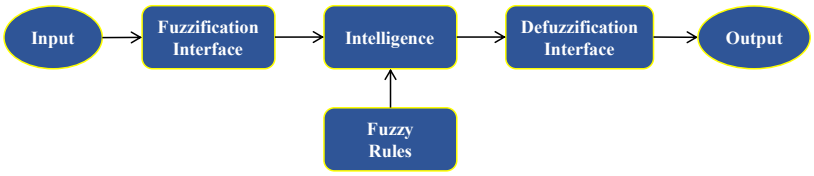


**Figure 8.1.** The schematic of a fuzzy logic system

## 8.2. Regression Modeling

Regression analysis was developed to examine the statistical connection between one or more independent variables and dependent variables. Due to its simplicity and versatility, the parabolic regression model is one of the most often used models for inspections. The following is an expression of this model:

$$y_i = b_0 + b_1 x_i + b_2 {x_i}^2 + \cdots + b_n {x_i}^n + \varepsilon \tag{8.1}$$

$$\varepsilon = y_i - \hat{y_i} \tag{8.2}$$

where $y_i$ is dependent variable, $x_i$ stands for the independent variable, $b_0$, $b_1$, $b_2$, $b_n$ are the parameter coefficients and $\varepsilon$ is the model error. The regression coefficients can be obtained by the Eq. 8.3:

$$b = (\acute{x}x)^{-1}\acute{x}y \tag{8.3}$$

Additionally, multiple regressions are a collection of numerical and factual techniques helpful for modeling and evaluating problems when the response of the subject is impacted by a number of variables.

The Mamdani FIS type was employed, and the Gaussian membership function (gauss2mf) was utilized to return the fuzzy membership calculated values using a combination of two Gaussian membership functions in the model. After that, linguistic coding was applied, as seen in Table 8.1. In Figure 8.2, the model's produced inputs are shown.

**Table 8.1.** The utilized linguistic coding for the developed model

| Radial rake angle (deg) | Axial rake angle (deg) | Cutting edge radius (µm) | Burr height (µm) | Rz (µm) |
|---|---|---|---|---|
| 6=L | -2=L | 10=L | L<350 | L<5 |

| | | | | |
|---|---|---|---|---|
| 8=M<br>10=H | 0=M<br>2=H | 15=M<br>20=H | 350≤M≤425<br>425<H≤500<br>VH>500 | 5≤M≤5.8<br>5.8<H≤6.3<br>VH>6.3 |

where L, M, H, and VH stand for low, medium, high, and very high, respectively. 27 rules in all were used to execute the model. Figure 8.3 illustrates the conceptually created rules-based fuzzy logic model used in this work. For defuzzification, the Mean of Maximum (MoM) approach was applied. The tracking of minimum and maximum compositional operations is what led to the fuzzy output.

In a combined mode of influencing cutting tool geometries, Figure 8.4 shows the fluctuation of the average entrance burr height and surface roughness. Figure 8.5 presents the fuzzy model that has been constructed for the machining responses. The fuzzy logic model's predictions for average burr height and surface roughness were 294.320 and 5.74 μm, respectively. It can be observed that when compared to experimental findings, the generated model accurately predicted the same cutting tool geometry for the lowest burr height. Additionally, it accurately identified two out of the tool's three geometric characteristics. Quadratic polynomial functions were employed in conjunction with the fuzzy logic system to model the quality of the drilled hole and anticipate the outcomes. Table 8.2 displays the generated functions. The surface roughness and burr height functions' respective confidence coefficients were %.80.04 and %.96.31. The fuzzy logic model's predictions for average burr height and surface roughness were 331.946 and 5.03 μm, respectively. In a comparison with experimental findings, the regression model has only identified the same cutting tool geometry for burr height. The surface quality prediction error and average entrance burr height according to fuzzy logic are 11.01 and 2.98, respectively. However, in the regression model, these percentages were 12.26 and 7.15 respectively. The observed and anticipated outcomes for the procedure are shown in Table 8.3 along with the computed error. Figure 8.6 illustrates the graphs for the average entrance burr height and surface roughness of the model. The model predictions have shown a good trend with the change of the radial, axial rake angles, and cutting-edge radius, beyond the expected and observed result values. Because both models can provide an adequate range of confidence in their prediction outcomes, they may be employed in both academic and industrial settings.




**Figure 8.2.** The generated inputs FIS model

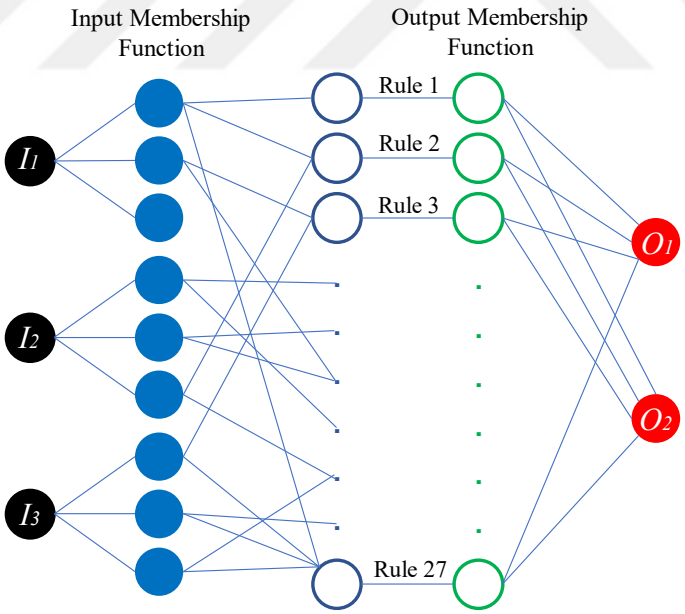


**Figure 8.3.** The schematic of the developed fuzzy logic model

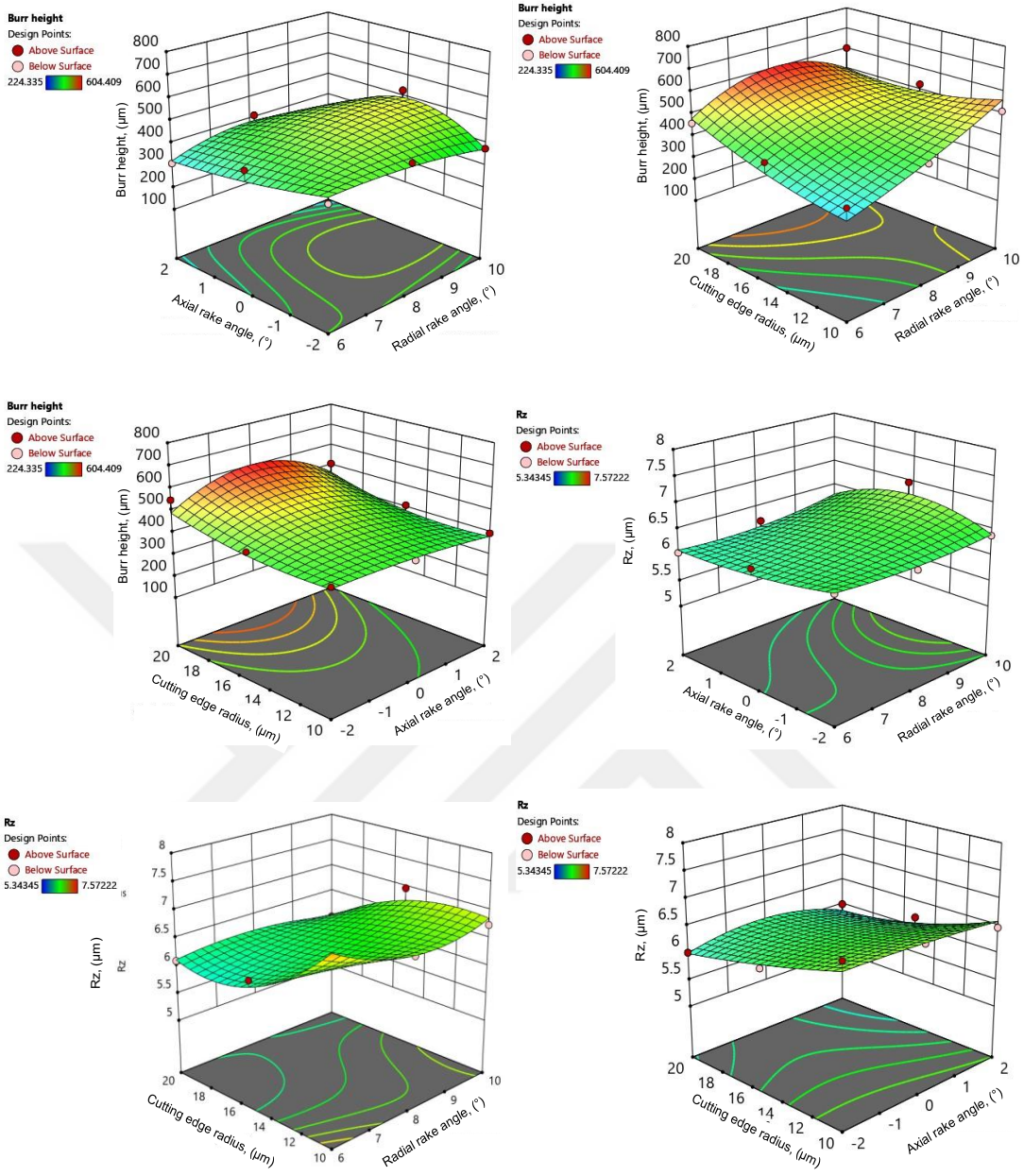


**Figure 8.4.** The variation of the average entry burr height and surface roughness in a combined mode of the influencing cutting tool geometries

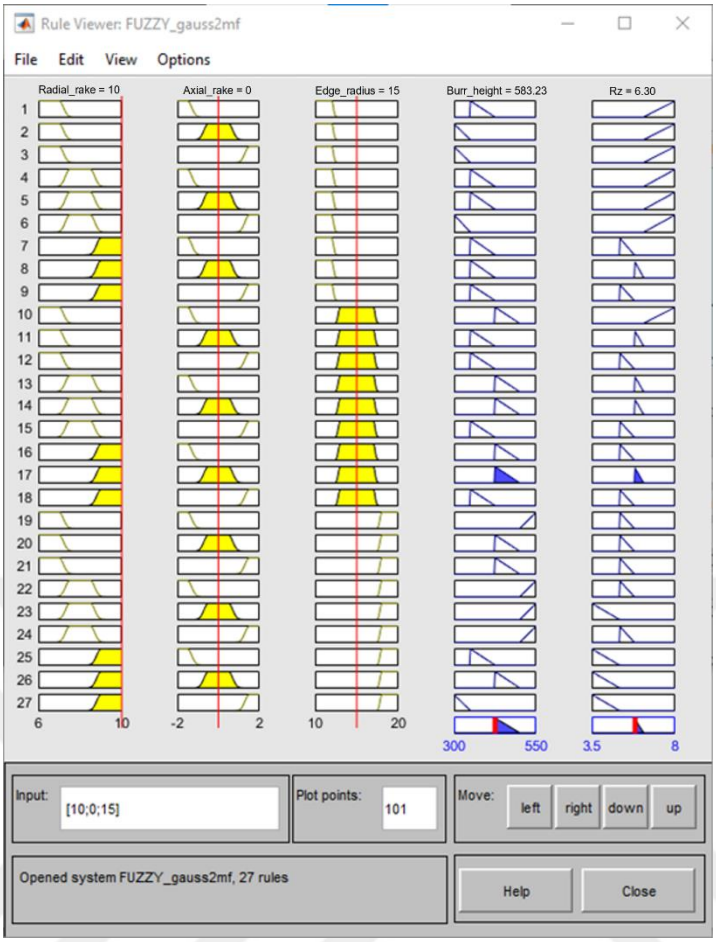


**Figure 8.5.** The developed fuzzy logic model in this study

**Table 8.2.** The developed regression model

| | | A | B | C | AB | AC | BC | $A^2$ | $B^2$ | $C^2$ | ABC | $A^2B$ | $A^2C$ | $AB^2$ | $AC^2$ | $B^2C$ | $BC^2$ |
|---|---|---|---|---|---|---|---|---|---|---|---|---|---|---|---|---|---|
| Burr | 479.03 | 66.91 | -19.28 | 96.04 | 8.59 | -59.75 | 3.34 | -50.2 | -72.01 | 33.76 | 12.85 | -28.98 | -66.88 | -87.98 | 5.32 | -57.89 | 4.68 |
| Rz | 6.35 | 0.29 | -0.11 | -0.24 | -0.04 | 0.05 | 0.006 | 0.09 | -0.14 | 0.09 | -0.11 | 0.01 | -0.25 | -0.23 | -0.41 | -0.11 | 0.05 |

**Table 8.3.** The obtained experimental and model results

| | | | | Experimental Results | | Regression Model Results | | | | Fuzzy Logic Model Results | | | |
|---|---|---|---|---|---|---|---|---|---|---|---|---|---|
| Run | Radial rake angle, (°) | Axial rake angle, (°) | Cutting edge radius, (µm) | Entry burr height, (µm) | Rz Bottom, (µm) | Entry burr height, (µm) | Rz Bottom, (µm) | % Burr Error | % Rz Error | Entry burr height, (µm) | Rz Bottom, (µm) | % Burr Error | % Rz Error |
| 1 | 6 | -2 | 10 | 395.33 | 7.57 | 353.57 | 8.01 | 10.5 | 5.81 | 452.18 | 7.21 | 14.3 | 4.76 |
| 2 | 6 | 0 | 10 | 355.46 | 7.25 | 378.16 | 7.56 | 6.3 | 4.28 | 427.96 | 7.24 | 20.4 | 0.14 |
| 3 | 6 | 2 | 10 | 296.02 | 7.25 | 258.74 | 7.87 | 12.5 | 8.55 | 373.24 | 6.97 | 26.0 | 3.86 |
| 4 | 8 | -2 | 10 | 428.68 | 6.9 | 466.73 | 6.32 | 8.8 | 8.41 | 472.59 | 6.86 | 10.2 | 0.58 |
| 5 | 8 | 0 | 10 | 404.88 | 6.68 | 499.92 | 6.99 | 23.4 | 4.64 | 413.98 | 6.94 | 2.2 | 3.89 |

| | | | | | | | | | | | | | |
|---|---|---|---|---|---|---|---|---|---|---|---|---|---|
| 6 | 8 | 2 | 10 | 398.87 | 6.47 | 389.09 | 6.76 | 2.4 | 4.48 | 384.03 | 6.94 | 3.7 | 7.26 |
| 7 | 10 | -2 | 10 | 534.11 | 6.43 | 479.50 | 5.87 | 10.2 | 8.71 | 508.55 | 6.71 | 4.7 | 4.35 |
| 8 | 10 | 0 | 10 | 513.02 | 6.74 | 521.27 | 6.23 | 1.6 | 7.57 | 555.31 | 6.83 | 8.2 | 1.34 |
| 9 | 10 | 2 | 10 | 439.66 | 6.84 | 419.03 | 6.47 | 4.6 | 5.41 | 424.97 | 6.83 | 3.3 | 0.15 |
| 10 | 6 | -2 | 15 | 407.59 | 6.37 | 389.08 | 5.97 | 4.5 | 6.28 | 465.94 | 6.66 | 14.3 | 4.55 |
| 11 | 6 | 0 | 15 | 409.77 | 6.27 | 417.02 | 6.69 | 1.7 | 6.70 | 403.94 | 6.59 | 1.4 | 5.10 |
| 12 | 6 | 2 | 15 | 310.77 | 6.05 | 300.95 | 6.32 | 3.1 | 4.46 | 389.29 | 6.32 | 25.2 | 4.46 |
| 13 | 8 | -2 | 15 | 441.19 | 6.25 | 442.50 | 6.74 | 0.2 | 7.84 | 471.58 | 6.27 | 6.8 | 0.32 |
| 14 | 8 | 0 | 15 | 418.37 | 6.21 | 479.03 | 6.86 | 14.5 | 10.47 | 427.56 | 6.35 | 2.2 | 2.25 |
| 15 | 8 | 2 | 15 | 412.64 | 6.19 | 371.54 | 6.45 | 9.9 | 4.20 | 385.72 | 6.13 | 6.5 | 0.97 |
| 16 | 10 | -2 | 15 | 377.44 | 6.38 | 395.51 | 6.95 | 4.7 | 8.93 | 376.76 | 6.17 | 0.1 | 3.29 |
| 17 | 10 | 0 | 15 | 529.00 | 6.97 | 440.63 | 6.37 | 16.7 | 8.61 | 583.23 | 6.3 | 10.2 | 9.61 |
| 18 | 10 | 2 | 15 | 271.23 | 6.14 | 341.73 | 6.55 | 25.9 | 6.68 | 328.89 | 6.13 | 21.2 | 0.16 |
| 19 | 6 | -2 | 20 | 508.28 | 6.09 | 492.11 | 6.41 | 3.1 | 5.25 | 568.72 | 6.1 | 11.8 | 0.16 |
| 20 | 6 | 0 | 20 | 458.45 | 6.09 | 523.40 | 6.66 | 14.1 | 9.36 | 504.66 | 6.14 | 10.0 | 0.82 |
| 21 | 6 | 2 | 20 | 382.04 | 6.07 | 410.67 | 5.03 | 7.4 | 17.13 | 458.99 | 5.84 | 20.1 | 3.79 |
| 22 | 8 | -2 | 20 | 548.23 | 6.01 | 485.78 | 5.03 | 11.3 | 16.31 | 585.01 | 5.88 | 6.7 | 2.16 |
| 23 | 8 | 0 | 20 | 519.24 | 6.11 | 525.65 | 6.30 | 1.2 | 3.11 | 522.72 | 5.95 | 0.6 | 2.62 |
| 24 | 8 | 2 | 20 | 509.65 | 6 | 421.51 | 5.50 | 17.2 | 8.33 | 549.75 | 5.87 | 7.8 | 2.17 |
| 25 | 10 | -2 | 20 | 242.96 | 5.59 | 331.95 | 5.80 | 36.6 | 3.76 | 304.8 | 5.74 | 25.4 | 2.68 |
| 26 | 10 | 0 | 20 | 604.41 | 5.99 | 427.50 | 6.20 | 29.2 | 3.51 | 595.11 | 5.97 | 1.5 | 0.33 |
| 27 | 10 | 2 | 20 | 224.34 | 5.34 | 331.95 | 5.10 | 47.9 | 4.49 | 294.32 | 5.81 | 31.2 | 8.80 |

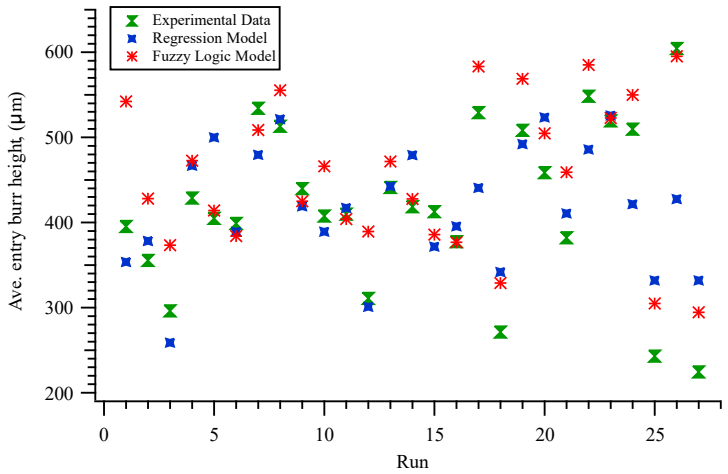

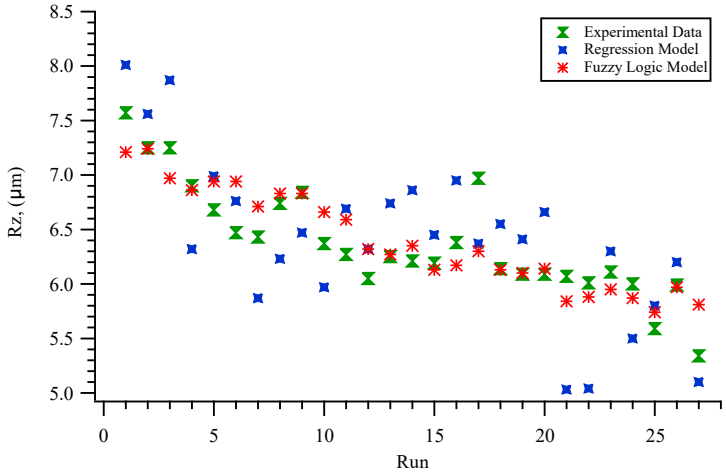


**Figure 8.6.** Comparison of the model predictions with the experimental results

## 8.3. Artificial neural networks (ANN) modeling

A multilayer perceptron (MLP) is made up of at least three layers, as seen in Figure 8.7. The yields ($R_i$) are acquired in the output layer while the inputs ($I_i$) are assigned in the input layer. Between the input and output layers, internal layers known as hidden layers operate; their number may be greater than one. When a correlation between a preset arrangement of input-output sets is formed, learning is complete. A neural network is a type of computing structure made up of many intricately connected processing units known as neurons. The neurons integrate weighted inputs from all directions and then apply a linear or non-linear operation on the outcome to determine the yield. The neurons are organized into layers and connected via an over-the-top network. A typical ANN that has been widely used in several research fields is the back propagation arrangement. The outputs of each layer are directly supplied to each neuron in the layer above in BPNs, which have different tiered feed forward arrangement engineering. Any analytic model may be unable to capture the intricate relationships between machined hole quality and affecting factors. The majority of conventional modeling approaches rely on assumptions that exhibit simplifications, which might provide inaccurate findings. On the other hand, the ANN method has a feature that makes it appropriate for modeling the quality expectation of machined holes; as a result, it is used in this thesis as the modeling tool.

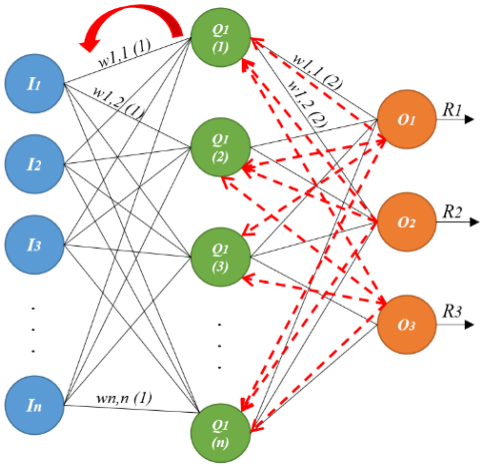


**Figure 8.7.** The schematic of neural network model and back propagation algorithm [18]

The net input to unit *i* in layer *m+1* and the unit's output are expressed in equations 8.4 and 8.5, respectively. *f* stands for the activation function of neurons in $(m+1)^{th}$ layer.

$$n_i^{m+1} = \sum_{j=1}^{s^m} w_{i,j}^{m+1} R_j^m + Q_i^{m+1} \tag{8.4}$$

$$R_i^{m+1} = f^{m+1}(n_i^{m+1}) \tag{8.5}$$

The experimental data for the burr heights and widths at both hole entry and exit as depicted in Figure 8.8 gathered and compiled in Table 8.4 were utilized to train the proposed models. In order for all the information to display a consistent connection, normalization is a technique used in neural networks. Otherwise, because one component's mathematical value is higher than the other, the neural network can infer that it is more important than the other. This phenomenon may worsen the network's capacity for generalization and lead to overfitting. As a result, all of the collected data were converted and standardized to have a mean value of zero and a standard deviation of 1. All inputs are equally important for the network's training after the normalization step. 70%, 10%, and 20% of the data in our model were used for training, validation, and testing, respectively. The data sets used for testing, validation, and training were all chosen at random. The appropriate number of neurons should be chosen in order to extend the network execution since it is general knowledge that having a high number of neurons in the hidden layer leads to overfitting and having a smaller number leads to underfitting.

The neurons with the lowest MSE are those that perceive the performance as being the best. The model has the following layers: 1 input, 2 hidden, and 1 output. There were 4, 8, 2, and 4 nods in the top layer, first and second concealed layers, and bottom layer, respectively. A trial-and-error approach was used to forecast the optimal performance. As a training function, the gradient descent back propagation with adaptive learning was chosen. Mean squared error (MSE) was used for the performance validation while TRAINGD and LEARNGDM were applied for the learning function. As shown in Fig. 8.9, the MSE of training the chosen ANN was around 0.005 in 59 epochs. The generated model's output and the outcomes are linearly correlated. The MSEs of the validation and testing groups are greater than those of the training group, as would be expected. Output=0.99*Input+2.937 is the best linear fit function, and $R^2$=0.9124 is the estimated correlation confidence coefficient. This outcome illustrates that the neural network can forecast an output level that is satisfactory for the needed input data. The results of the comparison between measured and ANN-predicted values are shown in Figure 8.10.

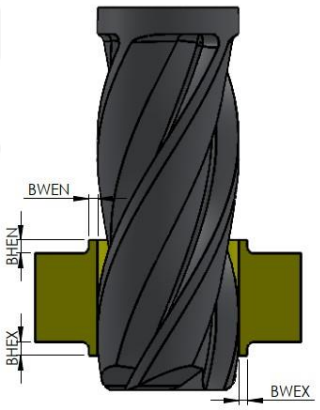


**Figure 8.8.** The schematic of the formed burrs

**Table 8.4.** Measured experimental results

| PA(°) | RRA (°) | ARA (°) | CER (μm) | BHEN (μm) | BHEX (μm) | BWEN (μm) | BWEX (μm) |
|---|---|---|---|---|---|---|---|
| 90 | 6 | -2 | 10 | 378.480 | 142.651 | 109.953 | 34.521 |
| 90 | 6 | 0 | 10 | 339.420 | 130.942 | 99.563 | 31.687 |
| 90 | 6 | 2 | 10 | 281.220 | 110.323 | 84.082 | 26.698 |
| 90 | 8 | -2 | 10 | 411.180 | 153.536 | 118.651 | 37.155 |
| 90 | 8 | 0 | 10 | 387.840 | 125.159 | 112.443 | 30.288 |
| 90 | 8 | 2 | 10 | 381.950 | 142.896 | 110.876 | 34.580 |
| 90 | 10 | -2 | 10 | 514.600 | 140.65 | 146.161 | 34.037 |
| 90 | 10 | 0 | 10 | 493.898 | 138.549 | 140.654 | 33.528 |

| | | | | | | | |
|---|---|---|---|---|---|---|---|
| 90 | 10 | 2 | 10 | 421.940 | 143.954 | 121.514 | 34.836 |
| 90 | 6 | -2 | 15 | 390.500 | 142.660 | 113.150 | 34.523 |
| 90 | 6 | 0 | 15 | 392.642 | 146.651 | 113.720 | 35.489 |
| 90 | 6 | 2 | 15 | 295.654 | 111.920 | 87.921 | 27.0846 |
| 90 | 8 | -2 | 15 | 423.441 | 159.567 | 121.913 | 38.615 |
| 90 | 8 | 0 | 15 | 401.065 | 146.942 | 115.961 | 35.559 |
| 90 | 8 | 2 | 15 | 395.452 | 148.956 | 114.468 | 36.047 |
| 90 | 10 | -2 | 15 | 360.948 | 197.269 | 105.290 | 47.739 |
| 90 | 10 | 0 | 15 | 509.580 | 188.651 | 144.826 | 45.653 |
| 90 | 10 | 2 | 15 | 256.970 | 162.354 | 77.631 | 39.289 |
| 90 | 6 | -2 | 20 | 489.250 | 182.354 | 139.418 | 44.129 |
| 90 | 6 | 0 | 20 | 440.365 | 165.548 | 126.415 | 40.062 |
| 90 | 6 | 2 | 20 | 365.455 | 134.950 | 106.489 | 32.657 |
| 90 | 8 | -2 | 20 | 528.456 | 197.845 | 149.847 | 47.878 |
| 90 | 8 | 0 | 20 | 500.003 | 186.125 | 142.278 | 45.042 |
| 90 | 8 | 2 | 20 | 490.600 | 184.640 | 139.777 | 44.682 |
| 90 | 10 | -2 | 20 | 229.340 | 194.659 | 70.282 | 47.107 |
| 90 | 10 | 0 | 20 | 583.601 | 216.590 | 164.515 | 52.414 |
| 90 | 10 | 2 | 20 | 230.684 | 197.446 | 70.639 | 47.781 |
| 60 | 6 | -2 | 10 | 216.744 | 112.661 | 52.780 | 23.005 |
| 60 | 6 | 0 | 10 | 195.651 | 102.657 | 48.646 | 20.963 |
| 60 | 6 | 2 | 10 | 164.223 | 89.156 | 42.486 | 18.206 |
| 60 | 8 | -2 | 10 | 234.402 | 120.654 | 56.241 | 24.638 |
| 60 | 8 | 0 | 10 | 221.798 | 100.607 | 53.771 | 20.544 |
| 60 | 8 | 2 | 10 | 218.618 | 111.261 | 53.147 | 22.719 |
| 60 | 10 | -2 | 10 | 290.249 | 109.456 | 67.187 | 22.351 |
| 60 | 10 | 0 | 10 | 279.069 | 108.793 | 64.996 | 22.216 |
| 60 | 10 | 2 | 10 | 240.212 | 112.659 | 57.380 | 23.005 |
| 60 | 6 | -2 | 15 | 223.235 | 110.367 | 54.052 | 22.537 |
| 60 | 6 | 0 | 15 | 224.3916 | 115.551 | 54.279 | 23.596 |
| 60 | 6 | 2 | 15 | 172.018 | 90.626 | 44.014 | 18.506 |
| 60 | 8 | -2 | 15 | 241.023 | 136.542 | 57.539 | 27.882 |
| 60 | 8 | 0 | 15 | 228.940 | 115.330 | 55.171 | 23.550 |
| 60 | 8 | 2 | 15 | 225.909 | 117.980 | 54.576 | 24.092 |
| 60 | 10 | -2 | 15 | 189.076 | 159.664 | 47.357 | 32.603 |
| 60 | 10 | 0 | 15 | 287.538 | 150.485 | 66.656 | 30.729 |
| 60 | 10 | 2 | 15 | 148.328 | 126.545 | 39.371 | 25.840 |
| 60 | 6 | -2 | 20 | 276.560 | 142.365 | 64.504 | 29.071 |
| 60 | 6 | 0 | 20 | 250.162 | 125.216 | 59.330 | 25.569 |
| 60 | 6 | 2 | 20 | 209.710 | 104.000 | 51.402 | 21.237 |
| 60 | 8 | -2 | 20 | 297.731 | 150.645 | 68.654 | 30.762 |
| 60 | 8 | 0 | 20 | 282.366 | 144.980 | 65.642 | 29.605 |
| 60 | 8 | 2 | 20 | 157.289 | 142.357 | 41.127 | 29.069 |
| 60 | 10 | -2 | 20 | 138.208 | 150.017 | 37.387 | 30.633 |
| 60 | 10 | 0 | 20 | 327.509 | 163.268 | 74.490 | 33.339 |
| 60 | 10 | 2 | 20 | 98.934 | 152.147 | 29.689 | 31.068 |
| 45 | 6 | -2 | 10 | 121.744 | 78.434 | 28.638 | 16.222 |

| | | | | | | | |
|---|---|---|---|---|---|---|---|
| 45 | 6 | 0 | 10 | 109.245 | 72.099 | 27.063 | 14.912 |
| 45 | 6 | 2 | 10 | 90.621 | 60.944 | 24.717 | 12.605 |
| 45 | 8 | -2 | 10 | 132.208 | 84.322 | 29.957 | 17.440 |
| 45 | 8 | 0 | 10 | 124.739 | 68.971 | 29.016 | 14.265 |
| 45 | 8 | 2 | 10 | 122.855 | 78.566 | 28.778 | 16.250 |
| 45 | 10 | -2 | 10 | 165.303 | 77.351 | 34.126 | 15.998 |
| 45 | 10 | 0 | 10 | 158.678 | 76.215 | 33.292 | 15.763 |
| 45 | 10 | 2 | 10 | 135.651 | 79.139 | 30.390 | 16.368 |
| 45 | 6 | -2 | 15 | 125.591 | 78.439 | 29.123 | 16.223 |
| 45 | 6 | 0 | 15 | 126.276 | 80.598 | 29.209 | 16.670 |
| 45 | 6 | 2 | 15 | 95.240 | 61.808 | 25.299 | 12.784 |
| 45 | 8 | -2 | 15 | 136.132 | 87.585 | 30.451 | 18.115 |
| 45 | 8 | 0 | 15 | 128.971 | 80.755 | 29.549 | 16.703 |
| 45 | 8 | 2 | 15 | 127.175 | 81.845 | 29.322 | 16.928 |
| 45 | 10 | -2 | 15 | 120.534 | 107.982 | 28.486 | 22.334 |
| 45 | 10 | 0 | 15 | 163.696 | 103.320 | 33.924 | 21.370 |
| 45 | 10 | 2 | 15 | 130.461 | 89.093 | 29.736 | 18.427 |
| 45 | 6 | -2 | 20 | 157.191 | 99.913 | 33.104 | 20.665 |
| 45 | 6 | 0 | 20 | 141.547 | 90.821 | 31.133 | 18.785 |
| 45 | 6 | 2 | 20 | 117.576 | 74.267 | 28.113 | 15.361 |
| 45 | 8 | -2 | 20 | 169.736 | 108.294 | 34.685 | 22.398 |
| 45 | 8 | 0 | 20 | 160.632 | 101.951 | 33.538 | 21.087 |
| 45 | 8 | 2 | 20 | 157.623 | 101.150 | 33.159 | 20.921 |
| 45 | 10 | -2 | 20 | 70.019 | 106.570 | 22.121 | 22.042 |
| 45 | 10 | 0 | 20 | 187.383 | 118.435 | 36.909 | 24.496 |
| 45 | 10 | 2 | 20 | 70.449 | 108.078 | 22.175 | 22.354 |

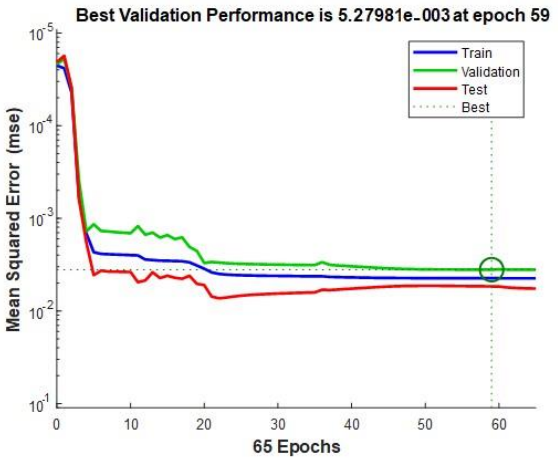


**Figure 8.9.** The MSE of training of the selected ANN

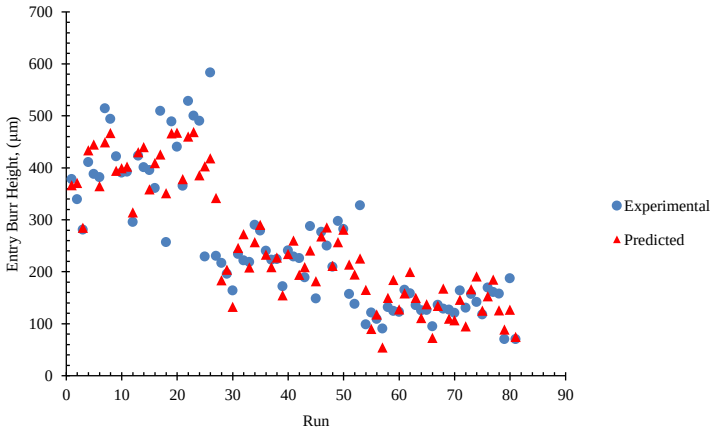


**Figure 8.10.** Comparison between the measured and predicted results by ANN

## 9. CONCLUSION

Long and tangled chips are produced during the machining process by the reduced lead content in brass alloys. Continuous chips in the drilling process cause a variety of issues, including dimensional errors in the finished components, built-up edges on the tools that lead to tool failure, accumulated chips that stop the continuous machining process, etc. Using scientific research and study, including experimental, analytical, and numerical analysis, the overall goal of this effort was to solve the aforementioned issues by developing a new generation of cutting tools, namely, flat bottom drill. The material characterization, metallographic, and mechanical characteristics of the environmentally friendly brass alloys CuZn40Pb2 (CW617N), CuZn38As (CW511L), and CuZn21Si3P (CW724R) have been investigated. The obtained measurements on microstructure, phase content, tensile strength, impact fracture energy, fracture toughness, and microhardness have all been thoroughly examined. To conduct a thorough investigation into the machinability, the effects of the process and alloying type have been evaluated with a focus on the flat bottom drilling operation. A predictive analytical cutting force model for flat bottom drills is developed using a mechanistic approach for both inclined and vertical plunging. The model is based on distributed elemental cutting over the tool radius while taking into consideration rake and relief faces, in accordance with the principles of orthogonal and oblique cuts. The parameters with the greatest significance were found after a study of the geometrical properties of the available flat bottom drills. In order to examine the dynamic behavior of the tools, flat bottom drills with different axial and radial rake angles have been created and put through modal analysis using finite element techniques. The stiffnesses, maximum total displacements, first six natural frequencies, and period of oscillation corresponding to the modes form have all been calculated for the designed tools. With a focus on the cutting forces, formed entrance and exit burr sizes, hole quality (surface roughness and dimensional correctness), as well as surface and sub-surface integrity, the effects of the cutting tool geometries, including axial rake, radial rake angles, edge radius, and plunging angle to the work material, have been studied. In the interim, the results of the developed predictive analytic model have been contrasted with the experimental data. To explain the results of the experiments, regression modeling and analysis of variance (ANOVA) methods were also employed. In accordance with the outcomes, the best cutting tool has been selected. For non-ferrous

materials, such as brass alloys, the performance of three different industrial coatings was compared to that of uncoated carbide flat bottom drills. Various microstructural circumstances, such as extruded, hot forged, and annealed, were taken into consideration in order to establish the impact of microstructure on the machining outputs in drilling brass alloys utilizing flat bottom drills. By taking into account radial and axial rake angles, cutting-edge radius in flat bottom drilling, and other factors, the impact of tool geometries on the machinability of the eco-friendly brass alloys was examined. Diverse deformations and microstructures were detected as a result of the different tool geometries and cutting parameters. Surface deformation and the creation of the new surface are significantly influenced by the cutting tool edge radius and radial rake angle. CrN coating was selected as the best material to be employed in flat bottom drilling operations. The lead-free brass alloy's tribological characteristics, such as micro-hardness, wear resistance, and corrosion resistance, is ultimately determined by this newly developed microstructure. The conducted research helped to establish fundamental understanding about the cutting forces, microhardness, surface and subsurface microstructure, and integrity issues pertinent to brass alloys when considering the impact of lead. The presence of Pb results in a notable improvement in reducing cutting forces, generated burr heights, surface and sub-surface integrity. Using artificial neural networks, flat bottom drilling has been performed while predicting the burr height and width as a result of the machining performance responses at both cutting tool entrance and exit. The effects of the cutting-edge radius and the axial, radial rake, and plunging angles were taken into account. An AI model was suggested and verified using results from experiments for this aim. The neural network was trained using experimental data that was gathered throughout all drilling tests in both the vertical and inclined directions. According to the results, the suggested ANN can accurately predict burr sizes within the bounds of the input values used to train it. To further predict the average burr height, hole entrance, and surface quality of drilled specimens, fuzzy logic and regression models were created. The most precise and efficient fuzzification and defuzzification techniques were discovered after several failed efforts. In the end, the experimental findings were contrasted with the predictions. Therefore, in commercial and academic applications, these models might be useful to avoid multiple expensive tests to forecast the drilling reactions as well as optimum cutting.

## REFERENCES


1. Zoghipour, N., Tascioglu, E., Atay, G., Kaynak, Y. (2020) Machining-induced surface integrity of holes drilled in lead-free brass alloy, Procedia CIRP, **87**, 148-152.
2. 05.10.2021]; Available from: The copper advantage a guide to working with copper and copper alloys, https://www.copper.org/publications/pub_list/pdf/a1360.pdf
3. 13.09.2012]; Available from: 01.10.2021]; Available from: Azom materials, Brass Alloys – Cast Alloys, zom.com/article.aspx?ArticleID=6281
4. 01.10.2021]; Available from: https://www.britannica.com/technology/brass-alloy#ref167380
5. 08.11.2021]; Available from: https://commons.wikimedia.org/wiki/File:Diagramme_binaire_Cu_Zn.svg
6. Nobel, C., Klocke, F., Lung, D., Wolf, S. (2014) Machinability enhancement of lead-free brass alloys, Procedia CIRP, **14**, 95-100
7. Zoghipour, N., Atay, G., Kaynak, Y. (2021) Modeling and optimization of drilling operation of lead-free brass alloys considering various cutting tool geometries and copper content, Procedia CIRP, **102**, 246-251
8. Davis, J.R., ASM source book in copper and copper alloys (2001) Metals Park: American Society for Metals, USA
9. Fontaine, A. La., Keast, V.J. (2006) Compositional distributions in classical and lead-free brasses, Materials Characterization, **57**, 424–429
10. Rajabi, Z., Doostmohammadi, H. (2018) Effect of addition of tin on the microstructure and machinability of α-brass, Materials Science and Technology, **34** (10), 1218-1227
11. Puathawee, S., Rojananan, S., Rojananan, S. (2013) Lead-free Cu-Si-Zn Brass with Tin Addition, Advanced Materials Research, **802**, 169-173
12. Oliver, J., Hertzman, S., Hutchinson, B. (2000) Dezincification of brass–a mechanistic study, Institute of Metals research, Stockholm, Swedish
13. Wessman, S., Oliver, J., Nylén, M. (2007) Effect of stress relieving heat treatment on the corrosion of brass, Swerea KIMAB Report, **541**, Stockholm, Swedish
14. Hutchinson, B., Oliver, J., Lindh-Ulmgren, E., (2007) Copper: better properties for innovative products. Stockholm: Investigations into the Dezincification of α-Brass; Corrosion and Metals Research Institute (KIMAB), **19**, 144–152.
15. Stålnacke, E., Claesson, E., Obitz, C., Lilja, M., Odqvist, J., Hagström, J., Rod, O. (2018) Corrosion microstructure interrelations in new low-lead and lead-free brass alloys, Materials Science and Technology, **36** (8), 917-924
16. Aytekin, K., (2018) Characterization of machinability in lead-free brass alloys, PhD Thesis, KTH Royal institute of technology, Sweden.
17. 10.11.2021]; Available from: https://www.epa.gov/laws-regulations/summary-safe-drinking-water-act
18. 1511.2021]; Available from: https://www.copper.org/applications/rodbar/pdf/A7038-brass-for-european-potable-water-applications.pdf
19. 12.11.2021]; Available from: https://rohs.exemptions.oeko.info/fileadmin/user_upload/RoHS_Pack_9/Exemption_6_c_/Exemption_6c__2015-10-mitsubishi-shindoh-rohs.pdf

20. Taha, M. A., El-Mahallawy, N. A., Hammouda, R. M., Moussa, T. M., Gheith, M. H. (2012) Machinability characteristics of lead free-silicon brass alloys as correlated with microstructure and mechanical properties, Ain Shams Engineering Journal, **3**, 383–392
21. Imai, H., Shufeng, L., Atsumi, H., Kosaka, Y., Kojima, A., Kondoh, K. (2010) Development of lead-free machinable brass with bismuth and graphite particles by powder metallurgy process, Materials Transactions, **51**, 855–859.
22. Imai, H., Kosaka, Y., Kojima, A., Li, S., Kondoh, K., Umeda, J., Atsumi, H. (2010) Characteristics and machinability of lead-free P/M Cu60–Zn40 brass alloys dispersed with graphite, Powder Technology, **198**, 417–421
23. Schultheiss, F., Johansson, D., Bushlya, V., Zhou, J., Nilsson, K., Ståhl, J. E. (2017) Comparative study on the machinability of lead-free brass, Journal of Clean Production, **149**, 366–377
24. Klocke, F., Nobel, C., Veselovac, D. (2016) Influence of tool coating, tool material, and cutting speed on the machinability of low-leaded brass alloys in turning, Materials in Manufacturing Processes, **31**, 895–1903
25. Nobel, C., Hofmann, U., Klocke, F., Veselovac, D., Puls, H. (2015), Application of a new, severe-condition friction test method to understand the machining characteristics of Cu–Zn alloys using coated cutting tools, Wear, 344-345
26. Gane, N. (1981) The effect of lead on the friction and machining of brass, Philosophical Magazine, **43** (3), 545–566
27. Kennedy, F.E., Voss, D. (1979) A reexamination of the wear of leaded brass on hardened steel, in: Proceedings of the International Conference of Wear of Materials, American Society of Mechanical Engineers, Dearborn, MI, USA, 89–96
28. Glardon, R., Finnie, I. (1983) A study of the friction and wear of cartridge and free cutting brass, Journal of Engineering Materials Technology, **105** (1) 31–35
29. Toulfatzis, A., Pantazopoulos, G., Paipetis, A. (2016) Microstructure and properties of lead-free brasses using post-processing heat treatment cycles, Materials Science and Technology, **32**, 1771–1781
30. Sundberg, R., Holm, R., Hertzman, S., Hutchinson, B. (2003) Dezincification (DA) and intergranular corrosion (IGA) of brass – influence of composition and heat treatment, Swedish Institute of Metals research, Stockholm, Sweden, **57** (11), 721-731
31. Toulfatzis, A.I., Pantazopoulos, G.A., David, C.N., Sagris, D.S., Paipetis, A.S. (2018) Final Heat Treatment as a Possible Solution for the Improvement of Machinability of Pb-Free Brass Alloys, Journal of Metals, **8** (8), 575
32. Atay, G. (2021) Investigation of machinability of lead-free brass materials forged with various conditions, Master Thesis, Marmara University Engineering and Pure Sciences Institute, Istanbul, Turkey, 20-60.
33. Aytekin, K., (2018) Characterization of machinability in lead-free brass alloys, Degree Project in Materials Design And Engineering, Second Cycle, 30 Credits Stockholm, Sweden
34. Atsumi, H., Imai, H., Li, S., Kondoh, K., Kousaka, Y., Kojima, A. (2011) High-strength, lead-free machinable α–β duplex phase brass Cu–40Zn–Cr–Fe–Sn–Bi alloys, Materials Science and Engineering: A, **529**, 275-281
35. Jewell, S., Kimball, S.M. (2014) Mineral Commodity Summaries, U.S. Department of the Interior, U.S. Geological Survey, Reston, Virginia, USA

36. Amaral, L., Quinta, R., Silva, T. E., Soares, R. MB., Castellanos, S. D., de Jesus, A.MP. (2018) Effect of lead on the machinability of brass alloys using polycrystalline diamond cutting tools, Journal of Strain Analysis, **1**, 14
37. Tam, PL., Schultheiss, F., Stahl, J-E., Nyborg, L. (2016) Residual stress analysis of machined lead-free and lead-containing brasses, Materials Science and Technology, **32** (17), 1789–1793
38. Çiçek, S., Altun, A., Zoghipour, N., Kaynak, Y. (2021) Designing a special cutting tool for high performance machining of CuZn40Pb2 brass alloy, Journal of Advances in Manufacturing Engineering, **2** (2), 25–32
39. Tascioglu, E., Zoghipour, N., Sharif, S., Kaynak, Y. (2022) Machining-induced surface integrity in brass alloys, Procedia CIRP, **108**, 654-659
40. Zoghipour, N., Tascioglu, E., Celik, F., Kaynak, Y. (2022) The influence of edge radius and lead content on machining performance of brass alloys, Procedia CIRP, **112**, 274-279
41. Toulfatzis, A. I., Pantazopoulos, G. A., David, C. N., Sagris, D. S., Paipetis, A. S. (2018) Machinability of Eco-Friendly Lead-Free Brass Alloys: Cutting-Force and Surface-Roughness Optimization, Journal of Metals, **8** (4), 250
42. Zoghipour, N., Yaratan, A. F., Kaynak, Y. (2021) Multi objective optimization of rough pocket milling strategies during machining of lead-free brass alloys using Desirability function and Genetic algorithms-based analysis, Procedia CIRP, **99**, 145-150
43. Fountas, N., Koutsomichalis, A., Kechagias, J. D., Vaxevanidis, N. M. (2019) Multi-response optimization of CuZn39Pb3 brass alloy turning by implementing Grey Wolf algorithm, N. A. Fountas et alii, Frattura ed Integrità Strutturale, **50**, 584-594
44. 06.06.2021]; Available from: https://www.sarbak.com.tr/en
45. Callister, W.D. (2007) Fundamentals of Materials Science and Engineering, 2nd ed. Wiley & Sons, 252.
46. Davis, J. R., Davidson, G. M., Lampman, S. R., Zorc, T. B. (1997) ASM Handbook, Heat Treating 4, ASM International, Materials Park, Ohio, 841-879.
47. Doostmohammadi, H., Moridshahi, H. (2015) Effects of Si on the microstructure, ordering transformation and properties of the Cu60Zn40 alloy, Journal of Alloys and Compounds, **640**, 401-407
48. Toulfatzis, A. I., Pantazopoulos, G. A., Paipetis, A. S. (2014) Fracture behavior and characterization of lead-free brass alloys for machining applications, Journal of Materials Engineering and Performance, **23**, 3193–3206
49. Wang, C. H. (1996) Introduction to fracture mechanics. Melbourne, Vic.: DSTO Aeronautical and Maritime Research Laboratory
50. ŞAR, E. (2020) Tensile opening mode fracture toughness measurements and size effect investigations with Brazilian disc type rock specimens, Master Thesis, Middle East Technical University
51. Ernst, H., Haggerty, W.A. (1958) The Spiral Point Drill - A New Concept in Drill Point Geometry, Transactions ASME, **80**, 1059-1072.
52. Altintas, Y. (2012) Manufacturing automation, metal cutting mechanics, machine tool vibrations, and CNC design, 2nd edition, University of British Columbia, Canada
53. Armarego. E.J.A. (1993) Material Removal Processes – An Intermediate Course, The University of Melbourne, Australia.

54. Armarego E.J.A., Brown, R.H. (1969) The Machining of Metals. Prentice-Hall.
55. Armarego, E.J.A., Pramanik, D., Smith, A.J.R., Whitfield, R.C. (1983) Forces and power in drilling computer aided predictions, Journal of Engineering Production, **6**, 149–174.
56. Armarego E.J.A., Uthaichaya. M. (1977) A mechanics of cutting approach for force prediction in turning operations, Journal of Engineering Production, **1** (1), 1–18.
57. Armarego E.J.A., Whitfield, R.C. (1985) Computer based modelling of popular machining operations for force and power predictions, CIRP Annals, **34**, 65–69.
58. Stabler, G.V. (1964) The chip flow law and its consequences. Proceedings of 5th Machine Tool Design and Research Conference, 243–251.
59. Stabler, G.V. (1951) Fundamental geometry of cutting tools, Proceedings of the Institution of Mechanical Engineers, **165**, 14–26
60. Luk. W.K. (1972) The direction of chip flow in oblique cutting, International Journal of Production Research, **10**, 67–76.
61. Lin, G.C.I., Mathew, P., Oxley, P.L.B., Watson, A.R. (1982) Predicting cutting force for oblique machining conditions, Proceedings of the Institution of Mechanical Engineers, **196**, 141–148.
62. Budak, E., Altintas, Y., Armarego, E.J.A. (1996) Prediction of milling force coefficients from orthogonal cutting data. ASME Journal of Manufacturing Science and Engineering, **118**, 216–224
63. Krystof. J. (1939) Berichte uber Betriebswissenschaftliche Arbeiten, Bd., **12**. VDI Verlag
64. Lee, E.H. Shaffer, B.W. (1951) Theory of plasticity applied to the problem of machining, Journal of Applied Mechanics, **18**, 405–413
65. Merchant, M.E. (1945) Mechanics of the metal cutting process, Journal of Applied Physics, **16**, 267–279
66. Huang, B.W. (2004) The Drilling Vibration Behavior of a Twisted Microdrill, Journal of Manufacturing Science and Engineering, **126** (4)
67. Ahmadi, K., Altintas, Y. (2013) Stability of lateral, torsional and axial vibrations in drilling, International Journal of Machine Tools and Manufacture, **68**, 63-74
68. Schmitz, T. L., Smith, K, S. (2009) Machining Dynamics, Frequency Response to Improved Productivity, Springer
69. Reinhall, P.G., Storti, D.W. (1986) Modeling and analysis of the dynamics of a drill penetrating a thin plate, ASME Journal of Applied Mechanics, **53**, 690–694
70. Tekinalp, O., Ulsoy, A.G. (1989) Modeling and finite element analysis of drill bit vibrations, ASME Journal of Vibration, Acoustics, Stress, and Reliability in Design, **111** (2), 148–155
71. Tekinalp, O., Ulsoy, A.G. (1990) Effects of geometric and process parameters on drill transverse vibrations, ASME Journal of Engineering for Industries, **112** (2), 189–194.
72. Rincon, D.M., Ulsoy, A.G. (1995) Complex geometry, rotary inertia and gyroscopic moment effects on drill vibrations, Journal of Sound and Vibration, **188** (5), 701–715.
73. Cheng, K. (2009) Machining Dynamics, Fundamentals, Applications and Practices, Springer Series in Advanced Manufacturing